ASSESSING THE CORROSION BEHAVIOUR OF STAINLESS STEELS WITH BIPOLAR ELECTROCHEMISTRY

A thesis submitted to
The University of Manchester for the degree of
Doctor of Philosophy (Ph.D.)
Department of Materials, School of Natural Sciences
Faculty of Science and Engineering

Yiqi Zhou

2020

Word counts: 79748

List of Figures

List of Tables

DECLARATION

No portion of the work referred to in this thesis has been submitted in support of an application for another degree or qualification at this, or any other, university, or other institute of learning.

COPYRIGHT STATEMENT

i. The author of this thesis (including any appendices and/or schedules to this thesis) owns certain copyright or related rights in it (the “Copyright”) and s/he has given The University of Manchester certain rights to use such Copyright, including for administrative purposes.

ii. Copies of this thesis, either in full or in extracts and whether in hard or electronic copy, may be made only in accordance with the Copyright Designs and Patents Act 1988 (as amended) and regulations issued under it or, where appropriate, in accordance with licensing agreements which the University has from time to time.

This page must form part of any such copies made.

iii. The ownership of certain Copyright, patents, designs, trade marks and other intellectual property (the “Intellectual Property”) and any reproductions of copyright works in the thesis, for example graphs and tables (“Reproductions”), which may be described in this thesis, may not be owned by the author and may be owned by third parties. Such Intellectual Property and Reproductions cannot and must not be made available for use without the prior written permission of the owner(s) of the relevant Intellectual Property and/or Reproductions.

iv. Further information on the conditions under which disclosure, publication and commercialisation of this thesis, the Copyright and any Intellectual Property and/or Reproductions described in it may take place is available in the University IP Policy (see http://documents.manchester.ac.uk/DocuInfo.aspx?DocID=487), in any relevant Thesis restriction declarations deposited in the University Library, The University Library’s regulations (see http://www.manchester.ac.uk/library/aboutus/regulations) and in The University’s policy on Presentation of Theses

Acknowledgement

During my PhD period, a lot of people give me the support and help in these three years, without them, I cannot finish this project.

First of all, I would like to thanks my academic supervisor – Prof Dirk Lars Engelberg. For his endless support, unpayable knowledge-share, communication, and guidance during my PhD study.

I am extremely indebted to Dr. Nicolas Stevens who gives me a lot of support and help from the electrochemistry. I also thanks to Mr Michael Faulkner, Mrs Xiangli (Shirley) Zhong, Dr. Teruo Hashimoto and Dr Arne Janssen for their help in scanning electron microscopy and related techniques. I highly acknowledge the help from Mr Garry Harrison who supports me in x-ray diffraction measurements.

I want to acknowledge and thank my colleagues in Corrosion Protection Centre. I would thank people in D26 who provides friendly and academic environment. I am particularly grateful to Dr Pierfranco Reccagni and Stephen Thornley for the help of writing, learning and discussing.

Finally, I would like to thank my parents, thanks for your supporting, no matter what happened, you always understand me and help me without reservations.

DEDICATION

Devoted to my girlfriend:

Lili Li

Abstract

Bipolar electrochemistry is a promising new method for corrosion screening and assessment of a wide range of materials and microstructures. The technique provides access to the full spectrum of anodic-to-cathodic electrochemical reactions in a single experiment, allowing in-situ observations of corrosion processes and rapid assessment of corrosion kinetic behaviour. The research reported in this PhD thesis is centred on exploring and developing innovative ways to apply bipolar electrochemistry techniques. The following overarching points summarise the four research directions, with key outputs listed below:

(1) Advancing the application of bipolar electrochemistry for corrosion research using type 420 ferritic/martensitic stainless steel with a segmented array bipolar electrode, in-situ observations of pit nucleation and growth, assessment of type 420 microstructure, and the effect of tempering on type 420 corrosion.
(2) Application on Duplex Stainless Steel 2205: introducing bipolar as a fast corrosion screening technique, measurement of corrosion kinetic behaviour, assessment of the effect of heat treatment on corrosion, and comparison to 2101 lean duplex and types 304L/316L: austenitic stainless steels.
(3) Technique development, introducing a modified bipolar approach, application of orthogonal feeder electrode arrangements, and simulating galvanic coupling of dissimilar stainless steels.
(4) Application of to test 2101 lean duplex weld microstructure, assessment of the effect of gravity on pit growt, and brass dezincification.

The potential and current density along a bipolar type 420 ferritic stainless steel electrode was measured using a segmented array electrode setup. The measured potential was quasi-linearly distributed distributed along the bipolar electrode (BPE), with the current density following an exponential Butter-Volmer-type relationship. The critical pitting potential and pit growth kinetics were measured. Pitting with general corrosion, pitting corrosion only, general corrosion, and cathodic reactions were observed. Pits nucleate near chromium carbides with the formation of oxide and chloride-rich particles deposited in the cathodic region. Pits grew into typical width-to-depth pit aspect ratios of 0.4-0.6, with electrolyte concentrations affecting pit growth. The best corrosion response was observed with tempering treatments at 250 ^{o}C.

Pitting corrosion kinetics of 2205 duplex stainless steel were determined at room temperature. Solution annealing heat treatments were applied to characterise the effect of microstructure on pit nucleation and growth resistance, with high temperature solution annealing indicating the highest resistance against pit growth. Selective phase dissolution was found to be associated with pittig corrosion in duplex stainless steel. Bipolar electrochemistry was also applied to contrast and compare the pitting corrosion resistance of austenitic 304L/316L with duplex 2101/2205 stainless steel.

A modified bipolar electrochemistry using application of an auxiliary potential to the BPE, was explored, allowing to test corrosion reactions in a far wider potential range. Approaches with perpendicular feeder electrode arrangements and two dissimilar stainless steel bipolar electrodes were explored.

Practical application of the bipolar technique was demonstrated with assessment of 2101 lean duplex weld microstructure, highlighting severe pitting corrosion occurring in the Heat-Affected Zone. Differences of corrosion susceptibility were associated with changes in ferrite-austenite fraction and local weld chemistry. The effect of gravity on pit growth kinetics and shape was revisited, with the pit depth found to be independent of sample orientation. Pits grown in the faceup orientation had the highest volume loss. Brass dezincification was explored as a test system to optimise corrosion product formation as a function of acting potential gradients.

1. Introduction

Bipolar defines as an object with two opposite extremes; the definition of the word “bipolar”is similar to the word “Janus”, a roman god has two faces looking in opposite directions shown as Figure 1- 1 [1]. For the bipolar electrode, the two opposite direction faces indicate the anode and cathode, but how does both anode and cathode occur on one bipolar electrode?

Figure 1- 1 Two face God Janus [1].

A potential is applied between the two feeder electrodes, an objective becomes bipolar electrode after set between the two feeder electrodes. The potential difference between the electrolyte and BPE is the driving force for the electrochemical reactions, due to a linear potential gradient between the feeder electrodes, so both anodic and cathodic reactions occurs along the BPE [2].

The application of bipolar electrochemistry varies from asymmetric partials production [1], wire formation [2]electrodeposition [3], sensor [4], anodic dissolution [5], microswimmer [6], and corrosion test [7,8]. The advantages of bipolar electrochemistry for these applications are no external electric connect, a potential gradient, and a simple experimental setup. In natural, corrosion on the bipolar electrode is known as the stray current corrosion, with the anodic corrosion reactions occur on one side and cathodic protection occurs on the other side [9].

Figure 1- 2 shows the amount of stainless steels manufactured from 2011 to 2018. The overall manusfatured stainless steel is increasing since 2011,

especially in China. Due to the stainless steels combined with good mechanical and corrosion properties, so stainless steel is widely used in the automobile, food, paper, oil, steam generator, and gas [10,11].

Figure 1- 2 The amount of stainless steel manufactured in the world [13].

Corrosion causes a lof of problems, in the US, the cost cost from corrosion is about 4.9% gross national product every year, and 40% of the cost can be avoided [12]Pitting corrosion is the localised breakdown of a passive film while the entire film remains to passivate [14]. The concentration of halide ions, applied potential, microstructure, and electrolyte temperature influence the pitting corrosion [15]. Pit requires the lacy cover, acts as a diffusion barrier, losing the lacy cover results the pit repassivate, unless the pit is under stable growth [16–18].

The structure of this thesis is scientific papers, divided into four main chapters (see Chapter 5). The first chapter (Chapter 6) gives four papers which include the theory of bipolar electrochemistry and corrosion behaviours of type 420 ferritic/martensitic stainless steel. The first paper introduces the current and potential distribution on the type 420 ferritic stainless steel bipolar electrode, and compare with 3-electrode potentio-static, and potentio-dynamic polarisation tests. The second paper introduces different corrosion response on type 420 ferritc stainless steel BPE and the pit growth kinetics under different applied potential. The third paper displays an in-situ, time lapse pitting corrosion test combined with bipolar electrochemistry with in-situ camera, to research the shape of cavities influence pit nucleation and pit electrolyte

changes the pit growth kinetics in type 420 ferritc stainless steel. The fourth paper gives the corrosion behaviour of type 420 martensitic stainless steel after different tempering treatment. The corrosion behaviours are measured by 3-electrode potentio-dynamic polarisation and bipolar electrochemistry tests, with the microstructure evolution is determined by the EBSD.

In Chapter 7, four papers are given related to DSS 2205. The first paper introduces a fast pitting corrosion test for DSS 2205 at room temperature. The second paper displays localised corrosion kinetics of DSS 2205 at room temperature. The third paper gives corrosion behaviour of DSS 2205 changed by heat treated. The corrosion behaviour is determined and compared from bipolar electrochemistry and simulated PREN and CPT, EBSD/SEM/EDX are used to analysis the microstructure evolution. The fourth paper compares corrosion behaviours between austenitic and duplex stainless steels from 3-electrode polarisation and bipolar electrochemistry.

In Chapter 8, three improved bipolar electrochemistry setups are introduced. The first paper introduces a modified BPE with a secondary applied potential on the BPE. The second paper gives 2-D bipolar electrochemistry with a secondary bipolar electrochemistry setup located perpendicular to the primary setup. The third paper is a creation of parallel BPE with an auxiliary potential, which can determine the galvanic corrosion between two parallel BPEs.

The fourth chapter (Chapter 9) introduces three applications of bipolar electrochemistry. The first paper gives the corrosion behaviour of a welded DSS 2101, including compare the crevice corrosion, transpassive corrosion, and pitting corrosion resistance with different microstructure on one welded DSS 2101. The second paper displays gravity influence the pitting corrosion. Sample with different surface orientation (faceup, perpendicular, and facedown) are used to simultate gravity influences pitting. The third paper shows the brass dezincification, to understand the different potential changes the formation and composition of the corrosion product.

References

[1] G. Loget, A. Kuhn, Bulk synthesis of Janus objects and asymmetric patchy particles, Journal of Materials Chemistry. 22 (2012) 15457–15474. doi:10.1039/c2jm31740k.

[2] S.E. Fosdick, K.N. Knust, K. Scida, R.M. Crooks, Bipolar electrochemistry, Angewandte Chemie - International Edition. 52 (2013) 10438–10456. doi:10.1002/anie.201300947.

[3] K. Nielsch, F. Müller, A.P. Li, U. Gösele, Uniform nickel deposition into ordered alumina pores by pulsed electrodeposition, Advanced Materials. 12 (2000) 582–586. doi:10.1002/(SICI)1521-4095(200004)12:8<582::AID-ADMA582>3.0.CO;2-3.

[4] W. Zhan, J. Alvarez, R.M. Crooks, Electrochemical sensing in microfluidic systems using electrogenerated chemiluminescence as a photonic reporter of redox reactions, Journal of the American Chemical Society. 124 (2002) 13265–13270. doi:10.1021/ja020907s.

[5] S. Morgenthaler, C. Zink, N.D. Spencer, Surface-chemical and -morphological gradients, Soft Matter. 4 (2008) 419–434. doi:10.1039/b715466f.

[6] T.R. Kline, W.F. Paxton, T.E. Mallouk, A. Sen, Catalytic nanomotors: Remote-controlled autonomous movement of striped metallic nanorods, Angewandte Chemie - International Edition. 44 (2005) 744–746. doi:10.1002/anie.200461890.

[7] S. Munktell, M. Tydén, J. Högström, L. Nyholm, F. Björefors, Bipolar electrochemistry for high-throughput corrosion screening, Electrochemistry Communications. 34 (2013) 274–277. doi:10.1016/j.elecom.2013.07.011.

[8] Y. Zhou, D.L. Engelberg, Application of a modified bi-polar electrochemistry approach to determine pitting corrosion characteristics, Electrochemistry Communications. 93 (2018) 158–161. doi:10.1016/j.elecom.2018.06.013.

[9] Z. Chen, D. Koleva, K. Van Breugel, A review on stray current-induced steel corrosion in infrastructure, Corrosion Reviews. 35 (2017) 397–423. doi:10.1515/corrrev-2017-0009.

[10] K.H. Lo, C.H. Shek, J.K.L. Lai, Recent developments in stainless steels, Materials Science and Engineering R: Reports. 65 (2009) 39–104. doi:10.1016/j.mser.2009.03.001.

[11] J.H. Qiu, Passivity and its breakdown on stainless steels and alloys, Surface and Interface Analysis. 33 (2002) 830–833. doi:10.1002/sia.1460.

[12] ASM International, The Effects and Economic Impact of Corrosion, in: Corrosion: Understanding the Basics, 2000: pp. 1–21.

[13] Taipei Doctors Union, Global crude steel output increases by 4.6% in 2018, Worldsteel Association. (2019) 1–3. https://www.coolloud.org.tw/node/89587.

[14] G.S. Frankel, Pitting Corrosion of Metals A Review of the Critical Factors, Journal of Electrochemistry Society. 145 (1998) 2186–2198. doi:10.5006/0010-9312-19.8.261.

[15] B. Krawczyk, P. Cook, J. Hobbs, D. Engelberg, Corrosion Behavior of Cold Rolled Type 316L Stainless Steel in HCl Containing Environments, Corrosion. 73 (2017) 1346. doi:/10.5006/2415.

[16] N.J. Laycock, R.C. Newman, Localised dissolution kinetics, salt films and pitting potentials, Corrosion Science. 39 (1997) 1771–1790. doi:10.1016/S0010-938X(97)00049-8.

[17] P. Ernst, R.C. Newman, Pit growth studies in stainless steel foils. I. Introduction and pit growth kinetics, Corrosion Science. 44 (2002) 927–941. doi:10.1016/S0010-938X(01)00133-0.

[18] P. Ernst, R.C. Newman, Pit growth studies in stainless steel foils. II. Effect of temperature, chloride concentration and sulphate addition, Corrosion Science. 44 (2002) 927–941. doi:10.1016/S0010-938X(01)00133-0.

2. Motivation

The Ph.D. project is "***Assessing the pitting corrosion behaviour of stainless steels by bipolar electrochemistry***".

Bipolar electrochemistry was recently used for pitting screening. However, only two published papers introduced the pitting corrosion tested by bipolar electrochemistry, and the pitting corrosion behaviour is only determined by the pit numbers and pit radius. The motivation for the research was to understand and develop bipolar electrochemistry for the pitting corrosion test. The aim was to investigate the pitting corrosion on different stainless steels. To analysis the pitting corrosion resisntance, which include the pit shapes, pit volume, pit depth, pitting growth kinetics, and critical pit volume/depth to form stable pits under a wide range of applied potential. Then compared with well know corrosion test method. Some modified bipolar electrochemistry setups can be designed, which are used to study the corrosion under wider potential range, galvanic corrosion, and localised corrosion competition.

The bipolar electrochemistry setups included the difference distance, potential, and current between the feeder electrodes. HCl was chosen as the testing electrolyte with concentration from 0.1 M to 0.05 M. Martensitic (type 420), ferritic (type 420), austenitic (type 316L and 304L), and duplex (type 2205, type 2101, and welded type 2101) stainless steels were chosen for corrosion behaviour research. Heat treatment was applied for type 420 and 2205 stainless steel to understand the corrosion changed by microstructure and phase evolution. Brass is used to studying the dezincification by bipolar electrochemistry.

3. Literature review

3.1 Bipolar electrochemistry

3.11 Background

The setup of bipolar electrochemistry is shown in Figure 3- 1[1]. A bipolar electrode (BPE) is set between the feeder electrodes in the electrolyte, with a potential/current applied on the feeder electrodes; results in a potential drop along the BPE surface is generated. With a sufficiently high applied potential, electrochemical reactions occur, the cathodic reactions occur close to the positive feeder electrode and inverse for anodic reactions [1–4]. A point on the BPE has an equal potential between the solution and BPE, which is a boundary to separate the cathodic and anodic reactions on the BPE [5].

Electrochemical reactions on the bipolar electrode was analysised by the modelling, and the parameters which will influence the electrochemical reactions are discussed. From Numerical Model analysis, four distinct time scale for ion transport and electrochemical reactions on the bipolar electrode; from BPE polarization or depolarisation, to capacitive electric double layers formation/relaxation, to onset or decay of faradaic reactions, and mass transport of the species. Mass transfer gradient might be created near the BPE surface, result in a longer diffusion time scale, if electrochemical reactions rate is quicker than mass transfer rate from or to the BPE surface. Bipolar electrode surface polarisation, faradaic charging accumulation, induced-charging electroosmotic flow, and ion concentration polarisation result in non-linearly potential on the BPE. The electrochemical reactions on the BPE also influence the potential and current distribution, e.g, the thicker oxide layers formed on the BPE anodic sites reduce discharging reactions, and then influence the Faradaic discharging occurs at the BPE cathodic sites. Three different regions can be determined on the charge, 1) net positive exceed charges accumulate at anodic sites, 2) net negative exceed charges accumulate at negative sites, and 3) a neutral case with net charge accumulation, these three regions influence the potential and current distributions on the BPE [6,7].

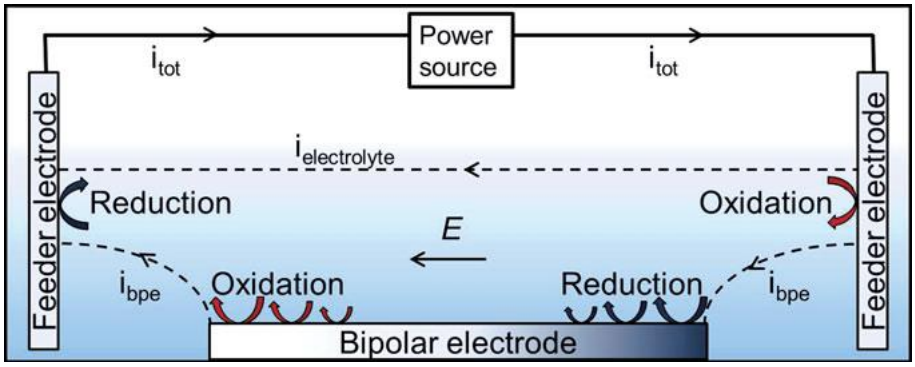

Figure 3- 1 The setup of the bipolar electrochemistry [1].

Bipolar electrochemistry became popular in the recent 20 years. The total number of cited papers related to bipolar electrochemistry is increasing from 20 in 1997 to 900 in 2015 shown in Figure 3- 2. The application for bipolar electrochemistry varied, from analytical chemistry to material science [8–10]. The potential gradient on the BPE allows to research the electrochemical reactions at different applied potential; the non-conduct wireless BPE setup allows small size, complex shape, and sensitivity to electric connect BPE could be used. A large array of BPE could be set in a single bipolar electrochemistry experiment; so the low cost is the other advantages for the bipolar electrochemistry used in the industry. Eardley [11] designs the bipolar electrochemistry setup to study the influence of the void fraction, phase geometry, and electrolyte conductivity to electrochemical relations. Janus-type particles are produced from bipolar electrochemistry, with the opposite sides created from different electrochemical reactions. As the non-contact BPE setup, the size of BPE could be micro or nano-scale [12–14]. Bipolar electrochemistry is also used in fluidized bed electrodes, to determine the energy consumption changed in different potential and particle sizes [15]. Functional molecular gradients are produced from the bipolar electrochemistry as the easy experiment setup and rapid experiment outcome [16]. Non-electric contact BPE setup allows the electric contacts between metals particles in three dimensional [17]. The electrochemical doping and electrochemical chlorination on a conductive polymer are changed by applied potential, which could be researched by bipolar electrochemistry [18].

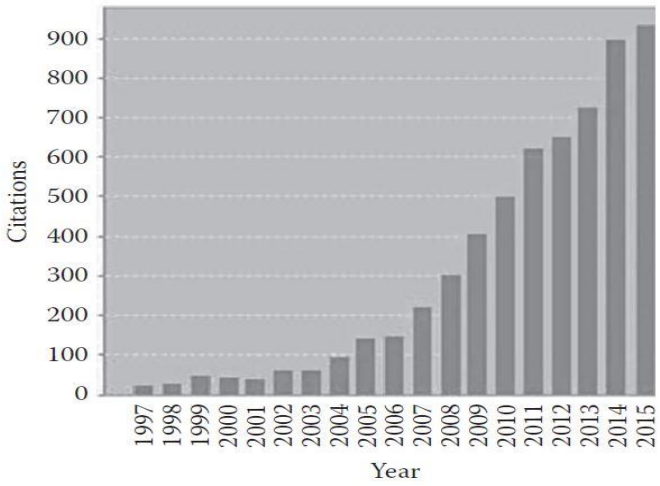

Figure 3- 2 Citations of published papers with the topic of "bipolar electrochemistry" from 1997 to 2015 [19]

3.12 Theory

3.121 Potential distribution

The potential on the BPE is similar, but the difference potential between the BPE and electrolyte solution result in different electrochemical reactions [4]. The potential gradient along the BPE is controlled by the applied potential between the feeder electrodes, BPE length and location, and electrolyte composition [1,5]. For a short length BPE, an extra high applied potential is required. For a high conductivity electrolyte, the potential drop was small, which cannot generate the electrochemical reactions.

One of the challenges of bipolar electrochemistry is the potential and current distributions on the BPE, which cannot be measured, due to a lack of external electric connection. Some methods are used to calculate, determine, or simulate the potential distribution on the BPE which includes: theoretical calculation, two reference electrode measurement, finite element method, and direct measurement.

Theoretical calculation

The theoretical potential across the BPE is calculated from Equation 3.1

$$\triangle \mathbf{E}_{\boldsymbol{BPE}} = \mathbf{E}_{\boldsymbol{tot}} \left(\frac{\mathrm{l_{BPE}}}{\mathrm{l_{Channel}}} \right) \qquad \text{Equation 3.1}$$

where $\triangle \mathbf{E}_{\boldsymbol{BPE}}$ is the potential distribution along the BPE, E_{tot} is the total potential difference between the feeder electrodes; l_{BPE} is the BPE length, and $l_{Channel}$ is the distance between the feeder electrodes [20].

Equation 3.1 indicates a linear potential distribution on the BPE, where the local potential could be calculated. However, Equation 3.1 has two main limitations for potential calculation. Firstly, calculate the potential distribution in a lower concentration electrolyte is not accurate. Without the BPE, the ideal potential gradient in the electrolyte is shown in Figure 3- 3 (a). The current between the two feeder electrodes is related to the applied potential (E_{tot}) and the electrolyte resistance (R_s). After a BPE is set between the feeder electrodes, the current could either pass through the electrolyte or BPE shown in Figure 3- 3 (b). For a low conductivity electrolyte, the electrolyte resistance (R_{S2}) is much higher than the BPE (R_{elec}). More current passes through the BPE, and the potential is proportional to the amount of current flow in the BPE. So the local potential changes at the BPE edges, which results in the potential gradient becoming non-linear potential on the BPE [4]. Secondly, the potential loss in the electrolyte as the electrochemical reactions is not considered in Equation 3.1 [5]. So, the calculated potential on the BPE is larger than the real potential distribution.

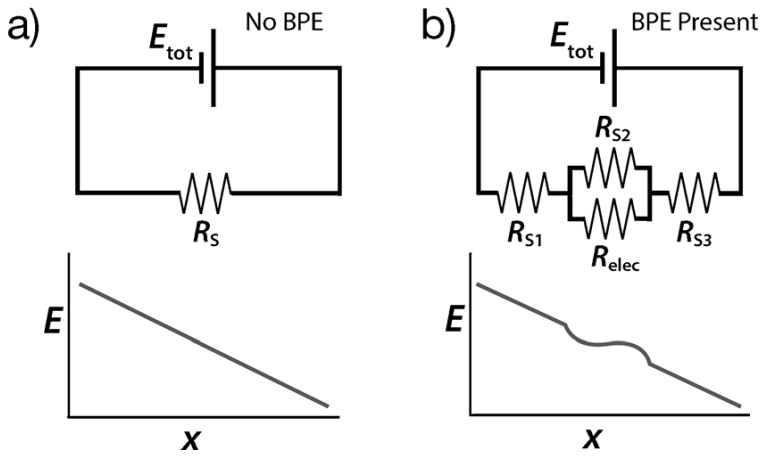

Figure 3- 3 The setup of bipolar electrochemistry, and the corresponding potential gradient without BPE in (a) and with BPE in (b) [4].

Two reference electrode measurement

The potential on the BPE could be measured by two reference electrode test method. The setup of two reference electrode is shown in Figure 3- 4. The potential difference between two points on the BPE surface could be determined by setting two reference microelectrodes set above the BPE [3,21], combined with the zero potential point (assume at the middle point of BPE). In this way, the local potential on the BPE could be measured. But this method had some limitations, the electrochemical reactions on the BPE are ignored [22]. Secondly, the electrochemical reactions between the reference microelectrode and BPE surface are also ignored [3].

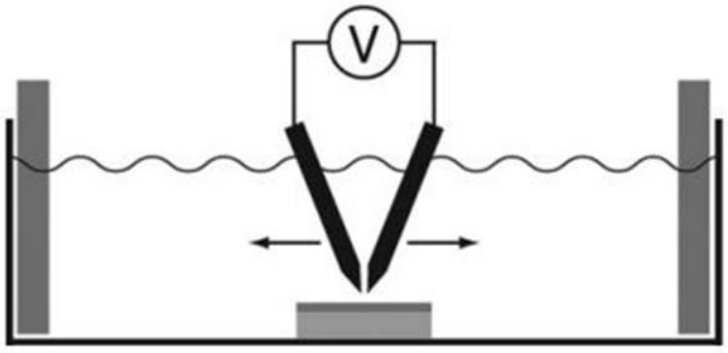

Figure 3- 4 The setup of two reference electrode measurement [21]

Finite element method (FEM)

FEM is applied to calculate the potential distribution on the BPE [23–25]. The potential is linearly reduced from +10V at the anodic edge to -10V at the cathodic edge in the 5.0 mM $Ru(bpy)_3^{2+}$ and 25.0 mM TPrA in 0.1 M phosphate buffer (pH 6.9) electrolyte from COMSOL Multiphysics simulation [23]. Hasheminedjad compares the potential on the BPE in phosphate buffered saline between the SPR image and COMSOL simulations, which showed the same potential distribution and the zero potential point location [25]. Potential distribution of the different shapes in phosphate buffer saline electrolytes is determined from COMSOL simulation and a prism-based surface plasmon resonance microscopy (SPR imaging). Both of the measurement show a linearly potential gradient with zero potential lines in the middle for all the different shape BPE, shown as Figure 3- 5 [24].

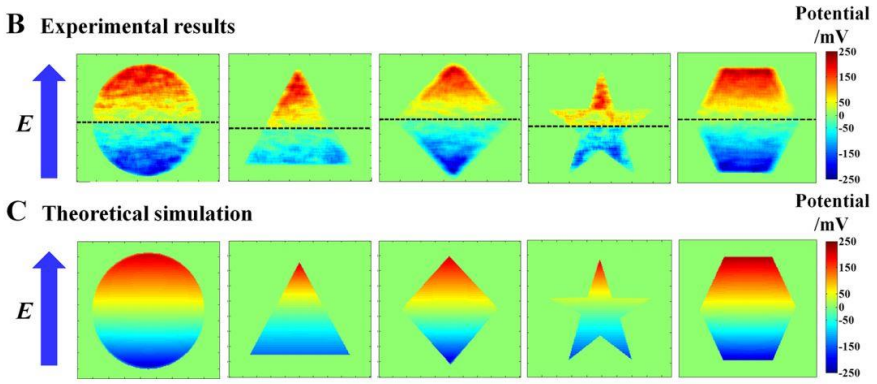

Figure 3- 5 The potential distribution on the BPE from experiment result and FEM (black line is the zero potential line) [24].

Direct measurement

To direct measure the local potential on the BPE, a Luggin probe connected to a reference electrode and the backside of BPE electric connect to a copper wire are used. To measure the local potential on the BPE, the Luggin probe is set above the BPE surface to record the potential change after switch on the bipolar electrochemistry. The setup of the direct measurement method is shown in Figure 3- 6 [2]. The local potential on the BPE can be measured by moving the location of the Luggin probe along the BPE surface.

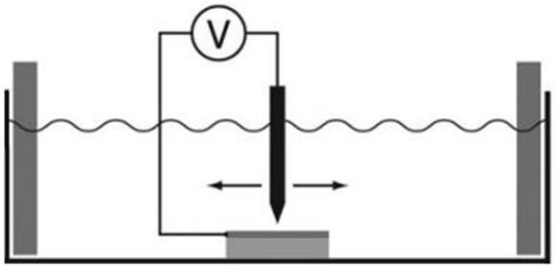

Figure 3- 6 The setup of Direct measurement [21].

This direct measurement setup loses some advantages (such as, non-wireless contact). But the measured potential distribution on the BPE are included the potential loss between the feeder electrodes and electrochemical reactions in the bipolar system (in the electrolyte and on the BPE surface). The other problem of this setup is the potential drop between the Luggin probe and the BPE surface. In the electrolyte of 0.5M H_2SO_4 + 5mM NaCl with 10 V on the feeder electrodes. Increasing the distance between the BPE and Lugin

probe from 100 µm to 300 µm, the recoreded potential on the same BPE location has few hundred microvolts drop [3].

3.122 Current distribution

The current has two pathways between the two feeder electrodes: either passed through the electrolyte or BPE, shown in Figure 3- 7 (a) and (b). The overall current density (i_{tot}) in the BPE system is the sum of current pass the electrolyte (i_e) and BPE (i_{BPE}). The concentration of the overall current passed through the BPE was related to the resistance of the electrolyte (R_e) and BPE (R_{BPE}). Figure 3- 7 (c) and (d) shows the local potential at the BPE oxidation and reduction edges, which is caused by part of the overall current (i_{BPE}) pass through the BPE. Figure 3- 7 (e) shows the ideal current distribution on the BPE, the highest current density at the BPE edges with the tiny current density was close to the centre of BPE [26].

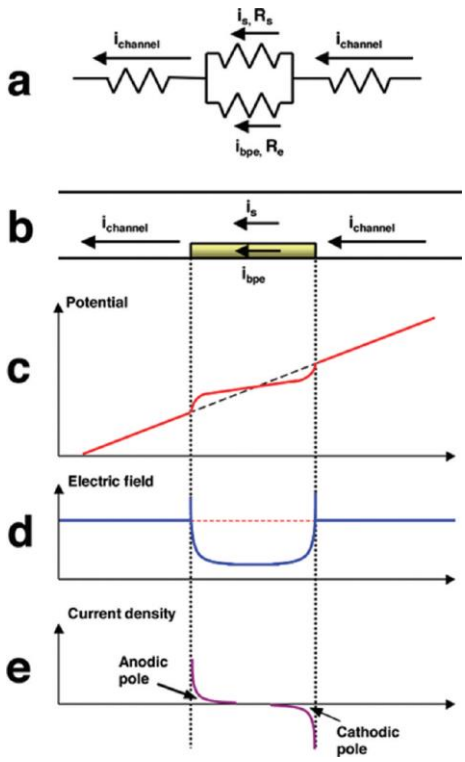

Figure 3- 7 (a) Equivalent circuit in (a) and simplified current distribution in the bipolar electrochemistry system, (c) and (d) shows the potential and electric field distribution between the two feeder electrodes, and (e) represents an ideal current distribution on the BPE [26].

The current on the BPE can not be direct measured. Some methods and setups are used to determine the current distribution on the BPE, including:

split bipolar electrode, Scanning Vibrating Electrode Technique (SVET), LEIS, electro generated chemiluminescence (ECL), Imaging Surface Plasmon Resonance (ISPR), Colorimetric pH indicator, and FEM.

Split bipolar electrode

The current distribution on the BPE could be directly measured from a split bipolar electrode setup, shown in Figure 3- 8. A non-conducting pellet is used to separate the intergrate BPE to small segment BPEs, and a Zero Resistance Ammeter (ZRA) is used to measure the current follows between the small segment BPEs [27,28]. Comparing the current density measured from split bipolar electrode setup and ECL density, the current density between these two menthod is similar at the same BPE length [5].

The limitations of spilt bipolar electrode setup includes the size of insulating materials between the split bipolar electrode influence the the value of the measured current [27]. The presence of the parasitic electrical current at the BPE edges results in a non-uniform potential and current density, so this setup only could determine the current distribution with a high applied potential difference across the BPE [29].

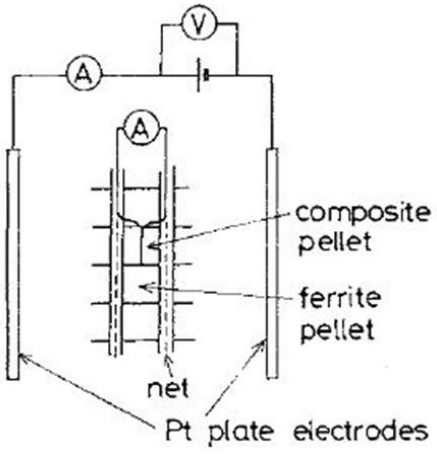

Figure 3- 8 The setup of spilt bipolar electrochemistry [27].

Scanning Vibrating Electrode Technique (SVET)

SVET is used to measuring small potential variations from the electrochemical reactions, and then convert into current density by a calibration routine [30]. The local potential is measured by a vibrating electrode above the sample

surface connect to a secondary auxiliary microelectrode [31]. The setup of SVET is shown in Figure 3- 9.

The main disadvantages of SVET are the current flow between anode and cathode under the vibrating electrode and some current returned to anode and cathode could not be detected. The sensitivity of SVET is not high enough, as the current density below 1 μA cm^{-2} could not be detected.The current flows in the electrolyte have three dimensional, but the SVET only could measure the current up to two directions. The movement and vibration of SVET probe, which increases oxygen transport on the sample surface, result in unbalanced the anodic and cathodic current [31,32]

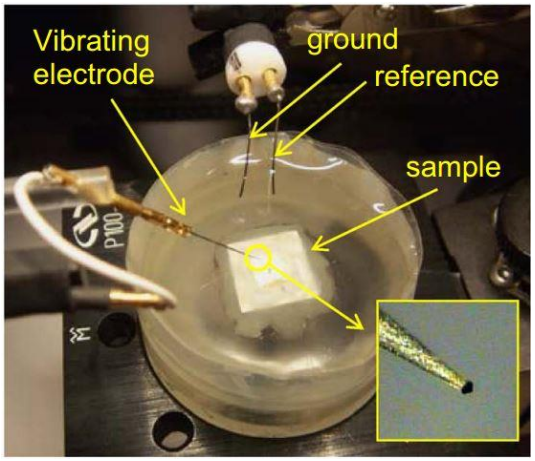

Figure 3- 9 The setup of Scanning Vibrating Electrode Technique (SVET) [31].

Local electrochemical impedance spectroscopy (LEIS)

LEIS is used to measure the local current in the close vicinity to the electrode. The resolution of the measured current is influenced by the dimension of microelectrode and the distance between the probe and electrode [33]. The setup of the LEIS is shown in Figure 3- 10, the local current density (i_{total}) on the BPE could be calculated from Equation 3.2:

$$i_{local} = \frac{\Delta V_{local}}{d} \times k \qquad \text{Equation 3.2}$$

where ΔV_{local} is the potential difference and d is the distance between two probes, and k is the conductivity of the electrolyte [33–35].

The limitation of the LEIS is the sensitivity of the measurement and probe size. The applied potential must be larger than 1 nV to get accurate current density [33]. The screening effect of the probe changes current density distribution unless the size of the probe is enough small [35].

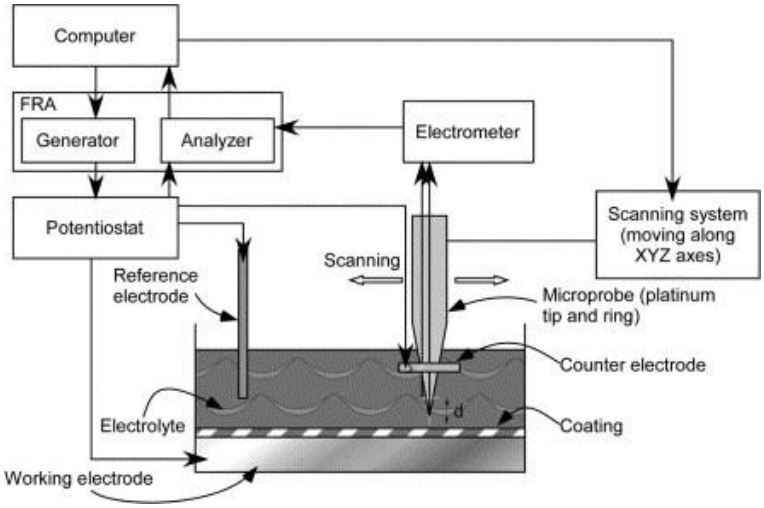

Figure 3- 10 The setup of the LEIS [34].

Electrogenerated chemiluminescence (ECL)

ECL is created to research the electrochemical reactions. ECL is setting the species at the electrode surfaces, and then electrochemical reactions active the species to excited states, which result in emit light [36]. The ECL intensity is related to the local potential and current density, which can be used to analysis the potential and current distribution on the BPE [37,38].

Figure 3- 11 gives the current distribution on the BPE measured from ECL. The electrolyte was 5.0 mM $Ru(bpy)_3^{2+}$ with 25.0 mM TPrA in 0.100 M phosphate buffer (pH 6.9). After increasing the potential between the feeder electrodes, the measured current density at the BPE edges became much larger. However, the current density in the middle region of the BPE is very small and almost independent of the different potential from the feeder electrodes. The main limitation of ECL used for current measurment is a critical potential was required to activate the ECL, so the current at low applied potential region cannot be measured [5].

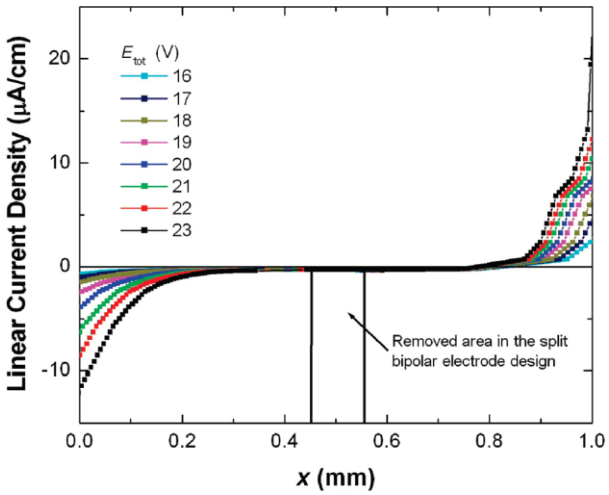

Figure 3- 11 The current density along the BPE as a function of different applied potential [5].

Imaging Surface Plasmon Resonance (iSPR)

iSPR could be used to determine the local current density via local change of refractive index, which is caused by electrochemical reactions. So the current density along the BPE could be visualized and evaluated from the different local electrochemical reactions [16].

Figure 3- 12 displays iSPR in the BPE anodic part from the different current density, here, the anodic reactions was $[Fe(CN)_6]^{4-}$ oxidized to $[Fe(CN)_6]^{3}$. To improve the accuracy of the current measurement, the iSPR images of the sample under OCP condition are used as reference. With increases the current output, the width of the current gradient decreased and shifted towards the middle of the BPE, as a larger potential distribution. The sigmoidal curve logarithmic relationship between the potential and concentration ratio of $[Fe(CN)_6]^{3-}$ to $[Fe(CN)_6]^{4-}$ with indicates the concentration of anodic electrochemical reactions [16].

The limitations for using iSPR to measure the current distribution on the BPE is the contamination sepcies is the bipolar system. Such as the generation of the second thiol deposits influences the refractive index, result in less accurate of the current density measurement [16]. For the stainless steel corrosion test. The electrolyte colour changes due to the Fe^{2+} and Fe^{3+} was generated, which influence the refractive index. So, the measured current density is not accurate in this system.

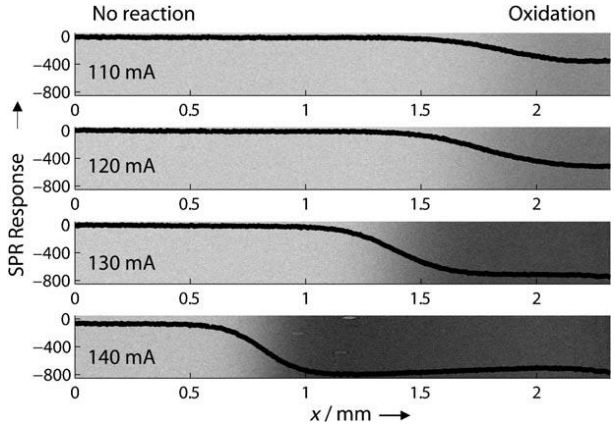

Figure 3- 12 The iSPR response changed by the refractive index when is $[Fe(CN)_6]^{4-}$ oxidized to $[Fe(CN)_6]^{3-}$ (the lines shows the mean intensity change in the iSPR)[16].

Colorimetric pH indicator

Figure 3- 13 gives a photo image of BPE with a colorimetric pH indicator. The colors of pH indicator changes from green at BPE reduction edge to red at the BPE oxidation edge. The pH values increases at the BPE reduction sites, as the generation of OH^-. The pH value reduces at the BPE oxidation sites, as the production of H^+. The generation rates of H^+ and OH^- from the electrochemical reactions could be used to calculate the local current density [38]. However, for the bipolar system, the electrochemical reactions only can generate H^+ and OH^-, if not, the current density calculation from the pH indicator are not accurate.

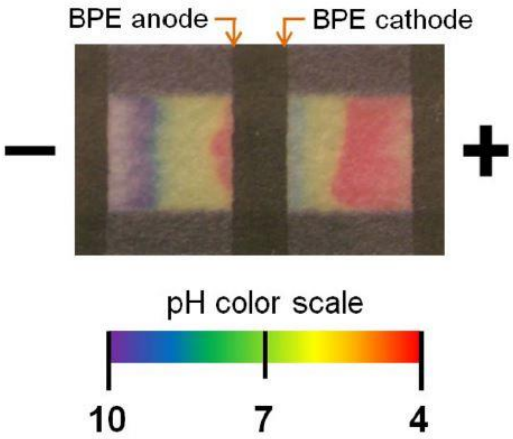

Figure 3- 13 Photo of BPE after the bipolar electrochemistry with a colorimetric pH indicator (top) and a standard pH colour scale (bottom) [38].

Finite element method (FEM)

Figure 3- 14 shows the current density from the COMSOL simulation with and without the BPE. The current density calculation is based on the electric field at 1.67 V cm^{-1}, electrolyte has the conductivity of 10^{-4} S cm^{-1} and BPE has the conductivity of 10^{-5} S cm^{-1}. Without the BPE, the current density distribution between the feeder electrodes is perpendicular to the feeder electrodes. After the BPE insertes in, the curvature lines of the current density is determined due to the BPE act as a pathway for the current flowing [3]. The limitation of COMSOL is the simplifying assumptions. For example, considering the electric field is homogeneity, the irreversible electron transfer reactions are limited, and only basic electrochemical reactions are considering in the bipolar system [3,22].

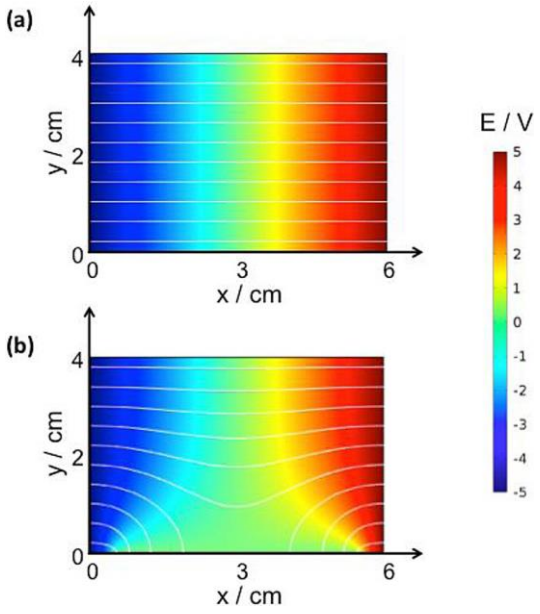

Figure 3- 14 FEM simulations of potential (coloured scale) and current (white line) without the BPE in (a) and with the BPE in (b) of a conductive substrate [3].

3.13 Application

The advantages of bipolar electrochemistry for electrochemistry research includes the easy setup, wireless non-contact BPE setup, fast experiment outcome, large active surface, and continuous potential gradient on the bipolar electrode. Bipolar electrochemistry is used in the asymmetric particles, electrodeposition, sensor, wire formation, anodic dissolution, microswimmer, and corrosion test.

Asymmetric Particles

Janus is named for Roman god who has two different direction faces shown in Figure 3- 15 [39]. As both anodic and cathodic reactions occurred at the two opposite sides on one particle. Janus particles is produced by different electrochemical reactions on the oppsite sites. The application is from electronic paper to autonomous swimmers [40,41].

The Janus particles are produced by the bipolar electrochemistry with suitable BPE size, composition, and shape. The easy experiment setup and a mass production yield of Janus particles are possible to achieved by the bipolar electrochemistry [40]. As non-contract wireless BPE, the Janus particles could be very small, the production of micro or nano size Janus particles are possible. But the micro or nano scale Janus particles are currently only produced in the lab, as an externally high applied potential is required to drive the electrochemical reactions. The other problems for micro or nano Janus particle product is the gas formation comes from electrochemistry reactions, which results in the direction of the BPE change during the bipolar electrochemistry experiment [39,41].

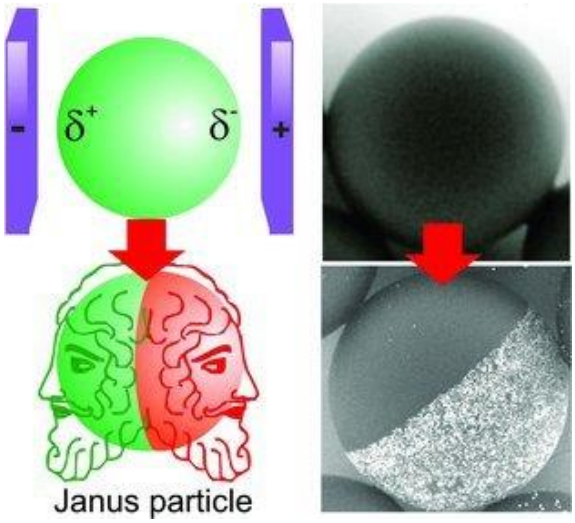

Figure 3- 15 Janus particles manufactured by the bipolar electrochemistry [39].

Electrodeposition

The deposition is depositing the materials on a surface with a suitable method, such as physical vapor deposition (PVD), chemical vapor deposition (CVD),

and sputtering [42,43]. The electrodeposition is widely used to decorate, which can improve the mechanical property and corrosion resistance [44,45].

The size, shape, thickness, and compositions of the deposited materials infleunced by different applied potential can be researched on the BPE in a single experiment [46]. Figure 3- 16 gives a BPE substrate which pre-modified 10 nm gold nanoparticles, and then immersing in the $HAuCl_4^-$ electrolyte with 5 V applied on the feeder electrodes. The gold nanoparticles size is increased in the cathodic site, caused by the electrodeposition. The size of the nanoparticls are related to the local applied potential, so the local applied potential influences the nano-particles growth kinetics could be determined [47]. Palladium particles are deposited on the carbon nano pipes from the bipolar electrochemistry, it is found that the thickness of deposited palladium partials various from 3 nm to 50 nm along the BPE, which is dependent on the local applied potential [48].

The electrodeposition from bipolar electrochemistry experiment could be used to collect different metals from fly ash. Usually, the fly ash contains 800-900 mg copper and 250-300 mg lead per kilogram. The fly ash is dangerous to storage unless the metals are extracted [49]. In the bipolar electrochemistry experiment, the copper and lead metals could be separated and collected at a different location on the BPE, then the flying ash is safe to storage and the collected copper and lead could be re-used.

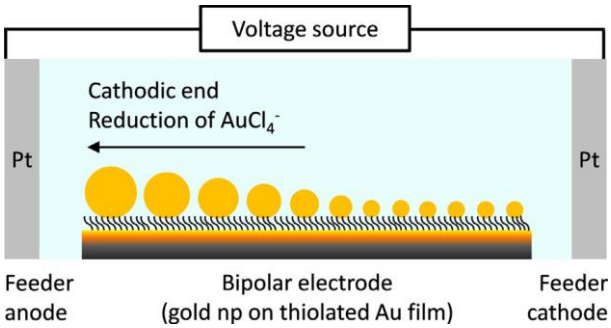

Figure 3- 16 Gold deposition size increase with a function of cathodic polarisation on the BPE [47].

Sensor

Bipolar electrochemistry is used for electroactive analyte, the local electrochemical reactions are determined from the intensity of ECL [50]. A setup of microdroplet sensor used for chemical and biological analysis is shown in Figure 3- 17. An ITO microband is chosen for the bipolar electrode with two micro reservoirs, one reservoir is used for the analyte and the other one is for the ECL measurement. The advantages of the microdroplet sensor are the simple setup, fast experimental outcome, high sensitivity, and wide dynamic response [51]. Senor based on bipolar electrochemistry is also used in the biological filed. Detection the adenosine in the cancer cell, as ferrocenes electrochemical reactions are used to measured the electrochemical reactions at the anodic part [52].

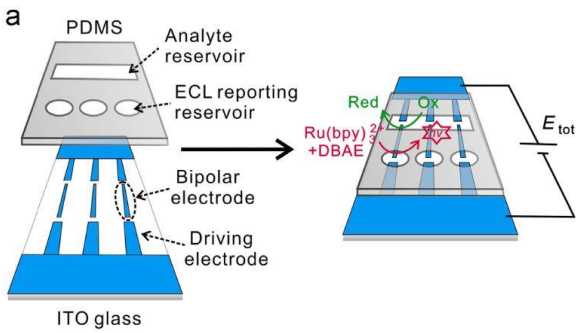

Figure 3- 17 The configuration of microdroplet sensor based on bipolar electrochemistry [51].

Wire formation

Bipolar electrochemistry is used to build an electric connection between two particles. This this achieved by electrochemical dissolution at one particle and electrodeposition reactions at the other particle, a extremely high potential between the particles is required [4].

Figure 3- 18 gives the process of electrical wire formation between two copper particles. One BPE copper processes the electrochemical oxidation reactions, oxidized to cupric ions. After a critical copper concentration is achived in the electrolyte, the electrochemical reductions reactions become the copper electrodeposition. So, a wire can be built between two copper particles. After the electrical wire is built and connect to the two particles, the wire growth

would stop as two BPEs become an integrated BPE [17]. A Schottky Diode (copper-silicon-copper) is manufactured from the bipolar electrochemistry. A silicon chip is set between two copper rings. Switching on the bipolar electrochemistry; then a copper wire is built and then connect to the the silicon chip. After the copper wire connect to the silicon chip switching the bipolar electrochemistry experiment in the opposite direction, allows the silicon chip connects to other copper particles. Mass production and the nano scale of the Schottky Diode are the main advantages from bipolar electrochemistry [53].

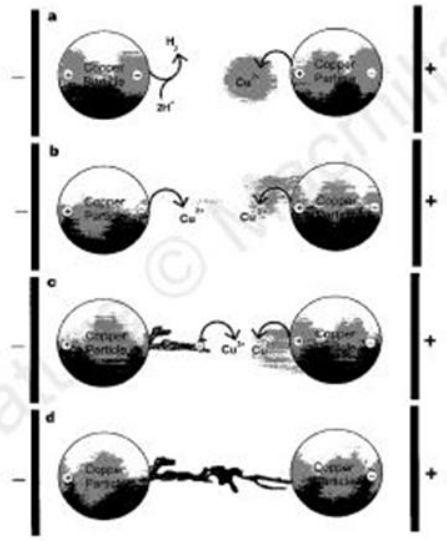

Figure 3- 18 The diagram of the process for a wire formed between two copper particles [17].

Anodic dissolution

Bipolar electrochemistry could be used to research the electrochemical etching. The average pore size and distribution on the silicon after etching in the HF solution changes as a function of the different applied potential. So, bipolar electrochemistry which produces a linearly potential gradient can be used [54].

Bipolar electrochemistry captures the DNA binds at the cathodic sites by determining the Ag dissolution rate. Figure 3- 19 shows the elemental distribution (EDX) on the anodic BPE after the Ag dissolution. The exposred area only measured the Au is caused by the selective dissolution of Ag. The Ag signals vanishes at a critical position on the BPE, which is the critical

potential for Ag dissolution. The detection of the Ag dissolution is easy, which can be detected by the naked eye [55]. Anodic dissolution rates of Ag is used to analyse the effect of driving force for the electrochemical reactions, as the solution flow and oxygen reduction reaction rate are increased by the catalyst [56,57].

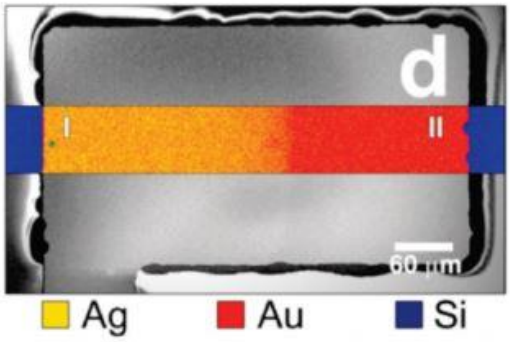

Figure 3- 19 EDX map of the anodic part of the BPE [55].

Microswimmer

The motion of the BPE is controlled by oxygen evolution, as the oxygen evolution breaks the interfacial tension between water and electrolyte [58,59]. Self-generation BPE is created based on the anodic dissolution reaction at one side on the BPE and cathodic deposition reactions at the opposite side on the BPE [12,17]. Self-generation also could be achieved by the hydrogen and oxygen evolution at the opposite BPE side. The rotation of microswimmers is also possible from Pt deposition at the BPE cathodic sides, and the rotation speed is linear to the electrochemical reactions rate. So researching the relationship between rotation speed and local applied potential could be used by bipolar electrochemistry [60,61].

Corrosion

Bipolar electrochemistry had recently been used for corrosion research. So far, only 5 papers are found using bipolar electrochemistry for corrosion test. Two of the them related to pitting corrosion and the left three papers are used for a fast corrosion screening to the steel which simulate the dew point corrosion conditions [1], determing the erosion-corrosion resistance of steel with different coating [2], and comparing the potential and current distribution

on the BPE and potentio-dynamic polarization from modelling [3]. In 2013, bipolar electrochemistry is used to test the corrosion behaviour of 304L stainless steel [62]. Figure 3- 20 shows an SEM image of type 304L stainless steel BPE. The applied potential between the two feeder electrodes was 5.4 V with the electrolyte of 1M H_2SO_4 for 120 minutes exposure. The rough surface on the stainless steel after bipolar electrochemistry experiment indicates intergranular corrosion occurs. The stainless steel surface becomes smooth toward the BPE centre, as less serious corrosion [62].

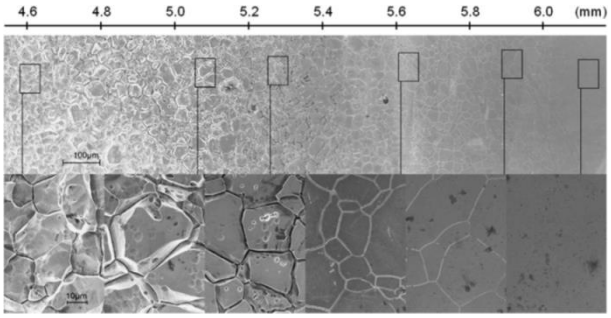

Figure 3- 20 An SEM image of intergranular corrosion on Type 304 stainless steel BPE [62].

Bipolar electrochemistry is used to rank the pitting corrosion resistance between Type 304, 2205, MV, SK, and SL stainless steels. The setup of the bipolar electrochemistry corrosion test shown in Figure 3- 21.The potentio-dynamic polarisation and pitting resistance equivalent number (PREN) are used to evaluating the corrosion resistance of these stainless steels measured from bipolar electrochemistry. PREN and polarisation tests proof the corrosion rank tested from bipolar electrochemistry is reliable [63].

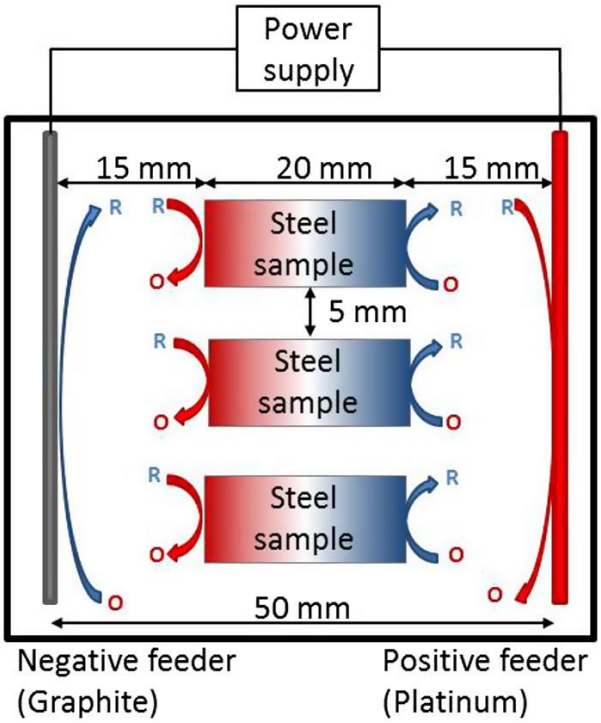

Figure 3- 21 Schematic figure of the bipolar array setup [63].

3.2 Stainless steel

3.21 Introduction

Stainless steel contains > 13% Cr (by weight) with the absence of the staining, rusting or corroding compare with the normal steels. The corrosion resistance of the stainless steel comes from a thin, stable, and passive with a thickness of 1-2 nm of microcrystalline chromium oxide (Cr_2O_3) film [65,66]. The passive film could be reformed/repaired at the damaged sites after a few seconds[66]. Cr element is one of the main element to increase the corrosion resistance, but other elements are also added to improve the mechanical and corrosion properties [67]. Stainless steels are used from automobiles, food, paper, oil, and gas due to the combination of good corrosion and mechanical properties [68,69].

3.22 Classification of stainless steel

Stainless steels are divided into 5 main different groups depending on the composition and microstructure. The 5 groups include ferritic stainless steel, austenitic stainless steel, martensitic stainless steel, duplex stainless steel,

and precipitation hardening stainless steel [70]. The main alloying elements and the corresponding concentration of different stainless is shown in Table 3. 1

Table 3. 1 Typical range of elements for a different type of stainless steel [70]

Category	Composition (wt%)					Others
	C	N	Cr	Ni	Mo	
Martensitic	>0.10	–	11–14	0–1	–	
	>0.15	–	16–18	0–2	0–2	
	<0.10	0.05	12–18	4–6	0–2	
Precipitation hardening	0.03–0.20	–	12–17	4–8	0–2	Al, Cu, Ti, Nb, V
	0.05–0.15	–	15–18	4–8	1–3	
Ferritic	<0.08	–	12–27	0–5	0–5	Ti
	<0.25	–	24–28	–	–	
Austenitic	<0.08	0.03–0.7	16–30	8–35	0–7	Cu, Ti, Nb, Mn
Duplex	<0.05	0.05–0.4	18–33	0–7	1–5	Mn

Ferritic stainless steel

Ferritic stainless steel has Cr % from 11 to 30 (wt%), and low concentration of C without N [71]. Ferritic stainless steel has a good corrosion resistance, high strength, moduli elasticity, and thermal conductivity. However, the formability and weldability properties are poor [72,73]. Ferritic stainless steel is non-magnetic and could be hardened by cold working [74]. The stress corrosion cracking corrosion (SCC) for ferritic stainless steel is excellent [75]. However, hydrogen embrittlement (HE) resistance for ferritic stainless steel is poor, as Laves phase particles are formed and the bcc phase has a high diffusivity and a low solubility of hydrogen [76].

Austenitic stainless steel

Austenitic stainless steel is the largest group in stainless steel as an excellent corrosion resistance, mechanical, and weldability properties at evaluated high temperatures [74]. Austenitic stainless steel has 200 and 300 series. Type 300 austenitic stainless steels has the composition of 16-26 % Cr and 10-22 % Ni. Type 200 austenitic stainless steels use the cheaper Mn (5-18%) to replace expensive Ni. Super-austenitic stainless steel has a super corrosion resistance than normal austenitic stainless steel, due to the addition of a high concentration of Mo (up to 6%) [71].

Martensitic stainless steel

Martensitic stainless has Cr concentration between 12-18% with C concentration < 1.2%, [77]. Martensitic stainless steel has a good mechanical and medium corrosion resistance, which is used in the steam generator, food processing blade, and mixer blade [78,79]. To manufacturing martensitic stainless steel, stainless steel is fully austenitizing from 950 - 1050 ^{o}C and followed by rapid quenching [80]. The austenitizing temperature, holding time, and quench speed affects the corrosion and mechanical properties [81,82]. Tempering is applied to improve the ductility, toughness and corrosion properties by the formation of the secondary phase and change the fraction volume of retained austenite [83–85].

Duplex stainless steel

Duplex stainless steel contains two phases - austenite and ferrite phase, each phase has at least 30% [86]. The application of duplex stainless steels varies from marine, chemical, and power plane due to the excellent mechanical and corrosion resistance properties [87,88]. Austenitic phase contributes the excellent corrosion and mechanical properties, and ferritic phase offers a high strength and good SCC resistance [89,90]. The ferritic phase has more Cr, Mo, Si, and W. Ni, Mn, and N are riched in austenitic phase [91].

Precipitation hardening stainless steel

Precipitation hardening stainless steel has an excellent hardness from the solution and aging heat treatment, some minor elements such as aluminium, copper, and titanium are added to achieve the precipitation hardening properties [77]. The crystal structure of the precipitation hardening stainless steel could be austenitic, semi-austenitic, or martensitic [92]. Precipitation hardening stainless steel has used the application wheren need ultra-high-strength, but only need reasonable ductility and corrosion resistance [93,94].

3.33 Effect of alloying elements

Stainless steel has the different alloying elements and concentration; each element has different contributed to the corrosion resistance and/or mechanical properties. Figure 3- 22 summarizes the common alloying elements which contributes to the corrosion resistance in the 3 electrode

potento-dynamic polarisation curve. The improvement of the corrosion resistance could be determined by the change of inactive, passive, and pitting potential range. Elements are added to increased $E_p$indicates the increased of the corrosion resistance, also the elements added to lower i_{pass} and I_{max} aslo improved corrosion resistance [95].

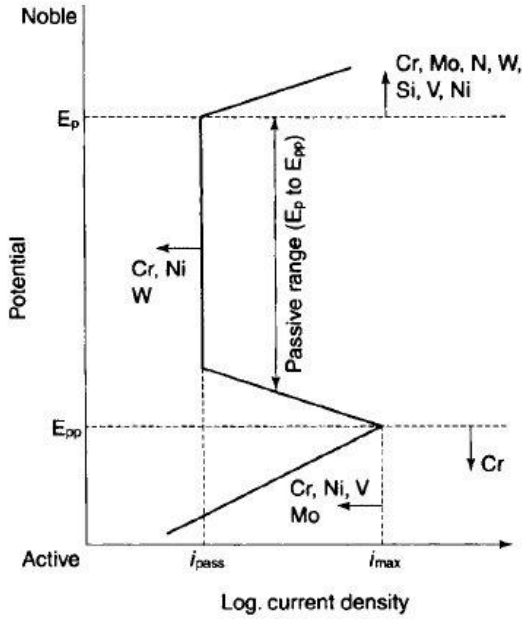

Figure 3- 22 The effect of alloying elements on the polarisation curve. E_{pp}: passivation potential, E_p: pitting potential, i_{pass}: passivate current density, i_{max}: active current density [95].

The functions of the common alloying elements in stainless steel is list:

Chromium (Cr): the most important element to increase the corrosion resistance by forming the the passive film (Cr_2O_3) [65,66]. Cr is the ferritic stabilizer in duplex stainless steel [70]. However, Cr could react with C to form chromium carbides ($Cr_{23}C_6$, Cr_7C_3, Cr_3C_2, Cr_3C, Cr_2C, and CrC), the Cr deletion region formed near chromium carbides, galvanic corrosion between the chromium carbides, and micro-crevice between the chornium carbides and stainless steel matix , all of them might result in localised corrosion [83,96,97]**.**

Nickel (Ni): Ni is the austenitic phase stabilizer in duplex stainless steel. The ductility, toughness, hardenability, and corrosion resistance properties are improved from a higher concentration of Ni [70,98]. A relative high Ni concentration (9%) can significantly reduce SCC and pitting corrosion [99].

However, the high concentration of Ni reduces the fatigue properties and increases the probability of the formation of sigma phase, which reduces the corrosion and mechanical properties [100].

Molybdenum (Mo): Mo is the ferritic stabilizer in duplex stainless steel. A higher concentration of Mo increases the mechanical strength and corrosion behaviours [70]. Mo increases the pitting potential by the reduction of the local chloride concentration from Mo complexes with chloride [101]. The formation of MoO_2 in the passive film could also increase the pitting corrosion resistance [102]. However, to avoid the formation of intermetallic phase, the concentration of Mo should be less than 4% [103].

Manganese (Mn): Mn was the austenitic phase stabilizer in duplex stainless steel, hot ductility, and solubility of nitrogen in stainless steel were improved by Mn [70]. But Mn reduced the corrosion resistance, by lowering the critical pitting potential and critical pitting temperature, and the formation of MnS inclusions offered the sites to nucleate the localised corrosion [104,105].

Carbon (C): Carbon is a strong austenitic stabilizer in duplex stainless steel. The hardness and strength properties could be increased by a higher concentration of carbon [70]. A high concentration of carbon also reduce the corrosion resistance due to the formation of chromium carbides [96,97].

Nitrogen (N): Nitrogen is a very strong austenitic stabilizer in duplex stainless steel. Nitrogen is used to replace the the expensive nickel [106]. Nitrogen is added to improve corrosion resistance and strength properties [70]. Nitrogen helps the pit repassivate by increasing the pH value by reach with H^+ to form NH_3 and $NH4^+$ [107]. The tensile strength, ductility, and elongation properties can also be improved by the addition of nitrogen [108]. However, if the concentration of nitrogen is too high, Cr_2N will be formed which reduces pitting corrosion [109].

Pitting corrosion behaviour could be theoretical and samply compared from the Pitting Resistance Equivalent Numbers (PREN). Higher PREN value indicates a higher pitting corrosion resistance. However, three different PREN equations are mentioned, related to the different factor of the alloying elements. The effective of Cr and Mo to the PREN is the same in these three

PREN formula. However, the coefficient of nitrogen is controversial, the factor varies from 16 to 30.

PREN=%Cr+3.3%Mo+16%N Equation 3.3 [110]

PREN=%Cr+3.3%Mo+20%N Equation 3.4 [111]

PREN=%Cr+3.3%Mo+30%N Equation 3.5 [112]

3.23 Heat treatment

The heat treatment is used to optimise the corrosion resistance and mechanical properties [70]. For martensitic stainless steel, the microstructure of martensite, undissolved with re-precipitated carbides, and retained austenite, changed by the heat treamtent, which result in the evolution of the hardness, strength toughness, wear resistance, and corrosion resistance [113].

For the heat treatment process, three parameters should be considered: 1, austenitizing temperature and holding time. 2, quenching rate. 3, tempering temperature and holding time. The tempering process had the largest impact on the mechanical and corrosion properties [114].

Austenitizing temperature

The austenitizing temperature range is between 950 and 1050 ℃, the most suitable austenitizing temperature depends on the composition of the stainless steel [114]. A higher austenitizing temperature increases the solubility of carbides, but suppresses the martensitic formation [115]. The retained austenite volume reduces the hardness, but it increases the pitting resistance. As the reduction the ovelall area of Cr depletion region and the increases the stability of the passive film and retards the formation of $Cr_{23}C_6$ [116,117].

Quenching rate

Relative slow quenching rate results in ferrite phase and dispersed carbides, not martensite [118]. A higher quench rate is preferred to avoid the carbides precipitation at the grain boundary. However, the suppressed carbon segregation reduce strength of the martentic stainless steel [114,119]. The prior austenite grain size for martensitic stainless steel is sensitive to the quenching rate [120].

Tempering temperature

The final microstructure and carbide precipitate can be adjusted by the different tempering process, results in different mechanical and corrosion properties. Tempering at 200 ℃, Fe_2C is formed with less internal stress. Tempering at 300 ℃, Fe_2C will transform to Fe_3C; then tempering up to 400-450 ℃, retained austenite was is completely transferred to martensite. Tempering between 450-600 ℃, the maximum secondary hardness will be achieved [121]. At tempering temperature from 200 to 400 ℃, a good toughness but a high residual stress is achieved [114]. Tempering from 480 to 720 ℃, the hardness and corrosion resistance are reduced as carbides precipitate [122,123]. The reversed austenite improves the corrosion resistance, as the reduction of the extent of Cr depletion and the increased of the passive film stability [116].

3.24 Passive film

A passive film with few nanometres thick is formed on the stainless steel surface in ambient temperature. The passive film contains two layers, an inner layer (n-type semiconductor) with enriched in chromium oxides, offered most corrosion resistance; and an outer layer (p-type semiconductor) with iron oxides and hydroxides [124]. The passive film is not static which changes with the environment [67]. The grain size of the stainless steel influences the passive film, a nano-crystalline grain size stainless steel results in a significant increase in mechanical, wear, and corrosion resistance properties [125]. Other parameters influences the passive film of the stainless steel include the alloying elements, applied potential, pH value, temperature, and exposure time:

Alloying elements

Cr, Ni, and Mo have to the positive effects to the corrosion resistance, but Pb give negative effects to the passive film. Increased Cr concentration, a homogenous, protective, and stability of the passive film are measured from the polarisation curve [126]. The critical pitting potential in 1N HCl is increasing with higher Cr in austenitic 20Cr-25Ni stainless steel, and no pitting is determined when Cr > 40% [102]. Ni is enriched in the passive film, which

located close to the base material [127]. Mo is present at internal Cr rich layers and Cr oxide/metal layers, which can increase the corrosion resistance by reducing the defects in the passive film [128]. In duplex stainless steel, Mo could optimize the corrosion resistance between the austentic and ferritx phases [129]. Pb prevents the oxygen vacancies diffuse outward, result in a lower passive film growth rate and a higher electric resistance [130].

Applied potential

The thickness of the passive film is increasing linearly to the applied potential in the passive region [67,131]. The corrosion resistance of the passive film is reduced after a critical potential, as the stability of Cr^{2+} is limited and Fe^{3+} is increased in the passive film [67]. The passive film composition is changed by the applied potential, $Fe(OH)_2$ is formed at the low potential in the passive film, then become FeOOH at the high potential [132].

pH value

The thickness of the passive film and concentration of Fe in the passive film is increasing with higher pH. Electrochemical quartz crystal microbalance (EQCM) is used to compare the thickeness of the passive film on Fe-25Cr and Fer-17Cr-33Mo stainless steel formed in acidic and alkaline electrolyte, the results show a thicker passive film formed at a higher pH environment, as a lower dissolution rate and more stability of iron oxide [133]. The concentration of Fe in the passive film on the Fe-15 Cr and Fe-20Cr alloys are pronounced in more alkaline solution [134]. Compare with 0.1M H_2SO_4 + 0.4M Na_2SO_4 solution, passive film are growing faster and dissolving slower in the more alkaline electrolyte (0.1M NaOH solution) [67].

Temperature

How will the electrolyte temperature influence the passive film was controversial. Some people mentions the electrolyte temperature could not influence the thickness and composition of the passive film, similar passive film formed in 0.5M NaCl from the room temperature to 90 ℃ [135]. However, the thickness of the passive film formed in HCl from 22 to 65 ℃ is also compared by other researchers, it is found that the thickness becomes thinner

at the higher temperature [67]. Some researchers find the composition of the passive film is changed by temperature. The corrosion resistance of the passive film is reduced as the less Cr and Mo in the passive film at higher electrplyte temperature [136].

3.3 Corrosion

Corrosion is the degradation of material exposure in the environment by chemical or electrochemical reactions. The applied potential, pH, environment, and temperature influenced the corrosion process and corrosion rate [137]. To process the electrochemistry reactions, four components are required: anode, cathode, electrolyte, and path connector. Electrolyte offeres the pathway for the ions movement and path connector allows the electrons transfer, the anode part suffers the corrosion process and cathode is used to balance the electrons from the anode [137].

For the corrosion process, anode and cathode could be either separate or at the same place, in the anodic reactions, the electrochemical reaction is [138]:

$M \rightarrow M^{n+} + ne^-$

The cathodic reactions depends on the nature of the environment [138]:

In neutral or basic electrolyte, oxygen reduction reactions occurs

$O_2+2H_2O+4e^- \rightarrow 4OH^-$

In acid electrolyte, a hydrogen evolution or oxygen reduction occurs either:

$2H^++2e^- \rightarrow H_2$ or $O_2+4H^++4e^- \rightarrow 2H_2O$

In some specific conditions, metal ions reduction is the cathodic reaction:

$M^{n+} + e^- \rightarrow M^{(n-1)+}$

Thermodynamic and kinetics are two important parameters for the corrosion process. Thermodynamic is used to distinguish the corrosion occur or not. The process of the corrosion is from an unstable high energy states to a stable low energy state. The driving force for corrosion is chemical energy. The corrosion

reactions could be spontaneously occurring if the free potential of products is lower than the reactants. Kinetics is used to study the corrosion rate [139].

Corrosion could be divided into general corrosion and localised corrosion.

3.31 General corrosion

General corrosion is a uniform corrosion of the entire surface of the alloy with a similar corrosion rate. In industry, the general corrosion rate < 3 miles per year is acceptable in most applications [140]. The location of the cathode and anode might be change with time during the general corrosion. Even general corrosion corroded tons of metal and alloy per year, but general corrosion would not result in a sudden failure and easy to calculate and measured. So general corrosion is less harm [138].

3.32 Localised corrosion

Localised corrosion is commonly detected, and thenode and cathode is physically separated. Localised corrosion is a concentrated attack on a small area, with the other area still in a protected state (cathode area). A large cathode and small anode results in a relative high corrosion rate [138]. The corrosion rate is hard to determine and calculate, as no significant material weight loss and hard to direct measure [139]. Five common type of localised corrosion will be introduced, including: stress crack corrosion (SCC), intergranular corrosion, galvanic corrosion, crevice corrosion, and pitting corrosion.

Stress corrosion crack (SCC)

The generation of the stress corrosion crack requires a combination of susceptible material, adequate stress, and a suitable corrosion environment, shown in Figure 3- 23. The applied stress should be lower than the yield stress, can come from either external stress or residual stress. SCC initiates at the surface flaws or localised corrosion sites, the pathway for crack could be either intergranular or transgranular, or sometimes combination of both [141]. SCC initiated near inclusion with specific composition and morphology in X70 pipeline steel. The inclusions enriched in Al is brittle and incoherent to the stainless steel matrix, which is easy to nucleate crack. But SCC could not be nucleates near Si rich inclusions, as the inclusion is easy to be deformed and

stable. [142]. The tensile stress could encourage the nucleation of SCC, but the compressive stress prevents the SCC nucleation. The crack also could penetrate to sample with a few hundred micrometres in depth, which is very harmful for materials [143].

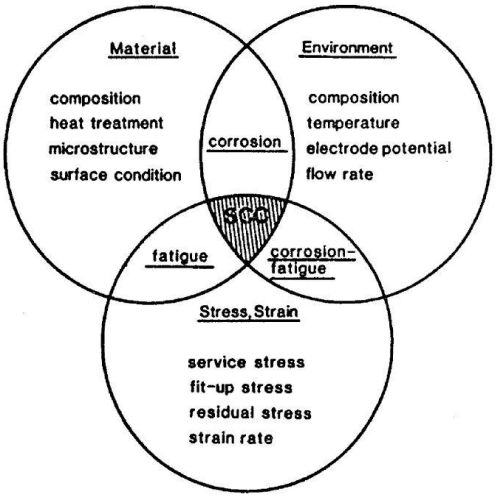

Figure 3- 23 The specific conditions are required for cracking to occur [141].

Intergranular corrosion

Intergranular corrosion results in the concentrated attack along the grain boundary, shown in Figure 3- 24 [139,144]. Compared with SCC, the corrosion depth for intergranular corrosion is relatively low; A sudden loss occurs after all the grains dissolved, and intergranular corrosion could transfer to SCC [145]. Sensitization of the stainless steel causes intergranular corrosion, which is cuased by the chromium carbides precipitate at the grain boundary during heat treatment. To reduce the sensitization damage, Ti, Nb, and Zn are added to stabilize the carbon during solution treatment. A uniform distribution of a high frequency of coincidence site lattices (CSL) boundaries in the stainless steel can also reduce the probability to nucleate the intergranular corrosion [146]. In austenitic stainless steel, sensitization occursd at tempering between 550 ℃ to 800 ℃, as $Cr_{23}C_6$ precipitates at the grain boundary [147]. For martensitic stainless steel, sensitization occurs at tempering temperature around 550 ℃, then, the degree of sensitization (DOS) is dramatically reduced with higher tempering temperature, from DOS of 40% at 550 ℃ to DOS of 2.8 % at 650 ℃ [148]

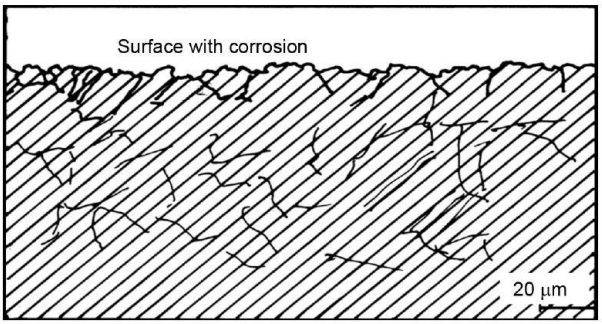

Figure 3- 24 Images of Intergranular corrosion [144].

Galvanic corrosion

Galvanic corrosion occurred when two dissimilar metals or alloys are electrically coupled in an electrolyte [149]. A galvanic current flows from one material to the other material [150]. The value of the galvanic current is influenced by the potential different of anode and cathode, solution resistance, and electrochemical reactions resistance on the anode and cathode [151]. In a galvanic cell, the anodic part is more active which suffers more corrosion, where the cathodic part is nobler and protected by anodic part [152].

Equation 3.8 is used to calculate the current density between the galvanic coupling [150–152]:

$$\mathrm{i_g} = \frac{\mathrm{E_c} - \mathrm{E_a}}{\mathrm{R_a} + \mathrm{R_c} + \mathrm{R_S}} \qquad \text{Equation 3.8}$$

$\mathrm{i_g}$ is the galvanic current, E_c and E_a are the corrosion potential of cathode and anode, R_a , R_c and R_s are the reaction resistance of anode, cathode and solution resistance.

The corrosion potential is used to distinguish the anode and cathode after two metals connects. But the reaction kinetics cannot be simply calculated by the potential different between anode and cathode, due to the corrosion products might be generated during the corrosion process [150,153]. The measured galvanic current density can also calculated from weight loss in the anode [154]. In some conditions, the cathodic part in a galvanic couple suffers the corrosion due to the electrolyte change, such as pH. Al is cathode after a couple with Zn in 3.5 % NaCl. However, pH increases in the electrolyte near

the Al from the cathodic reaction, which result in the corrosion in the cathodic part - Al [154].

Figure 3- 25 shows four different controlling modes in galvanic couples. If only the cathode is polarized, then the current density is controlled entirely by the cathode, called cathodic control. If only the anode ispolarized after coupling, the controlling mode is under the anodic control. With both of anode and cathode are not polarized, the controlling mode is under the resistance control. In most situations, both anode and cathode are polarized, which are called the mixed control [150]. Under the cathodic control, only the cathodic area is influenced by the galvanic corrosion. The opposite is for the anodic control, only anodic corrosion is affected by galvanic corrosion. For the mixed control mode, the ratio of cathode and anode surface area could change the galvanic corrosion [150,155].

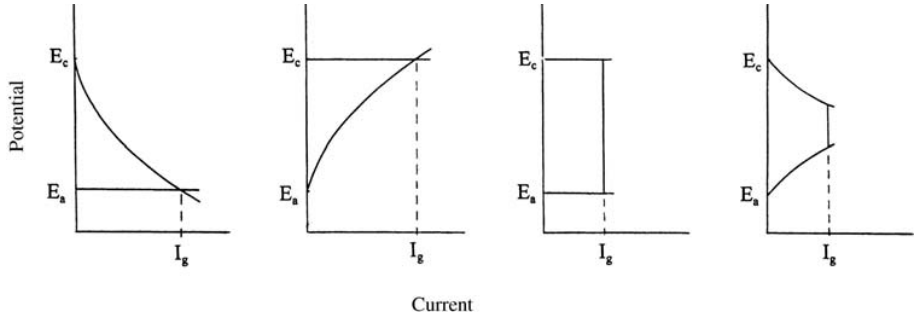

Figure 3- 25 Schematic illustration of anodic and cathodic polarisation curve under (a) cathodic control, (b) anodic control, (c) resistance control, and (d) mixed control [150].

Conductivity and thickness of the electrolyte are the other important factors in the galvanic corrosion. In a high conductivity electrolyte, the galvanic corrosion cannot uniformly distributed on the entire surface of the anode and cathode. In a low conductivity electrolyte, the galvanic corrosion can only concentrated in a narrow region between the anode and cathode. The thickness of the electrolyte influences the galvanic corrosion from: 1, change corrosion resistance, result in potential and current distributions across the galvanic coupling changes. 2, the cathodic reaction rate is controlled by diffusion length of the oxygen, which influences the anodic corrosion rate [156].

Crevice corrosion

Crevice corrosion is defined as an anode part located in a shielded or restricted environment, and the rest of the metal is the cathode. Crevice corrosion usually occurs in the welded structure, threaded components, and riveted plates [157]. Crevice corrosion is influenced by the geometry of crevice. As the openness of the crevice influenced the acidification process, potential distribution inside of crevice, and species diffuse out of crevice [158,159]. Crevice corrosion is also changed by the local applied potential, crevice length, pH value, oxygen concentration, Cl^- concentration, and electrolyte temperature [160,161]. Crevice corrosion is more dangerous than pitting corrosion, as it can initiated at a lower potential, temperature, and shorter induction time. The crevice corrosion could initiate without the Cl^- which is necessary for the pitting nucleation [162–164]. The crevice corrosion mechanism includes the metastable pitting corrosion mechanism, which is the metastable pits nucleated and growth in occluded crevice geometry; IR drop mechanism, which the potential in the crevice allows the crevice corrosion growth in active corrosion region; passive dissolution mechanism, which is pH gradual reduce to break the passive film, and then crevice corrosion could nucleate and growth growth [165].

Pitting corrosion

Pitting corrosion is the localised breakdown of a passive film on the metal surface followed by a rapid metal dissolution [166]. The halide ions influences the pitting corrosion, the harmful of the halide ions for the pitting corrosion decreased from Cl^-, Br^- and I^-. The fluoride ion could not promote the pitting corrosion by itself [167]. The pitting corrosion is also influenced by concentration aggressive ions, applied potential, and electrolyte temperature [168]. Three mechanisms of pit nucleation are discussed: penetration, mechanical breakdown, and adsorption [169]. Pitting corrosion has three stages: pit nucleation, metastable pitting, and stable pit growth[167]. Both the metastable and stable pit growth is under diffusion control [170]. The growth of a metastable pit requirs a lacy cover, which acts as a diffusion barrier to maintain the pit electrolyte at a high concentration of Cl^- and low pH [171]. Stable pits can only generates above a critical potential or temperature. The

passive film breakdown shows a step decrease with a higher temperature [172]. At a high applied potential, the metal dissolution inside of the pit is faster than metal ions diffuse out of the pit, so s salt film can be formed to stabilize the pit growth [173].

Figure 3- 26 shows three distinct parameters in the anodic 3 electrode potentio-dynamic polarisation curve: pitting potential range, passivation potential range, and activation potential range. The critical pitting potential is the lowest potential to nucleate the stable pitting corrosion. The passivation potential means the alloys in the passivate state which is protected by a passive film. The activation potential is the potential for metals suffering the general corrosion [174]. A repassivation potential in the pitting corrosion indicates the lowest potential for a growing pit continue expanding but cannot nucleate stable pit, so the repassivation potential is also called the protection potential [65,175]. The induction time in the pitting corroison defines as the time for the first pit nucleate [176,177].

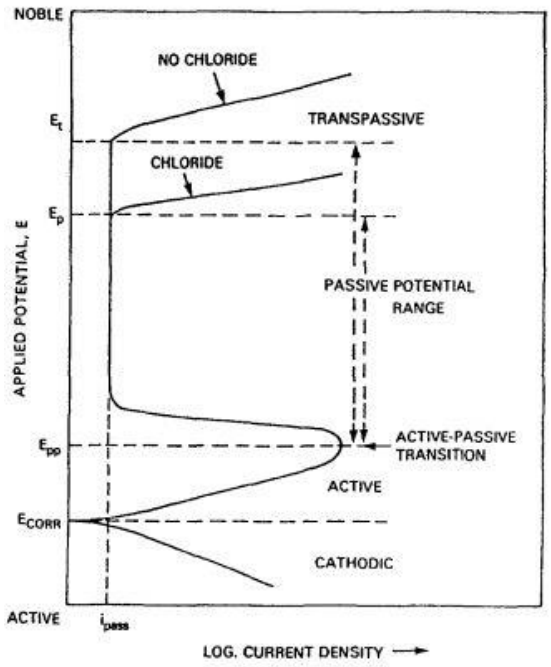

Figure 3- 26 Different regions of the potentio-dynamic polarisation curve [174].

3.4 Pitting

Pitting corrosion growth has three stages: pit nucleation, metastable pitting and stable pit growth [167]:

3.41 Pit nucleation

In stainless steel, the locations of pit nucleation is related to microstructure or metallurgical heterogeneities, such as inclusions, grain boundaries, and second phase precipitates[178]. Pit nucleation could be detected via a short, small current peak followed by sudden current drop in the electrochemistry test shown in Figure 3- 27 (a). The transients indicates the nucleation of a pitm but and then repassivatesuddenly. The repassivate pit volume loss is small, less than 0.01 μm^3. Figure 3- 27 (b) shows a current rise with a smoother step, which indicates a metastable pit nucleate and growth; but then the current density drop back to zero means the pit repassivate [170,179]. The probabilities of pit nucleation are influenced by the metal surface roughness. A smoother surface shows a lower frequency of pit nucleation but a higher probability for the pits under stable growth. The rough surface results in higher pit nucleation rate but lower chance for the nucleate pits transfer to stable pits [180].

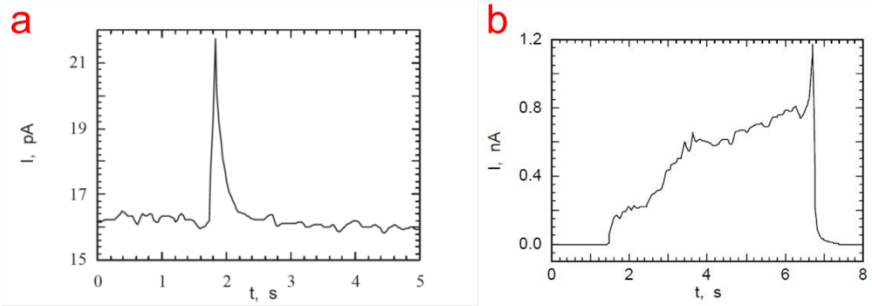

Figure 3- 27 (a) Current transient of a pit nucleate and (b) current transient of a metastable pit nucleate and growth for Type 304L stainless steel microelectrode [179].

Three mechanisms of passive film breakdown are discussed which includes the penetration, adsorption, and mechanical film breakdown [169,181,182].

Penetration mechanism

The penetration mechanism (in Figure 3- 28 (a)) is created by Hoar [181]. It is based the movement the ions through the passive film to reach the metal/passive interface under an electric field. The ions can penetrate the passive film through the imperfect regions. The ions penetrate rate is related to the potential across the passive film, and then the breakdown of the passive

film results in the pit corrosion [183,184]. Some researchers support the penetration mechanism [185,186]. However, some researchers disagree this mechanism, as Cl^- ions do not be detected in the passive film at and above the passivation potential. In other words, Cl^- can not penetrate the passive film [187,188].

Adsorption mechanism

The adsorption mechanism (in Figure 3- 28 (b)) is described by Uhlig [182]. It describes the competitive absorption between the aggressive ions; chromate and oxygen in the passive film. With a larger concentration of aggressive ions replace oxygen and chromate in the passive film, the passive film broken and then result in pit nucleation. Hoar [181] noticed a thinner passive film, caused by locally adsorbed aggressive ions and the breakdown of the passivity after a local high electric field strength. However, Bardwell rejects this mechanism, he notices the passive film under anodic galvanostatic charging at 5 $\mu A.cm^{-2}$ in pH 8.4 borated buffer solution with halide or halide-free. The same growth rate was found on the iron with and without halides, which is opposite to adsorption mechanism [189].

Mechanical film breakdown

Mechanical film breakdown mechanism (in Figure 3- 28 (c)) involves a continoues process of the passive film breakdown and repair. Stress sources, such as defects, impurities, misfits, and hydration result in tension stress. Then a high electric field could generate electrostriction pressure, results in compressive stress, the tension and compression stress, which breaks the passive film [169]. In Cl^- environment, the local breakdown sites are hard to repair due to the repassivate inhibitor Cl^- , so pit nucleation occurs [183]. Strehblow [190] finds a high concentration ions prevent the passive film repair. However, according to the mechanical film breakdown, a high current density is achieved after the pit nucleate, results in the formation of the salt film [191].

All theories could not explain the entire phenomenon of pit nucleation. A successful model should explain where the pit localised nucleation site and why the exist a critical pitting potential? How is the applied potential influencing

the induction time? How is the function of aggressive and inhibiting ions to the pitting nucleation, and role oxide film thickness contributes to the pit nucleation? One of the possible methods to answer these questions is the combination of two or more theories [176].

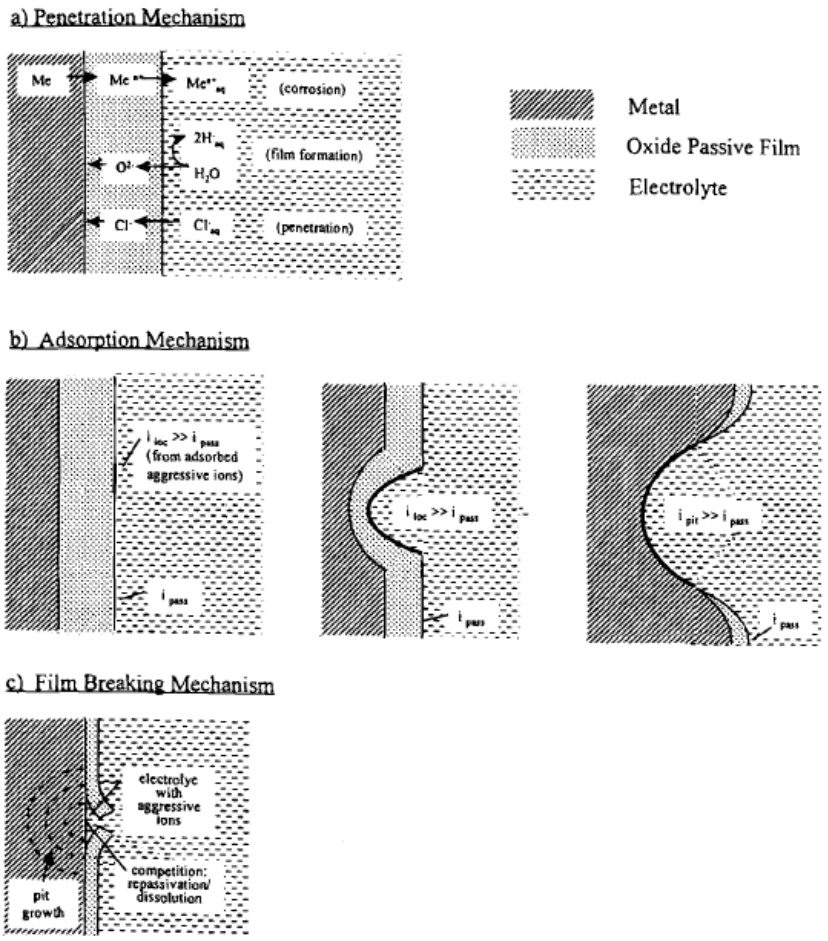

Figure 3- 28 Passive film breakdown mechanism: (a) Penetration, (b) adsorption, and (c) mechanical film breakdown [183].

The microstructural misfits might result in pitting corrosion. The misfits sites includes on the stainless steel included the chromium depletion region [96,97]**,** inclusions (e.g MnS) [104], grain boundary sites [192] and slip band sites [193]. Pits nucleate at the MnS inclusions, as the MnS can locally reduce the critical pitting potential and prevent the pit passivation [194,195]. The size of MnS changed the metastable pit lifetime and the distribution of the MnS influence the numbers of nucleated pits [196]. The pitting corrosion nucleates near the chromium carbides, as galvanic corrosion effect, Cr depletion area, or crevice

geometry. Micro galvanic corrosion is caused by more noble chromium carbides (cathode) and less noble surrounding region acted as the anode, pit nucleation associates with the galvanic effect [79,197]. The Cr depletion region is sensitive to localised corrosion as the low Cr concentration cannot formed the passive film [96,97]. The micro-cavities exists at the interface between the carbides and the matrix, the occulted geometry can accumulate to the aggressive electrolyte, then support the pit nucleation [198]. In martensitic stainless steel, pits nucleates at the sub-grain boundaries in martensitic grain or at grain boundaries between martensitic grains, due to a high grain orientation spread (GOS) [199]. For duplex stainless steel, the localised corrosion sites are related to selective phase dissolution of either ferrite or austenite, with the local environment and chemistry affects preferable dissolution sites [200]. In HCl environment, the selective phase dissolution and pitting preferentially nucleate in the ferrite. However, in HNO_3 or KOH environments, localised corrosion preferentially nucleates in the austenite phase [200,201].

The electrolyte temperature could decrease the pit repassivation potential (E_{rp}) and pit induction time(t_i) [202]:

$$E_{rp}=A+B \log(Cl^-) \qquad \text{Equation 3.9}$$

$$\text{Log } t_i= C+D \log(Cl^-) \qquad \text{Equation 3.10}$$

A, B, C, and D coefficients are temperature dependent. At a constant concentration of Cl^-, the pit repassivation potential is reduced at a higher electrolyte temperature. Since the passive film becomes more porosity from a higher electrolyte temperature [202].

3.42 Metastable pit growth

Frankel [183] defines the metastable pitting potential, that as pits initiate at a potential lower than the pitting potential, but it repassivated after a short time. The metastable pits in Type 302 stainless steel with 0.1M NaCl under the constant potential of 420 mV_{SCE} shown in Figure 3- 29. The sudden current increasing is caused by the pit nucleation and growth. Then the current dropped back to the background after a few seconds as the pit repassviate. A

good linear relationship is found between the metastable pitting potential and the stable pitting potential in the different concentration Cl^- electrolyte for Q235, X70, pure iron, and Type 316L stainless steel. So the metastable pitting potential is an important parameter to predict the stable pitting potential [203].

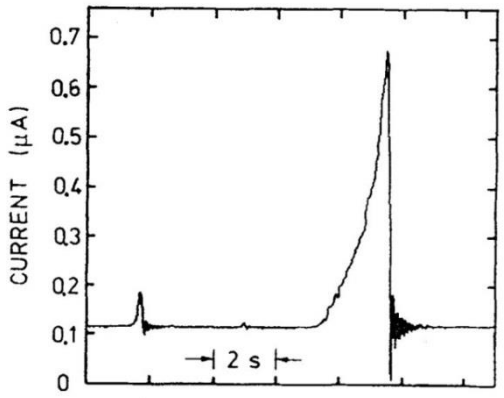

Figure 3- 29 Metastable pitting current for Type 302 stainless steel in 0.1M NaCl at 420mV$_{SCE}$ [204].

The growing of a metastable pit requires a lacy cover at the pit mouth, which acts as a diffusion barrier to maintain the aggressive pit electrolyte [171]. The lacy cover is the pre-exist passive film, the pores on the lacy cover allows ions exchange inside of pit and bulk electrolyte. The metastable pits repassived after the lacy cover break [204]. Whether the salt film formed during metastable pit growth or stable pit growth is controversial, Newman [173] mentions that the salt film isformed during metastable growth. However, Frankel [204] suggests the precipitation of a salt film in an indicator for the pit stable growth. So, no salt film forms during the metastable pit growth. Newman [172] then notices a salt film under metastable pit growth, but the composition is not the stable salt film ($FeCl_2$). The composition of the salt film is similar to the passive film of iron in H_2SO_4 electrolyte.

Metastable pits could growth below than the critical pitting potential and critical pitting temperature. Newman [172] researches the metastable pits in Type 904L stainless steel under 1M NaCl, the metastable pits could nucleate at 50℃, which is lower than the critical pitting temperature (CPT). Below the CPT, the numbers of nucleated metastable pits are increasing with higher

temperatures. The shape of the metastable pits become more open with the higher electrolyte temperature [205]. Metastable pits are determined in Type 304 stainless steel in 0.1M HCl at OCP, but the lifetime of the pit is up to a few seconds [206]. Frankel [204] studies the passive breakdown and metastable pit growth for Type 302 stainless steel in 0.1M HCl occurs at the potential of -210 mV_{SCE}, which is much lower than the critical pitting potential.

3.43 Stable pit growth

Stable pits could propagate without the lacy cover, as stable salt film formed [173]. For a stable pit, the pit depth is enough to act as a diffusion barrier to maintain the propagation. After the pit stable growth, the pit continues growth above the repassivation potential [207].

Stable pits only could be formed above a critical pitting potential or critical pitting temperature. The temperature changes critical pitting potential by the different electrochemical reactions, the salt film, and passive film properties. Figure 3- 30 shows the relationship between the temperature and the critical pitting potential. Above the room temperate, the critical pitting potential in 18-8 stainless steel is only slightly reduced with the increased temperature. The critical pitting potential is dramatically reduced below the room temperature , as the oxidation reduction: Fe^{2+}—Fe^{3+}+e^- occurs, which prevents the pitting corrosion reactions in $FeCl_3$ electrolyte [208]. The early stage of a stable pit growth also needs a lacy cover, and the critical concentration to precipitated the salt film at the pit bottom only occurs above CPT [209]. The composition of the salt film inside of the pit is $FeCl_2$, Newman [210] suggested no stable pits could be formed lower than the CPT. As the pits growth below CPT are in the salt film free states, which can stabilize the pit growth. On the other hand, the salt film retards the pit growth, as the salt film consumsthe acidity process, resulted in the pit repassivate. The passive film is largely intact below the CPT, so only metastable pit could be nucleated. [211]. The critical pitting potential becomes more negative with higher temperature. The effect of temperature influences the pitting potential variuos, the critical pitting potential in 0.5M NaCl + 0.1M $NaHCO_3$, the factors of the critical pitting potential changed by temperature is Incoloy > Type 304 stainless steel > Inconel 600 > Monel [212].

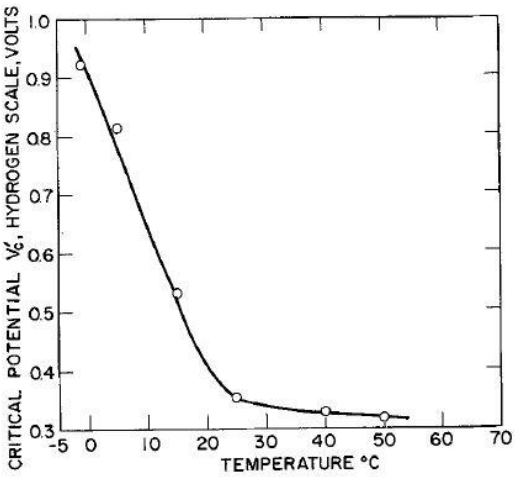

Figure 3- 30 The relationship between the critical pitting potential and electrolyte temperature in 0.1N NaCl for 18-8 stainless steel [208].

The critical pitting temperature measured from different methods is not the same. The critical pitting temperatures are compared for DSS 2205 in 1.6M $FeCl_3$ with pH=-0.2 from the electrochemical impedance spectroscopy (EIS), zero resistance ammeter, potentio-static and potentio-dynamic polarisation test. Potentio-static polarisaiton test showed the CPT value is about 50 ℃, higher than the measured CPT between 40 and 45 ℃ in the other corrosion test methods. Potentio-dynamic polarisation test has a higher CPT measurement, which is caused by the passive film increased by formerly applied potential in the passive potential region [213].

A critical potential is required to transient the metastable pit growth to stable pit growth, which is related to the formation of a stable salt film. The applied potential is proportional to the thickness of the salt film, which sustains the pit stable growth. As the salt film offers over 95% of the potential drop due to the high electric resistivity of 10^8 Ohm.cm^2 [214].

3.44 Pit growth rate

Three stages of over-potential controls the pitting corrosion shown in Figure 3- 31. At a low over-potential, the region is in the activation control region (region (I)) with a low current response, and all the current is consumed at the interface of metal/solution. Increasing the over-potential, the region (II) is reached, the pit growth is controlled by the current resistance or potential drop; the current is increased as the higher over-potential. In region (III) with a higher

over-potential, the pit growth is under diffusion controlled. Then current response is independent to the applied potential [215].

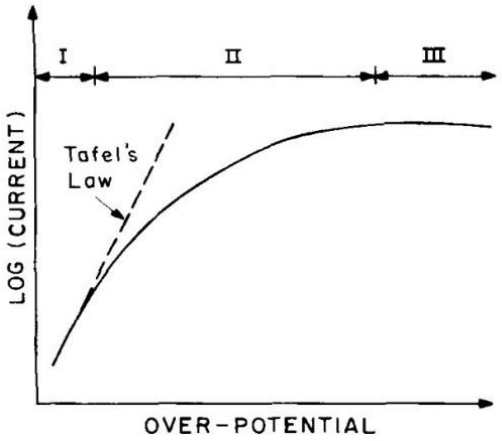

Figure 3- 31 Different over-potential regions of the electrochemical reactions [215].

The pit growth is time dependent and independent of the applied potential under the diffusion control. The pits growth in the Al at a constant applied potential shows that the pit depth (d) is proportional to the square root of time (t) [183].

The pit depth (L) growth with time (t) dependent is shown as Equation 3.11:

$$L = k\, t^{m}$$ Equation 3.11:

t is the time, k and m are the empirical constant and m usually < 1 [216].

The relationship between pit depth and time from Equation 3.11 is proofed by Cavanaugh [217], he measures the pit depth growth in AA7075 in 0.1M NaCl. The pit depth fitted well with Equation 3.11 in different pH, temperature and Cl^-. k is 4.8 with pH=10 at 40 ℃, m is varied in different experimental conditions, m=0.25 is in alkaline and high temperature environment and m=0.5 in neutral and low temperature environment which shown in Figure 3- 32. Competition between the pitting corrosion and general corrosion can retard the pit growth. The pit growth kinetics changes with environment, where pit growth is highest under cold, acid conditions and lowest under hot, alkaline conditions.

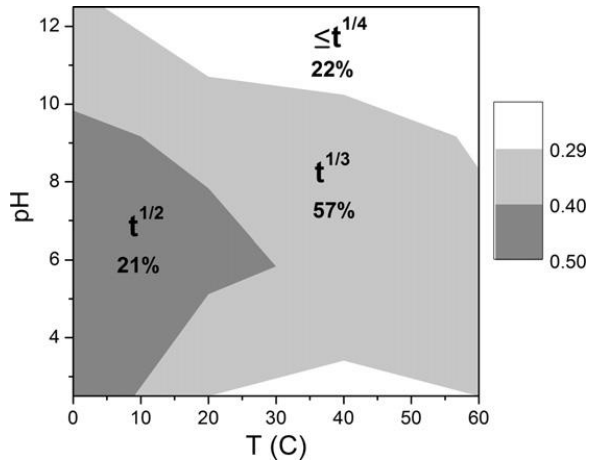

Figure 3- 32 The pit growth factor (k) as a function of temperature and the pH [217].

The pit volume is related to the applied potential. Newman [207] studies the pit growth kinetics with lacy cover for type 304 stainless steel in 1 M NaCl at 15 ℃ at a constant potential of 0.6 V_{SCE}, a semi-quantitative model based on concentration gradients and active/passive transitions are used to determine the pit growth and morphology. The pit growth in depth direction is independent of the applied potential due to the salt film precipitated. However, the pit growth in width direction is increased markedly with the applied potential as no salt film precipitate. So the pit volume is increasing with the higher applied potential.

The pit growth kinetics is potential independent, but it changes with experiment time. Newman [218] studies a single pit growth in Type 304 stainless steel in 1M sodium chloride + 0.04M sodium thiosulfate. It is found the value of n equal to 0.5 before 100 seconds and after 300 seconds; but the value of n becomes 2/3 between 100 seconds and 300 s seconds. Due to absence of the measured current density from Newman's experiment. Frankel [219] suggests the shape of the pit is a semi-circular shape pit, and then the calculated current density is proportional to $t^{-1/2}$ before 100 s and $t^{-1/3}$ after 100 seconds.

The pit growth rate in depth direction potential independent is rejected by Hunkeler [220]. He determines the pit growth rate in for Al foils in an alkaline environment, the value of k and m changes by Cl^- concentration and applied potential. It is found the value of k is influenced by the applied potential and

composition of the electrolyte, but m is independent constant to different applied potential. With increasing the applied potential from -750 V_{SCE} to -450 mV_{SCE}, and Cl^- concentration increased from 10^{-3} M $Cl^-$to 1M Cl^-. k varies between 2.76 and 22.22, but m is almost constant at around 0.5. So, the pit growth factors are both changed by the applied potential and electrolyte composition.

3.45 Electrolyte inside of pit

A low pH and high concentration of Cl^- is found in the pit electrolyte. The pit growth kinetics is controlled by pH and concentration of Cl^-. Wilde [221] uses liquid nitrogen to freeze the pit electrode to analysis the pH value and calculate the ratio of Fe^{2+}/Fe^{3+}. He find pH and ratio of Fe^{2+}/Fe^{3+} changes with the different applied potential shown in Table 3. 2. The pit electrolyte is taken from an artificial pit in Type304 stainless steel wires in 1M NaCl, different potential (from -0.2 V_{SCE} to +0.5 V_{SCE}) is applied until the dissolved volume reached to 0.32 cm. The measured pH varies from 0 to 3.6 with the corresponding ratio of Fe^{2+}/Fe^{3+} changes from 9.8 to 1.59. The pH increases with a lower ratio of Fe^{2+}/Fe^{3+}, caused by the hydrolysis reactions associated with the generation of Fe^{2+}. A lower pH could be achieved after a longer dissolution time at a more negative applied potential. So the increased pit growth rate is not only related to the generation of H^+, but also the concentration of Cl^- in the cavity.

Table 3. 2 Summary of pH and ratio of Fe^{2+}/Fe^{3+} with different applied potential for the artificial pit in Type 304 stainless steel with 1 M NaCl at room temperature [221].

	Control potential V(sce)	Period of exposure at fixed potential after 10 min at 0·500 V(sce) h	Observed pH (±0·1 unit)	Fe(II)/Fe(III)
1	0·500	4·0	3·6	1·59
2	0·100	20	3·5	3·9
3	0	19	2·0	5·6
4	−0·050	17	2·2	5·2
6	−0·100	24	2·0	5·4
8	−0·150	42	1·3	8·0
10	−0·200	61	0·0	9·8

Suzuki [222] analysis the artificial pits generated in 0.5N NaCl at 70℃ for three different austenitic stainless steels (304L, 316L, and 18Cr-16Ni-5Mo) under the galvanostatically condition (15 mA/cm^2). 200 μL pit electrolyte after each measurement is extracted for metallic and chloride ions analysis. The pH value and concentration of different ions (metal and chloride) for different

stainless steels are measured and compared showed as Table 3. 3. The value of pH is between -0.13 and 0.8 with chloride concentration from 3.78 N to 6.47 N. The lower pH value is also caused by the dissolving of Cr and Mo, as the same proportions to pH. The measured pH is lower than the thermodynamic calculation, as the hydroxyl-chloro complexes of dissolved metal ions and a higher concentration of Cl- ions results in higher measured pH.

Table 3. 3 The pH value and metallic/chloride ions in the artificial pits for Type 304L, 316L and 18Cr-16Ni-5Mo stainless steel [222].

Steel	pH	Metallic Ion (N)	Chloride Ion (N)	Steady State Potential (V, SCE)	Open Circuit Potential (V, SCE)
Type 304L	0.60 ~ 0.80	Fe^{2+} 2.31 Cr^{3+} 1.06 Ni^{2+} 0.34 Mo^{3+} – Mn^{2+} 0.06 Na^{+} 0.06 Total 3.83	3.87	-0.25 ~ -0.26	-0.31 ~ -0.32
Type 316L	0.06 ~ 0.17	Fe^{2+} 4.30 Cr^{3+} 1.50 Ni^{2+} 0.68 Mo^{3+} 0.14 Mn^{2+} 0.10 Na^{+} 0.08 Total 6.80	6.47	-0.20 ~ -0.22	-0.25 ~ -0.26
18Cr-16Ni-5Mo	-0.13 ~ 0.08	Fe^{2+} 3.26 Cr^{3+} 1.79 Ni^{2+} 0.95 Mo^{3+} 0.31 Mn^{2+} 0.09 Na^{+} 0.10 Total 6.50	6.20	-0.18 ~ -0.20	-0.24 ~ -0.26

The high Cl^- concentration with low pH for the pit electrolyte is also measured by Mankowski [223]. He studies the concentration of Cl^- inside of pit for 18Cr-12No-2Mo-Ti austenitic stainless steel in 0.5N NaCl + 0.1N H_2SO_4 at a constant potential (+860 mV_{NHE}) at 20℃. The maximum Cl^- concentration inside of the pit is 12 N, but Cl^- concentration reduces to 2 N after the pit lacy cover ruptured. The low pH value is caused by the hydrolysis of the corrosion products. The pit growth is under diffusion control as the pit growth rate decreaseswith a higher concentration of Cl^- inside of the pit.

3.46 Salt film inside of pit

The pit would be repassivated after the lacy cover rupture unless a stable salt film formed at the pit bottom [204]. The pit dissolution is controlled by the ions diffuse through the salt film [214]. After a critical metal cation reaches inside of the pit, then the stable salt film ($FeCl_2$) precipitated. The pit growth kinetics

is limited by the dissolution rate of the salt film and the metal ions concentration gradient inside of the pit [207].

Grimm [224] models a mass-transfer-limited dissolution of iron in the electrolyte contained a 4.0M $FeCl_2$, a salt film with two layer structure is formed from the AC impedance measurement. The salt film has a compact, inner layer with high field conduction and a porous and outer layer with low field conduction. The thickness of the inner layer is increasing with higher applied potential. The ionic-charge-carrier density in the film increases with higher limiting-current density. West [225] uses electro-hydrodynamic impedance to analysis the two-layer salt film. He notices the electrical resistance of the outer layer salt film is increasing with higher applied potential due to the porosity and thickness of salt film changed. Grimm [226] find the precipitation of the salt film consisted of an inner compact layer and out porous layer inside of for Fe-15Cr and Fe-25 Cr stainless steel in the $FeCl_2$ and NaCl electrolyte. A high electric conductive properties comes from the inner compact layer. Precipitation of the salt film limited the current plateau by mass transport of Fe^{2+} from the salt film to the bulk electrolyte.

3.47 Pit morphology

Both applied potential and exposure time changes the pit shape. Metastable pit shape changes from deep-like to dish-like with longer experimental time. More openness pit results in easier to repassivation as the shorter diffusion length; the pit shape change also caused by different electrolyte at the pit mouth and pit depth [227]. At a higher applied potential, the pit shape is disk-like [2]. The ratio of pit diameter to pit depth is increasing with higher temperature, as the dissolution at pit depth and pit diameter is not the same [228]. Williams [229] find the high occluded pits nucleates at low applied potential, and pits become more openness at higher applied potential.

The pit surface morphology is changed by applied potential. Figure 3- 33 shows the pit surface morphology changed at finish potential from the potentio-dynamic polarisation test. The pits are in the active state at low applied potential and in polishing state at a higher applied potential. The irregular etch pit surface comes from the selective corrosion of the specific

crystal plane in the pit. Pits in the polish state are close to hemi-spherical shape [230].

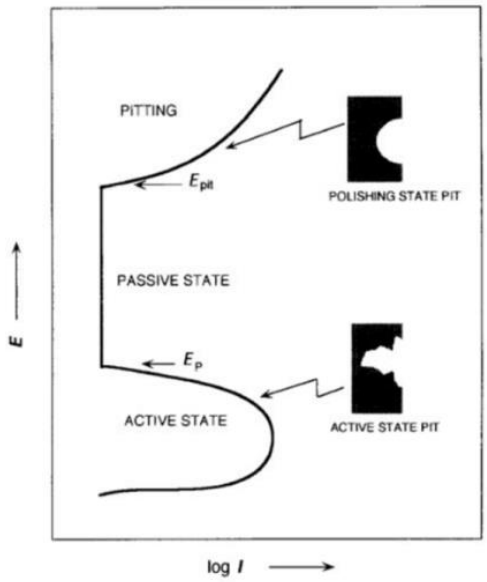

Figure 3- 33 Anodic polarisation curve for different pit state (polishing or active) with different potential range [230].

Pits surface morphology is also change with time. Schwenk [231] researches the pitting corrosion in type 304 stainless steel with 1M sodium chloride include and exclude 1N sulfuric acid and 0.5M sodium nitrate by a potentio-static technique. The pits initially grow as hemi-spherical, but then becomes dish like after long experiment time. Below the E_{pit}, the pit is etched with circular, hexagonal, or square edges. Above the E_{pit}, the pit surface becomes smooth and polished with fully isotropic. The pit surface contains etched surface as the preferential dissolution of the crystallographic plane due to the low current density. At a high current density, the dissolution rate inside of the pit becomes uniform which results in a smooth pit surface.

The electrolyte temperature influences the pit shapes. Newman [205] analysis the pits for Type 904L stainless steel polarized at 750mV_{SHE} with temperature from 10 ℃ to 2 ℃ lower than the CPT. Pits becomes more openness closer to the CPT. A new type large size metastable pit is nucleated at the temperature very close to CPT. The new type pits could not transfer to stable pits as an extreme anodic current density is required, which cannot be achieved. For the repassivate pits nucleates under the CPT had two different morphologies, one

issmall volume with small transients, and the other one was the polished surface for large transients. For metastable pits, the temperature influences the pit growth factor. The pit current density follows a law relationship $I \sim t^n$, below the CPT, n is from 0.5 to 1.5 which depends on the temperature.

Gravity influences the pit morphology by changing pit electrolyte distribution and stability of salt film in the pit. The faceup orientation samples generatethe dish like pits, pit shapes in the facedown orientation are narrow, and the pits in the perpendicular orientation have the intermediate shape [232]. Different pit shapes are caused by the stability of the salt film. Gravity removes the salt film at the pit bottom which results in narrow shape pits. For the faceup orientation, gravity encourages the salt film precipitate at pit bottom and results in either in the semi-circular or dish like pit [173,230,232]. The Cl^- concentration inside of the pits in the facedown and perpendicular orientations is lower than the faceup orientation. As gravity directly moves Cl^- out of the pit (facedown orientation), and indirectly removes the Cl^- at the pit mouth (PE orientation). So it is difficult to form the stable salt film for the FD and PE orientations [215,223,232]. For the facedown and perpendicular orientations, pit prefers propagated in depth direction for two reasons: 1, increasing the diffusion length to the keep aggressive electrolyte. 2, pit has a higher current density at a high aspect ratio shape [233–235].

3.5 References

[1] S. Munktell, Bipolar Electrochemistry for high throughput screening applications, ACTA Universitatis upsaliensis, 2016. http://urn.kb.se/resolve?urn=urn:nbn:se:uu:diva-277937.

[2] Y. Zhou, D.L. Engelberg, Application of a modified bi-polar electrochemistry approach to determine pitting corrosion characteristics, Electrochem. Commun. 93 (2018) 158–161. https://doi.org/10.1016/j.elecom.2018.06.013.

[3] N. Pébère, V. Vivier, Local electrochemical measurements in bipolar experiments for corrosion studies, ChemElectroChem. 3 (2016) 415–421. https://doi.org/10.1002/celc.201500375.

[4] S.E. Fosdick, K.N. Knust, K. Scida, R.M. Crooks, Bipolar electrochemistry, Angew. Chemie - Int. Ed. 52 (2013) 10438–10456. https://doi.org/10.1002/anie.201300947.

[5] F. Mavré, R.M. Crooks, J.A. Crooks, E. Sheridan, B.-Y. Chang, K.-F. Chow, A Theoretical and Experimental Framework for Understanding Electrogenerated Chemiluminescence (ECL) Emission at Bipolar Electrodes, Anal. Chem. 81 (2009) 6218–6225. https://doi.org/10.1021/ac900744p.

[6] A. Eden, K. Scida, N. Arroyo-Currás, J.C.T. Eijkel, C.D. Meinhart, S. Pennathur, Discharging behavior of confined bipolar electrodes: Coupled electrokinetic and electrochemical dynamics, Electrochim. Acta. 330 (2020). https://doi.org/10.1016/j.electacta.2019.135275.

[7] A. Eden, K. Scida, N. Arroyo-Currás, J.C.T. Eijkel, C.D. Meinhart, S. Pennathur, Modeling Faradaic Reactions and Electrokinetic Phenomena at a Nanochannel-Confined Bipolar Electrode, J. Phys. Chem. C. 123 (2019) 5353–5364. https://doi.org/10.1021/acs.jpcc.8b10473.

[8] A. Kuhn, R.M. Crooks, S. Inagi, A compelling case for bipolar electrochemistry, ChemElectroChem. 3 (2016) 351–352. https://doi.org/10.1002/celc.201500569.

[9] L. Koefoed, S.U. Pedersen, K. Daasbjerg, Bipolar electrochemistry—A wireless approach for electrode reactions, Curr. Opin. Electrochem. 2 (2017) 13–17. https://doi.org/10.1016/j.coelec.2017.02.001.

[10] G. Loget, A. Kuhn, Shaping and exploring the micro- and nanoworld using bipolar electrochemistry, Anal. Bioanal. Chem. 400 (2011) 1691–1704. https://doi.org/10.1007/s00216-011-4862-1.

[11] D.C. Eardley, D. Handley, S.P.S. Andrew, Bipolar electrolysis with intra phase conduction in two phase media, Electrochim. Acta. 18 (1973) 839–848. https://doi.org/10.1016/0013-4686(73)85036-4.

[12] G. Loget, A. Kuhn, Propulsion of microobjects by dynamic bipolar self-regeneration, J. Am. Chem. Soc. 132 (2010) 15918–15919. https://doi.org/10.1021/ja107644x.

[13] C. Warakulwit, T. Nguyen, J. Majimel, M.H. Delville, V. Lapeyre, P. Garrigue, V. Ravaine, J. Limtrakul, A. Kuhn, Dissymmetric carbon nanotubes by bipolar electrochemistry, Nano Lett. 8 (2008) 500–504. https://doi.org/10.1021/nl072652s.

[14] G. Loget, J. Roche, E. Gianessi, L. Bouffier, A. Kuhn, Indirect bipolar electrodeposition, J. Am. Chem. Soc. 134 (2012) 20033–20036. https://doi.org/10.1021/ja310400f.

[15] F. Goodridge, C.J.H. King, A.R. Wright, Performance studies on a bipolar fluidised bed electrode, Electrochim. Acta. 22 (1977) 1087–1091. https://doi.org/10.1016/0013-4686(77)80044-3.

[16] C. Ulrich, O. Andersson, L. Nyholm, F. Bjorefors, Formation of molecular gradients on bipolar electrodes, Angew. Chemie - Int. Ed. 47 (2008) 3034–3036. https://doi.org/10.1002/anie.200705824.

[17] J.C. Bradley, H.M. Chen, J. Crawrford, J. Eckert, K. Ernazarova, T. Kurzeja, M. Lin, M. McGee, W. Nadler, S.G. Stephens, Creating electrical contacts between metal particles using directed electrochemical growth, Nature. 389 (1997) 268–271. https://doi.org/10.1038/38464.

[18] S. Inagi, Y. Ishiguro, M. Atobe, T. Fuchigami, Bipolar patterning of conducting polymers by electrochemical doping and reaction, Angew. Chemie - Int. Ed. 49 (2010) 10136–10139. https://doi.org/10.1002/anie.201005671.

[19] L. Bouffier, D. Zigah, N. Sojic, A. Kuhn, Recent Advances in Bipolar Electrochemistry, in: Electroanal. Chem., 2017: pp. 20–110.

[20] G. Tisserant, J. Gillion, J. Lannelongue, Z. Fattah, P. Garrigue, J. Roche, D. Zigah, A. Kuhn, L. Bouffier, Single-Step Screening of the Potential Dependence of Metal Layer Morphologies along Bipolar Electrodes, ChemElectroChem. 3 (2016) 387–391. https://doi.org/10.1002/celc.201500313.

[21] C. Ulrich, O. Andersson, L. Nyholm, F. Björefors, Potential and current density distributions at electrodes intended for bipolar patterning, Anal. Chem. 81 (2009) 453–459. https://doi.org/10.1021/ac801871c.

[22] J.F.L. Duval, M. Minor, J. Cecilia, H.P. Van Leeuwen, Coupling of lateral electric field and transversal faradaic processes at the conductor/electrolyte solution interface, J. Phys. Chem. B. 107 (2003) 4143–4155. https://doi.org/10.1021/jp022459g.

[23] S.E. Fosdick, J.A. Crooks, B.Y. Chang, R.M. Crooks, Two-dimensional bipolar electrochemistry, J. Am. Chem. Soc. 132 (2010) 9226–9227. https://doi.org/10.1021/ja103667y.

[24] M. Li, S. Liu, Y. Jiang, W. Wang, Visualizing the Zero-Potential Line of Bipolar Electrodes with Arbitrary Geometry, Anal. Chem. 90 (2018) 6390–6396. https://doi.org/10.1021/acs.analchem.7b04881.

[25] M. Hasheminejad, Y. Fang, M. Li, Y. Jiang, W. Wang, H.Y. Chen, Plasmonic Imaging of the Interfacial Potential Distribution on Bipolar Electrodes, Angew. Chemie - Int. Ed. 56 (2017) 1629–1633. https://doi.org/10.1002/anie.201611235.

[26] F.O. Mavré, R.K. Anand, D.R. Laws, K.-F. Chow, B.-Y. Chang, J.A. Crooks, R.M. Crooks, Bipolar Electrodes: A Useful Tool for Concentration, Separation, and Detection of Analytes in Microelectrochemical Systems, (2010) 8766–8774. https://doi.org/10.1021/ac101262v.

[27] K. Kusakabe, S. Morooka, Y. Kato, Current paths and electrolysis efficiency in bipolar packed-bed electrodes, J. Chem. Eng. Japan. 15 (1982) 45–50. https://doi.org/10.1252/jcej.15.45.

[28] M. Sudoh, T. Kodera, H. Hino, H. Shimamura, Effect of anodic and cathodic reactions on oxidative degradation of phenol in an undivided bipolar electrolyzer, J. Chem. Eng. Japan. 21 (1988) 198–203. https://doi.org/10.1252/jcej.21.198.

[29] C. Comninellis, E. Plattner, P. Bolomey, Estimation of current bypass in a bipolar electrode stack from current-potential curves, J. Appl. Electrochem. 21 (1991) 415–418. https://doi.org/10.1007/BF01024577.

[30] A.M. Simões, A.C. Bastos, M.G. Ferreira, Y. González-García, S. González, R.M. Souto, Use of SVET and SECM to study the galvanic corrosion of an iron-zinc cell, Corros. Sci. 49 (2007) 726–739. https://doi.org/10.1016/j.corsci.2006.04.021.

[31] A.C. Bastos, M.C. Quevedo, O. V Karavai, M.G.S. Ferreira, Review—On the Application of the Scanning Vibrating Electrode Technique (SVET) to Corrosion Research, J. Electrochem. Soc. 164 (2017) C973–C990. https://doi.org/10.1149/2.0431714jes.

[32] H.S. Isaacs, Limitations of in situ current density mapping for vibrating electrodes close to metal surfaces, Corrosion. 46 (1990) 677–679. https://doi.org/10.5006/1.3585167.

[33] V.M. Huang, S.L. Wu, M.E. Orazem, N. Pébre, B. Tribollet, V. Vivier, Local electrochemical impedance spectroscopy: A review and some recent developments, Electrochim. Acta. 56 (2011) 8048–8057. https://doi.org/10.1016/j.electacta.2011.03.018.

[34] J.B. Jorcin, E. Aragon, C. Merlatti, N. Pébère, Delaminated areas beneath organic coating: A local electrochemical impedance approach, Corros. Sci. 48 (2006) 1779–1790. https://doi.org/10.1016/j.corsci.2005.05.031.

[35] E. Bayet, A Novel Way of Measuring Local Electrochemical Impedance Using A Single Vibrating Probe, J. Electrochem. Soc. 144 (2006) L87. https://doi.org/10.1149/1.1837562.

[36] M.M. Richter, Electrochemiluminescence (ECL), Chem. Rev. 104 (2004) 3003–3006. https://doi.org/10.1016/B978-044453125-4.50009-7.

[37] R. Liu, C. Zhang, M. Liu, Open bipolar electrode-electrochemiluminescence imaging sensing using paper-based microfluidics, Sensors Actuators, B Chem. 216 (2015) 255–262. https://doi.org/10.1016/j.snb.2015.04.014.

[38] C. Renault, K. Scida, K.N. Knust, S.E. Fosdick, R.M. Crooks, Paper-Based Bipolar Electrochemistry, J. Electrochem. Sci. Technol. 4 (2014) 146–152. https://doi.org/10.5229/jecst.2013.4.4.146.

[39] G. Loget, J. Roche, A. Kuhn, True bulk synthesis of Janus objects by bipolar electrochemistry, Adv. Mater. 24 (2012) 5111–5116. https://doi.org/10.1002/adma.201201623.

[40] G. Loget, D. Zigah, L. Bouffier, N. Sojic, A. Kuhn, Bipolar electrochemistry: from materials science to motion and beyond, Acc. Chem. Res. 46 (2013) 2513–2523. https://doi.org/10.1021/ar400039k.

[41] J.-C. Bradley, S. Babu, A. Mittal, P. Ndungu, B. Carroll, B. Samuel, Pulsed Bipolar Electrodeposition of Palladium onto Graphite Powder, J. Electrochem. Soc. 148 (2002) C647–C651. https://doi.org/10.1149/1.1391272.

[42] D. Grujicic, B. Pesic, Electrodeposition of copper: The nucleation mechanisms, Electrochim. Acta. 47 (2002) 2901–2912. https://doi.org/10.1016/S0013-4686(02)00161-5.

[43] K. Nielsch, F. Müller, A.P. Li, U. Gösele, Uniform nickel deposition into ordered alumina pores by pulsed electrodeposition, Adv. Mater. 12 (2000) 582–586. https://doi.org/10.1002/(SICI)1521-4095(200004)12:8<582::AID-ADMA582>3.0.CO;2-3.

[44] M. Sheffer, A. Groysman, D. Mandler, Electrodeposition of sol-gel films on Al for corrosion protection, Corros. Sci. 45 (2003) 2893–2904. https://doi.org/10.1016/S0010-938X(03)00106-9.

[45] K.M.S. Youssef, C.C. Koch, P.S. Fedkiw, Improved corrosion behavior of nanocrystalline zinc produced by pulse-current electrodeposition, Corros. Sci. 46 (2004) 51–64. https://doi.org/10.1016/S0010-938X(03)00142-2.

[46] S.O. Krabbenborg, J. Huskens, Electrochemically generated gradients, Angew. Chemie - Int. Ed. 53 (2014) 9152–9167. https://doi.org/10.1002/anie.201310349.

[47] A. Lundgren, S. Munktell, M. Lacey, M. Berglin, F. Björefors, Formation of Gold Nanoparticle Size and Density Gradients via Bipolar Electrochemistry, ChemElectroChem. 3 (2016) 378–382. https://doi.org/10.1002/celc.201500413.

[48] J.C. Bradley, S. Babu, P. Ndungu, Contactless tip-selective electrodeposition of palladium onto carbon nanotubes and nanofibers, Fullerenes Nanotub. Carbon Nanostructures. 13 (2005) 227–237. https://doi.org/10.1081/FST-200056245.

[49] M. Ahmaruzzaman, A review on the utilization of fly ash, Prog. Energy Combust. Sci. 36 (2010) 327–363. https://doi.org/10.1016/j.pecs.2009.11.003.

[50] W. Zhan, J. Alvarez, R.M. Crooks, Electrochemical sensing in microfluidic systems using electrogenerated chemiluminescence as a photonic reporter of redox reactions, J. Am. Chem. Soc. 124 (2002) 13265–13270. https://doi.org/10.1021/ja020907s.

[51] S. Wu, Z. Zhou, L. Xu, B. Su, Q. Fang, Integrating bipolar electrochemistry and electrochemiluminescence imaging with microdroplets for chemical analysis, Biosens. Bioelectron. 53 (2014) 148–153. https://doi.org/10.1016/j.bios.2013.09.042.

[52] H.W. Shi, M.S. Wu, Y. Du, J.J. Xu, H.Y. Chen, Electrochemiluminescence aptasensor based on bipolar electrode for detection of adenosine in cancer cells, Biosens. Bioelectron. 55 (2014) 459–463. https://doi.org/10.1016/j.bios.2013.12.045.

[53] J.C. Bradley, Z. Ma, S.G. Stephens, Electric field directed construction of diodes using free-standing three-dimensional components, Adv. Mater. 11 (1999) 374–378. https://doi.org/10.1002/(SICI)1521-4095(199903)11:5<374::AID-ADMA374>3.0.CO;2-Q.

[54] S. Morgenthaler, C. Zink, N.D. Spencer, Surface-chemical and -morphological gradients, Soft Matter. 4 (2008) 419–434. https://doi.org/10.1039/b715466f.

[55] K.F. Chow, B.Y. Chang, B.A. Zaccheo, F. Mavré, R.M. Crooks, A sensing platform based on electrodissolution of a Ag bipolar electrode, J. Am. Chem. Soc. 132 (2010) 9228–9229. https://doi.org/10.1021/ja103715u.

[56] I. Dumitrescu, R.K. Anand, S.E. Fosdick, R.M. Crooks, Pressure-driven bipolar electrochemistry, J. Am. Chem. Soc. 133 (2011) 4687–4689. https://doi.org/10.1021/ja111050h.

[57] S.E. Fosdick, R.M. Crooks, Bipolar electrodes for rapid screening of electrocatalysts, J. Am. Chem. Soc. 134 (2012) 863–866. https://doi.org/10.1021/ja210354m.

[58] J.-Z. Jiang, M.-H. Guo, F.-Z. Yao, J. Li, J.-J. Sun, J. Limtrakul, L. Bouffier, A. Kuhn, A. Kuhn, J. Wang, Propulsion of copper microswimmers in folded fluid channels by bipolar electrochemistry, RSC Adv. 7 (2017) 6297–6302. https://doi.org/10.1039/C6RA25162E.

[59] Y. Wang, R.M. Hernandez, D.J. Bartlett, J.M. Bingham, T.R. Kline, A. Sen, T.E. Mallouk, Bipolar electrochemical mechanism for the propulsion of catalytic nanomotors in hydrogen peroxide solutions, Langmuir. 22 (2006) 10451–10456. https://doi.org/10.1021/la0615950.

[60] G. Loget, A. Kuhn, Electric field-induced chemical locomotion of conducting objects, Nat. Commun. 2 (2011) 535–536. https://doi.org/10.1038/ncomms1550.

[61] P. Calvo-Marzal, K.M. Manesh, D. Kagan, S. Balasubramanian, M. Cardona, G.U. Flechsig, J. Posner, J. Wang, Electrochemically-triggered motion of catalytic nanomotors, Chem. Commun. (2009) 4509–4511. https://doi.org/10.1039/b909227g.

[62] D. Bankiewicz, E. Vainio, P. Yrjas, L. Hupa, G. Lisak, Application of bipolar electrochemistry to accelerate dew point corrosion for screening of steel materials for power boilers, Fuel. 265 (2020) 116886. https://doi.org/10.1016/j.fuel.2019.116886.

[63] C. Mele, F. Lionetto, B. Bozzini, An erosion-corrosion investigation of coated steel for applications in the oil and gas field, based on bipolar electrochemistry, Coatings. 10 (2020). https://doi.org/10.3390/coatings10020092.

[64] S. Munktell, M. Tydén, J. Högström, L. Nyholm, F. Björefors, Bipolar electrochemistry for high-throughput corrosion screening, Electrochem. Commun. 34 (2013) 274–277. https://doi.org/10.1016/j.elecom.2013.07.011.

[65] R.C. Newman, Understanding the corrosion of stainless steel, Corrosion. 57 (2001) 1030–1041. https://doi.org/10.5006/1.3281676.

[66] P.A. Schweitzer, Stainless steels, 4th ed., Elsevier Ltd, 2017. https://doi.org/10.1201/9781315140384.

[67] C.O.A. Olsson, D. Landolt, Passive films on stainless steels - Chemistry, structure and growth, Electrochim. Acta. 48 (2003) 1093–1104. https://doi.org/10.1016/S0013-4686(02)00841-1.

[68] I. Olefjord, The passive state of stainless steels, Mater. Sci. Eng. 42 (1980) 161–171. https://doi.org/10.1016/0025-5416(80)90025-7.

[69] J.H. Qiu, Passivity and its breakdown on stainless steels and alloys, Surf. Interface Anal. 33 (2002) 830–833. https://doi.org/10.1002/sia.1460.

[70] A. Iversen, Sheir's Corrosion, 2010.

[71] J.R. Davis, Alloy Digest Sourcebook: Stainless Steels, 1999. https://doi.org/10.2464/jilm.37.624.

[72] M.L. Lescoat, J. Ribis, Y. Chen, E.A. Marquis, E. Bordas, P. Trocellier, Y. Serruys, A. Gentils, O. Kaïtasov, Y. De Carlan, A. Legris, Radiation-induced Ostwald ripening in oxide dispersion strengthened ferritic steels irradiated at high ion dose, Acta Mater. 78 (2014) 328–340. https://doi.org/10.1016/j.actamat.2014.06.060.

[73] J. Wang, S. Qian, Y. Li, D.D. Macdonald, Y. Jiang, J. Li, Passivity breakdown on 436 ferritic stainless steel in solutions containing chloride, J. Mater. Sci. Technol. 35 (2019) 637–643. https://doi.org/10.1016/j.jmst.2018.10.030.

[74] J. WILLIAM D. CALLISTER, DAVID G. RETHWISCH, Fundamentals Materials science and Engineering : An Integrated Approach, 2015. 9781119230403.

[75] A.P. BOND, H.J. DUNDAS, Effects of Composition on the Stress Corrosion Cracking of Ferritic Stainless Steels, Corrosion. 24 (2013) 344–352. https://doi.org/10.5006/0010-9312-24.10.344.

[76] T.P. Perng, C.J. Altstetter, Comparison of Hydrogen Gas Embrittlement of Austenitic and Ferritic Stainless Steels., Metall. Trans. A, Phys. Metall. Mater. Sci. 18 A (1987) 123–134. https://doi.org/10.1007/BF02646229.

[77] G. George, H. Shaikh, Introduction to Austenitic Stainless Steels, Alpha Science International Ltd, 2011. https://doi.org/10.1533/9780857094018.37.

[78] R. Sola, R. Giovanardi, P. Veronesi, G. Poli, Effect of quenching method on the wear and corrosion resistance of stainless steel AISI 420 (TYPE 30Kh13), Met. Sci. Heat Treat. 54 (2013) 644–647. https://doi.org/10.1007/s11041-013-9564-1.

[79] K.H. Anantha, C. Örnek, S. Ejnermark, A. Medvedeva, J. Sjöström, J. Pan, Correlative Microstructure Analysis and In Situ Corrosion Study of AISI 420 Martensitic Stainless Steel for Plastic Molding Applications, J. Electrochem. Soc. 164 (2017) C85–C93. https://doi.org/10.1149/2.0531704jes.

[80] L.D. Barlow, M. Du Toit, Effect of austenitizing heat treatment on the microstructure and hardness of martensitic stainless steel AISI 420, J. Mater. Eng. Perform. 21 (2012) 1327–1336. https://doi.org/10.1007/s11665-011-0043-9.

[81] K. Chandra, V. Kain, N. Srinivasan, I. Samajdar, a. K. Balasubrahmanian, Temper Embrittlement and Corrosion Behaviour of Martensitic Stainless Steel 420, Adv. Mater. Res. 794 (2013) 757–765. https://doi.org/10.4028/www.scientific.net/AMR.794.757.

[82] A.N. Isfahany, H. Saghafian, G. Borhani, The effect of heat treatment on mechanical properties and corrosion behavior of AISI420 martensitic stainless steel, J. Alloys Compd. 509 (2011) 3931–3936. https://doi.org/10.1016/j.jallcom.2010.12.174.

[83] K.H. Anantha, C. Örnek, S. Ejnermark, A. Medvedeva, J. Sjöström, J. Pan, In Situ AFM Study of Localized Corrosion Processes of Tempered AISI 420 Martensitic Stainless Steel: Effect of Secondary Hardening, J. Electrochem. Soc. 164 (2017) C810–C818. https://doi.org/10.1149/2.1261713jes.

[84] I. Taji, M.H. Moayed, M. Mirjalili, Correlation between sensitisation and pitting corrosion of AISI 403 martensitic stainless steel, Corros. Sci. 92 (2015) 301–308. https://doi.org/10.1016/j.corsci.2014.12.009.

[85] L.C. Lim, M.O. Lai, J. Ma, D.O. Northwood, B. Miao, Tempering of AISI 403 stainless steel, Mater. Sci. Eng. A. 171 (1993) 13–19. https://doi.org/10.1016/0921-5093(93)90388-U.

[86] R. Gunn, Developments, grades and specifications, in: Duplex Stainl. Steels Microstruct. Prop. Appl., Woodhead Publishing, 1997: p. 3.

[87] H. Tan, Z. Wang, Y. Jiang, D. Han, J. Hong, L. Chen, L. Jiang, J. Li, Annealing temperature effect on the pitting corrosion resistance of plasma arc welded joints of duplex stainless steel UNS S32304 in 1.0M NaCl, Corros. Sci. 53 (2011) 2191–2200. https://doi.org/10.1016/j.corsci.2011.02.041.

[88] J. Nilsson, Overview Super duplex stainless steels, Mater. Sci. Technol. 8 (1992) 685–700.

[89] P. Lambert, Sustainability of metals and alloys in construction, Woodhead Publishing Limited, 2009. https://doi.org/10.1533/9781845695842.148.

[90] K.H. Lo, C.H. Shek, J.K.L. Lai, Recent developments in stainless steels, Mater. Sci. Eng. R Reports. 65 (2009) 39–104. https://doi.org/10.1016/j.mser.2009.03.001.

[91] Y. Jiang, H. Tan, Z. Wang, J. Hong, L. Jiang, J. Li, Influence of Creq/Nieq on pitting corrosion resistance and mechanical properties of UNS S32304 duplex stainless steel welded joints, Corros. Sci. 70 (2013) 252–259. https://doi.org/10.1016/j.corsci.2013.01.037.

[92] P. Shankar, U.K. Mudali, Corrosion of Austenitic Stainless Steels, 2002. https://doi.org/10.1533/9780857094018.363.

[93] V. Seetharaman, M. Sundararaman, R. Krishnan, Precipitation hardening in a PH 13-8 Mo stainless steel, Mater. Sci. Eng. 47 (1981) 1–11. https://doi.org/10.1016/0025-5416(81)90034-3.

[94] H. Nakagawa, T. Miyazaki, Effect of retained austenite on the microstructure and mechanical properties of martensitic precipitation hardening stainless steel, J. Mater. Sci. 34 (1999) 3901–3908.

https://doi.org/10.1023/A:1004626907367.

[95] A. Mandal, Processing-Microstructure-Microtexture-Property correlation of duplex stainless steels, 2016.

[96] M.W.A. Rashid, M. Gakim, Z.M. Rosli, M.A. Azam, Formation of Cr23C6during the sensitization of AISI 304 stainless steel and its effect to pitting corrosion, Int. J. Electrochem. Sci. 7 (2012) 9465–9477.

[97] P.J. Gellings, M.A. de Jongh, Grain boundary oxidation and the chromium-depletion theory of intercrystalline corrosion of austenitic stainless steels, Corros. Sci. 7 (1967) 413–421. https://doi.org/10.1016/S0010-938X(67)80054-4.

[98] Smith EH, Mechanical Engineer's Reference Book, 2001.

[99] S.A. Távara, M.D. Chapetti, J.L. Otegui, C. Manfredi, Influence of nickel on the susceptibility to corrosion fatigue of duplex stainless steel welds, Int. J. Fatigue. 23 (2001) 619–626. https://doi.org/10.1016/S0142-1123(01)00018-4.

[100] C.. Shek, K.. Wong, J.K.. Lai, D.. Li, Hot tensile properties of 25Cr-8Ni duplex stainless steel containing cellular (σ+γ2) structure after various thermal treatments, Mater. Sci. Eng. A. 231 (2002) 42–47. https://doi.org/10.1016/s0921-5093(97)00077-4.

[101] M. Kaneko, H.S. Isaacs, Effects of molybdenum on the pitting of ferritic- and austenitic-stainless steels in bromide and chloride solutions, Corros. Sci. 44 (2002) 1825–1834. https://doi.org/10.1016/S0010-938X(02)00003-3.

[102] K. Sugimoto, Y. Sawada, The role of molybdenum additions to austenitic stainless steels in the inhibition of pitting in acid chloride solutions, Corros. Sci. 17 (1977) 425–445. https://doi.org/10.1016/0010-938X(77)90032-4.

[103] R. Merello, F.J. Botana, J. Botella, M. V. Matres, M. Marcos, Influence of chemical composition on the pitting corrosion resistance of non-standard low-Ni high-Mn-N duplex stainless steels, Corros. Sci. 45 (2003) 909–921. https://doi.org/10.1016/S0010-938X(02)00154-3.

[104] M.P. Ryan, D.E. Williams, R.J. Chater, B.M. Hutton, D.S. McPhail, Why stainless steel corrodes, Nature. 415 (2002) 770–774. https://doi.org/10.1038/415770a.

[105] D.E. Williams, M.R. Kilburn, J. Cliff, G.I.N. Waterhouse, Composition changes around sulphide inclusions in stainless steels, and implications for the initiation of pitting corrosion, Corros. Sci. 52 (2010) 3702–3716. https://doi.org/10.1016/j.corsci.2010.07.021.

[106] T.S. Huang, W.T. Tsai, S.J. Pan, K.C. Chang, Pitting corrosion behaviour of 2101 duplex stainless steel in chloride solutions, Corros. Eng. Sci. Technol. 53 (2018) 9–15. https://doi.org/10.1080/1478422X.2017.1394020.

[107] R.F.A. Jargelius-Pettersson, Electrochemical investigation of the influence of nitrogen alloying on pitting corrosion of austenitic stainless steels, Corros. Sci. 41 (1999) 1639–1664. https://doi.org/10.1016/S0010-938X(99)00013-X.

[108] H. TSUGE, Y. TARUTANI, T. KUDO, The Effect of Nitrogen on the Corrosion Resistance of Stainless Steels, Corrosion. 36 (1988) 304–314.

[109] H.Y. Ha, H.S. Kwon, Effects of Cr2N on the pitting corrosion of high nitrogen stainless steels, Electrochim. Acta. 52 (2007) 2175–2180. https://doi.org/10.1016/j.electacta.2006.08.034.

[110] Z. Zhang, H. Jing, L. Xu, Y. Han, L. Zhao, J. Zhang, Influence of microstructure and elemental partitioning on pitting corrosion resistance of duplex stainless steel welding joints, Appl. Surf. Sci. 394 (2017) 297–314. https://doi.org/10.1016/j.apsusc.2016.10.047.

[111] L. Chen, H. Tan, Z. Wang, J. Li, Y. Jiang, Influence of cooling rate on microstructure evolution and pitting corrosion resistance in the simulated heat-affected zone of 2304 duplex stainless steels, Corros. Sci. 58 (2012) 168–174. https://doi.org/10.1016/j.corsci.2012.01.018.

[112] S.T. Kim, S.Y. Kim, I.S. Lee, Y.S. Park, M.C. Shin, Y.S. Kim, Effects of shielding gases on the microstructure and localized corrosion of tube-to-tube sheet welds of super austenitic stainless steel for seawater cooled condenser, Corros. Sci. 53 (2011) 2611–2618. https://doi.org/10.1016/j.corsci.2011.04.021.

[113] A. Rajasekhar, G. Madhusudhan Reddy, T. Mohandas, V.S.R. Murti, Influence of austenitizing temperature on microstructure and mechanical properties of AISI 431 martensitic stainless steel electron beam welds, Mater. Des. 30 (2009) 1612–1624. https://doi.org/10.1016/j.matdes.2008.07.042.

[114] R. Schneider, J. Perko, G. Reithofer, Heat treatment of corrosion resistant tool steels for plastic moulding, Mater. Manuf. Process. 24 (2009) 903–908. https://doi.org/10.1080/10426910902941553.

[115] L.D. Barlow, M. Du Toit, Effect of austenitizing heat treatment on the microstructure and hardness of martensitic stainless steel AISI 420, J. Mater. Eng. Perform. 21 (2012) 1327–1336.

[116] X. Lei, Y. Feng, J. Zhang, A. Fu, C. Yin, D.D. Macdonald, Impact of Reversed Austenite on the Pitting Corrosion Behavior of Super 13Cr Martensitic Stainless Steel, Electrochim. Acta. 191 (2016) 640–650. https://doi.org/10.1016/j.electacta.2016.01.094.

[117] S.Y. Lu, K.F. Yao, Y.B. Chen, M.H. Wang, N. Chen, X.Y. Ge, Effect of quenching and partitioning on the microstructure evolution and electrochemical properties of a martensitic stainless steel, Corros. Sci. 103 (2015) 95–104. https://doi.org/10.1016/j.corsci.2015.11.010.

[118] Some Metallurgical Principles, in: Introd. to Stainl. Steels, 1998: pp. 31–42.

[119] G.S. Ansell, S.J. Donachie, R.W. Messler, The effect of quench rate on the martensitic transformation in Fe-C alloys, Metall. Trans. 2 (1971) 2443–2449. https://doi.org/10.1007/BF02814881.

[120] Y. Tomita, K. Okabayashi, Effect of quench rate on microstructure and tensile properties of ALSL 4320 and 4340 steels, Metall. Trans. A. 18 (1987) 115–121. https://doi.org/10.1007/BF02646228.

[121] M. Seifert, D. Wieskämper, T. Tonfeld, S. Huth, Corrosion properties of a complex multi-phase martensitic stainless steel depending on the tempering temperature, Mater. Corros. 66 (2015) 1290–1298. https://doi.org/10.1002/maco.201508229.

[122] S.-Y. Lu, K.-F. Yao, Y.-B. Chen, M.-H. Wang, X.-Y. Ge, Influence of Heat Treatment on the Microstructure and Corrosion Resistance of 13 Wt Pct Cr-Type Martensitic Stainless Steel, Metall. Mater. Trans. a-Physical Metall. Mater. Sci. 46A (2015) 6090–6102. https://doi.org/10.1007/s11661-015-3180-1.

[123] H. Hill, S. Huth, S. Weber, W. Theisen, Corrosion properties of a plastic mould steel with special focus on the processing route, Mater. Corros. 62 (2011) 436–443. https://doi.org/10.1002/maco.200905570.

[124] R. Jiang, Y. Wang, X. Wen, C. Chen, J. Zhao, Effect of time on the characteristics of passive film formed on stainless steel, Appl. Surf. Sci. 412 (2017) 214–222. https://doi.org/10.1016/j.apsusc.2017.03.155.

[125] X.Y. Wang, D.Y. Li, Mechanical, electrochemical and tribological properties of nano-crystalline surface of 304 stainless steel, Wear. 255 (2003) 836–845. https://doi.org/10.1016/S0043-1648(03)00055-3.

[126] P. Schmuki, From Bacon to barriers: A review on the passivity of metals and alloys, J. Solid State Electrochem. 6 (2002) 145–164. https://doi.org/10.1007/s100080100219.

[127] R.D. Willenbruch, C.R. Clayton, M. Oversluizen, D. Kim, Y. Lu, An XPS and electrochemical study of the influence of molybdenum and nitrogen on the passivity of austenitic stainless steel, Corros. Sci. 31 (1990) 179–190. https://doi.org/10.1016/0010-938X(90)90106-F.

[128] M.F. Montemor, A.M.P. Simões, M.G.S. Ferreira, M. Da Cunha Belo, The role of Mo in the chemical composition and semiconductive behaviour of oxide films formed on stainless steels, Corros. Sci. 41 (1999) 17–34. https://doi.org/10.1016/S0010-938X(98)00126-7.

[129] H. Tian, X. Cheng, Y. Wang, C. Dong, X. Li, Effect of Mo on interaction between α/γ phases of duplex stainless steel, Electrochim. Acta. 267 (2018) 255–268. https://doi.org/10.1016/j.electacta.2018.02.082.

[130] W. Li, Z. Mi, S. Qin, L. Gao, J. He, L. Guo, L. Qiao, CS-AFM study on Pb-induced degradation of passive film on nickel-based alloy in high temperature and high pressure water, Corros. Sci. 144 (2018) 249–257. https://doi.org/10.1016/j.corsci.2018.08.054.

[131] F. Mohammadi, T. Nickchi, M.M. Attar, A. Alfantazi, EIS study of potentiostatically formed passive film on 304 stainless steel, Electrochim. Acta. 56 (2011) 8727–8733. https://doi.org/10.1016/j.electacta.2011.07.072.

[132] G. Lorang, M. Da Cunha Belo, A.M.P. Simões, M.G.S. Ferreira, Chemical Composition of Passive Films on AISI 304 Stainless Steel, J. Electrochem. Soc. 141 (1994) 3347–3356. https://doi.org/10.1149/1.2059338.

[133] P. Schmutz, D. Landolt, In-situ microgravimetric studies of passive alloys: Potential sweep and potential step experiments with Fe-25Cr and Fe-17Cr-33Mo in acid and alkaline solution, Corros. Sci. 41 (1999) 2143–2163. https://doi.org/10.1016/S0010-938X(99)00038-4.

[134] S. Haupt, H.H. Strehblow, A combined surface analytical and electrochemical study of the formation of passive layers on Fe Cr alloys in 0.5 M H2SO4, Corros. Sci. 37 (1995) 43–54. https://doi.org/10.1016/0010-938X(94)00104-E.

[135] S. Jin, A. Atrens, ESCA-Studies of the structure and composition of the passive film formed on stainless steels by various immersion temperatures in 0.1 M NaCl solution, Appl. Phys. A Solids Surfaces. 45 (1988) 83–91. https://doi.org/10.1007/BF00618768.

[136] X. Zhang, D.W. Shoesmith, Influence of temperature on passive film properties on Ni-Cr-Mo Alloy C-2000, Corros. Sci. 76 (2013) 424–431. https://doi.org/10.1016/j.corsci.2013.07.016.

[137] M.G. Fontana, Corrosion Engineering, Tata McGraw-Hill Education, 2005.

[138] Y. Lin, D. Yang, Corrosion and Corrosion Control Thoery, 2012. https://doi.org/10.1179/000705986798272190.

[139] K.R. Trethewey, Thermodynamic of corroison reactions, in: Corros. Students Sci. Eng., 1988: pp. 69–129.

[140] S. Ningshen, U.K. Mudali, Uniform Corrosion of Austenitic Stainless Steels, in: Corros. Austenitic Stainl. Steels, 2011: pp. 37–73. https://doi.org/10.1533/9780857094018.74.

[141] H.E.Hänninen, 6.01 Stress Corrosion Cracking, in: Compr. Struct. Integr., 2003: pp. 1–29.

[142] Z.Y. Liu, X.G. Li, C.W. Du, L. Lu, Y.R. Zhang, Y.F. Cheng, Effect of inclusions on initiation of stress corrosion cracks in X70 pipeline steel in an acidic soil environment, Corros. Sci. 51 (2009) 895–900. https://doi.org/10.1016/j.corsci.2009.01.007.

[143] B. Krawczyk, P. Cook, J. Hobbs, D.L. Engelberg, Atmospheric chloride-induced stress corrosion cracking of laser engraved type 316L stainless steel, Corros. Sci. 142 (2018) 93–101. https://doi.org/10.1016/j.corsci.2018.07.016.

[144] G. Brunner, Corrosion in Hydrothermal and Supercritical Water, Supercrit. Fluid Sci. Technol. 5 (2014) 591–619. https://doi.org/10.1016/B978-0-444-59413-6.00012-1.

[145] P. Kritzer, Corrosion in high-temperature and supercritical water and aqueous solutions: A review, J. Supercrit. Fluids. 29 (2004) 1–29. https://doi.org/10.1016/S0896-8446(03)00031-7.

[146] M. Shimada, H. Kokawa, Z.J. Wang, Y.S. Sato, I. Karibe, Optimization of grain boundary character distribution for intergranular corrosion resistant 304 stainless steel by twin-induced grain boundary engineering, Acta Mater. 50 (2002) 2331–2341. https://doi.org/10.1016/S1359-6454(02)00064-2.

[147] R.K. Dayal, N. Parvathavarthini, B. Raj, Influence of metallurgical variables on sensitisation kinetics in austenitic stainless steels, Int. Mater. Rev. 50 (2005) 129–155. https://doi.org/10.1179/174328005x14348.

[148] N. Alonso-Falleiros, M. Magri, I.G.S. Falleiros', Intergranular corrosion in a martensitic stainless steel detected by electrochemical tests, Corrosion. 55 (1999) 769–778. https://doi.org/10.5006/1.3284032.

[149] D.L. Zhang, W. Wang, Y. Li, An electrode array study of electrochemical inhomogeneity of zinc in zinc/steel couple during galvanic corrosion, Corros. Sci. 52 (2010) 1277–1284. https://doi.org/10.1016/j.corsci.2009.12.030.

[150] X.G. Zhang, Galvanic Corrosion, Uhlig's Corros. Handb. Third Ed. (2011) 123–143. https://doi.org/10.1002/9780470872864.ch10.

[151] Z.Z. Wang, Y.Y. Li, G.A. Zhang, Inhibitive effects of inhibitors on the galvanic corrosion between N80 carbon steel and 13Cr stainless steel under dynamic supercritical CO 2 conditions, Corros. Sci. 146 (2019) 121–133. https://doi.org/10.1016/j.corsci.2018.10.028.

[152] M. Pourbaix, Applications of electrochemistry in corrosion science and in practice, Corros. Sci. 14 (1974) 25–82. https://doi.org/10.1016/S0010-938X(74)80006-5.

[153] F. MANSFELD, J. V. KENKEL, Laboratory Studies of Galvanic Corrosion I. Two-Metal Couples, Corrosion. 31 (2013) 298–302. https://doi.org/10.5006/0010-9312-31.8.298.

[154] J.V.K. F. MANSFELD, D. H. HENGSTENBERG, Galvanic Corrosion of Al Alloys I. Effect of Dissimilar Metal, Corrosion. 30 (1974) 343–353.

[155] F. Mansfeld, J. V. Kenkel, Galvanic corrosion of Al alloys-III. The effect of area ratio, Corros. Sci. 15 (1975) 239–250. https://doi.org/10.1016/S0010-938X(75)80019-9.

[156] X.G. Zhang, E.M. Valeriote, Galvanic protection of steel and galvanic corrosion of zinc under thin layer electrolytes, Corros. Sci. 34 (1993) 1957–1972. https://doi.org/10.1016/0010-938X(93)90053-J.

[157] K.R. Trethewey, The mechanism of crevice corrosion, in: Corros. Students Sci. Eng., 1988: pp. 162–190.

[158] Q. Hu, G. Zhang, Y. Qiu, X. Guo, The crevice corrosion behaviour of stainless steel in sodium chloride solution, Corros. Sci. 53 (2011) 4065–4072. https://doi.org/10.1016/j.corsci.2011.08.012.

[159] D. Chen, E.H. Han, X. Wu, Effects of crevice geometry on corrosion behavior of 304 stainless steel during crevice corrosion in high temperature pure water, Corros. Sci. 111 (2016) 518–530. https://doi.org/10.1016/j.corsci.2016.04.049.

[160] A.M. Al-Zahrani, H.W. Pickering, IR voltage switch in delayed crevice corrosion and active peak formation detected using a repassivation-type scan, Electrochim. Acta. 50 (2005) 3420–3435. https://doi.org/10.1016/j.electacta.2004.12.017.

[161] G.R. Engelhardt, D.D. MacDonald, Possible distribution of potential and corrosion current density inside corroding crevices, Electrochim. Acta. 65 (2012) 266–274. https://doi.org/10.1016/j.electacta.2012.01.065.

[162] Y.H. Lee, Z. Takehara, S. Yoshizawa, The Enrichment of Hydrogen and Chloride Ions in The Crevice Corrosion of Steels, Corros. Sci. 21 (1981) 391–397.

[163] P. Chemistry, P. Academy, Crevice Corrosion of Stainless Steels In Sodium Chloride Solution, Corros. Sci. 18 (1978) 953–960.

[164] B.E. Wilde, E. Williams, The Relevance of Accelerated Electrochemical Pitting Tests to the Long-Term Pitting and Crevice Corrosion Behavior of Stainless Steels in Marine Environments, J. Electrochem. Soc. 118 (2007) 1057. https://doi.org/10.1149/1.2408246.

[165] N.J. Laycock, J. Stewart, R.C. Newman, The initiation of crevice corrosion in stainless steels, Corros. Sci. 39 (1997) 1791–1809. https://doi.org/10.1016/S0010-938X(97)00050-4.

[166] G.S. Frankel, Pitting Corrosion of Metals A Review of the Critical Factors, J. Electrochem. Soc. 145 (1998) 2186–2198. https://doi.org/10.5006/0010-9312-19.8.261.

[167] S. Pahlavan, S. Moazen, I. Taji, K. Saffar, M. Hamrah, M.H. Moayed, S. Mollazadeh Beidokhti, Pitting corrosion of martensitic stainless steel in halide bearing solutions, Corros. Sci. 112 (2016) 233–240. https://doi.org/10.1016/j.corsci.2016.07.008.

[168] B. Krawczyk, P. Cook, J. Hobbs, D. Engelberg, Corrosion behavior of cold rolled type 316L stainless steel in HCl containing environments, Corrosion. 73 (2017) 1346. https://doi.org//10.5006/2415.

[169] N. Sato, A theory for breakdown of anodic oxide films on metals, Electrochim. Acta. 16 (1971) 1683–1692. https://doi.org/10.1016/0013-4686(71)85079-X.

[170] S.M. G.Burstein, P.Pistorius, Evaluating the critical chemistry for repassivation at the corroding surface using mass transport model-based artificial pit experiments, Corros. Sci. 35 (1993) 57–62. https://doi.org/10.1016/0010-938X(93)90133-2.

[171] P.C. Pistorius, G.T. Burstein, Metastable Pitting Corrosion of Stainless Steel and the Transition to Stability, Philos. Trans. R. Soc. A Math. Phys. Eng. Sci. 341 (1992) 531–559. https://doi.org/10.1098/rsta.1992.0114.

[172] N.J. Laycock, Metastable Pitting and the Critical Pitting Temperature, J. Electrochem. Soc. 145 (1998) 2622. https://doi.org/10.1149/1.1838691.

[173] N.J. Laycock, R.C. Newman, Localised dissolution kinetics, salt films and pitting potentials, Corros. Sci. 39 (1997) 1771–1790. https://doi.org/10.1016/S0010-938X(97)00049-8.

[174] A.J. Sedriks, Plenary Lecture—1986: Effects of Alloy Composition and Microstructure on the Passivity of Stainless Steels , Corrosion. 42 (2011) 376–389. https://doi.org/10.5006/1.3584918.

[175] M. Pourbaix, L. Klimzack-Mathieiu, C. Mertens, J. Meunier, C. Vanleugenhaghe, L. de Munck, J. Laureys, L. Neelemans, M. Warzee, Potentiokinetic and corrosimetric investigations of the corrosion behaviour of alloy steels, Corros. Sci. 3 (1963) 239–259. https://doi.org/10.1016/S0010-938X(63)80030-X.

[176] J. Soltis, Passivity breakdown, pit initiation and propagation of pits in metallic materials - Review, Corros. Sci. 90 (2015) 5–22. https://doi.org/10.1016/j.corsci.2014.10.006.

[177] Z. SZKLARSKA-SMIALOWSKA, Review of Literature on Pitting Corrosion Published Since 1960, Corrosion. 27 (2013) 223–233. https://doi.org/10.5006/0010-9312-27.6.223.

[178] R.T. Loto, Electrochemical Corrosion Characteristics of 439 Ferritic, 301 Austenitic, S32101 Duplex and 420 Martensitic Stainless Steel in Sulfuric Acid/NaCl Solution, J. Bio- Tribo-Corrosion. 3 (2017) 24. https://doi.org/10.1007/s40735-017-0084-1.

[179] G.T. Burstein, Understanding Localized Corrosion through Electrochemical Measurements, ECS Trans. 3 (2007) 193–204.

[180] G.T. Burstein, S.P. Vines, Repetitive nucleation of corrosion pits on stainless steel and the effects of surface roughness, J. Electrochem. Soc. 148 (2001) B504–B516. https://doi.org/10.1149/1.1416503.

[181] T.P. Hoar, D.C. Mears, G.P. Rothwell, The relationships between anodic passivity, brightening and pitting, Corros. Sci. 5 (1965) 279–289. https://doi.org/10.1016/S0010-938X(65)90614-1.

[182] H.H. Uhlig, Adsorbed and Reaction-Product Films on Metals, J. Electrochem. Soc. 97 (1950) 215C. https://doi.org/10.1149/1.2777892.

[183] G.S. Frankel, Pitting corrosion of metals a review of the critical factors, 145 (1998) 2186–2198.

[184] H. Böhni, Breakdown of Passivity and Localized Corrosion Processes, Langmuir. 3 (1987) 924–930. https://doi.org/10.1021/la00078a010.

[185] T. Okada, Halide Nuclei Theory of Pit Initiation in Passive Metals, J. Electrochem. Soc. 131 (2006) 241. https://doi.org/10.1149/1.2115556.

[186] HUGH S. ISAACS, THE LOCALIZED BREAKDOWN AND REPAIR OF PASSIVE SURFACES DURING PITrING*, Corros. Sci. 29 (1989) 313–323.

[187] A.Schneider, D.Kuron, S.Hofmann, R.Kirchheim, AES ANALYSIS OF PITS AND PASSIVE FILMS FORMED ON Fe-Cr Fe-Mo and Fe-Cr-Mo ALLOYS, Corros. Sci. 31 (1990) 191–196. https://doi.org/10.1017/CBO9781107415324.004.

[188] V. Mitrovic-Scepanovic, B. MacDougall, M.J. Graham, The effect of Cl- ions on the passivation of Fe26Cr alloy, Corros. Sci. 27 (1987) 239–247. https://doi.org/10.1016/0010-938X(87)90020-5.

[189] J.A. Bardwell, B. MacDougall, G.I. Sproule, Use of SIMS to Investigate the Induction Stage in the Pitting of Iron, J. Electrochem. Soc. 136 (1989) 1331–1336. https://doi.org/10.1149/1.2096916.

[190] H. -H Strehblow, Nucleation and Repassivation of Corrosion Pits for Pitting on Iron and Nickel, Mater. Corros. 27 (1976) 792–799. https://doi.org/10.1002/maco.19760271106.

[191] T.R. Beck, R.C. Alkire, Occurrence of Salt Films during Initiation and Growth of Corrosion Pits, J. Electrochem. Soc. 126 (1979) 1662–1666. https://doi.org/10.1149/1.2128772.

[192] N.D. TOMASHOV, G.P. CHERNOVA, O.N. MARCOVA, Effect of Supplementary Alloying Elements On Pitting Corrosion Susceptibility Of 18Cr-14Ni Stainless Steel, Corrosion. 20 (2013) 166t-173t. https://doi.org/10.5006/0010-9312-20.5.166t.

[193] Y.R. Qian, J.R. Cahoon, Crack Initiation Mechanisms for Corrosion Fatigue of Austenitic Stainless Steel, Corros. 53 (1997) 129–135. https://doi.org/10.5006/1.3280442.

[194] R.C. Newman, H.S. Isaacs, B. Alman, Effects of sulfur compounds on the pitting behaviour of type 304 stainless steel, Corrosion. 38 (1982) 261–265.

[195] P. Marcus, A. Teissier, J. Oudar, The influence of sulphur on the dissolution and the passivation of a nickel-iron alloy-I. electrochemical and radiotracer measurements, Corros. Sci. 24 (1984) 259–268. https://doi.org/10.1016/0010-938X(84)90012-X.

[196] J. Stewart, D.E. Williams, THE INITIATION OF PITTING CORROSION ON AUSTENITIC STAINLESS STEEL: ON THE ROLE AND IMPORTANCE OF SULPHIDE INCLUSIONS, Corros. Sci. 33 (1992) 457–474. http://linkinghub.elsevier.com/retrieve/pii/0010938X9290074D.

[197] E.A. Culpan, A.G. Foley, The detection of selective phase corrosion in cast nickel aluminium bronze by acoustic emission techniques, J. Mater. Sci. 17 (1982) 953–964. https://doi.org/10.1007/BF00543513.

[198] K. Jung, K. Oh, D.-H. Nam, S. Ahn, S. Oh, H. Kwon, Effects of Centerline Segregation of Cr Carbides and Non-Metallic Inclusions on the Pitting Corrosion of Fe-13Cr-0.3C Stainless Steel Produced by Continuous Casting and Strip Casting, Corrosion. 73 (2017) 979–987. https://doi.org/10.5006/2384.

[199] V. Vignal, S. Ringeval, S. Thiébaut, K. Tabalaiev, C. Dessolin, O. Heintz, F. Herbst, R. Chassagnon, Influence of the microstructure on the corrosion behaviour of low-carbon martensitic stainless steel after tempering treatment, Corros. Sci. 85 (2014) 42–51. https://doi.org/10.1016/j.corsci.2014.03.036.

[200] C. Örnek, F. Léonard, S.A. McDonald, A. Prajapati, P.J. Withers, D.L. Engelberg, Time-dependent in situ measurement of atmospheric corrosion rates of duplex stainless steel wires, Npj Mater. Degrad. 2 (2018) 1–15. https://doi.org/10.1038/s41529-018-0030-9.

[201] S. Aoki, H. Yakuwab, K. Mitsuhashib, J. Sakaic, Dissolution Behavior of α and γ Phases of a Duplex Stainless Steel in a Simulated Crevice Solution, ECS Trans. 25 (2010) 17–22.

[202] J.-H. Wang, C.C. Su, Z. Szklarska-Smialowska, Effects of Cl − Concentration and Temperature on Pitting of AISI 304 Stainless Steel , Corrosion. 44 (2011) 732–737. https://doi.org/10.5006/1.3584938.

[203] Y. Tang, Y. Zuo, J. Wang, X. Zhao, B. Niu, B. Lin, The metastable pitting potential and its relation to the pitting potential for four materials in chloride solutions, Corros. Sci. 80 (2014) 111–119. https://doi.org/10.1016/j.corsci.2013.11.015.

[204] G.S. Frankel, L. Stockert, F. Hunkeler, H. Boehni, Metastable pitting of stainless steel, Corrosion. 43 (1987) 429–436. https://doi.org/10.5006/1.3583880.

[205] M.H. Moayed, R.C. Newman, Evolution of current transients and morphology of metastable and stable pitting on stainless steel near the critical pitting temperature, Corros. Sci. 48 (2006) 1004–1018. https://doi.org/10.1016/j.corsci.2005.03.002.

[206] Y. González-García, G.T. Burstein, S. González, R.M. Souto, Imaging metastable pits on austenitic stainless steel in situ at the open-circuit corrosion potential, Electrochem. Commun. 6 (2004) 637–642. https://doi.org/10.1016/j.elecom.2004.04.018.

[207] P. Ernst, R.C. Newman, Pit growth studies in stainless steel foils. I. Introduction and pit growth kinetics, Corros. Sci. 44 (2002) 927–941. https://doi.org/10.1016/S0010-938X(01)00133-0.

[208] H.P. Leckie, H.H. Uhlig, Environmental Factors Affecting the Critical Potential for Pitting in 18–8 Stainless Steel, J. Electrochem. Soc. 113 (2007) 1262. https://doi.org/10.1149/1.2423801.

[209] P. Ernst, R.C. Newman, Pit growth studies in stainless steel foils. II. Effect of temperature, chloride concentration and sulphate addition, Corros. Sci. 44 (2002) 927–941. https://doi.org/10.1016/S0010-938X(01)00133-0.

[210] R.C. Newman, 2001 W.R. Whitney award lecture: Understanding the corrosion of stainless steel, Corrosion. 57 (2001) 1030–1041. https://doi.org/10.5006/1.3281676.

[211] P.D. Krell, S. Li, H. Cong, Synergistic effect of temperature and HCl concentration on the degradation of AISI 410 stainless steel, Corros. Sci. (2017) 0–1. https://doi.org/10.1016/j.corsci.2017.03.027.

[212] C.J. Semino, P. Pedeferri, G.T. Burstein, T.P. Hoar, The localized corrosion of resistant alloys in chloride solutions, Corros. Sci. 19 (1979) 1069–1078. https://doi.org/10.1016/S0010-938X(79)80096-7.

[213] M. Hoseinpoor, M. Momeni, M.H. Moayed, A. Davoodi, EIS assessment of critical pitting temperature of 2205 duplex stainless steel in acidified ferric chloride solution, Corros. Sci. 80 (2014) 197–204. https://doi.org/10.1016/j.corsci.2013.11.023.

[214] H.S. Isaacs, The Behavior of Resistive Layers in the Localized Corrosion of Stainless Steel, J. Electrochem. Soc. 120 (1973) 1456. https://doi.org/10.1149/1.2403283.

[215] G.T. Gaudet, W.T. Mo, T.A. Hatton, J.W. Tester, J. Tilly, H.S. Isaacs, R.C. Newman, Mass-Transfer and Electrochemical Kinetic Interactions in Localized Pitting Corrosion, Aiche J. 32 (1986) 949–958. https://doi.org/10.1002/aic.690320605.

[216] G. Engelhardt, D.D. Macdonald, Unification of the deterministic and statistical approaches for predicting localized corrosion damage. I. Theoretical foundation, Corros. Sci. 46 (2004) 2755–2780. https://doi.org/10.1016/j.corsci.2004.03.014.

[217] M.K. Cavanaugh, R.G. Buchheit, N. Birbilis, Modeling the environmental dependence of pit growth using neural network approaches, Corros. Sci. 52 (2010) 3070–3077. https://doi.org/10.1016/j.corsci.2010.05.027.

[218] R.C. Newman, E.M. Franz, Growth and Repassivation of Single Corrosion Pits in Stainless Steel., Corrosion. 40 (1984) 325–330. https://doi.org/10.5006/1.3593930.

[219] G.S. FRANKEL, THE GROWTH OF 2-D PITS IN THIN FILM ALUMINUM, Corrosion. 30 (1990) 1203–1218.

[220] F. Hunkeler, H. Bohni, Determination of Pit Growth Rates on Aluminum Using a Metal Foil Technique., Corrosion. 37 (1981) 645–650. https://doi.org/10.5006/1.3577553.

[221] B.E. Wilde, E. Williams, The use of current/voltage curves for the study of localized corrosion and passivity breakdown on stainless steels in chloride media, Electrochim. Acta. 16 (1971) 1971–1985. https://doi.org/10.1016/0013-4686(71)85151-4.

[222] T. SUZUKI, M. YAMABE, Y. KITAMURA, Composition of Anolyte Within Pit Anode of Austenitic Stainless Steels in Chloride Solution, Corrosion. 29 (2013) 18–22. https://doi.org/10.5006/0010-9312-29.1.18.

[223] J. Mankowski, Z. Szklarska-Smialowska, Studies on accumulation of chloride ions in pits growing during anodic polarization, Corros. Sci. 15 (1975) 493–501. https://doi.org/10.1016/0010-938X(75)90015-3.

[224] R.D. Grimm, A.C. West, D. Landolt, AC impedance study of anodically formed salt film on iron in chloride solution, J. Electrochem. Soc. 139 (1992) 1622–1629.

[225] A.C. West, R.D. Grimm, D. Landolt, Electrohydrodynamic impedance study of anodically formed salt films on iron in chloride solutions, J. Electrochem. Soc. 330 (1992) 693–706.

[226] R.D.Grimm, D.Landolt, Salt films formed during mass-transport controlled dissolution of iron-chromium alloys in concentrated chloride media., Corros. Sci. 36 (1994) 1847–1868.

[227] W. Tian, N. Du, S. Li, S. Chen, Q. Wu, Metastable pitting corrosion of 304 stainless steel in 3.5% NaCl solution, Corros. Sci. 85 (2014) 372–379. https://doi.org/10.1016/j.corsci.2014.04.033.

[228] W. Tian, S. Li, N. Du, S. Chen, Q. Wu, Effects of applied potential on stable pitting of 304 stainless steel, Corros. Sci. 93 (2015) 242–255. https://doi.org/10.1016/j.corsci.2015.01.034.

[229] D.E. Williams, J. Stewart, P.H. Balkwill, The nucleation, growth and stability of micropits in stainless steel, Corros. Sci. 36 (1994) 1213–1235. https://doi.org/10.1016/0010-938X(94)90145-7.

[230] N. Sato, The stability of localized corrosion, Corros. Sci. 37 (1995) 1947–1967. https://doi.org/10.1016/0010-938X(95)00076-V.

[231] W. Schwenk, Theory Of Stainless Steel Pitting, Corrosion. 20 (1964) 129t-137t. https://doi.org/10.5006/0010-9312-20.4.129t.

[232] J. Mankowski, Z. Szklarska-Smialowska, The effect of specimen position on the shape of corrosion pits in an austenitic stainless steel, Corros. Sci. 17 (1977) 725–735. https://doi.org/10.1016/0010-938X(77)90068-3.

[233] J. Srinivasan, C. Liu, R.G. Kelly, Geometric evolution of flux from a corroding one-dimensional pit and its implications on the evaluation of kinetic parameters for pit stability, J. Electrochem. Soc. 163 (2016) C694–C703. https://doi.org/10.1149/2.1221610jes.

[234] M. Sakairi, A. Kageyama, Y. Kojima, Y. Oya, T. Kikuchi, Effect of aspect ratio of artificial pits formed on anodized Al by PRM on localized corrosion in chloride environments, Electrochem. Soc. 16 (2009) 19–28.

[235] P.C. Pistorius, G.T. Burstein, Aspects of the effects of electrolyte composition on the occurrence of metastable pitting on stainless steel, Corros. Sci. 36 (1994) 525–538. https://doi.org/10.1016/0010-938X(94)90041-8.

4. Experimental Procedures

4.1 Materials and sample preparation

The stainless steel used in this study included: Type 420, 304L, 316L, 2205, and 2101 stainless steel. The chemical composition is shown in Table 4. 1:

Table 4. 1 Chemical composition (wt%) of different stainless steel

	Cr	Ni	Mo	Mn	C	N	Fe	
304L	18.2	8.1	N/A	1.52	0.025	0.045	Bal	Austenite
316L	16.7	10.1	2.4	N/A	0.019	0.049	Bal	
2101	21.4	1.6	0.3	5.02	0.020	0.214	Bal	Duplex
2205	22.4	5.8	3.2	1.50	0.016	0.180	Bal	
420	13.7	N/A	N/A	0.39	0.46	N/A	bal	Ferritic/Martensitic

To manufacturing MSS 420. Type 420 stainless steel is put into the furnace at 950 ℃ for 1 hour and followed by water quenching. Then put them in the furnace with temperature from 250 ℃ to 700 ℃ for 1 hour and followed by air cooling. DSS 2205 is put into the furnace at different temperatures for 1 hour and followed by water quenching.

For the bipolar electrochemistry experiments, all samples are cut into 3 * 1 cm^2 (Length * Width) with different thicknesses. Samples are mounted in Araldite resin, followed by grinding to 1200 grit, with or without a polish at 1 μm diamond paste. After grinding and polishing, the samples are washed by deionized water and dry in hot air. For the 3-electrode polarisation test, the samples are cut into 2.5 * 2.5 cm, and the same surface preparation as BPE. For pitting corrosion changes by gravity in potentio-dynamic and potentio-static polarisation test. Samples are immersed in the 35% HNO_3 for 6 hours to grow a passive film on the sample surface, to avoid crevice corrosion at the sample edges. Then washed by soap water, electrically connect to a copper wire at the backside. The prepared samples are mounted in Araldite resin and followed by ground until 1200 girt. For the BPE, a plastic tube is immersed into the resin, used to change the surface orientation to achieve gravity influence the pitting corrosion.

For the Electron Backscattered Diffraction; the samples are grind to 4000 grits and polished until 0.25 µm diamond paste, then followed by fine polishing with OPS colloidal silica.

4.2 Bipolar electrochemistry

Bipolar electrochemistry setup

Figure 4- 1 shows an image of the bipolar electrochemistry setup, each feeder electrodes contain platinum with a surface area of 4 cm^2. The BPE is set in the middle of the feeder electrodes. The volume of electrolyte is 200ml with HCl from 0.01 to 0.1M. DC power sources (Keysight E36105A) are used to a power supply. The HCl environment was chosen to carry out pitting corrosion tests (chloride environment), by in parallel achieving large potential gradients acting across the BPE. We also carried out experiments using different concentrations of NaCl; however, with NaCl the cathodic reaction at the negative feeder limits the potential output between the feeder electrodes. Low concentrations of HCl were found to be the best choice for our experiments.

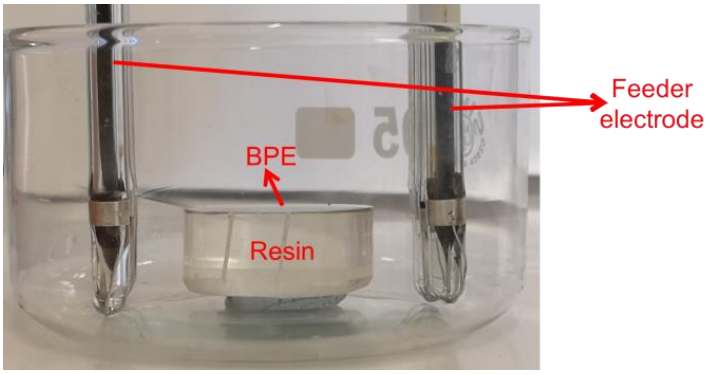

Figure 4- 1 Photo image of the bipolar electrochemistry setup.

Modified bipolar electrochemistry setup

Figure 4- 2 (a) shows the setup for the modified bipolar electrochemistry setup. For the sample preparation, a copper wire spot is welded at the back side of the BPE, and then mounted in the resin. The overall potential on the BPE is also controlled by the secondary potential; results in a wider potential range. Figure 4- 2 (b) displays a 2-D bipolar electrochemistry setup, which a secondary bipolar electrochemistry is set, which is perpendicular to the

primary bipolar electrochemistry. The secondary bipolar setup offers a secondary potential gradient on the BPE width, result in a wider and smoother potential gradient on the BPE. Figure 4- 2 (c) shows a two parallel BPEs setup, two parallel BPEs with a gap of 1mm are mounted in resin. One of the BPE is spot weld with copper wire at the back called the secondary BPE. The overall potential on the secondary BPE is controlled by a secondary applied potential and potential from feeder electrode. So, the potential difference between these two BPEs changes, which allows the generation of the galvanic corrosion between the two BPEs.

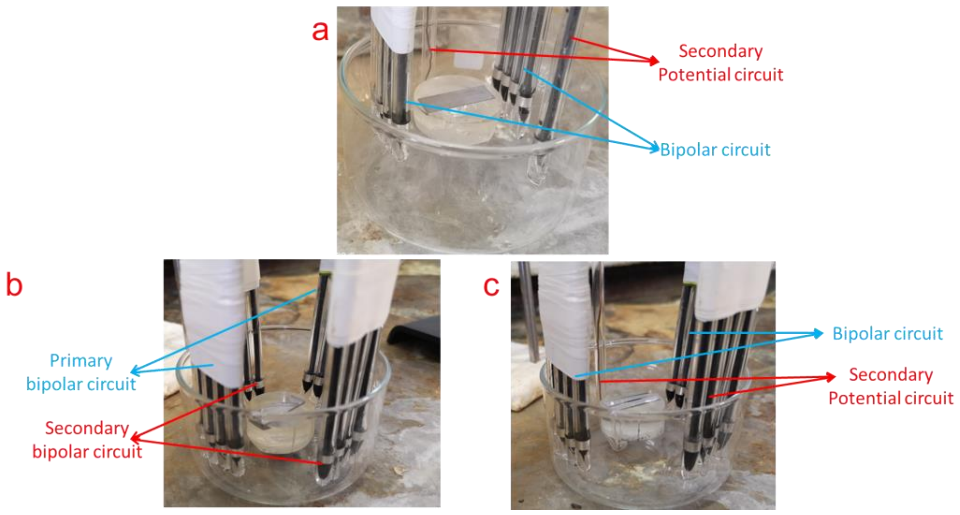

Figure 4- 2 The setup for (a) modified bipolar electrochemistry, (b) 2-D bipolar electrochemistry, and (c) parallel bipolar electrode.

Potential and current measurement setup

Figure 4- 3 (a) displays a spilt bipolar electrode, consists of small rectangle coupons. Each segment has an individual connection spot-welded to the back, and insulates to each other by electric insulation tape. Once packed the small rectangle coupons in a sequence, they have a dimension of a single BPE. Figure 4- 3 (b) shows the external connection of the split BPE. A Zero Resistance Ammeter (ZRA) is used to connect segment BPEs to measure the current flow. Figure 4- 3 (c) shows the setup for the potential distribution measurement. A Luggin probe is located above the BPE surface, and the other side connects to SCE reference electrode. The reported potential change vs OCP is the local potential change of the Lugin probe set. The

potential distribution along the BPE is measured by move the Luggin probe to different position on the BPE.

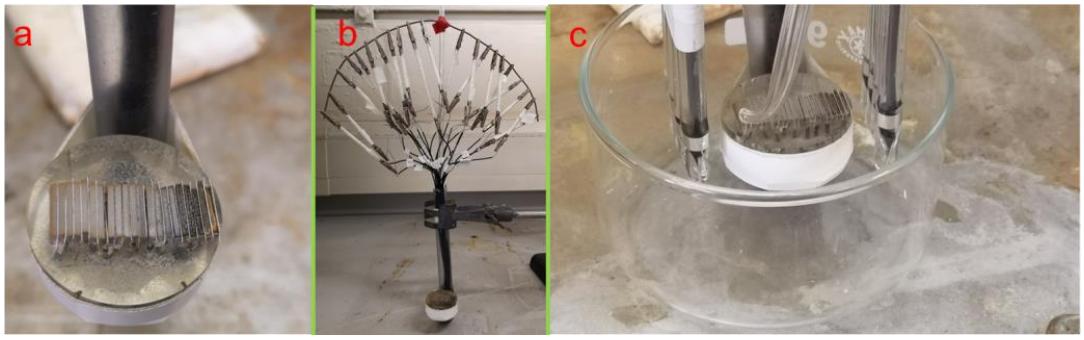

Figure 4- 3 (a) The split BPE, with (b) external connection, and (c) the potential and current measured setup.

4.3 Polarisation test

In this thesis, 3-electrode potentio-dynamic polarisation is used to determine the pitting corrosion properties of different stainless steels in HCl. 3-electrode potentio-static polarisation is used for Type 420, 304L and 316L stainless steel in 0.1M HCl. The IVIUM-Compactstat Potentiostat with corresponding IVIUM software is used to analyze the obtained polarisation curves. The current range is 100 mA with an accuracy of 0.2 % and the applied potential accuracy is 1 mV. The current response is recorded at a rate of 1 Hz.

Figure 4- 4 (a) gives the setup for the Avesta cell. The critical pitting potential is tested in the Avesta cell, without the generation of the crevice corrosion [1]. Crevice corrosion is avoided from the Avesta cell is due to a special design. A fine porous filter paper is attached to the sample which allows the distilled water pumped into a circular chamber and wetted the sample located in the base plate of the cell. The edges of the sample have no crevice corrosion due to the distilled water; the electrolyte concentration at the entire sample surface would not be changed due to the low density of water flow. Experiments show no crevice corrosion at elevated temperatures and high current density after post observation [2]. The exposed surface area in the Avesta cell is 1cm^2. Pt electrode is the counter electrode and the reference electrode was a saturated calomel electrode (SCE) reference electrode. Figure 4- 4 (b) is the setup for the polarisation test influenced by gravity. Due to the sample surface orientation in the Avesta cell cannot be adjusted. So, samples with spot

welded at the rear side covered by plastic tube is used, then the different surface orientation is achieved by bending the plastic tube.

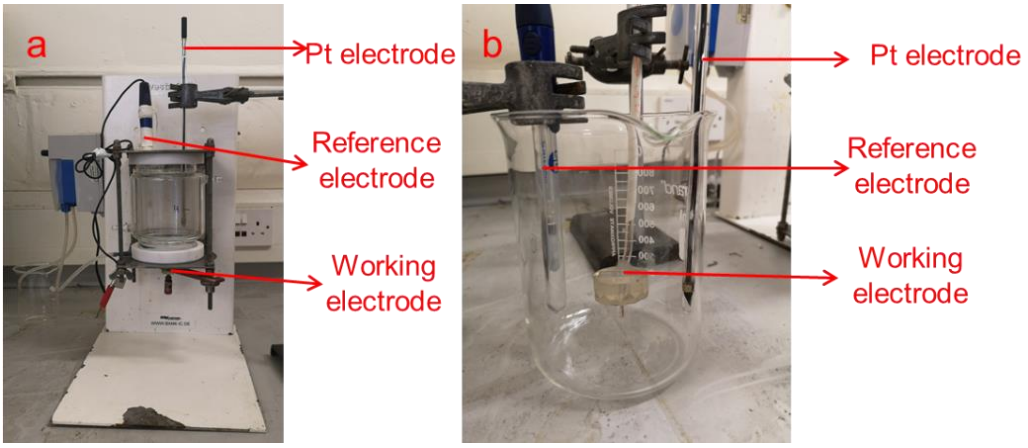

Figure 4- 4 The Avesta cell setup for polarisation test and (b) the standard cell for polarisation test.

4.4 Scanning Electron Microscopy (SEM)

SEM provides information on surface topography, crystalline structure, and chemical composition of the sample surface. Compare with the optical microscopy, SEM can focus on a rough surface sample, with a higher magnification. The other properties of the samples, such as crystal structure, chemical composition, and electrical properties can be determined by SEM which is not possible measured from the optical microscopy [3]. The SEM image is influenced by the acquisition of signals from the electron beam and interaction volume of the sample. Specially designed detectors are used to collect to different interaction of electron beams which could reveal a large data of information [4]. Figure 4- 5 shows the interaction volume on the sample surface of different signals can be detected.

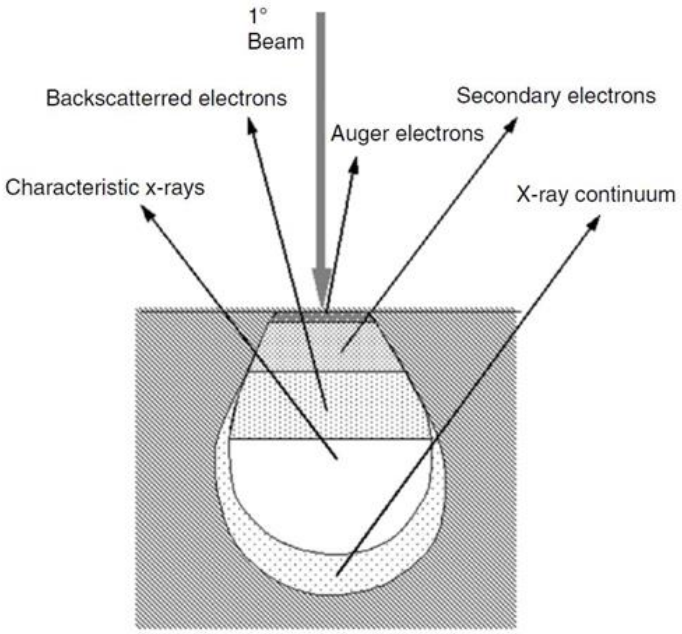

Figure 4- 5 Illustration of several signals generated by the electron beam–specimen interaction in the scanning electron microscope and the regions [5].

Secondary electrons (SE) mode is the most popular signal. As the incident electrons have relatively low energy, which result in a few nanometres depth of the sample surface is determined. So, SE is relatively accurate to produce the topological contrast of the sample [4].

Backscatter electrons (BSE) have the energy higher than 50 eV, from the elastic collision of the electron with the sample atoms. Sample with higher atomic number elements deflects more electrons, as a high number of positive ions on its nucleus. Compare with the image from SE mode, the atomic number of elements from the sample surfaces result in the contrast in the BSE image [4,6].

An energy-dispersive detector (EDX) is able to detect elements on the sample. A hole in the atom shell is created by the ejection of secondary electrons. An electron from the outer shell (higher energy) of the atom would replace the missing ejected electron, and then releases the characteristic X-ray. The released X-rays have a unique energy for each element, so the unique energy is used to identify the element [4].

SEM imaging is carried out to characterize the corrosion outcome. SEM and EDX analysis are measured from FEI Quanta 650, Quanta 250 and Sirion, Zeiss Ultra 55 and the Sigma, and Tescan Mira SEMs. SEM images are taken

from BSE and SE mode, with a typical working distance between 3 and 10 millimetres combined with acceleration voltage varies from 3 to 20 kV.

4.5 Electron Backscatter Diffraction (EBSD)

The electron backscatter diffraction (EBSD) is based on SEM, to a precise mapping of the microstructure for texture and crystallographic phases. For the EBSD measurement, the sample is titled to 70° to the incident beam. Then a characteristic pattern is formed by an electron beam diffracted from the sample, the characteristic pattern is called Kikuchi pattern. A detector is used to collect the diffracted electrons, so the microstructure of sample can be collected. Recently, the grain sizes up 0.1 μm is used to measured and analysed by the EBSD. Compare to TEM, easy sample preparation, large area of sample surface detection, specific area detection, and rapid and automated acquisition and analysis of the diffraction patterns are the main advantages of the application of EBSD [7,8]

A large tilted angle (70°) is used to maximize the intensity of backscattered electrons. Due to the low penetrating power of electrons, a damage-free surface is required to receive sufficiently high quality signals. So the mechanical damage and chemical contamination must be completely removed on the sample surface before the EBSD measurment. The sample surface with high electrically conductive is easier to get high quality data, without charging problems [9].

EBSD images and data are carried out using FEI Sirion, Zeiss Sigma, and Tescan Mira 3 SEMs. All SEMs are equipped with Oxford HKL Nordlys EBSD detector and Aztec software for data acquisition. The accelerating voltage is set to 15 kV with a working distance of 12 mm for Zeiss Sigma SEM, 16 mm for FEI Siron SEM, and 20 mm for Tescan Mira 3 SEM. The step sizes of the EBSD vary, which is depending on the magnification of the image (from x100 to x12000).

4.6 Laser Confocal Microscopy

The laser confocal microscopy combined with the laser and light source, which is used to obtain images with a large depth of field. The advantage of application of laser confocal microscopy for sample imaging is in focus across

the whole measured surface. The morphology data of the sample surface (e.g roughness) can be measured by the laser intensity information [10].

The light emitted from the laser light source focuses on the sample, and then the reflected singles is detected by a CCD camera, visible colour information for each pixel at the focal point is then measured. In the laser confocal optics, to obtaining images with height information across the entire screen, a pinhole is set in front of the photoreceptor to avoid no light from the focal point of the objective lens reaches the photoreceptor. The X-Y scan optics and objective lens are used to focus on the surface of the sample by the light emitted from the laser source. The X-Y scan optics is also used to select a large area to scan. The images from the reflected light are detected by pixel on the sample surface. During the scanning, the reflected intensity changes by moving Z axis. Pixel with the highest intensity indicates the focus thr point/height is under focused condition. So the laser intensity of each pixel on the sample surface can create the filed colour images, laser intensity images, or height images [10].

Keyence VK-X200K 3D laser scanning confocal microscope is used to analyze the general corrosion and localised corrosion. The wavelength of the violet laser is 408 nm. The frame memory images are 16 bits and the height measurement is 24 bits with the highest resolution of 2048*1036 [10].

4.7 Hardness Measurement

Hardness defined as a material's resistance to the indentation. The size of the indentation is related to the applied stress from indenter, which related to the hardness calculation [11]. The indentation size varies (from nano to macro), and type of hardness tests include Rockwell, Brinell, Knoop, and Vickers. Vickers hardness (HV) is a popular method to quantify the hardness due to the hardness value does not chaneged by the different test force [12]

For the Vickers hardness test, a pointed diamond pyramid with a square base is chosen for the indenter. An angle of 136^{o} exists between faces. Suitable applied stress is applied between the indenter and the sample. The average diagonal lengths (L) of the resulting indentation on the sample are measured,

and then Vickers hardness number (VHN or HV) could be calculated from Equation 4.1.

$$HV = \frac{KP}{L^2} \qquad \text{Equation 4.1}$$

K=1.854, P is the applied stress.

4.8 References

[1] R. Ovarfort, Critical pitting temperature measurements of stainless steels with an improved electrochemical method, Corrosion Science. 29 (1989) 987–993. doi:10.1016/0010-938X(89)90088-7.

[2] R. Ovarfort, New electrochemical cell for pitting corrosion testing, Corrosion Science. 28 (1988). doi:10.1016/0010-938X(88)90090-X.

[3] K.D. Vernon-Parry, Scanning Electron Microscopy : an introduction, III-Vs Review. 13 (2000) 40–44.

[4] M. Abd Mutalib, M.A. Rahman, M.H.D. Othman, A.F. Ismail, J. Jaafar, Scanning Electron Microscopy (SEM) and Energy-Dispersive X-Ray (EDX) Spectroscopy, Elsevier B.V., 2017. doi:10.1016/B978-0-444-63776-5.00009-7.

[5] W. Zhou, R.P. Apkarian, Z.L. Wang, Fundamentals of Scanning Electron Microscopy, Scanning Microscopy for Nanotechnology. (2007) 1–40. doi:10.1007/978-0-387-39620-0_1.

[6] R.F. Egerton, Physical Principles of Electron Microscopy, 2006. doi:10.1007/b136495.

[7] F.J. Humphreys, Characterisation of fine-scale microstructures by electron backscatter diffraction (EBSD), Scripta Materialia. 51 (2004) 771–776. doi:10.1016/j.scriptamat.2004.05.016.

[8] T.B. Britton, J. Jiang, Y. Guo, A. Vilalta-Clemente, D. Wallis, L.N. Hansen, A. Winkelmann, A.J. Wilkinson, Tutorial: Crystal orientations and EBSD - Or which way is up?, Materials Characterization. 117 (2016) 113–126. doi:10.1016/j.matchar.2016.04.008.

[9] A.D. Rollett, K. Barmak, Orientation Mapping, Fifth Edition, Elsevier, 2014. doi:10.1016/B978-0-444-53770-6.00011-3.

[10] 3D Laser Scanning Microscope VK-X100K/X105/X110 VK-X200K/X210 User's Manual, 2013.

[11] P. Moore, G. Booth, Mechanical testing of welds, in: The Welding Engineer′s Guide to Fracture and Fatigue, 2015: pp. 113–141. doi:10.1533/9781782423911.2.113.

[12] K. Herrman, Hardness measurement of metals - static methods, Hardness Testing - Principles and Applications. (2011) 26.

5. Overview of Publications and Presentations

This dissertation consisits 14 prepared manuscript, and 8 oral presentations are given for the academic conference.

(i) Presentation at European Corrosion Congress 2018, Krakow, Poland

Title: Application of Bipolar Electrochemistry to Characterise the Pitting Corrosion Behaviour of Type 420 Ferritic Stainless Steel

(ii) Presentation at SCI Electrochemistry Postgraduate Conference 2019, Newcastle, United Kingdom. (Win the first oral presentation price).

Title: Application of Bipolar Electrochemistry for Characterising the Corrosion Behaviour of Ferritic Stainless Steels.

(iii) Presentation 1st International Conference on Corrosion Protection and Application 2019, Chongqing, China

Title*:* Exploring the Application of Bipolar Electrochemistry – Providing Novel Insight for Corrosion Science and Engineering.

(iv) Presentation at European Corrosion Congress 2019, Seville, Spain.

Title: An Experimental Investigation into the Application of Bipolar Electrochemistry for Acid Corrosion Studies.

(v) Presentation at European Corrosion Congress 2020, online.

Title: Exploring the Application of Bipolar Electrochemistry – Novel Insight for Assessing Localised Corrosion in Corrosion Resistant Alloys

(vi) Presentation at European Corrosion Congress 2019, Seville, Spain

Title: Design of a Modified Bipolar Electrochemistry Approach for Corrosion Research and Engineering Application.

(vii) Presentation at European Corrosion Congress 2019, Seville, Spain.

Title: Application of Bipolar electrochemistry to research the gravity influences the pit shape and pit growth kinetics in stainless steel.

Chapter 6:

Ferritic Stainless Steel (Type 420)

(a) Background/Theory: Corrosion Electrochemistry with a Segmented Array Bipolar Electrode (Electrochimica Acta – Minor Correction)

(b) Microstructure: On the Application of Bipolar Electrochemistry to Characterise the Localised Corrosion Behaviour of Type 420 Ferritic Stainless Steel (Metals; doi.org/10.3390/met10060794)

(c) Time-lapse: Time-lapse Observation of Pitting Corrosion in Type 420 Ferritic Stainless Steel Using a Bipolar Electrochemistry Approach

(d) Heat Treatment: Accessing Full Spectrum of Corrosion Kinetic Behaviour of Tempered Type 420 Martensitic Stainless Steel

Chapter 7:

Duplex Stainless Steel (Type 2205)

(a) Screening: Fast testing of ambient temperature pitting corrosion in type 2205 duplex stainless steel by bipolar electrochemistry experiments (Electrochemistry Communications doi.org/10.1016/j.elecom.2020.106779)

(b) Kinetics: Estimating Pitting and Crevice Corrosion Growth Kinetics of Type 2205 Duplex Stainless Steel at Ambient Temperature

(c) Heat treatment: A new approach to assess the corrosion resistance of solution annealed duplex stainless steel microstructure (Corrosion Science – Under Review)

(d) Duplex vs. Austenitic: Application of Bipolar Electrochemistry for Characterising Corrosion Kinetics of Austenitic and Duplex Stainless Steels

Chapter 8:

Technique Development

(a) Modified: Application of a modified bi-polar electrochemistry approach to determine pitting corrosion characteristics (Electrochemistry Communications; doi.org/10.1016/j.elecom.2018.06.013)

(b) Orthogonal: Characterisation of localised corrosion growth kinetics with an orthogonal bipolar electrochemistry technique

(c) Galvanic: On the application of bipolar electrochemistry for simulating galvanic corrosion behaviour of dissimilar stainless steels (Electrochemistry Communications – Minor Corrosion)

Chapter 9:

Application

(a) Weld: Metallographic Screening of Duplex Stainless Steel Weld Microstructure with a Bipolar Electrochemistry Technique (Materials Characterisation; doi.org/10.1016/j.matchar.2020.110605)

(b) Gravity: Revisiting the effect of gravity on pitting corrosion

(c) Brass: Optimising Brass Dezincification with a Bipolar Electrochemistry Technique (Surfaces and Interfaces – Accept)

6 Theory of bipolar electrochemistry and Type 420 stainless steel

6.1 General introduction

One of the common techniques for the pitting corrosion resistance test was the critical pitting potential measured from 3-electrode potentio-dynamic polarisation test. However, the critical pitting potential was influenced by scan rate and previously applied potential before reach the pitting potential. For the post-analysis, the corrosion response on the specimen was accumulating of corrosion from all the previous potential. Bipolar electrochemistry was used for corrosion test from a linear potential generated along the BPE. So, the previous applied potential before the critical pitting potential and scan rate can be avoid. The potential and current distribution in the BPE could be determined from a split bipolar electrode setup. The corrosion behaviour of type 420 stainless steel was researched by bipolar electrochemistry. The crevice corrosion, pitting corrosion, general corrosion, and cathodic response are measured on the BPE. Post-observation is done by laser confocal microscopy and SEM. Combined with USB camera, the pit growth kinetics can be tested by in-situ carema. After the austenitizing treatment for the ferritic stainless steel, martensitic stainless steel was formed. Different tempering temperature is applied to optimize the corrosion and mechanical properties.

In the first paper of this chapter (chapter 6.2), the setup of split bipolar electrode was used to determine the potential and current distribution on the BPE. A polarisation curve replots from current and potential distribution on the BPE was used to compare to the traditional 3-electrode potentio-dynamic polarisation curve. A 3-electrode potentio-static polarisation test with different applied potential was also applied, to compare the corrosion response and current response with the corrosion and current distribution on the split bipolar electrochemistry.

The second paper (chapter 6.3) introduces the corrosion behaviour on type 420 ferritic stainless steel BPE. The microstructure of the stainless steel was analysis by the SEM/EBSD. Different corrosion response (pitting corrosion,

general corrosion, and cathodic deposition) on the BPE are measured by SEM. A wider and smoother potential gradient is generated on a larger BPE, then, the relationship between the pitting corrosion and local applied potential is researched.

The third paper (chapter 6.4) introduces an in-situ pit corrosion test method The In-situ time-lapse imaging, informed about pit nucleation frequencies and associated growth characteristics. Pit nucleatedand growth in the cavities with aspect ratio of 0.4 – 0.6, with fastest pit growth in prefer semi-circular shape (aspect ratio 0.5) cavity. Diluted pit electrolyte was applied to determined the influence to the pit growth kinetics.

The forth paper (chapter 6.5) introduces the corrosion changed by tempering temperatures for the martensitic stainless steel; the corrosion behaviuor was determined and compared from the 3-electrode potentio-dynamic polarisation and bipolar electrochemistry. The microstructure evolution were tested by the EBSD, and linked to the corrosion resistance change. The overall pitting volume and pit growth kinetics under different tempering temperature and applied potential are obtained. At last, the best tempering temperature with optimized hardness and pitting corrosion resistance is given.

6.2 Corrosion Electrochemistry with a Segmented Array Bipolar Electrode

Yiqi Zhou[*1], *Nicolas Stevens1*, *Dirk Lars Engelberg*[1,2]

(1) *Corrosion & Protection Centre, School of Materials, The University of Manchester, M13 9PL, Manchester, UK*

(2) Materials Performance Centre, The University of Manchester, M13 9PL, Manchester, UK

* Corresponding author: Yiqi.Zhou@postgrad.manchester.ac.uk

6.21 Highlights

Application of bipolar electrochemistry provides access to the full range of anodic-to-cathodic polarisation behaviours.

Potential and current distributions have been experimentally determined using a segmented array bipolar electrode.

The bipolar electrochemistry response is compared to conventional 3-electrode polarisation experiments.

Measurements of pitting corrosion kinetics have been obtained using bipolar electrochemistry.

6.22 Abstract

Bipolar electrochemistry was applied to determine the full spectrum of anodic-to-cathodic polarisation behaviour of stainless steel. The potential and current distributions at the sample surface were determined using a segmented array bipolar electrode. The measured potential shows a constant gradient along the bipolar electrode (BPE), with the current following an exponential Butler-Volmer relationship. Bipolar electrochemistry is compared to a conventional 3-electrode polarisation set-up, allowing determination of the critical pitting potential, general corrosion rates, and cathodic current responses. The application of bipolar electrochemistry is demonstrated via measurement of pit growth kinetics in ferritic stainless steel.

Keywords: Bipolar electrochemistry, Pitting, Stainless Steel, Butler-Volmer equation, Potentio-dynamic Polarisation

6.23 Introduction

The principle of bipolar electrochemistry is based on the application of a potential between two feeder electrodes, which provides an electric field

gradient between both feeder electrodes with immersion in a conductive electrolyte. Both oxidation and reduction reactions can simultaneously occur over a wide range of electrochemical potentials [1–3]. The oxidation reactions on the BPE occurring close to the negative feeder electrode and vice versa [1–4]. Bipolar electrochemistry was used in sensors, detectors, electrolysis, electro-deposition, electro-catalytic, corrosion and batteries [1,5,6]. Bipolar electrochemistry is now used for corrosion testing, as the simple setup provides a high throughput corrosion screening method, with full anodic-to-cathodic corrosion behaviour obtained on one electrode. The potential gradient along the BPE surface can be determined [1–4,7] with the potential across the BPE estimated by using Equation 1:

$$\triangle \mathbf{E}_{\boldsymbol{BPE}} = \mathbf{E}_{\boldsymbol{tot}} \left(\frac{\mathrm{l_{BPE}}}{\mathrm{l_{Channel}}} \right) \qquad \text{Equation 1:}$$

where $\triangle \mathbf{E}_{\boldsymbol{BPE}}$ is the acting potential across the BPE, E_{tot} is the total applied potential; l_{BPE} is the length of the BPE, and $l_{Channel}$ is the distance between the feeder electrodes.

The potential difference at the BPE surface has been determined using a two reference electrode setup, and Finite Element Method (FEM) employed to simulate the potential gradient along the BPE [8]. Scanning Vibrating Electrode Techniques (SVET) and Local Electrochemical Impedance Spectroscopy (LEIS) have also been used to determine the potential distribution along the BPE [2]. All these observations and simulations supported the presence of a linear potential gradient along the BPE with exposure to a conductive electrolyte.

To measure the current distribution along the BPE, split bipolar electrochemistry, modelling, SVET, LEIS, Electrogenerated Chemi-luminescence (ECL) and Imaging Surface Plasmon Resonance (ISPR) have been used so far [9–11]. For the split bipolar electrochemistry, Zero Resistance Ammeter (ZRA) monitoring is used to measure the current flow between discrete BPE segments [10,11]. Simulation and modelling approaches are employed to calculate the current along the BPE. These are typically limited by the application of simplified assumptions in these models,

for example, by considering and superimposing electric field homogeneity, limited irreversible electron transfer reactions, and the occurrence of only simple electrochemical reactions [2,12]. Local current can be evaluated from the measured local potential by SVET and LEIS [9,13], and ISPR has been used to visualize the current and potential distribution along the BPE by correlating experimentally measured results to electric field simulations [8,14]. The local current can also be determined experimentally via measuring the potential gradient from a pair of reference micro-electrodes [15,16]. ECL was used to measure the current density through electrochemical luminescence reactions [17,18]

The convential 3-electrode potentio-dynamic polarization test is one of the most common methods to determine corrosion bebavior [19,20]. However, it also has limiations, with, for example, the cathodic part resulting in irreversible damage of the electrode in certain corrosion systems, such indium tin oxide [21]. Hydrogen evlolution on Zn, Al, and Mg alloys can also affect subsequently measured polariszation curves (e.g [22]). At a low corrosion rates, current contributions can also derive from species/ions present in the electrolyte, which are kinetically more active [23]. Further, experimental parameters such as the scan rate can influence the corrosion behaviour, such as threshold pitting potential values [24,25]. Before reaching E_{pit}, the sample surface is typically passivated resulting in a more protectvie passvie film [26–28], with the measured E_{Pit} than higher compared to the “real E_{Pit}”. For potentio-static polarisation test, as the ohmic drop in solution, a finite potentio-static response time, and oxide formation results in the applied potential not truely representing potentio-static conditions [29]. Corrosion product development can also influence the net anodic current density, often augmented by inhomogeneous growth at flaws and fissures [30,31].

The aim of this paper is to experimentally determine the potential and current distributions along a BPE setup for corrosion screening application. A comparison to the potential and current distribution measured with traditional 3-electrode potentio-dynamic and potentio-static polarisation experiments is provided. The advantages of bipolar electrochemistry for corrosion screening

will be introduced via determination of pitting corrosion kinetics in ferritic stainless steel.

6.24 Materials and Methods

A type 420 ferritic stainless steel with a chemical composition (wt %) of 13.7 Cr, 0.46 C, 0.47 Si, and 0.39 Mn was used in this study. The size of the BPE was 30 * 10 * 1.2 mm^3 (length * width * thickness). Samples with 25 x 25 x 1.2 mm^3 (length * width * thickness) were used for all standard 3-electrode potentio-dynamic and potentio-static polarisation experiments. All samples were mounted in Araldite resin, and then ground to 1200 grit, followed by a final polishing step to 1 µm diamond paste finish.

A typical bipolar electrochemistry design is schematically shown in Figure 6.2-1 (a). A close-up view of the bipolar electrochemistry set-up is shown in Figure 6.2- 1 (b), with two platinum feeder electrodes each with 4 cm^2 surface area. The distance between the two feeder electrodes was set to 60 mm with BPE located in the centre. The applied potential on the feeder electrodes was 10 V for 30 min in 200 ml of 0.1 M HCl.

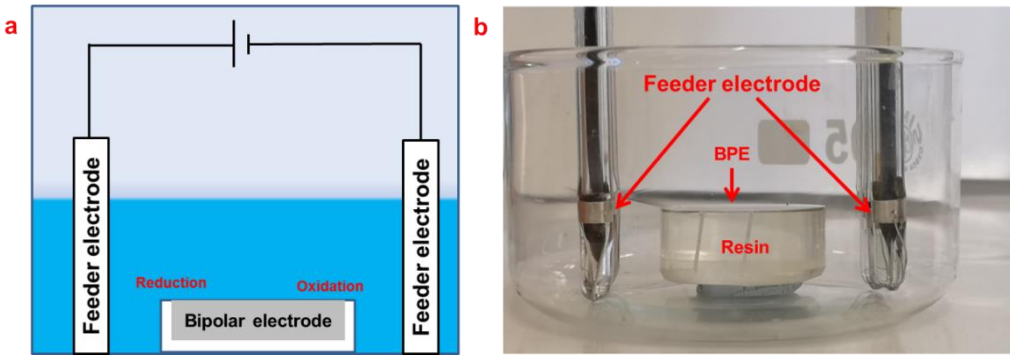

Figure 6.2- 1 (a) A typical setup for bipolar electrochemistry experiment, with (b) showing a close-up of the bipolar electrochemistry setup.

Figure 6.2- 2 provides the setup to measure the potential and current distributions. A segmented array BPE electrode consisting of 21 rectangle coupons (each 1.2 * 10 * 1.2 mm^3) was prepared. Each segment had an electrical connection spot-welded to the back, with each segment insulated to each other by electric insulation tapes. Once packed together in a sequence, they had the dimension of a single BPE. The copper wires at the back of the

segments were electric connected to each other to make up the segmented array BPE via metal clips.

To measure the current at individual segments, each coupon was connected to a Zero Resistance Ammeter (ZRA). The current flow was contained within the BPE electrode, with the ZRA only measuring the local current of each segment. The current was recorded for 10 min. For carrying out potential measurements, a Luggin capillary was located ≈ 1 mm above the BPE segments and connected to a reference electrode (SCE), as shown in Figure 6.2- 2. To measure the local potential changes during bipolar experiments, the OCP of the BPE was stabilised at first, then the bipolar electrochemistry experiment was turned on. The reported potential change was the difference of potential at each segment with respect to the measured OCP without bipolar control. Current measurements via ZRA were conducted in parallel.

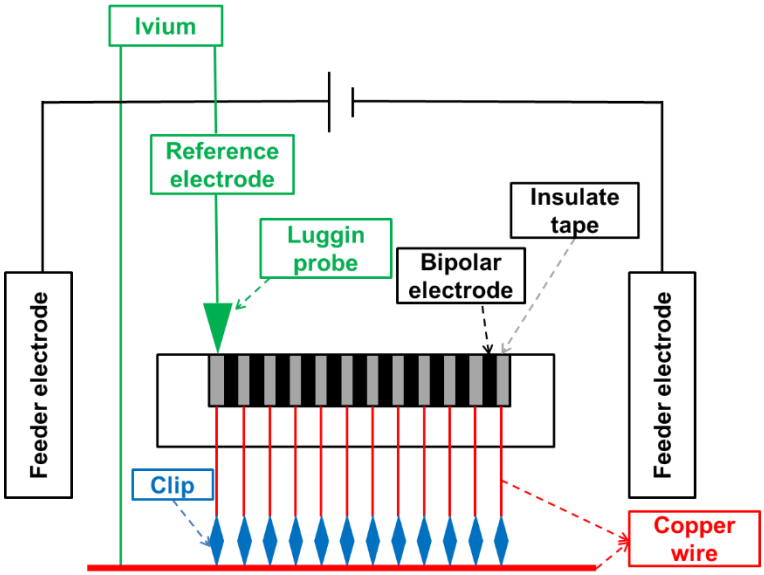

Figure 6.2- 2 The setup for bipolar electrochemistry to measure the local potential and current distributions.

For the 3-electrode polarization test, the samples were tested in an AVESTA cell at room temperature in 0.1M HCl. The counter electrode was a Pt electrode with a SCE reference electrode. The exposed surface area was 1 cm^2. An IVIUM-Compactstat potentiostat with IVIUM software was used to measure the OCP for 30 min, followed by potentio-dynamic polarisation tests. The scan rate of the potentio-dynamic tests was between 0.1 mV/s and 1 mV/s.

For the potentio-static polarisation test, OCP was stabilised for 30 min, followed by potentio-static polarisation test for 30 min at a potential range of -0.9 V_{OCP} to +0.9 $V_{OCP,}$ using a step potential change of 0.1 V.

After all the experiment, the sample was removed from the electrolyte, washed and rinsed in soap water, and dried in hot air. A Keyence VK-200K laser confocal scanning microscope was used to determine the corrosion morphology and pit topographies.

6.25 Results and Discussion

BPE potential and current evolution over time

The current distribution along the BPE should be balanced, with the overall cathodic current weighing out the anodic current. Figure 6.2- 3 gives the potential and current density changes over time at different locations along the BPE. From the BPE oxidation region to the reduction edge, the segmented BPE is labelled segment 1 to segment 21 respectively. In Figure 6.2- 3 (a), the measured potential of segment 1 first reduced from +1.0 V_{OCP} to +0.85 $V_{OCP,}$ and stabilised around +0.85 V_{OCP} with a variation of ± 0.05 V_{OCP}. The current density changes from +140 mA/cm^2 to +170 mA/cm^2. Segment 6 shows a lower change in potential, shown Figure 6.2- 3 (b), reduces to +0.37 V_{OCP} in the first few minutes and then stabilising around +0.35 V_{OCP} to +0.40 V_{OCP}. In parallel, the current density was fluctuating between +15 mA/cm^2 and +20 mA/cm^2. At the middle point of the BPE (segment 11) shown in Figure 6.2- 3 (c), the potential is between -0.06 V_{OCP} and -0.14 V_{OCP} with the current density reducing from +1.5 mA/cm^2 to -1.0 mA/cm^2. Figure 6.2- 3 (d) gives the potential and current density change in segment 16 with the potential changing to ≈ -0.24 V_{OCP} and the current density remaining between -30 mA/cm^2 and -40 mA/cm^2. Segment 21 contains the highest cathodic potential shown in Figure 6.2- 3 (e), representative of the cathodic edge of the BPE. The potential is fluctuating from -1.05 V_{OCP} to -0.95 V_{OCP}, with a change in current density from -190 mA/cm^2 to -160 mA/cm^2. All BPE segments show a reasonably constant potential and current density over time, hence each segment is under both galvanostatic and potentiostatic operation.

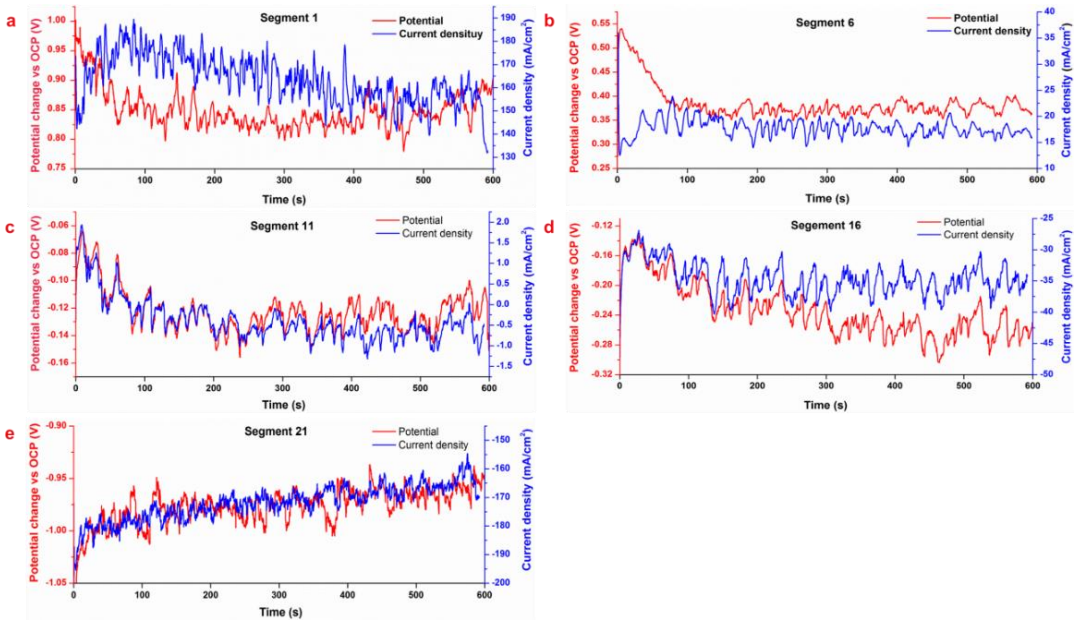

Figure 6.2- 3 The potential change over time with corresponding current density of the segmented array BPE for the (a) 1st segment (oxidation edge) (b), 6th segment, (c), 11th segment, (d), 16th segment, and (e) 21st segment (cathodic edge).

The influence of exposure time on the potential and current density was also investigated, using linear regression of the data in Figure 6.2- 3 at time different intervals between 0-200 s, 200-400 s and 400-600 s. The error bar is the standard deviation of the potential and current density with respect to the corresponding linear regression, revealing the fluctuations of potential and current density with time. Figure 6.2- 4 (a) shows that the change in potential and standard deviation for the first 200 s is the largest, significantly reducing to at 200-400 s and 400-600 s, which means the potential, is more stable with time after 200 s. In Figure 6.2- 4 (b), the current density and the standard deviation is highest at the oxidation edge with a reduction edge, and followed by the cathodic area. In the general corrosion site and middle point, the current density change is very small from 0-600 s.

In 1st segment, high potential and current density fluctuating are measured as the pitting corrosion and gas bubbles evolution (such as Cl_2 and H_2). From 6th segment, the tiny potential and current density fluctuating is caused by the electrochemical reactions in the electrolyte. At 21st segment, the undulating of potential and current density increases again as the gas evolution. The evolution of gas bubbles influence the current density by increase the current

resistance of the electrolyte and block part of the BPE surface. Gas generated and flows away make a dynamic electrolyte resistance, change the current flows in the BPE.

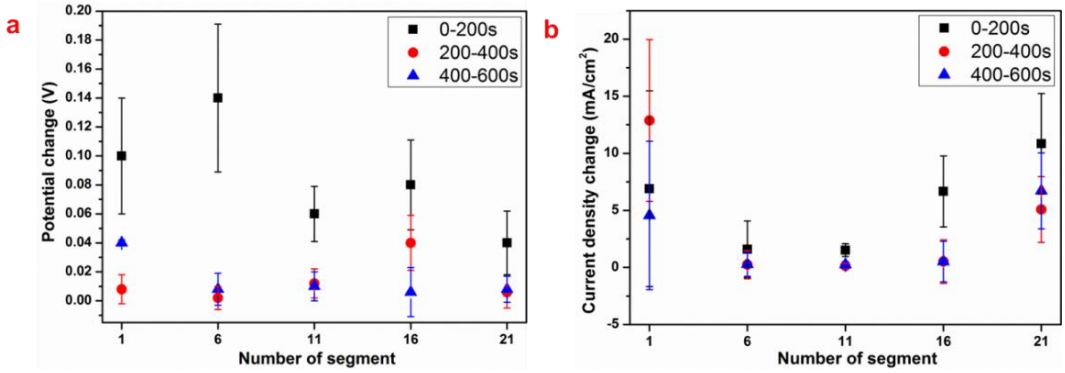

Figure 6.2- 4 (a) The change in potential and (b) current density as a function of BPE exposure time and segments 1, 6, 11, 16, 21.

BPE potential and current distribution

Figure 6.2- 5 (a) shows the mean current density and potential measured on the segmented array BPE. The potential distribution along the BPE is quasi-linear and increases from -1.0 V_{OCP} at the BPE reduction edge, to +0.9 V_{OCP} at the BPE oxidation edge. The current density distribution along the BPE is increasing from ≈ -180 mA/cm^2 to ≈ +180 mA/cm^2. A linear fit of potential and a polynomial fit of the current density along the BPE are superposed. Figure 6.2- 5 (b) gives the relationship between the current density and potential along the BPE by replotting the data from Figure 6.2- 5 (a). A simulated curve using the Butler-Volmer Equation is also shown, indicating the typical E-Log(i) relationship for activation controlled corrosion processed. The distribution of the potential and corresponding current density is similar as literatures [32]. The OCP is not at the centre of the sample, but off-set to the cathodic side. Part of the measured current density come from the electrochemical reactions in the electrolyte, results in the measured current density is not zero at the middle point.

The Butler-Volmer equation (Equation 2) is used to describe the relationship between the current density (i) and the over-potential (φ) in regions under activation control, with the resulting current density (i) considered the sum of the anodic and cathodic current density together [33].

$$i = i_0 \left[e^{\frac{(1-a)z\varphi F}{RT}} - e^{\frac{-az\varphi F}{RT}} \right]$$ Equation 2

i_0 is the exchange current density, a is the transfer coefficient (0.5); z is the numbers of electrons in the electrode reactions (n=2), F, R, T are Faraday's constant (96485 C.mol^{-1}), gas constant (8.314 J.mol^{-1}.K^{-1}), and absolute temperature (K). The exchange current density means the intrinsic rate of the electron transfer of an electrode reaction which is materials, construction and temperature dependent. Cathodic current at high anodic potential or anodic current at high cathodic potential can be neglected in the Butler-Volmer Equation [34]. The relationship between potential and current density between +0.2 V_{OCP} to +0.8 V_{OCP} and -0.2 V_{OCP} to -0.8 V_{OCP}, follow the Butler-Volmer equation which are i =0.7916 $e^{3.78}$ at anodic potential range and i =0.7639$e^{6.92}$ at cathodic potential range, and the exchange current density i_0 is similar for both anodic and cathodic potential.

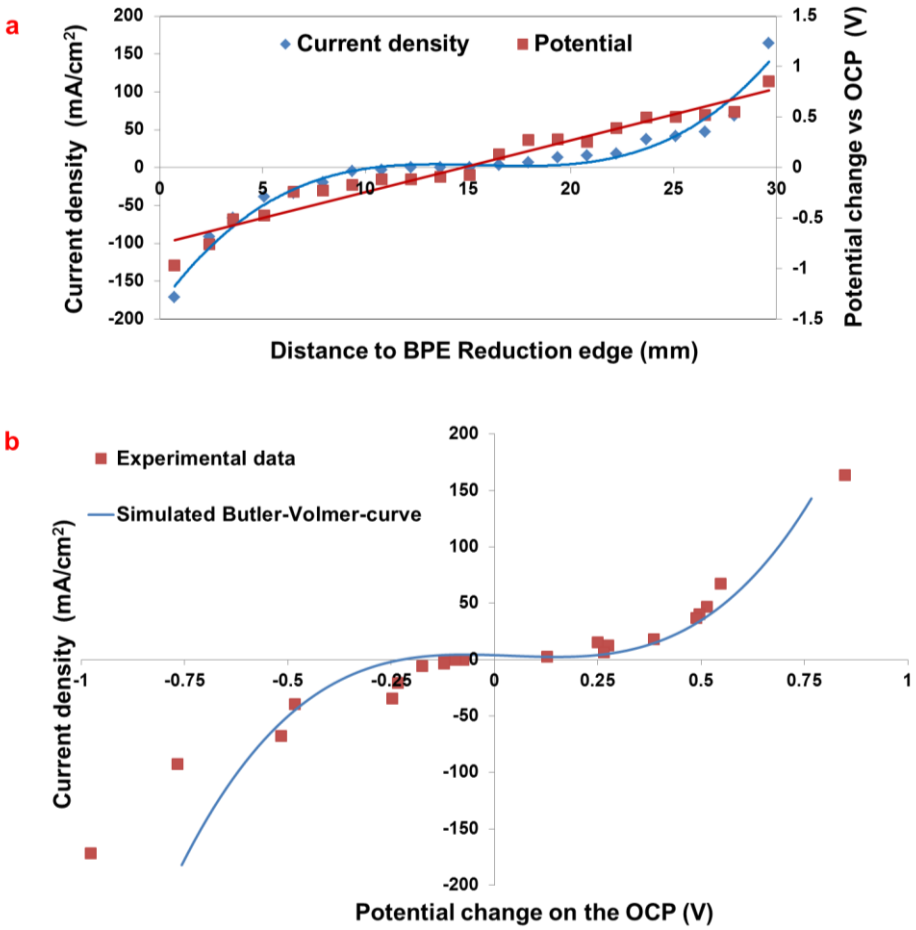

Figure 6.2- 5 Experimentally measured potential and current density distribution along the BPE and (b) the experimental relationship between potential and current density.

BPE application

Figure 6.2- 6 (a) shows a potentio-dynamic polarisation curve by re-plotting the current density distribution from Figure 6.2- 5 (b) on a log scale. In the potentio-dynamic polarisation test, cathodic region, activation region and localised corrosion can be identified from the local applied potential and corresponding current density. Figure 6.2- 6 (b) shows the BPE surface after testing, showing regions characteristic of crevice corrosion, pitting corrosion, general corrosion, and a cathodic region. By linking Figure 6.2- 6 (a) to Figure 6.2- 5 (a), the corrosion response with the corresponding potential (vs SCE) can be determined. The free corrosion potential is the boundary between general corrosion and the cathodic region, which is this, gives an OCP of -0.67 V_{SCE}. Two different pit covered lengths on the BPE are noticed; a shorter length (24 mm to BPE reduction edge) near the BPE sides and a longer length (24.5 mm) close to the BPE centre. E^1_{pit} has a lower potential than E^2_{pit}. E^2_{pit} is the pitting potential and E^1_{pit} is at the interface between crevice corrosion and stable pitting corrosion, with i^1_{pit} is 19.95 mA/cm^2 and i^2_{pit} is 31.62 mA/cm^2. All pits are open pits. The current density is suddenly increasing at -0.3 V_{SCE} due to the formation of a crevice between the BPE and the resin, as no pitting is detected at this potential on the BPE. So, the lower nucleation potential for crevice corrosion.

Table 6.2- 1 shows the different corrosion length with corresponding local potentials. The cathodic region has a length of 11.5 mm, followed by the general corrosion region from 11.5 mm to 24 mm (distance to the BPE reduction edge). The potential boundary between cathodic region and general corrosion region is -0.67 V_{SCE}. The crevice corrosion starts at 18.9 mm which relates -0.3 V_{SCE}. The stable pits start at the length of 24.0 mm which is 0.5 mm shorter than transition from crevice corrosion to stable pitting corrosion, indicates potential for stable pitting corrosion is +0.03 V_{SCE} higher.

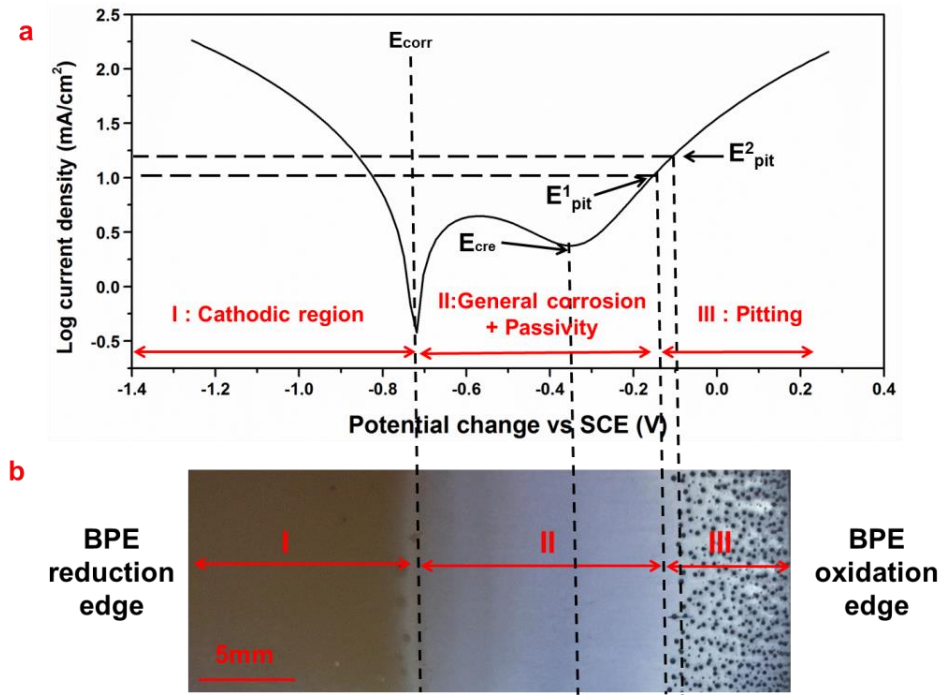

Figure 6.2- 6 (a) Potential and current response measured at the bipolar experiment. (b) Optical image of BPE surface after the bi-polar electrochemistry test for 30min.

Table 6.2- 1 The corrosion response on the BPE surface with the corresponding potential:

BPE surface response	Distance to BPE reduction edge (mm)	Response voltage (V_{SCE})
Pitting corrosion (2)	24.5 - 30.0	+0.25 - -0.02
Pitting corrosion (1)	24.0 - 24.5	-0.02 - -0.05
Crevice corrosion	18.9 - 30	+0.25 - -0.30
General corrosion	11.5 – 24.0	-0.05 - -0.67
Cathode region	0-11.5	-0.67 - -1.24

BPE vs Potentio-dynamic polarisation curve

The results of the BPE experiment are compared to the response from 3-electtode potentio-dynamic polarisation test. Figure 6.2- 7 shows the OCP for the potentio-dynamic polarisation experiment for the 3 different scan rates. No passive region is formed as the current density remains > 0.1 mA/cm^2. The measured E_{pit} was reduced with scan rate from 1 mV/s to 0.1 mV/s. The reduced E_{pit} with the lower scan rate, as the E_{pit} is time-dependent, so a higher scan rate result in a longer polarisation time to nucleate pit [35]. The cumulative electric charge (Q_C) also explains the E_{pit} change with the scan rate, which the Q_c influences to current density and time which related to the polarisation time [36]. The electrolyte used to carry out the bipolar

electrochemistry experiment for 30 min was also used for the 3-electrode potentio-dynamic polarisation test, with a scan rate of 1 mV/s. Comparison with the fresh HCl electrolyte, both of the OCP and E_{Pit} slightly changes, as the electrolyte was process by bipolar electrochemistry for 30 min. At high applied potential, highly active oxidants: Cl_2O, ClO_2, ClO^-, HClO, Cl* and HO_2^* (* indicates reactive free radicals) is generated [37]. After bipolar electrochemistry the experiment, the measured weight of the electrolyte was reduced by 1% possible due to gas evolution; the pH value increases. The current response between two feeder electrodes is reducing with time due to conductivity of electrolyte change. The weight, pH value, and electrolyte conductivity varied after the bipolar experiment indicates the electrolyte composition changes. For the polarisation curves replot from the BPE. The respond current density at same applied potential is higher.

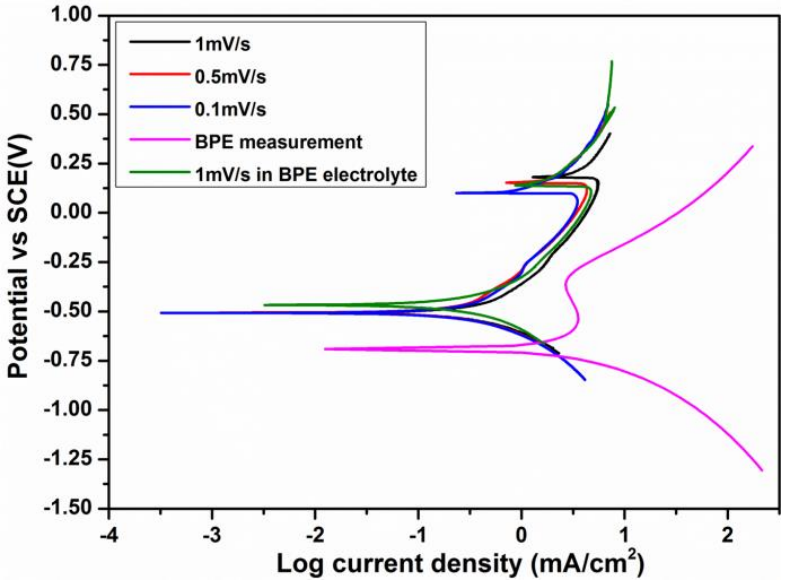

Figure 6.2- 7 3-electrode potentio-dynamic polarisation with different scan rate. The potential-current response from BPE. The polarisation test in BPE electrolyte after 30 min bipolar experiment with a scan rate of 1 mV/s.

Table 6.2- 2 shows E_{pit}, Corrosion rate (CR), and OCP from the 3-electrode potentio-dynamic polarisation test and bipolar electrochemistry experiment. CR is defined as the maximum current density before reaching E_{pit}. The E_{pit} and OCP from BPE measurement are both lower than the 3-electrode potentio-dynamic polarisation test. The CR is similar to the 3-electrode potentio-dynamic polarisation test with a scan rate of 0.1 mV/s. For the OCP,

the standard 3-electrode polarisations are all ≈ -0.5 V_{SCE}, whereas the BPE has an OCP of -0.67 V_{SCE}. Comparison between the fresh and pre-used BPE electrolyte, the OCP, CR, and E_{pit} change shows the electrolyte change affects the measurements.

The reasons for different OCP, corrosion rate, and E_{pit} between the 3-electrode potentio-dynamic polarisation and BPE polarisation curves are: (i) A large numbers of electrochemical reactions occurs in the BPE electrolyte as the high applied potential, which changes the electrolyte, (ii) The sample surface condition is already changed by previous applied potential before E_{pit} for the 3 electrode potentio-dynamic polarisation test, (iii) Ions are concentrated at feeder electrodes which changes the ion concentration at the BPE edges and hence affect the potential and current distribution on the BPE edges, (iv) The E_{pit} from the 3-electrode effects potentio-dynamic polarisation is influenced by the scan rate, but no scan rate applied for bipolar test, (v) The electrolyte is static in the 3-electrode potentio-dynamic polarisation, but dynamic in the bipolar experiment, (vi) The BPE has no IR drop between the anode and cathode, which exists in the 3-electrode potentio-dynamic polarisation test, (vii) Electrons generated from the electrochemical reactions in the electrolyte flow via BPE, influences ZRA reading. (viii). Crevice corrosion in the BPE increases the current in the anodic region, and to balance the anodic current, the cathodic current is also increased.

Table 6.2- 2 Comparison of pitting potential (E_{pit}), corrosion rate (CR) and free corrosion potential (E_{corr}) of each condition from Figure 6.2- 6.

	1mV/s	0.5mV/s	0.1mV/s	BPE measurement	1mV/s + BPE
E_{pit} (V)	+0.17	+0.15	+0.10	-0.04	+0.14
CR (mA/cm²)	+0.75	+0.63	+0.54	+0.55	+0.76
OCP(V)	-0.51	-0.51	-0.51	-0.67	-0.48

Figure 6.2- 8 shows the optical images for the 3-electrode potentio-dynamic polarisation terminated at +0.1 V_{SCE}, +0.3 V_{SCE} and +1.5 V_{SCE} with a scan rate of 1 mV/s. Figure 6.2- 8 (a) is a sample stopped before the E_{pit} reached (+0.1 V_{SCE}), only general corrosion occurred. Figure 6.2- 8 (b) is a sample at the potential slightly higher than E_{pit}, and pitting corrosion is detected. Figure 6.2-8 (c) is a sample polarised to +1.5 V_{SCE}; at such high potential, large semi-

spherical shape pits are clearly observed. A darker area surrounds each pit is clearly seen as more serous general corrosion from the aggressive pit electrolyte diffuse out of the pit. No passive region is measured in 3-electrode polarisation curves (Figure 6.2- 7), as the current density is very high in the anodic polarisation region. The stainless steel has low Cr concentration which is only slighter higher than the critical Cr concentration to from a passive film [38]. A large number of chromium carbides are observed on the sample surface, with chromium depletion region next the chromium carbide, so the general corrosion occurs before the E_{pit}, and pitting corrosion occurred at the Cr depletion region above the E_{pit}.

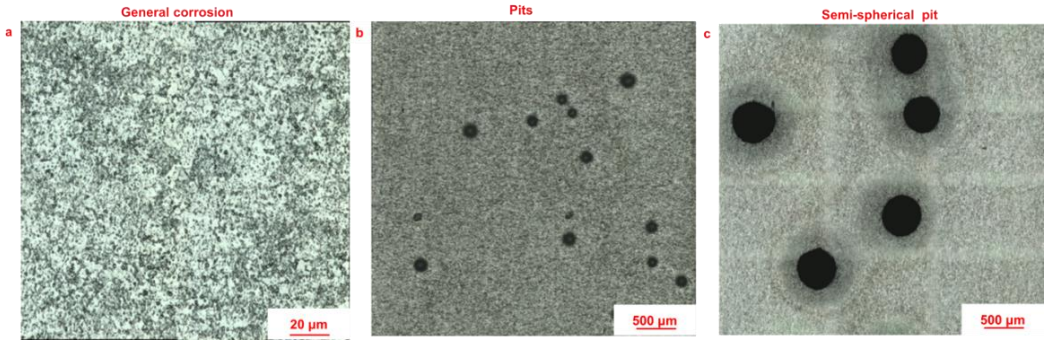

Figure 6.2- 8 Optical images of the stainless steel under potentio-dynamic polarisation stop at (a) +0.1 V_{SCE}, (b) +0.3 V_{SCE} and (c) +1.5 V_{SCE}.

BPE vs Potentio-static polarisation experiment

The experiments result from the BPE and 3-electrode potentio-static polarisation test in the Avesta cell. Figure 6.2- 9 gives the average current distribution for 30 min experiment on the BPE from two different methods. The first one is direct measure the current density from the spilt bipolar electrochemistry; the second one is measuring current response from different applied potential in the 3-electrode potentio-static polarisation test in the Avesta cell. The potentio-static polarisation potential is converted to the location on the BPE via the potential distribution on the BPE in Figure 6.2- 5 (a), so the current density distribution on the BPE can be estimated. The different corrosion response regions marked depend on the surface outcome of the BPE and potentio-static polarisation samples. The measured current density from the split BPE is higher than the potentio-static polarisation test.

Close to the centre of the BPE (5 to 25 mm), the current density from the split BPE is over 10 times higher than the potentio-static polarisation test. At the oxidation and reduciton edges of the BPE, the current density response is over 100 times higher from the split BPE. The higher current density at the BPE oxidation edge is caused by the crevice corrosion, to balance the current density at the anodic BPE, the current density at the BPE reduction edge is increased. In the middle part of the BPE, the current generated in the electrolyte can pass through the BPE as the low electric resistance, so the measured current from the split BPE in higher. Over 18 samples are need with each sample run 30 min for the potentio-static polarisation test. But for the BPE, only 1 sample is required to achieve the same outcome, which is time and sample saving. The potential boundary can be determined by the BPE, but for the potentio-static polarisation test, only a potential range for different corrosion outcome can be analysis, e.g pitting potential from potentio-static polarisation test is between +0.6 V_{SCE} and +0.7 V_{SCE}.

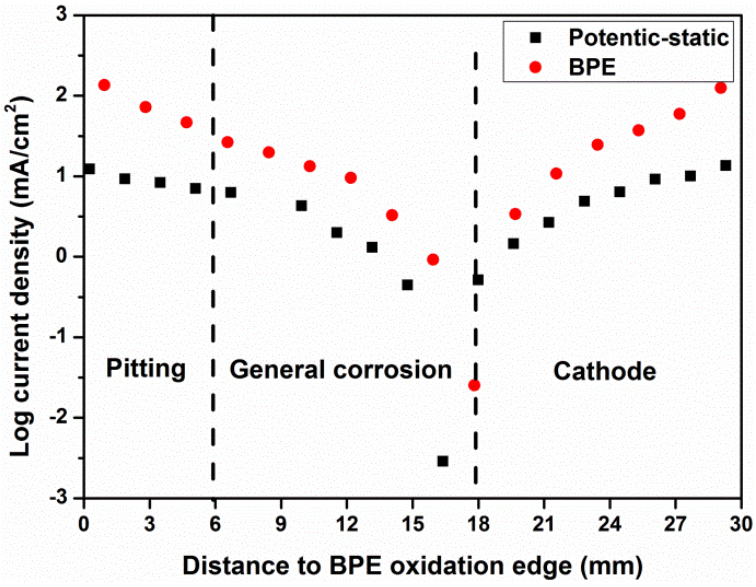

Figure 6.2- 9 The current density distribution on the BPE by direct measurement from segment BPEs and potentio-static polarisation test.

Pitting corrosion characteristics

The left side of the BPE is the BPE oxidation edge, the crevice corrosion is generated between the resin and BPE, here, only pitting corrosion is labelled and will be researched. Figure 6.2- 10 gives the pitting corrosion region of the

BPE, with this magnification, pits merged together and fully covered by the general corrosion next to the BPE oxidation edge. Some small size pits are also measured, which are the metastable pit. When pit close to each other or merge together, the continued growth pits are called the “champion pit” [39]. Before pit merge together, all pits show the circular shapes. At the region between the pitting and general corrosion, the surface is only part covered by the general corrosion. The general corrosion come from the pit electrolyte diffuse out of pit, with a low density of pit the electrolyte is not enough to corrode the whole sample surfaces, which only corrode the area near the pits.

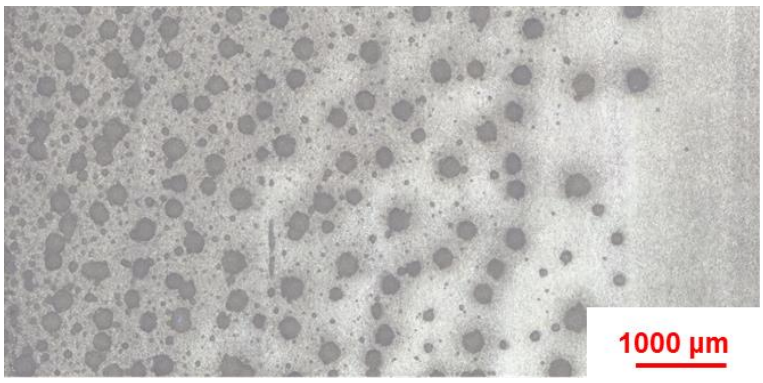

Figure 6.2- 10 The optical microscopy image of the pitting corrosion region on the BPE.

The pitting region is divided into 4 sub-regions, each region with a size of 1.5 x 4 mm^2 (length x width). The Region 1 is next to the BPE oxidation edge with the highest applied potential, region 4 has distance of 3-4 mm to the BPE oxidation edge. Figure 6.2- 11 (a) gives pit distribution in the different BPE region depend on the pit volume range. For the small volume pit (<10^4 μm^3), only measured in region 1, the small pits are repassivate pits, which cannot get enough current density. For a bigger volume pit (volume between 10^4 μm^3 and 10^5 μm^3), over 40 pits are found in region 1, 2, and 3, only 25 pits are found in region 4. For the pit volume over 10^5 μm^3, the numbers of pit are dramatically reduced in region 1 and 2 and slowly reduced in region 3 and 4. Pits with volume over 10^7 μm^3 are only measured in region 1 and region 2, caused by the pits merge together. Figure 6.2- 11 (b) offers the probability of nucleated pit grows to different volume in different BPE region. In region 1 and 2, over 55% of pit with volume less than 10^5 μm^3, only 20% pits can continue growth to a large size (over 10^6 μm^3). In the left two regions, the percentage

of pits growth to different pit volume (10^5, 10^6 and 10^7 μm^3) are similar ≈ 35%. In Figure 6.2- 11 (a), pits are concentrated with two volumes: 10^4 μm^3 and 10^6 μm^3 in all the BPE regions, the first peak indicates the metastable pit and the second peak is the stable pit. The pit volume act as the diffusion barrier for the pit growth, pit with large pit volume can be stable growth. Figure 6.2- 11 (b) shows at high applied potential region (region 1 and 2), over 60% pits are repassivate only 20% of pits can be stable growth. At low applied potential region (region 3 and 4), about 40% repassivates but >30% of pits can be stable growth. High applied potential can nucleate more pits, but more drastic competition between pits, result in not enough current for each pit to stable growth. For the low applied potential region, less pit is nucleated, but more current can be share to each pit, result in higher opportunities to become stable growth.

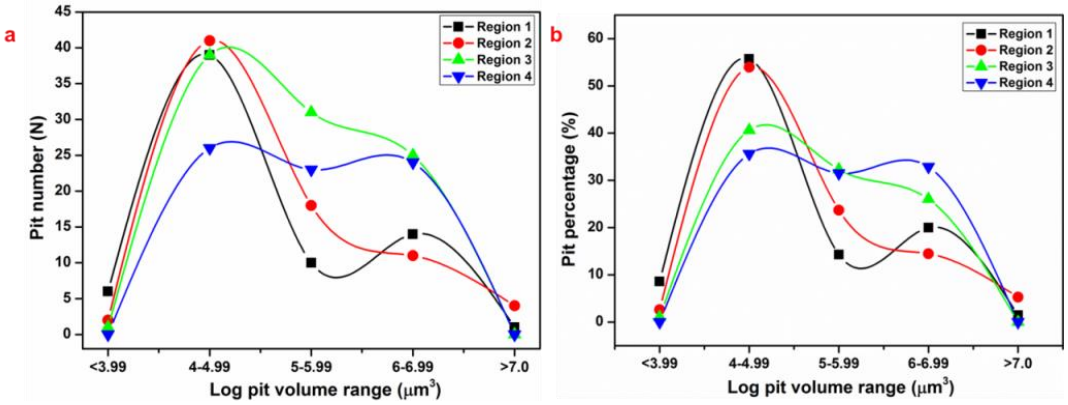

Figure 6.2- 11 Pit numbers (a) and percentage of pits (b) distribution with different BPE region depend on the pitting corrosion volume.

Figure 6.2- 12 (a) gives average pit growth factor calculate from deepest ten pits in each BPE region with the error bar stands for standard deviation. These deepest pits are nucleate at t=0 s. Pit growth kinetics typically follow a power law equation and independent to the applied potential [40,41].

$$d = Kt^b \qquad \text{Equation 3}$$

With (d) is the pit depth (μm), t is time (s), and (K) and (b) are experimental constants which influenced by temperature and pH value of the electrolyte, with typical values of (b) from 0.3 to 0.5. If we assume the value of (b) is 0.5, with (d) measurements from the confocal microscopy, and (K) values

calculated by solving Equation 3. The pit growth kinetics is independent to the local applied potential, so the pit growth factor is similar form region 1 to region 4. The pit growth factor is almost the similar around 2.9 between region 3 and 4. Pit growth factor in region 1 is lowest (about 2.6). The pit growth kinetics is reduced by pit merge together by a large number of nucleated pits. In region 2, the pit growth factor is 2.8, pits close to each other due to a large numbers of nucleated pits, result in less cathode area surround these pits, slightly reduce the pit growth factor. The standard deviations are reduced with lower applied potential as the pit growths has less influenced by pits close to each other or merge. Figure 6.2- 12 (b) gives the overall pit volume on the BPE, even the pit growth is independent to the applied potential, but the overall pit volume is related to the applied potential. The pit volume reduction is linearly along the BPE, similar to the linearly potential across the BPE.

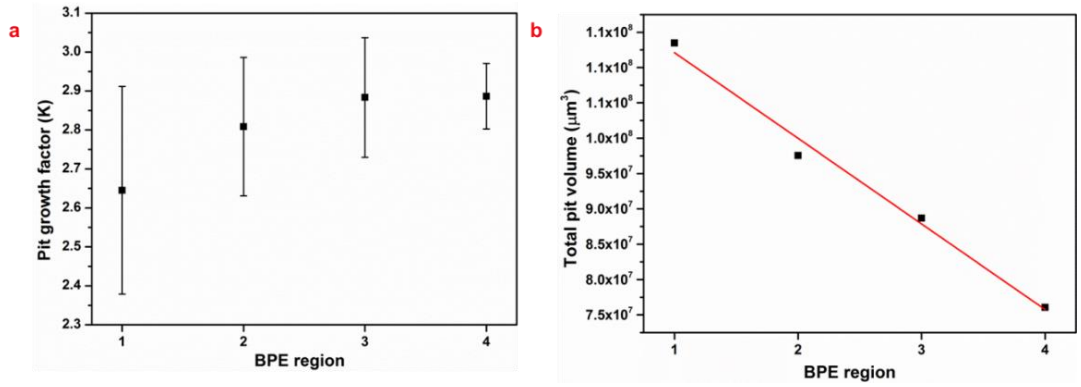

Figure 6.2- 12 The pit growth factor in different region on the BPE in (a) and the overall pit volume loss with different applied potential in (b).

6.26 Conclusions

BPE can obtain corrosion response over a large range of applied potentials which results in pitting corrosion, general corrosion, and a cathodic region, and the pit volume loss, pit growth kinetics, and the probability of the pit nucleation and stable growth under a wide range of applied potential are measured on one BPE sample. In contrast, with the conventional 3-electrode polarisation set-up, a similar breadth of results can only be achieved by carrying out numerous 3-electrode potentio-dynamic and potentio-static polarization experiments.

The split BPE is used to determine the potential and current density along the BPE, which match to Butler-Volmer equation under activation control. The OCP, E_{pit}, E_{corr}, corrosion rate, and the current density from BPE measurement and 3-electrode polarisation test vary. The gas evolution, electrochemical reactions in the electrolyte, and crevice corrosion in the BPE are the main reasons.

6.27 References

[1] Y. Zhou, D.L. Engelberg, Application of a modified bi-polar electrochemistry approach to determine pitting corrosion characteristics, Electrochemistry Communications. 93 (2018) 158–161.

[2] N. Pébère, V. Vivier, Local Electrochemical Measurements in Bipolar Experiments for Corrosion Studies, ChemElectroChem. 3 (2016) 415–421.

[3] S. Munktell, M. Tydén, J. Högström, L. Nyholm, F. Björefors, Bipolar electrochemistry for high-throughput corrosion screening, Electrochemistry Communications. 34 (2013) 274–277.

[4] S.E. Fosdick, K.N. Knust, K. Scida, R.M. Crooks, Bipolar electrochemistry, Angewandte Chemie - International Edition. 52 (2013) 10438–10456.

[5] J. Duval, J.M. Kleijn, H.P. Van Leeuwen, Bipolar electrode behaviour of the aluminium surface in a lateral electric field, Journal of Electroanalytical Chemistry. 505 (2001) 1–11.

[6] K. Wiesener, D. Ohms, G. Benczúr-Ürmössy, M. Berthold, F. Haschka, High power metal hydride bipolar battery, Journal of Power Sources. 84 (1999) 248–258.

[7] H. Termebaf, M. Shayan, A. Kiani, Two-Step Bipolar Electrochemistry: Generation of Composition Gradient and Visual Screening of Electrocatalytic Activity, Langmuir. 31 (2015) 13238–13246.

[8] C. Ulrich, O. Andersson, L. Nyholm, F. Björefors, Potential and current density distributions at electrodes intended for bipolar patterning, Analytical Chemistry. 81 (2009) 453–459.

[9] V.M. Huang, S.L. Wu, M.E. Orazem, N. Pébre, B. Tribollet, V. Vivier, Local electrochemical impedance spectroscopy: A review and some recent developments, Electrochimica Acta. 56 (2011) 8048–8057.

[10] R.K. Perdue, D.R. Laws, D. Hlushkou, U. Tallarek, R.M. Crooks, Bipolar electrode focusing: The effect of current and electric field on concentration enrichment, Analytical Chemistry. 81 (2009) 10149–10155.

[11] K. Kusakabe, S. Morooka, Y. Kato, Current paths and electrolysis efficiency in bipolar packed-bed electrodes, Journal of Chemical Engineering of Japan. 15 (1982) 45–50.

[12] J.F.L. Duval, M. Minor, J. Cecilia, H.P. Van Leeuwen, Coupling of lateral electric field and transversal faradaic processes at the conductor/electrolyte solution interface, Journal of Physical Chemistry B. 107 (2003) 4143–4155.

[13] H.S. Isaacs, The Effect of Height on the Current Distribution Measured with a Vibrating Electrode Probe, Journal of The Electrochemical Society. 138 (1991) 722.

[14] C. Ulrich, O. Andersson, L. Nyholm, F. Bjorefors, Formation of molecular gradients on bipolar electrodes, Angewandte Chemie - International Edition. 47 (2008) 3034–3036.

[15] O. Klett, L. Nyholm, Separation high voltage field driven on-chip amperometric detection in capillary electrophoresis, Analytical Chemistry. 75 (2003) 1245–1250.

[16] O. Ordeig, N. Godino, J. Del Campo, F.X. Muñoz, F. Nikolajeff, L. Nyholm, On-chip electric field driven electrochemical detection using a poly(dimethylsiloxane) microchannel with gold microband electrodes, Analytical Chemistry. 80 (2008) 3622–3632.

[17] M. Sentic, S. Arbault, B. Goudeau, D. Manojlovic, A. Kuhn, L. Bouffier, N. Sojic, Electrochemiluminescent swimmers for dynamic enzymatic sensing, Chemical Communications. 50 (2014) 10202–10205.

[18] K.F. Chow, F. Mavré, J.A. Crooks, B.Y. Chang, R.M. Crooks, A large-scale, wireless electrochemical bipolar electrode microarray, Journal of the American Chemical Society. 131 (2009) 8364–8365.

[19] S. Yang, D.D. Macdonald, Theoretical and experimental studies of the pitting of type 316L stainless steel in borate buffer solution containing nitrate ion, Electrochimica Acta. 52 (2007) 1871–1879.

[20] S. Frangini, N. De Cristofaro, Analysis of the galvanostatic polarization method for determining reliable pitting potentials on stainless steels in crevice-free conditions, Corrosion Science. 45 (2003) 2769–2786.

[21] W. Hao, Z. Cheng, L. Jin, J. Yiming, Electrochemical corrosion behaviors of ITO films at anodic and

cathodic polarization in sodium hydroxide solution, Proceedings, 2008 International Conference on Electronic Packaging Technology and High Density Packaging, ICEPT-HDP 2008. (2008) 6–9.

[22] H.Y. Ha, J.Y. Kang, J. Yang, C.D. Yim, B.S. You, Limitations in the use of the potentiodynamic polarisation curves to investigate the effect of Zn on the corrosion behaviour of as-extruded Mg-Zn binary alloy, Corrosion Science. 75 (2013) 426–433.

[23] INDIG ME, GROOT C, Some Limitations of the Linear Polarization Techniques in Evaluating Corrosion Behavior, Corrosion. 25 (1969) 455–461.

[24] S.F.. A.G.J.M.M. N. Birbilis, Electrochemical techniques for studying corrosion of reinforcing steel: Limitations and advantages, Corrosion Science. 61 (2005) 37–50.

[25] S. Al Saadi, Y. Yi, P. Cho, C. Jang, P. Beeley, Passivity breakdown of 316L stainless steel during potentiodynamic polarization in NaCl solution, Corrosion Science. 111 (2016) 720–727.

[26] C. Örnek, C. Leygraf, J. Pan, Passive film characterisation of duplex stainless steel using scanning Kelvin prove force microscopy in combination with electrochemical measurements, Npj Materials Degradation. 3 (2019) 8.

[27] J.M. Bastidas, C.L. Torres, E. Cano, J.L. Polo, Influence of molybdenum on passivation of polarised stainless steels in a chloride environment, Corrosion Science. 44 (2002) 625–633.

[28] G. Okamoto, Passive film of 18-8 stainless steel structure and its function, Corrosion Science. 13 (1973) 471–489.

[29] D.G. Kolman, Limitations of Potentiostatic Repassivation Techniques and Their Relationship to the Applicability of the High Field Approximation to the Repassivation of Titanium, Journal of The Electrochemical Society. 142 (2006) 2179.

[30] T. Cain, S.B. Madden, N. Birbilis, J.R. Scully, Evidence of the Enrichment of Transition Metal Elements on Corroding Magnesium Surfaces Using Rutherford Backscattering Spectrometry, Journal of The Electrochemical Society. 162 (2015) C228–C237.

[31] P. Meisterjahn, U. König, J.W. Schultze, Potentiostatic pulse measurements of oxide growth on zirconium, Electrochimica Acta. 34 (1989) 551–561.

[32] R. Kodým, K. Bouzek, D. Šnita, J. Thonstad, Potential and current density distributions along a bipolar electrode, Journal of Applied Electrochemistry. 37 (2007) 1303–1312.

[33] J.M. Rubi, S. Kjelstrup, Mesoscopic Nonequilibrium Thermodynamics Gives the Same Thermodynamic Basis to Butler−Volmer and Nernst Equations, The Journal of Physical Chemistry B. 107 (2003) 13471–13477.

[34] D.A. Noren, M.A. Hoffman, Clarifying the Butler-Volmer equation and related approximations for calculating activation losses in solid oxide fuel cell models, Journal of Power Sources. 152 (2005) 175–181.

[35] T. Haruna, D. Macdonald, Theoretcal Prediction of the Scan Rate Dependencies of the Pitting Potential and the Probabilily Distribution in the Induction Time, Journal of The Electrochemical Society. 144 (1997) 1574–1581.

[36] X.L. Zhang, Z.H. Jiang, Z.P. Yao, Y. Song, Z.D. Wu, Effects of scan rate on the potentiodynamic polarization curve obtained to determine the Tafel slopes and corrosion current density, Corrosion Science. 51 (2009) 581–587.

[37] I. Ignatov, O. Mosin, G. Gluhchev, S. Karadzhov, G. Miloshev, N. Ivanov, Studying Electrochemically Activated NaCl Solutions of Anolyte and Catholyte by Methods of Non-Equilibrium Energy Spectrum (NES) and Differential Non-Equilibrium Energy Spectrum (DNES), Journal of Medicine, Physiology and Biophysics. 20 (2016) 13–23.

[38] R.K. Dayal, N. Parvathavarthini, B. Raj, Influence of metallurgical variables on sensitisation kinetics in austenitic stainless steels, International Materials Reviews. 50 (2005) 129–155.

[39] N.J. Laycock, D.P. Krouse, S.C. Hendy, D.E. Williams, Computer Simulation of Pitting Corrosion of Stainless Steels, Interface, The Electrochemical Society. (2014) 65–71.

[40] P. Ernst, R.C. Newman, Pit growth studies in stainless steel foils. I. Introduction and pit growth kinetics, Corrosion Science. 44 (2002) 927–941.

[41] M.K. Cavanaugh, R.G. Buchheit, N. Birbilis, Modeling the environmental dependence of pit growth using neural network approaches, Corrosion Science. 52 (2010) 3070–3077.

6.3 On the Application of Bipolar Electrochemistry to Characterise the Localised Corrosion Behaviour of Type 420 Ferritic Stainless Steel

Yiqi Zhou[*1], *Dirk Lars Engelberg*[1,2]

(1) *Corrosion & Protection Centre, School of Materials, The University of Manchester, M13 9PL, Manchester, UK*

(2) Materials Performance Centre, The University of Manchester, M13 9PL, Manchester, UK

* Corresponding author: Yiqi.Zhou@postgrad.manchester.ac.uk

6.31 Highlights

The application of bipolar electrochemistry for observing pit growth kinetics and pit coalescence has been demonstrated.

$Cr_{23}C_6$, Cr_3C_2, and Cr_7C_3 have been identified as pit nucleation sites.

A critical dissolved pit volume has been observed for the transition to stable pit growth.

6.32 Abstract

Bipolar electrochemistry has been applied to Type 420 ferritic stainless steel in order to determine the full spectrum of anodic-to-cathodic polarisation behaviour. The occurrence of crevice corrosion, pitting corrosion in combination with general corrosion, pitting corrosion only, general corrosion only, followed by a cathodic region has been observed. Instances of pitting corrosion initiated near chromium-rich carbides with $Cr_{23}C_6$, Cr_3C_2, and Cr_7C_3 identified as pit nucleation sites. The observed pit growth kinetics were independent of the electrochemical over-potential. Characterisation of the pit size distributions supports the presence of a critical dissolved volume for the transition of metastable to stable pit growth and pit coalescence.

Keywords: stainless steel; bipolar electrochemistry; pitting corrosion; chromium carbides; pit growth factor.

6.33 Introduction

The application of bipolar electrochemistry provides access to the full spectrum of

Anodic-to-cathodic reactions along a bipolar electrode (BPE) [1–4]. In earlier studies, bipolar electrochemistry was applied for electro-syntheses, in photo electrochemical cells, for battery research, high throughput deposition of metals, and corrosion investigations [5–7]. In a nutshell, bipolar

electrochemistry combines a non-contact experimental setup with the ability of fast throughput corrosion screening, with access to all anodic and cathodic reactions in one experiment [1–3].

Stainless steels are prone to pitting corrosion in halide containing environments. In general, pitting corrosion is a rapid metal dissolution process, affected by the applied electrochemical potential, concentration of halides, microstructure, and electrolyte temperature [8,9]. At the pit initiation stage, all pits are considered to be metastable, followed by either re-passivation or the formation of stable pits [10,11]. The development of stable pits requires a critical pitting potential (Epit) and minimum critical pitting temperature (CPT) [12,13]. Changes in exposure temperature typically do not affect pit morphology, but the applied potential, microstructure condition, and Cl^-concentration can influence the resulting pit shape [1,9]. In duplex stainless steel, the pit morphology is also influenced by the ratio, size, and distribution of the austenite and ferrite crystallographic phases [14,15].

Ferritic stainless steels have a low thermal expansion, high yield strength and stiffness, and good deformation behaviour, with excellent stress corrosion cracking (SCC) resistance [16,17]. Type 420 ferritic stainless steel is a hardenable stainless steel grade, with a Cr concentration between 12% and 14% and a high carbon content [18]. Type 420 is typically in service with a martensitic microstructure, obtained via austenitisation treatment and quenching from annealed microstructures. The final microstructure contains chromium carbides, and the corrosion behaviour of this microstructure condition is dependent on austenitisation temperature, quench rate, and tempering treatments [19,20]. In its annealed condition, Type 420 stainless steel has a ferritic microstructure, which makes the microstructure easier to machine into shapes and structures [21]. After austenitisation treatment, the chromium carbides generally dissolve into the matrix, with subsequent tempering applied in order to improve the ductility and toughness by changing the microstructure, secondary phase and carbide distribution, and the fraction of the retained austenite [22–24].

The work reported in this paper provides insight into the pitting corrosion behaviour of annealed Type 420 ferritic stainless steel via the application of a bipolar electrochemistry approach. The aim is to obtain information about the

relationship between the electrochemical potential and the corrosion behaviour of this alloy, with a focus on determining pit nucleation sites and the associated growth kinetics.

6.34 Materials and Methods

Solution annealed Type 420 stainless steel with a composition (wt %) of 13.7 Cr, 0.46 C, 0.47 Si, 0.39 Mn, and Fe (bal.) was used in this study. The stainless steel had a hardness of 198.4 $HV_{0.5}$, indicating a soft annealed microstructure condition. Micro hardness was measured with a Buehler Micromet Tester, using an applied load of 4.903 N ($HV_{0.5}$), with the mean and standard deviation determined with five measurements.

Figure 6.3- 1a shows the setup for the bipolar electrochemistry testing. With a sufficiently high potential across the BPE, oxidation reactions occur close to the negative feeder electrode, and vice versa for the reduction reactions which occur close to the positive feeder electrode. Two different BPE samples were used for carrying out the bipolar experiments, with dimensions of 30 x 10 x 1.2 mm^3 (length x width x thickness) and 50 x 20 x 1.2 mm^3. The BPE samples were mounted in Araldite resin, with the exposed area ground to 1200 grit, followed by polishing to a 1 µm diamond paste finish. The shorter (30 mm) sample was used to explore the pit nucleation sites, with the longer (50 mm) sample then applied for studying pit growth, demonstrating the versatility of this technique.

The 30 mm long BPE had a distance of 60 mm between the feeder electrodes. For the 50 mm BPE, the distance between the two feeder electrodes was set to 75 mm. Both BPEs were centred between the two feeder electrodes, with an applied potentio-static potential of 10 V acting on the feeder electrodes. The electrolyte was 0.1 M HCl with a volume of 200 mL, with experiments carried out up to 30 min. The surface area of each platinum feeder electrode was 4 cm^2.

Figure 6.3- 1b demonstrates the potential gradient acting along the BPE, which was measured using a Luggin capillary connected to a saturated calomel electrode (SCE). The Luggin capillary was set ≈1mm above the centre line of the BPE surface, which was in turn connected to a copper wire and an IVIUM-Compactstat in order to determine the local potential. To measure the

local potential during the bipolar electrochemistry experiments, the open circuit potential (OCP) was stabilised first, and the power supply of the feeder electrodes was then switched on. The reported potential change on the y-axis is the difference of the measured potential with respect to OCP, which can be described as the acting over-potential along the BPE.

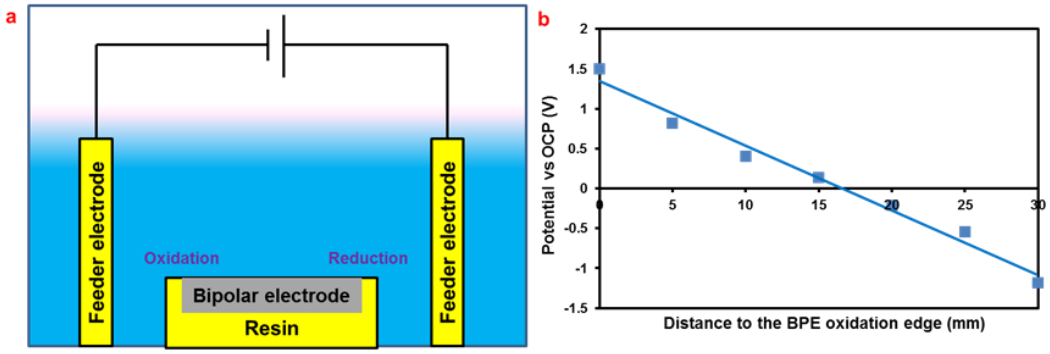

Figure 6.3- 1 (a) A schematic diagram of the bipolar electrochemistry setup, and (b) the measured potential distribution on the bipolar electrode (BPE) (30 mm length) using a Luggin capillary connected to the saturated calomel electrode (SCE).

All Type 420 ferritic BPE samples were washed with soap and dried in hot air after completing the bipolar electrochemistry experiments. The surface morphology of the tested samples was measured via laser scanning confocal microscopy, using a Keyence VK-X200K (Keyence Corporation, Osaka, Japan). For the electron backscatter diffraction (EBSD) and angle selective backscatter (AsB) microstructure analyses, the samples were ground to 4000 grit and polished to a 0.25 µm diamond paste finish, followed by fine polishing with oxide polishing suspensions (OPS) of colloidal silica. A Zeiss Sigma VP FEG-SEM (Zeiss, Jena, Germany) was used for scanning electron microscopy (SEM) imaging at 1.5 kV, with high resolution EBSD analysis carried out at 15 kV and a step size of 33 nm. An FEG-FEI Quanta 250 SEM (FEI Company, Hillsboro, OR, USA) was used for the energy dispersive x-ray (EDX) elemental analysis using 20 kV.

6.35 Results and Discussion

The microstructure of Type 420 stainless steel is shown in Figure 6.3- 2a, highlighting the different grain orientations of the annealed ferritic matrix. A small number of dark spots, shown by the arrows in Figure 6.3- 2a, were present in the micrograph, possibly due to the metallographic preparation

method (OPS polish). Chromium carbides were omnipresent in the matrix, with Figure 6.3- 2b showing typical morphologies in the form of one smaller (≈100 nm) and three larger ellipsoids (≈800 nm). The microstructure had typical chromium carbide sizes of up to ≈ 2 μm.

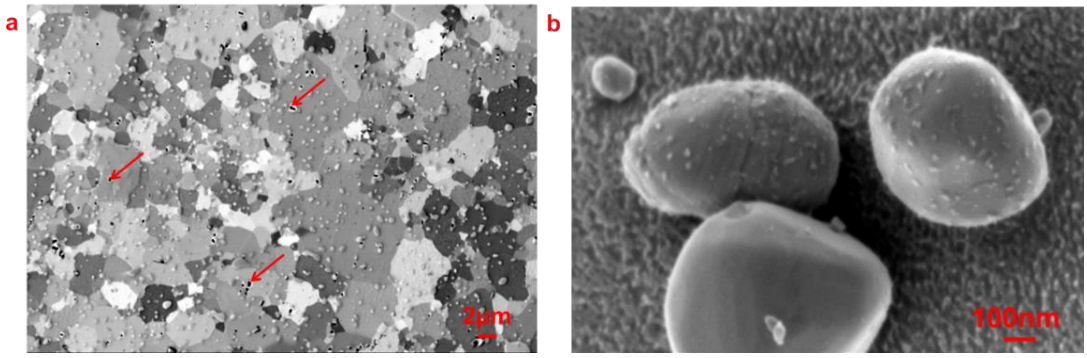

Figure 6.3- 2 (a) AsB SEM image of Type 420 stainless steel with the arrows showing voids, and (b) typical size and shape of chromium carbides.

Figure 6.3- 3a shows a SEM image of the Type 420 stainless steel with carbides present at triple junctions, along grain boundaries, and within grains, with the parameters of the possible carbides in this material listed in Table 6.3-1. The EDX images in Figure 3 confirm that all observed particles were chromium-rich carbides, with some containing higher Mn contents. The latter is related to the process annealing treatment, where Mn diffuses into the $M_{23}C_6$ [25]. $M_{23}C_6$ was homogenously distributed in the matrix, with the EBSD map in Figure 6.3- 3b showing the carbides, identified as $Cr_{23}C_6$, Cr_3C_2, and Cr_7C_3. The other two carbide types (Cr_3C, CrC) were not observed here in our study.

Table 6.3- 1 Database with crystallographic parameters for electron backscatter diffraction (EBSD) phase identification from Inorganic Crystal Structure Database (ICSD) and the Aztec EBSD software (Version 4.2, Oxford Instruments, Abingdon, UK).

Phase	A	B	C	Alpha	Beta	Gamma	Space Group
Fe3C	5.11 Å	6.78 Å	4.54 Å	90.00°	90.00°	90.00°	62
Iron bcc	2.87 Å	2.87 Å	2.87 Å	90.00°	90.00°	90.00°	229
Cr3C	5.12 Å	6.80 Å	4.58 Å	90.00°	90.00°	90.00°	62
Cr3C2	5.53 Å	11.49 Å	2.83 Å	90.00°	90.00°	90.00°	62
Cr7C3	4.53 Å	7.01 Å	12.14 Å	90.00°	90.00°	90.00°	62
Cr23C6	10.66 Å	10.66 Å	10.66 Å	90.00°	90.00°	90.00°	225
CrC	4.03 Å	4.03 Å	4.03 Å	90.00°	90.00°	90.00°	225

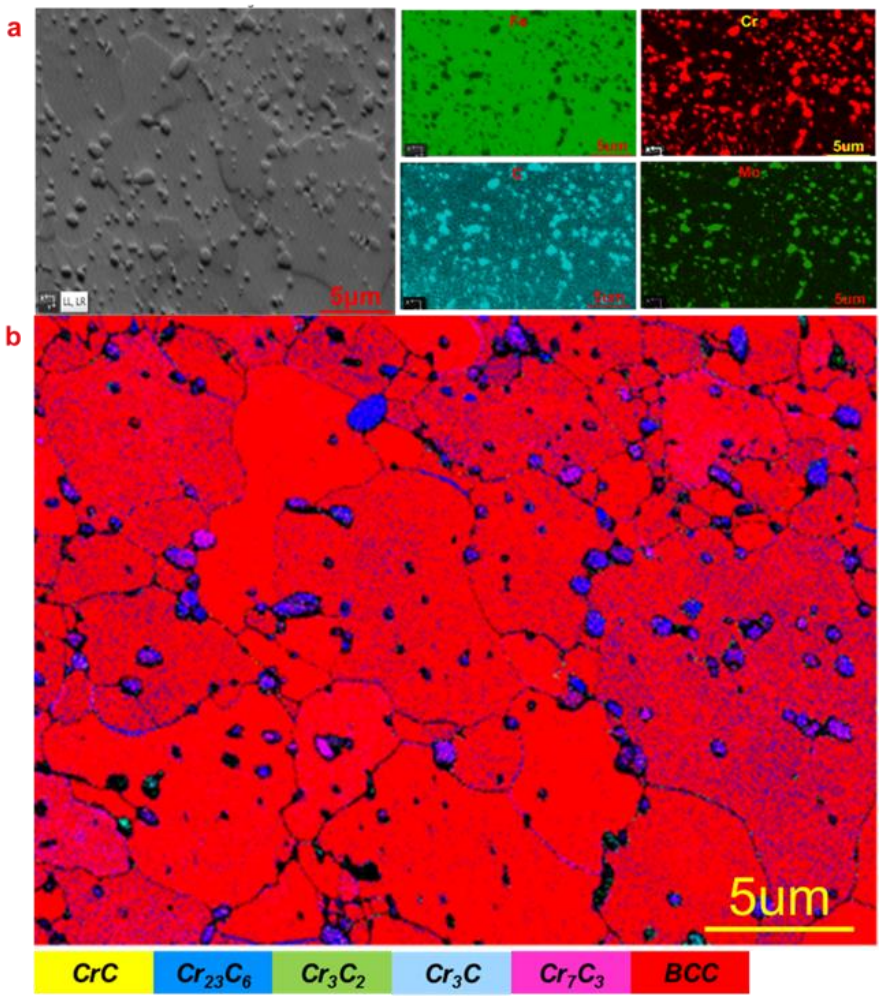

Figure 6.3- 3 (a) SEM image of Type 420 ferritic stainless steel with EDX elemental maps of Cr, Fe, C, and Mn, and (b) high-resolution EBSD map highlighting chromium carbides (BCC = body centred cubic, ferritic matrix).

Pit Nucleation Sites

Bipolar electrochemistry testing was carried out to identify the pit nucleation sites in this material. Figure 6.3- 4 shows the 30 mm long BPE electrode with three distinctive regions highlighted after bipolar testing. From the BPE oxidation edge on the left to the reduction edge on the right, the overall corrosion response showed crevice corrosion at the edges, pitting corrosion surrounded by general corrosion, general corrosion only, and a large cathodic region.

All observed pits were open pits without lacy metal covers. The region containing pits had a length of 6 mm measured from the oxidation edge, with general corrosion thereafter observed until a depth of 17 mm was reached.

The remaining 13 mm of the BPE was the cathodic region. The boundary between the anodic and cathodic site was not in the centre of the BPE electrode, due to non-symmetric differences in the anodic vs. cathodic current response. By comparing the corrosion response along the BPE and the potential distribution from Figure 1b, the critical pitting potential was estimated to be around +0.9 V_{OCP} for this sample.

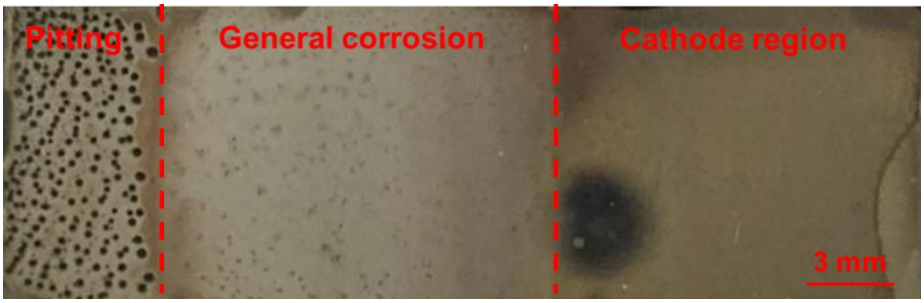

Figure 6.3- 4 Appearance of the 30 mm long BPE after bipolar electrochemistry testing for 30 min, with the left side showing large pits at the oxidation edge and the right side showing the reduction edge.

To identify the earliest onset of pit nucleation, the bipolar polarisation was applied for 5 s only, with Figure 6.3- 5a highlighting the typical pit nucleation sites (labelled with arrows). From the EDX maps, a strong Cr and C signal confirms that the observed particles here were all chromium rich carbides. Localised corrosion was initiated at the interface between chromium carbides and the matrix, caused by either micro-galvanic effects [21] or Cr depletion [28], in combination with occluded crevice geometries around some of these carbides [29]. Chromium carbides are typically more electrochemical noble, so they can easily act as cathodes, and the surrounding matrix can act as the anode [21]. The associated Cr depleted regions are typically caused by Cr diffusion to form chromium carbides. These regions contain significantly reduced Cr concentrations and are not able to form stable passive films, especially in low Cr containing ferritic stainless steels [28]. Figure 6.3- 5 b shows the EDX map of a pit with a diameter of 5 µm, showing a large number of chromium carbides inside the dissolved pit volume. Chromium carbides dropped into the formed pit cavity after the surrounding stainless steel was corroded away, with the carbides remaining inside this cavity due to their higher electrochemical nobility.

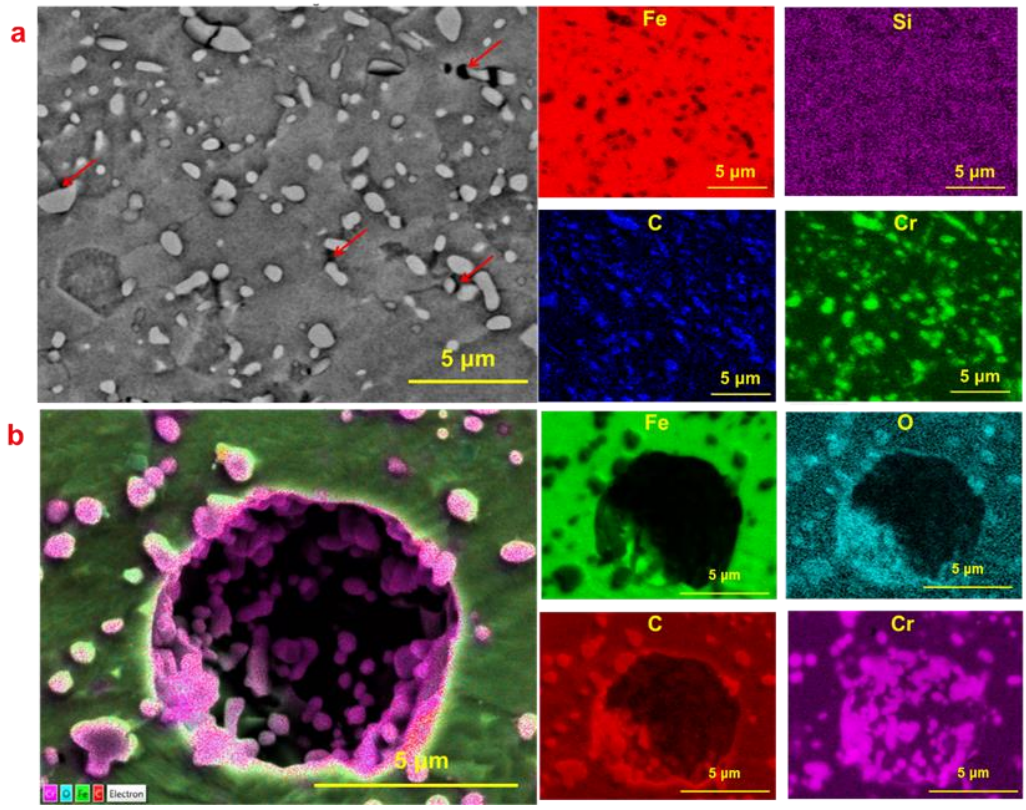

Figure 6.3- 5 (a) SEM images with EDX maps of Type 420 stainless steel after 5 s exposure time, with the arrow highlighting a pit nucleation site, and (b) EDX maps of a pitting with 5 um diameter with corresponding EDX maps.

Figure 6.3- 6 summarises the images of the region containing pitting corrosion after 5 min of bipolar electrochemistry exposure. Figure 6.3- 6a shows a pit with a diameter of 80 µm, surrounded by small voids which are indicative of the nucleation of several metastable pits. The circumference of the pit contained a ring of general corrosion. Pit growth ultimately results in the formation of an aggressive electrolyte (low pH, high Cl^- concentration) inside the pit [30]. The electrolyte can diffuse out and corrode the matrix surrounding the pit mouth, before the solution dilutes. Figure 6.3- 6b shows a higher magnification image of the pit mouth, with chromium carbides protruding out of the matrix, supporting the notion of their higher corrosion resistance.

Figure 6.3- 6c provides another SEM image of the outer part of the corroded pit circumference, with Figure 6.3- 6d showing an SEM image of the pit bottom. Grains with different heights can be seen, with larger sized chromium carbides at the surface. The cavities near the chromium carbides point towards the localised dissolution of the Type 420 matrix.

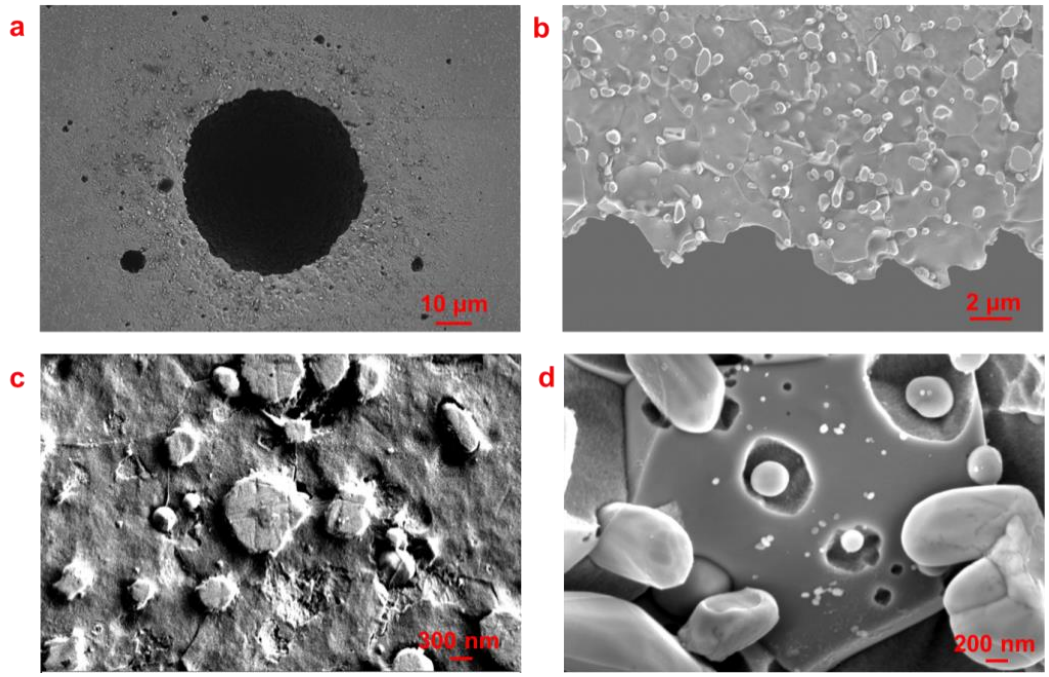

Figure 6.3- 6 (a) SEM image of a pit with a corroded circumference, (b) higher magnification image of the corroded circumference of the pit, (c) the corroded outer part of the pit ring, and (d) SEM image of the pit bottom.

General Corrosion Behaviour

Figure 6.3- 7a shows SEM images of the general corrosion region in Figure 6.3- 4 after polarising the BPE for 30 min. A large number of chromium carbides are also here protruding out of the matrix in the corroded regions. Individual grains of the corroded matrix can be seen, with Figure 6.3- 7b showing chromium carbides with typical sizes of ≈ 200 nm located at a grain boundary. The spherical shaped carbides remained at the grain surface, and ellipsoid chromium carbides were embedded within the matrix. Grains with different heights were observed within the general corrosion region, which were covered by fin-like surface structures, as shown in Figure 6.3- 7c,d. The presence of these fins points towards the formation of α-FeOOH with sedimentary amorphous layers, which have been reported to be either whisker, rod, or fin shaped [31]. α-FeOOH is generally transformed from γ-FeOOH, via the formation of Fe3O4 [32,33]. The presence of γ-FeOOH and α-FeOOH can improve the corrosion resistance, as they are stable and protective passive films. However, Fe_3O_4 reduces the corrosion resistance, as highly conductive

properties result in cathode, which accelerates the corrosion in the matrix [34,35].

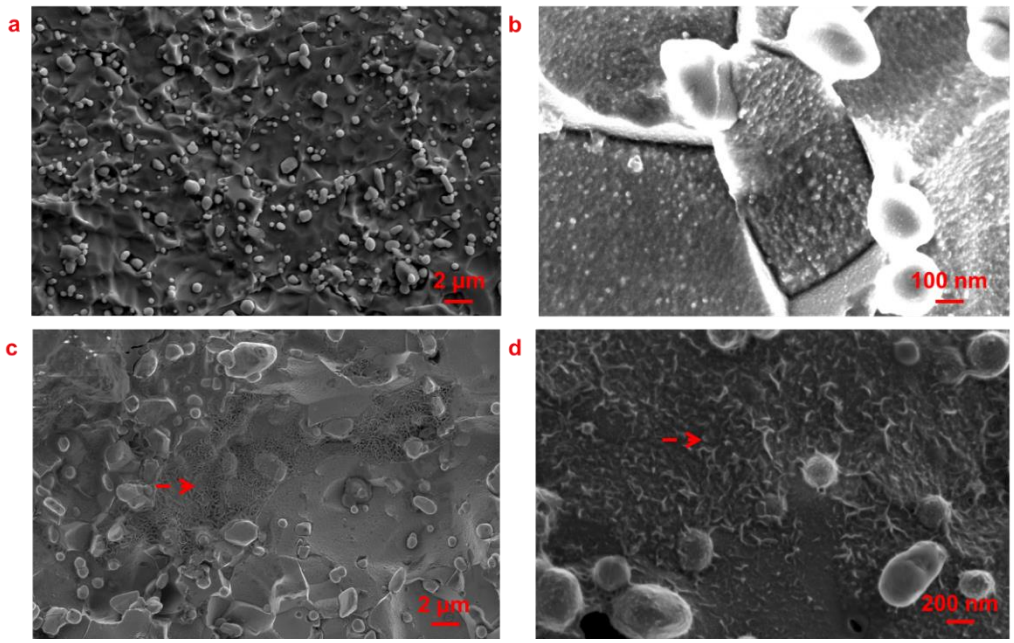

Figure 6.3- 7 General corrosion on the BPE, with (a) carbides protruding out of the matrix, (b) grains with different heights and carbides at grain boundaries, and (c, d) the presence of FeOOH.

Figure 6.3- 8 shows images of the cathodic site of the BPE, containing discrete particles. The particle length varied from 10 µm to 50 µm, and their presence is believed to be related to local electrochemical reactions. The EDX spectrum showed carbon, chloride, and oxygen rich particles, which could be easily removed by soap water cleaning.

Cl_2 and HClO are generated from electrochemical reactions in HCl electrolyte under high applied potentials [36]. Dissolved Cl_2 gas results in highly active oxidants: Cl2O, ClO_2, ClO^-, HClO, Cl^*, and $HO2^*$ (* indicates reactive free radicals) [36]. These highly active oxidants can diffuse to the cathodic sites and be deposited on the sample surface via electrochemical deposition reactions.

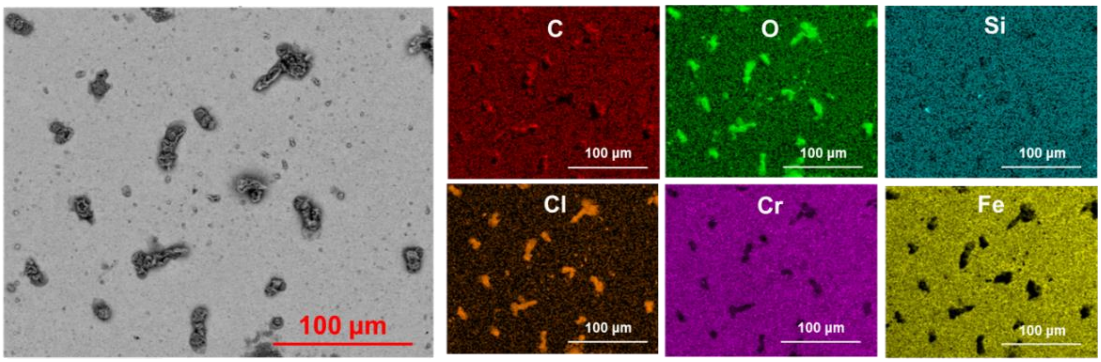

Figure 6.3- 8 SEM images and corresponding EDX images of the cathodic region on the BPE.

Pitting Corrosion Kinetics

The advantage of applying bipolar electrochemistry to pitting corrosion studies lies in the ability to observe pit nucleation and growth along the surface of the BPE, i.e., along the acting potential gradient. This allows researchers to investigate the earliest onset of pitting, the determination of pit growth kinetics, and associated pit coalescence.

An example of this is shown in Figure 6.3- 9, which shows the 50 mm long BPE after exposure to bipolar electrochemistry for 30 min. Here, on the longer electrode, four distinct regions can clearly be seen along the BPE surface, labelled A–D. The left side of the BPE is the BPE oxidation edge, which had the highest degree of localised corrosion. Closer inspection of the regions revealed the presence of a large crevice around the edge of the sample and pitting corrosion surrounded by general corrosion, followed by a region with pitting corrosion only, general corrosion only, and no corrosion at all. The latter is indicative of the cathodic region. All the observed pits were open pits with a lower applied potential, resulting in general corrosion.

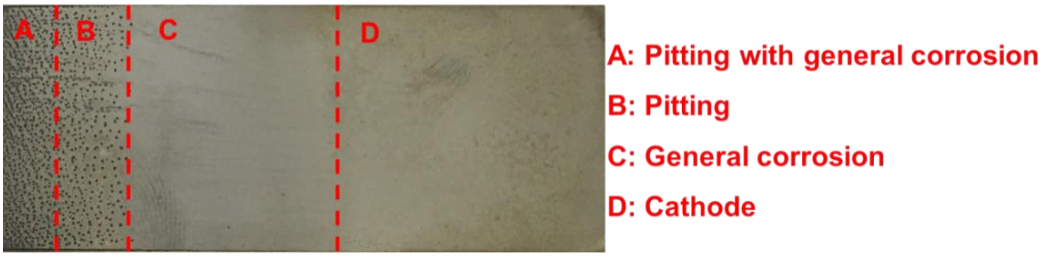

Figure 6.3- 9 The surface appearance of the 50 mm long BPE after 30 min bipolar exposure.

Figure 6.3- 10a shows an optical image of the oxidation edge, highlighting the crevice, and both regions containing pits (A, B) from Figure 6.3- 9. Close to the oxidation edge, pitting with general corrosion can be observed with a higher pit density. At a lower acting potential (further to the right), only pitting corrosion can be observed, with far fewer nucleated pits. Figure 6.3- 10b shows the 3D images of these regions, supporting the presence of a heavily corroded crevice, which developed between the BPE and the surrounding resin.

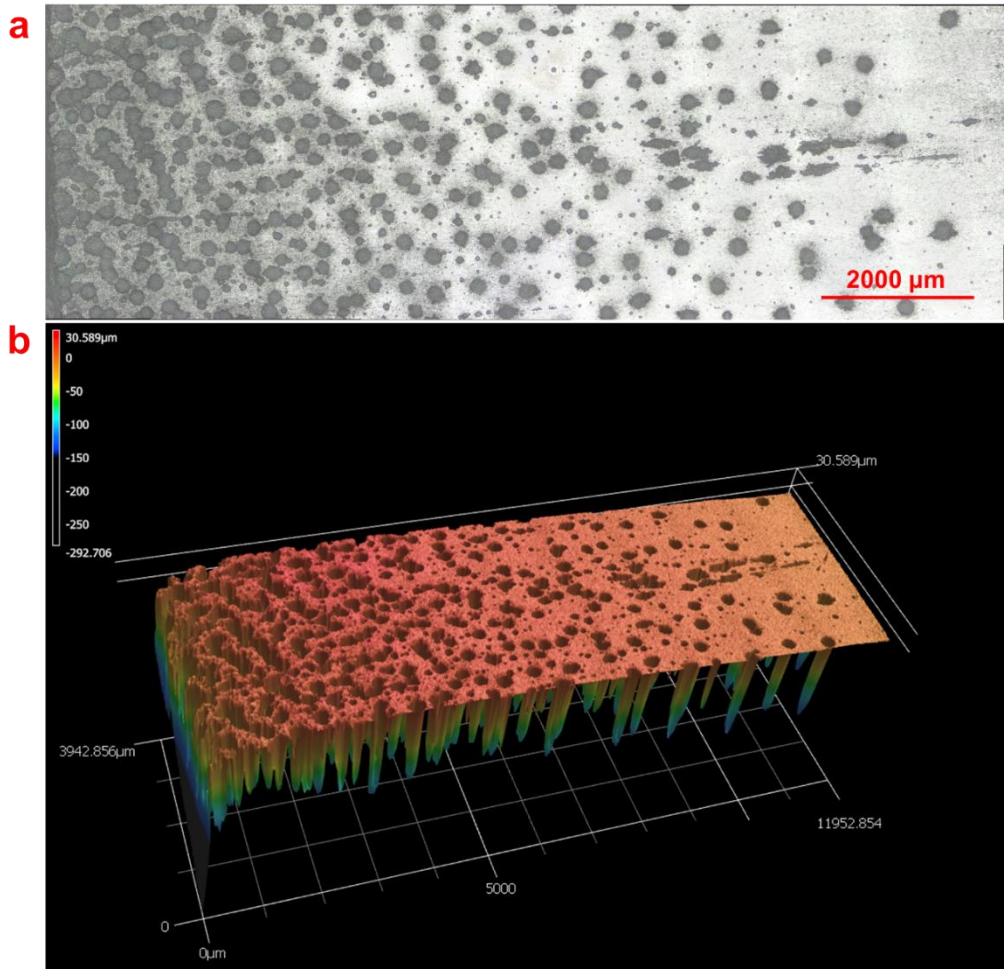

Figure 6.3- 10 (a) The optical image of the pitting corrosion region on BPE (50 mm), and (b) the corresponding 3D laser confocal image of this region.

The pit covered region in Figure 6.3- 9 was divided into seven sub-regions, each with a size of 1.5 × 4 mm^2 (length × width), as shown in Figure 6.3- 11a. Region I represented the highest potential close to the oxidation edge, with

region VII representing the lowest applied potential, 9 to 10.5 mm away from the oxidation edge. Region I contained the pit region with crevice, with regions II to IV showing pitting corrosion with general corrosion, whereas in regions V to VII, only pitting corrosion was observed. The pit density was reduced from region I to VII, with pits clearly coalesced in regions I, II, and III. The presence of numerous pits close to each other was found in regions IV and V, and predominantly isolated pits were found in regions VI and VII.

Figure 6.3- 11b shows the total dissolved pit volume in each of the seven regions, with the highest volume determined in region I and the lowest in region VII. The pit volume reduced exponentially from the BPE oxidation edge to the centre. Since the potential was linearly distributed along the length of the sample, an exponential potential vs. current relationship could be assumed [37].

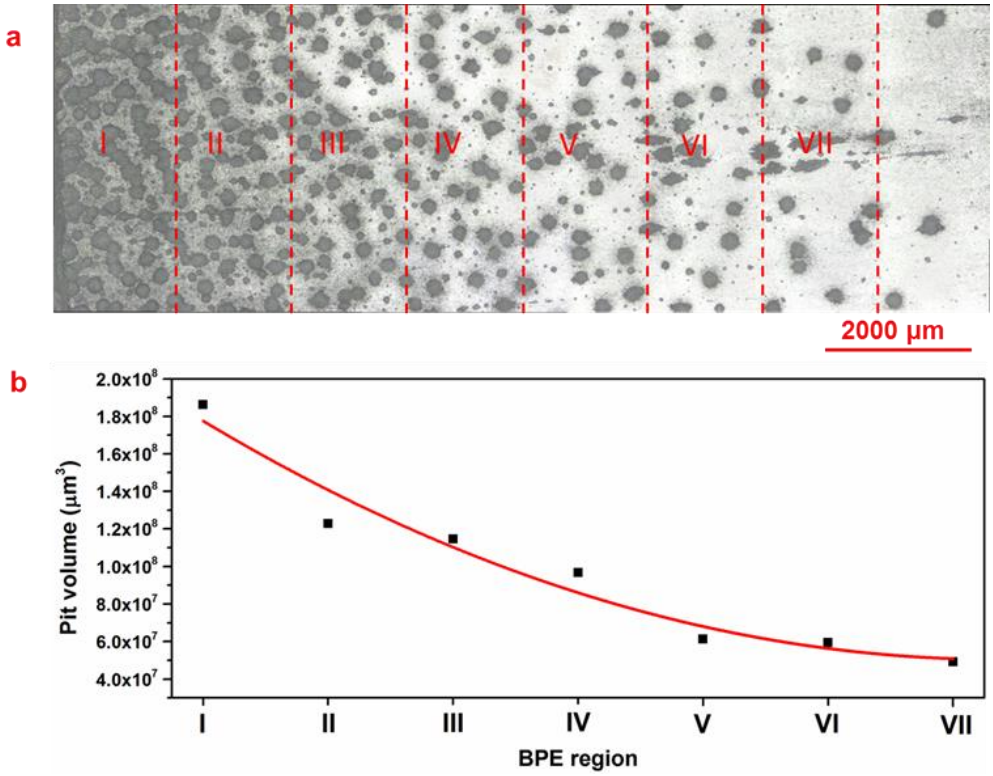

Figure 6.3- 11 (a) Overview of the seven pit covered regions, with (b) the corresponding pit volumes measured using laser confocal microscopy.

Figure 12a gives the number of pits with their corresponding pit volumes as a function of the seven investigated regions, with the reported data obtained via laser confocal microscopy. From regions III to VII, i.e., along a decreasing potential, the number and volume of pits decreased. Regions I and II gave a

slightly different response, with fewer pits but typically larger volumes. This observation is linked to the presence of a crevice in region I and the coalescence of larger pits in regions closer to the oxidation edge. From regions IV to VII, the pit numbers and the pit volumes were both clearly reduced, following the expected trend of fewer and smaller pits at lower applied potentials.

Figure 6.3- 12a describes the sizes of all pits found in regions I to VII, providing information about the total number of pits and their size distributions. The largest pits in regions II to VII had maximum values of $10^{+6.7}$ (0.005 mm^3) to 10^{+7} μm^3 (0.01 mm^3). Since the exposure time was constant for all regions, a lower slope here indicated that more pits with smaller volumes grew, pointing towards a higher pit nucleation frequency. The overall shapes of all the curves shown in Figure 6.3- 12a had similar features. Most of the curves contained two kinks, with one around a pit volume of $10^{+6.2}$ μm^3 (≈0.002 mm3) and the second around $10^{+6.6}$ μm^3 (≈0.004 mm^3), defined by the different slopes in Figure 6.3- 12a. These are also highlighted by the two horizontal lines.

The first kink can be explained for pits transforming from metastable to stable pit volumes, as the pit depth and overall volume act as diffusion lengths to stabilise pit growth [38]. The number of pits with stable and metastable volumes was not the same for all regions. The second kink possibly indicates the development of champion pits or pits that coalesced, resulting in significantly larger pit volumes. If we assume hemispherical pit shapes, the measured pit volumes would translate to a depth of 100 μm for achieving stable pit growth in this material. This means that at least two distinct populations of pits were present, defined by the observed critical volume. A number of smaller pits with dimensions up to the critical volume of $10^{+6.2}$ μm^3 (≈0.002 mm^3), followed by a larger accumulation of pits that were slightly larger, are present, evident by the lower slope of the curve defining larger pits.

Figure 6.3- 12b gives the average pit growth factor calculated from the deepest ten pits in each of the seven regions, with the error bar defined by the standard deviation of these measurements. The deepest pits were assumed to nucleate at t = 0 s, with pit growth kinetics following the power law relationship in Equation (1) [39]:

$$d = Kt^b \qquad \text{Equation (1)}$$

where (d) is the pit depth (μm), t is time (s), and K and b are experimental constants. The latter are influenced by the temperature and pH value of the electrolyte, with typical values of (b) from 0.3 to 0.5. If we assume the value of b = 0.5, with d measured from the laser confocal microscopy, the value of K can be calculated for each region.

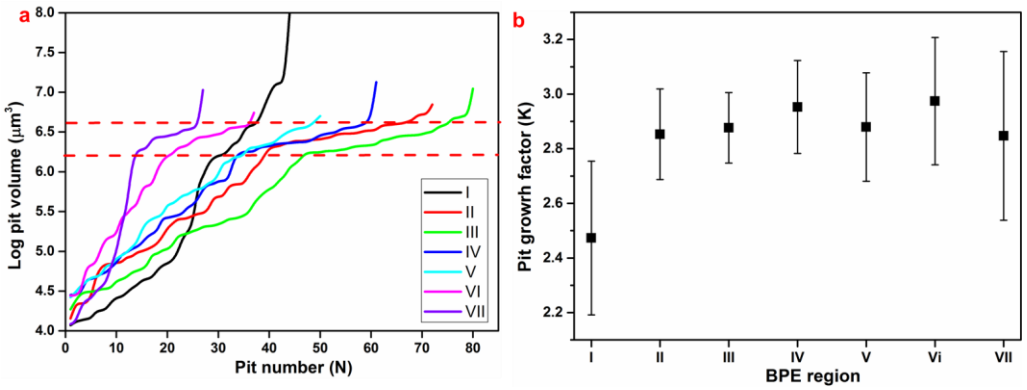

Figure 6.3- 12 (a) The relationship between pit number and corresponding pit volumes, and (b) the corresponding pit growth factor (K) for each region (I-VII) in Figure 6.3- 11.

The obtained K values in Figure 6.3- 12b confirm that the pit growth kinetics here were independent of the acting potential in each region. The 10 largest pits in each region had similar dimensions, resulting in pit growth factors (K) of around 2.9 from region II to IV. In region I, K was far lower at 2.5. The difference in pit growth kinetics in region (I) was caused by several pits merging together, reducing the number of larger pits seen in the overall distribution in Figure 12a. The presence of crevice corrosion also affected the maximum current up-take in this region, which most likely also contributed to a reduced pit growth factor. The coalescence of pits is also expected to affect the acting local potential, in parallel influencing pit growth kinetics [40].

The results reported in this investigation demonstrate the versatility of bipolar electrochemistry testing for corrosion research, providing access to a broad range of corrosion behaviours and mechanisms. In contrast, by using the conventional three-electrode polarisation set-up, a similar breadth of results can only be achieved by undertaking a large number of potentio-static polarisation experiments at different set potentials. With the bipolar screening technique, the occurrence of metastable pits, associated critical pitting potentials, and pit growth factors, as well as pit nucleation sites, can be

measured along one sample surface, in combination with far shorter experimental exposure times. The bipolar technique is, however, neither perfect nor fully understood yet, but the described advantages certainly warrant the further application and exploration of this method as a corrosion assessment tool.

6.36 Conclusions

(1) Bipolar electrochemistry allows a broad range of corrosion responses to be observed in a single experiment.

(2) $Cr_{23}C_6$, Cr_3C_2, and Cr_7C_3 are present in Type 420 stainless steel, with pits nucleating near these chromium-rich carbides.

(3) Pit nucleation, growth, and coalescence have been observed.

(4) Pit growth kinetics are independent of the acting potential.

(5) A critical pit volume for the transition from metastable to stable pits has been determined.

6.37 References

[1] Y. Zhou, D.L. Engelberg, Application of a modified bi-polar electrochemistry approach to determine pitting corrosion characteristics, Electrochem. Commun. 93 (2018) 158–161.

[2] S. Munktell, M. Tydén, J. Högström, L. Nyholm, F. Björefors, Bipolar electrochemistry for high-throughput corrosion screening, Electrochem. Commun. 34 (2013) 274–277.

[3] N. Pébère, V. Vivier, Local Electrochemical Measurements in Bipolar Experiments for Corrosion Studies, ChemElectroChem. 3 (2016) 415–421.

[4] R.M. Crooks, Principles of Bipolar Electrochemistry, ChemElectroChem. 3 (2016) 357–359.

[5] K. Wiesener, D. Ohms, G. Benczúr-Ürmössy, M. Berthold, F. Haschka, High power metal hydride bipolar battery, J. Power Sources. 84 (1999) 248–258.

[6] C.A.C. Sequeira, D.S.P. Cardoso, M.L.F. Gameiro, Bipolar Electrochemistry, a Focal Point of Future Research, Chem. Eng. Commun. 203 (2016) 1001–1008.

[7] Z. Qi, S. You, N. Ren, Wireless Electrocoagulation in Water Treatment Based on Bipolar Electrochemistry, Electrochim. Acta. 229 (2017) 96–101.

[8] Y. Yi, P. Cho, A. Al Zaabi, Y. Addad, C. Jang, Potentiodynamic polarization behaviour of AISI type 316 stainless steel in NaCl solution, Corros. Sci. 74 (2013) 92–97.

[9] B. Krawczyk, P. Cook, J. Hobbs, D. Engelberg, Corrosion Behavior of Cold Rolled Type 316L Stainless Steel in HCl Containing Environments, Corrosion. 73 (2017) 1346.

[10] M.H. Moayed, R.C. Newman, Evolution of current transients and morphology of metastable and stable pitting on stainless steel near the critical pitting temperature, Corros. Sci. 48 (2006) 1004–1018.

[11] S. Al Saadi, Y. Yi, P. Cho, C. Jang, P. Beeley, Passivity breakdown of 316L stainless steel during potentiodynamic polarization in NaCl solution, Corros. Sci. 111 (2016) 720–727.

[12] P.C. Pistorius, G.T. Burstein, Metastable Pitting Corrosion of Stainless Steel and the Transition to Stability, Philos. Trans. R. Soc. A Math. Phys. Eng. Sci. 341 (1992) 531–559.

[13] N.J. Laycock, Metastable Pitting and the Critical Pitting Temperature, J. Electrochem. Soc. 145 (1998) 2622.

[14] C. Örnek, F. Léonard, S.A. McDonald, A. Prajapati, P.J. Withers, D.L. Engelberg, Time-dependent in situ measurement of atmospheric corrosion rates of duplex stainless steel wires, Npj Mater. Degrad. 2 (2018) 1–15.

[15] K. Eguchi, T.L. Burnett, D.L. Engelberg, X-Ray tomographic characterisation of pitting corrosion in lean duplex stainless steel, Corros. Sci. 165 (2019) 108406.

[16] A.P. Bond, H.J. Dundas, Effects of Composition on the Stress Corrosion Cracking of Ferritic Stainless Steels, Corrosion. 24 (2013) 344–352.

[17] R.T. Newberg, H.H. Uhlig, Stress Corrosion Cracking of 18% Cr Ferritic Stainless Steels, J. Electrochem. Soc. 119 (1972) 981.

[18] Z.F. Yin, X.Z. Wang, L. Liu, J.Q. Wu, Y.Q. Zhang, Characterization of corrosion product layers from CO2corrosion of 13Cr stainless steel in simulated oilfield solution, J. Mater. Eng. Perform. 20 (2011) 1330–1335.

[19] K.H. Anantha, C. Örnek, S. Ejnermark, A. Medvedeva, J. Sjöström, J. Pan, In Situ AFM Study of Localized Corrosion Processes of Tempered AISI 420 Martensitic Stainless Steel: Effect of Secondary Hardening, J. Electrochem. Soc. 164 (2017) C810–C818.

[20] X. Lei, Y. Feng, J. Zhang, A. Fu, C. Yin, D.D. Macdonald, Impact of Reversed Austenite on the Pitting Corrosion Behavior of Super 13Cr Martensitic Stainless Steel, Electrochim. Acta. 191 (2016) 640–650.

[21] K.H. Anantha, C. Örnek, S. Ejnermark, A. Medvedeva, J. Sjöström, J. Pan, Correlative Microstructure Analysis and In Situ Corrosion Study of AISI 420 Martensitic Stainless Steel for Plastic Molding Applications, J. Electrochem. Soc. 164 (2017) C85–C93.
[22] A.F. Candelaria, C.E. Pinedo, Influence of the heat treatment on the corrosion resistance of the martensitic stainless steel type AISI 420, J. Mater. Sci. Lett. 22 (2003) 1151–1153.
[23] H. Nakagawa, T. Miyazaki, Effect of retained austenite on the microstructure and mechanical properties of martensitic precipitation hardening stainless steel, J. Mater. Sci. 34 (1999) 3901–3908.
[24] E. de Moor, S. Lacroix, A.J. Clarke, J. Penning, J.G. Speer, Effect of retained austenite stabilized via quench and partitioning on the strain hardening of martensitic steels, Metall. Mater. Trans. A Phys. Metall. Mater. Sci. 39 (2008) 2586–2595.
[25] M. Godec, D.A.S. Balantič, Coarsening behaviour of M23C6 carbides in creep-resistant steel exposed to high temperatures, Sci. Rep. 6 (2016) art. no. 29734.
[26] M. Du Toit, G.T. Van Rooyen, D. Smith, Heat-affected zone sensitization and stress corrosion cracking behaviour of 12 % chromium type 1.4003 ferritic stainless steel, Weld. World. 51 (2007) 41–50.
[27] A. Bjärbo, M. Hättestrand, Complex carbide growth, dissolution, and coarsening in a modified 12 pet chromium steel-an experimental and theoretical study, Metall. Mater. Trans. A Phys. Metall. Mater. Sci. 32 (2001) 19–27.
[28] P.J. Gellings, M.A. de Jongh, Grain boundary oxidation and the chromium-depletion theory of intercrystalline corrosion of austenitic stainless steels, Corros. Sci. 7 (1967) 413–421.
[29] K. Jung, K. Oh, D.-H. Nam, S. Ahn, S. Oh, H. Kwon, Effects of Centerline Segregation of Cr Carbides and Non-Metallic Inclusions on the Pitting Corrosion of Fe-13Cr-0.3C Stainless Steel Produced by Continuous Casting and Strip Casting, Corrosion. 73 (2017) 979–987.
[30] G.S. Frankel, L. Stockert, F. Hunkeler, H. Boehni, Metastable pitting of stainless steel, Corrosion. 43 (1987) 429–436.
[31] J. Liu, L.M. Wong, G. Gurudayal, L.H. Wong, S.Y. Chiam, S.F. Yau Li, Y. Ren, Immobilization of dye pollutants on iron hydroxide coated substrates: kinetics, efficiency and the adsorption mechanism, J. Mater. Chem. A. 4 (2016) 13280–13288.
[32] N. Dai, J. Zhang, Q. Chen, B. Yi, F. Cao, J. Zhang, Effect of the direct current electric field on the initial corrosion of steel in simulated industrial atmospheric environment, Corros. Sci. 99 (2015) 295–303.
[33] K. Asami, M. Kikuchi, In-depth distribution of rusts on a plain carbon steel and weathering steels exposed to coastal-industrial atmosphere for 17 years, Corros. Sci. 45 (2003) 2671–2688.
[34] L. Hao, S. Zhang, J. Dong, W. Ke, Evolution of corrosion of MnCuP weathering steel submitted to wet/dry cyclic tests in a simulated coastal atmosphere, Corros. Sci. 58 (2012) 175–180.
[35] M. Stratmann, K. Bohnenkamp, T. Ramchandran, The influence of copper upon the atmospheric corrosion of iron, Corros. Sci. 27 (1987) 905–926.
[36] I. Ignatov, O. Mosin, G. Gluhchev, S. Karadzhov, G. Miloshev, N. Ivanov, Studying Electrochemically Activated NaCl Solutions of Anolyte and Catholyte by Methods of Non-Equilibrium Energy Spectrum (NES) and Differential Non-Equilibrium Energy Spectrum (DNES), J. Med. Physiol. Biophys. 20 (2016) 13–23.
[37] J. Duval, J.M. Kleijn, H.P. Van Leeuwen, Bipolar electrode behaviour of the aluminium surface in a lateral electric field, J. Electroanal. Chem. 505 (2001) 1–11.
[38] W. Tian, S. Li, N. Du, S. Chen, Q. Wu, Effects of applied potential on stable pitting of 304 stainless steel, Corros. Sci. 93 (2015) 242–255.
[39] P. Ernst, R.C. Newman, Pit growth studies in stainless steel foils. I. Introduction and pit growth kinetics, Corros. Sci. 44 (2002) 927–941.
[40] N.J. Laycock, D.P. Krouse, S.C. Hendy, D.E. Williams, Computer Simulation of Pitting Corrosion of Stainless Steels, Interface, Electrochem. Soc. (2014) 65–71.

6.4 Time-lapse Observation of Pitting Corrosion in 13%Cr Ferritic Stainless Steel Using a Bipolar Electrochemistry Approach

Yiqi Zhou [a,*], *Dirk L. Engelberg* [a,b]

[a] Corrosion & Protection Centre, School of Materials, The University of Manchester, The Mill, M13 9PL, Manchester, United Kingdom

[b] Materials Performance Centre, Dalton Nuclear Institute, The University of Manchester, M13 9PL, Manchester, United Kingdom

* Corresponding author: Yiqi.Zhou@postgrad.manchester.ac.uk

6.41 Highlights

Pit nucleation and growth have been observed, in-situ, using a bipolar electrochemistry approach.

The development of champion pits in 13% Cr ferritic stainless steel is reported.

Pits nucleate in close to hemi-spherical cavities, and grow fastest in hemi-spherical cavity.

Pitting growth changed by diluted pit electrolyte is obtained.

6.42 Abstract

A bipolar electrochemistry approach has been applied to characterise pit nucleation and growth kinetics in 13% Cr ferritic stainless steel. In-situ time-lapse imaging, supported by laser confocal microscopy measurements, informs about pit nucleation frequencies and associated growth characteristics. The development of champion pits is observed. The features of the cavities which can support the pit nucleation and growth is researched. Pits can nucleate and growth in cavities with aspect ratio of 0.4-0.6, and then pit growth fastest in semi-circular cavity shape. The probability of pit growth is independent to the volume of the cavities and local applied potential. Dilutiing the pit electrolyte reduces the pit growth kinetics.

Keywords: Bipolar electrochemistry, pitting corrosion, pit growth kinetics, pit re-activation.

6.43 Introduction

The application of bipolar electrochemistry produces a linearly potential gradient between two feeder electrodes, resulting in a continuous spectrum of

anodic-to-cathodic electrochemical reactions occurring along the bipolar electrode (BPE) surface, with cathodic reactions occurring close to the positive feeder electrode, and in versa for anodic reactions [1–4]. The potential and current distribution on the BPE can be measured by split bipolar electrode, and the corrosion behaviour from the bipolar electrochemistry is compared with other well-known corrosion tests – potentio-dynamic and potentio-static polarisation test [EA paper]. Advantages of bipolar electrochemistry for corrosion test include: different corrosion results (crevice corrosion, pitting corrosion, general corrosion, and cathodic areas) are measured on one type 420 ferritic stainless steel BPE in a single experiment [5]; for type 2205 duplex stainless steel, the pitting corrosion can be nucleated at room temperature in 15 seconds, which pitting cannot be nucleated from other corrosion tests at room temperature [6], for welded lean 2101 duplex stainless steel, the crevice corrosion, transpassive corrosion, and pitting corrosion are direct compared with different microstructure conditions (base metal, heat affected zone, and fusion zone) on one sample in a single experiment [7]. Bipolar electrochemistry is used for study the dezincification of brass under different applied potential [S&I paper]. Furthermore, two different modified bipolar electrochemistry setups are created; for the first setup, the spatial distribution of reactions kinetics are modified, via application of a controlled potential to the BPE [2]. For the second setup, the galvanic corrosion between two stainless steels can tested from between a parallel bipolar electrodes setup [EEC paper].

The localised breakdown of the passive film can occur in a chloride-containing environment, typically resulting in pitting corrosion [8,9]. Pitting corrosion follows three general stages, with (i) pit nucleation, (ii) metastable pit growth, followed by (iii) stable pit growth [10,11]. Pit nucleation site is influenced by metallurgical variables, such as the presence of inclusion (e.g. MnS [12]), second phase particles (e.g. carbides [13]). The pitting corrosion is influenced by: the concentration of Cl^-, applied potential, and electrolyte temperature [14].The metastable pit growth requires a lacy cover act as a diffusion barrier to maintain a high concentration of Cl^- and low pH electrolyte [15,16]. The

stable pits can grow without a lacy cover, as pit depth, pit morphology or pit volume can act as diffusion barrier [17–19].

In this paper, bipolar electrochemistry has been applied to determine the pitting corrosion kinetic behaviour of 13% Cr ferritic stainless steel. In-situ, time-lapse imaging was used to observe the evolution of lateral pit dimensions over time. The features (volume/shape/depth) of the cavities can nucleate pitting growth at different local applied potential is researched, with laser confocal microscopy then used to obtain 3D topographies. The pitting growth kinetics between pits with/without diluted the pit electrolyte under a wide range applied potential is compared. This paper is focusing on determined the features of the cavities which can nucleate pitting corrosion and the dilution of the pit electrolyte influences the pit growth kinetics.

6.44 Materials and Methods

All experiments were carried out with an as-received 13% Cr Ferritic stainless steel (annealed Type 420) containing (wt%.) 13.7 Cr, 0.46 C, 0.47 Si, 0.39 Mn, and Fe (bal.) The material was in a solution annealed condition with hardness < 200 $HV_{0.5}$. Samples were mounted in Araldite resin, followed by grinding to 1200 grit, and a polishing treatment to 1 μm diamond paste finish, and followed by washed with deionized water and then dried in hot air.

Error! Reference source not found. (a) shows a sketch of the bipolar e lectrochemistry setup, a bipolar electrode (BPE) sample size of 30 * 10 * 1.2 mm^3 (length * width * thickness) was used, with the distance between the two feeder electrodes set to 60 mm. The BPE was set in the centre between the two feeder electrodes. The surface area of each of the two platinum feeder electrodes was 4 cm^2. The applied potential supported from Keysight E36105A power source between the two feeder electrodes was 10 V, with experiments carried out from 1 to 30 min in a cylindrical beaker containing 200 ml aqueous 0.1 M HCl solution. **Error! Reference source not found.** (b) g iving the mean recorded potential on the BPE. To measuring the potential on the BPE, spot welded at the rare side of the BPE and Luggin probe connect to reference electrode are required, which was introduced before [6]. The potentials were measured in increments of 5 mm along the sample surface,

and the measured potential at each point was stable with time until 10 minutes exposure. The potential distribution along the BPE is almost linearly. Slightly more positive potential measured at the BPE oxidation edge and more negative potential measured at the BPE reduction edge.

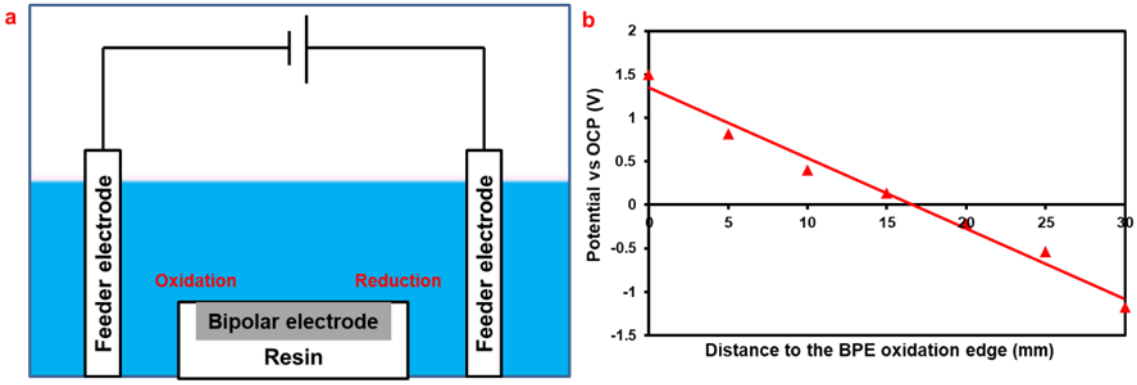

Figure 6.4- 1 (a) Schematic setup of the bipolar electrochemistry experiment, with (b) the measured potential offset distribution along a BPE electrode.

The surface of the BPE was imaged, in-situ, to determine the expansion of the pit cross-section area using a desktop digital USB microscope with up to 200x magnification. The microscope was mounted above the oxidation edge of the BPE, to obtain time-lapse information of the pit nucleation, lateral growth, repassivation, and coalescence of pits. All observed pits in the investigated 13% Cr ferritic stainless steel were open (without lacy covers), developing into circular cross-sectional shapes; thus providing direct access to pit radii (r) over time. The corresponding pit aspect ratios were then calculated by dividing the pit depth (d) by the pit diameter (2r). To measure pit nucleation and growth from different cavities, the BPE sample was taken out of the electrolyte and measured the pit morphology for every 1 minutes until 5 minutes, and then taken out for every 5 minutes until 30 minutes. The surface cleaned with water and soap, and then dried in hot air. The features of the cavities (volume, shape, and depth) which can support pitting nucleation and growth is determined by laser confocal microscopy. To understand the pit electrolyte influences the pitting growth kinetics, the pit electrolyte was certainly removing the sample from the washing. The BPE samples were conducted in 5 minutes intervals up to 30 minutes of exposure, and then compare the pit volume for BPE take out of electrolyte (remove the pit electrolyte) at constant time.

6.45 Results and Discussion

Bipolar Electrode

Figure 6.4- 2 shows the BPE with three distinctive regions after the bipolar electrochemistry experiment for 30 min.. Crevice corrosion, pitting corrosion surrounded with general corrosion, general corrosion and a cathode region are detected on the BPE. Multiply corrosion can be measured on the one BPE which means the bipolar electrochemistry for corrosion screening is sample and time saving. Crevice corrosion exists at the interface between the BPE and the resin. The pitting corrosion has a length of 6 mm. From 6 mm to 17 mm to the BPE oxidation edge, general corrosion is observed and the remaining 13 mm on the BPE is the cathodic region. The boundary between the anodic and cathodic sites is the OCP site but not located in the centre of the BPE.

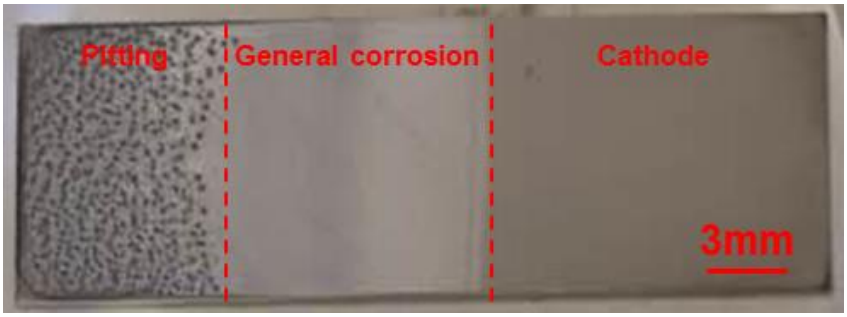

Figure 6.4- 2 Appearance of the BPE after the bipolar experiment after 30 min. exposure.

Snap-shots of the BPE surface taken every 30 seconds close to the BPE oxidation edge are shown in Figure 6.4- 3. The scale bar is uniform for all the optical images, and the left side of each image has higher applied potential. A large numbers of discrete sites (white spots) start to develop within the first 30 seconds. After 60 seconds, some of these sites develop a distinct dark centre, indicating lateral growth of some of these sites into pits. However, not all sites continue to grow at the same rate, with some clearly showing different growth rates. This means different pit geometries already develop at this early stage, even at a similar electrochemical potential, i.e. lateral distance from the BPE oxidation edge of the BPE [20]. From 90 seconds to 180 seconds, a number of sites continue to grow into larger pits, which are then surrounded by narrow

white rims. After 180 seconds, the density of the larger pits near the BPE oxidation edge is higher; as the probability for a pit to continue growth is larger at higher applied potentials.

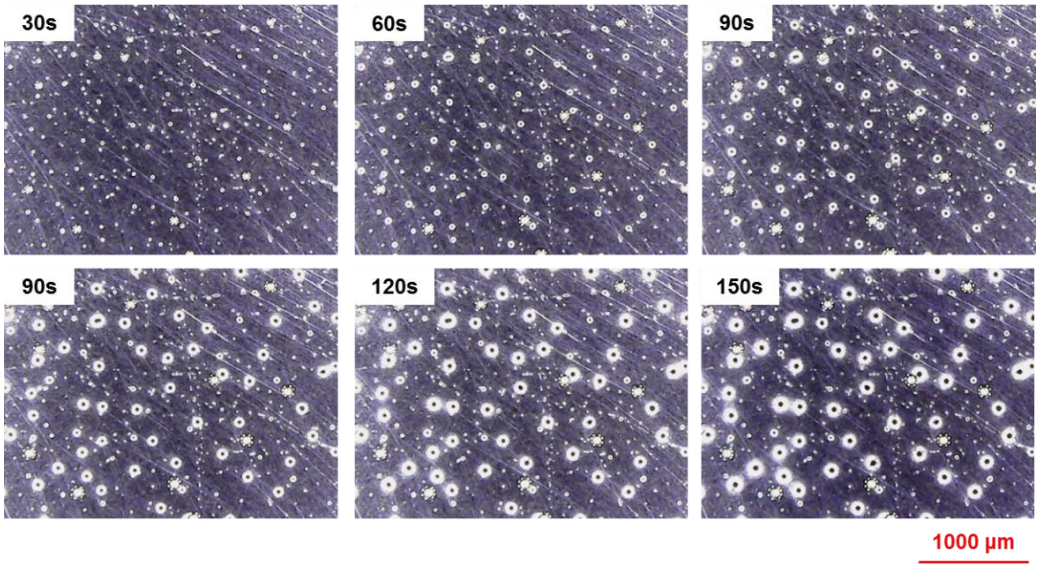

Figure 6.4- 3 Discrete snapshots of the BPE surface by using a digital camera close to the anodic edge at different time intervals (30-180s). The scale bar is representative for all images. The anodic edge is to the left of these images.

A further time-lapse view of the development of pits in the BPE oxidation region with exposure intervals up to 25 minutes is shown in Figure 6.4- 4. After 60 seconds of bipolar electrochemistry exposure, numerous white spots are present, which then further develop into considerable sizes, with white rims appearing around some of the pits. This rim is already visible at some of the larger sites after 60 seconds. Microscopic examination of the white rim revealed the presence of surface corrosion, possibly related to the aggressive electrolyte effluent from the open pit mouth. This effluent then results in general corrosion, manifested in a uniformly attacked circular area surrounding these pits.

Some of the observed pits continue to grow throughout all observed time frames, with some sites also indicating the development of effluent gas bubbles. This is most likely related to either hydrogen gas formation from cathodic reaction sites located at the BPE anodic surface or a supporting anodic gas evolution reaction [16,21].

In chloride containing environments with high applied potentials, electrochemical reactions can result in the formation of Cl_2O, ClO_2, ClO^-, HClO, Cl* and HO_2*, which can generate Cl_2 gas [22]. The latter case of chlorine gas evolution, however, is less likely, since this over-potential driven reaction would typically be expected close to the BPE oxidation edge where the highest over potential acts. Gas bubble formation seemed to occur predominantly along the specimen surface in between the observed anodic areas and not inside pits, where reactions are governed by the acidic, highly concentrated metal and chloride-ion containing liquor. The same argument also accounts for the occurrence of oxygen evolution reactions, which would be expected to form and evolve at higher over-potentials, with the reactions expected to be concentrated at the edge of the sample, in the region of the highest over-potential. This is certainly not observed here; with gas bubble evolution distributed over the anodic surface in local regions surrounding pits (Figure 6.4- 4). In general, most of the balancing cathodic reactions are expected to occur at the cathodic edge of the BPE (Figure 6.4- 2).

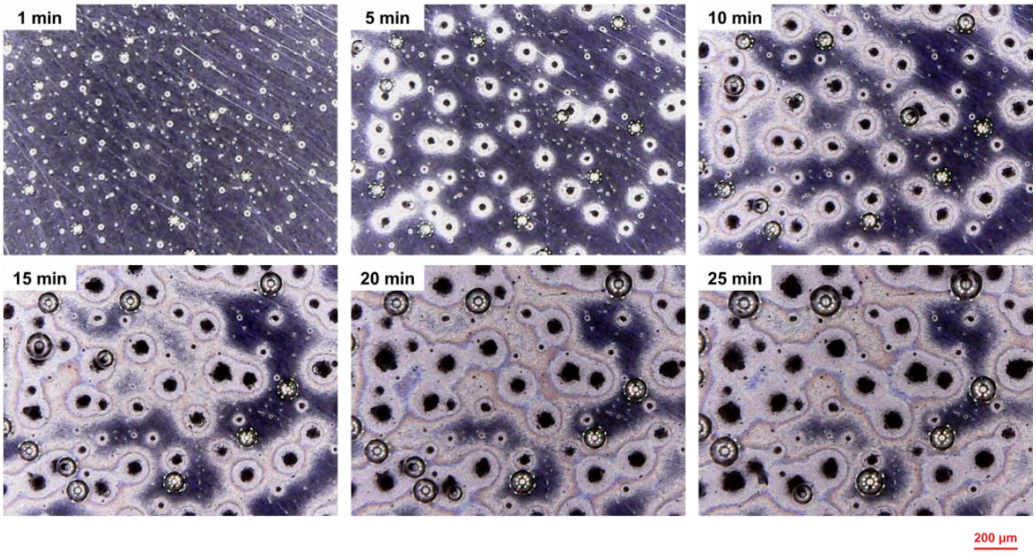

Figure 6.4- 4 Snapshots of the surface by using a digital camera close to the anodic edge at different time intervals (1-25 min). Gas bubbles formation and evolution is also observed.

After 10 min., the corroded circular areas around pits continue to expand radially, with a large fraction of pit openings also becoming visible. Anodic reactions were taking place inside pits, evident by the expansion of several

pits, supported by an anodic rim surrounding these pits. After 15 min., more general corrosion covering the surface is obvious, with corroded regions of different sites linking up. The general corrosion expands at higher potential, near the BPE oxidation edge, and after 25 min. the BPE surface at the anodic edge is totally covered by pits surrounded by regions with general corrosion. These corroded regions are also connected across the surface, with isolated sites of the original surface making up the regions in between, providing access for local gas evolution reactions. This infers that either oxygen or chlorine gas evolution takes place in these regions, or alternatively that local cathodic reactions are able to support the development of large corrosion sites within the anodic polarised region, close to anodic edge.

Figure 6.4- 5 summarise the frequency of growing pits as a function of the time intervals shown in Figure 6.4- 3 and Figure 6.4- 4, indicating that the number of actively growing pits is reduced from 56 to 42 within the first 120 seconds of exposure. From 120 to 180 seconds, the number of growing pits remained constant. The total number of growing pits significantly reduces up to 30 min. of exposure, from initially 61 initiation sites to 15, facilitating the development of “champion pits” [20,23,24]. The latter pits are certainly the survivors of this thorough pit analysis scheme, with pit growth stopped and re-initiated every 30 seconds (up to 5 min. of exposure), and then stopped every 5 min. thereafter.

To further distinguish whether pits grow or re-passivate, the development of the cross-sectional surface areas of pits (pit mouth) were re-compared over time. It is observed that some pits seem to stop growing at the early stages of the experiment, but after several surrounding pits stopped growing, the available current seems to be able to activate previously re-passivated pits. This is also the reason why the number of growing pits from 60-300 seconds is slightly larger than the number of growing pits observed in the 30-60 seconds interval. Inspection of the time-lapse intervals in Figure 6.4- 3 and Figure 6.4- 4 also confirm that only a few pits nucleated during the later stages of the experiment.

The reduction in the number of pits is most likely related to the increase in pit surface area competing for the available current [23]. Pits with a large number of active neighbouring pits are ;more likely to re-passivate, due to a depression of the effective potential and available maximum current around each pit [24]. Some pits are inherently more stable than others, for example, based on their geometries. These are then able to develop into champion pits, on the expense of stifling most surrounding, typically less stable pits [20,24]. Stifled pits will not consume anodic current further promoting the stability of champion pits.

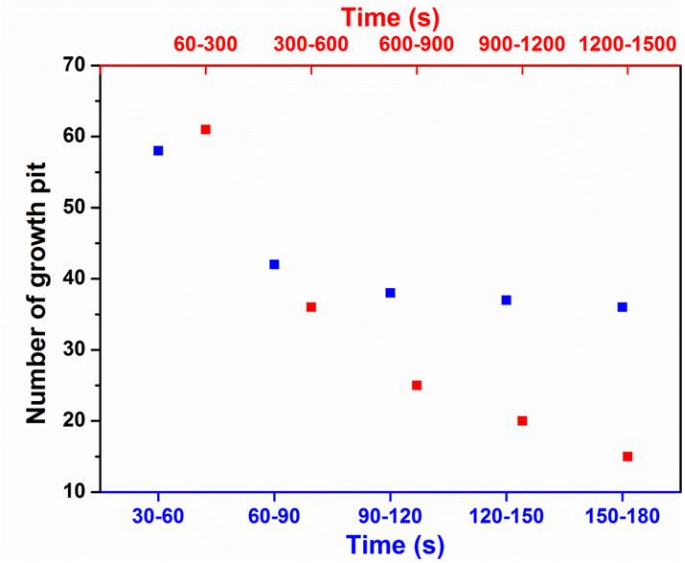

Figure 6.4- 5 Frequency of pits growing pits for the time intervals shown in Figure 6.4-3 for every 30 seconds, and compare to the intervals in Figure 6.4- 4 for every 5 minutes.

Pit Growth from Different Cavities

To find out the features of cavities which allow pits nucleation and growth with different applied potential and exposure time.. 10 growing pits (until 5 mins exposure) from different cavities at high applied potential (near the BPE oxidation edge) is research, show in Figure 6.4- 6. 15 growing pits (until 30 mins exposure) from different cavities at low applied potential (near BPE centre) is research show in Figure 6.4- 7.

Figure 6.4- 6 (a) gives the growth rate of ten pits exposure up to 5 min.. The pit growth rate pit growth in depth per minute. A larger pit growth percentage indicates faster pit growth rates. Pits with the highest growth rate (> 8 μm/min)

are in Group A1, and the lowest growth rate are in the Group C1 (< 5.5 μm/min). Group B1 makes up the pits in between these two arbitrary chosen values.

Figure 6.4- 6 (b) shows the average aspect ratio of the cavities in the different groups (A1-C1), with the error bars describing the population standard deviation. All cavities have initially a higher aspect ratio, decreasing over time, indicates those reactive pits prefer growth in the pit mouth direction. Here, an aspect ratio of 0.5 describes a perfectly hemispherical cavity shape. The cavities in Group A1 have aspect ratio fluctuations between 0.65 and 0.55, with cavities in Group B1 containing aspect ratio from 0.65 to 0.45, and cavities in Group C1 has aspect ratio reductions from 0.55 to 0.42. Pits nucleate in the cavities with aspect ratio between 0.4 and 0.6, with higher frequencies of the cavities with hemispherical shapes (aspect ratio ≈ 0.55) result in a quicker pit growth speed.

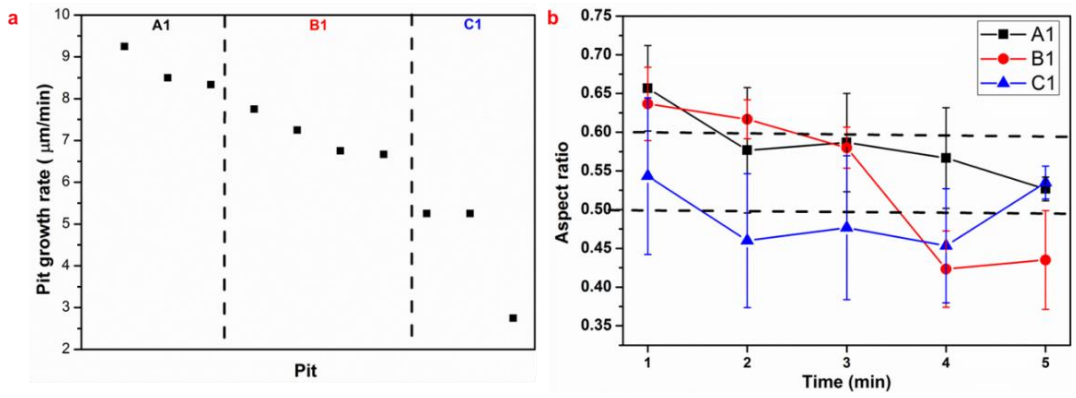

Figure 6.4- 6 (a) Pit growth rate (μm/min) for 10 chosen pits, which divided into three arbitrary groups (A1-C1), depending on their pit growth rates, with (b) showing a summary of the mean aspect ratio change of the different group (A1-C1).

Figure 6.4- 7 (a) shows the pit growth rate of the fifteen pits shown in highlighting 5 different groups (A2, B2, C2, D2, and E2) exposure from 5 min. to 30 min.. Group A2 has the highest pit growth rate, with the E2 showing the lowest pit growth rate. Figure 6.4- 7 (b) gives the average cavities aspect ratio of the cavities measured by every 5 min. with exposure up to 30 min.. The overall aspect ratio for each group is reducing with time, from 0.58 to below 0.38 after 30 min. of exposure. Group A2 has aspect ratios between 0.58 and 0.46, Group B2 between 0.55 and 0.46, Group C2 from 0.55 to 0.45, Group

D2 between 0.57 and 0.42, and Group E2 between 0.51 and 0.38. Pits with higher frequency nucleate from the hemispherical topographies cavity (aspect ratio ≈ 0.5) can achieve a higher pit growth percentage (A2-E2).

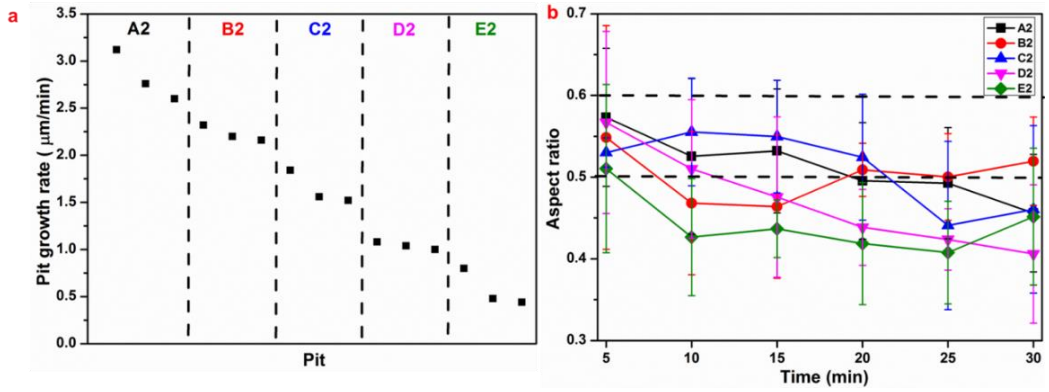

Figure 6.4- 7 (a) The pit growth rate (μm/min) showing five groups (A2 - E2), with (b) showing the mean aspect ratio change of these groups from 5 to 30 min. of bipolar exposure.

Here, the volume of the cavities and the local applied potential do not influence the pit nucleation and growth. For the cavities which cannot support the pit nucleation, they had either smaller or larger volume and with either higher or lower applied potential than the cavities which allows pit nucleated and growth. The cavities which nucleate the pitting corrosion is the shape related, explained by IR drop mechanism. Pickering [24,25] created the IR drop mechanism to analysis the localised corrosion in the stainless steel, the localised corrosion is caused by the anodic current density (I) and the solution resistance (R) inside of corrosion. A critical potential ($\triangle\varphi^*$) indicates the potential difference at the mouth and at the active/passive transition in the pit solution's polarization curve. With a high applied potential (IR >$\triangle\varphi^*$), the local potential inside of pit is in the active region, not the passive region, so the pit can propagate [26–29]. With a large aspect ratio, $\triangle\varphi^*$ is very large, result in IR inside of the pit need longer time or cannot reach the critical value, as pit electrolyte is easier to diffuse out. For a small aspect ratio, the current density is low, and the pits wall are under passivate condition, cannot reach $\triangle\varphi^*$ [29–32].

From Figure 6.4- 6 and Figure 6.4- 7, the pit nucleate from the cavities with aspect ratio from 0.4-0.6, independent to the pit volume and pit depth, as the

IR reaches the critical potential with a suitable aspect ratio, here is 0.4-0.6. Pits nucleated from the cavities with aspect ratio ≈ 0.5 grow fastest, caused by less time for critical IR value. The depth and volume of the cavities do not influence the pit nucleation, as pits nucleated from the cavities with a depth ≈ 90 μm, and some pits also repassivate at the early stage of pitting corrosion. Due to a large volume of the cavities, electrolyte resistance need a longer time to reach the critical value, result in slower pit growth rate. The maximum pit growth rate is about 10 μm/min at 5 min., but the growth rate is only ≈ 3 μm/min at 30 min. The pit shapes become dish-like for longer exposure time, as the current is often limited via diffusion control, which limited the pit growth to the depth direction.

Pit Growth Kinetics

Pit growth typically follows a power law Equation 1 [34,35].

$$d = Kt^b \qquad \text{Equation 1}$$

With (d) is the pit depth (μm), t is time (s), and (K) and (b) are experimental constants, with typical values of (b) from 0.3 to 0.5, influenced by temperature and the pH value of the electrolyte [35]. (b). If assume the (b) is 0.5, with (d) measured from the laser confocal microscopy, and (K) calculated by solving Equation 1.

Figure 6.4- 8 gives the pit growth factors change with time between pits in Additive mode (BPE takes out of the electrolyte at a constant time, and then set back to run experiment) and Continue mode (BPE take out of the electrolyte only the experiment finish). Ten largest pits without merge together are chosen, assume t = 0 s, the average pit growth factor is calculated with the error bars describing the standard deviation. The pit growth factor in the Continue mode is slightly reducing from 3.8 at 5 min. to 3.4 at 30 min., the pit growth factor in the Additive mode is largely decreasing from 3.4 at 5 min. to 2.4 at 30 min..

The pit growth factor in the Continue mode is stable with time but not in the Additive mode, and the difference of the pit growth factor between the two modes are increasing with longer exposure time. The pit growth factor in the

Continue mode is almost the same, as the pit growth is under diffusion control; the pit growth factor slightly reduced with longer exposure time might be caused by pit competition and limited cathodic area. When pit close to each other, the cathode area surrounded the pits is limited, cannot support enough cathodic current to sustain a high pit growth kinetics [37,38]. After a longer exposure time, more serious competition from less cathodic area and more numbers of pit surrounded the growing pit, result in the pit growth kinetics is slightly reduced. For the pit growth kinetics in the Additive mode, it is largely reduced after longer exposure time, as the pit electrolyte was removed at constant time. Larger cavities volume results in a longer time is required for the cavities transfer from general corrosion to pitting corrosion, so the real time for the cavities under pitting corrosion growth is less, result in lower pit growth kinetics.

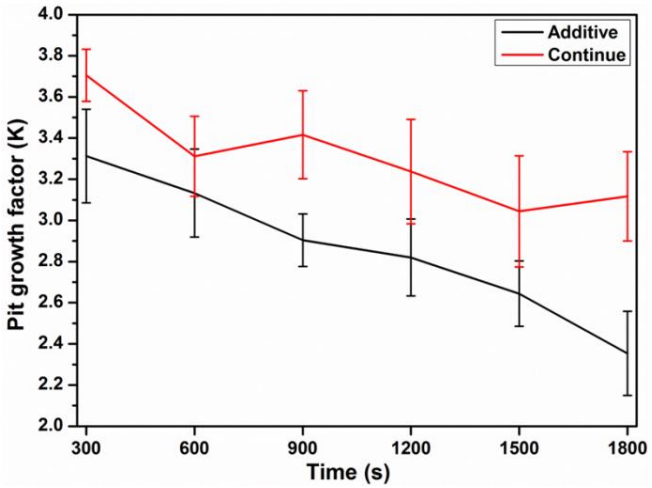

Figure 6.4- 8 The pit growth factor for two different pit growth modes with different exposure time.

Pit Volume Growth Statistics

Figure 6.4- 9 gives pit volume linearly distribute on the BPE with increasing exposure time for both modes. For the Continue mode, the pit volume is increasing from 0.06 mm^3 at 5 min. to 0.43 mm^3 at 30 min.. For the Additive mode, the pit volume increases from 0.04 mm^3 at 5 min. to 0.38 mm^3 at 30 min.. The overall pit metal loss in the Continue mode is higher than the Additive mode. As the electrolyte in the cavities need time to reach the critical IR for pit nucleation,

as the pit electrolyte in the Additive mode are removed at constant time. However, after the pit reactive from the cavities, the corrosion kinetics still follows the pit growth kinetics, so the overall pit volume is still linearly increase with longer exposure time. Figure 6.4- 9 (b) gives the difference of the pit volume gaps between the two modes. The pit volume gap is only 0.02 mm^3 at 5 minutes, and then dramatically increasing to 0.07 mm^3 at 10 minutes. From exposure at 10 minutes to 30 minutes, the difference of the metal loss volume is slowing increasing from 0.07 mm^3 to over 0.09 mm^3. Here, the pit volume gap largely increased to 10 minutes and then slowly increase until 30 minutes, as the pit competition and cathode area surrounded the pit. When pits merge together, the pit expansion rate is changed as the local effective applied potential or chloride concentration inside of pits are changed [24]. Less cathodic area surrounded the pit after close to other pits, which result in pit competition which also changes the pit growth kinetics. Before 10 minutes, the pit density is little and pit size is small, which means enough cathodic area next to the pits and less pit completion with the surrounding the pits. So, the pit growth in the Continue mode with less restriction. But after 10min, pits are close to each other and even merge together, so the pit volume expansion is restricted in the Continue mode, so the pit volume difference between these two mode is only slowly increasing with time.

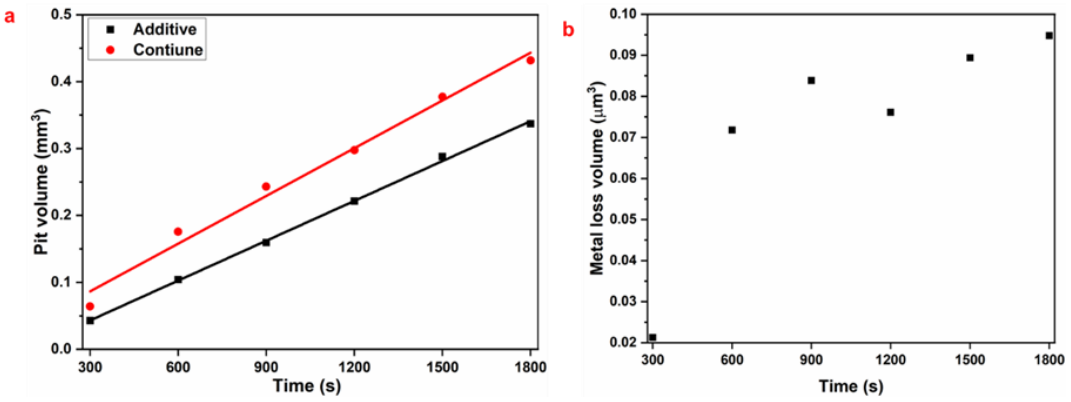

Figure 6.4- 9 The pit volume on the BPE change with time for the Additive and Continue mode.

Figure 6.4- 10 shows the pitting distribution on the BPE as a function of pit volume for difference exposure time. The Additive mode in Figure 6.4- 10 (a) shows most pits have the volume between 3 – 30 * 10^3 μm^3 for all the exposure time, which means a lot of nucleated pits can growth this volume, which might

be the critical pit volume for the new pits after 5 min. exposure. After 10 min., the numbers of pits in this volume is reduced, and continue reduced with longer exposure time, as fewer new nucleated pits, the current is consumed by the pre-exist pits (cavities) growth to a bigger volume. So some large volume pits are measured after longer exposure time from the cavities with the aspect ratio ≈ 0.5. Figure 6.4- 10 (b) shows in the pit distribution in the Continue mode. At 5 min., more pits are nucleated in the Continue mode, as the BPE in the Additive modes was taken out of the electrolyte for every 1min. current from the re-passivate pit can nucleate new pits. Most of the pits have the volume of $3 * 10^4$ μm^3. At 10 min., the average pit volume increased to $3 * 10^5$ μm^3. At 15 min., most of the pits have the pit volume with $3 * 10^5$ μm^3, but the numbers of pits are reduced, caused by pits merge. After 20 min., the pits with the volume over $3 * 10^6$ μm^3 are measured.

In the Continues mode, two peaks on the pit volume distribution are determined. The pits in the first peak are the metastable pits, and the pits in the second peak are the stable pits. The stable pits always have large pit volume can act as a diffusion barrier [39]. At 5 and 10 minutes, only one peak is determined, which might be most of them has potential to be stable pits. The numbers of stable growth pit reduced as the pits nucleated until 20 minutes exposure, as these growing pits are merge together. From 20 to 30 minutes exposure, these stables pits has similar pit volume, indicates pit competition reduce the pit growth kinetics, and less large size pits as the pits merge together. In the Additive mode, only one peak is determined for all the exposure time, indicates, pit volume cannot distinguish pit with stable growth or repassivate, and the probabilities of the pit can growth from the cavities with suitable aspect ratio. So, the pit growth in the Additive mode is the cavities shape dependent and the pit growth kinetics in the Continue mode is volume dependent.

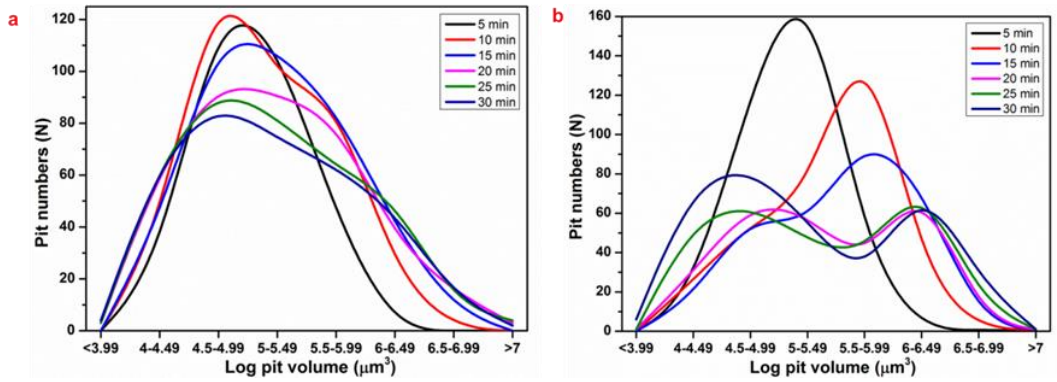

Figure 6.4- 10 Pit distribution on the BPE as a function of bipolar electrochemistry exposure time and pitting volume range in (a) Additive and (b) Continue modes.

6.46 Conclusions

- Bipolar electrochemistry has been combined with time-lapse, in-situ imaging techniques to observe pit growth behaviour.
- The number growing pits reduce with time before reaching a plateau, with pit coalescence resulting in the development of champion pits.
- Local dissolution around pits is observed, due to general corrosion.
- The faster growing pits comes from an initial hemi-spherical cavity.
- Pit growth factor is potential independent but related to pit electrolyte.
- The dissolved pit volume increases linearly with time and applied potential.
- The pit growth is volume dependent but pit growth from cavities are cavity shape related.

6.47 References

[1] S. Munktell, M. Tydén, J. Högström, L. Nyholm, F. Björefors, Bipolar electrochemistry for high-throughput corrosion screening, Electrochem. Commun. 34 (2013) 274–277.

[2] Y. Zhou, D.L. Engelberg, Application of a modified bi-polar electrochemistry approach to determine pitting corrosion characteristics, Electrochem. Commun. 93 (2018) 158–161.

[3] N. Pébère, V. Vivier, Local electrochemical measurements in bipolar experiments for corrosion studies, ChemElectroChem. 3 (2016) 415–421.

[4] S.E. Fosdick, K.N. Knust, K. Scida, R.M. Crooks, Bipolar electrochemistry, Angew. Chemie - Int. Ed. 52 (2013) 10438–10456.

[5] Y. Zhou, D.L. Engelberg, On the application of bipolar electrochemistry to characterise the localised corrosion behaviour of type 420 ferritic stainless steel, Metals (Basel). 10 (2020) 794.

[6] Y. Zhou, D.L. Engelberg, Fast testing of ambient temperature pitting corrosion in type 2205 duplex stainless steel by bipolar electrochemistry experiments, Electrochem. Commun. 117 (2020) 106779.

[7] Y. Zhou, A. Kablan, D.L. Engelberg, Metallographic screening of duplex stainless steel weld microstructure with a bipolar electrochemistry technique, Mater. Charact. 169 (2020) 110605.

[8] S. Pahlavan, S. Moazen, I. Taji, K. Saffar, M. Hamrah, M.H. Moayed, S. Mollazadeh Beidokhti, Pitting corrosion of martensitic stainless steel in halide bearing solutions, Corros. Sci. 112 (2016) 233–240.

[9] S. Frangini, N. De Cristofaro, Analysis of the galvanostatic polarization method for determining reliable

pitting potentials on stainless steels in crevice-free conditions, Corros. Sci. 45 (2003) 2769–2786.

[10] S. Al Saadi, Y. Yi, P. Cho, C. Jang, P. Beeley, Passivity breakdown of 316L stainless steel during potentiodynamic polarization in NaCl solution, Corros. Sci. 111 (2016) 720–727.

[11] S.M. G.Burstein, P.Pistorius, Evaluating the critical chemistry for repassivation at the corroding surface using mass transport model-based artificial pit experiments, Corros. Sci. 35 (1993) 57–62.

[12] M.P. Ryan, D.E. Williams, R.J. Chater, B.M. Hutton, D.S. McPhail, Why stainless steel corrodes, Nature. 415 (2002) 770–774.

[13] K.H. Anantha, C. Örnek, S. Ejnermark, A. Medvedeva, J. Sjöström, J. Pan, In Situ AFM Study of Localized Corrosion Processes of Tempered AISI 420 Martensitic Stainless Steel: Effect of Secondary Hardening, J. Electrochem. Soc. 164 (2017) C810–C818.

[14] B. Krawczyk, P. Cook, J. Hobbs, D. Engelberg, Corrosion behavior of cold rolled type 316L stainless steel in HCl containing environments, Corrosion. 73 (2017) 1346.

[15] G.S. Frankel, L. Stockert, F. Hunkeler, H. Boehni, Metastable pitting of stainless steel, Corrosion. 43 (1987) 429–436.

[16] J. Srinivasan, R.G. Kelly, Evaluating the critical chemistry for repassivation at the corroding surface using mass transport model-based artificial pit experiments, J. Electrochem. Soc. 163 (2016) C768–C777.

[17] N.J. Laycock, Metastable Pitting and the Critical Pitting Temperature, J. Electrochem. Soc. 145 (1998) 2622.

[18] N.J. Laycock, R.C. Newman, Localised dissolution kinetics, salt films and pitting potentials, Corros. Sci. 39 (1997) 1771–1790.

[19] W. Tian, S. Li, N. Du, S. Chen, Q. Wu, Effects of applied potential on stable pitting of 304 stainless steel, Corros. Sci. 93 (2015) 242–255.

[20] M.I. Suleiman, R.C. Newman, The use of very weak galvanostatic polarization to study localized corrosion stability in stainless steel, Corros. Sci. 36 (1994) 1657–1665.

[21] M. Naghizadeh, D. Nakhaie, M. Zakeri, M.H. Moayed, Effect of Thiosulfate on Pitting Corrosion of 316SS, J. Electrochem. Soc. 162 (2014) C71–C77.

[22] I. Ignatov, O. Mosin, G. Gluhchev, S. Karadzhov, G. Miloshev, N. Ivanov, Studying electrochemically activated naCl solutions of anolyte and catholyte by methods of non-Equilibrium energy spectrum (NES) and differential non-equilibrium energy spectrum (DNES), J. Med. Physiol. Biophys. 20 (2016) 13–23.

[23] M. Ghahari, D. Krouse, N. Laycock, T. Rayment, C. Padovani, M. Stampanoni, F. Marone, R. Mokso, A.J. Davenport, Synchrotron X-ray radiography studies of pitting corrosion of stainless steel: Extraction of pit propagation parameters, Corros. Sci. 100 (2015) 23–35.

[24] N.J. Laycock, D.P. Krouse, S.C. Hendy, D.E. Williams, Computer simulation of pitting corrosion of stainless steels, Interface, Electrochem. Soc. (2014) 65–71.

[25] R.P. Frankenthal, H.W. Pickering, On the Mechanism of Localized Corrosion of Iron and Stainless Steel I. Electrochemical Studies, J. Electrochem. Soc. 119 (1972) 1297–1304.

[26] R.P. Frankenthal, H.W. Pickering, On the Mechanism of Localized Corrosion of Iron and Stainless Steel II. Morphological Studies, J. Electrochem. Soc. 119 (2007) 1304.

[27] A.M. Al-Zahrani, H.W. Pickering, IR voltage switch in delayed crevice corrosion and active peak formation detected using a repassivation-type scan, Electrochim. Acta. 50 (2005) 3420–3435.

[28] H.W. Pickering, The role of electrode potential distribution in corrosion processes, Mater. Sci. Eng. A. 198 (1995) 213–223.

[29] G.F. Kennell, R.W. Evitts, K.L. Heppner, A critical crevice solution and IR drop crevice corrosion model, Corros. Sci. 50 (2008) 1716–1725.

[30] H.W. Pickering, The significance of the local electrode potential within pits, crevices and cracks, Corros. Sci. 29 (1989) 325–341.

[31] E.A. Nystrom, An Approach for Estimating Anodic Current Distributions in Crevice Corrosion from Potential Measurements, J. Electrochem. Soc. 141 (2006) 358.

[32] Y. Xu, On Electric Field Induced Breakdown of Passive Films and the Mechanism of Pitting Corrosion, J. Electrochem. Soc. 140 (2006) 3448.

[33] Y. Xu, The Initial Potential and Current Distributions of the Crevice Corrosion Process, J. Electrochem. Soc. 140 (2006) 658.

[34] Z. Szklarska-Smialowska, Pitting corrosion of aluminum, Corros. Sci. 41 (1999) 1743–1767.

[35] P. Ernst, R.C. Newman, Pit growth studies in stainless steel foils. I. Introduction and pit growth kinetics, Corros. Sci. 44 (2002) 927–941.

[36] M.K. Cavanaugh, R.G. Buchheit, N. Birbilis, Modeling the environmental dependence of pit growth using neural network approaches, Corros. Sci. 52 (2010) 3070–3077.

[37] M.T. Woldemedhin, M.E. Shedd, R.G. Kelly, Evaluation of the maximum pit size model on stainless steels under thin film electrolyte conditions, J. Electrochem. Soc. 161 (2014) E3216–E3224.

[38] M.T. Woldemedhin, M.E. Shedd, R.G. Kelly, Evaluation of the maximum pit size model on stainless steels under atmospheric conditions, J. Electrochem. Soc. 58 (2014) 41–50.

[39] M.H. Moayed, N.J. Laycock, R.C. Newman, Dependence of the Critical Pitting Temperature on surface roughness, Corros. Sci. 45 (2003) 1203–1216.

6.5 Accessing The Full Spectrum of Corrosion Kinetic Behaviour of Tempered Type 420 Martensitic Stainless Steel

Yiqi Zhou[*1], *Dirk Lars Engelberg*[1,2]

1. Corrosion & Protection Centre, School of Materials, The University of Manchester, M13 9PL, Manchester, UK
2. Materials Performance Centre, The University of Manchester, M13 9PL, Manchester, UK

* Corresponding author: Yiqi.Zhou@postgrad.manchester.ac.uk

6.51 Highlights

The corrosion behaviour of different tempered treated martensitic stainless steel is observed and compared.

The full spectrum of anodic-to-cathodic electrochemical response is accessible for observation.

Pitting corrosion and intergranular corrosion are observed, related to chromium carbides precipitate.

Microstructure of martensitic stainless steel changed by different tempered treatment is determined.

6.52 Abstract

Bipolar electrochemistry produces a linear potential gradient between two feeder electrodes, providing access to the full spectrum of anodic-to-cathodic electrochemical reaction responses on the BPE. Type 420 martensitic stainless steel has been used to investigate microstructure evolution and corrosion behaviour change with different tempered temperatures. Tempered at 250 ^{o}C, 400 ^{o}C, and 700 ^{o}C reveals to the occurrence of pitting corrosion. E_{pit} and pit volume have been used to analysis the pitting corrosion resistance behaviour. Tempering at 550 ^{o}C, only intergranular corrosion is observed. $Cr_{23}C_6$ is determined for all the tempered conditions, with Cr_7C_3 and CrC are observed for tempering at 550 ^{o}C. Chromium carbides preferred precipitate at the grain boundaries.

Keywords: Bipolar electrochemistry, stainless steel, pitting corrosion, chromium carbides, intergranular corrosion

6.53 Introduction

Martensitic stainless steel has high wear resistance, high hardness, and medium corrosion resistance. Applications include steam generators, food

processing blades, and mixer blades [1,2]. However, martensitic stainless steel is susceptible to localised corrosion in chloride electrolyte [3,4]. To manufacture of martensitic stainless steel, the stainless steel is held at the austenitization temperature (950-1050 ^{o}C) for a period of time, and followed by rapid quenching [5–7]. Different austenitization temperatures, holding times, quench rate and tempering treatment changes corrosion behaviour and mechanical properties [8–11]. Tempering treatments influence the formation of the chromium carbides, from M_3C to M_7C_3 and then into $M_{23}C_6$, which changes the hardness [12,13]. The tempering process also change the volume of retained austenite, result in different yield strength, tensile strength, elongation and absorbed energy [14,15].

Localised breakdown of the passive film can result in pitting in stainless steel in the chloride-containing environment [16,17]. Pitting corrosion nucleates at the local weak part, such as Cr depleted region [18]. Pitting corrosion has three general stages, from (i) pit nucleation, (ii) metastable pit growth, to (iii) stable pit growth [23,24]. The metastable pit growth requires a lacy cover act as a diffusion barrier to maintain a high concentration of Cl^- and low pH electrolyte [25,26]. Stable pit growth is associated with a critical electrochemical potential (E_{pit}) or a critical pitting temperature (CPT) [23,24. Stable pits have a lager pit volume or depth, act as the diffusion barrier, can growth without lacy cover [25,26].

Bipolar electrochemistry has become valuable for corrosion testing. The method is favoured due to the non-contact set up, easy experiment setup, and being able to observe multiple corrosion responses during a single experiment [27–29]. A linear potential gradient is established along with the interface of the electrolyte and bipolar electrode (BPE); as a result, both anodic and cathodic reactions are simultaneously occurring along the BPE [27–30]. The potential and current distribution on the BPE was determined by split BPE, and corrosion behaviours are compared between bipolar electrochemistry, potentio-dynamic, and potentio-static polarisation test [EA paper]. Bipolar electrochemistry is a powerful corrosion test method, which nucleates the pitting corrosion on DSS 2205 at room temperature, which traditional corrosion test cannot not [31], and the pitting corrosion changed by microstructure also

can be easily measured by bipolar electrochemistry [32]. Furthermore, brass dezincification and galvanic corrosion can also be researched by bipolar electrochemistry [S&I paper][EC paper].

This paper describes the contribution of tempered temperatures to corrosion behaviour and mechanical property with the microstructure evolution of type 420 martensitic stainless steel. The corrosion behaviour is determined from the 3-electrode potentio-dynamic polarisation test and bipolar electrochemistry experiment. The pitting corrosion is measured from 3D laser surface scanning confocal microscopy. Hardness tests are also test the tempered martensitic stainless steel.. The microstructure is assessed using Scanning Electron Microscopy (SEM) with EDX, and Electron Backscatter Diffraction (EBSD).

6.54 Materials and Methods

As-received Type 420 stainless steel samples with the composition (wt %) of 13.7 Cr, 0.46 C, 0.47 Si, 0.39 Mn and (Bal.) Fe were used in this study. A CWF Laboratory Chamber Furnace was used for heat treatment; the stainless steel was austenitizing at 950 ^{o}C for one hour followed by water quenching; then, the samples were tempered at 250 ^{o}C, 400 ^{o}C, 550 ^{o}C, or 700 ^{o}C for one hour, followed by cooling in air. For the bipolar electrochemistry experiments, BPEs had dimensions of 30 * 10 * 1.2 mm^3 (length * width * thickness). The BPE samples were mounted in Araldite resin and then prepared by grinding up to 1200 grit. For the 3-electrode potentio-dynamic polarization test, the samples cut into 25 * 25 mm* 1.2 mm^3 (length * width * thickness) were grind to 1200 grit. For EBSD analysis; the sample was cut to a dimension of 25 * 25 mm * 1.2 mm^3 (length * width * thickness), then grinded to 4000 grit and polished until 0.25 µm diamond pastes, then followed by a fine polishing (OPS Colloidal Silica). Micro hardness tests were carried out with a Buehler Micromet Tester using an applied load of 4.903N ($HV_{0.5}$).

For the 3-electrode potentio-dynamic polarization test, the samples were tested in an AVESTA cell at room temperature in 0.1M HCl. A platinum electrode and SCE reference electrode were used, in combination with a CS2350 Bipotentiostat and CS Studio 5 software to test 3-electrode potentio-

dynamic polarisation curves. The Open Circuit Potential (OCP) was stabilized for 10 min, followed by potentio-dynamic polarisation tests from -200 mV_{OCP} to in excess of +1500 mV_{OCP} with a scan rate of 1 mV/s.

Figure 6.5- 1 (a) shows the bipolar electrochemistry setup. The applied potential between the feeder electrodes was 10 V, with both feeder electrodes set 60 mm apart, and the BPE centred between the two feeder electrodes. The surface area of each platinum feeder electrodes was 4 cm^2. All experiments were conducted in 200 ml of 0.1M HCl for 5 min. Figure 6.5- 1 (b) gives the average potential and standard deviation over 600 seconds along BPE sample surface for every 5mm, and a linearly tendency line was used to connect all the measured points. The setup of the potential measurement was introduced before [31]. The measured potential each point along the BPE was almost stable with time.

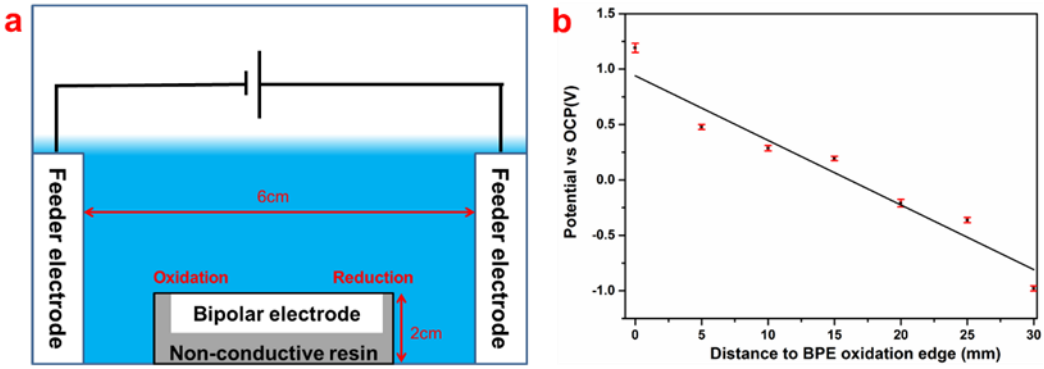

Figure 6.5- 1 (a) Schematic diagram of the bipolar electrochemistry set-up with (b) the potential distribution measured along the BPE.

After the bipolar electrochemistry experiment, the BPE was placed in an ultrasonic bath for 10 min to break and remove lacy pit covers, then cleaned with soap water and dried in hot air. A Keyence VK-200K laser confocal microscope was used to measure the corrosion morphology. All measured regions had a width of 4 mm, with the overall length depending on the pitting covered length on the BPE. A Zeiss Sigma VP FEG-SEM was used for EDX analysis from the Aztec software at 20 kV. A Tescan Mira 3 LC FEG-SEM was used to acquire SEM and EBSD images; for the EBSD, the step size was 110

nm for the microstructure analysis of the matrix and 3.25 nm for the chromium carbides detection at 15 kV.

6.55 Results and Discussion

Potentio-dynamic polarisation tests

3-electrode potentio-dynamic polarisation curves as a function of tempering temperature are shown in Figure 6.5- 2. Each electrochemical test was carried out thrice and the results show consistent and reproducible. The OCP for all tempered samples remain similar ≈ -0.5 V_{SCE}. The E_{pit} for the MSS 420 without tempering *is around* 0.11 V_{SCE}. When tempering at 250 ^{o}C, E_{pit} is increased to +0.17 V_{SCE} with two hoops determined in the passive region. The second hoop indicates a passive film formation at Cr-depleted regions [33]. When tempered at 400 ^{o}C, E_{pit} reduces to -0.03 V_{SCE}. After tempering at 550 ^{o}C, no pitting corrosion is observed from the polarisation curves and after post observation, as a continues chromium carbides formed at grain boundaries result in intergranular corrosion [34,35]. For tempered at 700 ^{o}C, E_{pit} increases to +0.12 V_{SCE}. However, no passive region is formed as the current density remains > 0.1 mA/cm^2, and pits are determined for post observation. All results of polarisation studies are collected in Table 6.5- 1.

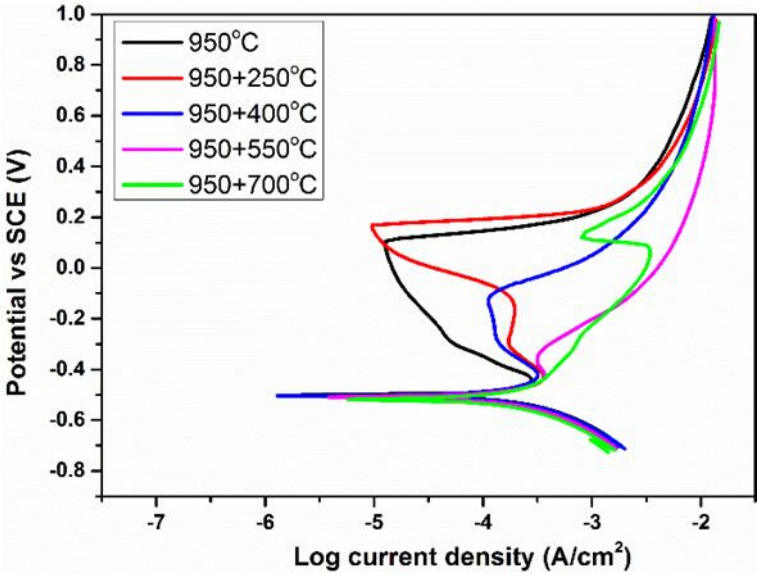

Figure 6.5- 2 3-electrode potentio-dynamic polarisation curves for all tempered sample in 0.1 M HCl solution at RT.

Table 6.5- 1 Pitting potentials obtained for different temperature tempered martensitic after polarisation in 0.1 M HCl electrolyte at RT.

	E_{corr}	$E_{ave.corr}$	E_{pit}	$E_{ave.pit}$
950	-0.495	-0.501±0.006	0.10	0.11±0.01
	-0.505		0.10	
	-0.505		0.12	
950+250	-0.516	-0.513±0.003	0.18	0.17±0.01
	-0.513		0.17	
	-0.511		0.16	
950+400	-0.517	-0.515±0.002	-0.04	-0.03±0.01
	-0.515		-0.03	
	-0.513		-0.03	
950+550	-0.514	-0.510±0.004	/	/
	-0.510		/	
	-0.506		/	
950+700	-0.528	-0.527±0.001	0.10	0.12±0.02
	-0.527		0.12	
	-0.527		0.13	

Bipolar electrochemistry

All tempered treatments stainless steels are tested by bipolar electrochemistry experiment, with two BPE appearances were determined. Figure 6.5- 3 shows the corrosion response on the BPE after tempered at (a) 400 ^{o}C and (b) 550 ^{o}C, different corrosion response is separated by red dash lines. The left sides of the images are the BPE oxidation edge. From the BPE oxidation edge to BPE reduction edge, an active-passive-transpassive polarisation response is shown.. The crevice corrosion length is longer than pitting corrosion, indicates the crevice corrosion nucleates at a lower applied potential. When tempering at 550 ^{o}C, crevice corrosion, general corrosion, and cathode area are detected. MSS 420 tempered in the other temperatures, show crevice corrosion, pitting corrosion, passive region, and general corrosion; the left region is the cathode area.

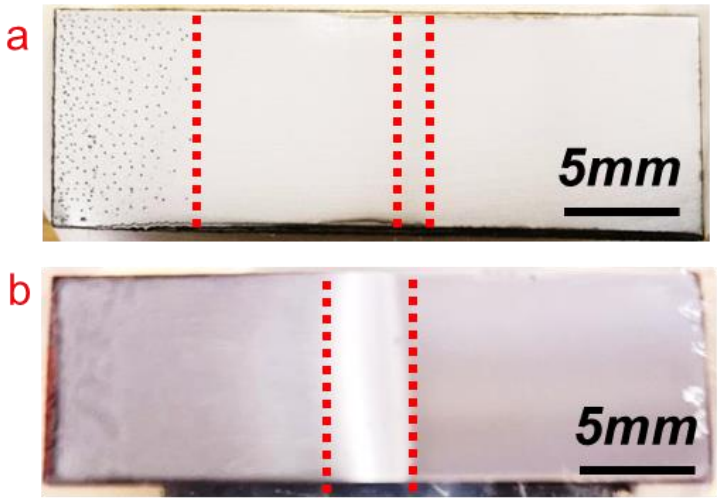

Figure 6.5- 3 Images of MSS 420 BPE after tempered at (a) 400 ºC and (b) 550 ºC for 5 min exposure.

Figure 6.5- 4 gives the pitting covered region located in the BPE with different tempered treatments. No pitting corrosion is measured after tempered at 550 ºC, same as the polarisation test. The left sides of all BPEs are BPE oxidation edge. To demonstrate the reproducibility of these results, three independent tests were carried out using identical sample dimensions and parameters. The pit covered length changed by different tempered temperature, indicates different critical pitting potential. The black voids are the pitting corrosion, even a potential gradient exist along the BPE surface, Here, the large size pits are stable pits and the small size pits are metastable pits. MSS 420 tempered temperature below 400 ºC, only nucleate the lacy covered pits. Pits become open pits after tempered at 700 ºC. The general corrosion (black area) surrounded the pits at high applied potential is only determined after tempering at 700 ºC. High magnification of these two pits are shown in Figure 6.5- 5

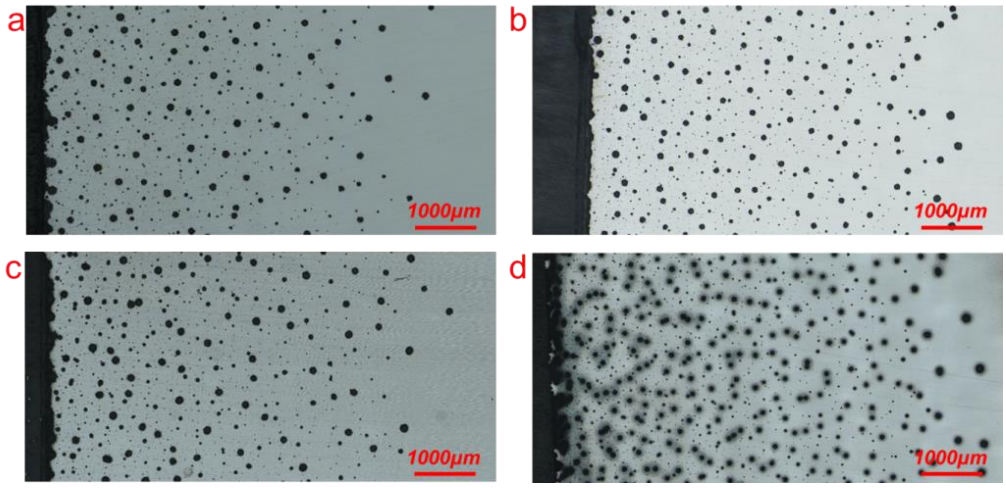

Figure 6.5- 4 Optical images of the pit-covered region after bipolar electrochemistry experiments under different tempering temperatures (a) no tempering, (b) 250 °C, (c) 400 °C, and (d) 700 °C.

Figure 6.5- 5 (a) gives a pit after tempered at 250 °C. The pit edge is not smooth, and some lacy cover is found partly collapsed into the pits, which is retained lacy cover after the ultrasonic bath. Figure 6.5- 5 (b) gives a pit on the BPE tempered at 700 °C, the pit mouth is circle. A rougher surface is detected surrounded the pit, which come from the pit electrolyte diffuse out and corrode the surface [36]. Compare with Figure 6.5- 2, from the potentio-dynamic polarisation test , the passive film are only found tempered below 400 °C, the passive layers acts as the lacy cover and retard the pit electrolyte diffuse out. No passive film is found after tempered at 700 °C, so no lacy cover is determined. .

Both of the 3 electrode potentio-dynamic polarisation and bipolar electrochemistry tests shows similar result, passive film only formed for tempered lower than 400 oC; no pitting is determined when tempered at 550 oC, and pits nucleated for tempered at 700 °C shows different morphology than other tempered temperatures.

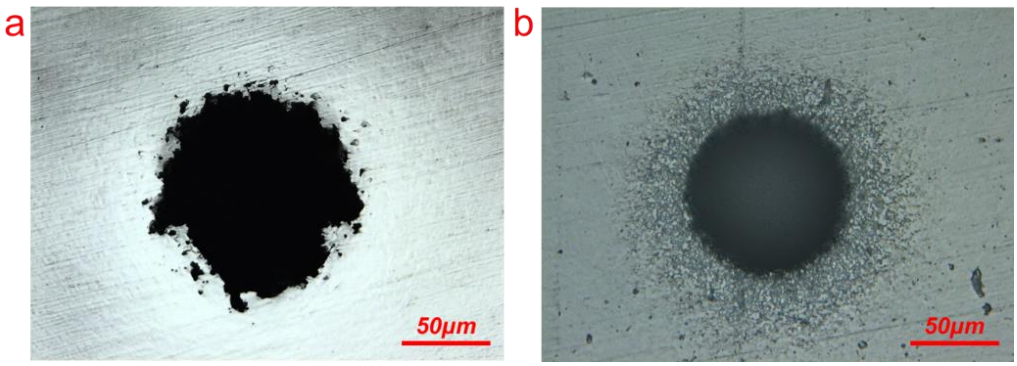

Figure 6.5- 5 Optical images of single pits on the BPE after tempered at (a) 250 °C and (b) 700 °C.

EBSD

Figure 6.5- 6 gives the EBSD images of MSS 420 after different tempered treatments. The scale bar is the same for all the images. No reverted austenite is measured, as no Ni in this MSS 420 [37]. A prior austenite boundary is marked in Figure 6.5- 6 (a). The martensitic phase inside the prior austenite grain has a similar grain orientation. Both retained austenite and martensitic grain sizes change by tempered process. The average area of retained austenite is 17.7 μm^2 without tempering, 11.9 μm^2 for tempering at 250 °C, 7.3 μm^2 for tempering at 400 °C, 5.82 μm^2 for tempering at 550 °C, and 6.24 μm^2 for tempering at 700 °C. The average grain diameter of lath martensitic grain size is 1.67 μm without tempering, 1.46 μm for tempering at 250 °C, 1.19 μm for tempering at 400 °C, 1.07 μm for tempering at 550 °C, and 1.35 μm for tempering at 700 °C. Grain size influences the pitting corrosion behaviour; the fine grain sizes reduces the metastable pit nucleation, but increase the probability to form a stable pit [38].

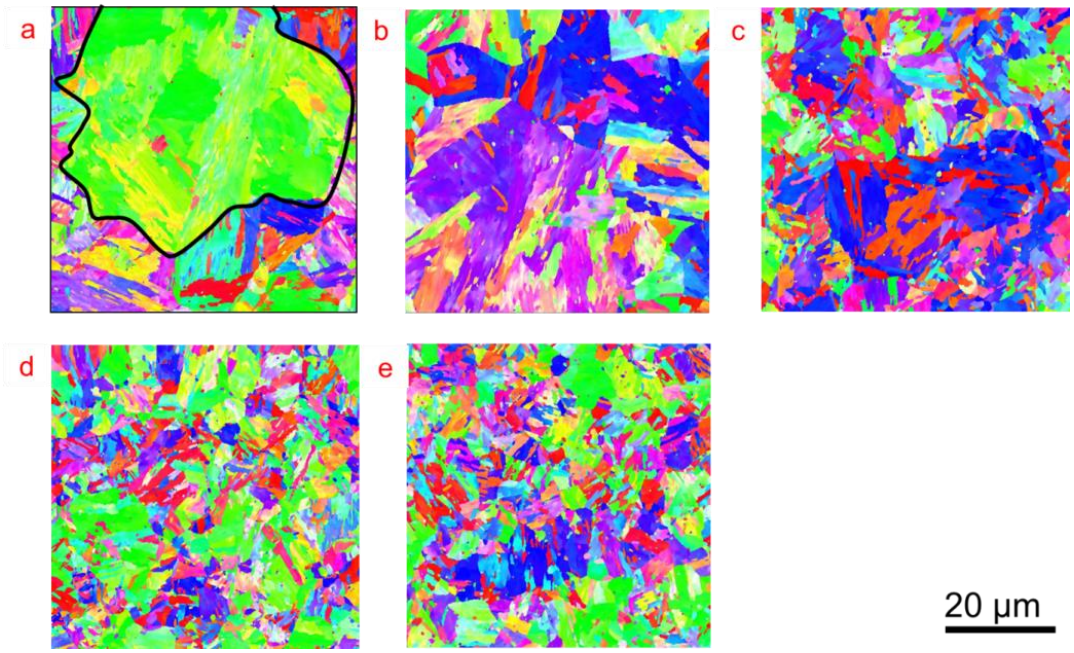

Figure 6.5- 6 The EBSD images of MSS 420 followed by (a) without tempering treatment, tempering temperature at (b) 250 ^{o}C, (c) 400 ^{o}C, (d) 550 ^{o}C and (e) 700 ^{o}C.

To identify the chromium carbides, crystallographic parameters of all possible chromium carbides are listed in Table 6.5- 2. These are obtained from the Inorganic Crystal Structure Database (ICSD) and the Aztec software used for EBSD phase acquisition. The scale bar is the same for all EBSD images. Figure 6.5- 7 shows as-received stainless steel without austenitization treatment, contains a uniform distribution of $Cr_{23}C_6$. Figure 6.5- 7 (b) shows most of the carbides are dissolved into the matrix after austenitization treatment. When tempering at 250 ^{o}C, some tiny amount of $Cr_{23}C_6$ is determined at the grain boundary. After tempering at 400 ^{o}C, larger size and more numbers of. When tempering at 550 ^{o}C, CrC, Cr_7C_3, and $Cr_{23}C_6$ are continues formed at the grain boundaries, result in a continue chromium depletion region, hence intergranular corrosion occurs. Only a tiny amount of CrC and Cr_7C_3 has been determined as most of CrC and Cr_7C_3 transformed and stabilized to $Cr_{23}C_6$ [10,12,35]. For MSS 420 tempered at 700 ^{o}C, only $Cr_{23}C_6$ is determined. The Cr diffusion rate is high at high temperature, which form the large size chromium carbides ≈ 2 µm [39]. The chromium carbides prefer precipitate at the grain boundary as the higher diffusion rate at the grain boundary [40]. It was found, the pitting corrosion nucleated next to the

chromium carbides [36]. The Cr_3C, Cr_3C_2, and Fe_3C are not measured for both ferritic stainless steel and martensitic stainless steel with different tempering treatments.

Table 6.5- 2 Database with crystallographic geometry parameters for EBSD phase identification

Phase	a	b	c	Alpha	Beta	Gamma	Space Group	Phase
Fe3C	5.11 Å	6.78 Å	4.54 Å	90.00 °	90.00 °	90.00 °	62	BCT
Cr3C	5.12 Å	6.80 Å	4.58 Å	90.00 °	90.00 °	90.00 °	62	
Cr3C2	5.53 Å	11.49 Å	2.83 Å	90.00 °	90.00 °	90.00 °	62	
Cr7C3	4.53 Å	7.01 Å	12.14 Å	90.00 °	90.00 °	90.00 °	62	
Cr23C6	10.66 Å	10.66 Å	10.66 Å	90.00 °	90.00 °	90.00 °	225	FCC
CrC	4.03 Å	4.03 Å	4.03 Å	90.00 °	90.00 °	90.00 °	225	

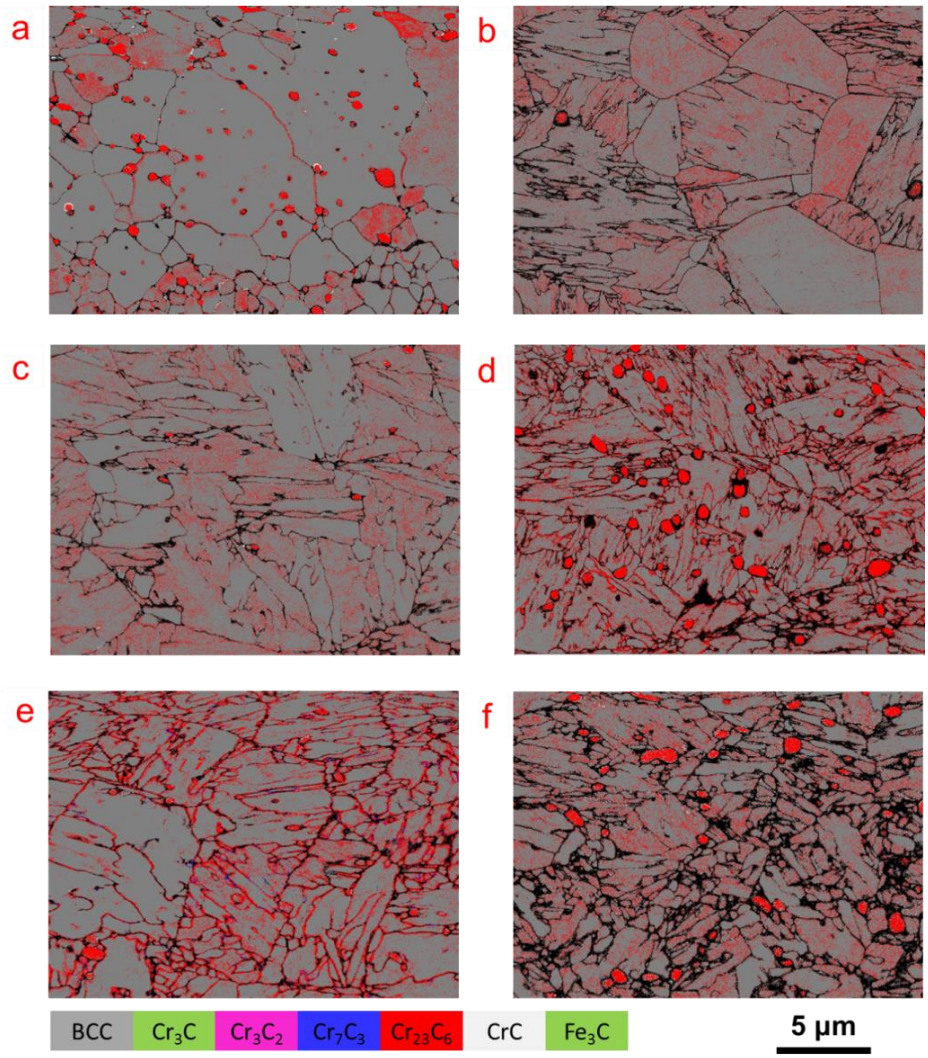

Figure 6.5- 7 The type of chromium carbide and the distribution in (a) as-received ferritic stainless steel, and only austenitization treatment and water quenched in (b), and tempering from (c) 250 ºC, (d) 400 ºC, (e) 550 ºC, to (f) 700 ºC.

Post-test observation

Four different pits are determined after 3-electrode potentio-dynamic polarisation test. All large size pits are the open pits due to the high finished potential. Figure 6.5- 8 (a) shows a circular cross-section pit, the bottom of the pit is clean with a diameter ≈ 300 μm. Some white particles (chromium carbides) stand in front of the matrix, indicates higher corrosion resistance than the matrix. Figure 6.5- 8 (b) shows two elliptical pits; the surface area between the two pits is rough, caused by the general corrosion. The bigger pit has a diameter ≈ 500 μm with the corrosion product inside the pit; from EDX analysis, the corrosion product has high concentration of Cr, O, and Cl, and lower Fe. During pit growth, Cr and Fe dissolve, react with Cl ions and O_2, and then form the oxides and chlorides; less Fe in the corrosion product as a higher diffusion rate out to the pit [41]. The corrosion rate and pit morphology are also changed by the porosity of corrosion product [42,43]. Figure 6.5- 8 (c) shows a circular pit with a diameter of 200 μm, and the diameter of the surrounding general corrosion is > 500 μm. General corrosion is caused by the pit electrolyte diffuse out of the pit. Pit with general corrosion are found in 3-electrode polarisation test for all tempered MSS 420, but not in the BPE. This is related to the final high applied potential, pits become open pits allow a large amount of pit electrolyte diffuse out. All pits are found before tempered lower than 400 ^{o}C. When MSS 420 tempered at 700 ^{o}C, only one type of pit is found shown in Figure 6.5- 8 (d). A spherical shape about 200 μm and a circular pit ring with a diameter of 300 μm surround the pit. The surface roughness is rougher at inner part of pit ring (near the pit) and smoother at outer part of pit ring (far to pit ring). Here, all pits are found with general corrosion surrounded with it, due to the pit electrolyte diffuse out.

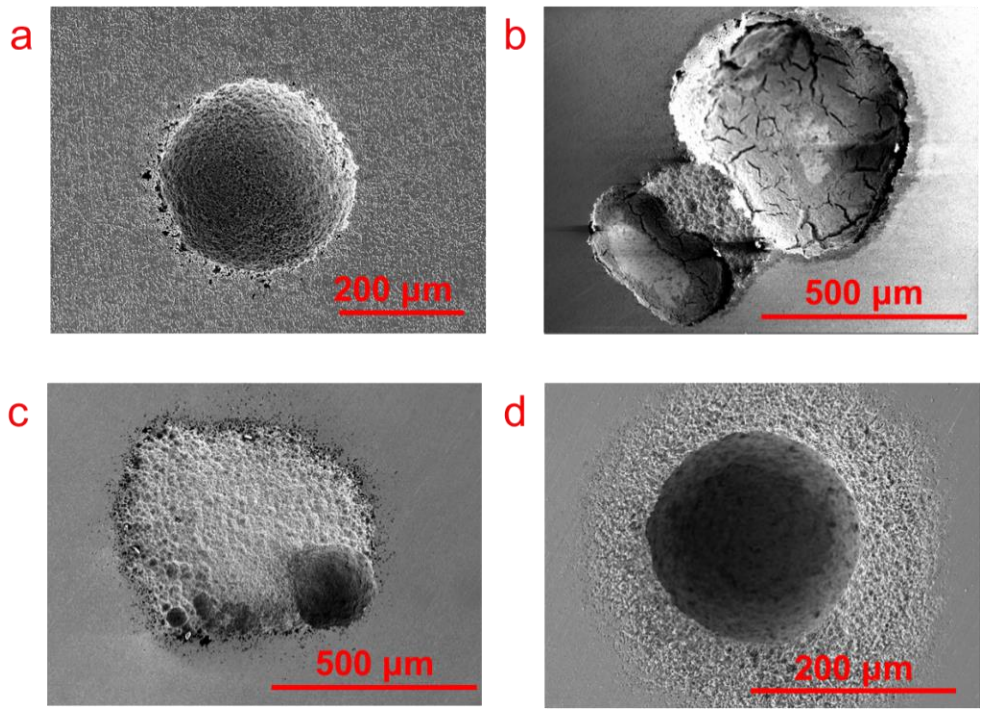

Figure 6.5- 8 Different pit morphologies after the potentio-dynamic polarisation test for (a), (b), and (c) measured at tempered lower than 400 °C and pit measured after tempering at 700 °C in (d).

Figure 6.5- 9 (a) gives an SEM image of the pit ring after tempering at 250 °C. The chromium carbides are clearly seen, with some cavities, which are the metastable pits. Figure 6.5- 9 (b) shows the intergranular corrosion after tempered at 550 °C, each grain is clearly seen, the grain dropping especially regions with similar grain sizes. Figure 6.5- 9 (c) gives the surface roughness of inner part of pit ring close to the pit after tempering at 700 °C, the ellipsoid shape chromium carbides are standing proud of the surface. At a higher magnification of the outer part of pit ring show in Figure 6.5- 9 (d). The sample surface is smoother than inner pit ring, and two cavities surrounding the chromium carbides are seen. Compared to Figure 6.5- 2, the high current density before E_{pit} is the selective corrosion at chromium depletion region, which shown here, the area surrounding the chromium carbides is preferably dissolved, same as literature [36].

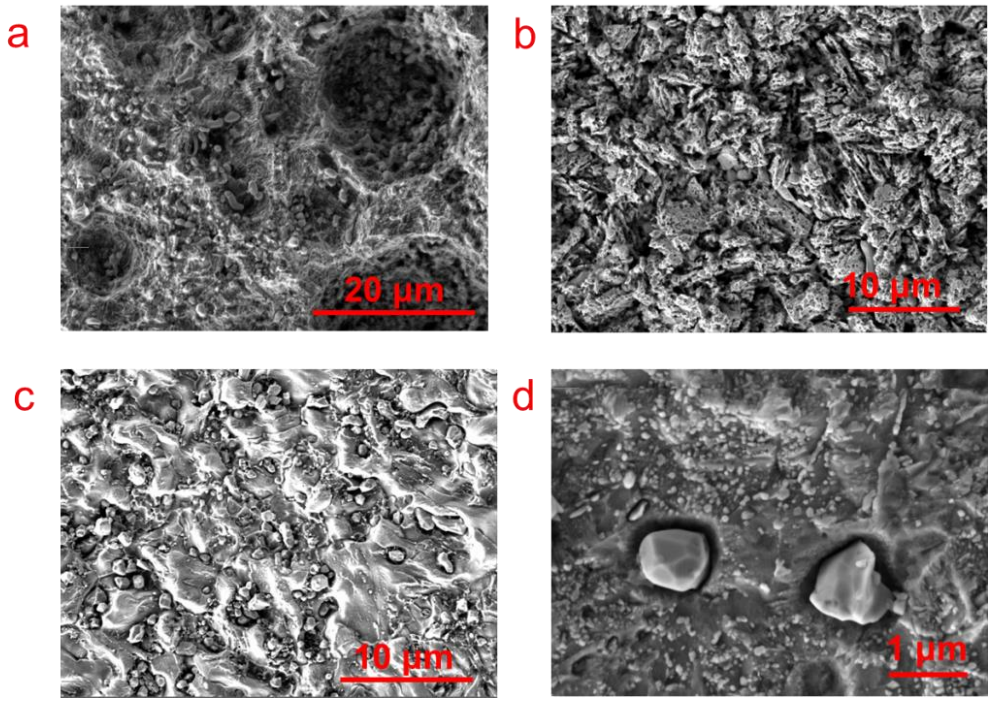

Figure 6.5- 9 The general corrosion after potentio-dynamic polarisation test in the corroded circular area around pits for (a) tempered at 250 ºC and (b) Intergranular corrosion for tempered temperature at 550 ºC. General corrosion of the inner part of pit ring after tempered at 700 ºC in (c) and a high magnification of outer part of pit ring in (d).

The hardness of tempered MSS 420 is the avergae of 5 measurements with the error bars describes the standard deviation. Figure 6.5- 10 (a) shows the hardness is similar until tempered at 400 ºC ≈ 570 $HV_{0.5}$. The hardness reduces to 370 $HV_{0.5}$ and 250 $HV_{0.5}$ after tempering at 550 ºC and 700 ºC. The hardness is slightly decreased after tempering at 250 ºC due to the smaller retained austenite grain size [44]; then slightly increased in hardness for tempered at 400 ºC, as new carbides formed, referred to a secondary hardening effect [45]. After tempered at 550 ºC, the hardness is dramatically reduced as the formation of large number and big chromium carbides. Figure 6.5- 10 (b) shows the concentration of chromium in the matrix, which is the average of 10 points in the matrix with the error bar for the standard deviation. A critical concentration of chromium to form a protective passive film is about 12 %. For tempering below 400 ºC, the chromium concentration > 12%, is enough to form a stable passive film. After tempering at 550 ºC, the chromium concentration is < 12%, so the corrosion occurs in the chromium depletion results in intergranular corrosion. With tempering at 700 ºC, the chromium is

≈11.5%, which also cannot form the passive film, the localised corrosion occurs near the chromium carbides result in the pitting nucleation.

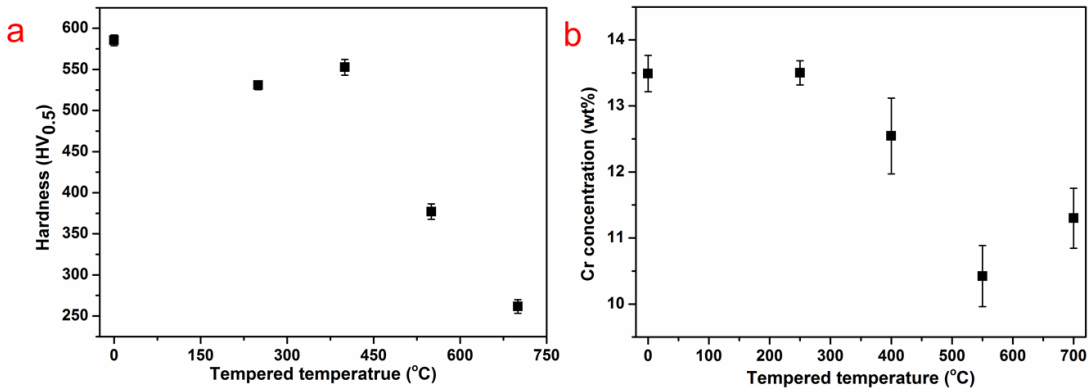

Figure 6.5- 10 (a) The hardness and (b) the Cr concentration evolution with different tempered temperatures.

Corrosion behaviour

Figure 6.5- 11 gives the E_{pit} from 3-electrode polarisation test and pit covered length on the BPE with different tempered temperatures. The E_{pit} and pit covered length is the average value from three independent experiment with same experiment conditions and the error bar is the standard deviation. Due to a linear potential distribution on the BPE, so a longer pit covered length indicates a lower pit nucleation potential. From the E_{pit}, the corrosion resistance rank is 250 ^{o}C > 700 ^{o}C > no tempered treatment ≈ 400 ^{o}C, and from the pit covered length, the rank is 250 ^{o}C > no tempered treatment > 400 ^{o}C > 700 ^{o}C. After tempered at 700 ^{o}C, E_{pit} displays a high corrosion resistance but also a longer pit covered length; this is caused no passive film formed, and the pit formation is more time dependent, fast scan rate (10mV/s) result in higher E_{pit} and 5 min. bipolar exposure had a longer pit covered length.

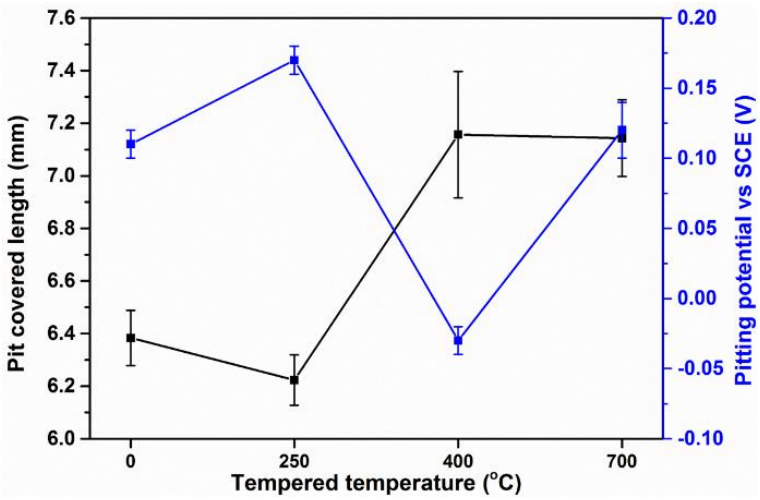

Figure 6.5- 11 The length of pit covered region on the BPE and E_{pit} measured from the 3-electrode polarisation test.

Figure 6.5- 12 (a) displays the average metal loss volume with standard deviation of pitting and crevice corrosion from three independent BPEs with same experiment conditions. The crevice corrosion volume is between the resin and the BPE oxidation edge. Both of pitting and crevice corrosion volume on the BPE shows the similar tendency of different tempered temperatures, a larger corrosion volume is found after tempered at 400 ^{o}C and 700 ^{o}C, and smallest corrosion volume exist for tempered at 250 ^{o}C. From the corrosion volume, the corrosion resistance rank is 250 ^{o}C > no tempered treatment > 400 ^{o}C ≈ 700 ^{o}C. Figure 6.5- 12 (b) gives the pits along the BPE were divided into five equal-sized regions, with each region spanning a size of 1 x 4 mm^2 (length * width). Region 1 represents the highest potential close to the oxidation edge, and region 5 located 4 to 5 mm away from the oxidation edge, with lowest applied potential. Due to a linear potential gradient along the BPE, the pitting corrosion volume is reduced from region 1 to region 5. Here, the pit volume slightly increases from the region 1 to region 2, as most of the available current was consumed by the large crevice at the oxidation edge corrosion, limited current density suppresses the pitting corrosion growth in region 1. From region 2 to region 5, the pit volume is reduced due to the lower acting applied potential. The pit volume in each region almost follows 700 ^{o}C > 400 ^{o}C > no tempered treatment >250 ^{o}C which is similar to the rank of overall localised volume on the BPE. So, the pit growth kinetics in all applied potential

region is lowest after tempered at 250 ^{o}C and highest for tempered at 700 ^{o}C in all different applied potential region.

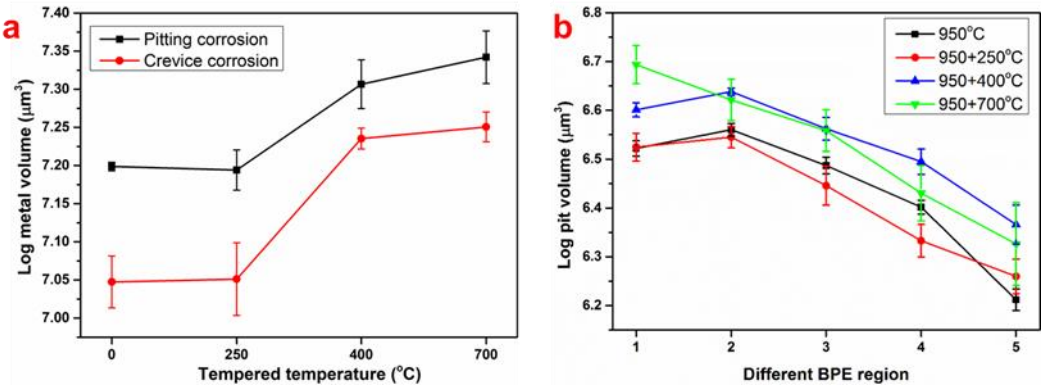

Figure 6.5- 12 (a) The overall pitting and crevice corrosion volume on the BPE and (b) pitting corrosion volume along the BPE after different tempered temperature.

The pitting corrosion determined from bipolar electrochemistry and 3-electrode potentio-dynamic polarisation test gives the same rank of the pitting resistance of the tempered type 420 martensitic stainless steel. Unlike the 3-electrode potentio-dynamic polarisation test, which only offer the critical pitting potential, the advantage of using bipolar electrochemistry for corrosion test include the pit growth kinetics under different applied potential region and the crevice corrosion also can be determined compared and compared at the same time. To optimise the corrosion and hardness behaviour of the type 420 martensitic stainless steel, tempered at 250 ^{o}C is the best choice, due the highest corrosion resistance (high E_{pit} and low pit growth kinetics) and relative high hardness value (>500 $HV_{0.5}$). Tempered at 550 ^{o}C and 700 ^{o}C should be avoid, as the hardness and corrosion resistance are dramatically reduced, due to a large numbers and large size chromium carbides formed.

6.56 Conclusions

- Bipolar electrochemistry is used to determine corrosion behaviour of tempered MSS 420 different applied potential in a single experiment.
- Intergranular corrosion appears with tempering *at* 550 ^{o}C due to continues chromium carbides at the grain boundary.

- The pitting corrosion resistance rank is tempered at 250 ^{o}C > no tempering > 400 ^{o}C > 700 ^{o}C, based on the pit volume and pit covered length, same to the corrosion resistance rank of the E_{pit} in 3-electrode polarisation test.
- The grain size and chromium carbides change with tempering treatments.
- $Cr_{23}C_6$ is determined for all the tempering samples, and CrC and Cr_7C_3 are only measured for sample tempering at 550 ^{o}C.
- The chromium carbides formed predominantly at the grain boundaries.

6.57 References

[1] K.H. Anantha, C. Örnek, S. Ejnermark, A. Medvedeva, J. Sjöström, J. Pan, Correlative Microstructure Analysis and In Situ Corrosion Study of AISI 420 Martensitic Stainless Steel for Plastic Molding Applications, J. Electrochem. Soc. 164 (2017) C85–C93.

[2] A.F. Candelaria, C.E. Pinedo, Influence of the heat treatment on the corrosion resistance of the martensitic stainless steel type AISI 420, J. Mater. Sci. Lett. 22 (2003) 1151–1153.

[3] P.D. Krell, S. Li, H. Cong, Synergistic effect of temperature and HCl concentration on the degradation of AISI 410 stainless steel, Corros. Sci. (2017) 0–1.

[4] S. Marcelin, N. Pébère, S. Régnier, Electrochemical investigations on crevice corrosion of a martensitic stainless steel in a thin-layer cell, J. Electroanal. Chem. 737 (2015) 198–205.

[5] L.D. Barlow, M. Du Toit, Effect of austenitizing heat treatment on the microstructure and hardness of martensitic stainless steel AISI 420, J. Mater. Eng. Perform. 21 (2012) 1327–1336.

[6] C. Brasileiro, Effects of Heat Treatment Conditions on Microstructure and Mechanical Properties of AISI 420 Steel, (2014) 5857–5867.

[7] R. Schneider, J. Perko, G. Reithofer, Heat treatment of corrosion resistant tool steels for plastic moulding, Mater. Manuf. Process. 24 (2009) 903–908.

[8] X. Lei, Y. Feng, J. Zhang, A. Fu, C. Yin, D.D. Macdonald, Impact of Reversed Austenite on the Pitting Corrosion Behavior of Super 13Cr Martensitic Stainless Steel, Electrochim. Acta. 191 (2016) 640–650.

[9] C. García De Andrés, L.F. Álvarez, V. López, J.A. Jiménez, Effects of carbide-forming elements on the response to thermal treatment of the X45Cr13 martensitic stainless steel, J. Mater. Sci. 33 (1998) 4095–4100.

[10] A.N. Isfahany, H. Saghafian, G. Borhani, The effect of heat treatment on mechanical properties and corrosion behavior of AISI420 martensitic stainless steel, J. Alloys Compd. 509 (2011) 3931–3936.

[11] K.H. Anantha, C. Örnek, S. Ejnermark, A. Medvedeva, J. Sjöström, J. Pan, In Situ AFM Study of Localized Corrosion Processes of Tempered AISI 420 Martensitic Stainless Steel: Effect of Secondary Hardening, J. Electrochem. Soc. 164 (2017) C810–C818.

[12] S.-Y. Lu, K.-F. Yao, Y.-B. Chen, M.-H. Wang, X.-Y. Ge, Influence of Heat Treatment on the Microstructure and Corrosion Resistance of 13 Wt Pct Cr-Type Martensitic Stainless Steel, Metall. Mater. Trans. a-Physical Metall. Mater. Sci. 46A (2015) 6090–6102.

[13] C. Köse, R. Kaçar, The effect of preheat & post weld heat treatment on the laser weldability of AISI 420 martensitic stainless steel, Mater. Des. 64 (2014) 221–226.

[14] H. Nakagawa, T. Miyazaki, Effect of retained austenite on the microstructure and mechanical properties of martensitic precipitation hardening stainless steel, J. Mater. Sci. 34 (1999) 3901–3908.

[15] E. de Moor, S. Lacroix, A.J. Clarke, J. Penning, J.G. Speer, Effect of retained austenite stabilized via quench and partitioning on the strain hardening of martensitic steels, Metall. Mater. Trans. A Phys. Metall. Mater. Sci. 39 (2008) 2586–2595.

[16] S. Pahlavan, S. Moazen, I. Taji, K. Saffar, M. Hamrah, M.H. Moayed, S. Mollazadeh Beidokhti, Pitting corrosion of martensitic stainless steel in halide bearing solutions, Corros. Sci. 112 (2016) 233–240.

[17] S. Frangini, N. De Cristofaro, Analysis of the galvanostatic polarization method for determining reliable pitting potentials on stainless steels in crevice-free conditions, Corros. Sci. 45 (2003) 2769–2786.

[18] K. Chandra, V. Kain, R. Tewari, Microstructural and electrochemical characterisation of heat-treated 347 stainless steel with different phases, Corros. Sci. 67 (2013) 118–129.

[19] S.M. G.Burstein, P.Pistorius, Evaluating the critical chemistry for repassivation at the corroding surface

using mass transport model-based artificial pit experiments, Corros. Sci. 35 (1993) 57–62.

[20] G. Meng, Y. Li, Y. Shao, T. Zhang, Y. Wang, F. Wang, Effect of Cl - on the properties of the passive films formed on 316l stainless steel in acidic solution, J. Mater. Sci. Technol. 30 (2014) 253–258.

[21] G.S. Frankel, L. Stockert, F. Hunkeler, H. Boehni, Metastable pitting of stainless steel, Corrosion. 43 (1987) 429–436.

[22] J. Srinivasan, R.G. Kelly, Evaluating the critical chemistry for repassivation at the corroding surface using mass transport model-based artificial pit experiments, J. Electrochem. Soc. 163 (2016) C768–C777.

[23] N.J. Laycock, Metastable Pitting and the Critical Pitting Temperature, J. Electrochem. Soc. 145 (1998) 2622.

[24] C.J. Semino, P. Pedeferri, G.T. Burstein, T.P. Hoar, The localized corrosion of resistant alloys in chloride solutions, Corros. Sci. 19 (1979) 1069–1078.

[25] J. Srinivasan, M.J. McGrath, R.G. Kelly, Mass Transport and Electrochemical Phenomena Influencing the Pitting and Repassivation of Stainless Steels in Neutral Chloride Media, Electrochem. Soc. 58 (2014) 1–11.

[26] N.J. Laycock, R.C. Newman, Localised dissolution kinetics, salt films and pitting potentials, Corros. Sci. 39 (1997) 1771–1790.

[27] Y. Zhou, D.L. Engelberg, Application of a modified bi-polar electrochemistry approach to determine pitting corrosion characteristics, Electrochem. Commun. 93 (2018) 158–161.

[28] S. Munktell, M. Tydén, J. Högström, L. Nyholm, F. Björefors, Bipolar electrochemistry for high-throughput corrosion screening, Electrochem. Commun. 34 (2013) 274–277.

[29] N. Pébère, V. Vivier, Local electrochemical measurements in bipolar experiments for corrosion studies, ChemElectroChem. 3 (2016) 415–421.

[30] R.M. Crooks, Principles of Bipolar Electrochemistry, ChemElectroChem. 3 (2016) 357–359.

[31] Y. Zhou, D.L. Engelberg, Fast testing of ambient temperature pitting corrosion in type 2205 duplex stainless steel by bipolar electrochemistry experiments, Electrochem. Commun. 117 (2020) 106779.

[32] Y. Zhou, A. Kablan, D.L. Engelberg, Metallographic screening of duplex stainless steel weld microstructure with a bipolar electrochemistry technique, Mater. Charact. 169 (2020) 110605.

[33] T. Moisio, M. Mannerkoski, The influence of tempering on the anodic polarization of a precipitation hardening low-C martensitic stainless steel, Corros. Sci. 9 (1969) 129–135.

[34] I. Taji, M.H. Moayed, M. Mirjalili, Correlation between sensitisation and pitting corrosion of AISI 403 martensitic stainless steel, Corros. Sci. 92 (2015) 301–308.

[35] N. Alonso-Falleiros, M. Magri, I.G.S. Falleiros', Intergranular corrosion in a martensitic stainless steel detected by electrochemical tests, Corrosion. 55 (1999) 769–778.

[36] Y. Zhou, D.L. Engelberg, On the application of bipolar electrochemistry to characterise the localised corrosion behaviour of type 420 ferritic stainless steel, Metals (Basel). 10 (2020) 794.

[37] Y.Y. Song, X.Y. Li, L.J. Rong, D.H. Ping, F.X. Yin, Y.Y. Li, Formation of the reversed austenite during intercritical tempering in a Fe-13%Cr-4%Ni-Mo martensitic stainless steel, Mater. Lett. 64 (2010) 1411–1414.

[38] A. Abbasi Aghuy, M. Zakeri, M.H. Moayed, M. Mazinani, Effect of grain size on pitting corrosion of 304L austenitic stainless steel, Corros. Sci. 94 (2015) 368–376.

[39] S.K. Bonagani, V. Bathula, V. Kain, Influence of tempering treatment on microstructure and pitting corrosion of 13 wt.% Cr martensitic stainless steel, Corros. Sci. 131 (2018) 340–354.

[40] M. Godec, D.A.S. Balantič, Coarsening behaviour of M23C6 carbides in creep-resistant steel exposed to high temperatures, Sci. Rep. 6 (2016) art. no. 29734.

[41] M.G. Alvarez, J.R. Galvele, The mechanism of pitting of high purity iron in NaCl solutions, Corros. Sci. 24 (1984) 27–48.

[42] T.Q. Ansari, J.-L. Luo, S.-Q. Shi, Modeling the effect of insoluble corrosion products on pitting corrosion kinetics of metals, Npj Mater. Degrad. 3 (2019) 1–12.

[43] H. Ha, C. Taxen, K. Williams, J. Scully, Effects of selected water chemistry variables on copper pitting propagation in potable water, Electrochim. Acta. 56 (2011) 6165–6183.

[44] F. Hu, K.M. Wu, T.P. Hou, A.A. Shirzadi, Tempering stability of retained austenite in nanostructured dual phase steels, Mater. Sci. Technol. 29 (2013) 947–953.

[45] A.A. Salih, M.Z. Omar, S. Junaidi, Z. Sajuri, Effect of different heat treatment on the SS440C martensitic stainless steel, Aust. J. Basic Appl. Sci. 5 (2011).

7 Application for the characterisation of 2205 duplex Stainless Steel

7.1 General introduction

DSS 2205 had a good combination of the mechanical and corrosion resistance properties. Pitting corrosion cannot be determined on DSS 2205 at room temperature from traditional corrosion tests (such as 3-electrode potentio-dynamic and potentio-static poalrisation). However, bipolar electrochemistry can nucleate pits on DSS 2205 < 15 seconds at room temperature. The crevice, pitting, general corrosion and cathodic area DSS 2205 in 0.1M HCl were researched. Heat treatments were applied on DSS 2205 to change the microstructure, alloying elements redistribution and ratio of ferrite and austenite, result in different corrosion behaviour. The relationship between the microstructure evolution and corrosion resistance changed was researched. The corrosion behaviour of 304L, 316L, 2101, and 2205 was tested by bipolar electrochemistry, the corrosion resistance is compared with traditional corrosion test: PREN and 3 electrode potentio-dynamic polarisation tests.

The first paper (chapter 7.2) introduces the pitting corrosion test on DSS 2205 at room temperature from the bipolar electrochemistry, pit nucleated at the ferrite phase. At 15 seconds, the pits were generated on the BPE. Pitting corrosion, passive region, general corrosion with the cathodic area was determined on one BPE sample. Three independent results proof bipolar electrochemistry test was repeatable.

The second paper (chapter 7.3) displays the pitting corrosion, localised corrosion, and general corrosion kinetics of DSS 2205 at room temperature from 150s to 900s in 0.1M HCl. Cirtical pitting potential reduces and the height differences between the two phases increase with longer exposure time.

The third paper (chapter 7.4) gives introduces the corrosion behaviours of DSS 2205 changed by different heat treatments. Pitting, general corrosion, and cathode region with the passive region were measured. Corrosion resistance was ranked by critical pitting potential and pitting volume. The microstructures DSS 2205 were obtained by the EBSD with EDX. Simulated

CPT and PREN was used to evaluate the pitting corrosion measured from bipolar electrochemistry . The optimized tempering temperatures were chosen from lowest critical pitting potential and lowest pit volume.

The forth paper (chapter 7.5) introduces the corrosion behaviours of four stainless steels from the bipolar electrochemistry. The pitting corrosion resistance was tested and compared from PREN, 3-electrode potentio-dynamic polarisation test, and bipolar electrochemistry. The pitting resistance of different stainless steel was ranked by critical pitting potential and overall pitting volume. Transpassive corrosion was determined on DSS 2101. For DSS, the microstructure of austenite pit lacy cover. Ferrite corroded away in pitting corrosion but it retained in transpassive corrosion.

7.2 Fast Testing of Ambient Temperature Pitting Corrosion in Type 2205 Duplex Stainless Steel by Bipolar Electrochemistry Experiments

Yiqi Zhou[*1], *Dirk Lars Engelberg*[1,2]

1. Corrosion & Protection Centre, School of Materials, The University of Manchester, M13 9PL, Manchester, UK
2. Materials Performance Centre, The University of Manchester, M13 9PL, Manchester, UK

* Corresponding author: Yiqi.Zhou@postgrad.manchester.ac.uk

7.21 Highlights

Room temperature pitting corrosion testing of Type 2205 duplex stainless steel has been successfully carried out.

Pit nucleation and growth can be observed using bipolar electrochemistry testing.

Corrosion pits form by selective dissolution of the ferrite, with lacy covers related to remaining austenite grains.

7.22 Abstract

Commercial grade type 2205 duplex stainless steel is resistant to localised corrosion at room temperature. With the application of bipolar electrochemistry, pitting and crevice corrosion can be probed at room temperature, with corrosion pits nucleated in 0.1M HCl within 15 seconds of exposure. The evolution of localised corrosion kinetics as a function of applied electrochemical potential is discussed. Pit nucleation occurred at the interface between ferrite and austenite, growing into the ferrite phase. Pits with lacy covers formed via selective dissolution of the ferrite.

Keywords: Duplex stainless steel, Pitting corrosion, Crevice corrosion, Bipolar electrochemistry, SEM/EDX.

7.23 Introduction

Bipolar electrochemistry produces a linear potential gradient across two feeder electrodes, providing access to the full spectrum of anodic-to-cathodic electrochemical responses [1]. This technique has been introduced to investigate corrosion properties of stainless steels [2-4]. The technique provides simultaneous access to both anodic and cathodic reactions, a simple

and wireless (non-contact) experimental setup, and provides a method for high throughput screening [1–4].

Duplex stainless steels (DSS) contain a balanced fraction of ferrite (α) and austenite (γ) [5,6], with the materials widely used in marine, chemical environment, and power plants due to their excellent mechanical and corrosion resistance properties [7,8]. However, DSS are not immune to localised corrosion [9,10], with pits even observed under atmospheric exposure at elevated temperature [11]. The concentration of chloride, the applied electrochemical potential, and the electrolyte temperature are key factors that influence the nucleation of crevice and pitting corrosion [12–17]. For Type 2205 DSS, the critical pitting temperature (CPT) is typically measured with potentio-dynamic and potentio-static polarisation techniques, or electrochemical impedance spectroscopy (EIS) [18]. In general, pitting corrosion in annealed 2205 DSS is expected at temperature far in excess of 30°C [18–20]. The CPT can be estimated for exposure to 6% $FeCl_3$ on basis of the chemical composition using ASTM G48 Method E: CPT (°C) = (2.5 × %Cr) + (7.6 × %Mo) + (31.9 × %N) – 41. The corresponding PREN number is then determined with PREN = %Cr + 3.3 × %Mo+ 30 × %N, with higher PREN values indicating better pitting corrosion resistance [21,22].

The aim of this manuscript is to introduce bipolar electrochemistry corrosion screening tests for DSS at ambient temperature. The experimental setup and instantaneous outcome of this test (<15 seconds) are the main advantages of bipolar electrochemistry over standard test methods, such as, for example, ASTM G48-E5 or CPT testing with electrochemical methods. The nucleation and growth of both pitting and crevice corrosion can easily be observed and characterised, here in our manuscript supported by pit topography measurements using 3D laser surface scanning confocal microscopy.

7.24 Materials and Methods

Type 2205 DSS with a composition (wt %) of 22.4% Cr, 0.016% C, 0.4% Si, 5.8% Ni, 1.5% Mn, 3.2% Mo, 0.18% N, and Fe (bal.) was used in this study. The as received material was in the solution annealed condition, with a PREN

of 38.4 and an estimated CPT using ASTM G48 of 45°C for 6% $FeCl_3$. The ratio of the austenite and ferrite was ≈50/50. Pits were found to nucleate in the same DSS 2205 material at 50°C and 30% relative humidity after long-term atmospheric environment exposure [23].

The bipolar electrodes (BPE) had a dimension of 30 mm * 10 mm * 2.4 mm (L * W * D), with the samples first mounted in Araldite resin and then prepared by grinding to 1200 grit, followed by polishing to 1 µm diamond paste finish. For the potentio-dynamic polarisation tests, the sample was cut to 30 mm * 30 mm * 2.4 mm (L * W * D), and also finished via grinding and polishing to 1 µm, ready for testing in the Avesta cell.

For 3-electrode potentio-dynamic polarisation, all samples were tested in an AVESTA cell [12] at room temperature in 0.1M HCl. A Pt counter electrode and Saturated Calomel Electrode (SCE) reference electrode were used, in combination with an IVIUM-Compactstat and IVIUMsoft software to measure potentio-dynamic polarisation curves. The open circuit potential (OCP) was measured for 10 min, followed by potentio-dynamic polarisation tests from -200 mV_{OCP} to +1200 mV_{OCP} using a scan rate of 1 mV/s.

Figure 7.2- 1 (a) gives the setup of the bipolar electrochemistry experiments. A Keysight E36232A DC power supply was used to apply the feeder electrode potential. A constant current (galvanostatic) of 1.2 A was applied between the Platinum feeder electrodes, with a set distance between the feeder electrode of 60 mm, and the BPE centred between the two feeder electrodes. Each feeder electrode had a surface area of 4 cm^2, and all experiments were conducted in 200 ml of 0.1M HCl. Bipolar electrochemistry experiments were run for 15, 30, 150 and 300 seconds to investigate pit growth kinetics, with the surface after exposure analysed for pit nucleation sites.

Figure 7.2- 1 (b) shows the setup for measuring the acting potential along the BPE. A copper-wire was spot welded to the backside of the BPE, and a Luggin capillary connected to a Saturated Calomel Electrode (SCE) set ≈ 1mm above the BPE surface. To measure local potential changes during the bipolar electrochemistry experiments, the OCP was first recorded and the power

supply then switched on. The reported potential change on the y-axis is the difference of measured potential with respect to the OCP. The potentials were measured along the BPE surface in increments of 5 mm, with the Luggin capillary following the centreline of the sample.

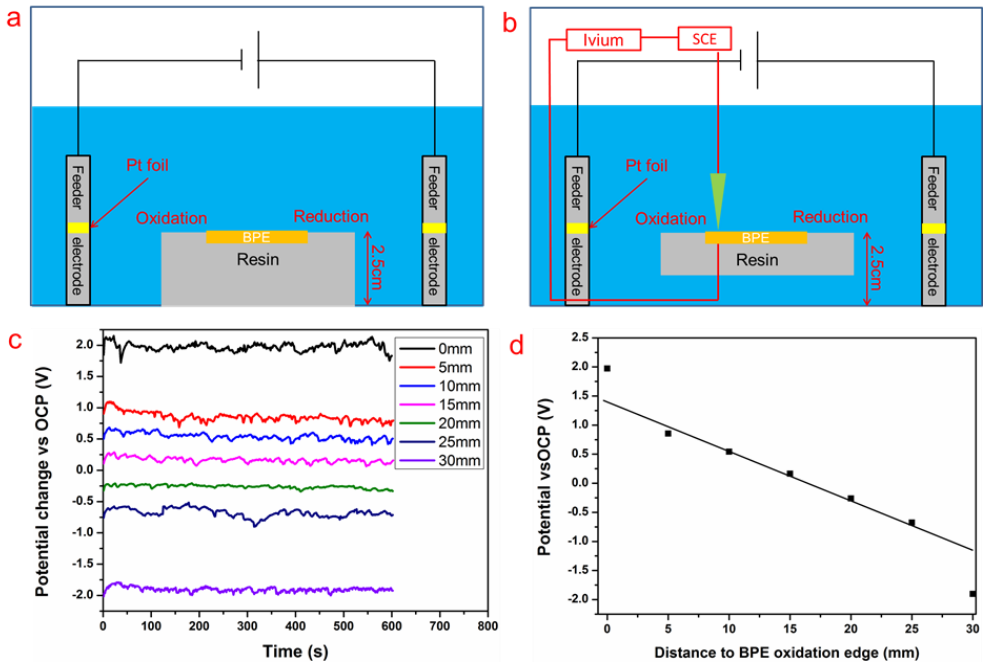

Figure 7.2- 1 (a) Schematic setup of the bipolar electrochemistry experiment, and (b) the bipolar electrochemistry set-up for local potential measurements using a Luggin capillary. (c) The potential change vs time at different locations on the BPE (0 - 30 mm) and (d) measured potential distribution along the BPE (potential change vs OCP).

Figure 7.2- 1 (c) gives the potential change vs. OCP at the different locations. These values (e.g 0 mm, 5 mm) describe the distance with respect to the oxidation edge of the sample (bipolar electrode). The observed noise at each point is caused by local turbulences due to gas formation reactions. The applied potential here is able to generate Cl_2 and H_2 gas, which in turn over longer time periods then change the electrical resistance of the electrolyte. Figure 7.2- 1 (d) shows the potential distribution along the BPE, with the recorded potential at each point showing the average potential over the first 10 minutes of exposure. The potential distribution is quasi-linear along the centre of the BPE, with the potential at the oxidation edge indicating slightly increased potential responses; i.e. more positive at the oxidation edge, and more negative at the reduction edge. The superimposed trend line shows a

linear approximation of all points, with the measured potentials at the BPE edges (0 mm and 30 mm) off-set with respect to the line. This may be attributed to measurements uncertainties close to the edge of the sample.

After each experiment, the sample was removed from the electrolyte, washed and rinsed in soap water, and dried in hot air. A Keyence VK-200K laser confocal scanning microscope was used to determine the corrosion morphology and pit topographies. A Zeiss Sigma VP FEG-SEM was used for imaging and EDX analysis. EDX mapping was carried out using Aztec software at 20 kV, to characterise the chemical compositions of both phases and to observe areas containing selective dissolution around pits.

7.25 Results and Discussion

3-electrode Potentio-dynamic Polarisation Testing

The standard potentio-dynamic polarisation curve in 0.1M HCl is shown in Figure 7.2- 2 (a), displaying an OCP of 0 $V_{SCE.}$ During anodic polarisation, the current density remains low in the passive region up to +0.9 $V_{SCE,}$ where the current then increased significantly up to > 0.1 mA/cm^2. No pits were found, which is in line with literature observations [18–20]. Figure 7.2- 2 (b) shows a 3D laser confocal topography image after testing, showing different grains with outlined interphase boundaries between ferrite and austenite. Grains with higher height is the ferrite and lower grains indicates the austenite. The sharp increase in current density at +0.9 V_{SCE} is caused by the onset of trans-passive corrosion, ultimately leading into oxygen evolution with higher applied potentials [24]. The critical pitting temperature of Type 2205 DSS is far above room temperature, yielding difficulties to induce pits using standard polarisation tests. Pitting corrosion in DSS 2205 can be induced by using higher electrolyte temperatures or with the presence of microstructure susceptibilities, such as chi-/sigma-phase or Cr-Nitrides.

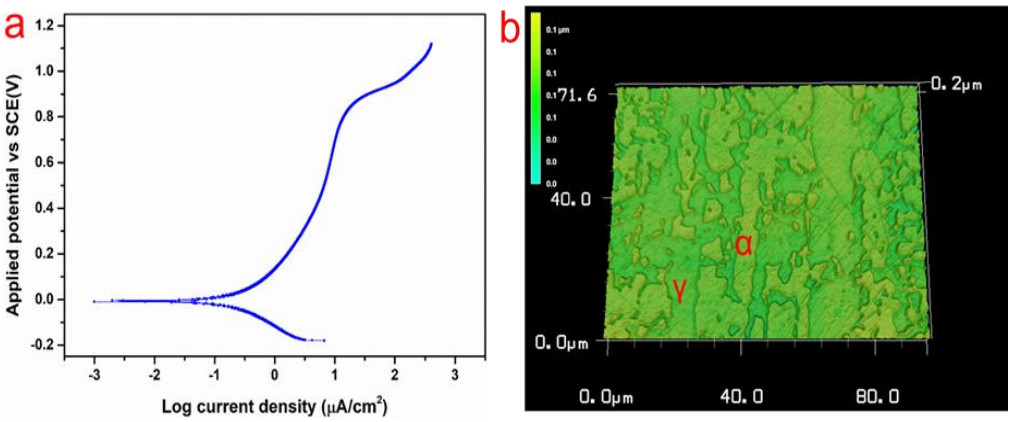

Figure 7.2- 2 (a) The 3-electrode potentio-dynamic polarisation curves for Type 2205 stainless steel at room temperature, and (b) 3D laser confocal topography image after potentio-dynamic polarisation testing.

Bipolar Electrochemistry Testing

Figure 7.2- 3 (a) gives optical images of the rectangular BPE surface after testing in 0.1M HCl for 300 seconds at room temperature. The left side of the image shows the oxidation edge (close to the negative feeder electrode), with the surface covered by crevice corrosion, pitting corrosion, surrounded by a passive region and general corrosion. Further to the reduction edge (to the right) the balancing cathodic reactions then take place. From 0 mm to 4 mm to the BPE oxidation edge, pitting corrosion is observed, with crevice corrosion observed up to a distance of 5 mm. From 4 mm to 8 mm, a passive region is present, and from 8 mm to 10 mm general corrosion is observed. The region beyond 10 mm (10-30 mm) shows no corrosion at all, and most of this region can be attributed to the balancing cathodic reactions. The higher magnification image in Figure 7.2- 3 (b) highlights the crevice, which occurred at the interface between the resin and the BPE. Comparing these regions to the measured potentials in Figure 7.2- 1 (b), indicates that the crevice nucleated at a potential of ≈0.8 $V_{.OCP,}$ which is slightly lower than the observed pitting potential region of ≈0.9 $V_{.OCP}$. The surface of the BPE here shows an active-passive-trans-passive polarisation response, which is mapped onto the rectangular area of the BPE.

The higher resolution image of the anodic regions is shown in Figure 7.2- 3 (b), clearly indicating the presence of large open, hemispherical pits. Crevice

corrosion also exists between the resin and the BPE, with the most serious crevice found close to the BPE oxidation edge due to the highest acting potential. The length of pit covered region and crevice covered region are marked in Figure 7.2- 3 (b). Crevice corrosion can be nucleated at a lower applied potential than pitting corrosion.

Figure 7.2- 3 impressively shows that the BPE provides access to all the different regions of a potentio-dynamic test on one sample surface, providing access to the full spectrum of anodic to cathodic reactions (& kinetics) along the surface. Here in our study we focus on crevice and pitting corrosion, but far more information can be extracted from the BPE surface.

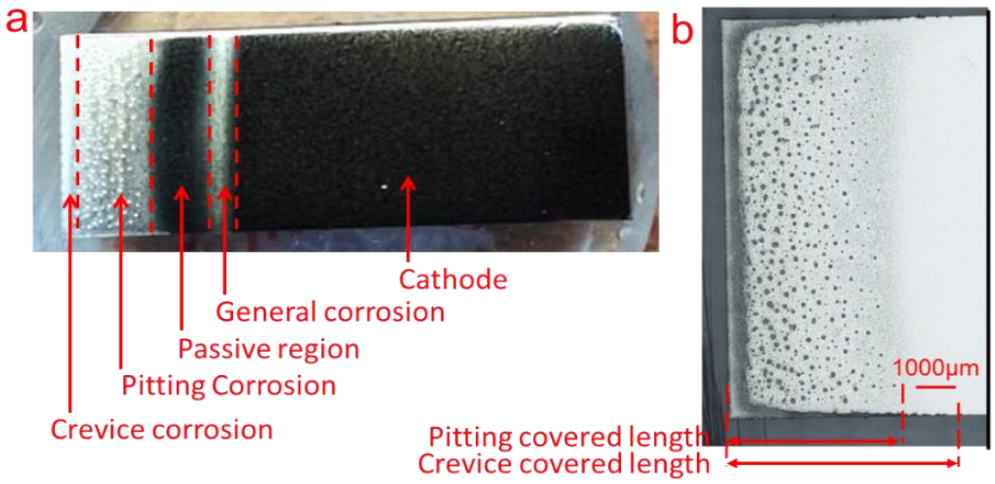

Figure 7.2- 3 (a) View of the bipolar electrode after 300 seconds of exposure, outlining the different corrosion regions along the sample surface; (b) higher magnification zoomed optical image of the localised corrosion region

Pitting corrosion occurs during this test at room temperature, highlighting the capability of bipolar electrochemistry as an effective corrosion screening technique. Compared to the conventional 3-electrode test set-up, the BPE surface does not undergo a temporal evolution of the passive surface film. During conventional 3-electrode testing, the potential is swept through the passive region typically at ever increasing potentials, building up the surface film until either trans-passivity sets-in or the critical pitting potential is reached. The surface film locally breaks down at local passive film imperfections or microstructure heterogeneities, typically associated with temperatures in

excess of 40°C for grade 2205 DSS. This obviously means that the thickness and possibly composition of the passive film on the BPE is inherently different to the passive film developed during potentio-dynamic polarisation testing. Here, the acting potential is able to locally break down the passive film at room temperature. The BPE test results in pitting corrosion, whereas, the conventional 3-electrode set-up only provides observations of trans-passive corrosion or oxygen evolution at room temperature.

During the OCP measurement, the DSS 2205 sample is spontaneously passive due to high concentration of >20% Cr in the passive film. The thickness of the passive film increases with exposure time, so the corrosion resistance is increased for DSS [25–27]. When DSS is probed using potentio-dynamic polarisation test, a thicker passive film can be formed when sweeping through the lower potential regions (in the passive region). The transportation of Cl^- within the passive film will be retarded by thickening the passive film [28,29]. The passive film on the stainless steel consists of two layers, n-type inner layer and p-type outer layer, and the n-type inner layer contributes the corrosion resistance during the polarisation process [30]. The passive film breaks down due to both structural and compositional changes, which is in turn is related to the applied potential. A higher applied potential results initially in thickening of the passive film, with in parallel formation of a less dense outer layer due to anodic Fe dissolution. The underlying alloy surface layer is believed to become more dense via Ni and Mo enrichment. Higher applied potentials then result in rapid Cr dissolution with associated film breakdown, leading to pit nucleation [31–33]. This supports our observation here, that the high potential applied during BPE testing reduces the corrosion resistance of the stainless steel passive layer, providing access to pit nucleation and growth characteristics at room temperature.

Pitting Corrosion and Microstructure

Figure 7.2- 4 (a) shows the occurrence of pitting corrosion on the BPE after only 15 seconds of exposure, resulting in the formation of pits with diameters of a few micrometres. Some small nucleation sites are present at the interface between the ferrite and the austenite, with corrosion typically growing into the

ferrite phase. The lateral spread of the linear potential gradient along the surface of the BPE provides access to the earliest occurrence of pit nucleation. Figure 7.2- 4 (b) summarises pitting corrosion on the BPE after 30 seconds. The diameter of the open pits is around 20 μm, indicating the development of stable pits, with Figure 7.2- 4 (c) showing typical pit nucleation sites at the interface between the austenite and ferrite phase, further expanding into the ferrite. Small isolated pits are also observed inside the ferrite, but most pits nucleate at the interface and more rapidly grow into larger, more stable pits. Figure 7.2- 4 (d) shows a pit grown into the ferrite, with the remains of the austenite phase resulting in a lacy cover type appearance. Some parts of the lacy cover here are already collapsed into the pit after the surrounding ferrite phase was corroded away. The formation of lacy cover pits in DSS 2205 seems similar to previous observation of lacy cover pit formation in lean DSS [10]**.**

Figure 7.2- 4 (e) gives an elongated pit grown by consuming the ferrite phase, supporting previous observations that the austenite phase remains, unless all the surrounding ferrite is dissolved away. Figure 7.2- 4 (f) also shows a large pit with a diameter of 80 μm. The edge of the pit is not smooth, and regions with remaining austenite phase exist at the pit edge, shown as arrows in the figure. The size of the austenite phase is small compared to the overall pit size, so the pit appears hemi-spherical. The ferrite seemed to preferentially dissolve, with local attack resulting into the formation of pits. No uniform attack of other phases was observed, supporting localised corrosion rather than the occurrence of trans-passive corrosion here. During trans-passive corrosion, the austenite is often found to dissolve preferentially (Figure 7.2- 2b).

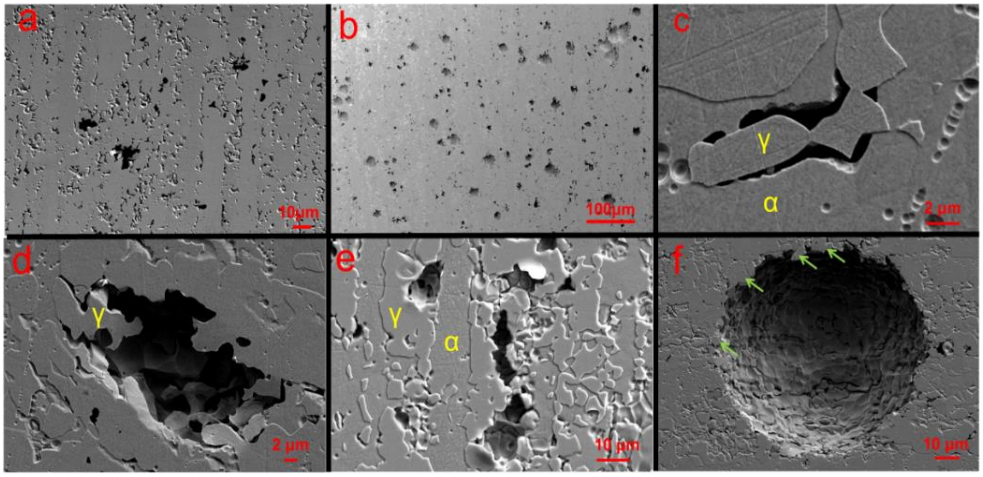

Figure 7.2- 4 (a) Pitting corrosion after 15 seconds of BPE exposure, (b) after 30 seconds, with (c) a typical pit nucleation site after 15 min exposure, and (d-f) fully grown pits with typical dimensions and topographies,(f) a pit it with a diameter of 80 µm.

For EDX analysis, 10 points of each phase were measured, and the average composition calculated, with the standard deviation based on ten measurements. For the austenite phase, the composition is Cr% 21.8 ± 0.4, Ni% 7.0 ± 0.2, and Mo% 2.8 ± 0.2; and for the ferrite phase Cr% 24.5 ± 0.2, Ni% 4.7 ± 0.1, and Mo% 4.3 ± 0.1. For the N content, we assumed that N is saturated in the ferrite phase (0.05 wt%) and all the other nitrogen is therefore enriched in the austenite phase. These compositions give maximum PREN values of 40 for the ferrite and 41 for the austenite. The different chemical signature of each phase was used for identification.

The composition difference between the ferrite and austenite result in the different electrochemical passivation reactions supporting local galvanic activity, the difference in PREN between two phases here is only 1, as the content of nitrogen cannot be directly determined and is only estimated. The difference in (wt%) of Cr, Mo, and Ni is similar to observations in other DSS 2205 microstructure [34], where Scanning Kelvin Probe Force Microscopy (SKPFM) measurements indicated at least a 40 mV potential difference between ferrite and austenite.

Repeatability of Measurements

A linear potential gradient acts along the BPE, resulting in a gradient controlled corrosion response. To demonstrate the reproducibility of these results, three independent tests were carried out using identical sample dimensions and parameters. Figure 7.2- 5 (a) gives the length of pitting and crevice corrosion measured from the oxidation edge on the BPE, with the absolute length of these regions related to the applied potential. All 3 samples show similar results, with the length of crevice corrosion along the interface mounting to 5.3 mm, with pitting corrosion terminating at a length of 4.4 mm (measured from the oxidation edge). It is readily established here that crevice corrosion can nucleate at far lower applied potentials (≈ 0.1 V_{OCP}) than pitting corrosion [35].

For Figure 7.2- 5 (b) and (d), all pits and crevices along the BPE were divided into four equal-sized regions, with each region spanning a size of 1 x 10 mm (L x W). Region 1 represents the highest potential close to the oxidation edge, with region 4 representing lower applied potentials, 3 to 4 mm away from the oxidation edge. The volume of the crevice corrosion region is the sum of the crevice volume at the BPE oxidation edge and the sides. Figure 7.2- 5 (b) summarises the volume of crevice corrosion along the BPE, clearly demonstrating the sudden reduction from region 1 to region 2, and then decreasing into region 4. This is caused by the lower acting potentials at regions further away from the oxidation edge. After region 2, the length of interface between the resin and BPE is constant, the crevice volume is only influenced by the applied potential, i.e. acting potential gradient.

Figure 7.2- 5 (c) gives the corresponding pit volumes. The corroded pit volumes increased from region 1 to region 2. Here, the higher applied potential results in lower pit volumes, since most of the available current was consumed by the large crevice at the oxidation edge. In region 1, larger crevice corrosion area results in less current available for pitting corrosion. The pit volumes from region 2 to region 4 then follow the gradually decreasing potential, with the pitting corrosion volume reduced with lower acting potential. The average crevice corrosion volume in region 1 is about 0.06 mm^3, representing 95% of the corroded volume.

Figure 7.2- 5 (d) shows the maximum pit depth of the 4 different regions. The maximum pit depth is determined by averaging the deepest ten pits in each region. If we now assume that pit growth kinetics follows $d = Kt^n$, with (d) pit depth (μm), (t) time (s), and (K), (n) experimental constants [13,36], we see that the maximum depth between region 1 and 4 only varies by 10%, indicating very similar growth kinetics of the ten deepest pits in all four regions. This implies, that the presence of smaller pits is related to either pits that stifled during the pit growth process, or pits nucleated far later along the process timeline, only being able to grow to smaller sizes. These results show that the pit growth (maximum depth) was potential independent, and most likely related to a limiting parameter.

The power of using bipolar electrochemistry screening for characterising difficult to assess corrosion systems is demonstrated, opening up novel routes for corrosion testing and fast throughput screening techniques.

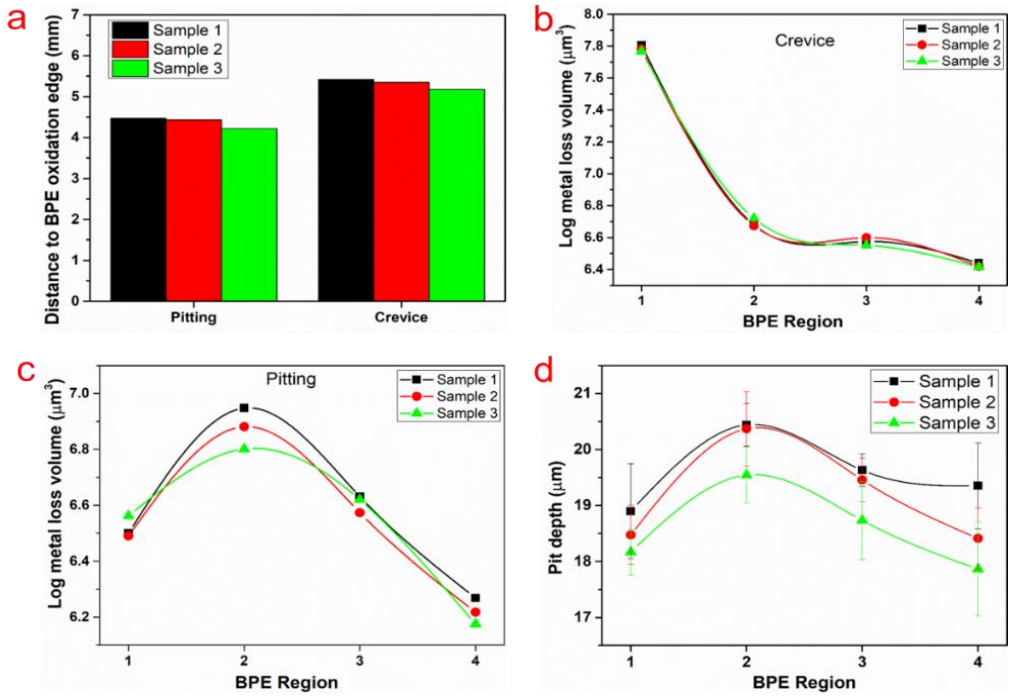

Figure 7.2- 5 (a) The maximum distance of pitting and crevice corrosion measured perpendicular to the BPE oxidation edge after exposure for 150 seconds. 3 samples were used here for data verification, showing (b) the metal loss from crevice corrosion and (c) metal loss from pitting corrosion, and (d) maximum pit depth of the three different samples.

7.26 Conclusions

- Potentio-dynamic corrosion testing did not result in localised corrosion.
- Crevice corrosion, pitting corrosion and general corrosion have been observed under bipolar electro-chemistry control in Type 2205 DSS.
- Pitting corrosion can be observed on Type 2205 stainless steel after only 15 seconds of bipolar exposure in 0.1M HCl.
- Pit nucleation typically occurs at the ferrite-austenite interface, with pit growth via dissolution of the ferrite phase.
- Hemispherical pits with lacy covers were formed by ferrite dissolution, with the remaining austenite forming the lacy covered regions.
- The applied potential affects the overall dissolved volume, with the observed maximum pit depth indicating limiting pit growth.

7.27 References

[1] Y. Zhou, D.L. Engelberg, Application of a modified bi-polar electrochemistry approach to determine pitting corrosion characteristics, Electrochem. Commun. 93 (2018) 158–161. https://doi.org/10.1016/j.elecom.2018.06.013.

[2] S. Munktell, M. Tydén, J. Högström, L. Nyholm, F. Björefors, Bipolar electrochemistry for high-throughput corrosion screening, Electrochem. Commun. 34 (2013) 274–277. https://doi.org/10.1016/j.elecom.2013.07.011.

[3] S. Munktell, L. Nyholm, F. Björefors, Towards high throughput corrosion screening using arrays of bipolar electrodes, J. Electroanal. Chem. 747 (2015) 77–82. https://doi.org/10.1016/j.jelechem.2015.04.008.

[4] N. Pébère, V. Vivier, Local Electrochemical Measurements in Bipolar Experiments for Corrosion Studies, ChemElectroChem. 3 (2016) 415–421. https://doi.org/10.1002/celc.201500375.

[5] J.H. Potgieter, P.A. Olubambi, L. Cornish, C.N. Machio, E.S.M. Sherif, Influence of nickel additions on the corrosion behaviour of low nitrogen 22% Cr series duplex stainless steels, Corros. Sci. 50 (2008) 2572–2579. https://doi.org/10.1016/j.corsci.2008.05.023.

[6] Z. Zhang, Z. Wang, Y. Jiang, H. Tan, D. Han, Y. Guo, J. Li, Effect of post-weld heat treatment on microstructure evolution and pitting corrosion behavior of UNS S31803 duplex stainless steel welds, Corros. Sci. 62 (2012) 42–50. https://doi.org/10.1016/j.corsci.2012.04.047.

[7] H. Tan, Z. Wang, Y. Jiang, D. Han, J. Hong, L. Chen, L. Jiang, J. Li, Annealing temperature effect on the pitting corrosion resistance of plasma arc welded joints of duplex stainless steel UNS S32304 in 1.0M NaCl, Corros. Sci. 53 (2011) 2191–2200. https://doi.org/10.1016/j.corsci.2011.02.041.

[8] J. Nilsson, Overview Super duplex stainless steels, Mater. Sci. Technol. 8 (1992) 685–700. https://doi.org/10.1179/mst.1992.8.8.685.

[9] S.M. Sharland, A Review of The Theoretical Modelling of Crevice and Pitting Corrosion, Corros. Sci. 27 (1987) 289–323.

[10] K. Eguchi, T.L. Burnett, D.L. Engelberg, X-Ray tomographic characterisation of pitting corrosion in lean duplex stainless steel, Corros. Sci. 165 (2019) 108406. https://doi.org/10.1016/j.corsci.2019.108406.

[11] C. Örnek, F. Léonard, S.A. McDonald, A. Prajapati, P.J. Withers, D.L. Engelberg, Time-dependent in situ measurement of atmospheric corrosion rates of duplex stainless steel wires, Npj Mater. Degrad. 2 (2018) 1–15. https://doi.org/10.1038/s41529-018-0030-9.

[12] B. Krawczyk, P. Cook, J. Hobbs, D. Engelberg, Corrosion Behavior of Cold Rolled Type 316L Stainless Steel in HCl Containing Environments, Corrosion. 73 (2017) 1346. https://doi.org//10.5006/2415.

[13] G.S. Frankel, Pitting Corrosion of Metals A Review of the Critical Factors, 145 (1998) 2186–2198.

[14] J.W. Oldfield, W.H. Sutton, Crevice Corrosion of Stainless Steels: I. A Mathematical Model, Br. Corros. J. 13 (1978) 13–22. https://doi.org/http://dx.doi.org/10.1179/000705978798358671.

[15] A.M. Al-Zahrani, H.W. Pickering, IR voltage switch in delayed crevice corrosion and active peak formation detected using a repassivation-type scan, Electrochim. Acta. 50 (2005) 3420–3435. https://doi.org/10.1016/j.electacta.2004.12.017.

[16] N. Corlett, L.E. Eiselstein, N. Budiansky, Chapter 2.03 Crevice Corrosion, in: Shreir's Corros., 2010: pp. 753–771.

[17] G.R. Engelhardt, D.D. MacDonald, Possible distribution of potential and corrosion current density inside corroding crevices, Electrochim. Acta. 65 (2012) 266–274. https://doi.org/10.1016/j.electacta.2012.01.065.

[18] N. Ebrahimi, M. Momeni, A. Kosari, M. Zakeri, M.H. Moayed, A comparative study of critical pitting temperature (CPT) of stainless steels by electrochemical impedance spectroscopy (EIS), potentiodynamic and potentiostatic techniques, Corros. Sci. 59 (2012) 96–102. https://doi.org/10.1016/j.corsci.2012.02.026.

[19] N. Ebrahimi, M.H. Moayed, A. Davoodi, Critical pitting temperature dependence of 2205 duplex stainless steel on dichromate ion concentration in chloride medium, Corros. Sci. 53 (2011) 1278–1287. https://doi.org/10.1016/j.corsci.2010.12.019.

[20] M. Adeli, M.A. Golozar, K. Raeissi, Pitting corrosion of SAF2205 duplex stainless steel in acetic acid containing bromide and chloride, Chem. Eng. Commun. 197 (2010) 1404–1416. https://doi.org/10.1080/00986441003626151.

[21] S. Kim, S. Kim, I. Lee, Y. Park, M. Shin, Y. Kim, Effects of shielding gases on the microstructure and localized corrosion of tube-to-tube sheet welds of super austenitic stainless steel for seawater cooled condenser, Corros. Sci. 53 (2011) 2611–2618. https://doi.org/10.1016/j.corsci.2011.04.021.

[22] L.H. Guilherme, P. Reccagni, A. V Benedetti, C.S. Fugivara, D.L. Engelberg, Corrosion Assessment of ASME Qualified Welding Procedures for Grade 2101 Lean Duplex Stainless Steel, Corrosion. 75 (2019) 1216–1229. https://doi.org/10.5006/3257.

[23] C. Örnek, X. Zhong, D.L. Engelberg, Low-Temperature Environmentally Assisted Cracking of Grade 2205 Duplex Stainless Steel Beneath a MgCl 2 :FeCl 3 Salt Droplet, Corrosion. 72 (2016) 384–399. https://doi.org/10.5006/1888.

[24] C. Örnek, M. Långberg, J. Evertsson, G. Harlow, W. Linpé, L. Rullik, F. Carlà, R. Felici, E. Bettini, U. Kivisäkk, E. Lundgren, J. Pan, In-situ synchrotron GIXRD study of passive film evolution on duplex stainless steel in corrosive environment, Corros. Sci. 141 (2018) 18–21. https://doi.org/10.1016/j.corsci.2018.06.040.

[25] P. Brüesch, K. Müller, A. Atrens, H. Neff, Corrosion of stainless steels in chloride solution: An XPS investigation of passive films, Appl. Phys. A Solids Surfaces. 38 (1985) 1–18. https://doi.org/10.1007/BF00618720.

[26] R. Jiang, Y. Wang, X. Wen, C. Chen, J. Zhao, Effect of time on the characteristics of passive film formed on stainless steel, Appl. Surf. Sci. 412 (2017) 214–222. https://doi.org/10.1016/j.apsusc.2017.03.155.

[27] C. Örnek, C. Leygraf, J. Pan, Passive film characterisation of duplex stainless steel using scanning Kelvin prove force microscopy in combination with electrochemical measurements, Npj Mater. Degrad. 3 (2019) 8. https://doi.org/10.1038/s41529-019-0071-8.

[28] K. Sugimoto, Y. Sawada, The role of molybdenum additions to austenitic stainless steels in the inhibition of pitting in acid chloride solutions, Corros. Sci. 17 (1977) 425–445. https://doi.org/10.1016/0010-938X(77)90032-4.

[29] J. Moon, H.Y. Ha, S.J. Park, T.H. Lee, J.H. Jang, C.H. Lee, H.N. Han, H.U. Hong, Effect of Mo and Cr additions on the microstructure, mechanical properties and pitting corrosion resistance of austenitic Fe-30Mn-10.5Al-1.1C lightweight steels, J. Alloys Compd. 775 (2019) 1136–1146. https://doi.org/10.1016/j.jallcom.2018.10.253.

[30] T. Haruna, D.D. Macdonald, Breakdown of Passive Films on Metals, Zairyo-to-Kankyo. 47 (2014) 78–85. https://doi.org/10.3323/jcorr1991.47.78.

[31] M. Långberg, C. Örnek, J. Evertsson, G.S. Harlow, W. Linpé, L. Rullik, R. Felici, E. Bettini, U. Kivisäkk, E. Lundgren, J. Pan, Redefining passivity breakdown of super duplex stainless steel by electrochemical operando synchrotron near surface X-ray analyses, Npj Mater. Degrad. 3 (2019) 22. https://doi.org/10.1038/s41529-019-0084-3.

[32] C.O.A. Olsson, D. Landolt, Passive films on stainless steels - Chemistry, structure and growth, Electrochim. Acta. 48 (2003) 1093–1104. https://doi.org/10.1016/S0013-4686(02)00841-1.

[33] G. Okamoto, Passive film of 18-8 stainless steel structure and its function, Corros. Sci. 13 (1973) 471–489. https://doi.org/10.1016/0010-938X(73)90031-0.

[34] P. Reccagni, L.H. Guilherme, Q. Lu, M.F. Gittos, D.L. Engelberg, Reduction of austenite-ferrite galvanic activity in the heat-affected zone of a Gleeble-simulated grade 2205 duplex stainless steel weld, Corros. Sci. 161 (2019). https://doi.org/10.1016/j.corsci.2019.108198.

[35] B.E. Wilde, E. Williams, The Relevance of Accelerated Electrochemical Pitting Tests to the Long-Term Pitting and Crevice Corrosion Behavior of Stainless Steels in Marine Environments, J. Electrochem. Soc. 118 (2007) 1057. https://doi.org/10.1149/1.2408246.

[36] M.K. Cavanaugh, R.G. Buchheit, N. Birbilis, Modeling the environmental dependence of pit growth using neural network approaches, Corros. Sci. 52 (2010) 3070–3077. https://doi.org/10.1016/j.corsci.2010.05.027.

7.3 Estimating Pitting and Crevice Corrosion Growth Kinetics of Type 2205 Duplex Stainless Steel at Ambient Temperature

Yiqi Zhou[*1], *Dirk Lars Engelberg*[1,2]

1. Corrosion & Protection Centre, School of Materials, The University of Manchester, M13 9PL, Manchester, UK

2. Materials Performance Centre, The University of Manchester, M13 9PL, Manchester, UK

* Corresponding author: Yiqi.zhou@postgrad.manchester.ac.uk

7.31 Highlights

Pitting, crevice corrosion, and general corrosion are measured on DSS 2205 at room temperature by bipolar electrochemistry.

Pit growth kinetics and crevice corrosion development with time and applied potential are reported.

Critical pitting and crevice potential are related to the exposure time.

The probability of pit nucleation and growth is discussed.

7.32 Abstract

Bipolar electrochemistry produces a linear potential gradient across the bipolar electrode (BPE), provides a full spectrum of anodic-to-cathodic electrochemical responses. Pitting, crevice, and general corrosion are nucleated on DSS 2205 BPE at room temperature. The critical pit depth and the probability of pits under stable growth are measured. Pit nucleation site is either in the ferrite phase or at the interface between ferrite and austenite. The critical pitting and crevice corrosion potential and the evolution of localised corrosion are discussed. Pit growth kinetics under different applied potential is calculated, and the “champion pit” is introduced. General corrosion shows ferrite suffers more corrosion, the height difference between ferrite and austenite increases with time.

Keywords: Duplex stainless steel, Pitting corrosion, Crevice corrosion, Bipolar electrochemistry, SEM/EBSD.

7.33 Introduction

A bipolar electrode (BPE) is set between the feeder electrodes in the electrolyte with a potential drop across the BPE surface. With a sufficiently high applied potential drop, the cathodic reactions occur close to the positive

feeder electrode and inverse for anodic reactions [1,2]. The applications of bipolar electrochemistry various from analytical chemistry to material science [3–5]. Recently, bipolar electrochemistry is used to study stainless steel corrosion behaviours; the pit radius on Type 304 stainless steel is decreasing from the BPE oxidation edge to the BPE center [6]. The rank of pitting resistance measured from different stainless steel by bipolar electrochemistry is the same as the corrosion response from 3-electrode potentio-dynamic polarization and pitting resistance equivalent number (PREN) [7]. The relationship between the potential-current curves measured from the bipolar electrochemistry and 3-electrode potentio-dynamic polarization test is similar [8]. A modified bipolar electrochemistry is created by a secondary potential superposed on the BPE, used to study the corrosion evolution from the cathodic region, passive region, pitting corrosion, and trans-passive corrosion [9].

Duplex stainless steel contains austenite and ferrite phase, with the application varied from marine, chemical, and power plane due to the excellent mechanical and corrosion resistance properties [10–12]. The composition of duplex stainless steel influences the pitting corrosion resistance, such as PREN = %Cr + 3.3 × %Mo+ 30 × %N [13], and critical pitting temperature (CPT) (°C) = (2.5 × %Cr) + (7.6 × %Mo) + (31.9 × %N) – 41 according to the ASTM G48-11 Method E. Usually, the CPT for DSS 2205 is higher than room temperature [14–17]. But microstructure susceptibilities, such as Cr depletion regions next to secondary precipitations (sigma/chi), result in pitting at room temperature [18].

Bipolar electrochemistry was successfully applied to nucleate pitting corrosion at room temperature on DSS 2205 without secondary precipitations. The aim of the manuscript is to research to evolution of pitting corrosion, crevice corrosion, and general corrosion on DSS 2205 at room temperature with different applied potential on the bipolar electrode. The corrosion morphology is determined by laser confocal microscopy, and the microstructure and composition of DSS 2205 are identified by EBSD/SEM/EDX.

7.34 Materials and Methods

Type 2205 stainless steel with the composition (wt %) of 22.4% Cr, 0.016% C, 0.4% Si, 1.5% Mn, 0.18% N, and Fe (bal.) was used in this study. The duplex stainless steel was as received condition. BPEs had the dimensions of 30 mm * 10 mm * 2.4 mm (L * W * D). For the potentio-dynamic polarisation test, the sample was cut to 30 mm * 30 mm * 2.4 mm (L * W * D). The BPEs were mounted in Araldite resin, then prepared by grinding up to 1200 grit and followed by polish to 1 µm diamond paste. For EBSD analysis; the samples ground to 2400 grit and polished to 0.25 µm with diamond paste, and then followed by a fine polishing (OPS Colloidal Silica).

Figure 7.3- 1 (a) gives the setup of the bipolar electrochemistry. A Keysight E36232A Autoranging DC power supply was used. A constant current (1.2 A) was applied between the feeder electrodes with a distance of 60 mm. The BPE was set at the centre of the feeder electrodes. Each Platinum feeder electrode had a surface area of 4 cm^2. Bipolar electrochemistry experiments were run until 900 seconds had elapsed, with an interval of 150 seconds to investigate the corrosion evolution. The electrolyte was HCl (0.1 M, 200 mL). Figure 7.3- 1 (a) shows the potential distribution along the BPE, measured by with a Luggin probe, and the recorded potential vs OCP at each location is stable with time [19]. The potential was the average record potential from 0 to 600 seconds. The superimposed trend line showed a linear approximation of all points, but the measured potentials at the BPE edges (0 mm and 30 mm) were far away off-set with respect to the line. This may be attributed to measurements uncertainties close to the edge of the sample.

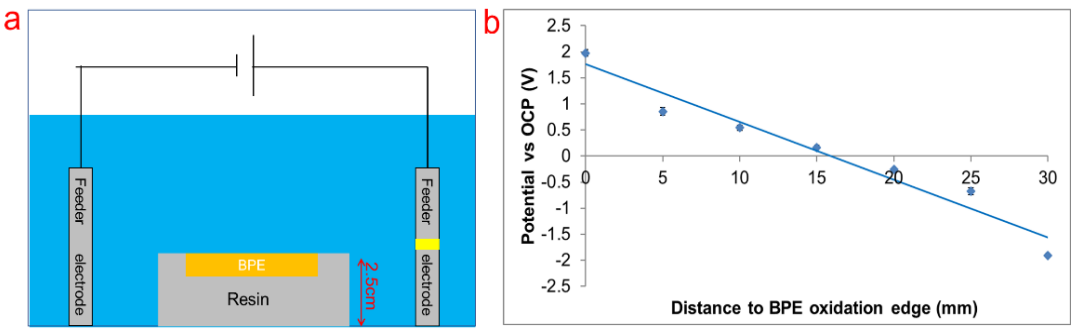

Figure 7.3- 1 (a) Schematic setup of the bipolar electrochemistry and (b) measured potential along the BPE (potential change vs OCP).

7.35 Results and Discussion

EBSD

Figure 7.3- 2 gives an EBSD image of DSS 2205, only austenite and ferrite phase are determined, with no secondary precipitations. The austenitic phase is isolated by the ferritic phase; so here the austenitic phase is more prone to collapse if the all surrounding ferritic phase is dissolved, which supports the view that no lacy cover has been observed for the large size pits after the corrosion tests. The ratio of the austenite and ferrite is about 50/50. For the austenite phase, the concentration (wt%) of Cr is 21.8%, Ni is 7.0%, and Mo is 2.8%; for the ferrite phase, Cr is 24%, Ni is 4.7%, and Mo is 4.3%. The austenite phase contains a higher concentration of Ni, but a lower concentration of Cr and Mo. The elemental partitioning between austenite and ferrite phase result in different passivation behaviours during polarisation and different potential measured by SKPFM [20].

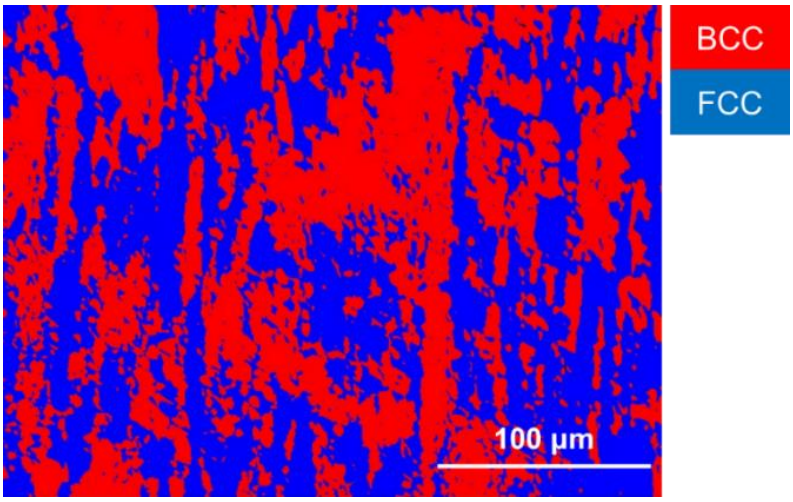

Figure 7.3- 2 The EBSD image of Type 2205 stainless steel.

Bipolar Electrochemistry Testing

Figure 7.3- 3 gives an optical image of the BPE surface after 900 seconds. From BPE oxidation edge to reduction edge, crevice corrosion, pitting corrosion, passive region, general corrosion, and cathodic region are determined. The surface of the BPE shows the full active-passive-trans-passive polarisation response. From 0 mm to 5 mm to the BPE oxidation edge,

pitting corrosion is observed, with crevice corrosion observed up to a distance of 6 mm. From 5 mm to 10 mm general corrosion is observed. The region beyond 10 mm (10-30 mm) shows no corrosion at all, and most of this region can be attributed to the balancing cathodic reactions. The length of pit covered region increases with time, and the growth direction is toward to the BPE reduction edge. At 150s, no general corrosion region is measured. At 300s, general corrosion is nucleated. The expansion direction of the general corrosion is toward to the BPE oxidation edge, shown as an arch. At 900s, general corrosion connects to pitting corrosion, and the colour of the general corrosion close to the pitting is lighter than close to the cathodic region, indicates less serious of general corrosion.

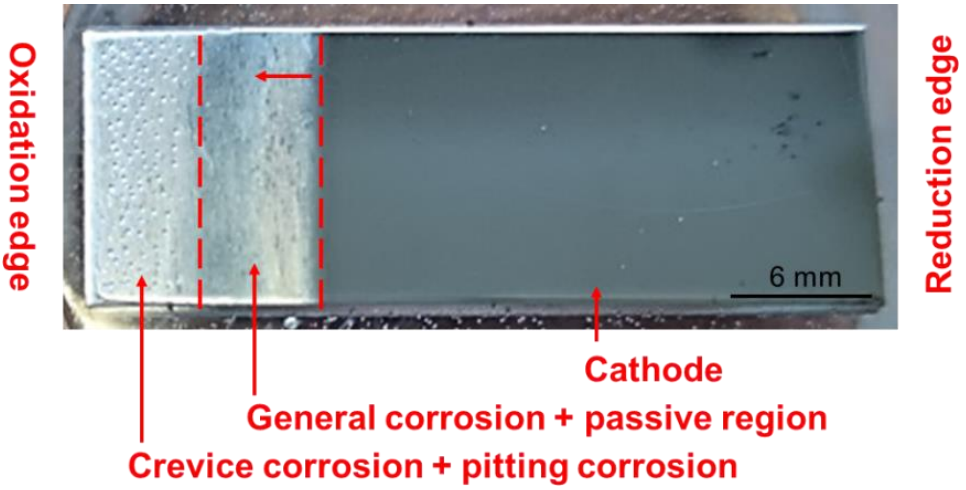

Figure 7.3- 3 View of the bipolar electrode after 900 seconds of exposure, outlining the different corrosion regions along the sample surface.

Figure 7.3- 4 gives the optical images of BPE contain the localised corrosion with different exposure time. The left side of the image is the BPE oxidation edge. The length of the pit covered region and crevice covered region is marked. Crevice corrosion, pitting corrosion, and general corrosion is measured on the BPE. All the large size pits are open pits. The crevice corrosion is found between the resin and BPE, the most serious crevice corrosion is nucleated between the resin and BPE oxidation edge due to the highest applied potential. The length of the pit covered length is shorter than crevice length, indicates the crevice corrosion is 0.1 V_{SCE} higher than pitting corrosion. The average pit size is increasing with longer exposure time. After

750s, pits close to each other, and then merge together. The width of the crevice corrosion mouth at the BPE oxidation edge increases slightly with time, as the openness of the crevice corrosion influence the acidification process and potential distribution inside of crevice, more openness crevice encourages the aggressive electrolyte diffusion out of the crevice which reduces or retard the crevice corrosion expansion [21–26].

For the bipolar electrode, a full spectrum of anodic-to-cathodic response can be measured on one BPE. Here, the anodic corrosion evolution, include crevice corrosion, pitting corrosion, and general corrosion will be researched. The competition of the crevice corrosion and pitting corrosion should be considered, and pit growth kinetics changed by pit close to each other or merge together will be discussed.

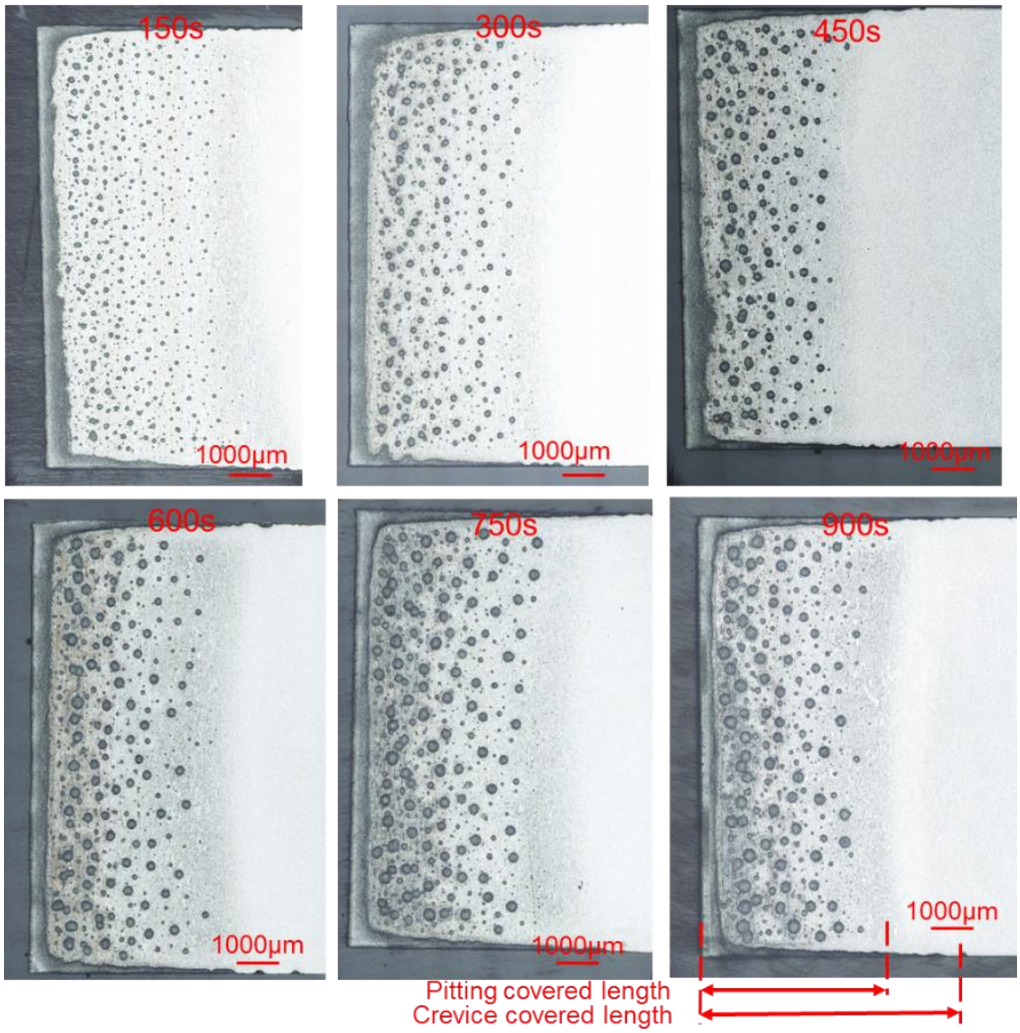

Figure 7.3- 4 Higher magnification zoomed optical image of the localised corrosion region

Localised corrosion morphology

Figure 7.3- 5 displays the optical images of pitting and crevice corrosion and corresponding surface roughness lines one the BPE after 900s. Figure 7.3- 5 (a) gives the pits with a diameter over 300 μm or less than 100 μm. The large pits are the stable pits; as the large volume can act as a diffusion barrier to keep the aggressive pit electrolyte [27–30]. A line across a pit with a diameter around 300 μm and depth 70 μm is given, the pit radius (150 μm) > depth (70 μm) indicates the pit is the disk-like shape. For a single phase stainless steels, the pit shape is related to applied potential, alloy composition, and Cl^- concentration [9,31]. For duplex stainless steel, the pit morphology is also related by the ratio, size, and distribution of austenite and ferrite [32]. The surface line at the pit bottom is not smooth, caused by the selective phase corrosion. Figure 7.3- 5 (b) gives the crevice corrosion between the resin and BPE oxidation edge. The maximum height of the crevice is 70 μm next to the resin. Toward the BPE, the height of the crevice is slightly increased to 40 μm and then the crevice wall in reached, which is the boundary for crevice corrosion and pitting corrosion. The height of sudden diminishes can be explained by the IR drop mechanism. IR drop is the potential drop inside of the localised corrosion caused by the anodic current density (I) and solution resistance (R). A critical potential ($\triangle\varphi^* = IR^*$) is given to indicate the potential difference at the crevice mouth and active/passive transition in the crevice solution's polarization curve. When $IR > IR^*$, the local potential inside of crevice is in the active region, so the crevice corrosion can propagate [33–36]. The sudden height change in the crevice corrosion is in the condition of $IR < IR^*$, so the crevice wall is in passive region.

Figure 7.3- 5 (c) offers the crevice corrosion at the interface between the resin and BPE sides, which has a distance of 3 mm to the BPE oxidation edge. The maximum crevice depth is ≈ 70 μm, similar to the crevice height at the BPE oxidation edge, which indicates the corrosion kinetics is under diffusion control. The maximum crevice height is also located next to the resin, caused by longer

growth time. Crevice corrosion nucleated at the interface between the resin and BPE, and then growth toward to the BPE. Longer nucleation time, result in higher depth. A crevice wall with sudden height change is also found at the interface of BPE pit covered region and crevice corrosion.

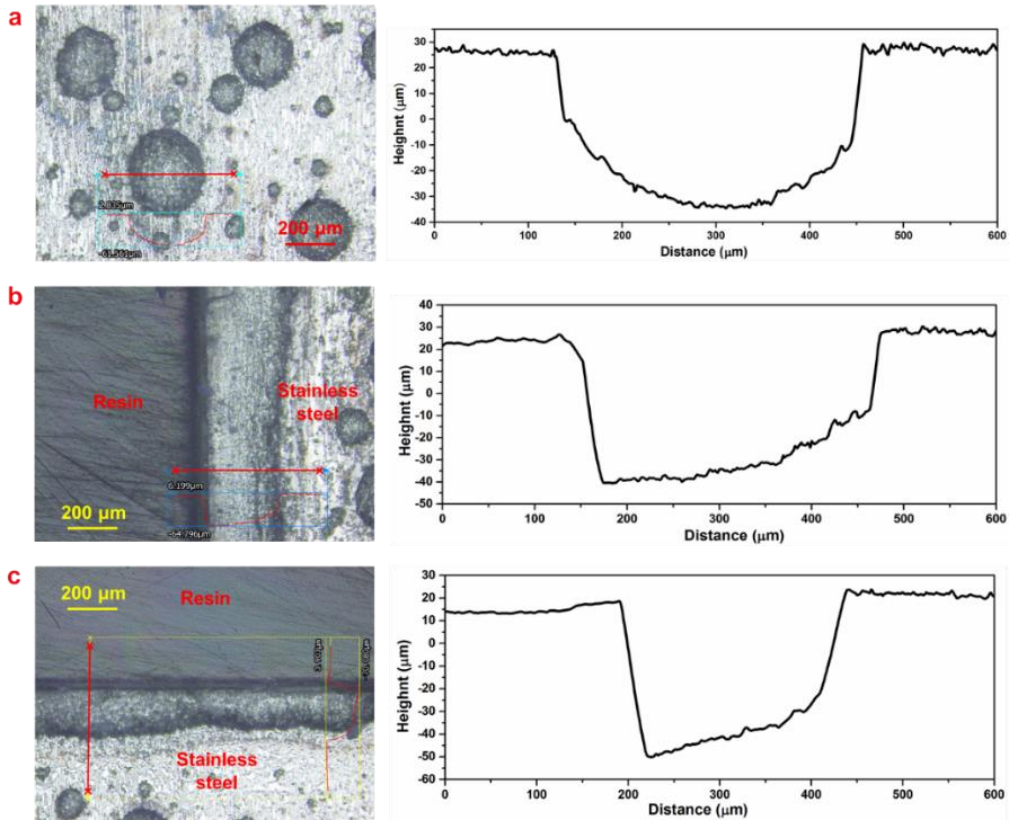

Figure 7.3- 5 The surface morphology across the (a) pitting corrosion, (b) crevice corrosion between resin and BPE oxidation edge and (c) crevice corrosion between resin and BPE side after exposure 900s.

Here, the deepest crevice depth is not related to the local applied potential, as the deepest crevice depth in Figure 7.3- 5 (b) and (c) was the same. However, the applied potential changes the width of crevice mouth, more openness cervices are generated at higher applied potential, the crevice mouth is about 400 µm at the BPE oxidation edge, but the crevice mouth only ≈250 µm was nucleated at the BPE sides.

Figure 7.3- 6 (a) shows the crevice corrosion at the interface between the resin and BPE oxidation edge. The top part is the resin and the bottom part is the BPE pit covered region. The surface appearance in the crevice corrosion close to the resin is not the same as next to the pit region. Figure 7.3- 6 (b) gives

the surface morphology of the crevice corrosion close to the resin; austenite and ferrite have similar height; corrosion shows general corrosion not selective phase corrosion as the more aggressive electrolyte. Large crevice depth and cup-like geometry (one side of the crevice is the resin, suffer no corrosion) can maintain the aggressive electrolyte. Figure 7.3- 6 (c) shows the crevice corrosion near the pit covered region. A yellow line is marked to distinguish crevice corrosion bottom and crevice wall; the upper part is the crevice bottom and the lower part is the crevice wall. Both sides show the selective phase corrosion. Austenite and ferrite with different height are seen, indicates the selective phase corrosion. Figure 7.3- 6 (d) shows the crevice corrosion in the middle part of the crevice at the BPE oxidation edge, shows different grains with outlined interphase boundaries between ferrite and austenite. Here, the corrosion becomes selective grain boundary corrosion.

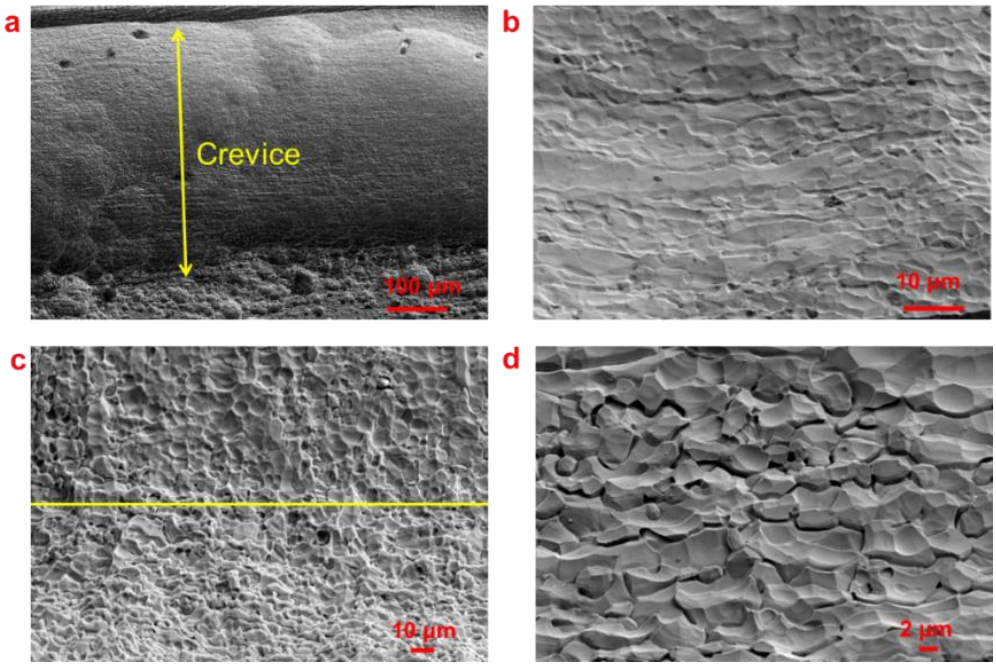

Figure 7.3- 6 (a) The crevice corrosion between the resin and the BPE oxidation edge. (b) the crevice corrosion near the resin. (c) crevice corrosion near the BPE pitting region, (d) crevice corrosion in the middle of the crevice.

Different surface morphology inside of the crevice is measured, from general corrosion, selective grain boundary corrosion, and selective phase corrosion. The corrosion evolution is related to the local electrolyte (different Cl^- concentration and pH) and applied potential.

Figure 7.3- 7 (a) gives shows the BPE pit covered region. Some small nucleation sites are present at the interface between the ferrite and the austenite, with corrosion typically grow into the ferrite phase. Some relative voids nucleated inside of the ferrite phase are the repassivated pits. Figure 7.3- 7 (b) displays a small pit with and the surrounding area shows grains with higher height. The pits stay inside of the ferrite phase. Inside of the pit, grains are clearly seen, from the selective phase corrosion. Figure 7.3- 7 (c) gives a lacy covered pit, with the ferrite phase corrodes away and the remains the austenite phase become the lacy cover, some part of the lacy cover collapse into the pit after the surrounding ferrite phase is removed. Figure 7.3- 7 (d) gives the surface morphology at the pit bottom, some grains stand in front of the matrix with the grain boundary are clearly seen. The corrosion response is the combination of selective phase corrosion and selective grain boundary corrosion.

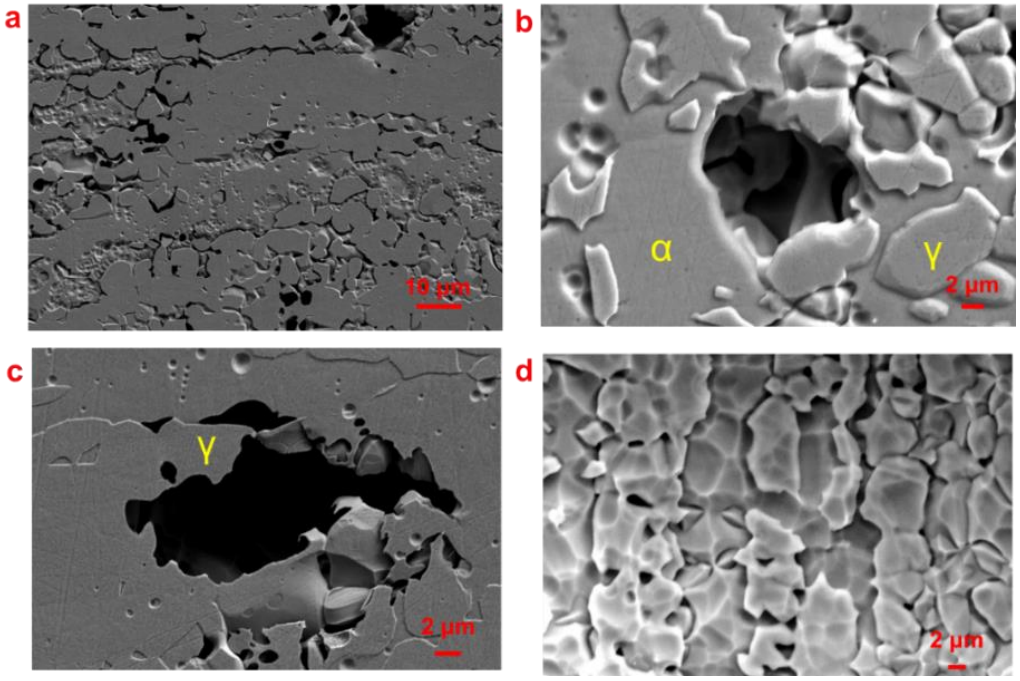

Figure 7.3- 7 (a) Overview of pit covered region, typical pit nucleation sites in (a) and (b) after exposure 900s. and (d) SEM image inside of pit.

No pits are measured in the austenite. The pits nucleated at the interface between austenite and ferrite have the potential to be stable growth, but pit nucleated inside of ferrite will be repassivate, and the pit nucleated inside of ferrite is related to the Cr_2N [11,37]. Pit mouth propagation direction follows

the shape of the ferrite phase [19], same as localised corrosion propagation in the depth direction, proofed the selective phase corrosion inside of pitting and crevice corrosion.

Localised corrosion growth kinetics

Figure 7.3- 8 (a) shows the pit percentage with different depths on the BPE exposed from 150s to 900s. Pit depth between 10 μm and 20 μm is over 20% at all the time. For exposure at 150s, about 90% of pits have the depth < 20 μm. At 300s, over 60% pits with depth from 20 μm to 30 μm. At 450s, about 55% pits contain the depth between 30 μm and 40 μm. At 600s and 750s, < 40% pits have the depth from 40 μm to 50 μm. At 900s, most pits (≈ 30%) have a depth over 50 μm. Figure 7.3- 8 (b) displays the percentage of the stable pit (depth > 20 μm) on the BPE at 900s. BPE was divided into four equal-sized regions, with each region spanning a size of 1 x 10 mm (L x W). Region 1 represents the highest potential close to the oxidation edge, with region 4 representing lower applied potentials, 3 to 4 mm away from the oxidation edge. In Region 1, over 50% pits are found are the stable pits after 750s. In Region 2 and Region 3, the percentage of stable pits in Region 3 is higher before 750s, then becomes similar after 750s. In Region 4, the percentage of the stable pit is lower than Region 2 before 600s, but after it, the pit percentage is largest in all regions.

Figure 7.3- 8 (c) gives the pit growth factor on the BPE from 150s to 900s. If we now assume that pit growth kinetics follows $d = Kt^n$, with (d) pit depth (μm), (t) time (s), and (K), (n) experimental constants [38,39], the maximum pit depth is determined by averaging the deepest ten pits in each region, with the error bar means the standard deviation. It was found the pit growth kinetics was independent of the applied potential on the DSS 2205 [19]. Here, the pit growth factor is stable before 450s but slight increases after 450s. Figure 7.3- 8 (d) gives pit growth kinetics on the BPE at 150s and 900s. The pit growth factor is independent of the applied potential. However, the pit growth factor at 900s is higher than 150s.

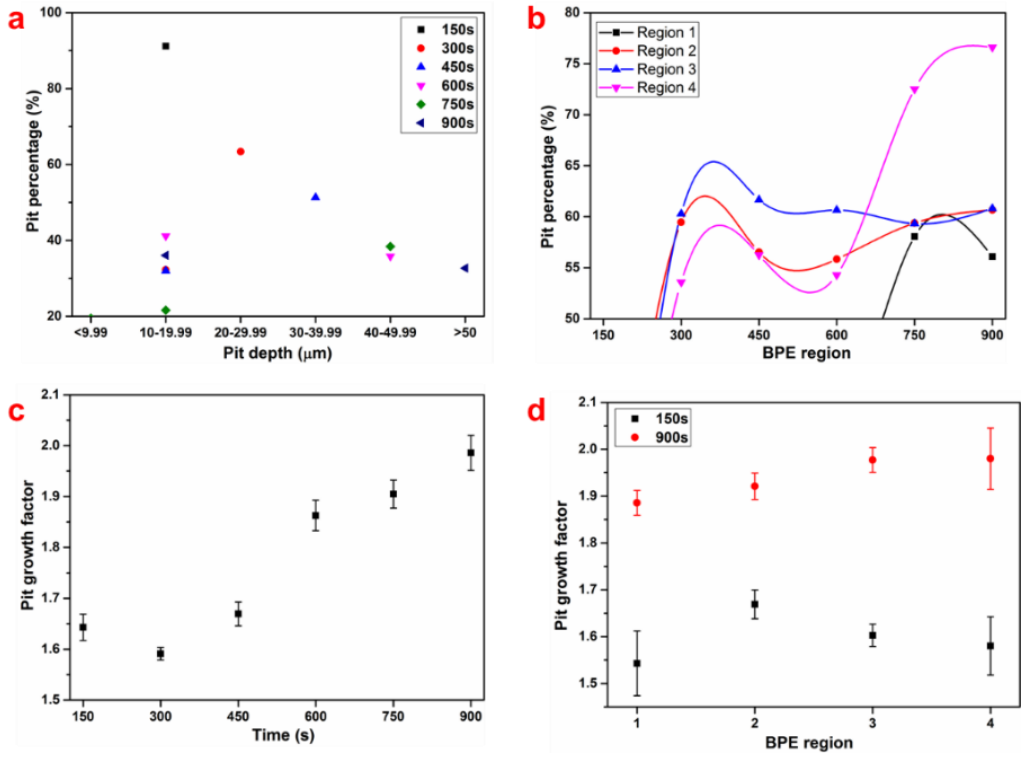

Figure 7.3- 8 (a) The percentage of pits with different depth and exposure time, (b) pit percentage (> 20 μm) at different BPE region at 900s. (c) Pit growth kinetics at different exposure time and (d) the pit growth factor at 150s and 900s along BPE.

Over 20% pits with the depth between 10 μm and 20 μm are found in all the time, which is the critical pit depth for metastable pit transfer to stable pits. The stable pit is growing result in the deeper pits, but the pit percentage of the corresponding large pit is reduced, caused by new pit nucleation and previous pit repassivate. In Region 1, the stable pits percentage < 50%, as a large number of pits are nucleated, result in a lower probability of stable growth. After at 750s, the stable pit percentage is increased, as fewer pit numbers from pits merge. The stable pit percentage in Region 3 is higher before 750s, but pits merge in Region 2 increases the stable pit percentage after 750s. In Region 4, the percentage of stable pits dramatically increased after 600s, as less new pit nucleated. Pit growth factor increased at 450s is caused by the "champion pits", on the expense of stifling most surrounding, typically less stable pits [40,41]. Stifled pits will not consume anodic current further promoting the stability of champion pits, so the champion pit grows faster. At 900s, the pit growth factor is similar from region 1 to region 4, but large pit merge exists in Region 1 and Region 2, as the champion pits disappeared

after pits merge. After pits merge together, the pit electrolyte and effective potential changes, result in lower pit growth factor.

Figure 7.3- 9 (a) gives the pit volume on different BPE regions and exposed time. The pit volume is increasing with time. The pit volume increase rate is similar between Region 1 and Region 4. Pit volume in Region 2 is higher than Region 3, but the pit volume increase rate in Region 2 is faster. Figure 7.3- 9 (b) gives the crevice volume on different BPE regions. The crevice volume is the sum of the crevice volume at the BPE oxidation edge and the sides. The crevice volume in Region 1 is much larger than other regions, as the crevice at the BPE oxidation edge and the resin. The crevice volume increase rate is similar in all BPE regions. Figure 7.3- 9 (c) gives the percentage of pit volume over the localised corrosion volume, which is the sum of pitting and crevice corrosion volume. All BPE regions show the pit volume percentage is increasing with time. Pit volume increase rate in Region 1 and Region 2 is relatively slow, and Region 3 and Region 4 have a similar pit volume increase rate. Figure 7.3- 9 (d) shows the relationship between localised corrosion and exposure time. The pit volume increase rate (from 0.02 mm^3 to 0.19 mm^3) is higher than the crevice corrosion (from 0.08 to 0.31 mm^3), indicates faster pit volume expansion.

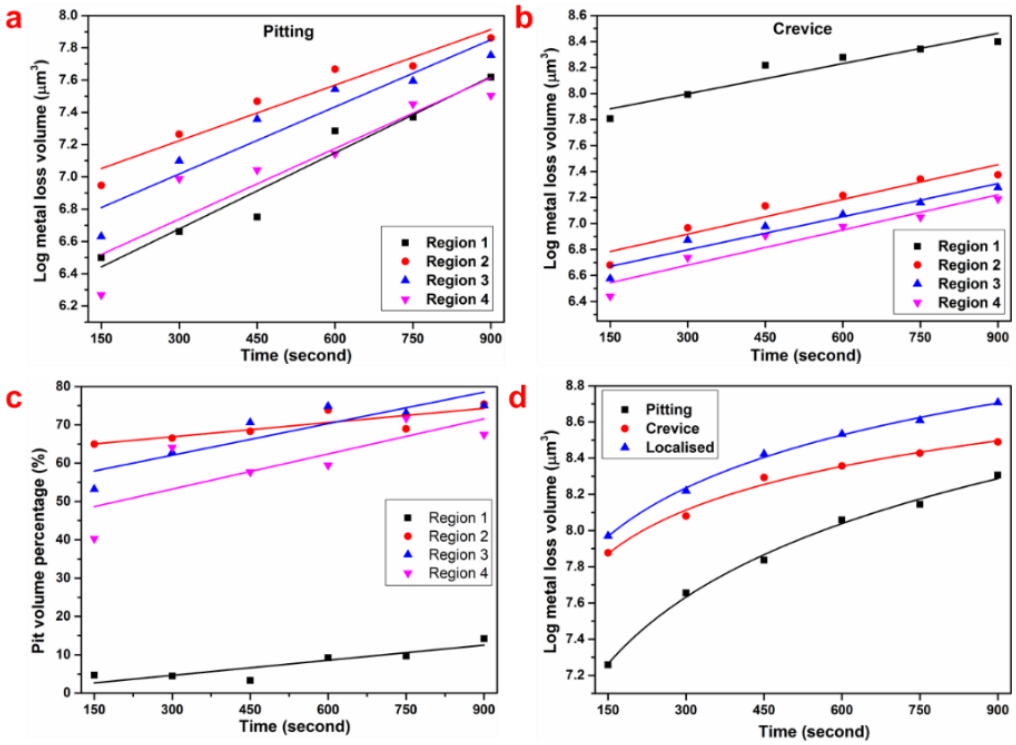

Figure 7.3- 9 (a) Pitting and (b) crevice corrosion volume change with time on different BPE regions, (c) the percentage of pit volume change with time along BPE, and (d) the overall corrosion volume change with time.

The pit volume is similar in Region 1 and Region 4, caused by the crevice corrosion. Here, in Region 1, the higher applied potential results in lower pit volumes, since most of the available current was consumed by the large crevice at the oxidation edge [19]. Pit volume increase rate in Region 3 is faster than Region 2, related to the effective cathodic area surrounded the pit. The cathode area surrounds the pit is less in Region 2 as larger overall pitting corrosion area, resulting in the less cathodic current. Hence the pit volume expansion rate is retarded [42,43]. The crevice volume increase rate is similar in all BPE regions, as the location for cervices corrosion is limited, only exist between the BPE and the resin. Pit volume percentage increase rate in Region 1 and Region 2 is slower, as the competition between the crevice corrosion. But the pit volume percentage increases with time, as the large pit nucleation area.

Figure 7.3- 10 (a) gives the maximum depth of the pitting and crevice corrosion from 150s to 900s. Interesting, the depth of corrosion linearly increases with time. The depth of crevice corrosion is larger than the pitting corrosion and the depth difference between pitting and crevice corrosion is increasing with time. Figure 7.3- 10 (b) gives pitting and crevice corrosion covered length change from150s to 900s, the pit and crevice covered length are shown in Figure 7.3-4. The pit covered length increases from 4.5 to 4.8 mm and the crevice covered length increases from 5.4 to 5.9 mm.

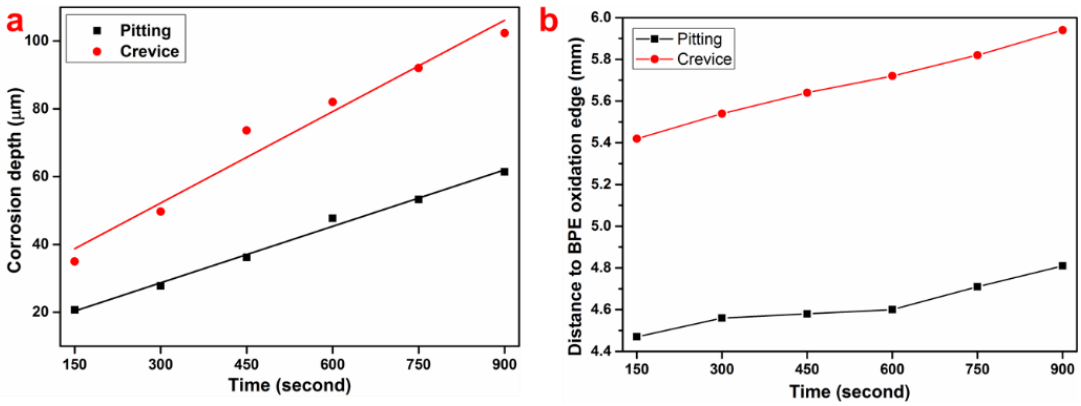

Figure 7.3- 10 (a) The maximum pit and crevice depth change with time and (b) the pit and crevice covered length change with time.

The corrosion depth is linear with time, do not follow the pit growth equation; it might be caused by the corrosion competition or limited experiment time. The pit depth might come from the champion pit with pit growth kinetics accelerated by the surrounding pits. For the crevice corrosion, competition between the crevice corrosion and pitting corrosion influence the crevice growth kinetics. Another reason is the short experiment time, so the corrosion kinetics is linear with time in this time range. The critical pitting and crevice corrosion potential are reduced with a longer time. From the point defect model, the pit nucleation is time-dependent, so longer exposure time can nucleate pit at a lower applied potential [44]. The cumulative electric charge (Q_C) explains the critical corrosion potential is time dependent, indicates lower pitting potential with longer exposure time [45,46].

General corrosion

Figure 7.3- 11 (a) shows the general corrosion region at 900s, phases with different height are clearly seen. 3 different regions on the BPE are analysed by the EDX; one is in the pitting corrosion, the second one is at the interface between the pitting and general corrosion, and the last region is the general corrosion. The EDX results show the ferrite is the preferred corrode phase and austenite is the retains phase in all regions. Figure 7.3- 11 (b) gives the height difference between the ferrite and austenite phase in the general corrosion region from 150s to 900s. The value of height at each phase is the average height of the phase with standard deviation. The measured location is next to the BPE centre, which suffers the most serious corrosion. The height of each phase is the average height with the standard deviation. The height difference between ferrite and austenite is linearly increasing with longer exposure time. At 150s, no height difference between the ferrite and austenite. At 300s, the height difference is 0.02 μm. At 450s, the height difference increases to 0.05 μm. At 600s, the austenite phase is 0.06 μm higher than ferrite. After 750s, the height difference increases to 0.08 μm and then becomes 0.10 μm at 900s. Figure 7.3- 11 (c) gives the surface roughness between the ferrite and

austenite phases in the general corrosion region near to the BPE centre. A line analysis across the austenite and ferrite phase is used to determine the height difference. Higher austenite phase indicates less corrosion, and the height difference between the two phases increases with exposure time. The surface roughness of each phase is not smooth, and is observed by attenuating roughness. The smoothest surface seems to appear at the ferrite and austenite interface. Both pitting and general corrosion nucleated at the interface between the ferrite and austenite, the point where the passive film is most susceptible.

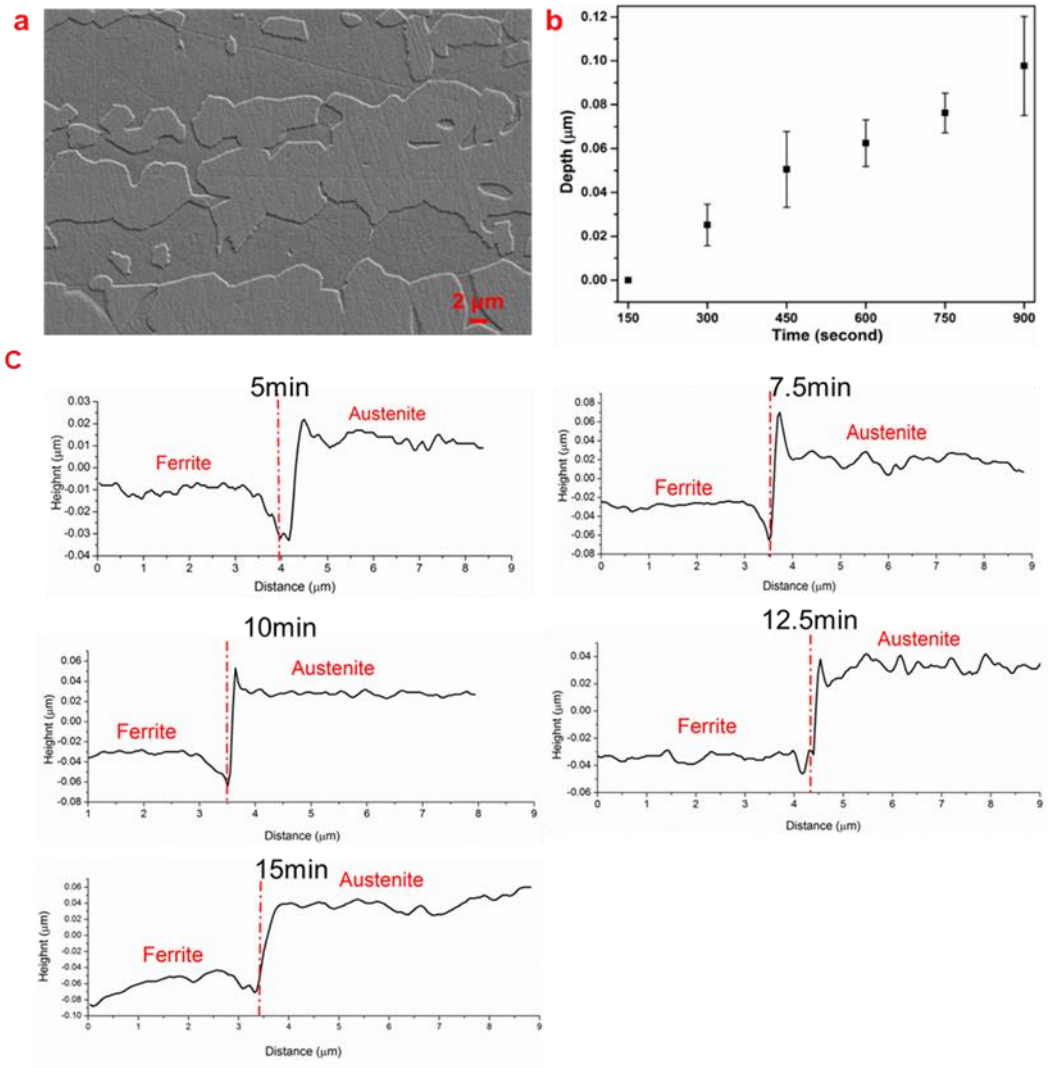

Figure 7.3- 11 (a) SEM image of the optical image on the BPE after 900s and (b) the height different between ferrite and austenite in the general corrosion with different time.

7.36 Conclusions

- Bipolar electrochemistry produces crevice corrosion, pitting corrosion and general corrosion in one DSS 2205 BPE at room temperature.
- Ferrite enriched in Cr and Mo prefers to corrode away and austenite with a higher concentration of Ni retains.
- The shape of the ferrite phase influences the metastable pit shape and pit growth direction.
- Selective phase corrosion, selective grain boundary corrosion, and uniform corrosion are found inside of crevice corrosion.
- The applied potential affects the overall localised corrosion volume, but pit growth kinetics is independent of the potential.
- The critical localised potential is reduced with longer exposure time.
- The height difference between ferrite and austenite is linearly increased with time.

7.37 References

[1] A. Eden, K. Scida, N. Arroyo-Currás, J.C.T. Eijkel, C.D. Meinhart, S. Pennathur, Discharging behavior of confined bipolar electrodes: Coupled electrokinetic and electrochemical dynamics, Electrochim. Acta. 330 (2020). https://doi.org/10.1016/j.electacta.2019.135275.

[2] A. Eden, K. Scida, N. Arroyo-Currás, J.C.T. Eijkel, C.D. Meinhart, S. Pennathur, Modeling Faradaic Reactions and Electrokinetic Phenomena at a Nanochannel-Confined Bipolar Electrode, J. Phys. Chem. C. 123 (2019) 5353–5364. https://doi.org/10.1021/acs.jpcc.8b10473.

[3] A. Kuhn, R.M. Crooks, S. Inagi, A Compelling Case for Bipolar Electrochemistry, ChemElectroChem. 3 (2016) 351–352. https://doi.org/10.1002/celc.201500569.

[4] L. Koefoed, S.U. Pedersen, K. Daasbjerg, Bipolar electrochemistry—A wireless approach for electrode reactions, Curr. Opin. Electrochem. 2 (2017) 13–17. https://doi.org/10.1016/j.coelec.2017.02.001.

[5] G. Loget, A. Kuhn, Shaping and exploring the micro- and nanoworld using bipolar electrochemistry, Anal. Bioanal. Chem. 400 (2011) 1691–1704. https://doi.org/10.1007/s00216-011-4862-1.

[6] S. Munktell, M. Tydén, J. Högström, L. Nyholm, F. Björefors, Bipolar electrochemistry for high-throughput corrosion screening, Electrochem. Commun. 34 (2013) 274–277. https://doi.org/10.1016/j.elecom.2013.07.011.

[7] S. Munktell, L. Nyholm, F. Björefors, Towards high throughput corrosion screening using arrays of bipolar electrodes, J. Electroanal. Chem. 747 (2015) 77–82. https://doi.org/10.1016/j.jelechem.2015.04.008.

[8] N. Pébère, V. Vivier, Local Electrochemical Measurements in Bipolar Experiments for Corrosion Studies, ChemElectroChem. 3 (2016) 415–421. https://doi.org/10.1002/celc.201500375.

[9] Y. Zhou, D.L. Engelberg, Application of a modified bi-polar electrochemistry approach to determine pitting corrosion characteristics, Electrochem. Commun. 93 (2018) 158–161. https://doi.org/10.1016/j.elecom.2018.06.013.

[10] R. Gunn, Developments, grades and specifications, in: Duplex Stainl. Steels Microstruct. Prop. Appl., Woodhead Publishing, 1997: p. 3.

[11] H. Tan, Z. Wang, Y. Jiang, D. Han, J. Hong, L. Chen, L. Jiang, J. Li, Annealing temperature effect on the pitting corrosion resistance of plasma arc welded joints of duplex stainless steel UNS S32304 in 1.0M NaCl, Corros. Sci. 53 (2011) 2191–2200. https://doi.org/10.1016/j.corsci.2011.02.041.

[12] J. Nilsson, Overview Super duplex stainless steels, Mater. Sci. Technol. 8 (1992) 685–700. https://doi.org/10.1179/mst.1992.8.8.685.

[13] S. Kim, S. Kim, I. Lee, Y. Park, M. Shin, Y. Kim, Effects of shielding gases on the microstructure and localized corrosion of tube-to-tube sheet welds of super austenitic stainless steel for seawater cooled condenser, Corros. Sci. 53 (2011) 2611–2618. https://doi.org/10.1016/j.corsci.2011.04.021.

[14] N. Ebrahimi, M. Momeni, A. Kosari, M. Zakeri, M.H. Moayed, A comparative study of critical pitting temperature (CPT) of stainless steels by electrochemical impedance spectroscopy (EIS), potentiodynamic and potentiostatic techniques, Corros. Sci. 59 (2012) 96–102. https://doi.org/10.1016/j.corsci.2012.02.026.

[15] N. Ebrahimi, M.H. Moayed, A. Davoodi, Critical pitting temperature dependence of 2205 duplex stainless steel on dichromate ion concentration in chloride medium, Corros. Sci. 53 (2011) 1278–1287. https://doi.org/10.1016/j.corsci.2010.12.019.

[16] M. Adeli, M.A. Golozar, K. Raeissi, Pitting corrosion of SAF2205 duplex stainless steel in acetic acid containing bromide and chloride, Chem. Eng. Commun. 197 (2010) 1404–1416. https://doi.org/10.1080/00986441003626151.

[17] C. Örnek, X. Zhong, D.L. Engelberg, Low-Temperature Environmentally Assisted Cracking of Grade 2205 Duplex Stainless Steel Beneath a MgCl 2 :FeCl 3 Salt Droplet, Corrosion. 72 (2016) 384–399. https://doi.org/10.5006/1888.

[18] Y. Kim, S. Kim, H. Kim, C. Park, Y. Choi, C. Park, Effects of the precipitation of secondary phases on the erosion-corrosion of 25 % Cr duplex stainless steel, Corros. Sci. 152 (2019) 202–210. https://doi.org/10.1016/j.corsci.2019.03.006.

[19] Y. Zhou, D.L. Engelberg, Fast testing of ambient temperature pitting corrosion in type 2205 duplex stainless steel by bipolar electrochemistry experiments, Electrochem. Commun. 117 (2020) 106779. https://doi.org/10.1016/j.elecom.2020.106779.

[20] P. Reccagni, L.H. Guilherme, Q. Lu, M.F. Gittos, D.L. Engelberg, Reduction of austenite-ferrite galvanic activity in the heat-affected zone of a Gleeble-simulated grade 2205 duplex stainless steel weld, Corros. Sci. 161 (2019). https://doi.org/10.1016/j.corsci.2019.108198.

[21] S.E. Lott, The Role of Inclusions on Initiation of Crevice Corrosion of Stainless Steel, J. Electrochem. Soc. 136 (2006) 973. https://doi.org/10.1149/1.2096896.

[22] J.W. Oldfield, W.H. Sutton, Crevice Corrosion of Stainless Steels: II. Experimental studies, Br. Corros. J. 13 (2013) 104–111. https://doi.org/10.1179/000705978798276258.

[23] Q. Hu, G. Zhang, Y. Qiu, X. Guo, The crevice corrosion behaviour of stainless steel in sodium chloride solution, Corros. Sci. 53 (2011) 4065–4072. https://doi.org/10.1016/j.corsci.2011.08.012.

[24] Q. Hu, Y.B. Qiu, X.P. Guo, J.Y. Huang, Crevice corrosion of Q235 carbon steels in a solution of NaHCO3 and NaCl, Corros. Sci. 52 (2010) 1205–1212. https://doi.org/10.1016/j.corsci.2010.01.006.

[25] D. Chen, E.H. Han, X. Wu, Effects of crevice geometry on corrosion behavior of 304 stainless steel during crevice corrosion in high temperature pure water, Corros. Sci. 111 (2016) 518–530. https://doi.org/10.1016/j.corsci.2016.04.049.

[26] G. Karlberg, G. Wranglen, On the mechanism of crevice corrosion of stainless Cr steels, Corros. Sci. 11 (1971) 499–510. https://doi.org/10.1016/S0010-938X(71)80017-3.

[27] M.H. Moayed, N.J. Laycock, R.C. Newman, Dependence of the Critical Pitting Temperature on surface roughness, Corros. Sci. 45 (2003) 1203–1216. https://doi.org/10.1016/S0010-938X(02)00215-9.

[28] W. Tian, S. Li, N. Du, S. Chen, Q. Wu, Effects of applied potential on stable pitting of 304 stainless steel, Corros. Sci. 93 (2015) 242–255. https://doi.org/10.1016/j.corsci.2015.01.034.

[29] N.J. Laycock, Metastable Pitting and the Critical Pitting Temperature, J. Electrochem. Soc. 145 (1998) 2622. https://doi.org/10.1149/1.1838691.

[30] N.J. Laycock, R.C. Newman, Localised dissolution kinetics, salt films and pitting potentials, Corros. Sci. 39 (1997) 1771–1790. https://doi.org/10.1016/S0010-938X(97)00049-8.

[31] B. Krawczyk, P. Cook, J. Hobbs, D. Engelberg, Corrosion Behavior of Cold Rolled Type 316L Stainless Steel in HCl Containing Environments, Corrosion. 73 (2017) 1346. https://doi.org//10.5006/2415.

[32] C. Örnek, F. Léonard, S.A. McDonald, A. Prajapati, P.J. Withers, D.L. Engelberg, Time-dependent in situ measurement of atmospheric corrosion rates of duplex stainless steel wires, Npj Mater. Degrad. 2 (2018) 1–15. https://doi.org/10.1038/s41529-018-0030-9.

[33] A.M. Al-Zahrani, H.W. Pickering, IR voltage switch in delayed crevice corrosion and active peak formation detected using a repassivation-type scan, Electrochim. Acta. 50 (2005) 3420–3435. https://doi.org/10.1016/j.electacta.2004.12.017.

[34] H.W. Pickering, The role of electrode potential distribution in corrosion processes, Mater. Sci. Eng. A. 198 (1995) 213–223. https://doi.org/10.1016/0921-5093(95)80076-7.

[35] G.F. Kennell, R.W. Evitts, K.L. Heppner, A critical crevice solution and IR drop crevice corrosion model, Corros. Sci. 50 (2008) 1716–1725. https://doi.org/10.1016/j.corsci.2008.02.020.

[36] H.W. Pickering, The significance of the local electrode potential within pits, crevices and cracks, Corros. Sci. 29 (1989) 325–341. https://doi.org/10.1016/0010-938X(89)90039-5.

[37] L. Chen, H. Tan, Z. Wang, J. Li, Y. Jiang, Influence of cooling rate on microstructure evolution and pitting corrosion resistance in the simulated heat-affected zone of 2304 duplex stainless steels, Corros. Sci. 58 (2012) 168–174. https://doi.org/10.1016/j.corsci.2012.01.018.

[38] M.K. Cavanaugh, R.G. Buchheit, N. Birbilis, Modeling the environmental dependence of pit growth using neural network approaches, Corros. Sci. 52 (2010) 3070–3077. https://doi.org/10.1016/j.corsci.2010.05.027.

[39] G.S. Frankel, Pitting Corrosion of Metals A Review of the Critical Factors, 145 (1998) 2186–2198.

[40] M.I. Suleiman, R.C. Newman, The use of very weak galvanostatic polarization to study localized corrosion stability in stainless steel, Corros. Sci. 36 (1994) 1657–1665. https://doi.org/10.1016/0010-938X(94)90060-4.

[41] N.J. Laycock, D.P. Krouse, S.C. Hendy, D.E. Williams, Computer Simulation of Pitting Corrosion of Stainless Steels, Interface, Electrochem. Soc. (2014) 65–71. https://doi.org/10.1149/2.F05144IF.

[42] M.T. Woldemedhin, M.E. Shedd, R.G. Kelly, Evaluation of the Maximum Pit Size Model on Stainless Steels under Thin Film Electrolyte Conditions, J. Electrochem. Soc. 161 (2014) E3216–E3224. https://doi.org/10.1149/2.023408jes.

[43] M.T. Woldemedhin, M.E. Shedd, R.G. Kelly, Evaluation of the Maximum Pit Size Model on Stainless Steels under Atmospheric Conditions, J. Electrochem. Soc. 58 (2014) 41–50. https://doi.org/10.1149/2.023408jes.

[44] T. Haruna, D. Macdonald, Theoretcal Prediction of the Scan Rate Dependencies of the Pitting Potential and the Probabilily Distribution in the Induction Time, J. Electrochem. Soc. 144 (1997) 1574–1581.

[45] Y. Yi, P. Cho, A. Al Zaabi, Y. Addad, C. Jang, Potentiodynamic polarization behaviour of AISI type 316 stainless steel in NaCl solution, Corros. Sci. 74 (2013) 92–97. https://doi.org/10.1016/j.corsci.2013.04.028.

[46] X.L. Zhang, Z.H. Jiang, Z.P. Yao, Y. Song, Z.D. Wu, Effects of scan rate on the potentiodynamic polarization curve obtained to determine the Tafel slopes and corrosion current density, Corros. Sci. 51 (2009) 581–587. https://doi.org/10.1016/j.corsci.2008.12.005.

7.4 A new approach to assess the corrosion resistance of solution annealed duplex stainless steel microstructure

Yiqi Zhou[*1], Dirk Lars Engelberg[1,2]

1. Corrosion & Protection Centre, School of Materials, The University of Manchester, M13 9PL, Manchester, UK

2. Materials Performance Centre, The University of Manchester, M13 9PL, Manchester, UK

* Corresponding author: Yiqi.zhou@postgrad.manchester.ac.uk

7.41 Highlights

- Solution annealing heat treatments have been applied to tailor microstructure characteristics of type 2205 duplex stainless steel.

- Standard electrochemical corrosion tests have been compared to novel bipolar electrochemistry assessments.

- The room temperature pitting corrosion resistance of type 2205 was determined, yielding information about pit nucleation sites and pit growth characteristics.

- The as received microstructure had the highest pit nucleation resistance, with high-temperature solution annealing revealing reduced pit growth rates.

- New insights for microstructure design to optimise corrosion resistance are discussed.

7.42 Abstract

The corrosion resistance of solution annealing heat-treated type 2205 duplex stainless steel microstructures was assessed with a bipolar electrochemistry technique. Chemical element partitioning in both crystallographic phases was correlated to simulations of critical pitting temperatures. The as-received microstructure had the highest pit nucleation resistance, with high-temperature solution annealing treatment revealing reduced pit growth rates. Pit nucleation occurred either within the ferrite phase or at ferrite-austenite interfaces, with the resulting pit shape affected by the microstructure characteristics. The results of this study are discussed in the framework of microstructure design for enhanced corrosion resistance in duplex stainless steels.

Keywords: Bipolar electrochemistry, duplex stainless steel, pitting corrosion, solution annealing

7.43 Introduction

Duplex stainless steels (DSS) are generally chosen for critical applications based on their excellent mechanical properties, superior corrosion resistance compared to most other stainless steels, and their unrivalled crack propagation resistance [1–3]. In the solution annealed microstructure condition, DSS only consist of ferrite (α) and austenite (γ) [4,5]. The ferrite typically provides stiffness and chloride-induced stress corrosion cracking (SCC) resistance, with the austenite contributing ductility and hydrogen embrittlement (HE) resilience.

The occurrence of pitting corrosion in stainless steels is linked to a heterogeneous breakdown of the passive surface film, followed by highly localised metal dissolution via metastable and stable pit growth [6,7]. Most work on pit initiation and growth has been undertaken on austenitic and ferritic stainless steels, with metastable pits showing the presence of characteristic lacy metal covers, which act as diffusion limiting barrier. These barriers then result in the accumulation of increased anion concentrations within pits [8,9]. Transition to stable pit growth typically results via the loss of these lacy covers, with the overall pit depth and morphology then acting as diffusion limiting parameter [10,11]. The shape and topography of pits is therefore an important factor in determining growth characteristics and associated kinetic behaviour.

In DSS, the localised corrosion resistance is more complex as different elements partition to the different crystallographic phases present, with ferrite generally becoming enriched in Cr and Mo, and the austenite in Ni, Mn, and N. The chemical fingerprint of each phase facilitates the corrosion characteristics, with the pitting corrosion behaviour typically limited by the weaker ferrite phase [12,13]. Changes in the ferrite-to-austenite volume fraction typically comes with a redistribution of alloying elements within the two phases. The latter redistribution can be achieved, for example, via application of solution annealing heat treatments with the aim to optimise the corrosion resistance and associated mechanical properties without introducing further deleterious phases [14–17].

In contrast, the heat affect zone (HAZ) of DSS 2205 (22%Cr-5%Ni) has also been associated with reduced corrosion resistance, based on adversely distributed alloying elements in both the ferrite and austenite phase [18]. For DSS 2205 and Super DSS 2507 (25%Cr-7%Ni), the highest critical pitting temperature (CPT) is achieved when both the ferrite and austenite have the same pitting resistance equivalent number (PREN). From ASTM G48 Method E, the CPT (°C) is calculated by CPT = 2.5 × %Cr + 7.6 × %Mo + 31.9 × %N – 41, with the PREN assessed via PREN = %Cr + 3.3 × %Mo+ 30 × %N [19]. These equations point towards a key influence of three main alloying elements (Cr, Mo and N), positively affecting pitting corrosion resistance. However, for lean DSS 2101 (21%Cr-1%Ni), an optimized PREN between ferrite and austenite cannot be achieved by heat treatments [20]. Lower temperature annealing treatment might precipitate other phases, such as sigma phase, chi phase, and chromium nitride, which all reduce the corrosion resistance [21–23].

Bipolar electrochemistry provides access to the full spectrum of anodic-to-cathodic electrochemical reactions in a single experiment [24]. The non-contact setup provides a rapid experimental outcome, with this method typically used for corrosion screening of stainless steels [25–28]. In the work reported here, the microstructure evolution of DSS 2205 with solution annealing treatments of up to 1350 °C was characterised, with bipolar electrochemistry applied to assess and compare the pitting corrosion resistance of all microstructure at room temperature. The results are discussed in the framework of pit nucleation and propagation to design enhanced DSS microstructures.

7.44 Materials and Methods

DSS 2205 with a chemical composition (wt %) of 22.4 Cr, 0.016 C, 0.4 Si, 5.8 Ni, 1.5 Mn, 3.2 Mo, 0.18 N, and Fe (bal.) was used in this study. The as received (AR) material was in the solution annealed condition with a PREN value of 38.4 and an estimated CPT using ASTM G48 of 45 °C. Heat treatments were performed at 1000 °C, 1150 °C, 1250 °C, 1300 °C, and 1350 °C in a CWF chamber furnace. The samples were held for 1 hour at the set temperature, followed by rapid cooling in water.

For bipolar electrochemistry testing, all bipolar electrodes (BPEs) had a dimension of 30 x 10 x 1.2 mm^3 (length x width x thickness). Samples were mounted in Araldite resin and then prepared by grinding up to 1200 grit, and polished to 1 μm diamond paste finish. For the 3-electrode potentio-dynamic polarization test, the samples were also finished to 1 μm diamond paste. For EBSD analysis, the samples were further polished to 0.25 μm diamond paste, followed by an OPS Colloidal Silica fine polish.

Figure 7.4- 1 (a) shows the setup of bipolar electrochemistry. A Keysight E36105A was used for power supply. A constant current (1 A) was applied between the feeder electrodes with at a distance of 60 mm, and the BPE was centred between the feeder electrodes. Each Pt feeder electrode had a surface area of 4 cm^2. All experiments run for 900 seconds in 200 ml of 0.1M HCl. To measure the acting potential along the BPE, a copper-wire was spot welded to the rear of the BPE, and a Luggin capillary connected to a saturated calomel electrode (SCE) set ≈ 1mm above the BPE surface. To measure local potential changes on the BPE, the open circuit potential (OCP) was first recorded and the power supply of the bipolar system then switched on. The reported potential on the y-axis was the difference of measured potential with applied bipolar electrochemistry vs. OCP. Potentials were measured along the BPE surface in increments of 5 mm, with the Luggin capillary following the centreline of the sample. Figure 7.4- 1 (b) shows the potential distribution along the BPE, with the recorded potential at each point showing the average potential over the first 600 seconds of exposure. The potential distribution is quasi-linear along the centre of the BPE, with the potential at both edges indicating slightly increased potential responses; i.e. more positive at the oxidation edge, and more negative at the reduction edge. The superimposed trend line shows a linear approximation of all points, with the measured potentials at the BPE edges (0 mm and 30 mm) off-set with respect to the line.

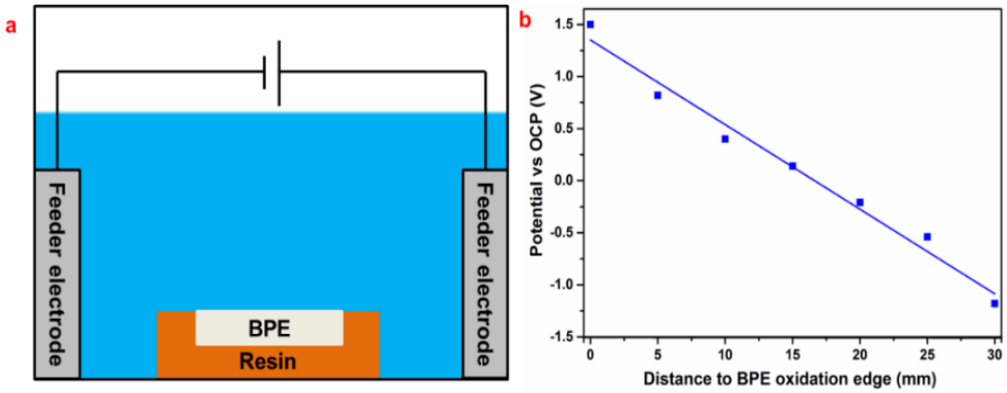

Figure 7.4- 1 (a) Schematic setup of the bipolar electrochemistry experiment, and (b) measured potential distribution along the BPE (potential change vs OCP).

For 3-electrode potentio-dynamic polarisation, all samples were tested in an AVESTA cell at room temperature in 0.1M HCl. A Pt counter electrode and SCE reference electrode were used, in combination with an IVIUM-Compactstat and IVIUMsoft software to measure potentio-dynamic polarisation curves. The OCP was measured for 600 seconds, followed by potentio-dynamic polarisation tests from -200 mVOCP to +1200 mVOCP using a scan rate of 1 mV/s.

After the experiment, the samples were removed from the electrolyte, cleaned with soap water, and dried in hot air. A Keyence VK-200K laser confocal microscope was used to measure the corrosion topography. The measured regions had a width of 4 mm, with the overall length depending on the pit covered length on the BPE. SEM imaging and EDX analysis was carried out in a Zeiss Sigma VP FEG-SEM at 20 kV, using Aztec software for analysis. Electron Backscatter Diffraction (EBSD) was carried out in a Sirion FEG-SEM and Zeiss Sigma VP FEG-SEM at 20 kV, with a step size of 0.14 µm and 3.8 µm, respectively. The small step size was employed over typical areas of 125.5 x 93.2 µm2, to inform about the presence of other crystallographic phases, with the large step size applied to characterise the size and distribution of ferrite vs. austenite.

7.45 Results and Discussion

Microstructure Characterisation

The microstructures of the wrought as received and all solution annealing heat-treated samples are summarised in Figure 7.4- 2. The microstructures only contained ferrite and austenite, with no other visible precipitates or tertiary phases present. The microstructures were also inspected for the potential presence of quench-in chromium nitrides (CrN), which can form during rapid cooling. No signs of quench-in CrN were found.

In the AR specimen and the sample annealed at 1000 ^{o}C, the austenite phase is evenly distributed in the form of elongated islands within the ferritic matrix. Both microstructures had along the rolling direction elongated ferrite- and austenite-containing regions, showing typical ribbon-like morphologies of wrought DSS microstructure. The island-shaped austenite grains grow larger, whereas ferrite grains become wider gradually as the annealing temperature increases up to 1250 ^{o}C. For specimens annealed at temperature in excess of 1250 ^{o}C, the microstructure developed a different morphology. As the microstructure transforms into ferrite at such temperature, the austenitic phase dissolves and reforms through a solid-state phase transformation during the cooling process. High temperature heat treatments then produce ferritic grains, surrounded by reformed secondary austenite. The cooling rate then affects the overall composition of both phases, with further cooling then also resulting in intragranular or plate-like Widmansstaetten austenite needles. Grain boundary austenite is present in Figure 7.4- 2 (e,f), with Widmanstaetten austenite found after the 1350 ^{o}C annealing treatment in Figure 7.4- 2 (f).

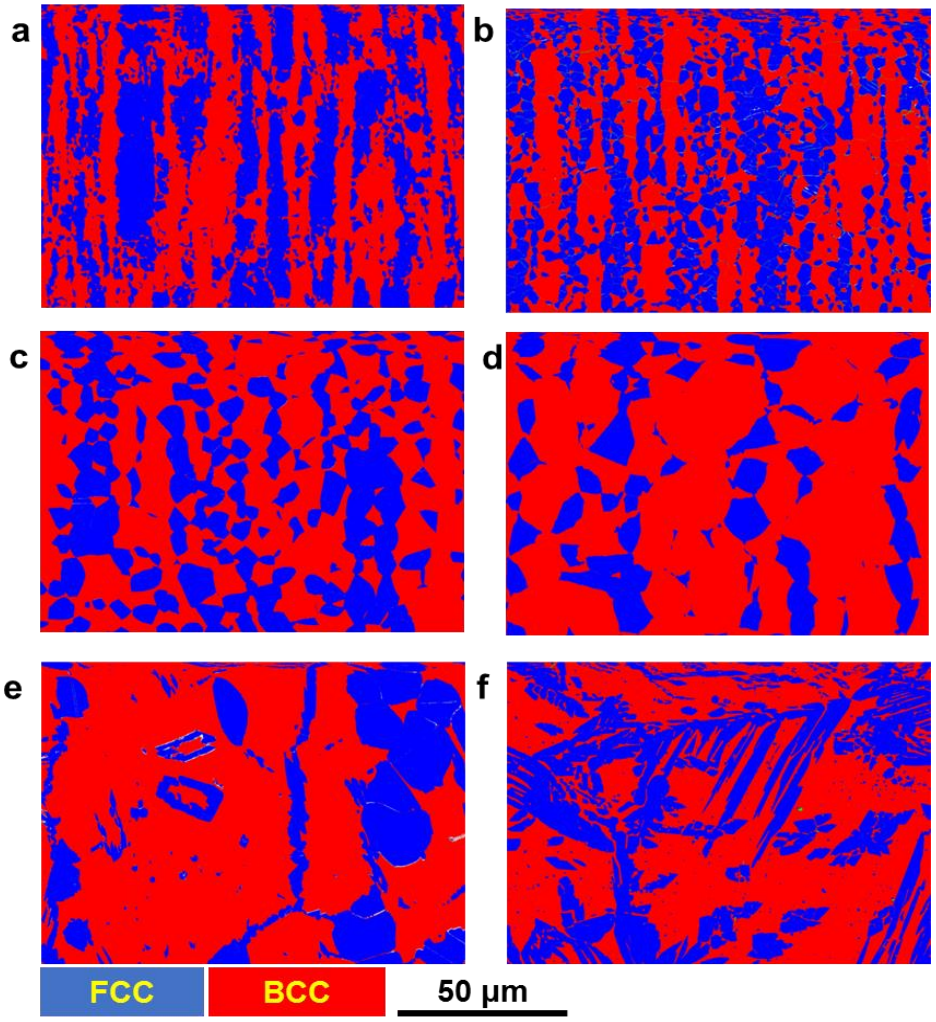

Figure 7.4- 2 The EBSD of DSS 2205 with different heat treatment temperature, from (a) AR, (b) 1000 ºC, (c) 1150 ºC, (d) 1250 ºC, (e) 1300 ºC, to (f) 1350 ºC, with the latter showing Widmannstaetten austenite needles

The diameter of the austenite and ferrite phase regions at different temperatures is shown in Figure 7.4- 3 (a). Both phase diameters become larger at higher annealing temperature, with the austenite-to-ferrite transformation resulting in significant differences in grain diameters. For specimen heat treated below 1250 ºC, the grain size in both ferrite and austenite phase are monotonically increasing with increasing temperature, due to the balanced distribution of both phases. However, for specimen heat treated over 1300 ºC, the ferrite size is significantly increased, due to the high temperature transformation of austenite into δ-ferrite. Longer heat treatment at these temperatures can intermittently produce fully ferritic microstructures [29]. The resulting grain size has been reported to influence the overall

corrosion behaviour, with for example, DSS 2202 (22%Cr-2%Ni) showing higher current densities potentio-static polarisation tests with larger grain sizes [30]. Figure 7.4- 3 (b) summarises the change in ferrite to austenite phase fraction with annealing temperature, supporting all previous observations of the effect of annealing temperature on the phase transformations. For specimens annealed at 1350 ^{o}C, the final ferrite concentration reduces, as more austenite reforms due to far longer diffusion times for elements during the heat treatment and cooling schedule.

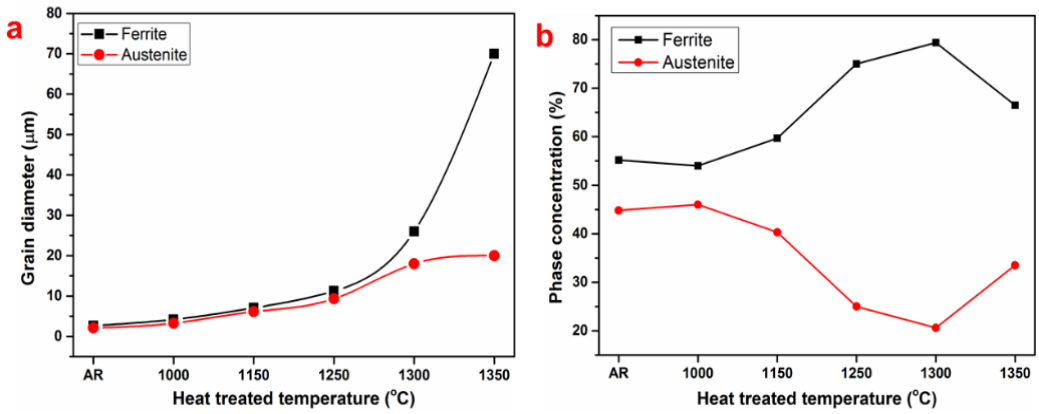

Figure 7.4- 3 (a) Average diameter ferrite and austenite grain size and (b) concentration of ferrite and austenite phase.

Figure 7.4- 4 gives large area EBSD maps of specimen annealed at 1300 ^{o}C and 1350 ^{o}C. The specimen annealed at 1350 ^{o}C produces coarse grained ferrite that favoured the formation of austenite in specific areas. Austenite has three locations and morphologies, (i) a continuous phase at prior-ferrite grain boundaries, (ii) acicular-type Widmanstätten plates growing into ferrite grains, (iii) and discrete intragranular regions. At a relatively high annealing temperatures, the concentration of grain boundary allotriomorphs austenite and the Widmänstten austenite increased significantly. Many of the intragranular austenite grains reveal significant grain growth to assume more spheroidal shapes. It is also observed that the austenite grains do not exhibit any preferred growth direction.

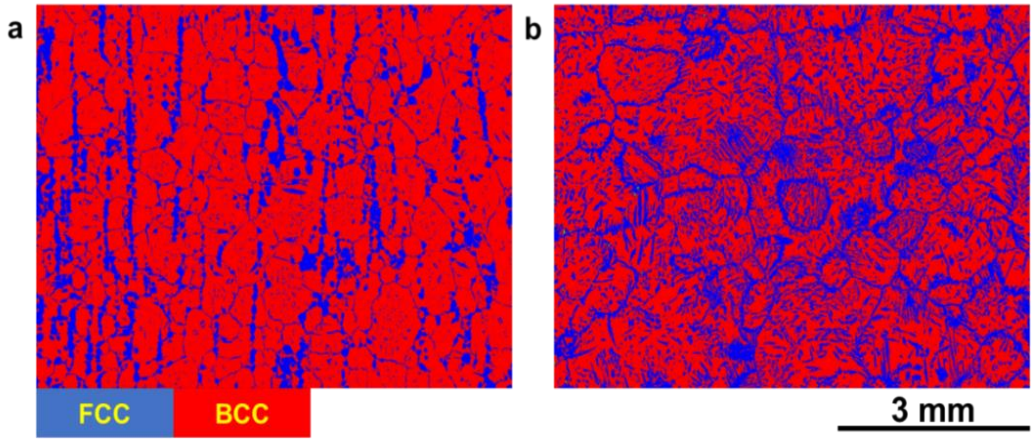

Figure 7.4- 4 The EBSD of DSS 2205 at a low magnification after heat treated at (a) 1300 ºC and (b) 1350 ºC.

Element Partitioning & PREN

The concentrations of the three major alloying elements Cr, Ni, and Mo as a function of annealing temperature are listed in Table 7.4- 1. Ten random EDX measurements at each phase have been obtained and the mean value is calculated with the standard deviation. For specimen annealed below 1250 oC, both Cr and Mo are enriched in the ferrite, whereas Ni is concentrated in the austenite phase. With higher annealing temperatures, the concentration of Cr and Mo in the ferrite phase decreases, with the Ni increasing; at the same time, the concentration of Cr and Mo in the austenite slightly increases. For specimen annealed over 1300 ºC, the three key elements Cr, Ni, and Mo are balanced in both the ferrite and austenite phase. The alloying elements diffuse relatively slowly in the solid state; hence, they cannot partition between ferrite and austenite.

Table 7.4- 1 Alloying elements contents of tested specimens

	Phase	Cr	Ni	Mo
AR	BCC	24.5±0.2	4.7±0.1	4.3±0.1
	FCC	21.8±0.4	7.0±0.2	2.8±0.2
1000 °C	BCC	25.1±0.2	4.1±0.2	4.7±0.2
	FCC	21.6±0.2	7.0±0.2	2.9±0.1
1150 °C	BCC	24.2±0.2	4.8±0.1	4.3±0.1
	FCC	21.7±0.5	7.2±0.1	2.9±0.1
1250 °C	BCC	23.3±0.2	4.7±0.2	4.2±0.3
	FCC	21.6±0.3	6.8±0.3	3.2±0.3
1300 °C	BCC	23.3±0.1	5.6±0.1	4.1±0.1
	FCC	23.1±0.2	6.0±3.0	3.9±0.2
1350 °C	BCC	22.4±0.1	5.8±0.1	4.1±0.1
	FCC	22.1±0.5	6.5±0.2	3.5±0.2

Figure 7.4- 5 plots data from Table 7.4- 1, highlighting differences between ferrite and austenite elemental compositions. The largest difference is present for specimen annealed at 1000 ^{o}C, and then reduces with increasing annealing temperature, reaching a minimum for samples annealed at 1300-1350 ^{o}C, the corrosion behaviour of each phase is related to the chemical composition, which was revealed by scanning kelvin probe force microscopy (SKPFM). The larger the difference of Cr, Mo, and Ni within the two phases, the higher was the observed Volta potential difference between the two phases, resulting in lower corrosion resistance [18]. These observations are also supported by PREN and CPT simulations, with the CPT calculated from ASTM G48 Method E. Table 7.4- 1 provides data to simulation the expected PREN and CPT values for each phase, with the concentration of nitrogen assumed to reach saturateion in the ferrite. The latter is assumed to reach a maximum of 0.05% N, with the rest then partitioned into the austenite phase. Here we do not consider the possibility of nitrogen loss during the annealing treatment [31,32].

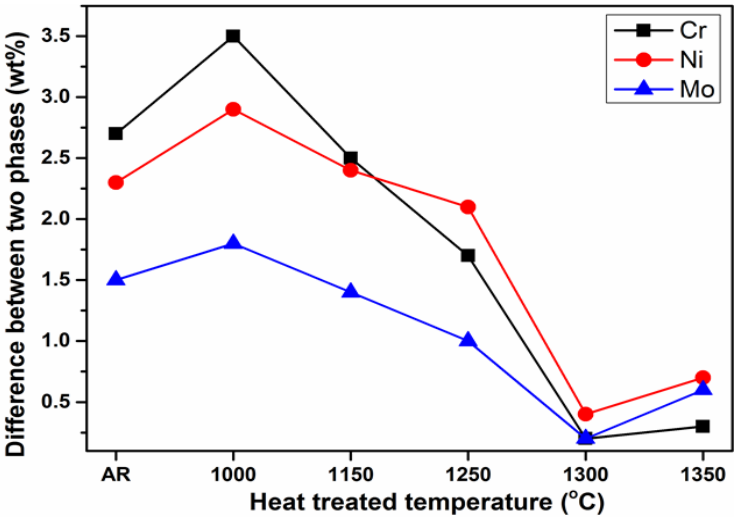

Figure 7.4- 5 The main alloying elements difference between two phases after difference annealed temperatures.

Figure 7.4- 6 shows the CPT and PREN of the ferrite and austenite at different heat treatment temperatures. The austenite phase has typically higher PREN values except for the 1000 ^{o}C annealed sample. Pits are therefore expected to nucleate in the ferrite phase, with the pitting corrosion resistance (the weaker PREN phase) following 1000 ^{o}C > AR > 1150 ^{o}C > 1250 ^{o}C > 1300 ^{o}C > 1350 ^{o}C. Two distinct groups are apparent in Figure 7.4- 6, with all high temperature treatments 1250-1350 ^{o}C having far higher PREN in the ferrite, compared to the lower temperature treatments, but the inverse was observed for the austenite; here the lower temperature treatments had higher PREN values.

In contrast for the CPT simulations, the ferrite phase indicated a higher CPT for heat treatments lower than 1150 ^{o}C, but for heat treatments at 1250 ^{o}C and above, the austenite phase had a higher CPT. The pitting corrosion resistance according to CPT calculations (lower CPT phase) is ranked as follows: 1250 ^{o}C > 1300 ^{o}C> 1350 ^{o}C > 1150 ^{o}C > AR ≈ 1000 ^{o}C. The pitting corrosion resistance rank from CPT and PREN are not the same, due to different weight factors of the Cr, Mo, and N.

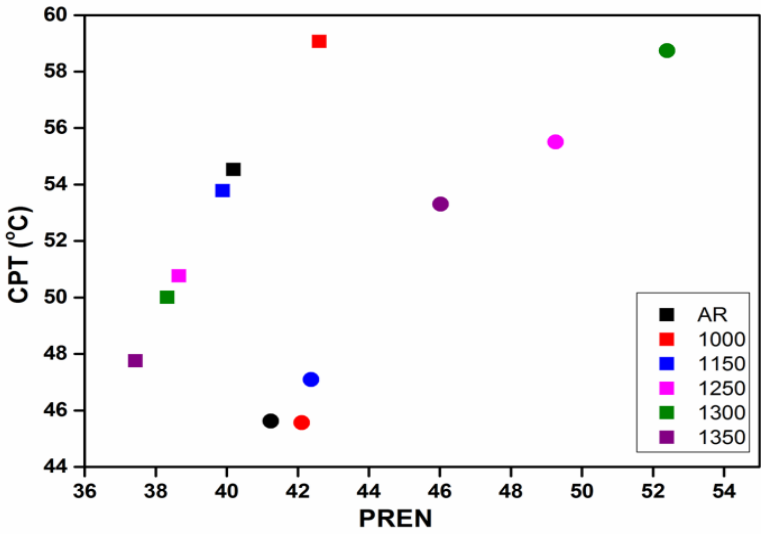

Figure 7.4- 6 Simulated CPT and PREN values for ferrite and austenite after different solution treatments, with the ferrite shown in squares and the austenite with circles.

(CPT = 2.5 × %Cr + 7.6 × %Mo + 31.9 × %N – 41; PREN = %Cr + 3.3 × %Mo+ 30 × %N)

Pitting corrosion test

Figure 7.4- 7 shows the 3-electrode potentio-dynamic polarisation curves at room temperature for the different annealing treatments. The measured OCP values have minor differences, indicating slightly modified passive film properties. The passive current density response is similar in all samples and remained very low. The current density exceed 0.1 mA/cm^2 at around +0.9 V_{SCE}, but no pits were observed in the experiment, in line with literature observation where no pits are expected in DSS 2205 in 0.1M HCl at room temperature [33,34]. The sharp increase in current density at + 0.9 V_{SCE} is caused by the onset of trans-passive corrosion, ultimately leading into oxygen evolution with higher applied potentials [35].

All polarization studies are summarised in Table 7.4- 2, with the lowest OCP found after annealing at 1250 ^oC. The passive region is estimated via the range of anodic potentials where the current density remains below 0.1 mA/cm^2. The passive current density for specimen annealed at 1350 ^oC is slightly higher, which is in line with literature observations [36]. The latter has been attributed to better passive film properties caused by larger grain size sizes [36].

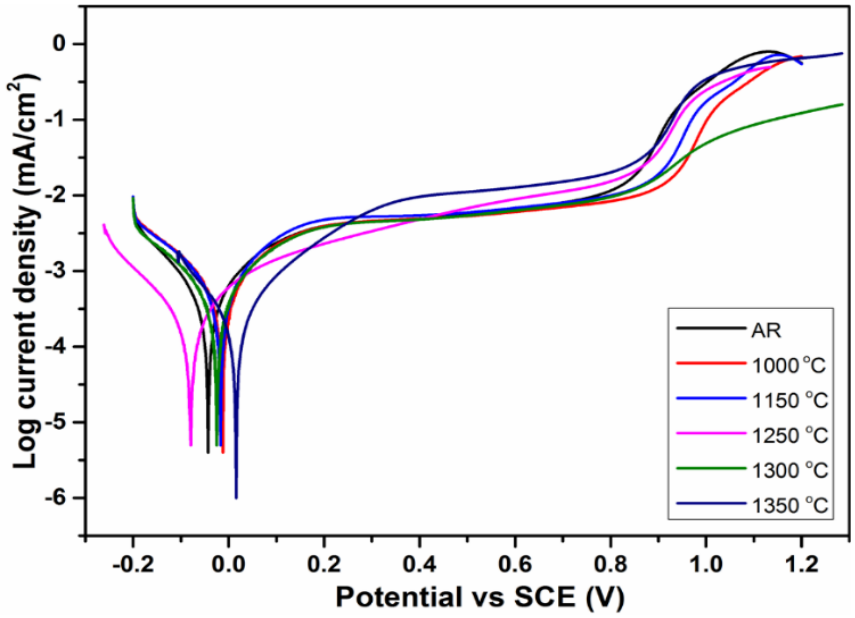

Figure 7.4- 7 The 3-electrode potentio-dynamic polarisation curves for DSS 2205 at room temperature at different annealed temperature.

Table 7.4- 2 OCP, passive region, and passive current density obtained for tested specimens after polarization in 0.1M HCl at room temperature.

	OCP (V_{SCE})	Passive region(V_{SCE})	Passive current density (mA/cm^2)
AR	-0.043	0.926	0.011
1000 °C	-0.012	1.042	0.008
1150 °C	-0.017	0.987	0.010
1250 °C	-0.079	1.021	0.012
1300 °C	-0.025	1.436	0.010
1350 °C	0.016	1.268	0.044

Bipolar electrochemistry was applied to reveal the localised corrosion resistance of DSS 2205 at room temperature. The methodology for carrying out these tests has been introduced in [27]. Figure 7.4- 8 (a) gives an optical image of the rectangular BPE surface after testing in 0.1M HCl in the as received condition. Due to the linear potential gradient acting along the BPE, the surface shows different corrosion behaviour as a function of distance to the sample edge. The left side (labelled A) is the oxidation edge, showing crevice corrosion, pitting corrosion, and general corrosion, with the right (labelled C) accommodating the balancing cathodic reactions. Figure 7.4- 8 (b) gives the pit-covered region of all tested samples with the different annealing

treatments. The lengths of the regions containing pits were affected by microstructure, with the difference in length indicating different critical pitting potentials for pit nucleation. All pits on the BPE are open pits, without lacy covers.

1250 ^{o}C heat treatment resulted in pits with predominantly circular-shapes, with higher temperature annealing showing more elliptical shapes, with in parallel localised corrosion at grain boundaries. Pits growing in close proximity to each other or merged pits influence overall pit growth rate, as the local effective applied potential and chloride concentration inside of pits changes [37]. When pit grow close to each other, the cathode area surrounding the pit is reduced, often providing not enough cathodic current to sustain a high pit growth rate [38]. Crevice corrosion is also found at the interface between the resin and sample at the oxidation edge. Crevices typically nucleate at lower applied potentials compared to corrosion pits, which is also observed on the samples in Figure 7.4- 8 (b)

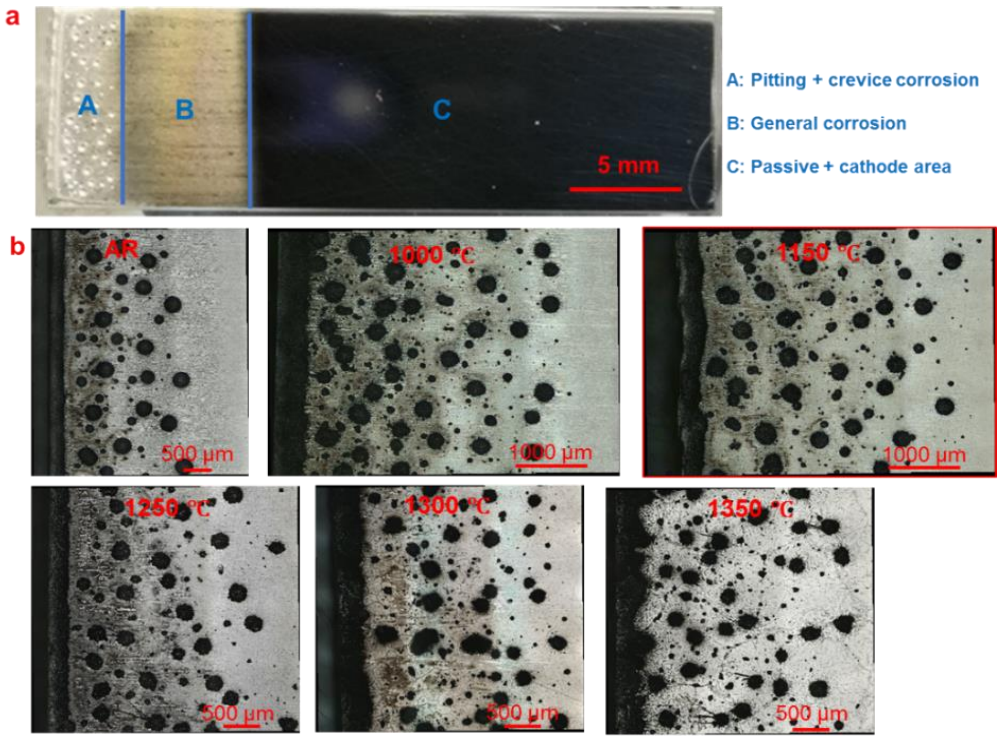

Figure 7.4- 8 View of the AR DSS 2205 bipolar electrode, outlining the different corrosion regions along the sample surface; (b) higher magnification zoomed optical image of the localised corrosion region after all annealing conditions.

Pit Nucleation & Growth

The bipolar treated samples were assessed and inspected in more details. Figure 7.4- 9 (a) and (b) show two pit nucleation sites, found on samples annealed at 1150 ^{o}C and 1250 ^{o}C. Pit nucleation inside ferrite grain can be seen, with the other site showing pits growing at ferrite–austenite boundaries. Inside the austenite phase, there are no pits. The ferrite phase is preferentially corroding away. Figure 7.4- 9 (c) gives pit nucleation sites at the ferrite phase, and along a network of grain boundary austenite in the specimen annealed at 1350 ^{o}C, this explains the localised corrosion observed of the BPE at the grain boundary measured in Figure 7.4- 8 (b) after annealing at 1300 ^{o}C.

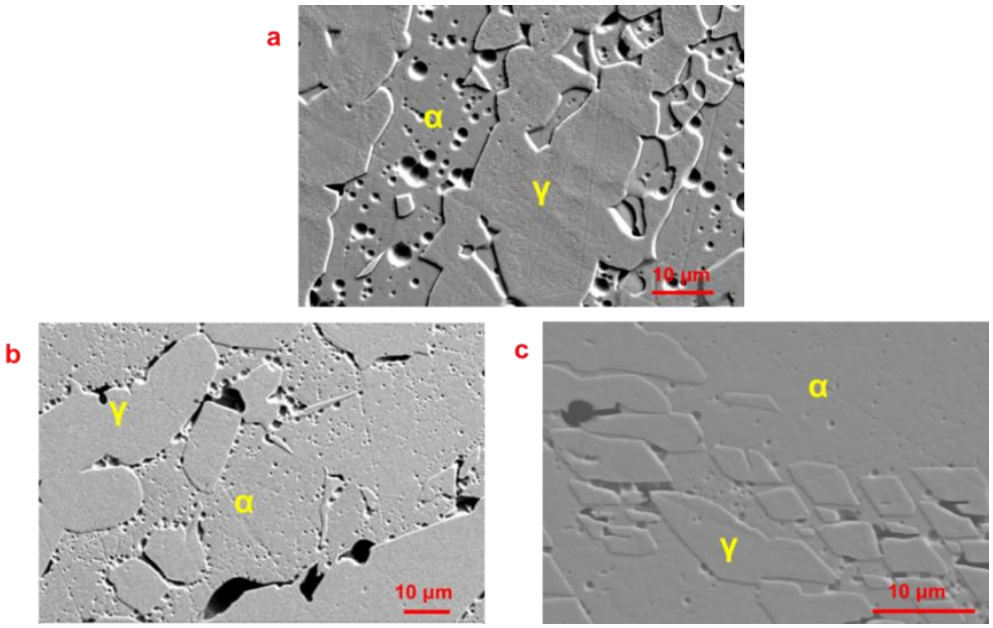

Figure 7.4- 9 The pitting corrosion sites at the specimen after annealed at (a) 1150 ^{o}C and (b) 1250 ^{o}C and (c) 1350 ^{o}C.

Figure 7.4- 10 (a) shows a pit grown into the ferrite, with the remains of the austenite phase resulting in a lacy cover type appearance. Some parts of the lacy cover here are already collapsed into the pit after the surrounding ferrite phase was corroded away. The formation of lacy cover pits in DSS 2205 seems similar to the previous observation of lacy cover pit formation in lean DSS [13], and supports observations reported in [27]. Figure 7.4- 10 (b) gives a fully grown pit after consuming the ferrite phase, supporting previous observations that the austenite phase remains unless all the surrounding

ferrite is dissolved away. Large sized pits on the BPE always had open pits, with Figure 7.4- 10 (c) showing a pit with a diameter of 60 μm. The edge of the pit is not smooth, as remaining austenite phase exist. The size of austenite phase is small compared to the overall pit size, so the pit appears hemi-spherical.

Microstructure changes invoked by annealing heat treatments influences metastable pit growth. After the pit grows to a large hemi-spherical size, it becomes independent to the microstructure, as the ferrite and austenite size is small compared to the overall pit mouth. Slightly elongated pit is present after annealing at 1300 ^{o}C, which is in turn related to the large size of the ferrite grains. The ferrite size also influences the shape and morphology of the lacy covers, which then affects the pit growth kinetics by affecting the ion exchange from inside the pit to the outside bulk electrolyte [13].

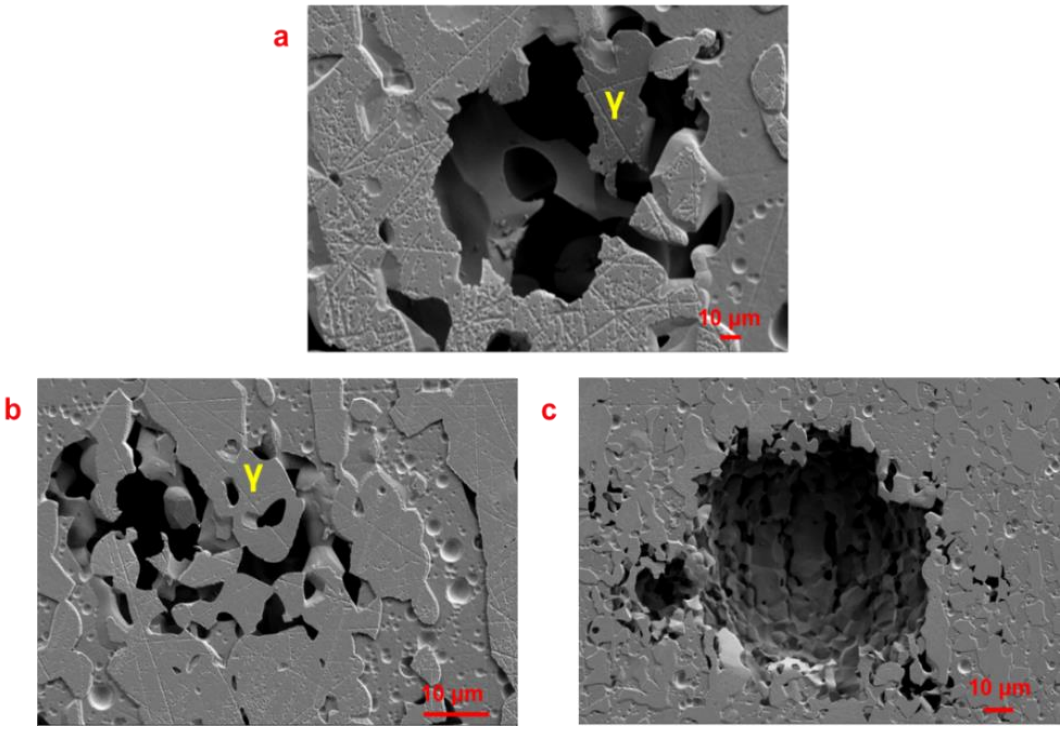

Figure 7.4- 10 The pitting propagation for the specimen annealed at 1000 ^{o}C.

Pit Shape and Morphology

The pit depth measured via confocal microscopy is correlated to the overall pit volume of each pit in Figure 7.4- 11 (a) (a-c) for all different annealed

temperatures. Equation 1 and 2 are introduced to provide an estimate of the measured pit shape. Equation 1 assumes a perfectly hemi-spherical shape, when the depth (d) is the same value as the radius (r).

The pit depth and volume of each pit are then compared to different shape factors ($\boldsymbol{\alpha}$ = 0.5, 1, 2), which is reflected by the three reference curves shown in Figure 7.4- 11. If we keep the pit depth (d) constant, these curves are then indicative of either wide and shallow pits ($\boldsymbol{\alpha}$ = 0.5; e.g. the radius is twice the depth), perfectly hemispherical pits ($\boldsymbol{\alpha}$ = 1), or deep and narrow pits ($\boldsymbol{\alpha}$ = 2; where the radius is half the depth).

$$\mathbf{V} = \frac{\mathbf{1}}{\mathbf{2}} \times \frac{\mathbf{4}}{\mathbf{3}} \times \boldsymbol{\pi} \times \mathbf{d} \times \mathbf{r}^{\mathbf{2}} \qquad \text{Equation 1}$$

$$\boldsymbol{d} = \boldsymbol{\alpha} \times \boldsymbol{r} \qquad \text{Equation 2}$$

All pits are chiefly concentrated at two different depths; one group is less than 40 μm deep, and the other depth group is over 100 μm deep. It seems that a pit depth of 40 μm may act as the critical threshold parameter for the development of metastable to stable pits. Stable pits have a large pit volume/depth ratio which act as diffusion barrier.

Figure 7.4- 11 (b) shows the pit shape with pit depth less than 40 μm; the smaller pits show a nice trend from "wide" (as received) to more a narrow shape with higher annealing temperature. This is related to grain size and the ferrite-austenite ratio in DSS [39,40]. For example, the pit growth in DSS 2205 is found to grow more in depth, but in DSS 2202 pits grow along the surface [41]. Figure 7.4- 11 (c) shows the pit shape when pit depth > 100 μm, the larger pits also show a very nice trend with higher annealing temperature slightly deeper pits, but they become more semi-circular than smaller pits. For the specimen annealing at 1350 ^{o}C, the pits shape is the same for small and large pits. The maximum pit depth is increasing with higher annealing temperature up to 1250 ^{o}C, then the maximum pit depth becomes constant. The maximum pit depth becomes similar after annealing over 1250 ^{o}C, as the formation of austenite inside and at the grain boundary of the ferrite. The effect of austenite acts as a barrier to reduce the pit growth kinetics and the nitrogen loss to increase the pit growth kinetics are cancelled.

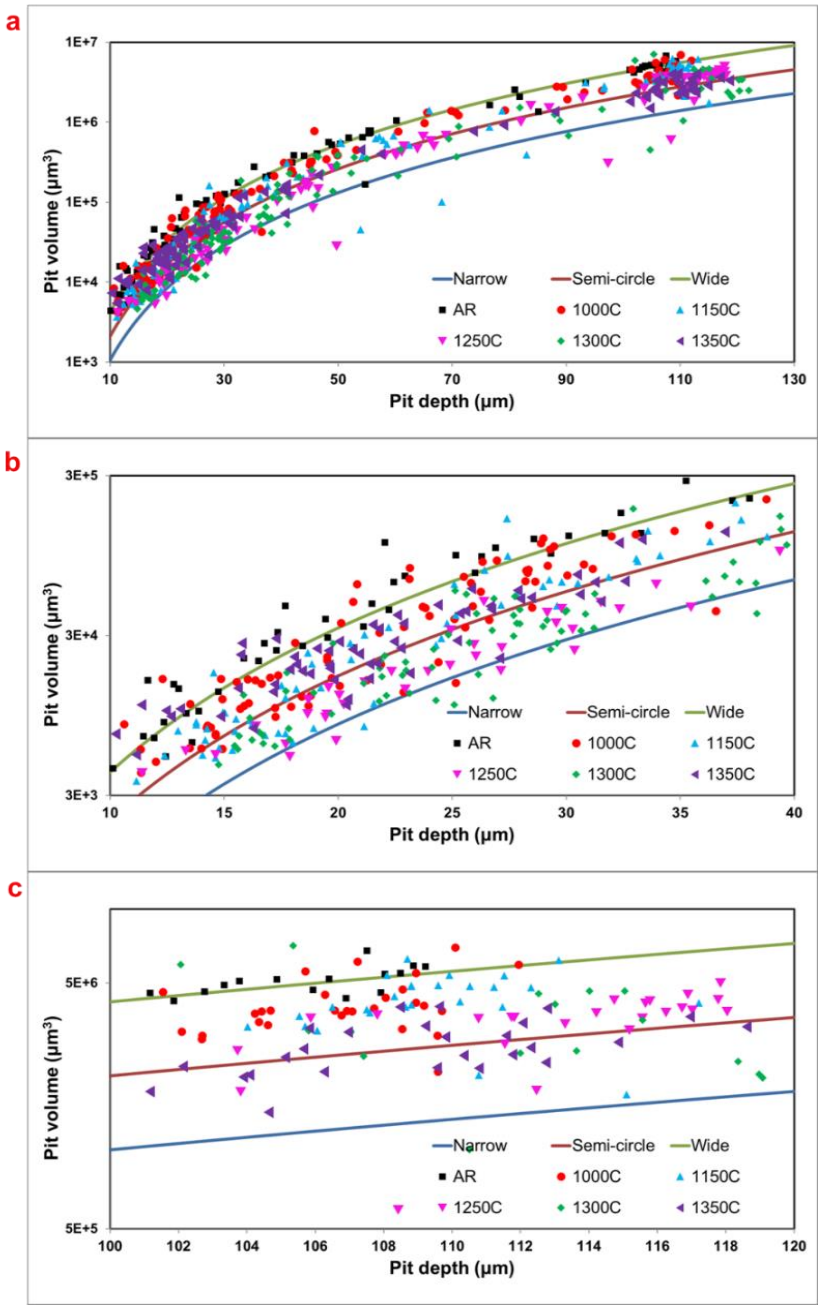

Figure 7.4- 11 (a) Pit depth and the corresponding volume on the BPE with different annealed temperature. With the pit shape of (b) pit depth from 10-40 µm and (c) pit depth from 100 – 120 µm.

Comparison & Optimisation

Figure 7.4- 12 (a) gives the overall pit volume vs pit covered length for each heat treatment condition. A longer pit covered length indicates a lower critical pitting potential, so higher susceptibility. The shortest pit covered region is measured in the AR condition (2.5 mm). For specimen annealed at 1000 ^{o}C, the pit covered length reaches the maximum ≈ 4.4 mm. Then continues

reducing to 3.1mm for specimen annealed at 1250 ^{o}C. From specimen annealing over 1300 ^{o}C, the pit covered length increases from 3.1 mm to 3.5 mm. A larger pit volume indicates a higher pit growth kinetics, even the pit growth in the depth direction is potential independent, but the overall pit volume is related to the applied potential [27]. The pit volume increases from AR to annealed at 1000 ^{o}C, then reduces with higher annealed temperatures. The pitting corrosion resistance is AR > 1250 ^{o}C > 1300 ^{o}C > 1350 ^{o}C > 1150 ^{o}C > 1000 ^{o}C from the pit covered length on the BPE. But the rank for the pit growth kinetics is different, which is 1000 ^{o}C > 1150 ^{o}C > 1250 ^{o}C ≈ AR > 1300 ^{o}C > 1350 ^{o}C.

Figure 7.4- 12 (b) displays the overall pit volume vs PREN values, indicating that smaller pit volumes have a lower PREN. This is opposite to higher PREN indicating a higher pit corrosion resistance, because PREN is only used to estimate the critical pitting potential, which cannot used to estimate the pit growth kinetics. The rank of the pitting resistance from the critical pitting potential and pit volume is not the same, as the nitrogen give a more contribution effect to the pit growth kinetics and size/shape of ferrite/austenite also affect the pit growth kinetics. N reduces the pit growth kinetics, as N increases the pH value inside of pit electrolyte from reach with H^{+} to form NH_3 and $NH4^{+}$ [42]. The pit growth kinetics also run for 900 seconds, but the pit nucleation time is less than 15 seconds [27], so the nitrogen influence the pit growth kinetics for a longer time. The shape of austenite and ferrite is also an important factor for pit growth rate, as only ferrite is corroded away, so the remained austenite can act as a wall to reduce the pit growth. The specimen after annealing over 1300 ^{o}C has the grain boundary austenite which can reduce the pit growth kinetics even with a more nitrogen loss condition.

Interestingly, specimens annealed at 1000 ^{o}C have a ratio of ferrite and austenite of 50:50, but the corrosion resistance is the lowest. In contrast, the highest difference in alloying elements exists in this microstructure between ferrite and austenite (Figure 7.4- 3b), so the galvanic effect between the phases may accelerate the corrosion rate. For the specimen heat-treated over 1300 ^{o}C, the critical pitting potential increases. The possible reason is the concentration of ferrite and elements distribution, the critical current to

nucleate pitting corrosion need a higher applied potential due to a large concentration of ferrite, and the alloying elements between the ferrite and austenite is more homogenous, so the galvanic corrosion between the two phases is very small, which cannot enhance the corrosion rate.

Figure 7.4- 12 clearly shows differences of the initiation behaviour via the pit covered length with pit growth information supported by the overall dissolved pit volume. With this in mind, all high temperature treatments seem to have smaller dissolved volumes, with the as received material providing the highest resistance against pit nucleation. These results demonstrate the application of bipolar electrochemistry for assessing, comparing, and ranking the localised corrosion performance of duplex stainless steel at room temperature. Key for optimising the corrosion resistance seems to be related to the chemical signature of both crystallographic phases, and in particular their interplay. This observation provides the means for developing microstructures with improved resistance to pit growth.

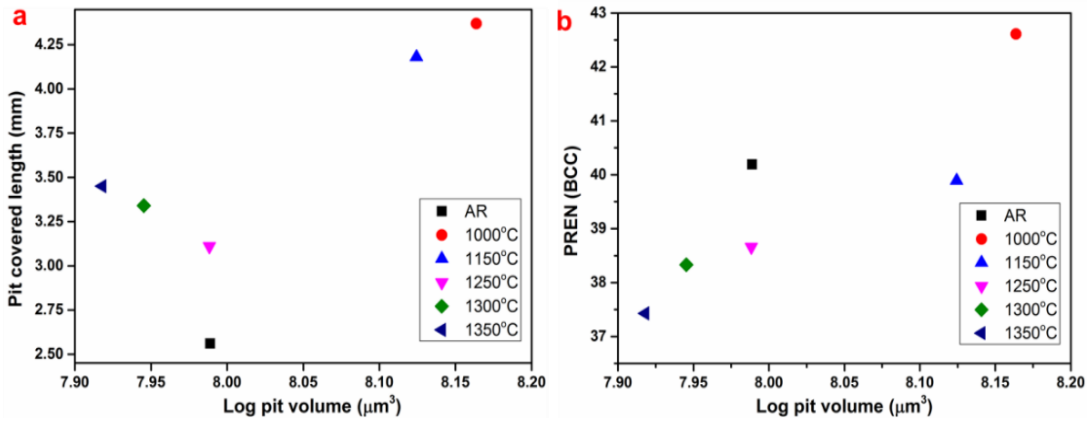

Figure 7.4- 12 (a) the pit covered length and (b) PREN of ferrite phase vs overall pit volume loss on the BPEs.

7.46 Conclusions

The volume of ferrite increases with higher annealing temperatures, but the difference in galvanic behaviour between ferrite and austenite reduces significantly.

The element distribution affected the pit growth behaviour, with the lowest dissolved pit volume observed on samples with the lowest difference in chemical composition of both phases.

Corrosion pits nucleated within ferrite and the interface between ferrite and austenite.

The critical pitting potential, pit growth kinetics, and pit shapes changed with solution treatments, and the rank of critical pitting potential/temperature is not the same when assessed with PREN, CPT, and bipolar electrochemistry.

Bipolar electrochemistry was for the first time successfully applied to assess and rank duplex 2205 microstructure characteristics at room temperature.

7.47 References

[1] H. Tan, Z. Wang, Y. Jiang, D. Han, J. Hong, L. Chen, L. Jiang, J. Li, Annealing temperature effect on the pitting corrosion resistance of plasma arc welded joints of duplex stainless steel UNS S32304 in 1.0M NaCl, Corros. Sci. 53 (2011) 2191–2200. https://doi.org/10.1016/j.corsci.2011.02.041.

[2] J. Nilsson, Overview Super duplex stainless steels, Mater. Sci. Technol. 8 (1992) 685–700. https://doi.org/10.1179/mst.1992.8.8.685.

[3] S.T. Kim, S.H. Jang, I.S. Lee, Y.S. Park, Effects of solution heat-treatment and nitrogen in shielding gas on the resistance to pitting corrosion of hyper duplex stainless steel welds, Corros. Sci. 53 (2011) 1939–1947. https://doi.org/10.1016/j.corsci.2011.02.013.

[4] J.H. Potgieter, P.A. Olubambi, L. Cornish, C.N. Machio, E.S.M. Sherif, Influence of nickel additions on the corrosion behaviour of low nitrogen 22% Cr series duplex stainless steels, Corros. Sci. 50 (2008) 2572–2579. https://doi.org/10.1016/j.corsci.2008.05.023.

[5] Z. Zhang, Z. Wang, Y. Jiang, H. Tan, D. Han, Y. Guo, J. Li, Effect of post-weld heat treatment on microstructure evolution and pitting corrosion behavior of UNS S31803 duplex stainless steel welds, Corros. Sci. 62 (2012) 42–50. https://doi.org/10.1016/j.corsci.2012.04.047.

[6] G.S. Frankel, Pitting corrosion of metals a review of the critical factors, J. Electrochem. Soc. 145 (1998) 2186–2198. https://doi.org/10.5006/0010-9312-19.8.261.

[7] S.M. G.Burstein, P.Pistorius, Evaluating the critical chemistry for repassivation at the corroding surface using mass transport model-based artificial pit experiments, Corros. Sci. 35 (1993) 57–62. https://doi.org/10.1016/0010-938X(93)90133-2.

[8] J. Srinivasan, R.G. Kelly, Evaluating the critical chemistry for repassivation at the corroding surface using mass transport model-based artificial pit experiments, J. Electrochem. Soc. 163 (2016) C768–C777. https://doi.org/10.1149/2.0661613jes.

[9] J. Srinivasan, C. Liu, R.G. Kelly, Geometric evolution of flux from a corroding one-dimensional pit and its implications on the evaluation of kinetic parameters for pit stability, J. Electrochem. Soc. 163 (2016) C694–C703. https://doi.org/10.1149/2.1221610jes.

[10] P. Ernst, R.C. Newman, Pit growth studies in stainless steel foils. I. Introduction and pit growth kinetics, Corros. Sci. 44 (2002) 927–941. https://doi.org/10.1016/S0010-938X(01)00133-0.

[11] W. Tian, S. Li, N. Du, S. Chen, Q. Wu, Effects of applied potential on stable pitting of 304 stainless steel, Corros. Sci. 93 (2015) 242–255. https://doi.org/10.1016/j.corsci.2015.01.034.

[12] B. Deng, Y. Jiang, J. Gong, C. Zhong, J. Gao, J. Li, Critical pitting and repassivation temperatures for duplex stainless steel in chloride solutions, Electrochim. Acta. 53 (2008) 5220–5225. https://doi.org/10.1016/j.electacta.2008.02.047.

[13] K. Eguchi, T.L. Burnett, D.L. Engelberg, X-Ray tomographic characterisation of pitting corrosion in lean duplex stainless steel, Corros. Sci. 165 (2019) 108406. https://doi.org/10.1016/j.corsci.2019.108406.

[14] H.Y. Ha, M.H. Jang, T.H. Lee, J. Moon, Interpretation of the relation between ferrite fraction and pitting corrosion resistance of commercial 2205 duplex stainless steel, Corros. Sci. 89 (2014) 154–162. https://doi.org/10.1016/j.corsci.2014.08.021.

[15] L. F. Garfias-Mesias, J. M. Sykes, C. D. S. Tuck, The effect of phase compositions on the pitting corrosion of 25 Cr duplex stainless steel in chloride solutions, Corros. Sci. 38 (1996) 1319–1330.

[16] L.Q. Guo, M. Li, X.L. Shi, Y. Yan, X.Y. Li, L.J. Qiao, Effect of annealing temperature on the corrosion behavior of duplex stainless steel studied by in situ techniques, Corros. Sci. 53 (2011) 3733–3741. https://doi.org/10.1016/j.corsci.2011.07.019.

[17] N. Lopez, M. Cid, M. Puiggali, Influence of σ-phase on mechanical properties and corrosion resistance of duplex stainless steels, Corros. Sci. 41 (1999) 1615–1631. https://doi.org/10.1016/S0010-938X(99)00009-8.

[18] P. Reccagni, L.H. Guilherme, Q. Lu, M.F. Gittos, D.L. Engelberg, Reduction of austenite-ferrite galvanic activity in the heat-affected zone of a Gleeble-simulated grade 2205 duplex stainless steel weld, Corros. Sci. 161 (2019). https://doi.org/10.1016/j.corsci.2019.108198.

[19] S. Kim, S. Kim, I. Lee, Y. Park, M. Shin, Y. Kim, Effects of shielding gases on the microstructure and localized corrosion of tube-to-tube sheet welds of super austenitic stainless steel for seawater cooled condenser, Corros. Sci. 53 (2011) 2611–2618. https://doi.org/10.1016/j.corsci.2011.04.021.

[20] L. Zhang, W. Zhang, Y. Jiang, B. Deng, D. Sun, J. Li, Influence of annealing treatment on the corrosion resistance of lean duplex stainless steel 2101, Electrochim. Acta. 54 (2009) 5387–5392. https://doi.org/10.1016/j.electacta.2009.04.023.

[21] R.A. Perren, T. Suter, C. Solenthaler, G. Gullo, P.J. Uggowitzer, H. Böhni, M.O. Speidel, Corrosion resistance of super duplex stainless steels in chloride ion containing environments: Investigations by means of a new microelectrochemical method. II. Influence of precipitates, Corros. Sci. 43 (2001) 727–745. https://doi.org/10.1016/S0010-938X(00)00088-3.

[22] E. Angelini, B. De Benedetti, F. Rosalbino, Microstructural evolution and localized corrosion resistance of an aged superduplex stainless steel, Corros. Sci. 46 (2004) 1351–1367. https://doi.org/10.1016/j.corsci.2003.09.024.

[23] Z. Wei, J. Laizhu, H. Jincheng, S. Hongmei, Effect of ageing on precipitation and impact energy of 2101 economical duplex stainless steel, Mater. Charact. 60 (2008) 50–55. https://doi.org/10.1016/j.matchar.2008.07.002.

[24] N. Pébère, V. Vivier, Local electrochemical measurements in bipolar experiments for corrosion studies, ChemElectroChem. 3 (2016) 415–421. https://doi.org/10.1002/celc.201500375.

[25] Y. Zhou, D.L. Engelberg, Application of a modified bi-polar electrochemistry approach to determine pitting corrosion characteristics, Electrochem. Commun. 93 (2018) 158–161. https://doi.org/10.1016/j.elecom.2018.06.013.

[26] Y. Zhou, A. Kablan, D.L. Engelberg, Materials characterization metallographic screening of duplex stainless steel weld microstructure with a bipolar electrochemistry technique, Mater. Charact. 169 (2020) 110605. https://doi.org/10.1016/j.matchar.2020.110605.

[27] Y. Zhou, D.L. Engelberg, Fast testing of ambient temperature pitting corrosion in type 2205 duplex stainless steel by bipolar electrochemistry experiments, Electrochem. Commun. 117 (2020) 106779. https://doi.org/10.1016/j.elecom.2020.106779.

[28] Y. Zhou, D.L. Engelberg, On the application of bipolar electrochemistry to characterise the localised corrosion behaviour of type 420 ferritic stainless steel, Metals (Basel). 10 (2020) 794. https://doi.org/doi.org/10.3390/met10060794.

[29] K. Vijayalakshmi, V. Muthupandi, R. Jayachitra, Influence of heat treatment on the microstructure,ultrasonic attenuation and hardness of SAF 2205 duplex stainless steel, Mater. Sci. Eng. A. 529 (2011) 447–451. https://doi.org/10.1016/j.msea.2011.09.059.

[30] C. David, F. Ruel, F. Krajcarz, C. Boissy, S. Saedlou, V. Vignal, Effect of grain size on the anodic dissolution of lean duplex UNS S32202 austenitic-ferritic stainless steel, Corrosion. 75 (2019) 1450–1460. https://doi.org/10.5006/3218.

[31] H. Tan, Y. Jiang, B. Deng, T. Sun, J. Xu, J. Li, Effect of annealing temperature on the pitting corrosion resistance of super duplex stainless steel UNS S32750, Mater. Charact. 60 (2009) 1049–1054. https://doi.org/10.1016/j.matchar.2009.04.009.

[32] V.A. Hosseini, S. Wessman, K. Hurtig, L. Karlsson, Nitrogen loss and effects on microstructure in multipass TIG welding of a super duplex stainless steel, Mater. Des. 98 (2016) 88–97. https://doi.org/10.1016/j.matdes.2016.03.011.

[33] N. Ebrahimi, M.H. Moayed, A. Davoodi, Critical pitting temperature dependence of 2205 duplex stainless steel on dichromate ion concentration in chloride medium, Corros. Sci. 53 (2011) 1278–1287. https://doi.org/10.1016/j.corsci.2010.12.019.

[34] M. Adeli, M.A. Golozar, K. Raeissi, Pitting corrosion of SAF2205 duplex stainless steel in acetic acid containing bromide and chloride, Chem. Eng. Commun. 197 (2010) 1404–1416. https://doi.org/10.1080/00986441003626151.

[35] C. Örnek, M. Långberg, J. Evertsson, G. Harlow, W. Linpé, L. Rullik, F. Carlà, R. Felici, E. Bettini, U. Kivisäkk, E. Lundgren, J. Pan, In-situ synchrotron GIXRD study of passive film evolution on duplex stainless steel in corrosive environment, Corros. Sci. 141 (2018) 18–21. https://doi.org/10.1016/j.corsci.2018.06.040.

[36] X.Y. Wang, D.Y. Li, Mechanical and electrochemical behavior of nanocrystalline surface of 304 stainless steel, Electrochim. Acta. 47 (2002) 3939–3947. https://doi.org/10.1016/S0013-4686(02)00365-1.

[37] N.J. Laycock, D.P. Krouse, S.C. Hendy, D.E. Williams, Computer simulation of pitting corrosion of stainless steels, Interface, Electrochem. Soc. (2014) 65–71. https://doi.org/10.1149/2.F05144IF.

[38] M.T. Woldemedhin, M.E. Shedd, R.G. Kelly, Evaluation of the maximum pit size model on stainless steels under thin film electrolyte conditions, J. Electrochem. Soc. 161 (2014) E3216–E3224. https://doi.org/10.1149/2.023408jes.

[39] H.J. Sussmann, Understanding why PREN alone cannot be used to select duplex stainless steels, in: NACE Int. Conf., 2015: pp. 1–10.

[40] H. Hwang, Y. Park, Effects of heat treatment on the phase ratio and corrosion resistance of duplex stainless steel, Mater. Trans. 50 (2009) 1548–1552. https://doi.org/10.2320/matertrans.MER2008168.

[41] C. Örnek, F. Léonard, S.A. McDonald, A. Prajapati, P.J. Withers, D.L. Engelberg, Time-dependent in situ measurement of atmospheric corrosion rates of duplex stainless steel wires, Npj Mater. Degrad. 2 (2018) 1–15. https://doi.org/10.1038/s41529-018-0030-9.

[42] R.F.A. Jargelius-Pettersson, Electrochemical investigation of the influence of nitrogen alloying on pitting corrosion of austenitic stainless steels, Corros. Sci. 41 (1999) 1639–1664. https://doi.org/10.1016/S0010-938X(99)00013-X.

7.5 Application of Bipolar Electrochemistry for Characterising Corrosion Kinetics of Austenitic and Duplex Stainless Steels

Yiqi Zhou[*1], *Dirk Lars Engelberg*[1,2]

1. Corrosion & Protection Centre, School of Materials, The University of Manchester, M13 9PL, Manchester, UK

2. Materials Performance Centre, The University of Manchester, M13 9PL, Manchester, UK

* Corresponding author: Yiqi.Zhou@postgrad.manchester.ac.uk

7.51 Highlights

Bipolar electrochemistry has been applied to characterise the corrosion behaviour of austenitic and duplex stainless steels.

The full spectrum of anodic-to-cathodic electrochemical response is accessible for observation.

Pit growth kinetics and 3D pit ratio development are reported.

Trans-passive corrosion and selective phase dissolution are observed and discussed for duplex stainless steels.

7.52 Abstract

Bipolar electrochemistry produces a linear potential gradient across the bipolar electrode, which provides access to the full spectrum of anodic-to-cathodic electrochemical responses. Type 304L and 316L austenitic stainless steels are compared to Type 2101 and 2205 duplex stainless steels in relation to their corrosion behaviour and pit growth kinetics. The critical pitting potential obtained via 3 electrode potentio-dynamic polarisation and bipolar electrochemistry is compared, with changes and differences in pit aspect ratio development discussed. Selective corrosion of the ferrite phase has been observed for both duplex stainless steels, with trans-passive dissolution of austenite phase in the lean Type 2101 duplex stainless steel.

Keywords: Bipolar electrochemistry, stainless steel, pitting corrosion, pitting potential, trans-passive corrosion

7.53 Introduction

Bipolar electrochemistry has recently been used to test corrosion behaviour due to the simplicity of the experimental setup. A wireless non-contact sample is used, which allows corrosion screening to take place in real time [1–3]. A potential gradient is created between two feeder electrodes which results in a continuous spectrum of anodic to cathodic electrochemical reactions simultaneously occurring at the bipolar electrode (BPE). The full corrosion response can be observed by using one sample with a potential gradient acting along the surface [1–4].

Different types of stainless steel are used for application in demanding environment, with the aim to optimise corrosion resistance and performance of component microstructure. Type 316L stainless steel has a higher localised corrosion resistance, due to containing 2-3% Mo [5]. Type 304L stainless steel has great formability, weldability, and excellent corrosion resistance in nitric acid electrolyte [6]. Type 2205 duplex stainless steel has the potential to replace austenitic stainless steels, as better pitting, stress corrosion cracking (SCC) resistance, and better mechanical properties [7–10]. Type 2101 stainless steel has an economic benefit over Type 2205; the expensive Ni and Mo are replaced by Mn and N, whilst maintaining superior corrosion resistance over some austenitic counterparts [11–13].

Pitting corrosion is caused by the local breakdown of the passive film [14]. The local breakdown sites are typically related to microstructure or metallurgical heterogeneities, such as inclusions, grain boundaries, or other second phase precipitates, often resulting in locally weakened passive films [15]. For duplex stainless steel, localised corrosion also related to selective phase dissolution of either the ferrite or austenite, with the local environment and chemistry affecting dissolution sites [7]. In HCl environment, the selective phase dissolution and pitting preferentially nucleates in the ferrite. In HNO_3 or KOH environments, localised corrosion preferentially nucleates in the austenite phase [16–18]. The applied potential, alloy composition, electrolyte composition, and temperature are the key parameters influence the localised corrosion in stainless steels [14,19], with the occurrence of pitting corrosion also influenced by the size and ratio of ferrite-austenite in duplex stainless

steel [20,21]. Once initiated, stable pit growth typically occurs under diffusion control and becomes independent of the applied potential [22]. The initial pit size is typically larger at higher applied potentials, and thus the probability of a metastable pit transforming into a stable pit is greater [2,23].

7.54 Materials and Methods

Four types of stainless steels (Type 304L, 316L, 2101, and 2205) have been investigated with their compositions (wt%) shown in Table 7.5- 1. The PREN (pitting resistance equivalent number = % Cr+3.3 % Mo +16 % N) value was used to rank these pitting corrosion resistance [24].

Table 7.5- 1 The chemical composition (wt%) of Type 304L, 316L, 2101 and 2205 stainless steel with their PREN values.

	Cr	Ni	Mo	Mn	C	N	Fe	PREN
304L	18.2	8.1	N/A	1.52	0.025	0.045	Bal	18.9
316L	16.7	10.1	2.4	N/A	0.019	0.049	Bal	25.4
2101	21.4	1.6	0.3	5.02	0.020	0.214	Bal	25.7
2205	22.4	5.8	3.2	1.50	0.016	0.180	Bal	33.2

For the bipolar electrochemistry experiment, all BPE samples had the exposed surface area of 30 × 10 mm^2 (length x width) with varying thickness. The BPE samples were mounted in Araldite resin and ground up to 1200 grit. To analysis the microstructure, samples were further polished to a 1 μm diamond paste finish. For Electron backscattered diffraction (EBSD) analysis, the samples had a final polish with 0.25 μm diamond paste, followed by a fine polish with OPS (colloidal silica).

For the 3-electrode potentio-dynamic polarization test, samples were cut into 25 × 25 mm^2 (length x width) and ground to 1200 grit. The samples were then tested in an AVESTA cell at room temperature in 0.1M HCl. A Pt electrode and SCE (Saturated Calomel Electrode) reference electrode were used; An IVIUM-Compactstat with IVIUMsoft software was used to measure potentio-dynamic polarisation curves. The open circuit potential (OCP) was stabilised for 10 min., followed by potentio-dynamic polarisation tests from -200mV_{OCP} to +1200mV_{OCP} with a scan rate of 1 mV/s.

A sketch of the bipolar electrochemistry setup is shown as Figure 7.5- 1 (a). A constant current (1 A) was applied between the feeder electrodes, which was set at a distance of 60 mm. The BPE was set in the middle between the feeder electrodes. Each Pt feeder electrode had a surface area of 4 cm^2. Bipolar electrochemistry experiments were run for 5, 10 and 15 min. for each type of stainless steel. The electrolyte was 0.1M HCl with a volume of 200 ml. Figure 7.5- 1 (b) gives the setup for local potential measurements on the BPE. The copper wire was connecting to the backside of the sample. A Luggin probe was located ≈ 1-2 mm above the sample surface, and connected to the Ivium Compactstat via SCE reference electrode. The bipolar electrochemistry experiment was switched on after the OCP stabilised, and the potential measured for 10 minutes thereafter. Then moved the Luggin probe to a new position, repeated the potential measured process. All potentials were measured in increments of 5 mm along the BPE surface.

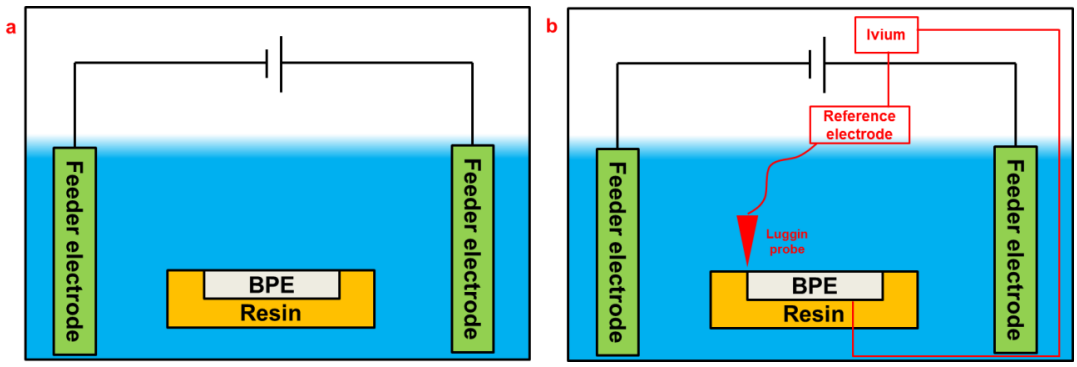

Figure 7.5- 1 1 (a) Setup for bipolar electrochemistry experiment and (b) the setup for the potential measurement on the BPE.

Figure 7.5- 2 (a) shows the potential distribution along the BPE, which is almost linearly reduced from BPE oxidation edge to the BPE reduction edge, the local potential is the average from 10 min. measurements. Figure 7.5- 2 (b) gives the potential change vs. OCP at the different locations. The local applied potential is almost constant with time, some noises are determined. The observed noise at each point is caused by local turbulences due to gas formation reactions. The applied potential here is able to generate Cl_2 and H_2 gas, which in turn over longer time periods then change the electric resistance of the electrolyte.

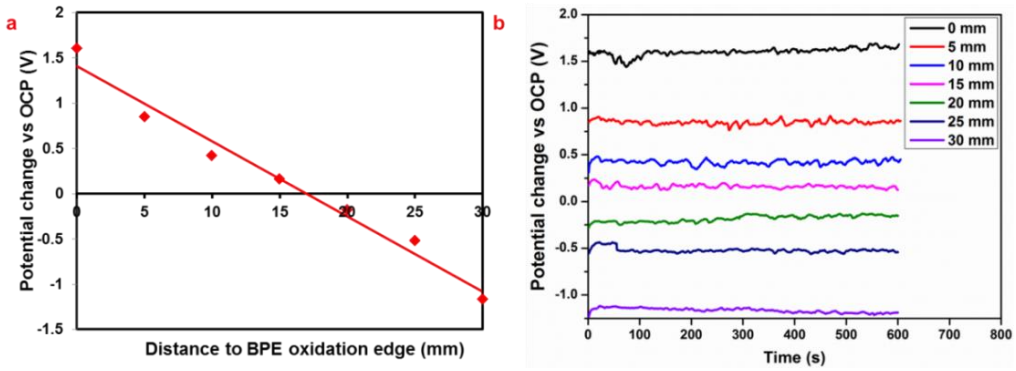

Figure 7.5- 2 (a) The measured potential distribution along the BPE (potential change vs, OCP) and (b) the potential change vs time with different location on the BPE.

After the bipolar electrochemistry experiment, the BPE sample was removed from the electrolyte, placed in an ultrasonic bath for 10 min., to break and remove the lacy pit covers, and then washed in soap water and dried in hot air. A Keyence VK-200K laser confocal microscope was used to determine the pit morphology. The measured regions had a width of 4 mm, with the overall pit covered length. An FEI Quanta 650 FEG SEM was used for imaging and EDX analysis. EBSD maps have been obtained using a Tescan Mira 3 LC FEG-SEM at 15kV.

7.55 Results and Discussion

Potentio-dynamic polarisation tests

The critical pitting potentials (E_{pit}) from the 3 electrode potentio-dynamic polarisation tests in the Avesta cell are summarised in Figure 7.5- 3. For Type 304L stainless steel, the pitting potential is the lowest at +0.4 V_{SCE} with Type 316L stainless steel having an E_{pit} of +0.5 V_{SCE}. E_{pit} for Type 2101 stainless steel is about +0.47 V_{SCE} and no E_{pit} is observed for Type 2205 stainless steel at the room temperature. The OCP of different stainless steel vary from -0.01 to -0.18 $V_{vs\ SCE}$, indicating slight differences in the passive film resistance. The optical images after conducting the potentio-dynamic polarisation tests in Figure 7.5- 3 show open circular pits for Type 304L stainless steel, lacy cover circular pits in Type 316L stainless steel, and lacy cover elongated irregular-shaped pits in Type 2101 stainless steel. The lacy cover at the pit mouth acts as a diffusion barrier, allowing the aggressive electrolyte to remain inside of pit by providing pit stability; the lacy cover is removed at higher applied

potential once the pit becomes stable [25]. For Type 2205 stainless steel, only one small pit-shaped localised corrosion site with a radius of 10 μm has been found after inspecting the whole sample surface exposed during this test. No pits are typically expected in Type 2205 stainless steel in 0.1M HCl at room temperature [9,10].

The optical images in Figure 7.5- 3 (b) show the surface after polarisation testing, with the surface appearance dominated by the highest applied potential (or current), which overshadows most of the corrosion reactions that had occurred at lower potentials.

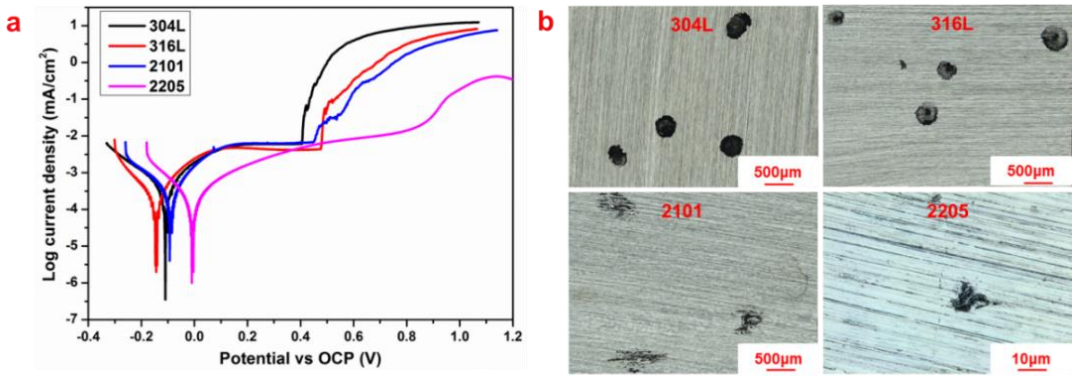

Figure 7.5- 3 (a) Potentio-dynamic polarisation curves of different stainless steels and (b) the corresponding optical images after potentio-dynamic polarisation test in 0.1M HCl at RT.

Bipolar electrochemistry

Figure 7.5- 4 shows the images of the four investigated stainless steels after the bipolar electrochemistry experiment for exposure 15 min., the left side showing the BPE oxidation edge). The scale bar is uniform for all the optical images. Type 304L stainless steel shows pitting corrosion at the BPE oxidation edge, with pits have a length of 10 mm. At a distance of 20 mm from the oxidation edge, some deposits are present, indicating possible chemical or electrochemical reactions that had occurred at the cathodic side. For Type 316L stainless steel, pits nucleate at a distance of 8 to 13 mm from the oxidation edge, indicating at higher anodic potentials close to the edge, no dissolution occurred. A line exists at 17 mm, which defines here the boundary of the anodic and cathodic regions. Close to the oxidation edge, transpassive

corrosion is observed in Type 2101 stainless steel, with large pits then present at a distance in excess of 1 mm. For Type 2205 stainless steel, pits nucleate at the BPE oxidation edge, followed by selective phase dissolution, with both having a length of 7 mm. All BPE stainless steels show crevice corrosion at the interface of the BPE and resin. The crevice corrosion has a longer length than pit covered length, indicates a lower nucleation potential.

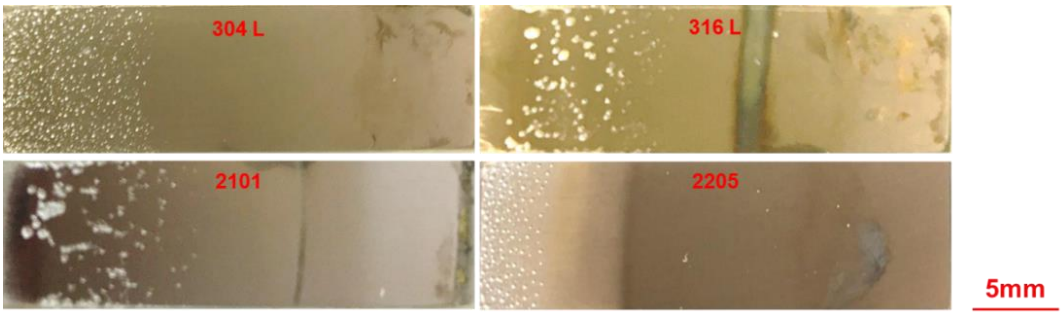

Figure 7.5- 4 Optical images of the four investigated stainless steels after bipolar electrochemistry control for 15 min.

Figure 7.5- 5 shows snapshots of the temporal development of the regions shown in Figure 7.5- 4, summarising the length and development of the pit covered regions of the different stainless steels. The scale bar is the same for all images and the left side of the images are the BPE oxidation edge. For both Types 316L and 304L stainless steels, only pitting corrosion is observed. For Type 2101 stainless steel, trans-passive corrosion is determined at higher applied anodic potential, and pitting corrosion at a lower potential is observed. For Type 2205 stainless steel, pitting corrosion surrounded by selective phase corrosion is found near the BPE oxidation edge and selective phase corrosion closer to BPE centre.

After 5 min., pits nucleated near the BPE oxidation edge for Types 304L and 2205 stainless steels. The pit numbers are reducing from the BPE oxidation edge to the BPE centre, representing the potential reduction along the length of the sample. For Type 316L and 2101 stainless steels, pits do not nucleate at the BPE oxidation edge. Type 2101 stainless steel shows transpassive corrosion at the BPE oxidation edge, but for the Type 316L stainless steel, no transpassive corrosion is observed after the experiment, showing a distinct difference between both materials. For Type 316L stainless steel,

transpassive corrosion has been reported in 0.1M HCl at a potential in excess of 2.2 V_{OCP} [2]. In the bipolar experiment here, the maximum applied potential at the BPE edge is about 1.4 V_{OCP}, cannot support transpassive corrosion. For Type 316L stainless steel, pitting corrosion need a longer induction time at higher applied potential as a thicker passive film is formed, resulting in almost no corrosion. The latter is also supported by gas evolution (possibly H_2 or Cl_2) close the oxidation edge, which seems to be more dominant than the dissolution reaction.

After 10 min., the pit covered length in Type 304L stainless steel remained constant, but pits near the BPE oxidation edge merged and became far larger. For Types 2101 and 316L stainless steel, further pits nucleated and the pit-covered region grew closer to the BPE oxidation edge. For Type 2205 stainless steel, the pit covered region increased towards the BPE centre, with the overall pit sizes increasing.

After 15 min., a large number of pits in Type 2101 stainless steel merged together, which resulted in elongated, more rectangular shaped pits. For Types 316L and 2205 stainless steels, pits near the BPE oxidation edge became larger. Overall, pits at more anodic applied potential have higher opportunities to become stable pits. For Type 304L stainless steel, some pits remained the same size as observed after 5 minutes of bipolar exposure. Some of the observed pits overgrew others in size at the same potential region, indicating the metastable and stable pits.

Type 304L stainless steel has the largest number pits, but the pit especially near the BPE oxidation edge is smaller compared to three stainless steels. The larger number pit is caused by Type 304L stainless steel being more susceptible to pit nucleation, which in turn results in a smaller current density for each pit, with the higher pit density resulting in smaller sized pits. In Type 316L and 2101 stainless steels, fewer but much bigger pits are present close to the BPE oxidation edge. This of course results in far higher current density for each pit; hence these pits can grow rapidly. Pits observed in Type 2205 stainless steel obviously required a higher potential compared to all other stainless steels, with far fewer pits observed towards the centre of the BPE. A

gradient of pit sizes is clearly present in all samples along the potential gradient on the BPE sample.

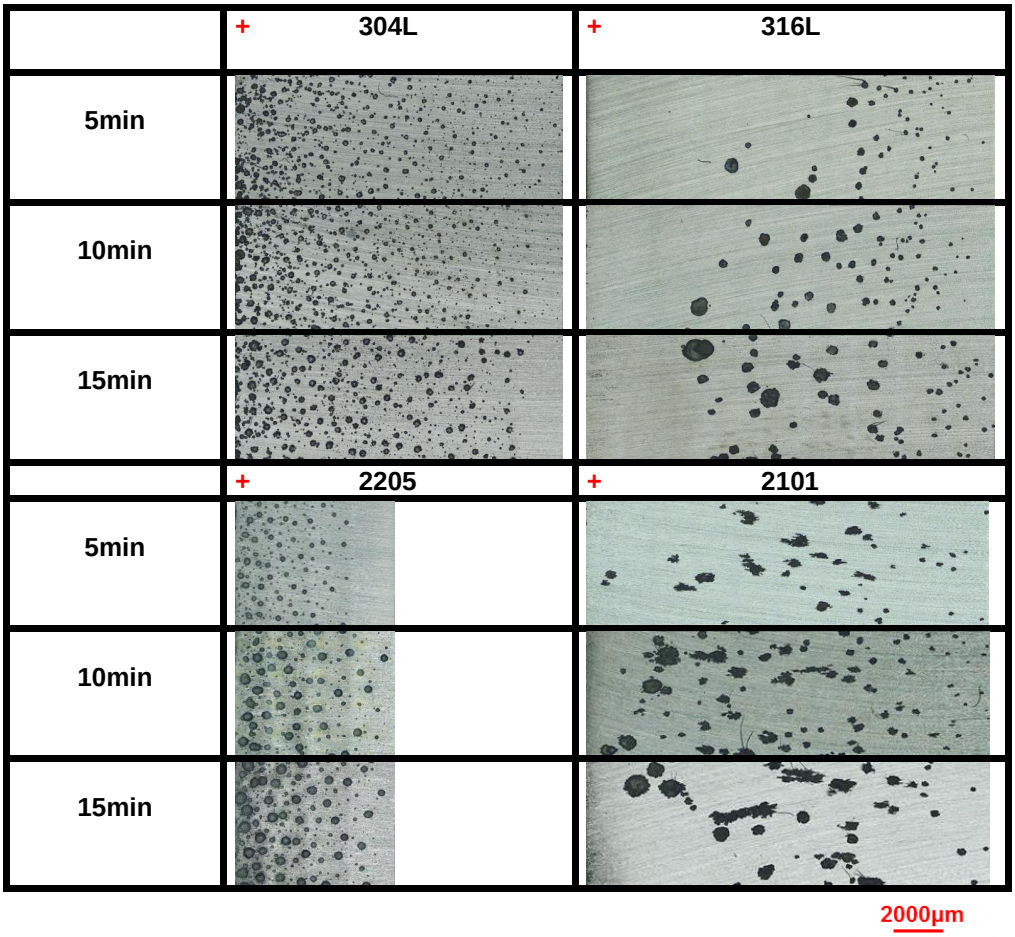

Figure 7.5- 5 Optical images of the pit-covered region after conducting bipolar electrochemistry experiments for 5 min., 10 min., and 15 min. The BPE oxidation edge is on the left in all images ("+" = oxidation edge).

Critical pitting potentials

Table 7.5- 2 gives the overall pit covered length on the BPE, the critical pitting potential (E_{pit}), and total pit volume of all stainless steels are determined on the BPE after 5 min., of bipolar electrochemistry exposure. E_{pit} is obtained by correlating the measured potential distribution along the BPE (in Figure 7.5- 2 a) to the location of observed pits on the sample surface. The critical pitting potential obtained via bipolar electrochemistry is the lowest for Types 316L and 2101 stainless steel, and highest for Type 2205 stainless steel. The pitting potential for Type 304L stainless steel is surprisingly higher than for Type 316L and 2101 stainless steel, which is most likely caused by pitting corrosion at

higher applied potential region, pits plunder current at the lower applied potential region, results in the current is not enough to nucleate pitting corrosion. So the pit covered length for Type 304L stainless steel is higher due to more serious pitting corrosion near BPE oxidation edge.

Passive film thickness, structure and composition result in the different pitting potential determined from the BPE samples and potentio-dynamic polarisation samples, and bipolar electrochemistry test can nucleate pitting corrosion on Type 2205 stainless steel at room temperature, which 3-electrde potentio-dynamic cannot.

During the OCP process, the corrosion resistance is improved by Fe preferred dissolved and enrich in Cr in the passive film [26]. When materials are probed using potentio-dynamic polarisation tests, a thicker passive film can form when sweep through lower potentials, the thickness of the passive film is related to the polarised time in the passive region. The transportation of Cl^- within the passive film will be retard by thicken the passive film [27–29], increases the pitting induction time, result in higher E_{pit} in the potentio-dynamic polarisation test. In the passive region, The outer surface of will enrich in Cr, Mo and Ni, as the Fe selectively dissolves, improves the corrosion behaviour [29]. The corrosion resistance of passive film on the BPE is not enhance by OCP and sweep through passive region, which therefore results in a lower pitting induction potential. So the E_{pit} from 3-electrode potentio-dynamic polarisation test is higher than the pitting potential on the BPE except Type 304L stainless steel shown in Table 7.5- 2.

The passive film on the stainless steel consist of n-type inner layer and p-type outer layer which the corrosion resistance mainly from the n-type inner layer [30]. After a critical potential, the stability of Fe surpass Cr in the passive film, result in lower corrosion resistance. From the Point Defect Model (PDM), at a high applied potential, the cation vacancy can quickly diffuse, result in the pitting corrosion [31]. At the same time, the film growth rate also increased due to high diffusion rate, but high diffusion rate limits time for atoms/ions diffuse to correct position, results in more defects and donors in the passive film. So the corrosion resistance of the passive film reduced. [32–35]. Less Cr

concentration and more defects in passive film and high Cl^- diffusion rate are the reasons for pitting corrosion is nucleated in Type 2205 BPE at room temperature [36,37].

For the pit volume, Type 304L stainless steel has the largest volume which can proof a large number of current was consumed, pit growth at high applied potential protect the lower applied potential region. With the lowest pit volume observed in Type 2205 stainless steel. Types 316L and 2101 stainless steels contain similar pit volumes, with the overall rank of all pit volumes reflecting the PREN values in Table 7.5- 1.

Table 7.5- 2 Summary of the length of the pit containing region, critical pitting potential ,and total pit volume obtained from the BPE experiments, wth the critical pitting potential (Epit) from potentiodynamic polarisation shown for comparison.

	Pit region (mm) (distance to BPE oxidation edge)	BPE length of the region containing pits vs OCP (V)	E_{pit} from potentio-dynamic polarisation tests (V)	Log total pit volume (μm^3)
304L	0-10.6	1.41-0.53	0.5	8.12
316L	4.6-13.2	1.03-0.32	0.63	7.74
2101	1.0-13.2	1.33-0.32	0.55	7.73
2205	0-7.2	1.41-0.82	/	7.68

Microstructure corrosion susceptibility

After the bipolar experiment, transpassive and pitting corrosion are both observed in Type 2101 stainless steel. Pitting corrosion surrounded with selective phase corrosion and pure selective phase corrosion are observed in Type 2205 stainless steel. The selective phase dissolution and transpassive corrosion are not observed after potentio-dynamic polarisation testing. Figure 7.5- 6(a) shows an elongated pit in Type 2101 stainless steel, with remnants of the lacy cover. The pit shown here is the result of selective phase corrosion, which has also been observed in lean Type 2202 stainless steel [7]. Figure 7.5- 6 (b) and (c) are images of the selective phase corrosion in Type 2101 stainless steel. Figure 7.5- 6 (b) shows a rougher, more dissolved surface as at a higher applied potential.

In contrast, Figure 7.5- 6 (d) gives a circular pit shape with an open mouth in Type 2205 stainless steel; the radius of the pit is about 100 μm, the rougher

surface near the pit mouth is caused by selective phase corrosion. The pit edge is not smooth, some phase are still retained; but compare with the whole pit, the phases are very small, so pit mouth is still like a circular like. Figure 7.5- 6 (e) shows the corrosion surrounding the pitting mouth region. The surface is rough, and grains with different height are clearly seen. A number of black sites can clearly be seen, indicates the metastable pits. Figure 7.5- 6 (f) gives a region closer to the BPE centre, only the grain boundaries are seen without height difference between austenite- ferrite phases, resulting in more general corrosion attack.

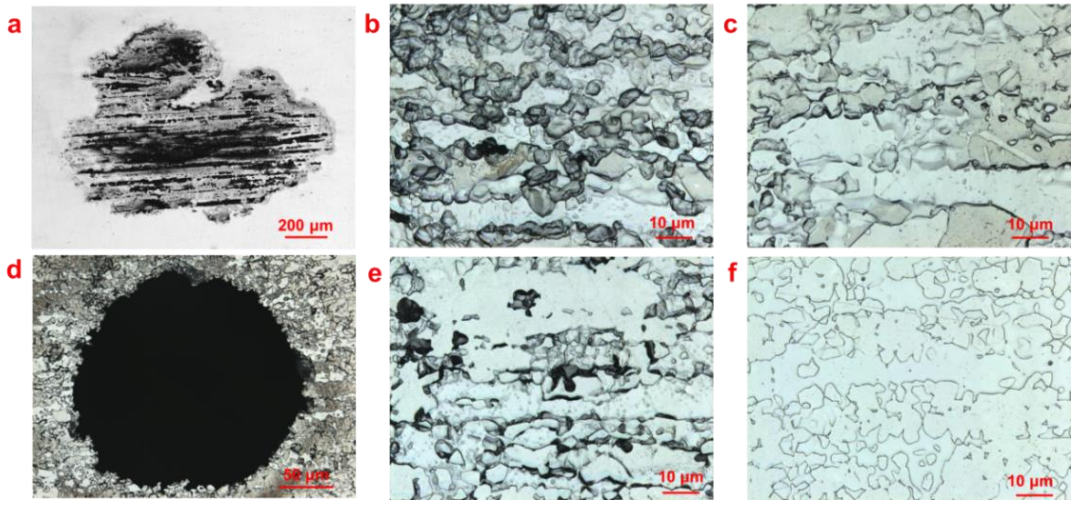

Figure 7.5- 6 Optical images of Type 2101 stainless steel after the bipolar electrochemistry experiment with (a) pitting corrosion, (b) selective phase corrosion at a higher applied potential, and (c) at a lower applied potential. Corrosion response for Type 2205 stainless steel is shown, with in (d) pitting corrosion, and more selective and general corrosion (e) and only general corrosion in (f) at lower applied potentials.

Figure 7.5- 7 gives the corresponding EBSD images of Type 2101 and 2205 stainless steels. The scale bar is the same for both of EBSD images. The ratio of ferrite to austenite is 52/48 for Type 2101 stainless steel and 55/45 for Type 2205 stainless steel. For Type 2101 stainless steel, the distribution of the austenitic phase is more continuous and not isolated by the ferritic phase, and it is easier for the austenitic phase to exist as lacy cover after the surrounding ferritic phase is dissolved away via selective phase corrosion. For Type 2205 stainless steel, the austenitic phase is not continues and isolated by the ferritic phase; so here the austenitic phase is more prone to collapse if the all surrounding ferritic phase is dissolved, which supports the view in Figure 7.5-

6 (d), small phases retained at the pit edge, but too small which cannot be lacy cover for large size pits.

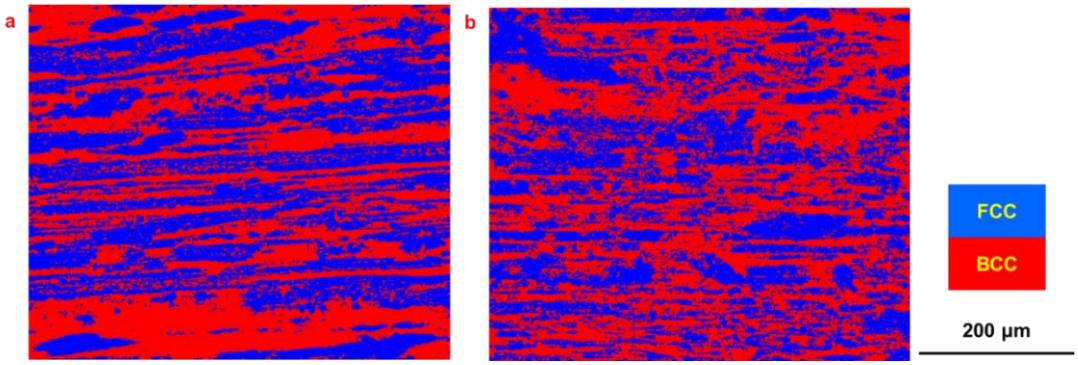

Figure 7.5- 7 EBSD maps of (a) Type 2101 stainless steel and (b) Type 2205 stainless steel (FCC = austenite; BCC = ferrite)

Figure 7.5- 8 (a) shows a region with transpassive corrosion in Type 2101 stainless steel. Ten random EDX measurements at each phase have been obtained and the mean value with standard deviation of the Cr concentration (wt %) are used to distinguish the ferritic and austentic phase. In the austenitic phase, Cr is 20.9 ± 0.6 %. For the ferritic phase, Cr is 22.7 ± 0.7 %. From the EDX analysis, the corroded phase is the austenite here, with the ferritic retained. Figure 7.5- 8 (e) gives an SEM image of another area with transpassive corrosion, and the corresponding EBSD image is given in Figure 7.5- 8 (f). The EBSD image also supports the observation that the retained phase is the ferrite, with the austenite clearly dissolved. In the transpassive region, the passive film becomes more defective, less crystalline and dense, so phases with high Cr have higher resistant to dissolution at the trans-passive corrosion potential [29,38,39].

Figure 7.5- 8 (b) shows an SEM image of the pit lacy cover for Type 2101 stainless steel, the Cr concentration for the lacy cover is 20.9 ± 1.1 % which supports that the lacy cover is the austenite phase, with the surrounding ferritic phase corroded. The ferritic phase preferentially corrodes in reducing acids as austenite has a higher corrosion potential than the ferrite, and micro-galvanic corrosion can occur [40,41]. The potential difference between ferrite and austenite is related to the elements in these two phases [42].

Figure 7.5- 8 (c) shows the selective phase corrosion surrounding the pits in Type 2205 stainless steel. The preferably corroded phase is the ferritic phase which contains 22.6 ± 0.4 % Cr and 3.8 ± 0.2 % Mo, and the retained austenitic phase has 20.3 ± 0.8 % Cr and 2.6 ± 0.4 % Mo. Some circular voids are seen in the ferritic phase and the interface between ferrite and austenite, which are possibly metastable pits. The ferritic phase in Figure 7.5- 8 (d) is dissolved, but no obviuos metastable pits are observed due to the lower local applied potential.

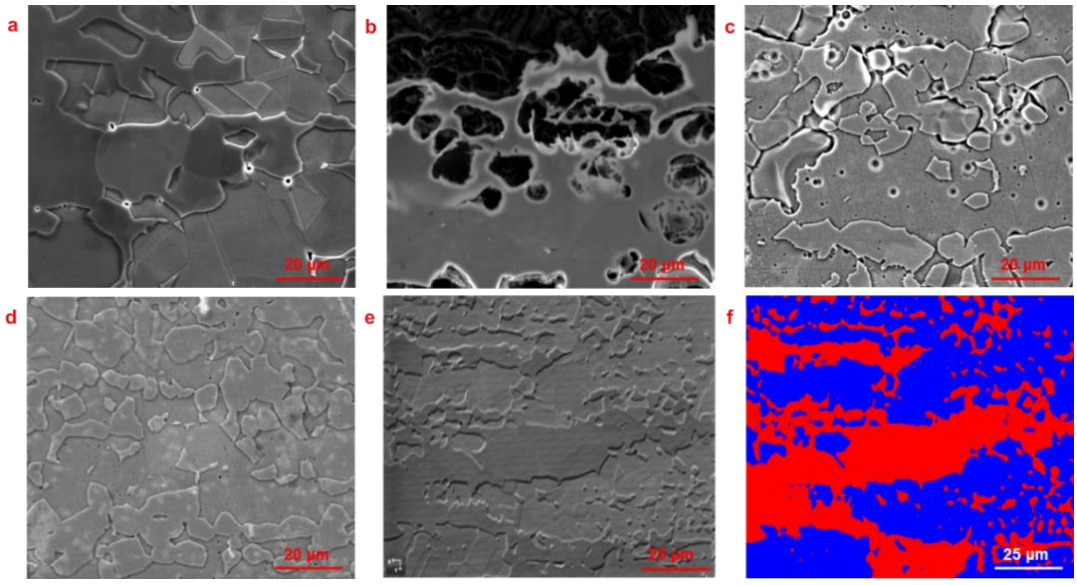

Figure 7.5- 8 (a) Trans-passive corrosion and (b) pit lacy cover in Type 2101 stainless steel. Corrosion in Type 2205 stainless steel surrounding (c) pits and (d) selective phase corrosion at lower applied potential. (e) Trans-passive corrosion in Type 2101 stainless steel and (f) the corresponding EBSD map.

Figure 7.5- 9 (a) gives the total pit volume of all stainless steels for 5 to 15 min. of bipolar exposure, generally showing an increase over exposure time. Type 304L stainless steel has the largest pit volume, with both Types 316L and 2205 stainless steels having the smallest pit volume. After 5 min., Type 2101 stainless steel has a similar pit volume to Type 316L stainless steels, but after 10 min., the pit volume in Type 2101 stainless steel becomes far larger. Figure 7.5- 9 (b) gives the total pit cross-sectional surface area of all pits over time. Types 316L and 2205 stainless steel have the smallest overall pit cross-sectional surface area. Type 304L stainless steel has the largest pit cross-

section area after 5 min., and after 10 min. The total pit cross-sectional area for Type 304L and 2101 stainless steel become similar.

For Type 316L and 2205 stainless steels, the total pit volume is similar but Type 2205 stainless steel has a larger total pit cross-section area. Deeper pits exist in Type 316L stainless steel, as they prefer to grow in depth and pits in Type 2205 stainless steel are shallower, with larger surface cross sections. For Type 304L stainless steel, the total pit cross-sectional area increase is less than the total pit volume change. Type 2101 stainless steel has a similar total pit cross-sectional area as Type 304L stainless steel, but a far smaller total pit volume. This indicates pits in Type 2101 stainless steel are shallower than pits in Type 304L stainless steel.

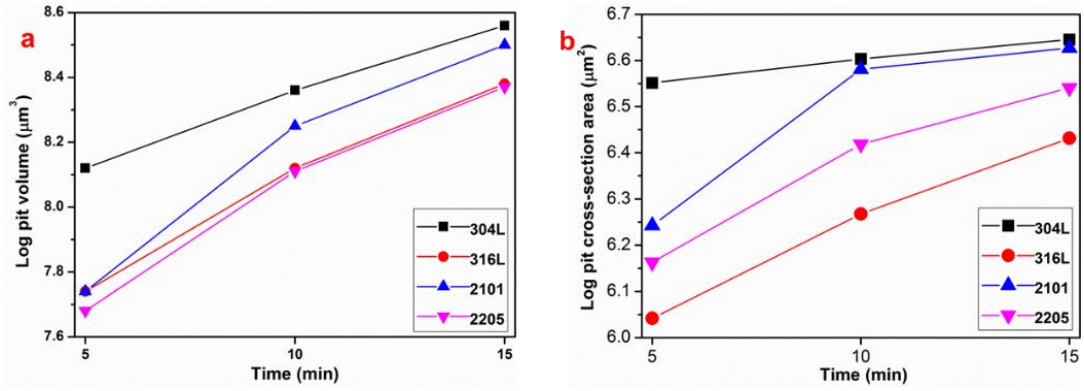

Figure 7.5- 9 (a) Pit volume development with (b) change in pit cross-sectional area over time.

Pit growth kinetics

Pit depth maxima for the three discrete time intervals are summarised in Figure 7.5- 10 (a) showing an increase of depth of all pits over time. Type 304L has the deepest pits, with Type 2205 showing the lowest depth of attack. If we now assume that the deepest pits in all stainless steels nucleated at t=0 s, and at a constant exponential square-root growth behaviour over time ($t^{0.5}$), a value for the pit growth factor (k) can then be estimated following Equation 1, where (y) is the pit depth, (k) is the pit growth factor and (t) is the pit growth time [14,43,44]:

$$\mathbf{y = k\, t^{0.5}} \qquad \text{Equation 1}$$

Figure 7.5- 10 (e) gives the obtained pit growth factor (k) for the first 5, 10, and 15 minutes of exposure, confirming the largest pit growth factor for Type 304 stainless steels. For both duplex stainless steels, the pit growth factor is smaller than in both austenitic stainless steels, and seems almost constant over time; a smaller pit growth factor indicates here a better pitting corrosion resistance. As expected, Type 2205 shows by far the best performance. For Type 2101 stainless steel, the pit growth factor is somehow fluctuating, by first increasing and then decreasing over time. This is related to the irregular pit growth, associated with the lateral coalescence of pits shown in Figure 7.5- 4, and selective corrosion of ferrite phase. For Type 2205 stainless steel, the size of the lateral pit coalescence is reduced compared to type 2101. This may also be related to the less pronounced connectivity of the ferrite phase in type 2205, which is part of the selective dissolution-associated pitting corrosion mechanism in these alloys.

Figure 7.5- 10 (b) to (d) gives a summary of all individual pit volumes over time for all stainless steels. For Type 304L stainless steel, the number of pits is increasing from 322 at 5 min. to 380 at 10 min., followed by a sudden decrease to 269 at 15 min. This shows that a large number of pits first initiate and nucleate, and then merge during subsequent growth with longer exposures. This is also reflected in the large pits reaching total pit volumes > 10^8 μm^3. These overall dimensions are reflected in Figure 7.5- 5, with pits reaching dimensions in excess of 100's of µm in diameter.

Interestingly, pit nucleation seems to continue for most stainless steels over time, evident in Figure 7.5- 5 by increasing length of the pit covered regions, resulting in a direct competition between pit nucleation and either stable growth or coalescence. For Type 316L stainless steel, the number of pits is increasing from 47 at 5 min., to 57 at 10 min. and then 63 at 15 min., indicating the pit nucleating rate is larger than the pit coalescence rate. The number of pits is also an order of magnitude lower compared to Type 304 stainless steel, resulting in more widely spaced nucleation sites. For Type 2101 stainless steel, from 5 to 15 min., the pit numbers increased from 49 to 93, but then significantly reduced to 42, due to the lateral growth and coalescence of pits. For Type 2205 stainless steel, the pit numbers are constant, with values of

around 160, indicating that the pit nucleation rate is similar to the pit coalescence rate. The latter is supported by the observations in Figure 7.5- 5, showing an increase in pit-covered area over time, which can only be maintained by the nucleation of new pits and growth via, coalescence of existing pits.

Figure 7.5- 10 (b) shows that Type 316L and 2101 stainless steels have similar total pit numbers and average pit volumes. The number of pits in Type 304L stainless steels is the highest, with the lowest numbers observed in Type 316L and 2205 stainless steel. All samples have a sudden increase in pit volume when the largest pits merge. Figure 7.5- 10 (c) gives the pit volume and number of pits at 10 min., with the sizes and numbers both increased for 304L, 316L, and 2101 stainless steels. For Type 2205 stainless steel, a larger average pit volume was determined.

Figure 7.5- 10 (d) confirms that the pit numbers in Type 2101 stainless steel are reduced due to pit coalescence. Both Type 316L and 2205 stainless steels have largely increased average pit volumes. In general, pit numbers and size in Type 316L and 2201 stainless steels are similar. Type 2205 stainless steel has the best pitting corrosion resistance as the least pit volume, and smaller pit size than Type 316L and 2101 stainless steels.

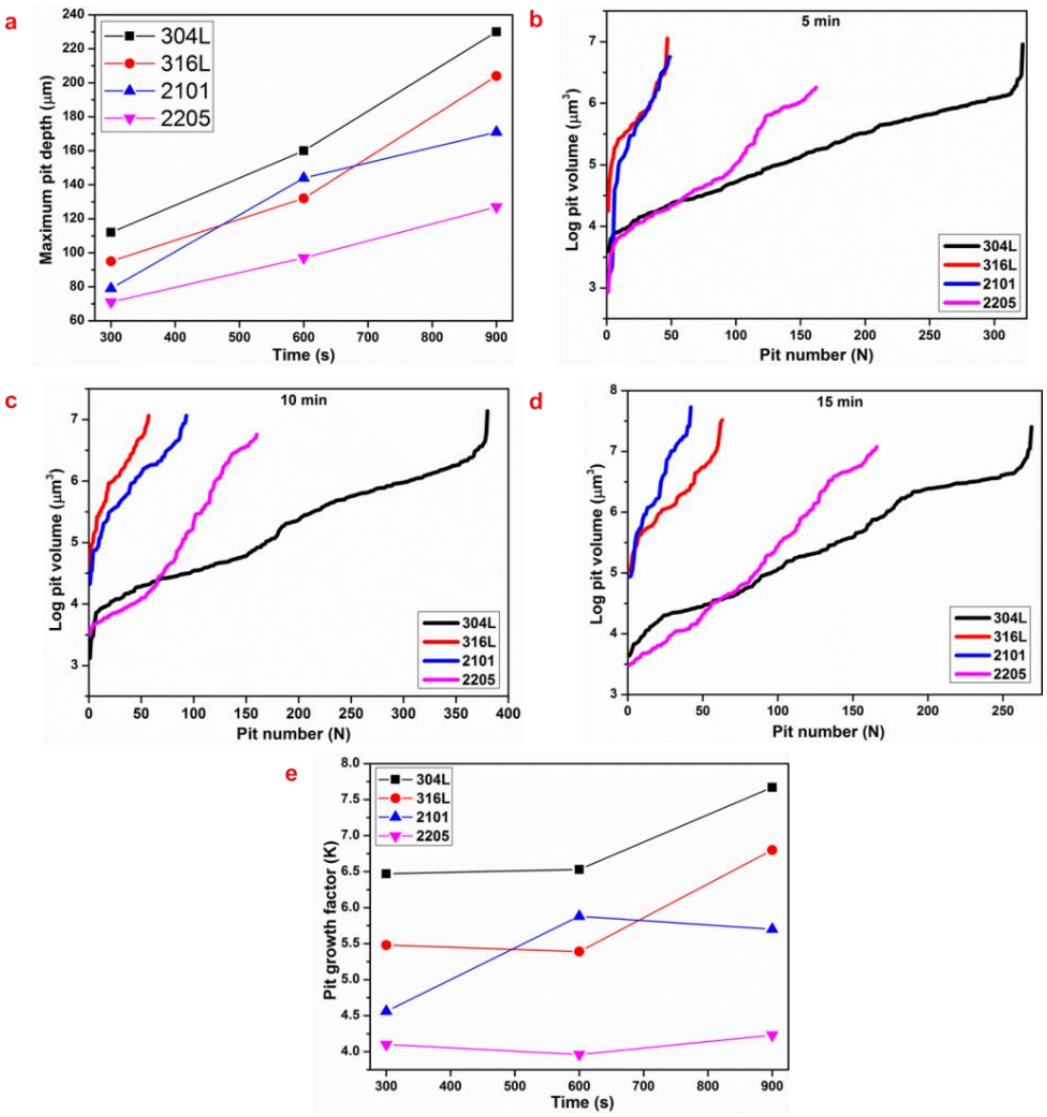

Figure 7.5- 10 (a) The change in pit depth with bipolar exposure from 5 to 15 min. Individual pit volumes vs. number of pits at (b) 5 min., (c) 10 min. and (d) 15 min. of exposure, with (e) giving the pit growth factor k for the data in (a).

Figure 7.5- 11 (a) and (b) shows the optical images of Type 304L and 2205 BPE stainless steels after 15 min. exposure, the BPEs are divided into three regions. Region I has the highest applied potential and region III has the lowest applied potential. 10 largest pits are chosen from each region (* only 8 pits were chosen in Region III for Type 2205 stainless steel). Figure 7.5- 11 (c) shows the mean pit growth factor calculated from Equation 1 in different regions and stainless steels, and the error bar stands for the standard deviation. The pit growth factor is ≈ 5 for the Type 304L stainless steel, higher the pit growth factor ≈ 4 for Type 2205 stainless steel. The pit growth factor in

different region is almost the same, indicates independent to the local applied potential, as the pit growth is diffusion control.

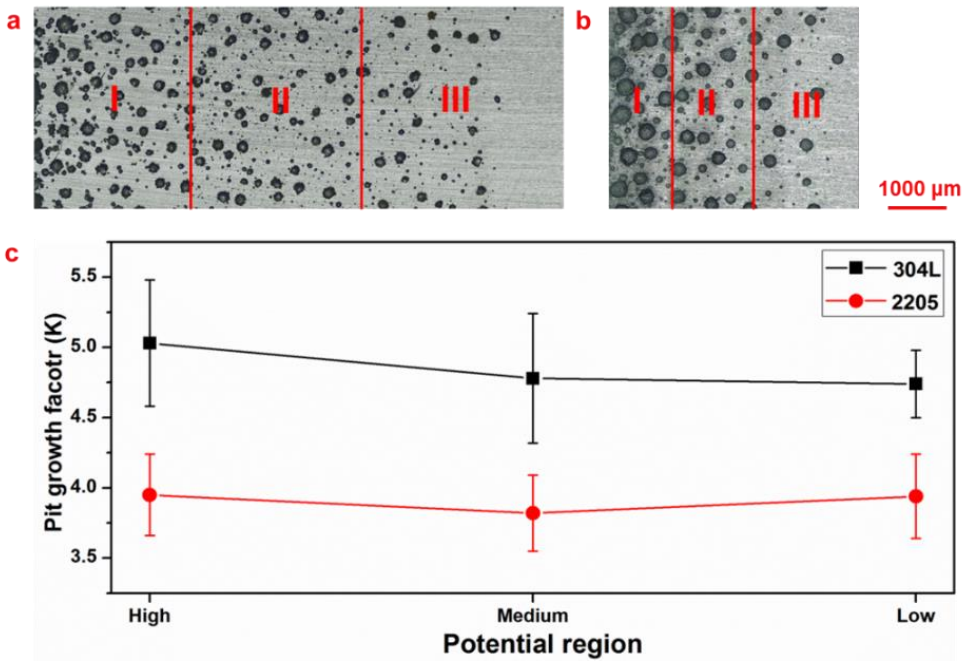

Figure 7.5- 11 BPE was divided into three regions depend on the local potential for Type (a) 304L and (b) 2205 stainless steel. (c) The average pit growth factor for 10 pits with different region.

Pit aspect ratio

The development of pit aspect ratio is summarised in Figure 7.5- 12, measured via laser confocal microscopy at (a) 5 min. and (b) 15 minutes. Equation 2 and Equation 3 are introduced to provide an estimate of the measured volume. The pit depth and volume of each pit is compared to different shape factors ($\boldsymbol{\alpha}$ = 0.5, 1, 2), with three reference curves shown, indicative for either perfectly hemispherical pit shapes, narrower pits or deeper pits. The figures show for a certain depth (d) different pit volumes, which gives information about the overall pit shape. A shallow/dish-like appearance ($\boldsymbol{\alpha}$ = 0.5), is compared to a perfectly hemi-spherical shape ($\boldsymbol{\alpha}$ = 1), versus a narrower, bottle-neck/deep pit ($\boldsymbol{\alpha}$ = 2).

$$\boldsymbol{V = \frac{1}{2} \times \frac{4}{3} \times \pi \times d \times r^2} \qquad \text{Equation 2}$$

$$\boldsymbol{d = \alpha \times r} \qquad \text{Equation 3}$$

Figure 7.5- 12 (a) shows that all pits in Type 2205 stainless steel have either near-hemispherical or slightly shallower shapes. Most pits in type 2101 stainless steel have a wide shape, related to their lateral growth. This is in line with observations of wide corrosion patches and more lateral growth of corrosion pits observed in lean 2202 duplex stainless steel wires after long-term atmospheric corrosion tests [11]. Shallower corrosion sites indicate a higher tendency for re-passivation. Pits in Type 304L stainless steel have a wider spread of ratios, with smaller pits more on the shallower side, and larger pit far deeper than any other investigated stainless steel in this study. This indicates that the pits can readily change shape over time, and grow in more bottle-neck, deeper with size. The change in shape is associated with pits around 30-60 μm in depth. The Mo-alloyed Type 316 stainless steel has a broad distribution of pit shapes, ranging from deep to very shallow morphologies, as the addition of Mo, which support pit re-passivation result in shallower pits [45].

Figure 7.5- 12 (b) shows the pit shape for all stainless steels at 15 min. of bipolar exposure. The pit shape of Type 2205 and 2101 stainless steels remained similar to the distribution observed after 5 min., with however far deeper pits. For Type 304L and 316L stainless steels, most large size pits are now far deeper than the pits observed after in 5 min., as pits are now between the semi-circular and deep pit reference lines. For austenite stainless steel, stable pits are typically close to semi-circular shape [46], which is found for the pits in Type 316L stainless steel, but the pit shape change over exposure time in deeper, more bottle-neck shaped pits in Type 304L stainless steel, as when pits close to each other, less available cathode area surround the pits, which retard the pit growth, so the pits prefers growth in pit depth. For duplex stainless steel, the concentration of ferrite and the size of ferrite/austenite can influence the pit shape, with pits shallower than in their austenitic counterparts.

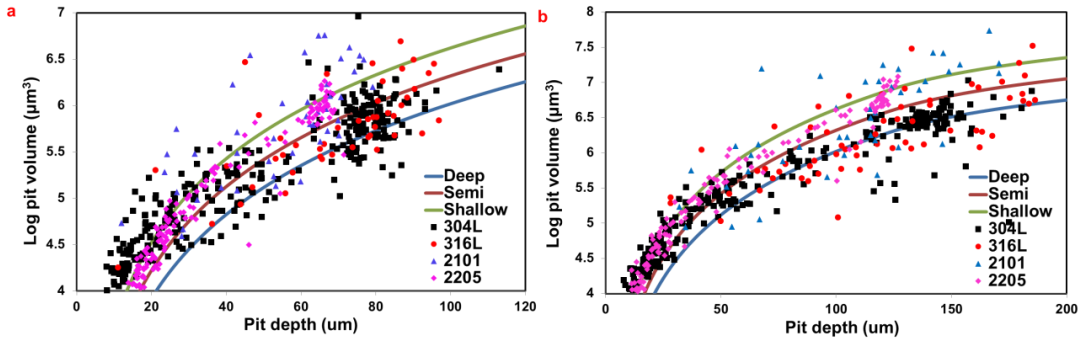

Figure 7.5- 12 Pit depth and volume of Type 304L, 316L, 2101, and 2205 stainless steel at (a) 5 min. and (b) 15 min.

7.56 Conclusions

- Bipolar electrochemistry offers a linear potential gradient on the BPE, allows the anodic and cathodic reaction occurring on the BPE simultaneous.
- Bipolar electrochemistry can test the pitting corrosion for Type 2205 stainless steel at room temperature.
- Pit volume, pit growth kinetics, and pit numbers under a wide range of potential can be measured on one BPE in a single experiment.
- The pit volume is increased with higher applied potential, but pit growth kinetics is independent to the potential.
- Type 304L, 316L and 2101 stainless steel had pits with lacy covers, with only open pits observed in Type 2205 stainless steel. Pits are shallower in duplex stainless steel, compared to their austenitic counterparts.
- The overall pitting corrosion resistance decreased from Type 2205 ≈ 316L > 2101 > 304L stainless steel, with the same order observed from potentio-dynamic polarisation tests.
- The E_{pit} is higher in potentiodynamic scans, related to thickness, composition and structure of the passive film.
- Trans-passive corrosion in Type 2101 stainless steel, result in preferably dissolved the austenitic phase; in Type 2101 and 2205 stainless steel, pitting corrosion occurred via selective phase dissolution of the ferritic phase.

7.57 References

[1] S. Munktell, M. Tydén, J. Högström, L. Nyholm, F. Björefors, Bipolar electrochemistry for high-throughput corrosion screening, Electrochemistry Communications. 34 (2013) 274–277.

[2] Y. Zhou, D.L. Engelberg, Application of a modified bi-polar electrochemistry approach to determine pitting corrosion characteristics, Electrochemistry Communications. 93 (2018) 158–161.

[3] N. Pébère, V. Vivier, Local Electrochemical Measurements in Bipolar Experiments for Corrosion Studies, ChemElectroChem. 3 (2016) 415–421.

[4] S.E. Fosdick, K.N. Knust, K. Scida, R.M. Crooks, Bipolar electrochemistry, Angewandte Chemie - International Edition. 52 (2013) 10438–10456.

[5] G. Meng, Y. Li, Y. Shao, T. Zhang, Y. Wang, F. Wang, Effect of Cl - on the properties of the passive films formed on 316l stainless steel in acidic solution, Journal of Materials Science and Technology. 30 (2014) 253–258.

[6] U. Kamachi Mudali, B.M. Ananda Rao, K. Shanmugam, R. Natarajan, B. Raj, Corrosion and microstructural aspects of dissimilar joints of titanium and type 304L stainless steel, Journal of Nuclear Materials. 321 (2003) 40–48.

[7] C. Örnek, F. Léonard, S.A. McDonald, A. Prajapati, P.J. Withers, D.L. Engelberg, Time-dependent in situ measurement of atmospheric corrosion rates of duplex stainless steel wires, Npj Materials Degradation. 2 (2018) 10.

[8] R. Magnabosco, N. Alonso-Falleiros, Pit morphology and its relation to microstructure of 850°C aged duplex stainless steel, Corrosion. 61 (2005) 130–136.

[9] N. Ebrahimi, M.H. Moayed, A. Davoodi, Critical pitting temperature dependence of 2205 duplex stainless steel on dichromate ion concentration in chloride medium, Corrosion Science. 53 (2011) 1278–1287.

[10] M. Adeli, M.A. Golozar, K. Raeissi, Pitting corrosion of SAF2205 duplex stainless steel in acetic acid containing bromide and chloride, Chemical Engineering Communications. 197 (2010) 1404–1416.

[11] T.S. Huang, W.T. Tsai, S.J. Pan, K.C. Chang, Pitting corrosion behaviour of 2101 duplex stainless steel in chloride solutions, Corrosion Engineering Science and Technology. 53 (2018) 9–15.

[12] R.T. Loto, C.A. Loto, Potentiodynamic Polarization Behavior and Pitting Corrosion Analysis of 2101 Duplex and 301 Austenitic Stainless Steel in Sulfuric Acid Concentrations, Journal of Failure Analysis and Prevention. 17 (2017) 672–679.

[13] C. Köse, R. Kaçar, The effect of preheat & post weld heat treatment on the laser weldability of AISI 420 martensitic stainless steel, Materials and Design. 64 (2014) 221–226.

[14] G.S. Frankel, Pitting Corrosion of Metals A Review of the Critical Factors, 145 (1998) 2186–2198.

[15] R.T. Loto, Electrochemical Corrosion Characteristics of 439 Ferritic, 301 Austenitic, S32101 Duplex and 420 Martensitic Stainless Steel in Sulfuric Acid/NaCl Solution, Journal of Bio- and Tribo-Corrosion. 3 (2017) 24.

[16] S. Aoki, H. Yakuwab, K. Mitsuhashib, J. Sakaic, Dissolution Behavior of α and γ Phases of a Duplex Stainless Steel in a Simulated Crevice Solution, ECS Transactions. 25 (2010) 17–22.

[17] W.T. Tsai, J.R. Chen, Galvanic corrosion between the constituent phases in duplex stainless steel, Corrosion Science. 49 (2007) 3659–3668.

[18] M. Hoseinpoor, M. Momeni, M.H. Moayed, A. Davoodi, EIS assessment of critical pitting temperature of 2205 duplex stainless steel in acidified ferric chloride solution, Corrosion Science. 80 (2014) 197–204.

[19] B. Krawczyk, P. Cook, J. Hobbs, D. Engelberg, Corrosion Behavior of Cold Rolled Type 316L Stainless Steel in HCl Containing Environments, Corrosion. 73 (2017) 1346.

[20] H.J. Sussmann, Understanding Why PREN Alone Cannot Be Used to Select Duplex Stainless Steels, in: NACE International Conference, 2015: pp. 1–10.

[21] H. Hwang, Y. Park, Effects of Heat Treatment on the Phase Ratio and Corrosion Resistance of Duplex Stainless Steel, Materials Transactions. 50 (2009) 1548–1552.

[22] S.M. G.Burstein, P.Pistorius, The Nucleation and Growth of Corrosion Pits on Stainless Steel, Corrosion Science. 35 (1993) 57–62.

[23] R.C. Newman, E.M. Franz, Growth and Repassivation of Single Corrosion Pits in Stainless Steel., Corrosion. 40 (1984) 325–330.

[24] D.H. Kang, H.W. Lee, Study of the correlation between pitting corrosion and the component ratio of the dual phase in duplex stainless steel welds, Corrosion Science. 74 (2013) 396–407.

[25] N.J. Laycock, R.C. Newman, Localised dissolution kinetics, salt films and pitting potentials, Corrosion Science. 39 (1997) 1771–1790.

[26] R. Jiang, Y. Wang, X. Wen, C. Chen, J. Zhao, Effect of time on the characteristics of passive film formed on stainless steel, Applied Surface Science. 412 (2017) 214–222.

[27] K. Sugimoto, Y. Sawada, The role of molybdenum additions to austenitic stainless steels in the inhibition of pitting in acid chloride solutions, Corrosion Science. 17 (1977) 425–445.

[28] J. Moon, H.Y. Ha, S.J. Park, T.H. Lee, J.H. Jang, C.H. Lee, H.N. Han, H.U. Hong, Effect of Mo and Cr additions on the microstructure, mechanical properties and pitting corrosion resistance of austenitic Fe-30Mn-10.5Al-1.1C lightweight steels, Journal of Alloys and Compounds. 775 (2019) 1136–1146.

[29] C. Örnek, M. Långberg, J. Evertsson, G. Harlow, W. Linpé, L. Rullik, F. Carlà, R. Felici, E. Bettini, U. Kivisäkk, E. Lundgren, J. Pan, In-situ synchrotron GIXRD study of passive film evolution on duplex stainless steel in corrosive environment, Corrosion Science. 141 (2018) 18–21.

[30] T. Haruna, D.D. Macdonald, Breakdown of Passive Films on Metals, Zairyo-to-Kankyo. 47 (2014) 78–85.

[31] D. Macdonald, The Point Defect Model for Bi-Layer Passive Films, Journal of the Electrochemical Society. 139 (1992) 3434–3449.

[32] A. Fattah-alhosseini, F. Soltani, F. Shirsalimi, B. Ezadi, N. Attarzadeh, The semiconducting properties of passive films formed on AISI 316 L and AISI 321 stainless steels: A test of the point defect model (PDM), Corrosion Science. 53 (2011) 3186–3192.

[33] L. V. Taveira, M.F. Montemor, M. Da Cunha Belo, M.G. Ferreira, L.F.P. Dick, Influence of incorporated Mo and Nb on the Mott-Schottky behaviour of anodic films formed on AISI 304L, Corrosion Science. 52 (2010) 2813–2818.

[34] J. Amri, T. Souier, B. Malki, B. Baroux, Effect of the final annealing of cold rolled stainless steels sheets on the electronic properties and pit nucleation resistance of passive films, Corrosion Science. 50 (2008) 431–435.

[35] S. Al Saadi, Y. Yi, P. Cho, C. Jang, P. Beeley, Passivity breakdown of 316L stainless steel during potentiodynamic polarization in NaCl solution, Corrosion Science. 111 (2016) 720–727.

[36] C.O.A. Olsson, D. Landolt, Passive films on stainless steels - Chemistry, structure and growth, Electrochimica Acta. 48 (2003) 1093–1104.

[37] G. Okamoto, Passive film of 18-8 stainless steel structure and its function, Corrosion Science. 13 (1973) 471–489.

[38] I. Betova, M. Bojinov, T. Laitinen, K. Mäkelä, P. Pohjanne, T. Saario, The transpassive dissolution mechanism of highly alloyed stainless steels I. Experimental results and modelling procedure, Corrosion Science. 44 (2002) 2675–2697.

[39] M. Itagaki, T. Mori, K. Watanabe, Channel flow double electrode study on electrochemical oscillation during copper dissolution in acidic chloride solution, Corrosion Science. 41 (1999) 1955–1970.

[40] C. Örnek, D.L. Engelberg, SKPFM measured Volta potential correlated with strain localisation in microstructure to understand corrosion susceptibility of cold-rolled grade 2205 duplex stainless steel, Corrosion Science. 99 (2015) 164–171.

[41] S. Aoki, K. Ito, H. Yakuwa, M. Miyasaka, J. Sakai, Potential Dependence of Preferential Dissolution Behavior of a Duplex Stainless Steel in Simulated Solution inside Crevice, Zairyo-to-Kankyo. 60 (2011) 363–367.

[42] P. Reccagni, L.H. Guilherme, Q. Lu, M.F. Gittos, D.L. Engelberg, Reduction of austenite-ferrite galvanic activity in the heat-affected zone of a Gleeble-simulated grade 2205 duplex stainless steel weld, 161 (2019).

[43] M.K. Cavanaugh, R.G. Buchheit, N. Birbilis, Modeling the environmental dependence of pit growth using neural network approaches, Corrosion Science. 52 (2010) 3070–3077.

[44] O.O. Fatoba, R. Leiva-Garcia, S. V. Lishchuk, N.O. Larrosa, R. Akid, Simulation of stress-assisted localised corrosion using a cellular automaton finite element approach, Corrosion Science. 137 (2018) 83–97.

[45] A. Pardo, M.C. Merino, A.E. Coy, F. Viejo, R. Arrabal, E. Matykina, Pitting corrosion behaviour of austenitic stainless steels - combining effects of Mn and Mo additions, Corrosion Science. 50 (2008) 1796–1806.

[46] J. Mankowski, Z. Szklarska-Smialowska, The effect of specimen position on the shape of corrosion pits in an austenitic stainless steel, Corrosion Science. 17 (1977) 725–735.

8 Bipolar electrochemistry technique development

8.1 General introduction

Some modified bipolar electrochemistry setups were designed for corrosion test. The first design could test corrosion behaviour under a wider range of applied potential. The second design was used determined the localised corrosion competition between the pitting and crevice corrosion. The galvanic corrosion between different materials under a wide range of applied potential could be tested by the third parallel bipolar electrochemistry setup.

The first paper (chapter 8.2) introduces a modified bipolar electrochemistry setup to measure the corrosion response on 316L ss. A secondary potential was applied on the BPE to control the overall potential on the BPE. Corrosion response and the pit morphology changed by potential were determined on the modified BPE. Open dish-like pits and transpassive corrosion can be achieved from the modified bipolar electrochemistry.

The second paper (chapter 8.3) introduces a two-dimensional bipolar electrochemistry setup. In this setup, a secondary bipolar electrochemistry set perpendicular to the primary bipolar electrochemistry. The localised corrosion growth (pitting and crevice corrosion) kinetics and the competition between them were determined. The competition between the pitting and localised corrosion can be controlled by the potential from the second bipolar electrochemistry setup.

The third paper (chapter 8.4) introduces a parallel bipolar electrode setup, which is used to measure the galvanic corrosion. For this setup, two parallel BPEs with a constant gap are used. One of the BPE connects to an externally applied potential. The overall potential on the secondary BPE could be adjusted by a secondary applied potential, then the galvanic corrosion between the two BPEs were controlled. The galvanic effect changed by the different secondary potential was determined the volume of the localised corrosion changed on the BPE.

8.2 Application of a Modified Bi-polar Electrochemistry Approach to Determine Pitting Corrosion Characteristics

Yiqi Zhou[*1], *Dirk Lars Engelberg* [1,2]

1.Corrosion & Protection Centre, School of Materials, The University of Manchester, M13 9PL, Manchester, UK

2.Materials Performance Centre, The University of Manchester, M13 9PL, Manchester, UK

* Corresponding author: Yiqi.Zhou@postgrad.manchester.ac.uk

8.21 Highlights

- A modified bi-polar electrochemistry approach is introduced, by exposing a potentio-statically controlled sample to a potential gradient.
- The spatial distribution of anodic to cathodic bi-polar reaction characteristics can be controlled.
- Application of the new approach is demonstrated via determination of pitting corrosion characteristics in austenitic stainless steel.

8.22 Abstract

The application of bi-polar electrochemistry produces a linear potential gradient between two feeder electrodes, allowing the full spectrum of anodic to cathodic reaction kinetics to be controlled. A modified bi-polar approach is introduced, by superimposing a constant electrochemical potential to the potential gradient, thereby controlling the location and spatial distribution of anodic to cathodic reactions along the exposed sample surface. Application of this approach is demonstrated by controlling the extent of pitting corrosion in austenitic stainless steel as a function of the applied potential.

Keywords: Bi-polar electrochemistry, stainless steel, pitting corrosion, potentio-static polarisation

8.23 Introduction

Bi-polar electrochemistry produces a linear potential gradient between two feeder electrodes. A metallic sample exposed to such a potential gradient solicits spatially separated anodic to cathodic electro-chemical reactions along the sample surface [1–5]. This provides the means to obtain a continuous spectrum of electrochemical polarisation characteristics on one sample surface, as a function of distance between both feeder electrodes. Applying

bi-polar electrochemistry therefore provides a wireless, non-contact setup for fast throughput corrosion screening [1, 6, 7].

The occurrence of pitting corrosion results in rapid metal dissolution confined to small areas at the sample surface [8–10]. The developed pit shapes and associated reaction kinetics vary as pits grow into different morphologies, for example, by either providing mass-transport related stability via growth in depth, or by predominantly propagating and coalescencing along the sample surface [11]. Potentiodynamic polarization is typically used to determine the critical pitting potential (E_{pit}), with a current density in excess of 1 mA/cm^2 often regarded as the pit initation threshold [12]. The stability and growth criteria of corrosion pits is also linked to the pit stability product (P), estimated by multiplying the current density (i) inside a pit with the maximum pit depth (d). This infers that either deeper pits or the presence of a suitably high current density [13] facilitates stable pit growth. Stability products between 0.3 and 0.6 $A.m^{-1}$ are considered to provide the environmental envelope for stable pit growth in austenitic stainless steel [14], with the pit aspect ratio playing herein an important role, defined by the pit depth to width relationship [15].

The aim of this communication is to investigate a modified bi-polar experimental set-up for controlling the spatial location of potential gradients and associated reaction characteristics along an exposed sample surface. The viability of this approach is demonstrated by controlling pit growth and stability characteristics in an austenitic stainless steel.

8.24 Materials and Methods

The material used in this study was a Type 316L stainless steel with (wt%) 16.7 Cr, 10.1 Ni, 2.4 Mo, 0.019 C, 0.049 N and (bal.) Fe, which was cut into rectangular coupons of 30mm x 10mm x 1mm (L x W x T). A copper wire was spot welded to the back-side of the coupon, and then mounted in Araldite resin, followed by preparation of the exposed sample surface to a 1um diamond paste finish.

A sketch of the modified bi-polar electrochemistry experiment with two DC power sources (Keysight E36105A) is shown in Figure 8.2- 1(a). The first power source supplies the potential for the bi-polar feeder electrode setup,

with the second power source controlling the potential of the bipolar electrode (BPE). Pt electrodes were used as feeder and counter electrodes. The area of both Pt feeder electrodes was 4 cm^2, with an additional Pt counter electrode of 1 cm^2 positioned 25 mm away from the BPE sample surface. This set up offers the means to provide a potential gradient between both feeder electrodes along the BPE surface, by in parallel superimposing and controlling the potential of the BPE via application of a second potential. The latter provides a way to control the spatial distribution of the anodic to cathodic reactions occurring along the sample surface, schematically shown by the potential gradients in Figure 8.2- 1 (b). All potentials were measured in increments of 5 mm along the BPE sample surface, using a Luggin capillary connected to a Saturated Calomel Electrode (SCE).

The electrolyte used for all experiments was 0.1M HCl, with the distance between the two feeder electrodes set to 60 mm. The potential applied between the two feeder electrodes was 10V, with the applied potential to the BPE between 0V and +4V. Figure 8.2- 1 (b) shows the measured potential distribution along the surface of the BPE as a function of the superimposed applied potential. The potential is linearly distributed along the surface of the bipolar electrode, with the applied potential via the second power source then providing an offset to the overall potential gradient. All experiments were carried out for the duration of 0.5 hrs. For running the experiment, the power supply for bipolar electrochemistry was switched on first, followed by applying a static potential to the BPE. It should be noted that the formation of several secondary reaction species can occur in HCl solutions with application of large over-potentials, including Cl_2O, ClO_2, ClO-, HClO, Cl* and HO_2* [16]. This may result in the formation of gaseous species, which certainly affects the measured potentials distribution over time.

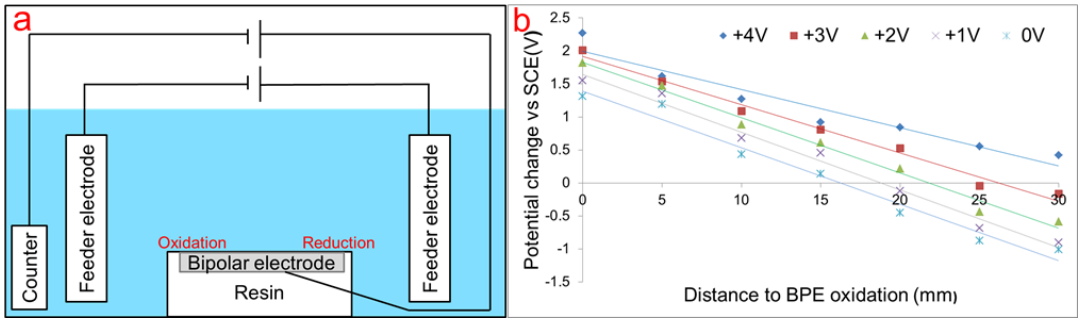

Figure 8.2- 1 Setup for modified bi-polar electrochemistry arrangement, with (b) sketch of the potential distribution along the BPE under different applied potentials (0 to +4V).

After the experiments, the BPE samples were removed from the electrolyte rinsed and dried for surface topography analysis. The pit depth (d), width (w), cross-sectional surface area (A), and total volume of each pit (V) was obtained by 3D laser scanning microscopy, using a Keyence VK-X200K microscope. For measuring the total volume for pits with lacy metal covers, the samples were placed in an ultrasonic bath for 10 min, to collapse and remove the lacy cover. The pit aspect ratio for each pit was determined, describing the pit depth to width (d / w) ratio, calculated from Keyence measurements. The dissolved pit volume density is calculated by normalising the measured pit volume over the total measured area (7 mm^2). The mean of at least *7* measurements is reported, with error bars describing the standard deviation.

8.25 Results and Discussion

A collage of all sample surfaces after carrying out the modified bi-polar electrochemistry experiment is shown in Figure 8.2- 2 (a). Pitting corrosion characteristics along the length of the exposed samples, as a function of the superimposed potentio-statically applied potentials (0 to +4V) are reported. There are five distinctive surface characteristics, which are labelled and separated by boundaries. Region I contains surface corrosion only, followed by large open pits observed in Region II, mixed pit characteristics (both open and with lacy covers) in Region III, exclusively lacy-cover pits in the Region IV, with Region V showing no sign of corrosion or dissolution at all.

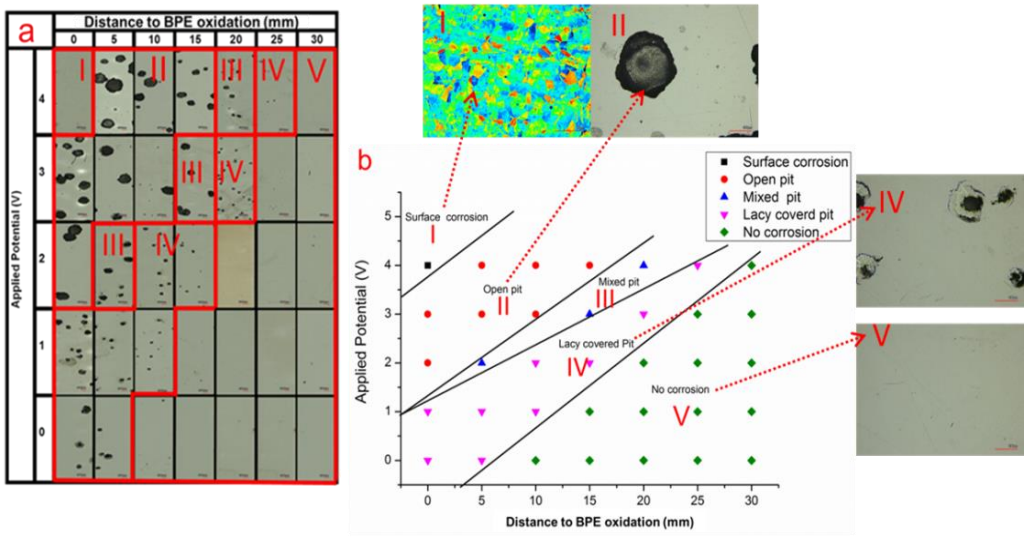

Figure 8.2- 2 Surface corrosion characteristics of the BPE under different applied potentials as a function of distance along the surface, with (b) a summary of the observed corrosion type; the sample surfaces was assessed every 5mm length increment, from 0mm to 30mm. Optical images of region II, IV, and V and a surface topography colour map of region I support observation of the different corrosion characteristics.

With the application of bi-polar electrochemistry and a superimposed applied potential, the sizes of pits are smaller with increasing distance from the BPE oxidation edge, until no corrosion occurs, indicative of passivity and cathodic behaviour (region V). At a constant distance from the BPE edge, surface corrosion characteristics change with increasing applied potential, from cathodic response (region V), to lacy-cover pits at low applied potentials (region IV), to stable open pits at higher applied potentials (region II), and finally to trans-passive surface corrosion (region I). Figure 8.2- 2 (b) summarises all observations, demonstrating the effect of applied potential on controlling localised corrosion characteristics along the surface of the BPE, concluding that potentio-static control of the BPE therefore provides a tool for controlling the spatial distribution of local reaction characteristics.

Figure 8.2- 3 (a) gives the dissolved pit volume density along the surface of the BPE in relation to the applied potential. A larger pit volume density indicates higher corrosion rates, since a constant exposure time was used for all experiments. The pit volume density shows for all applied potentials a quasi-linear relationship versus the distance along the surface of the sample. Overall, the total dissolved pit volume increased with higher applied potentials,

transitioning from lacy cover pitting corrosion to stable, open pit growth. This is possible when the pit either reaches a critical depth or the supplied current reaches a critical threshold [17]. At an applied potential of +4V, the highest overall pit volume density is found at a distance of 5 - 10 mm, which is similar to the pit volume density at the anodic edge (0 mm) with +3V applied. This indicates that both regions have similar localised corrosion characteristics, supporting the role of applied potential to BPE in controlling the location of electrochemical reactions along the sample surface. At the anodic edge of the to +4V polarised sample, only general corrosion was observed, resulting in the sudden drop of the measured pit volume in Figure 8.2- 3 (a).

Figure 8.2- 3 (b) highlights pit aspect ratio variations from 0.2 to >1.0, with pits inside the rectangle all showing open pit characteristics, and the ones outside the rectangle all containing lacy covers. Additonally, all open pits have a depth to width aspect ratio between 0.2 and 0.4, indicating shallow, dish shaped topographies. Lacy covered pits have higher aspect ratios, typically in excess of 0.4, resulting in far deeper ellipsoidal to hemispherical pit shapes. An aspect ratio of 0.5 means that pits have a hemi-spherical appearance, with ratios in excess of 0.5 to 1 resulting in an elongated bottle shape, schematically shown Figure 8.2- 3 (b). These observations are supported by Figure 8.2- 2 (b), showing that open pit morphologies are typically associated with either locations close to the oxidation edge, or the presence of high applied potentials (+3 to +4V). This indicates that the current density in these regions is large enough to support stable pit growth, without the need for diffusion limited deep pit geometries or lacy metal covers.

The presence of lacy cover pits in Figure 8.2- 3 (b), synonymous for a diffusion barrier, is characteristic of lower applied potentials or regions further away from the BPE oxidation edge. This indicates that pits grow deeper at lower potentials, to establish longer diffusion pathways to prevent re-passivation. So, lacy cover pits typically grow to a certain depth before they lose their covers, transforming into open, stable pits.

In our case, a shallow dish shape with low aspect ratio is characteristic for open pits, summarised from Figure 8.2- 3 (b). This means that for stable pit

growth, the presence of a limiting current density would provide a driving force for expanding the shallow pit area, but once the current density drops below a critical threshold, the self-protecting pit growth mechanisms would result in higher aspect ratios and lacy pit covers, as predominantly the pit depth increases. This can be observed by either increasing the distance to the BPE oxidation edge, or by reducing the applied potentio-static potential at a given distance. This technique can be used to grow different pit shapes and, for example, examine the effect of pit morphology and stability on pit-to-crack transition.

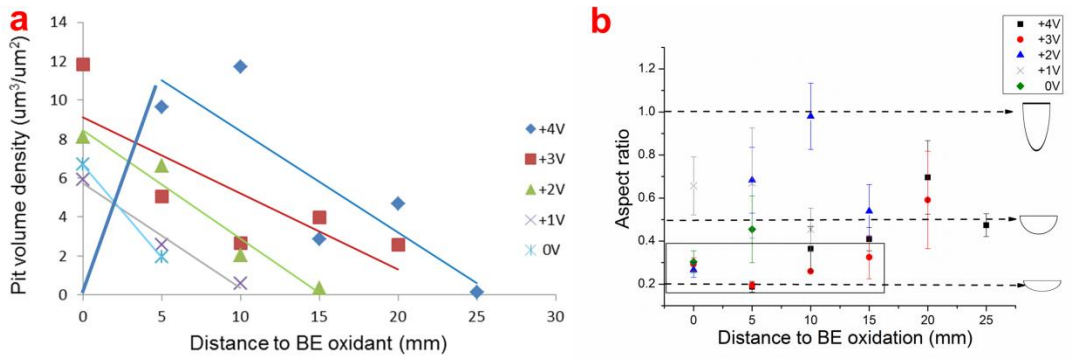

Figure 8.2- 3 Pit volume density at different locations along the BPE as function of applied potentials, with (b) summary of pit aspect ratio along the sample surface. Typical pit shapes for each aspect ratio are also shown. The rectangle shows aspect ratios of open pits.

8.26 Conclusions

A modified bi-polar electrochemistry approach has been introduced, comprising of a potentio-statically controlled sample within a bi-polar potential gradient. The spatial distribution of anodic to cathodic bi-polar reaction characteristics can be controlled, demonstrated via observing pitting corrosion characteristics in austenitic stainless steel. The transition from lacy covered pits to open pitting corrosion has been determined, indicating a change to open, dish-like pits with aspect ratios below 0.4. The presence of lower potentials results in deeper, higher aspect ratio pits and the formation of lacy pit covers.

8.27 References

[1] S. Munktell, Bipolar Electrochemistry for high throughput screening applications, ACTA Universitatis upsaliensis, 2016.

[2] S.E. Fosdick, K.N. Knust, K. Scida, R.M. Crooks, Bipolar electrochemistry, Angew. Chemie - Int. Ed. 52 (2013) 10438–10456.

[3] L. Koefoed, S.U. Pedersen, K. Daasbjerg, Bipolar electrochemistry—A wireless approach for electrode reactions, Curr. Opin. Electrochem. 2 (2017) 13–17.

[4] S. Munktell, M. Tydén, J. Högström, L. Nyholm, F. Björefors, Bipolar electrochemistry for high-throughput corrosion screening, Electrochem. Commun. 34 (2013) 274–277.

[5] G. Tisserant, Z. Fattah, C. Ayela, J. Roche, B. Plano, D. Zigah, B. Goudeau, A. Kuhn, L. Bouffier, Generation of metal composition gradients by means of bipolar electrodeposition, Electrochim. Acta. 179 (2015) 276–281.

[6] S. Munktell, L. Nyholm, F. Björefors, Towards high throughput corrosion screening using arrays of bipolar electrodes, J. Electroanal. Chem. 747 (2015) 77–82.

[7] Z.A. Fattah, Applications of bipolar electrochemistry : from materials science to biological systems, Universite Sciences et Technologies, 2013.

[8] Y. Yi, P. Cho, A. Al Zaabi, Y. Addad, C. Jang, Potentiodynamic polarization behaviour of AISI type 316 stainless steel in NaCl solution, Corros. Sci. 74 (2013) 92–97.

[9] S. Frangini, N. De Cristofaro, Analysis of the galvanostatic polarization method for determining reliable pitting potentials on stainless steels in crevice-free conditions, Corros. Sci. 45 (2003) 2769–2786.

[10] S. Yang, D.D. Macdonald, Theoretical and experimental studies of the pitting of type 316L stainless steel in borate buffer solution containing nitrate ion, Electrochim. Acta. 52 (2007) 1871–1879.

[11] C. Örnek, F. Léonard, S.A. McDonald, A. Prajapati, P.J. Withers, D.L. Engelberg, Time-dependent in situ measurement of atmospheric corrosion rates of duplex stainless steel wires, Npj Mater. Degrad. 2 (2018) 10.

[12] B. Krawczyk, P. Cook, J. Hobbs, D. Engelberg, Corrosion Behavior of Cold Rolled Type 316L Stainless Steel in HCl Containing Environments, Corrosion. 73 (2017) 1346.

[13] J. Srinivasan, R.G. Kelly, On a recent quantitative framework examining the critical factors for localized corrosion and its impact on the galvele pit stability criterion, Corrosion. 73 (2017) 613–633.

[14] F.A. Almuaili, S.A. McDonald, P.J. Withers, D.L. Engelberg, Application of a Quasi In Situ Experimental Approach to Estimate 3-D Pitting Corrosion Kinetics in Stainless Steel, J. Electrochem. Soc. 163 (2016) C745–C751.

[15] H.W. Pickering, The role of electrode potential distribution in corrosion processes, Mater. Sci. Eng. A. 198 (1995) 213–223.

[16] I. Ignatov, O. Mosin, G. Gluhchev, S. Karadzhov, G. Miloshev, N. Ivanov, Studying Electrochemically Activated NaCl Solutions of Anolyte and Catholyte by Methods of Non-Equilibrium Energy Spectrum (NES) and Differential Non-Equilibrium Energy Spectrum (DNES), J. Med. Physiol. Biophys. 20 (2016) 13–23.

[17] P. Ernst, N.J. Laycock, M.H. Moayed, R.C. Newman, The mechanism of lacy cover formation in pitting, Corros. Sci. 39 (1997) 1133–1136.

8.3 Characterisation of localised corrosion growth kinetics with an orthogonal bipolar electrochemistry technique

Yiqi Zhou[*1], *Dirk Lars Engelberg* [1,2]

1.Corrosion & Protection Centre, School of Materials, The University of Manchester, M13 9PL, Manchester, UK

2.Materials Performance Centre, The University of Manchester, M13 9PL, Manchester, UK

* Corresponding author: Yiqi.Zhou@postgrad.manchester.ac.uk

8.31 Highlights

- A two-dimensional bipolar electrochemistry approach is introduced, by exposing two orthogonal bipolar electrochemistry setups.
- The spatial distribution of anodic to cathodic bipolar reaction characteristics can be controlled.
- Application of the new approach is demonstrated via determination of pitting and crevice corrosion growth kinetics.
- Competition between pitting corrosion and crevice corrosion is discussed.

8.32 Abstract

A linearly potential is generated between two feeder electrodes, which allows the anodic and cathodic reactions occurring on a bipolar electrode (BPE) simultaneously. Two-dimensional bipolar electrochemistry setup is introduced by two bipolar electrochemistry setups orthogonal to each other, allows the corrosion behaviour over a wider potential range can be determined. Application of two-dimensional bipolar electrochemistry also can measure the pitting and crevice corrosion growth kinetics at the same increased potential and competition between them as a function of different applied potential.

Keywords: Bipolar electrochemistry, stainless steel, pitting corrosion, crevice corrosion

8.33 Introduction

Bipolar electrochemistry creates a potential gradient between two feeder electrodes which results in a continuous spectrum of anodic to cathodic reactions simultaneously occurring along the BPE [1–3]. As the simplicity of the experimental setup, wireless non-contact BPE sample, high throughout corrosion screening, and multiple corrosion response along one BPE in a single experiment; bipolar electrochemistry is recently used for the corrosion accessing [1–4]. But the application of bipolar electrochemistry for corrosion

test still has some limitations, one of the limitations is limited potential along the BPE as low potential from the bipolar electrodes. To overcome it, a secondary applied potential can be applied on the BPE, so corrosion at a wider potential is achieved [2]. The other limitation is a steep potential gradient with a high potential across a short length BPE, result in corrosion response only appears in a narrow potential range cannot be measured. So, the two-dimensional bipolar electrochemistry can be applied to solve these two issues. Two-dimensional bipolar electrochemistry is used for electrochemical sensing and high throughput screen of electrocatalytic activity, which offers a wider potential gradient [5].

Localised corrosion is defined as a localised breakdown of the sample with a passive film, which result in pitting and crevice corrosion [6]. The nucleation sites of pitting corrosion is the local weak part on the passive film, such as inclusions, grain boundaries, or second phase precipitates [7]. The pitting and crevice corrosion are both influenced by the concentration of Cl^-, applied potential, and electrolyte temperature [8–10]. Crevice geometry can change the crevice corrosion, from acidification process, potential distribution inside of crevice, and the possibility of species inside of crevice diffuse out [11–13]. Pit growth kinetics is independent of the applied potential, but the pit volume loss increases with higher applied potential [14,15]. Three common crevice corrosion growth mechanism are discussed, includes metastable pitting corrosion mechanism, which is the metastable pits nucleated and growth inside of crevice as the occluded geometry. IR drop mechanism, which is the potential drop in the crevice from the crevice electrolyte resistance, crevice can growth in the active state location. Passive dissolution mechanism, which is pH gradual reducing to a critical value to break the passive film, result in the crevice corrosion nucleates and growth [16–21]. Crevice corrosion is more dangerous than pitting corrosion as initiated at a lower potential, lower temperature, shorter induction time, and crevice corrosion can initiate and growth without the Cl^-, but Cl^- is necessary for the pitting corrosion nucleation and growth [18,22,23].

The aim of the manuscript is to investigate a two-dimensional bipolar electrochemistry setup for controlling the spatial location of potential gradients

to analysis the localised corrosion on the BPE. The viability of this approach is demonstrated by pitting and crevice corrosion growth kinetics and the competition between them under a higher potential range with smooth potential gradient on the BPE via the two-dimensional bipolar electrochemistry setup.

8.34 Materials and Methods

The material used in this study was as annealed Type 420 stainless steel with (wt%) 13.7 Cr, 0.46 C, 0.47 Si, 0.39 Mn and (bal.) Fe, the BPE sample was 30 * 10 * 1 mm^3 (length * width * thickness). BPEs were mounted in Araldite resin, followed by grind the exposed sample surface with 1200 grit, washed with soap water and followed by dry in hot air.

The sketch of the bipolar electrochemistry setup is shown as Figure 8.3- 1(a), a constant potential (10 V) was applied between the feeder electrodes with a distance of 60 mm. The BPE was set in the centre between the feeder electrodes. The oxidation reactions occurred near the negative feeder electrode, and vice versa. Figure 8.3- 1 (b) shows the two-dimensional bipolar electrochemistry setup, a secondary pair of the feeder electrodes was set perpendicular to the primary feeder electrode setup. The primary bipolar electrochemistry setup offered a potential gradient along the BPE length and the secondary bipolar electrochemistry setup offered a secondary potential gradient along the BPE width. The distance between secondary feeder electrodes was also 60 mm. Both the primary and secondary feeder electrodes were Pt electrode with a surface area of 4 cm^2. The electrolyte used for the experiment was 0.05 M HCl with a volume of 200 ml. All the experiments run for 5 min.. The main and support bipolar electrochemistry were switched on simultaneously during the bipolar experiment.

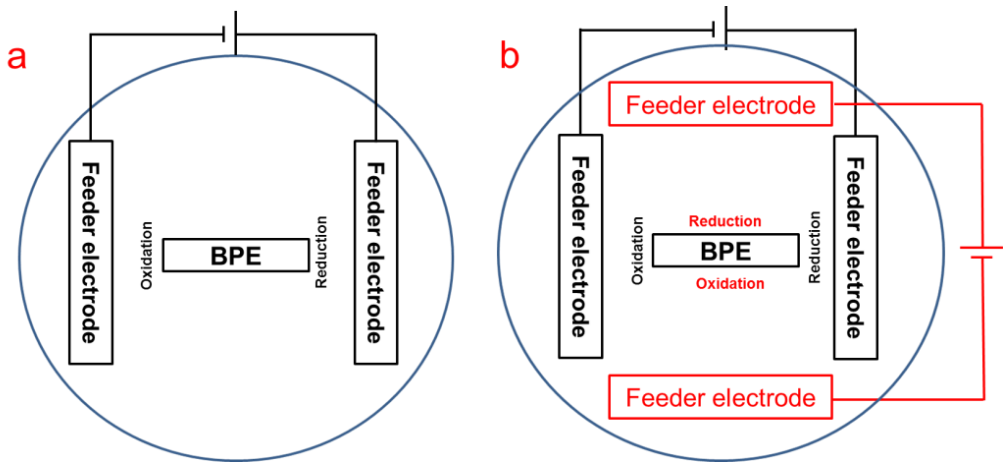

Figure 8.3- 1 (a) Setup of bipolar electrochemistry, and (b) setup of two-dimensional bipolar electrochemistry, the red colour is the secondary bipolar circuit and the black colour is the primary bipolar circuit.

Figure 8.3- 2 (a) shows the potential distribution along the length of BPE with only switch on the primary bipolar circuit, the x-axis is the distance to BPE oxidation edge and the y-axis is the corresponding potential change vs OCP. The potential distribution along the BPE length is almost linearly. To measure local potential changes during the bipolar experiments, a copper-wire was electric connected to the backside of BPE, and a Luggin capillary connected to a saturated calomel electrode (SCE) set ≈ 1mm above the centreline of BPE surface. The OCP was stabilised at first, and then switched on the power supply. The reported potential change on the y-axis is the difference of measured potential with respect to the OCP. The potentials were measured along the BPE surface in increments of 5 mm. The measured potential was constant with time for all the measured point on the BPE. The recorded potential in Figure 8.3- 2 (a) at each point is the average potential change vs OCP in 5 min.. Figure 8.3- 2 (b) gives the potential distribution on the width of BPE only from the secondary bipolar circuit; the x-axis is the distance along with the BPE width. Both potential at secondary BPE oxidation sites and the potential gradient across the BPE width became larger with a higher secondary bipolar potential. The recorded potential in Figure 8.3- 2 at each point is the average potential change vs OCP in 5 min.

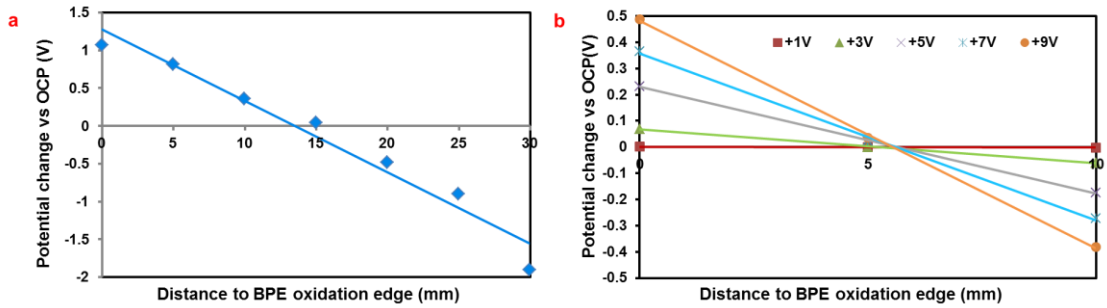

Figure 8.3- 2 The potential distributions along the length of BPE with only run the primary bipolar electrochemistry and (b) the potential along the width of BPE only switch on the secondary bipolar electrochemistry.

Figure 8.3- 3 (a) shows 5 different regions on the BPE width, depend on the different distance to the secondary BPE oxidation edge. The width of each region is 2 mm and the measured length equal to the localised corrosion covered length. With a higher potential from the secondary bipolar circuit, the local potential is increased in region 1 and 2, reduced in region 4 and 5; and neutral in region 3. Figure 8.3- 3 (b) gives four different regions along the BPE length. The size of each region was 2 * 10 mm^2 (length * width). The volume of pitting and crevice corrosion in each region is measured by laser confocal microscopy and compared with different secondary bipolar potential from secondary feeder electrodes.

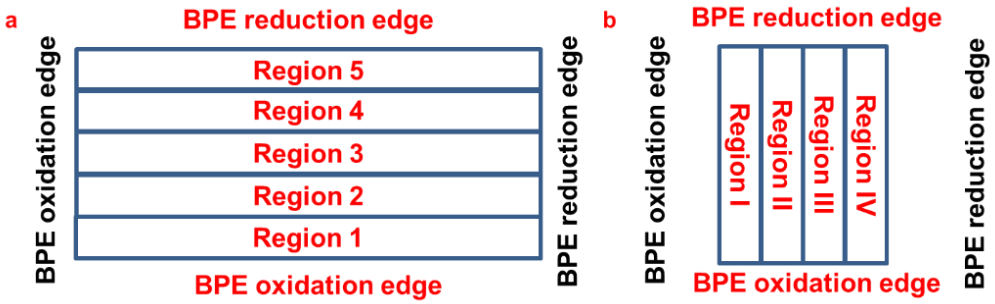

Figure 8.3- 3 Sketch of five different regions along the BPE width and (b) four regions along the BPE length.

After the bipolar electrochemistry experiment, the BPE samples were removed from the electrolyte, cleaned with soap water and dried the surface by hot air for the surface analysis. The corrosion volume was obtained by 3D laser scanning microscopy using Keyence VK-X200K microscopy.

8.35 Results and Discussion

Localised corrosion appearance

Figure 8.3- 4 (a) gives the locations of different corrosions on the BPE. The crevice corrosion generated at the interface of the resin and the BPE. A longer crevice covered length than pitting corrosion, indicates a lower nucleation potential. The general corrosion starts at the potential after the crevice corrosion stops. Between the general and pitting corrosion, a narrow passive region is determined, shows no corrosion at all. Figure 8.3- 4 (b) shows localised corrosion on the BPE without secondary bipolar potential, the pit size and pit density from region 1 to 5 is similar at this magnification. From region I to IV, the pit size is still similar, but pit density is reduced as the potential reduction. Some small pits are observed, which are the metastable pits. After applying the secondary bipolar potential, pit density changes; for +1 V from the secondary feeder electrode, the pitting size and density from region 1 to 5 is similar, as by a small secondary potential change is not enough to largely influence the corrosion. Increasing the secondary bipolar potential to +3 V, the pit covered length in region 1 is slightly longer than region 5. After applied at +5 V, the pit covered length is obviously increased in region 1 and reduced in region 5. Region 1 appears a darker area on the surface, caused by the general corrosion. The general corrosion comes from the pit electrolyte diffuse out of pits. As a large numbers of pits can offer enough pit electrolytes to corrode the BPE surface. After applied on the secondary feeder electrode over +7 V, pit covered length are dramatically increased in region 1 and 2, and largely reduced in region 4 and 5.

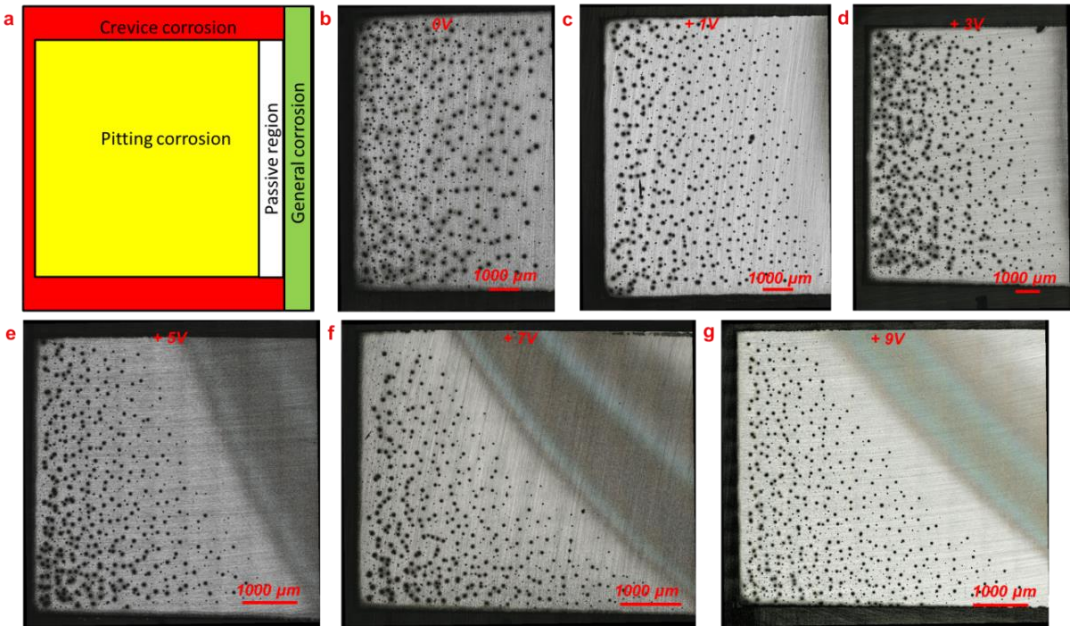

Figure 8.3- 4 The schematic diagram of the different corrosion on the BPEs. The localised corrosion region with potential from the secondary bipolar circuit from (b) 0 V, (c) + 1V, (d) + 3V, (e) +5V, (f) +7V and (g) +9V.

Figure 8.3- 5 gives the localised corrosion volume along the BPE only with primary bipolar electrochemistry (10V). To demonstrate the reproducibility of these results, five independent tests were carried out using identical sample dimensions and parameters. The corrosion volume from pitting and crevice corrosion is compared from region I to IV in these five independent samples. The volume of the crevice corrosion region is the sum of the crevice volume at the BPE oxidation edge and sides. Figure 8.3- 5 (a) shows the pit volume change from region I to IV, the largest overall pit volume (≈0.022 mm^3) is measured in region I and smallest pit volume (≈0.004 mm^3) is found in region IV. Figure 8.3- 5 (b) shows the crevice volume is highest (≈ 0.089 mm^3) in region I and lowest (≈ 0.003 mm^3) in region IV. Both of pitting and crevice corrosion in all regions has a similar volume in the 5 independent samples. So the bipolar electrochemistry for the corrosion test is repeatable and reliable.

Between region I and II, the crevice volume drop is larger than crevice volume drop in other regions. As the crevice also nucleates between the oxidation edge and the resin in region I, which has the largest corrosion volume due to the highest applied potential. At the same time, the pitting volume gap between region I and II is smaller than the pit volume gap between other

regions. The higher applied potential results in lower pit volumes, since most of the available current was consumed by the crevice corrosion at the oxidation edge. In region I, larger crevice corrosion results in less current available for pitting corrosion. So, the crevice corrosion is easier to gain enough current density to growth when compete with pitting corrosion.

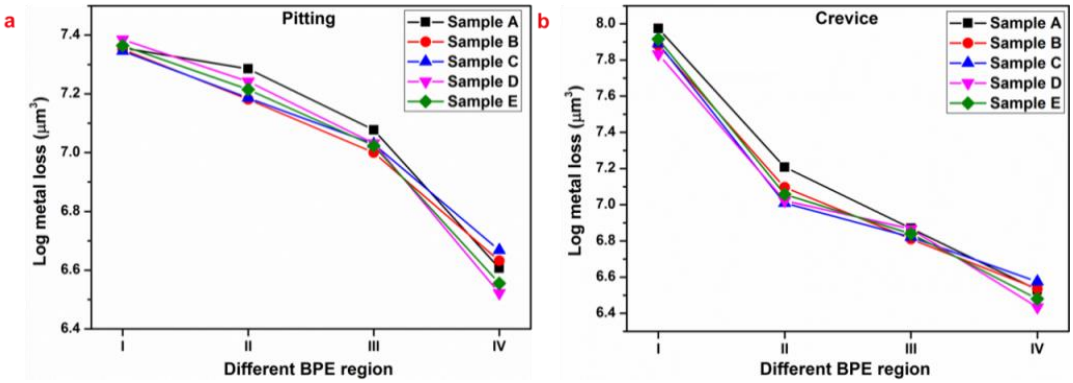

Figure 8.3- 5 Volume of (a) pitting corrosion and (b) crevice corrosion along the BPE with 5 different samples.

Advantages of bipolar electrochemistry test

The advantages of using the bipolar electrochemistry used for the corrosion test include the pit growth factor, corrosion volume, pits nucleation and growth probability under a wide range potential can be determined on one BPE. Figure 8.3- 6 gives the pits in Sample A in Figure 8.3- 5. Figure 8.3- 6 (a) shows the mean pit growth factor calculated from Equation 1, the mean pit growth factor is calculated from the deepest 10 pits in each region with the error bar stands for the standard deviation [24,25]. The pits nucleate at t=0 s.

$$\mathbf{y = k\, t^{0.5}} \qquad \text{Equation 1}$$

y is the pit depth (μm), k is the pit growth factor and t is the pit growth time (s).

The pit growth factor is around 2.75 from region I to IV, as pit growth factor is under diffusion control, independent to the applied potential [15]. Figure 8.3- 6 (b) gives the overall corrosion volume, which is linearly distribution from region I to IV, similar as the linearly potential distribution. Figure 8.3- 6 (c) gives the pit numbers in the BPE, which is almost linearly reduced from Region I to IV, as the pit nucleation probabilities is a function of applied potential [26].

Figure 8.3- 6 (d) gives the percentage of the pits with different depth, the percentage of pit depth < 45 μm is highest in region I, but the percentage of the pits > 60 μm in Region IV is highest. More pits are nucleated at a high applied potential, but the current density for each pit is small. So more pit repassivate. At a low applied potential, fewer pit nucleates but each pit gain enough current, which is easier become stable growth. The pits nucleation rate is higher at high applied potential, but lower probability for these pits become stable growth.

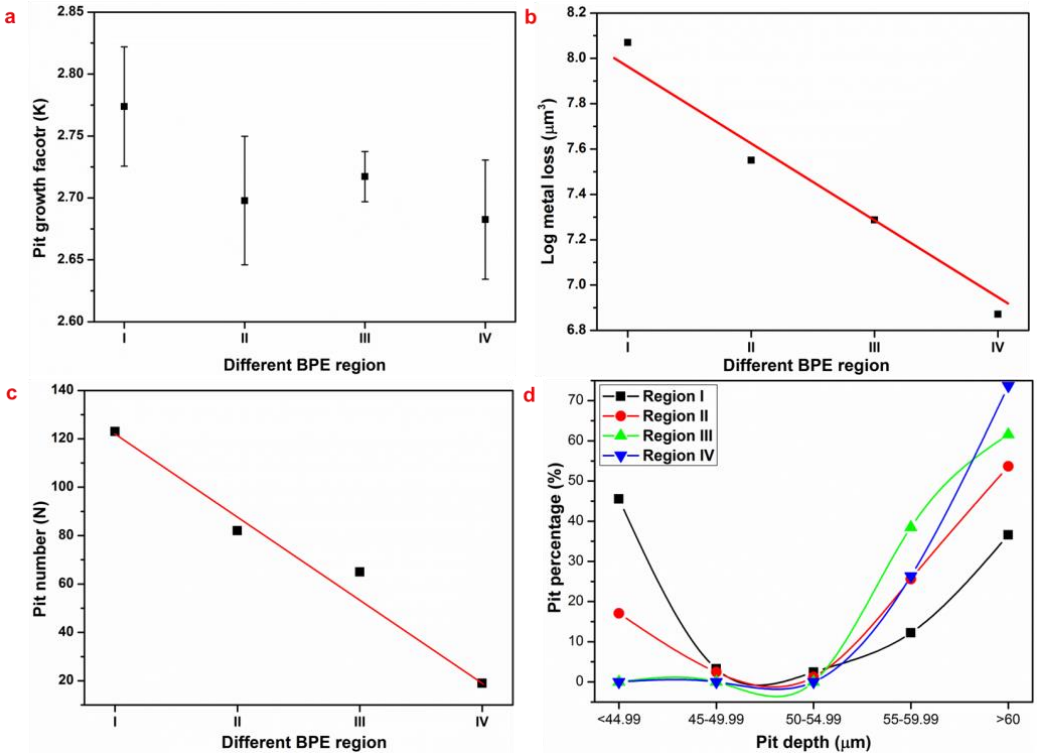

Figure 8.3- 6 The pit growth factor and (b) the localised corrosion volume along the BPE, (c) the numbers of pits and (d) the probability of the nucleate pit growth to different pit depth.

Overall localised corrosion on the BPE

Figure 8.3- 7 (a) gives the localised corrosion volume change with different secondary bipolar potential. The overall localised corrosion volume on the BPE is almost the same under different secondary bipolar potential, as the overall potential changed on the BPE is zero. Figure 8.3- 7 (b) shows the pit volume is slightly reduced with a higher secondary bipolar potential, but the crevice corrosion volume stays the similar value. This is caused by the

competition of the pitting and crevice corrosion, as the crevice corrosion can get more current than pitting corrosion. So the volume reduced in cathodic area as local potential reduced is smaller than the increase of the pit volume in anodic sites. Increasing the higher secondary bipolar potential, larger pit volume reduces at the cathodic sites, because the pit volume increase at anodic site is restricted, but both competition with crevice corrosion and competition between pits after they close to each other. So the overall pit volume is reduced with higher secondary bipolar potential. The crevice corrosion can get enough current, so the volume increased by in the anodic region and reduced in the cathodic region is balance. The crevice volume independent to secondary bipolar potential, but the pitting corrosion volume is reduced by higher secondary bipolar potential.

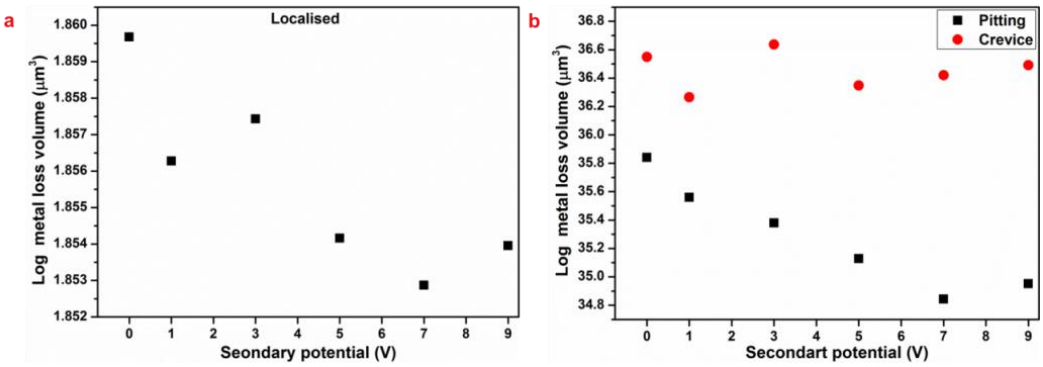

Figure 8.3- 7 The localised corrosion volume on the BPE with (b) the pitting and crevice corrosion volume on the BPE under different secondary bipolar electrochemistry potential.

Localised corrosion along the BPE width

Figure 8.3- 8 (a) shows the maximum pitting covered length on BPE width with different secondary bipolar potentials. Increasing the secondary bipolar potential, the pit volume increases in region 1 and 2, reduces in region 4 and 5, and constant in region 3, similar potential distribution on the BPE from secondary bipolar electrochemistry. In Figure 8.3- 8 (b), the crevice corrosion volume increased rate in region 1 is highest, as a longer distance between the BPE and the resin, which can nucleate the crevice corrosion. The crevice corrosion volume increase speed is lower in region 2, as the length of the BPE and resin is constant. Crevice corrosion volume increase is only caused by

the higher applied potential. Crevice corrosion volume is almost constant at region 3 and region 4, as the local potential change on the BPE is neglected in region 3 and 4. Crevice corrosion is largely reduced at region 5, which come from both of the the lower local potential and shorter length (between BPE side and resin) to nucleate the crevice corrosion.

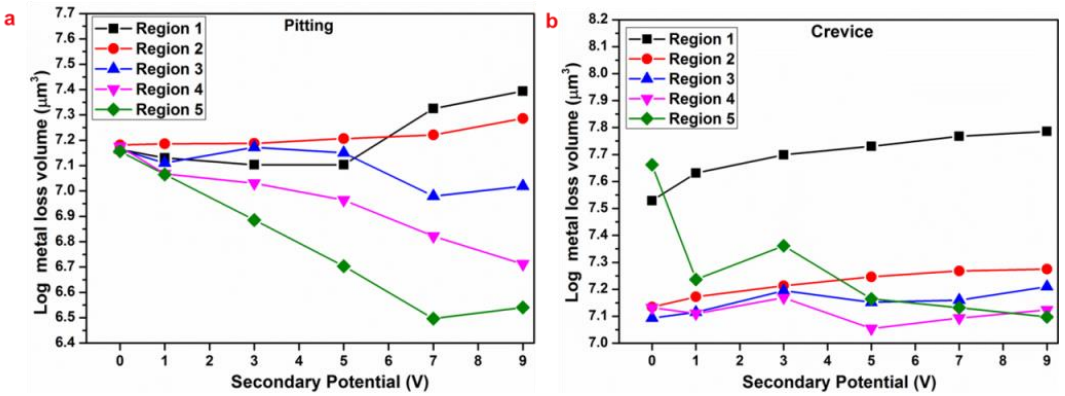

Figure 8.3- 8 The corrosion volume from (a) pitting corrosion and crevice corrosion in (b) with different secondary bipolar electrochemistry potential from region 1 to 5.

Figure 8.3- 9 shows the pit volume change caused by the different secondary bipolar potential. It is calculated from the measured volume under different secondary bipolar potential minus the volume at the same region without switch on the secondary bipolar potential. A zero line is marked, indicates zero corrosion volume changes secondary bipolar potential. In Figure 8.3- 9 (a), pit volume is almost the same before +5 V applied on the secondary bipolar potential in region 1, So most of extra current generated by higher secondary applied potential is consumed by crevice corrosion expansion. After +7 V, the pit volume increases volume increases which means pit can gain some of the extra current to grow from high increased current. In region 2, the pit volume is almost the same before +7 V on the secondary bipolar potential; enough current to support the pit expansion at +9 V. In region 3, the pitting corrosion is always slightly reduced after +7 V from secondary bipolar potential, as pit covered area is reduced by the negative applied potential. The reduced area also influences the pit volume expansion. After region 4, the pit volume is reduced after +1 V from the secondary bipolar potential, as the pit generation area is largely reduced higher cathodic potential from the secondary bipolar potential.

Figure 8.3- 9 (b) gives the crevice corrosion volume change from region 1 to 5 with different secondary bipolar potential. The crevice corrosion volume is increased in region 1, 2, and 3 even only at +1 V from the secondary bipolar potential. So, the crevice corrosion expansion at lower increased potential is easier than pitting corrosion. With a higher applied secondary bipolar potential, the larger crevice corrosion volume in region 1, 2 and 3 is largely increased. After region 4, the crevice corrosion volume is slightly reduced as the higher local negative applied potential. In region 5, the crevice corrosion is largely reduced, as both more negative applied potential and shorter length to nucleate the crevice corrosion in region 5. Both of region 4 and 5 show the crevice corrosion volume is reduced at a higher secondary bipolar potential.

Figure 8.3- 9 (c) offers the overall localised corrosion volume on the BPE changed from different secondary bipolar potential. In region 1, the localised corrosion volume is increased from 1.25 μm^3 at +1 V to 1.78 μm^3 at +9 V from the secondary bipolar potential. In region 2, the increased corrosion volume becomes smoother, from 1.12 μm^3 at +1 V to 1.41 μm^3 at +9 V. As lower increased potential and a shorter crevice corrosion length to nucleate crevice corrosion. In region 3, the localised corrosion volume is also constant with tiny fluctuating, as the neutral applied potential. In region 4, the change of the localised corrosion volume becomes negative, as a higher secondary bipolar potential results in a more negative volume local applied potential in this region. In region 5, the reduction of the localised corrosion volume reduction is larger than region 4 as a shorter crevice corrosion length to nucleate the crevice corrosion and a more local negative applied potential.

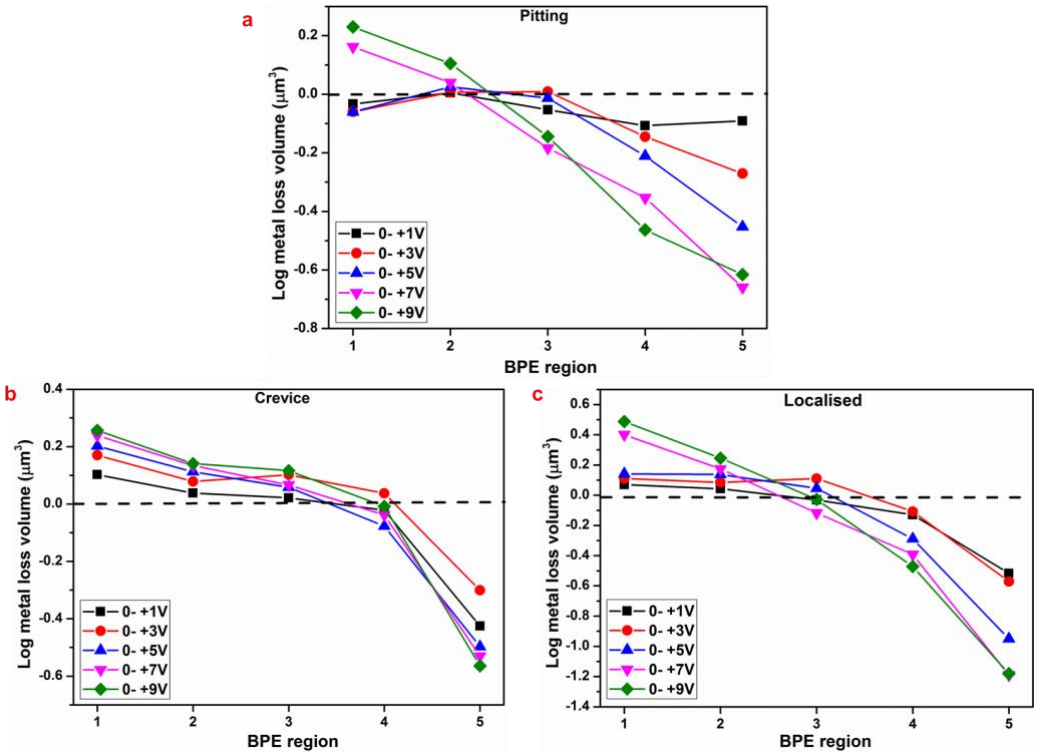

Figure 8.3- 9 The volume of (a) pitting corrosion and (b) crevice corrosion different secondary bipolar potential from region 1 to 5, and (c) the overall localised volume change on the BPE.

Localised corrosion along the BPE length

Figure 8.3- 10 (a) shows pitting corrosion along the BPE length with different secondary bipolar potential. In region I, the overall pit volume is similar which is independent to the secondary bipolar potentials. As the overall neutral potential change is neutral in this region. In region II, the pit volume is similar before +7 V from the secondary bipolar potential. Above +7 V, the pit volume is reduced with higher secondary bipolar potential, as pit volume in region 5 on the BPE width is reduced. In region III, the reduction of the pit volume starts at +5 V from the secondary bipolar potential. In region IV, the secondary bipolar potential can change the pit volume is only at +1 V. The secondary bipolar potential required to reduce the pit volume is decreasing from Region I to IV, which similar to the potential required to change the pit covered area in Region 1 to 5.

Figure 8.3- 10 (b) shows the crevice volume along the BPE length with different secondary bipolar potential. In region I, the crevice corrosion volume

is constant which is independent to secondary bipolar potential. In region II, the crevice corrosion volume is constant until +5 V from the secondary bipolar potential and then the crevice corrosion is slightly reduced at higher secondary applied potential. In region III, the reduction of the crevice crevice corrosion volume begins at +3 V from the secondary bipolar potential. In region IV, the reduction of the crevice corrosion volume is reduced after at +1 V from the secondary bipolar potential.

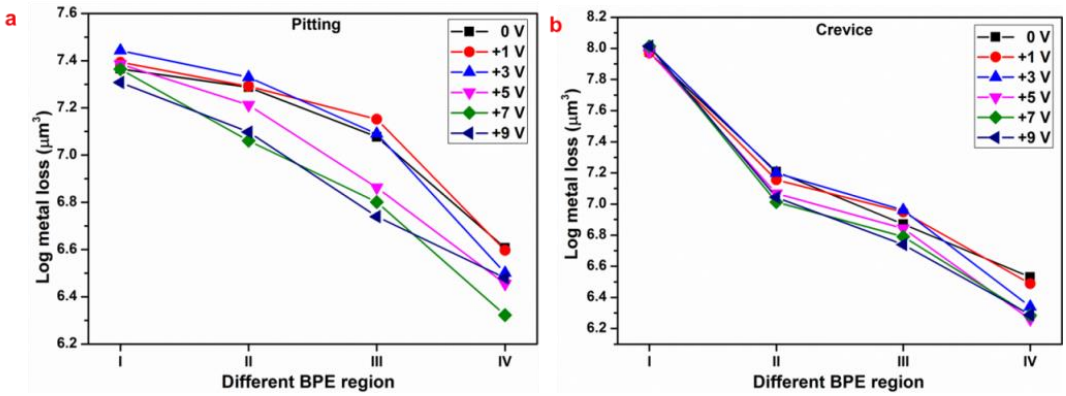

Figure 8.3- 10 The volume of (a) pitting corrosion and (b) crevice corrosion change with different secondary bipolar potential from region I to IV.

The crevice corrosion is more dangerous than the pitting corrosion, as lower critical potential to nucleate the crevice corrosion, crevice corrosion volume growth faster and easier with competition to the pitting corrosion. The crevice covered length is longer than the pit covered length, so the crevice corrosion nucleates at a lower applied potential than the pitting potential. At a small increment potential, the crevice corrosion can gain enough current to expand but pit volume is constant. At a high applied potential, the crevice corrosion volume increases faster than the metal loss volume from the pitting corrosion. So, crevice corrosion is the “winner” during the competition with pitting corrosion.

8.36 Conclusions

Bipolar electrochemistry is successful used accessing the localised corrosion, such as the pit growth factor, localised corrosion kinetics; pit nucleation rate and pit growth probability of under a wide range of applied different potential on one sample can be measured. Pit growth kinetics is independent to the

local applied potential, but the localised corrosion volume is proportional to the applied potential; higher pit nucleation rate but a lower stable pit is measured at a high local applied potential. Two-dimensional bipolar electrochemistry is created to get as a wider potential range and smoother potential gradient on the BPE. Crevice corrosion can be nucleated at a lower applied potential than pitting corrosion. Crevice corrosion can expand at lower applied potential with competition to the pitting corrosion. Crevice corrosion volume expands faster than pitting corrosion at higher applied potential.

8.37 References

[1] S. Munktell, M. Tydén, J. Högström, L. Nyholm, F. Björefors, Bipolar electrochemistry for high-throughput corrosion screening, Electrochemistry Communications. 34 (2013) 274–277.

[2] Y. Zhou, D.L. Engelberg, Application of a modified bi-polar electrochemistry approach to determine pitting corrosion characteristics, Electrochemistry Communications. 93 (2018) 158–161.

[3] N. Pébère, V. Vivier, Local Electrochemical Measurements in Bipolar Experiments for Corrosion Studies, ChemElectroChem. 3 (2016) 415–421.

[4] S.E. Fosdick, K.N. Knust, K. Scida, R.M. Crooks, Bipolar electrochemistry, Angewandte Chemie - International Edition. 52 (2013) 10438–10456.

[5] S.E. Fosdick, J.A. Crooks, B.Y. Chang, R.M. Crooks, Two-dimensional bipolar electrochemistry, Journal of the American Chemical Society. 132 (2010) 9226–9227.

[6] S.M. Sharland, A Review of The Theoretical Modelling of Crevice and Pitting Corrosion, Corrosion Science. 27 (1987) 289–323.

[7] R.T. Loto, Electrochemical Corrosion Characteristics of 439 Ferritic, 301 Austenitic, S32101 Duplex and 420 Martensitic Stainless Steel in Sulfuric Acid/NaCl Solution, Journal of Bio- and Tribo-Corrosion. 3 (2017) 24.

[8] B. Krawczyk, P. Cook, J. Hobbs, D. Engelberg, Corrosion Behavior of Cold Rolled Type 316L Stainless Steel in HCl Containing Environments, Corrosion. 73 (2017) 1346.

[9] A.M. Al-Zahrani, H.W. Pickering, IR voltage switch in delayed crevice corrosion and active peak formation detected using a repassivation-type scan, Electrochimica Acta. 50 (2005) 3420–3435.

[10] J.W. Oldfield, W.H. Sutton, Crevice Corrosion of Stainless Steels: I. A Mathematical Model, British Corrosion Journal. 13 (1978) 13–22.

[11] S.E. Lott, The Role of Inclusions on Initiation of Crevice Corrosion of Stainless Steel, Journal of The Electrochemical Society. 136 (2006) 973.

[12] Q. Hu, G. Zhang, Y. Qiu, X. Guo, The crevice corrosion behaviour of stainless steel in sodium chloride solution, Corrosion Science. 53 (2011) 4065–4072.

[13] D. Chen, E.H. Han, X. Wu, Effects of crevice geometry on corrosion behavior of 304 stainless steel during crevice corrosion in high temperature pure water, Corrosion Science. 111 (2016) 518–530.

[14] S.M. G.Burstein, P.Pistorius, The Nucleation and Growth of Corrosion Pits on Stainless Steel, Corrosion Science. 35 (1993) 57–62.

[15] P. Ernst, R.C. Newman, Pit growth studies in stainless steel foils. I. Introduction and pit growth kinetics, Corrosion Science. 44 (2002) 927–941.

[16] P.C. Pistorius, G.T. Burstein, Metastable Pitting Corrosion of Stainless Steel and the Transition to Stability, Philosophical Transactions of the Royal Society A: Mathematical, Physical and Engineering Sciences. 341 (1992) 531–559.

[17] J.N. Al-Khamis, H.W. Pickering, IR Mechanism of Crevice Corrosion for Alloy T-2205 Duplex Stainless Steel in Acidic-Chloride Media, Journal of The Electrochemical Society. 148 (2001) B314.

[18] P. Chemistry, P. Academy, Crevice Corrosion of Stainless Steels In Sodium Chloride Solution, Corrosion Science. 18 (1978) 953–960.

[19] H.K. Shu, F.M. Al-Faqeer, H.W. Pickering, Pitting on the crevice wall prior to crevice corrosion: Iron in sulfate/chromate solution, Electrochimica Acta. 56 (2011) 1719–1728.

[20] S.E. Lott, R.C. Alkire, The variation of solution composition during the initiation of crevice corrosion on stainless steel, Corrosion Science. 28 (1988) 479–484.

[21] N.J. Laycock, J. Stewart, R.C. Newman, The initiation of crevice corrosion in stainless steels, Corrosion Science. 39 (1997) 1791–1809.

[22] Y.H. Lee, Z. Takehara, S. Yoshizawa, The Enrichment of Hydrogen and Chloride Ions in The Crevice Corrosion of Steels, Corrosion Science. 21 (1981) 391–397.

[23] B.E. Wilde, E. Williams, The Relevance of Accelerated Electrochemical Pitting Tests to the Long-Term Pitting and Crevice Corrosion Behavior of Stainless Steels in Marine Environments, Journal of The Electrochemical Society. 118 (2007) 1057.

[24] M.K. Cavanaugh, R.G. Buchheit, N. Birbilis, Modeling the environmental dependence of pit growth using neural network approaches, Corrosion Science. 52 (2010) 3070–3077.

[25] O.O. Fatoba, R. Leiva-Garcia, S. V. Lishchuk, N.O. Larrosa, R. Akid, Simulation of stress-assisted localised corrosion using a cellular automaton finite element approach, Corrosion Science. 137 (2018) 83–97.

[26] D.E. Williams, J. Stewart, P.H. Balkwill, The nucleation, growth and stability of micropits in stainless steel, Corrosion Science. 36 (1994) 1213–1235.

8.4 On the Application of Bipolar Electrochemistry for Simulating Galvanic Corrosion of Dissimilar Stainless Steels

Yiqi Zhou[*1], Jiantao Qi[2], Dirk Lars Engelberg [1,3]

1.Corrosion & Protection Centre, Department of Materials, The University of Manchester, M13 9PL, Manchester, UK

2.College of New Energy, China University of Petroleum (East China), 266580, Qingdao China

3.Materials Performance Centre, The University of Manchester, M13 9PL, Manchester, UK

* Corresponding author: Yiqi.Zhou@postgrad.manchester.ac.uk

8.41 Highlights

- A bipolar electrochemistry method has been introduced for the characterisation of galvanic corrosion,
- Assessment of the galvanic coupling of two dissimilar stainless steel grades has been demonstrated,
- Type 304L austenitic stainless steel is more cathodic compared to type 420 ferritic stainless steel with exposure to HCl environment,
- An applied secondary potential controlled the overall galvanic corrosion response.

8.42 Abstract

The application of a bipolar electrochemistry technique to simulate the galvanic corrosion behaviour of dissimilar stainless steels is introduced. The technique allows comparison of the bipolar response by controlling the extent of localised corrosion as a function of an applied off-set potential. The setup was explored for simulating the galvanic performance of type 420 ferritic and type 304L austenitic stainless steel, yielding information about the anodic-vs-cathodic behaviour of both materials. The introduced approach provides a novel methodology to simulate the effect of galvanic coupling on the corrosion behaviour of stainless steels.

Keywords： Bipolar electrochemistry, stainless steel, pitting corrosion, crevice corrosion, galvanic corrosion

8.43 Introduction

Bipolar electrochemistry produces a potential gradient between two feeder electrodes, resulting in a continuous spectrum of anodic-to-cathodic electrochemical reactions occurring along the exposed surface [1–3]. This technique has already found application in synthesizing nano-sized palladium precipitates as well as bipolar Janus

particles [4,5]. Bipolar electrochemistry is now increasingly been explored for corrosion testing, as it significantly reduces experiment time and number of samples required; providing a simple experimental set-up with no contact needed between the sample and the apparatus [1–3,6,7]. A bipolar screening technique has also been applied for to assess susceptibility of lean duplex 2101 stainless steel welds, providing information about microstructure corrosion propensity [8]. Observation of the corrosion behaviour under even wider potential gradients can be achieved by using a modified bipolar electrochemistry approach via applying a direct off-set potential to the bipolar electrode (BPE) [1].

Localised corrosion, such as pitting and crevice corrosion, is typically caused by a local breakdown of the passive film [9,10]. Both pitting and crevice corrosion are influenced by the applied potential, halide concentration, pH value of the environment and temperature [11,12], with bipolar electrochemistry providing an experimental set-up for ambient temperature pitting corrosion testing of duplex stainless steel [7]. Crevice corrosion is influenced by the crevice geometry [13,14] and considered far more dangerous as crevices initiate at lower potentials and temperatures, as well shorter induction times. They can also grow without the presence of excessive halide ion concentrations [15,16].

In contrast, galvanic corrosion occurs when two metals or alloys with different electrochemical potentials are electrically coupled in the presence of a connecting electrolyte [17–19]. In a galvanic cell, the anodic part is where dissolution occurs, whereas the cathodic part is typically protected, i.e. cathodic reactions occur [20,21]. Galvanic corrosion is controlled by the exposed area ratio of anodic vs. cathodic sites. The electrochemical potential difference and distance between anode and cathode, electrolyte film thickness, and electrochemical reactions resistance also play an important role [22,23]. The standard guide ASTM G71-81 provides the framework for conducting and evaluating galvanic corrosion tests in electrolytes; however small currents from dissimilar galvanic couples, such as dissimilar stainless steels or different stainless steel microstructure are often challenging to measure. A wire beam electrode technique has recently been introduced for galvanic corrosion research [22,24], but the electrode size and distance between both electrodes severely limits the spatial resolution of this technique.

A new bipolar electrochemistry set-up is introduced here, where the anode and cathode of two dissimilar metals are directly compared to each other. This then provides the possibility to control potential differences between the two dissimilar

metal coupons, allowing simulation of the galvanic behaviour of each material. Corrosion potential gradients from a wide range of metallic systems can therefore be measured, ranked and compared using one test set-up. The viability of this approach is demonstrated by controlling the corrosion potential of two dissimilar stainless steels, here demonstrated by comparing austenitic type 304L with ferritic type 420. These two stainless steels have slightly different electrochemical open circuit potentials (OCP) and associated activation behaviours. Such differences are also present, for example, when the two phases in a duplex stainless steel microstructure are compared [22,23]. The electrochemical potential between the ferrite and austenite phase can also change via heat treatment, resulting in distinct changes of the anodic vs cathodic behaviour of these phases. The set-up presented in here can be explored, for example, to simulate these galvanic differences via application of different offset potentials [24,25].

8.44 Materials and Methods

The materials used in this study was annealed type 304L austenitic and type 420 ferritic stainless steels with their chemical compositions given in Table 8.4- 1

Table 8.4- 1 Chemical compositions of type 304L and 420 stainless steel

(wt%)	Cr	Ni	C	N	Mn	Bal
304L	18.2	8.1	0.025	0.045	/	bal.
420	13.7	/	0.46	/	0.39	bal.

Rectangular coupons with dimensions of 30 * 5 * 1 mm^3 (length * width * thickness) for type 304L stainless steel and 30 * 6 * 1 mm^3 for type 420 stainless steel were prepared. A copper wire was spot-welded to the rear of the type 420 and the type 304L coupon, which allowed a potential to be applied to either electrode (e.g. see the set-up in [1]). Both rectangular stainless steel coupons were then placed next to each other with a gap of 1 mm between them to avoid direct electrical contact. This bipolar electrode (BPE), made up of both stainless steels, was then embedded in Araldite resin, followed by grinding to a 1200 grit finish.

A sketch of the bipolar electrochemistry set-up is shown in Figure 8.4- 1 (a), with two Keysight E36105A power sources used in this arrangement. The

inner power source supplies both feeder electrodes (primary circuit), producing the potential gradient along the centred BPE. With a sufficiently high potential across the BPE, oxidation reactions occur next to the negative feeder electrode, and vice versa for the reduction reactions close to the positive feeder. The two Pt feeder electrodes and the Pt auxiliary electrode had each a surface area of 4 cm^2. The auxiliary electrode was positioned at the same height as the other two feeder electrodes, with a distance of ≈ 25 mm away from the BPE, the auxiliary electrode was located away from the primary feeder electrodes.

A second power source was connected to an auxiliary electrode, to be able to control and change the electrochemical potential of either the type 420 or the type 304L sample. The idea here is to be able to compensate (or further increase) differences in the corrosion behaviour of both dissimilar metals by applying an off-set potential to one of the electrodes. Both stainless steels are expected to assume a mixed potential, if both coupons are electrically connected to each other, resulting in galvanic coupling. Since both stainless steels are here in this set-up not in contact, the applied off-set potential needs to bridge the gap between both electrochemical potentials, directly simulating the galvanic corrosion response.

Figure 8.4- 1 (b) shows the specimen arrangement using two dissimilar metal coupons. Two different bipolar experiments were carried out to probe the galvanic effect of both electrodes in close proximity to each other. In the first set-up, the type 420 stainless steel is electrically connected to the auxiliary electrode (secondary circuit), and the type 304L sample only embedded in the resin. In the second set-up, the type 304L sample is electrically connected to the auxiliary electrode, with the type 420 isolated in the resin.

Figure 8.4- 1 (c) describes how the extent of crevice and pitting corrosion was assessed and compared. A small difference in exposed sample area size was chosen to be able to access information about anodic vs. cathode area effects. The interfaces between the metal coupons and the resin were labelled site I and site II, to unambiguously be able to assess and categorise the development of crevices at both interfaces. The labelled regions on both

coupons had each a width of 1 mm, with 5 regions identified on the type 304L and 6 regions present on the type 420 samples. The corrosion response in these regions is compared to each other, yielding information about the corrosion response of both meals exposed to the bipolar potential gradient.

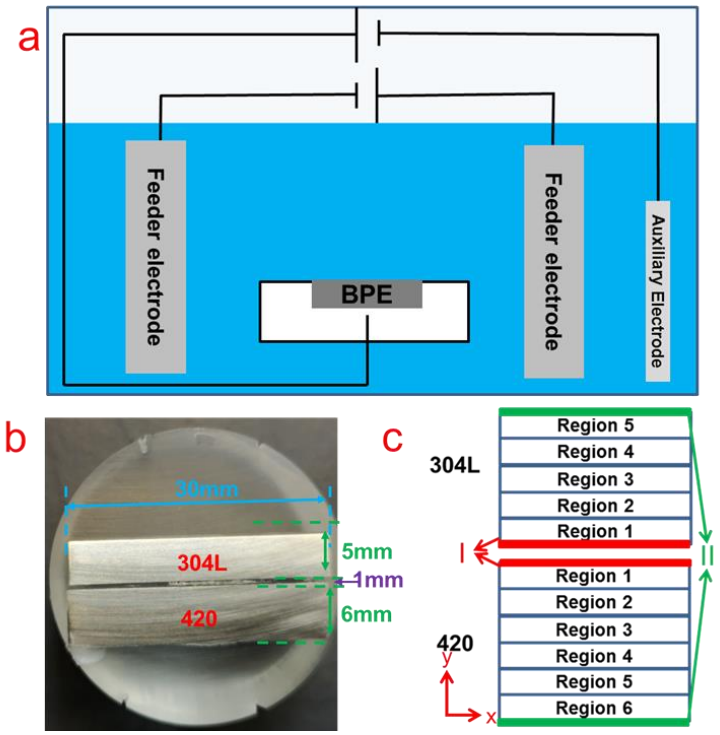

Figure 8.4- 1 (a) Sketch of the the bipolar electrochemistry set-up and (b) top-view of a bipolar electrode with the two dissimilar metals (type 304L and 420 stainless steel), with (c) the different regions of the BPE with the two (I and II) crevice corrosion sites highlighted.

The electrolyte used was 200 ml of 0.1M HCl, and the distance between the two feeder electrodes was set to 60 mm. The BPE was centred between the two feeder electrodes. The potential applied between the primary feeder electrodes was 10 V, with the externally auxiliary applied potential on the auxiliary circuit varied between 0 V and +3 V. The duration of each experiment was 10 min. For the experiment, the power supply for bipolar electrochemistry and auxiliary applied potential were switched on simultaneously.

An IVIUM-Compactstat combined with IVIUMsoft software was also used to determine the OCP of both stainless steels individually. A saturated calomel electrode (SCE) was used as reference electrode, which was then either connected to the type420 stainless steel or the type 304L sample. The mixed

corrosion potential of our electrode configuration was also obtained by electrically connecting both type 304L and 420 stainless steels with each other and measured vs. SCE.

After the experiment had finished, the BPE was removed from the electrolyte, rinsed in deionized water and dried for subsequent surface topography analysis. For pitting and crevice corrosion analysis, the samples were placed in an ultrasonic bath with deionized water to collapse and remove lacy pit covers. The dissolved pit volumes were measured by using a 3D Keyence VK-X200K laser confocal microscope. The differences in dissolved volume and the visual appearance was used to compare the corrosion behaviour of both stainless steels.

8.45 Results and Discussion

The measured OCP for type 304L stainless steel in 0.1M HCl is -0.11 V_{SCE}, slightly higher than the -0.51 V_{SCE} measured for type 420 stainless steel. We would therefore expect the Type 420 stainless steel to act as the anode after coupling with type 304L stainless steel, in-line with galvanic corrosion test reported in the literature [19,25]. The mixed OCP is -0.36 V_{SCE} after connecting both electrodes (types 304L and 420 stainless steels) with each other. The potential difference between the Pt electrode vs. type 420 electrode is +0.98 V_{SCE}, and vs. type 304L electrode is +0.58 V_{SCE}. It should be noted that for all these initial measurements, the primary feeder circuit was turned off.

Once the primary bipolar circuit is switched on, an electrical field develops between both feeder electrodes, resulting in a potential gradient acting along the centred BPE. he potential distribution is quasi-linear along the centre of the BPE, with the potential at the oxidation edge resulting in slightly increased potential responses; i.e. slightly more positive at the oxidation edge, and more negative at the reduction edge. Similar gradients have also been obtained for a number of other stainless steel samples [1,6,7].

Figure 8.4- 2 shows optical images of the anodic side of both stainless steels with only the primary bipolar circuit acting on them (0V) and with different applied secondary potentials via the auxiliary electrode. The values (+1V, etc.)

on the top of each image indicate the different secondary potentials, with for all measurements the primary bipolar circuit set to 10 V.

Without applying a secondary potential (0V), far more pits are observed on type 420 supporting the anodic characteristics of type 420 BPE compared to type 304L stainless steel. Region (1) of the type 304L coupon even shows an area depleted in corrosion pits, indicating galvanic protection possibly exerted by far more current consumption of the type 420 electrode. In this set-up, both materials are only exposed to the primary BPE circuit, with the same potential gradient acting along both electrodes. No difference in pit density and distribution would be expected if both electrodes had the same electrochemical corrosion behaviour; however, it is clear in this arrangement that the Type 420 stainless steel is able to partially protect the adjacent region of the type 304L sample.

With increasing the applied potential on the type 420 sample, the pit-covered length in region 1 on the 304 sample is gradually reduced from +1 V to +3 V (Figure 8.4- 2). This is caused by the availability of galvanic current ($\mathrm{i_g}$), the potential between galvanic couples and the current shown in Equation 1 [18,22,25]

$$\mathrm{i_g} = \frac{\mathrm{E_c} - \mathrm{E_a}}{\mathrm{R_a} + \mathrm{R_c} + \mathrm{R_S}} \qquad \text{Equation 1}$$

E_c and E_a are the potential of cathode and anode, $\mathrm{R_a}$ and $\mathrm{R_c}$ are the reaction resistance of anode and cathode, and R_s is the solution resistance. With a higher potential between the standard BPE and the secondary BPE (assume $\mathrm{R_a}$, $\mathrm{R_c}$ and $\mathrm{R_s}$ is constant), differences in galvanic currents ($\mathrm{i_g}$) are generated. The presence of similar electrochemical potentials of both samples then results in shorter pit-covered length along both electrodes in region 1, as shown in Figure 8.4- 2. Differences in the overall response of the various regions containing corrosion pits are apparent with increasing secondary potentials, in particular along the interface between both dissimilar stainless steel samples.

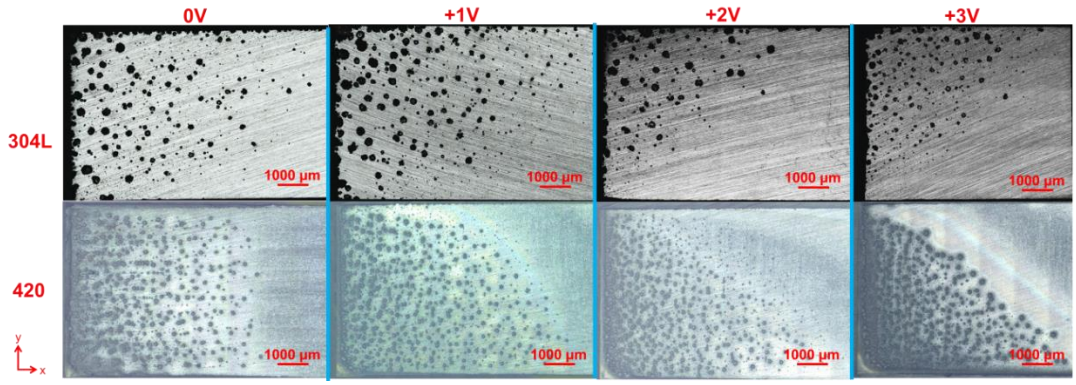

Figure 8.4- 2 Optical images of the corrosion pit covered areas on standard type 304L and type 420 as a function of applied secondary potentials from 0 V to +3 V.

Comparing the attack of both stainless steels without superimposed secondary potential (0 V), it is apparent that the type 304L has in general far fewer pits and far less corrosion close to the interface with the type 420 sample. Interestingly, individual pits nucleated at slightly lower potentials on type 304L electrode, showing small pits further to the right in most images shown in Figure 8.4- 2. The type 420 sample draws more current to the sample surface, leaving the region of the type 304L sample close to the adjacent interface un-attacked. The effect of the secondary applied potential on both the standard type 304L and type 420 is apparent, with a secondary applied potential immediately indicating a reduction of corrosion on type 304L. The corrosion attack on type 420 also becomes more asymmetric, with pits nucleating at higher potentials (shorter pit-covered length) due to the galvanic protection.

To quantify these observations, the length and volume of all corrosion pits and crevice containing regions was measured by laser confocal microscopy. Figure 8.4- 3 (a) shows the length of crevices on both materials as a function of applied auxiliary potential to the other sample. The length of the observed crevice (I) at the interface between both samples is obviously reducing with increasing potential, which can also be seen in Figure 8.4- 2. The crevice in type 420 at the interface away from the type 304L sample (site II, Figure 8.4- 1) is increasing in length. Interestingly, no effect is observed on the 304L stainless steel crevice in region 5, as the galvanic current cannot reach the end of this region due to the longer distance to the cathode.

Figure 8.4- 3 (b) shows the total dissolved corrosion volume as a function of the applied secondary potentials to the other sample, which is the sum of both pitting and crevice corrosion. The type 304L sample always has lower overall pit volumes, indicating far better pitting corrosion resistance. Both type 304L and 420 BPEs show similar trends, having less localised corrosion as a function of higher applied auxiliary potentials.

Figure 8.4- 3 (c) shows the corrosion volume in each region for type 304L. Without the superimposed secondary polarisation the corrosion volume is similar in all regions. A larger corrosion volume is measured in region 5, related to the crevice corrosion (site II). Increasing the applied secondary potential to the 420 counter electrode, results in more regions on Type 304L being protected and a reduction of the corrosion volume is apparent. Region 1 is protected with a superimposed potential > +1 V, with the corrosion volume in region 3 reduced at +2 V, and region 4 after a potential of +3 V. The application of a higher secondary potential to the type 420 sample resulted in far less corrosion and larger protected areas on type 304L stainless steel. The overall change in corrosion behaviour of both electrodes is demonstrated, pointing towards a combined effect of the effect of galvanic coupling and material characteristics.

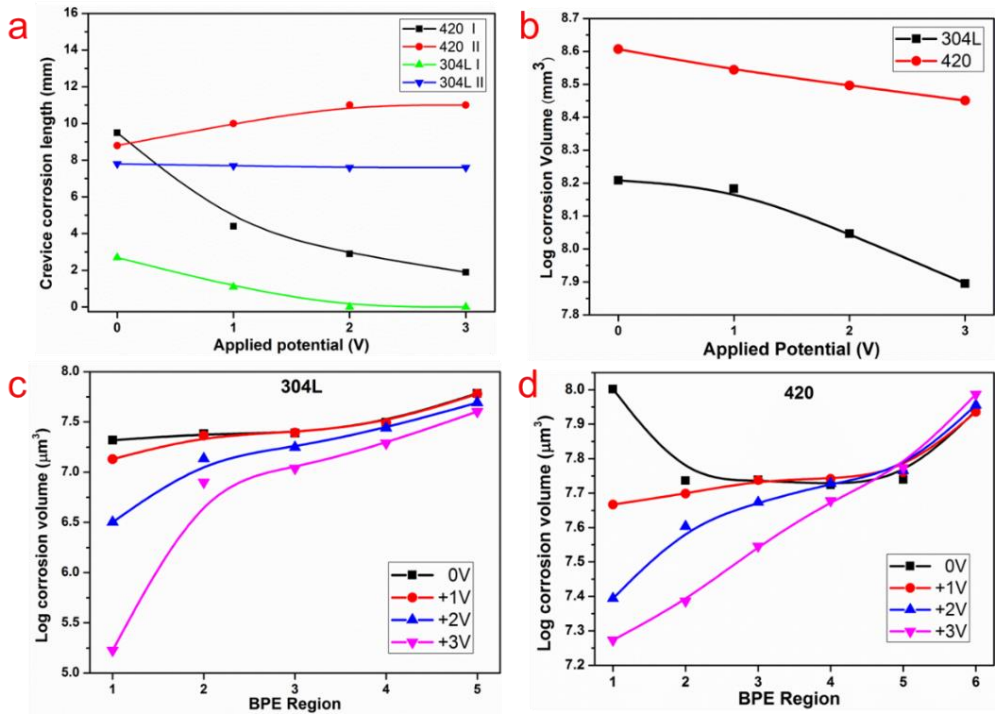

Figure 8.4- 3 (a) The crevice covered length and (b) the overall corrosion volume on the standard BPE with different auxiliary potentials. The corrosion volume in (c)Type 304L standard BPEs and (d) Type 420 standard BPEs in different regions and different auxiliary potentials.

Figure 8.4- 3 (d) summarizes the corroded volume of the type 420 sample. With only the primary bipolar gradient acting on the sample, the type 420 shows the highest corrosion volume in region 1, as both the crevice geometry in site I and the galvanic current increase the total corrosion volume. The observed corrosion is similar from region 2 to region 5, which indicates no galvanic effect. In region 6, the corrosion volume increased again due to the crevice at site II. Introducing a secondary potential of up to +3 V to the 304L, results in a significant reduction of the dissolved volume in the adjacent type 420 sample from region 1 to region 3.

Interestingly, the corrosion volume of the type 420 dropped by nearly an order of magnitude close to the interface. For both materials, the localised corrosion volume is reduced with higher applied secondary potentials as more galvanic current is generated from the larger potential difference. So, the galvanic protection on the cathode is a function of distance to the anode and the potential difference between both stainless steel samples.

In comparison to, for example, the wire beam electrode (WBE) technique [26], the bipolar approach introduced here produces far more controllable means to assess galvanic coupling of two dissimilar metals. Several different routes are currently explored for ranking the microstructure response as a function of galvanic potential. The introduced method has the potential advantage to quantify the galvanic corrosion behaviour of dissimilar metals under a wide range of applied potential by using a simple sample set-up and fast corrosion screening.

8.46 Conclusions

A bipolar electrochemistry approach has been introduced to measure the galvanic corrosion between two dissimilar stainless steels. The galvanic corrosion response is controlled by the secondary potential applied, providing assessment of the galvanic coupling of two dissimilar stainless steel grades.

The type 304L austenitic stainless steel was more cathodic than the type 420 ferritic stainless steel, with the applied secondary potential controlling the overall galvanic corrosion response.

8.47 References

[1] Y. Zhou, D.L. Engelberg, Application of a modified bi-polar electrochemistry approach to determine pitting corrosion characteristics, Electrochem. Commun. 93 (2018) 158–161.

[2] S. Munktell, M. Tydén, J. Högström, L. Nyholm, F. Björefors, Bipolar electrochemistry for high-throughput corrosion screening, Electrochem. Commun. 34 (2013) 274–277.

[3] N. Pébère, V. Vivier, Local electrochemical measurements in bipolar experiments for corrosion studies, ChemElectroChem. 3 (2016) 415–421.

[4] J.C. Bradley, S. Babu, P. Ndungu, Contactless tip-selective electrodeposition of palladium onto carbon nanotubes and nanofibers, Fullerenes Nanotub. Carbon Nanostructures. 13 (2005) 227–237.

[5] G. Loget, D. Zigah, L. Bouffier, N. Sojic, A. Kuhn, Bipolar electrochemistry: from materials science to motion and beyond, Acc. Chem. Res. 46 (2013) 2513–2523.

[6] Y. Zhou, D.L. Engelberg, On the application of bipolar electrochemistry to characterise the localised corrosion behaviour of type 420 ferritic stainless steel, Metals (Basel). 10 (2020) 794.

[7] Y. Zhou, D.L. Engelberg, Fast testing of ambient temperature pitting corrosion in type 2205 duplex stainless steel by bipolar electrochemistry experiments, Electrochem. Commun. 117 (2020) 106779.

[8] Y. Zhou, A. Kablan, D.L. Engelberg, Materials characterization metallographic screening of duplex stainless steel weld microstructure with a bipolar electrochemistry technique, Mater. Charact. 169 (2020) 110605.

[9] G.S. Frankel, Pitting corrosion of metals a review of the critical factors, J. Electrochem. Soc. 145 (1998) 2186–2198.

[10] S.M. Sharland, A review of the theoretical modelling of crevice and pitting corrosion, Corros. Sci. 27 (1987) 289–323.

[11] B. Krawczyk, P. Cook, J. Hobbs, D. Engelberg, Corrosion behavior of cold rolled type 316L stainless steel in HCl containing environments, Corrosion. 73 (2017) 1346.

[12] G.R. Engelhardt, D.D. MacDonald, Possible distribution of potential and corrosion current density inside corroding crevices, Electrochim. Acta. 65 (2012) 266–274.

[13] Q. Hu, G. Zhang, Y. Qiu, X. Guo, The crevice corrosion behaviour of stainless steel in sodium chloride solution, Corros. Sci. 53 (2011) 4065–4072.

[14] D. Chen, E.H. Han, X. Wu, Effects of crevice geometry on corrosion behavior of 304 stainless steel during crevice corrosion in high temperature pure water, Corros. Sci. 111 (2016) 518–530.

[15] P. Chemistry, P. Academy, Crevice corrosion of stainless steels in sodium chloride solution, Corros. Sci. 18 (1978) 953–960.

[16] Y.H. Lee, Z. Takehara, S. Yoshizawa, The Enrichment of Hydrogen and Chloride Ions in The Crevice Corrosion of Steels, Corros. Sci. 21 (1981) 391–397.

[17] D.L. Zhang, W. Wang, Y. Li, An electrode array study of electrochemical inhomogeneity of zinc in zinc/steel couple during galvanic corrosion, Corros. Sci. 52 (2010) 1277–1284.

[18] Z.Z. Wang, Y.Y. Li, G.A. Zhang, Inhibitive effects of inhibitors on the galvanic corrosion between N80 carbon steel and 13Cr stainless steel under dynamic supercritical CO 2 conditions, Corros. Sci. 146 (2019) 121–133.

[19] Z.F. Yin, M.L. Yan, Z.Q. Bai, W.Z. Zhao, W.J. Zhou, Galvanic corrosion associated with SM 80SS steel and Ni-based alloy G3 couples in NaCl solution, Electrochim. Acta. 53 (2008) 6285–6292.

[20] M. Pourbaix, Applications of electrochemistry in corrosion science and in practice, Corros. Sci. 14 (1974) 25–82.

[21] X.G. Zhang, E.M. Valeriote, Galvanic protection of steel and galvanic corrosion of zinc under thin layer electrolytes, Corros. Sci. 34 (1993) 1957–1972.

[22] G. Song, B. Johannesson, S. Hapugoda, D. StJohn, Galvanic corrosion of magnesium alloy AZ91D in contact with an aluminium alloy, steel and zinc, Corros. Sci. 46 (2004) 955–977.

[23] J.X. Jia, G. Song, A. Atrens, Influence of geometry on galvanic corrosion of AZ91D coupled to steel, Corros. Sci. 48 (2006) 2133–2153.

[24] Y.J. Tan, Wire beam electrode: A new tool for studying localised corrosion and other heterogeneous electrochemical processes, Corros. Sci. 41 (1999) 229–247.

[25] Y.Y. Li, Z.Z. Wang, X.P. Guo, G.A. Zhang, Galvanic corrosion between N80 carbon steel and 13Cr stainless steel under supercritical CO 2 conditions, Corros. Sci. 147 (2019) 260–272.

[26] L. Pang, Z. Wang, Y. Zheng, X. Lai, X. Han, On the localised corrosion of carbon steel induced by the in-situ local damage of porous corrosion products, J. Mater. Sci. Technol. 54 (2020) 95–104.

9 Application of bipolar electrochemistry

9.1 Introduction

Bipolar electrochemistry can be used in a wider application. Such as measuring and comparing the corrosion changed by microstructure evolution, such as welded DSS. The pitting corrosion influenced by microstructure evolution under a wide range of applied potential could be measured in a single experiment. The gravity influenced pitting corrosion under a wide range of applied potential can be easily determined from the bipolar electrochemistry setup. For brass dezincification, 3-electrode potentio-dynamic polarisation test was used but it had some limitations. Such as the brass surface conditions changed by previous applied potential, the current response is influenced by the corrosion product. However, bipolar electrochemistry for the brass dezincification research can avoid these problems.

The first paper (chapter 9.2) introduces the corrosion test of a welded DSS 2101. Bipolar electrochemistry tested the crevice, transpassive, and pitting corrosion in the three zones (FZ, HAZ, and BM) of welded DSS 2101. The different corrosion resistance was caused by different microstructure and alloying elements partitions. The pitting corrosion in HAZ was lowest, however, the crevice corrosion and transpassive corrosion resistance was lowset in the HAZ.

The second paper (chapter 9.3) introduces three different sample surface exposure orientations: (faceup, perpendicular, and facedown) to simulate the gravity influences the pit corrosion by bipolar electrochemistry. Gravity changed the current density distribution on the BPE, but potential distribution on the BPW was independent to gravity. The pit shapes and pit growth kinetics changed by gravity in a wide range of applied potential, but the gravity did not change the pit depth.

The third paper (chapter 9.4) gives the brass dezincification. The change of the corrosion product films by different applied potential could be determined along the BPE. The optimized potential to grow a dense and thick corrosion products which can reduce further dezincification were measured. At high

applied potential, corrosion products cannot be formed. In this stage, the Cu ions dissolution rate could be controlled, which was used in the application, such as Sterilization.

9.2 Metallographic Screening of Duplex Stainless Steel Weld Microstructure with a Bipolar Electrochemistry Technique

Yiqi Zhou[*1], *Abdulaziz Kablan*[2], *Dirk Lars Engelberg*[1,2]

1.Corrosion & Protection Centre, School of Materials, The University of Manchester, M13 9PL, Manchester, UK

2.Materials Performance Centre, The University of Manchester, M13 9PL, Manchester, UK

* Corresponding author: Yiqi.Zhou@postgrad.manchester.ac.uk

9.21 Highlights

- A bipolar electrochemistry screening approach is introduced to reveal local corrosion susceptibility of weld microstructures.
- A lean duplex stainless steel weld has been assessed with the most severe etch response found at the Fusion Zone (FZ) - Heat-Affected Zone (HAZ) interface.
- The ferrite selectively dissolved forming corrosion pits, with the austenite dissolving at higher applied potentials.
- Differences of local weld susceptibility were associated with changes in ferrite-austenite fraction and local weld chemistry.

9.22 Abstract

A novel bipolar electrochemistry screening method to reveal corrosion susceptibility of weld microstructures is introduced. This metallographic method is applied to characterise the weld microstructure of a lean duplex stainless steel. The corrosion behaviour of the Fusion Zone (FZ), Heat Affected Zone (HAZ) and Base Metal (BM) was revealed, with the most severe etch response found at the interface between Fusion Zone (FZ) – Heat Affected Zone (HAZ). Transpassive and crevice corrosion were more significant in the FZ, with the highest corrosion resistance observed in the BM. The observed behaviour was linked to differences in local element distributions and the ferrite-to-austenite phase fraction. Corrosion pits formed via preferential dissolution of the ferrite, with the austenite preferentially dissolving in the transpassive region.

Keywords: Bipolar electrochemistry, Stainless steel, Corrosion screening, Weld Microstructure, Heat Affected Zone

9.23 Introduction

Bipolar electrochemistry produces a quasi-linear potential gradient along the interface of a bipolar electrode (BPE), resulting in access to full spectrum of anodic-to-cathodic electrochemical reactions [1–5]. This technique can be applied to assess corrosion properties of stainless steels, by using a simple experimental setup which is also designed for high throughput material screening. Bipolar screening techniques have been applied to assess room temperature pitting corrosion in type 316 austenitic and type 2205 duplex stainless steel [1,5] as well as for observations of localised corrosion in type 420 ferritic stainless steel [6].

Duplex stainless steels (DSS) are typically based on balanced phase fractions of ferrite (α) and austenite (γ), with excellent mechanical properties and corrosion resistance [7–10]. However, DSS are susceptible to localised corrosion, with pitting observed under atmospheric exposure at elevated temperature [11]. Lean duplex stainless steel, such as grade 2101 (21%Cr-1%Ni) has attracted a lot of attention, as the Ni and Mo are replaced by Mn and N, whilst maintaining superior corrosion resistance over type 304L stainless steel [12–14]. During welding, DSS is typically subjected to a series of thermal cycles, with unfavourable phase transformation and non-metallic precipitations then located in the HAZ or within the FZ. Heat input is one of the factors to determine the cooling rate of the welding process. Generally, a relatively high heat input is beneficial to the microstructure as more austenite reforms during the cooling stage. However, deleterious secondary phases can always precipitate in most DSS microstructures, such as σ and χ, lowering the corrosion resistance [9,15–17]. At low heat inputs, the ferrite to austenite transformation is suppressed, resulting in lower austenite fraction in the HAZ and FZ. As a consequence of this unbalanced ratio of microstructure phases, the mechanical and corrosion resistance properties are greatly affected [9,13,15,18]. To improve the corrosion resistance of welded lean DSS, post-weld heat treatment can be applied [15,19]. In welded lean DSS 2101, the pitting corrosion resistance can also be improved by using 90 % N_2+10 % H_2 as backing gas [20]. In contrast, post-weld cleaning treatments have not been found to be effective for improving the pitting corrosion resistance of lean DSS

2101, which has been attributed to the presence of manganese-rich oxide particles [21].

Pitting corrosion is the localised breakdown of a passive film, followed by rapid metal dissolution [22]. Pitting corrosion often nucleates at MnS or Cr depleted region [23], but in DSS, localised corrosion nucleation sites also relate to selective phase dissolution of either the ferrite or austenite, with the local environment and chemistry affecting dissolution sites [24,25]. Pitting corrosion is influenced by the concentration of Cl^-, applied potential, and electrolyte temperature [26], and the size and ratio of ferrite-austenite [27]. Metastable pit growth requires a lacy cover to act as a diffusion barrier to maintain a high concentration of Cl^- and low pH electrolyte [28,29]. In lean DSS 2202, the size of the ferrite phase influences the porosity of lacy cover, which affects pitting corrosion via changing the ion exchange inside the pit to the bulk electrolyte [30]. Stable pit growth is associated with a critical electrochemical potential (E_{pit}) above a critical pitting temperature (CPT) [31,32]. Stable pits can grow without lacy covers, as the large pit volume/depth act as the diffusion barrier [33,34].

In the work reported here, the bipolar electrochemistry technique was explored for weld microstructure characterisation, clearly demonstrating applicability of this technique for corrosion susceptibility screening. The main advantage is the direct observation of different corrosion responses, comparing the BM, HAZ, and FZ at different applied potentials. This observation can then be correlated to the microstructure of DSS 2101, determined by Electron Backscattered Diffraction (EBSD) analysis.

9.24 Materials and Methods

A lean DSS 2101 with a composition (wt %) of 21.4 Cr, 1.6 Ni, 5.02 Mn, 0.3 Mo, 0.21 N, 0.02 C, and Fe (bal.) was used in this study. Two rectangular DSS 2101 samples were welded together using a plasma + TIG machine welding process. The weld seam was then reworked according to DIN EN ISO 5817 D. Samples for electrochemical testing were prepared, with each sample containing a combination of base material (BM), heat affected zone (HAZ), and the fusion zone (FZ).

Standard 3-electrode potentiodynamic polarisation tests were carried out in an AVESTA cell at room temperature using an aqueous 0.1M HCl solution. A platinum electrode and Saturated Calomel Electrode (SCE) reference electrode were used, in combination with a CS2350 Bipotentiostat and CS Studio-5 software. The open circuit potential (OCP) was stabilised for 10 min, followed by potentiodynamic polarisation tests from -200 mV_{OCP} until the current density exceeded 0.1 mA/cm^2, using a scan rate of 1 mV/s.

A bipolar electrode (BPE) is shown in Figure 9.2- 1 (a) with a dimension of 30 mm x 22 mm x 5 mm (Length * Width * Thickness). The FZ had a width of 7 mm, and the BM had a width of 15 mm, with the HAZ located in between the FZ and BM. The surface was prepared to 1200 grit, followed by polishing to 1 µm diamond paste finish. The sides of the BPE were ground to 800 grit, and a lacquer then applied to cover all side faces and the bottom. For the potentiodynamic polarisation tests, the samples were cut to 30 * 30 * 5 mm^3 (Length * Width * Thickness) and finished via grinding and polishing to 1 µm, ready for testing in the Avesta cell. For the EBSD analysis, the sample was ground to 4000 grit and polished to 0.25 µm diamond paste finish, followed by a fine polishing using OPS Colloidal Silica.

The schematic in Figure 9.2- 1 (b) demonstrates the setup for the bipolar electrochemistry experiments. A Keysight E36232A DC power supply was used as a power source for the feeder electrodes. A constant current (galvanostatic) of 1 A was applied between the feeder electrodes, with the distance between the electrodes set to 60 mm, and the BPE centred in between. Each platinum feeder electrode had a surface area of 4 cm^2, and the experiment was conducted in 200 ml of 0.1M HCl for 5 min.

After corrosion testing, all samples were removed from the electrolyte, washed and rinsed in soap water, and dried in hot air. A Keyence VK-200K laser confocal scanning microscope was used to determine corrosion morphologies. A Zeiss Sigma VP FEG-SEM was used for SEM imaging, EDX and EBSD analysis. EDX mapping was carried out using Aztec software at 20 kV to characterise the chemical compositions of the ferrite and austenite phase, and to analyse areas around pits where selective dissolution is most susceptible.

The EDX detector used was an x-max 150 detectors from oxford instrument. For EBSD, a step size with 1.26 µm was applied for the microstructure and phase analysis at 20 kV.

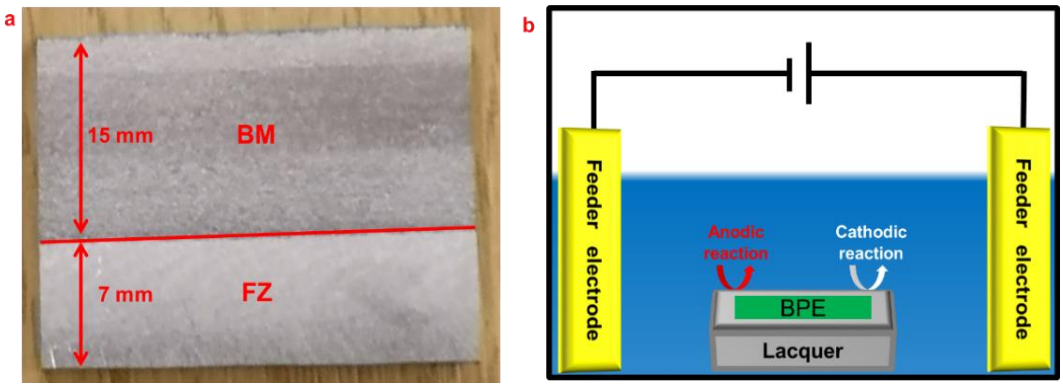

Figure 9.2- 1 (a) The top view of the welding lean DSS 2101, with (b) schematic diagram of the bipolar electrochemistry set-up.

9.25 Results and Discussion

An EBSD map of the DSS 2101 weld microstructure is shown in Figure 9.2- 2 (a), with the BM, HAZ, and FZ outlined and marked. The microstructure of the as received BM consists of austenite and ferrite, with both phases elongated along the processing direction Hardness testing was carried out with 15 equally spaced indents, with the mean and standard deviation of all measurements reported. The BM has a hardness of 230±14 HV_{10}, indicating an annealed microstructure condition. The width of the HAZ is ≈ 500 µm. In the HAZ, the microstructure closer to the FZ has a different morphology compared to the microstructure on the BM side. In the FZ, columnar ferrite grains are formed due to their growth along temperature gradients during welding; at the centre of the FZ, more equiaxed ferrite grains are then formed with secondary austenite grains located at grain boundaries. Austenite in the FZ has three locations and morphologies, (i) a continuous phase at prior-ferrite grain boundaries, (ii) acicular-type Widmanstätten plates growing into ferrite grains, and (iii) discrete intragranular regions.

EBSD assessment revealed a ratio of ferrite/austenite in the BM of ≈50:50. A ratio of ferrite/austenite in the HAZ of 63:36 and even 77:23 in the FZ were found, showing regions with unbalanced ferrite/austenite fractions. Nitrogen loss is often observed in fusion based welding processes, which can easily

result in unbalanced phase fractions in the HAZ. This combined with even fast cooling rates results then in a reduced diffusion time in the FZ, resulting in far higher ferrite phase fraction of up to 77% here. This is well above the recommended ferrite envelope of 30-65% for BM and 40–65% for the HAZ, according to API technical report 938-C**.**

Figure 9.2- 2 (b-d) give an overview of the chemical composition of the EBSD map in Figure 9.2- 2 (a), highlighting the distribution of Cr, Mn, and Ni. The microstructure of the BM reflects the different concentrations of these 3 alloying elements, with higher Cr and lower Mn concentrations in the ferrite. However, in the HAZ and the FZ, both ferrite and austenite have similar Cr concentrations. The FZ has a lower Mn content, which in turn contains more Ni, indicating that a Ni-over alloyed filler materials was used for the welding process. The over alloyed Ni should promote austenite formation in the FZ [35]. However, the EBSD map in Figure 2(a) clearly shows a significantly reduced fraction of austenite, predominantly reformed at grain boundaries. Overall, the FZ seems to have a fairly homogenous concentration of all major alloying elements.

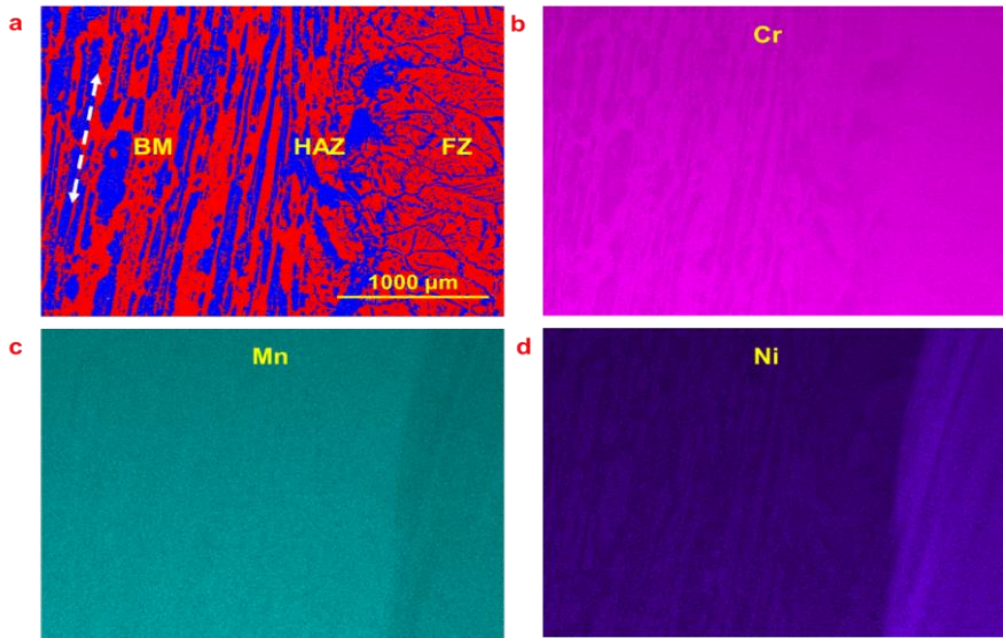

Figure 9.2- 2 (a) EBSD map of the DSS 2101 microstructure (blue: austenite, red: ferrite), with the arrow showing the process direction of the base material. The distribution of corresponding major chemical elements of this region is shown in (b) for Cr, in (c) for Mn, and in (d) for Ni.

Table 9.2- 1 displays the chemical composition of the welded DSS 2101 in the different regions. 10 points of each phase were measured, and the average composition calculated, with the standard deviation based on ten measurements. Due to the insensitivity of the EDX techniques to nitrogen, the nitrogen content of the single phase could not be measured. In the HAZ and FZ, the chemical element distribution between the ferrite and austenite are similar. In this region, both the ferrite and austenite transformed into a fully ferritic structure upon welding, with the austenite then re-forming during the subsequent cooling period. The reformed austenite here is expected to have a similar composition to the ferrite. The Cr and Ni can only diffuse relatively slowly in the solid state; hence, they could not partition between ferrite and austenite in the FZ and HAZ. The partitioning of alloying elements (Cr and Ni) between ferrite and austenite is not discernible in the FZ and HAZ, which is supported by the measurements inTable 9.2- 1 and the maps in Figure 9.2- 2.

Table 9.2- 1 Alloying elements concentration in welded lean DSS 2101.

	Phase	Cr	Ni	Mn
BM	Austenite	20.2 ± 0.3	1.9 ± 0.1	5.3 ± 0.1
	Ferrite	22.2 ± 0.1	1.3 ± 0.1	4.7 ± 0.1
HAZ	Austenite	21.1 ± 0.3	1.6 ± 0.2	5.1 ± 0.2
	Ferrite	21.5 ± 0.4	1.5 ± 0.1	4.9 ± 0.1
FZ	Austenite	21.1 ± 0.2	3.2 ± 0.4	4.2 ± 0.2
	Ferrite	21.3 ± 0.2	2.9 ± 0.3	4.2 ± 0.2

Potentio-dynamic polarisation

Two standard potentiodynamic polarisation curves of DSS 2101 BM and a sample containing BM+HAZ+FZ in 0.1M HCl are shown in Figure 9.2- 3. Each electrochemical test was carried out in triplicates using the Avesta cell with the results consistent and reproducible. The corrosion potential (E_{corr}) for the BM and the BM+HAZ+FZ was about -0.069 V_{SCE} and -0.134 V_{SCE}, respectively. A slightly different corrosion potential indicates minor differences in the microstructure passive film resistance. The BM has a far larger passive potential region with an increase in current (E_{pit}) at around +0.620 V_{SCE}. For the sample contains BM+HAZ+FZ, the passive region is shorter, and the E_{pit} reduced to +0.438 V_{SCE}. The HAZ+FZ containing sample is far more susceptible to localised corrosion. All results of polarization studies are collected in Table 9.2- 2.

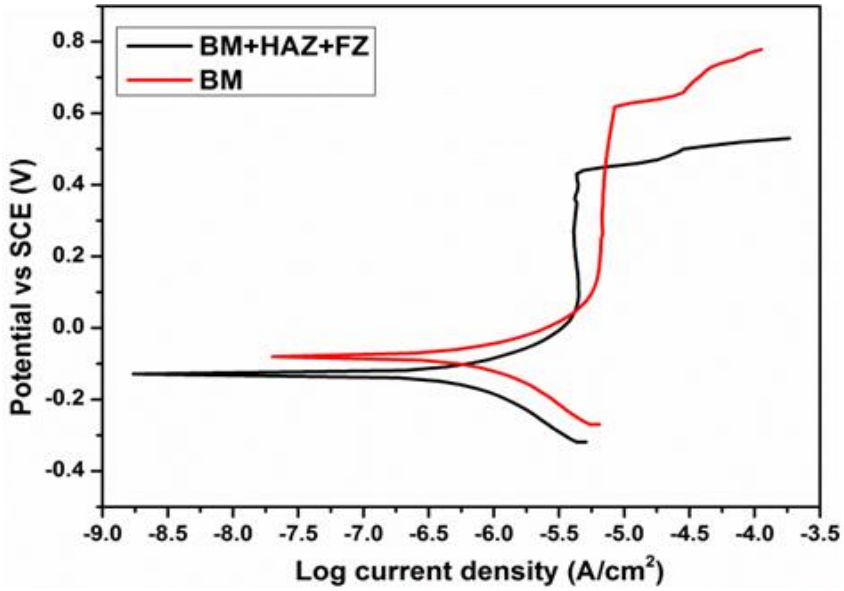

Figure 9.2- 3 Standard 3-electrode potentio-dynamic polarisation curves for DSS 2101 BM and BM+HAZ+FZ using 0.1M HCl at room temperature.

Table 9.2- 2 Pitting potentials obtained for welded lean DSS 2101 after polarization in 0.1M HCl solution at room temperature.

	E_{corr} (V_{SCE})	$E_{av.corr}$	E_{pit} (V_{SCE})	$E_{av.pit}$
BM	-0.062	-0.069±0.01	+0.617	+0.620±0.007
	-0.064		+0.615	
	-0.080		+0.628	
BM+HAZ+FZ	-0.128	-0.134±0.01	+0.441	+0.438±0.004
	-0.129		+0.439	
	-0.145		+0.434	

Bipolar Electrochemistry Testing

Figure 9.2- 4 (a) displays an optical image of welded DSS 2101 containing BM, HAZ, and FZ after exposure for 5 min. to the bipolar electrochemistry corrosion screening method. From the oxidation edge (left side) to the reduction edge (right side), crevice corrosion, transpassive corrosion, pitting corrosion, and an un-attacked passive region, followed by the balancing cathodic region are observed. A higher resolution image of the anodic region is shown in Figure 9.2- 4 (b), with crevice corrosion present at the interface between sample and lacquer. Transpassive corrosion is observed next to the crevice at the oxidation edge, as shown in Figure 9.2- 4 (b). When it comes to the distribution of corrosion pits, a clear difference between FZ, HAZ, and BM is apparent, with the most susceptible region clearly visible along the HAZ. Far larger corrosion sites with corrosion pits spreading further along the length of the sample is observed.

Figure 9.2- 4 (b) also reveals that the pit density in the FZ is the lowest, followed by the BM and the highest pit density in the HAZ. The latter indicates a far lower pitting potential in that region, with at higher potentials pits transforming into transpassive corrosion. From the polarisation curves in Figure 9.2- 3, it is apparent that the BM+HAZ+FZ have lower corrosion resistance in HCl compared to the BM alone, which also reflected here in Figure 9.2- 4. Both FZ and HAZ show unbalanced ratio of ferrite/austenite. However, the FZ has a higher corrosion resistance, related to the higher Ni content, confirmed in Table 9.2- 1. Here the interface Fusion Zone (FZ) - Heat Affected Zone (HAZ) had the most severe etch response.

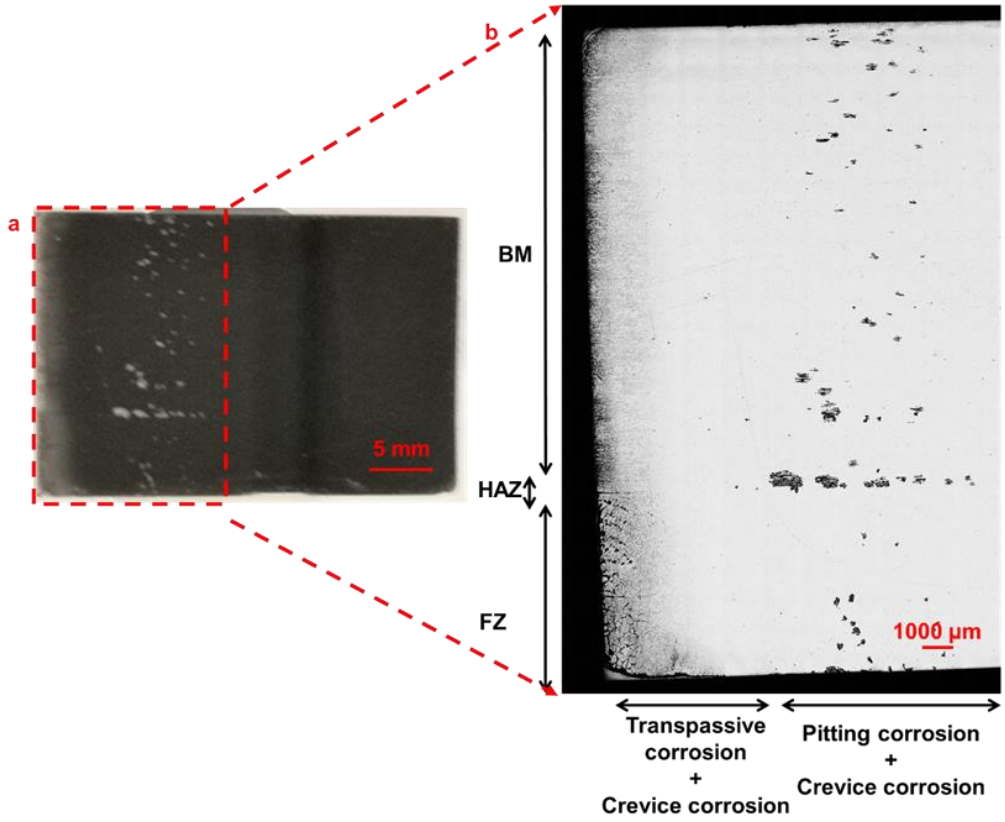

Figure 9.2- 4 (a) Optical images of the bipolar electrode after the corrosion test; (b) higher magnification zoomed optical image of the localised corrosion region, outlining the different corrosion regions along the sample surface.

Bipolar Potential Distribution

To measure the potential distribution along the BPE, a copper-wire was spot welded to the back-side of the bipolar electrode, and a Luggin capillary is connected to a SCE reference electrode. The Luggin capillary was set ≈ 1mm

above the surface. To measure local potential changes during the bipolar electrochemistry experiment, the OCP is first recorded, and then the power supply of the bipolar experiment switches on. The reported potential change on the y-axis is the difference of measured potential under bipolar control with respect to the OCP. The potentials are measured along the surface in increments of 5 mm, with the Luggin capillary following the centreline of the sample.

Figure 9.2- 5 (a) (a) gives the potential change vs. OCP at different locations. The value of the numbers (0 mm, 5 mm, etc.) indicates the distance to the oxidation edge. The observed noise at each point is caused by local turbulences due to gas formation reactions. The applied potential here is able to generate Cl_2 and H_2 gas, which in turn over longer time periods then changes the electric resistance of the electrolyte.

Figure 9.2- 5 (b) shows the potential distribution along the electrode, with the recorded potential at each point showing the average potential over 5 minutes of exposure. The potential distribution is quasi-linear along the centre of the electrode, with the potential at the oxidation edge indicating a slightly increased potential responses; i.e. more positive, and more negative at the reduction edge. The superimposed trend line shows a linear approximation of all points, with the potentials at the edges (0 mm and 30 mm) off-set due to the edge effect of the electrode. In Figure 9.2- 4 (b), the transpassive corrosion potential of the BM and the FZ are similar (≈ +0.95 V_{OCP}). The HAZ had the lowest pitting potential (≈ +0.28 V_{OCP}), with pits present up to a potential of ≈ +0.70 V_{OCP}. The pitting potential in the BM and FZ were similar (≈ +0.35 V_{OCP}), reaching up to a maximum potential in the BM of ≈ +0.60 V_{OCP}, compared to ≈ +0.57 V_{OCP} in the HAZ.

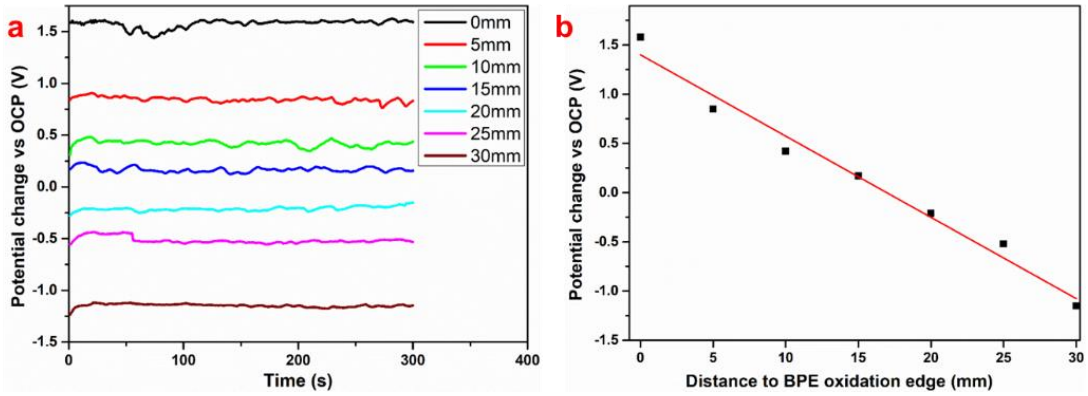

Figure 9.2- 5 (a) The potential change vs time at different locations on the bipolar electrode and (b) measured mean potential (potential change vs OCP) measured at 5 mm increments.

Corrosion Morphology

The SEM images in Figure 9.2- 6 show higher resolution impressions of corrosion pits at the different weld regions. The microstructure shows the austenite (bright white) and the ferrite (dark) in all regions. Figure 9.2- 6 (a) shows the pits in the FZ, with the austenite phase (at prior-ferrite grain boundaries and inside of the ferrite) retained, and the ferrite dissolved away. The remaining austenite produces lacy cover type pit appearance. Some parts of the lacy cover here are already collapsed into the pit after the surrounding ferrite phase was dissolved and could not support the austenite anymore. Figure 9.2- 6 (b) displays pitting corrosion in the BM, with pit morphologies following the process direction of the ferrite phase. The ferrite phase also selectively dissolved here in this region. The austenite phase remained, assembling a continuous network of large austenite grains.

Figure 9.2- 6 (c) and (d) show pitting corrosion in the HAZ at lower applied potentials, further away from the oxidation edge. In the HAZ, the austenite also remains, clearly showing the interface between BM and FZ. Figure 9.2- 6 (e) and (f) show that the largest pits are formed at the HAZ, much larger than those at the BM and FZ, indicating higher pit growth kinetics. These pits grew predominantly along the HAZ. It seemed to becomes more difficult for pits to grow into the BM, with the pit expansion possibly affected by the large remaining austenite islands acting as a preventative wall to pitting corrosion. In the FZ, a higher volume fraction of ferrite is here typically present, thus

offering more pathways for pit propagation. The HAZ is here clearly more sensitive to pitting corrosion.

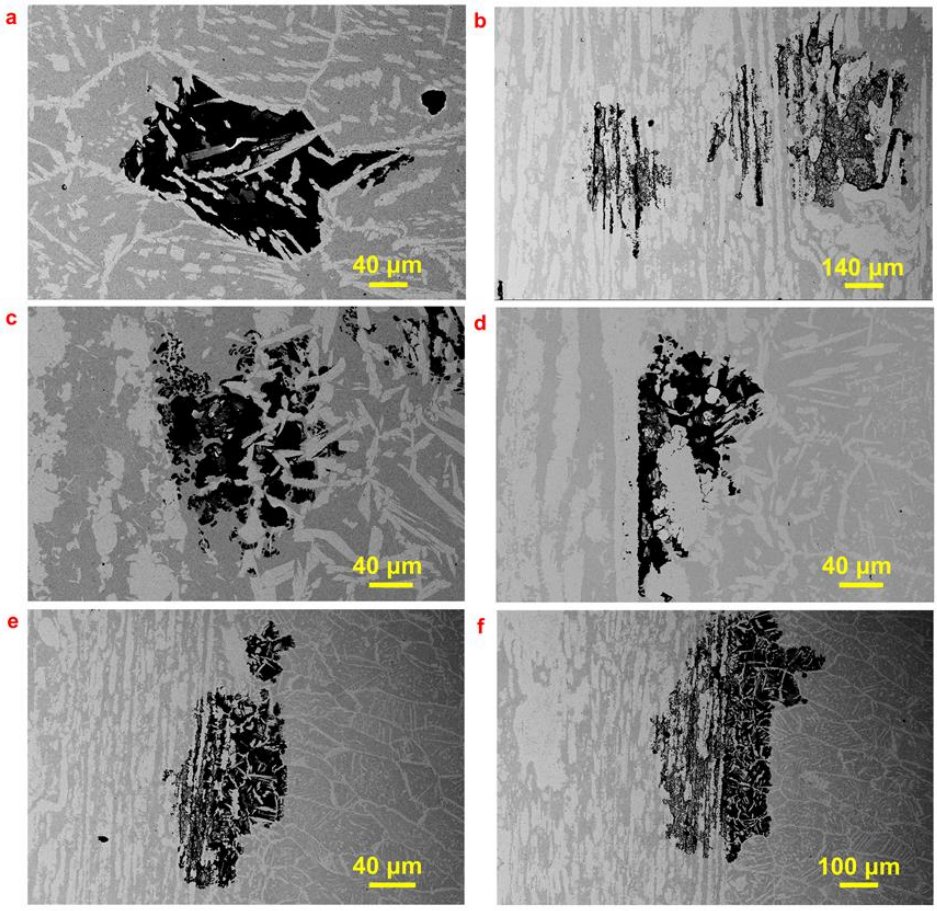

Figure 9.2- 6 SEM images of corrosion pits in the (a) FZ and (b) BM. The pitting corrosion in HAZ is shown with (c,d) representing lower applied potential and (e,f) at higher potentials (closer to the oxidation edge).

Trans-passive corrosion

Figure 9.2- 7 (a) gives a SEM image of the oxidation edge of the bipolar electrode, indicating that the observed crevice corrosion in the FZ is far more serious than in the BM, displaying a larger crevice volume. In the FZ, some corrosion sites are observed following prior-ferrite grain boundaries. The grains drop if the surrounding phase is dissolved away. In the BM, no localised corrosion is observed except for crevice corrosion at the interface with the lacquer.

Figure 9.2- 7 (b) displays the transpassive corrosion in the FZ. Austenite preferentially corrodes away starting often from grain boundaries, as the passive film becomes more defective, less crystalline and dense during transpassive corrosion. Hence, phases with higher Cr content have better corrosion resistance in this potential region [36]. Inside prior-ferrite grain, the intragranular austenite (as seen lower in height) dissolved preferentially here shown in Figure 9.2- 7 (c). Some localised corrosion is also found at the interface between austenite and ferrite. Figure 9.2- 7 (d) shows transpassive corrosion in the BM highlighting the presence of grains with different height. Figure 9.2- 7 (e) shows the transpassive corrosion in the HAZ. Overall, the HAZ had less transpassive corrosion, showing only small height difference between the ferrite and austenite phase.

During transpassive corrosion, austenite preferentially dissolved, resulting in selective corrosion. The FZ is more sensitive to crevice corrosion and transpassive corrosion, with a larger crevice width and localised corrosion caused by transpassive corrosion. HAZ suffers the least transpassive corrosion, as the least height difference between austenite and ferrite was found. The results in this paper demonstrated the effect of chemical composition on the observed corrosion morphologies in duplex stainless steel.

A lower volume fraction of austenite and nitrogen loss in the HAZ during welding typically result in reduced pitting corrosion resistance [37]. The latter can be restored by balancing local nitrogen concentrations, for example, via using nitrogen-containing shielding atmospheres during welding. The higher volume fraction of ferrite in the HAZ can also be avoided or reduced by, for example, optimizing cooling times or introducing subsequent annealing heat treatments [38]. The difference in chemical compositions of the two phases typically results in ferrite dissolving preferentially during pitting corrosion in chloride containing environments as demonstrated by recent studies on lean duplex stainless steel [14,30]

For welded DSS, details of the corrosion behaviour in relation to microstructure evolution can be obtained from bipolar electrochemistry tests. For 3-electrode potentiodynamic polarisation testing, the critical pitting

potential and preferentially dissolved phase in each region can be probed. However, for applying bipolar electrochemistry screening, both the critical pitting potential and associated microstructure susceptibility can be measured and compared. At the same time, pit growth kinetics and pit nucleation propensities can be determined.

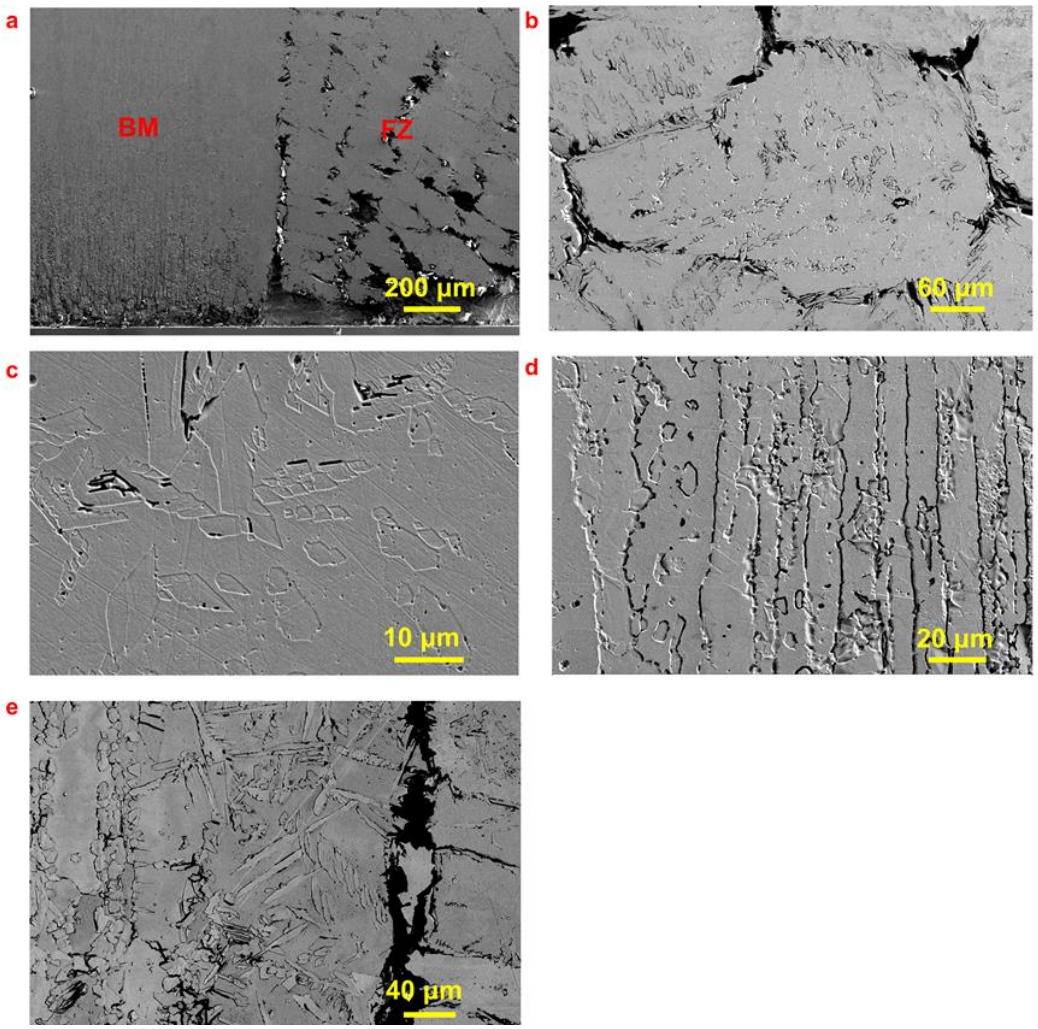

Figure 9.2- 7 The SEM images of transpassive corrosion for welded lean DSS 2101 at (a) the oxidation edge, (b) and (c) in the FZ, (d) in the BM, and (e) in the HAZ.

9.26 Conclusions

Bipolar electrochemistry metallographic screening tests have successfully been carried out, highlighting the most susceptible regions of welded lean DSS 2101 in a single experiment.

Crevice corrosion, transpassive corrosion and pitting corrosion are observed, with differences of microstructure susceptibility clearly identified.

The HAZ has the largest pits, with pits developing also at the lowest potential.

The FZ showed more transpassive corrosion and crevice corrosion.

Pits nucleated in the selectively dissolving ferrite phase, but transpassive corrosion nucleated in the austenite phase in all weld microstructure regions.

9.27 References

[1] Y. Zhou, D.L. Engelberg, Application of a modified bi-polar electrochemistry approach to determine pitting corrosion characteristics, Electrochem. Commun. 93 (2018) 158–161. https://doi.org/10.1016/j.elecom.2018.06.013.

[2] S. Munktell, M. Tydén, J. Högström, L. Nyholm, F. Björefors, Bipolar electrochemistry for high-throughput corrosion screening, Electrochem. Commun. 34 (2013) 274–277. https://doi.org/10.1016/j.elecom.2013.07.011.

[3] S. Munktell, L. Nyholm, F. Björefors, Towards high throughput corrosion screening using arrays of bipolar electrodes, J. Electroanal. Chem. 747 (2015) 77–82. https://doi.org/10.1016/j.jelechem.2015.04.008.

[4] N. Pébère, V. Vivier, Local Electrochemical Measurements in Bipolar Experiments for Corrosion Studies, ChemElectroChem. 3 (2016) 415–421. https://doi.org/10.1002/celc.201500375.

[5] Y. Zhou, D.L. Engelberg, Fast testing of ambient temperature pitting corrosion in type 2205 duplex stainless steel by bipolar electrochemistry experiments, Electrochem. Commun. 117 (2020) 106779. https://doi.org/10.1016/j.elecom.2020.106779.

[6] Y. Zhou, D.L. Engelberg, On the Application of Bipolar Electrochemistry to Characterise the Localised Corrosion Behaviour of Type 420 Ferritic Stainless Steel, Metals (Basel). 10 (2020) 794. https://doi.org/doi.org/10.3390/met10060794.

[7] J.H. Potgieter, P.A. Olubambi, L. Cornish, C.N. Machio, E.S.M. Sherif, Influence of nickel additions on the corrosion behaviour of low nitrogen 22% Cr series duplex stainless steels, Corros. Sci. 50 (2008) 2572–2579. https://doi.org/10.1016/j.corsci.2008.05.023.

[8] Z. Zhang, Z. Wang, Y. Jiang, H. Tan, D. Han, Y. Guo, J. Li, Effect of post-weld heat treatment on microstructure evolution and pitting corrosion behavior of UNS S31803 duplex stainless steel welds, Corros. Sci. 62 (2012) 42–50. https://doi.org/10.1016/j.corsci.2012.04.047.

[9] H. Tan, Z. Wang, Y. Jiang, D. Han, J. Hong, L. Chen, L. Jiang, J. Li, Annealing temperature effect on the pitting corrosion resistance of plasma arc welded joints of duplex stainless steel UNS S32304 in 1.0M NaCl, Corros. Sci. 53 (2011) 2191–2200. https://doi.org/10.1016/j.corsci.2011.02.041.

[10] J. Nilsson, Overview Super duplex stainless steels, Mater. Sci. Technol. 8 (1992) 685–700. https://doi.org/10.1179/mst.1992.8.8.685.

[11] C. Örnek, F. Léonard, S.A. McDonald, A. Prajapati, P.J. Withers, D.L. Engelberg, Time-dependent in situ measurement of atmospheric corrosion rates of duplex stainless steel wires, Npj Mater. Degrad. 2 (2018) 1–15. https://doi.org/10.1038/s41529-018-0030-9.

[12] T.S. Huang, W.T. Tsai, S.J. Pan, K.C. Chang, Pitting corrosion behaviour of 2101 duplex stainless steel in chloride solutions, Corros. Eng. Sci. Technol. 53 (2018) 9–15. https://doi.org/10.1080/1478422X.2017.1394020.

[13] E.M. Westin, C.O.A. Olsson, S. Hertzman, Weld oxide formation on lean duplex stainless steel, Corros. Sci. 50 (2008) 2620–2634. https://doi.org/10.1016/j.corsci.2008.06.024.

[14] L.H. Guilherme, P. Reccagni, A. V Benedetti, C.S. Fugivara, D.L. Engelberg, Corrosion Assessment of ASME Qualified Welding Procedures for Grade 2101 Lean Duplex Stainless Steel, Corrosion. 75 (2019) 1216–1229. https://doi.org/10.5006/3257.

[15] Y. Jiang, H. Tan, Z. Wang, J. Hong, L. Jiang, J. Li, Influence of Creq/Nieq on pitting corrosion resistance and mechanical properties of UNS S32304 duplex stainless steel welded joints, Corros. Sci. 70 (2013) 252–259. https://doi.org/10.1016/j.corsci.2013.01.037.

[16] B. Deng, Z. Wang, Y. Jiang, T. Sun, J. Xu, J. Li, Effect of thermal cycles on the corrosion and mechanical properties of UNS S31803 duplex stainless steel, Corros. Sci. 51 (2009) 2969–2975. https://doi.org/10.1016/j.corsci.2009.08.015.

[17] M. Watthée-Delmotte, J. Poirier, Effects of solution treatment and continuous cooling on σ-phase precipitation in a 2205 duplex stainless steel, Mater. Sci. Eng. A. 311 (2006) 220. https://doi.org/10.1016/S0921-5093(01)00911-X.

[18] T. Ogawa, T. Koseki, Effect of composition profiles on metallurgy and corrosion behavior of duplex stainless steel weld metals, Weld. J. 68 (1989) 181.

[19] Y. Yang, Z. Wang, H. Tan, J. Hong, Y. Jiang, L. Jiang, J. Li, Effect of a brief post-weld heat treatment on the microstructure evolution and pitting corrosion of laser beam welded UNS S31803 duplex stainless steel, Corros. Sci. 65 (2012) 472–480. https://doi.org/10.1016/j.corsci.2012.08.054.

[20] E.M. Westin, M.M. Johansson, R.F.A. Pettersson, Effect of nitrogen-containing shielding and backing gas on the pitting corrosion resistance of welded lean duplex stainless steel LDX 2101® (EN 1.4162, UNS S32101), Weld. World. 57 (2013) 467–476. https://doi.org/10.1007/s40194-013-0046-2.

[21] M.M. Johansson, E.M. Westin, J. Oliver, R.F.A. Pettersson, Localized corrosion resistance of welded austentic and lean duplex stainless steel, Weld. World. 55 (2011) 19–27. https://doi.org/doi.org/10.1007/BF03321316.

[22] G.S. Frankel, Pitting Corrosion of Metals A Review of the Critical Factors, J. Electrochem. Soc. 145 (1998) 2186–2198. https://doi.org/10.5006/0010-9312-19.8.261.

[23] K. Chandra, V. Kain, R. Tewari, Microstructural and electrochemical characterisation of heat-treated 347 stainless steel with different phases, Corros. Sci. 67 (2013) 118–129. https://doi.org/10.1016/j.corsci.2012.10.011.

[24] W.T. Tsai, J.R. Chen, Galvanic corrosion between the constituent phases in duplex stainless steel, Corros. Sci. 49 (2007) 3659–3668. https://doi.org/10.1016/j.corsci.2007.03.035.

[25] M. Hoseinpoor, M. Momeni, M.H. Moayed, A. Davoodi, EIS assessment of critical pitting temperature of 2205 duplex stainless steel in acidified ferric chloride solution, Corros. Sci. 80 (2014) 197–204. https://doi.org/10.1016/j.corsci.2013.11.023.

[26] B. Krawczyk, P. Cook, J. Hobbs, D. Engelberg, Corrosion Behavior of Cold Rolled Type 316L Stainless Steel in HCl Containing Environments, Corrosion. 73 (2017) 1346. https://doi.org//10.5006/2415.

[27] H. Hwang, Y. Park, Effects of Heat Treatment on the Phase Ratio and Corrosion Resistance of Duplex Stainless Steel, Mater. Trans. 50 (2009) 1548–1552. https://doi.org/10.2320/matertrans.MER2008168.

[28] G.S. Frankel, L. Stockert, F. Hunkeler, H. Boehni, Metastable pitting of stainless steel, Corrosion. 43 (1987) 429–436. https://doi.org/10.5006/1.3583880.

[29] J. Srinivasan, R.G. Kelly, Evaluating the Critical Chemistry for Repassivation at the Corroding Surface Using Mass Transport Model-Based Artificial Pit Experiments, J. Electrochem. Soc. 163 (2016) C768–C777. https://doi.org/10.1149/2.0661613jes.

[30] K. Eguchi, T.L. Burnett, D.L. Engelberg, X-Ray tomographic characterisation of pitting corrosion in lean duplex stainless steel, Corros. Sci. 165 (2019) 108406. https://doi.org/10.1016/j.corsci.2019.108406.

[31] N.J. Laycock, Metastable Pitting and the Critical Pitting Temperature, J. Electrochem. Soc. 145 (1998) 2622. https://doi.org/10.1149/1.1838691.

[32] C.J. Semino, P. Pedeferri, G.T. Burstein, T.P. Hoar, The localized corrosion of resistant alloys in chloride solutions, Corros. Sci. 19 (1979) 1069–1078. https://doi.org/10.1016/S0010-938X(79)80096-7.

[33] J. Srinivasan, M.J. McGrath, R.G. Kelly, Mass Transport and Electrochemical Phenomena Influencing the Pitting and Repassivation of Stainless Steels in Neutral Chloride Media, Electrochem. Soc. 58 (2014) 1–11.

[34] N.J. Laycock, R.C. Newman, Localised dissolution kinetics, salt films and pitting potentials, Corros. Sci. 39 (1997) 1771–1790. https://doi.org/10.1016/S0010-938X(97)00049-8.

[35] J. Pilhagen, R. Sandström, Influence of nickel on the toughness of lean duplex stainless steel welds, Mater. Sci. Eng. A. 602 (2014) 49–57. https://doi.org/10.1016/j.msea.2014.01.093.

[36] I. Betova, M. Bojinov, T. Laitinen, K. Mäkelä, P. Pohjanne, T. Saario, The transpassive dissolution mechanism of highly alloyed stainless steels I. Experimental results and modelling procedure, Corros. Sci. 44 (2002) 2675–2697. https://doi.org/10.1016/S0010-938X(02)00073-2.

[37] E.M. Westin, S. Hertzman, Element distribution in lean duplex stainless steel welds, Weld. World. 58 (2014) 143–160. https://doi.org/10.1007/s40194-013-0108-5.

[38] L. Zhang, W. Zhang, Y. Jiang, B. Deng, D. Sun, J. Li, Influence of annealing treatment on the corrosion resistance of lean duplex stainless steel 2101, Electrochim. Acta. 54 (2009) 5387–5392. https://doi.org/10.1016/j.electacta.2009.04.023.

9.3 Revisiting the Influence of Gravity on Pitting Corrosion

Yiqi Zhou[*1], *Dirk Lars Engelberg* [1,2]

(1) Corrosion & Protection Centre, School of Materials, The University of Manchester, M13 9PL, Manchester, UK

(2) Materials Performance Centre, The University of Manchester, M13 9PL, Manchester, UK

* Corresponding author: Yiqi.Zhou@postgrad.manchester.ac.uk

9.31 Highlights

Gravity influences pit volume, pit growth kinetics, and pit shape.

Corrosion pits in the Faceup (FU) orientations have the largest pit volume.

Pits in the Perpendicular (PE) and Facedown (FD) orientations show similar corrosion behaviour.

Pits in the FU orientation are semi-circular to dish-shaped, with far narrower pits observed in both the PE and FD orientations.

9.32 Abstract

Bipolar electrochemistry creates a linear potential gradient along the bipolar electrode (BPE), resulting in access to the full spectrum of anodic to cathodic electrochemical reactions. The pitting corrosion behaviour of Types 316L and 304L stainless steels with different exposed surface orientations is revisited, highlighting that pit growth kinetics and the resulting pit shapes are severely affected by gravity. The largest overall pit volumes with the fastest growing pits are found in the Faceup (FU) orientation. Pits have similar metal loss and pit growth rate when exposed Perpendicular (PE) and Facedown (FD) orientations. Pit shapes in the FU orientation are either semi-circular or dish-shaped, with the PE and FD orientations both resulting in far more narrower, ellipsoid shaped pits. Pit growth kinetics is independent of applied potential, supporting diffusion limited growth regimes for estimating the maximum pit depth.

Keywords: Bipolar electrochemistry, stainless steel, pitting corrosion, gravity, pit shape, pit growth kinetics

9.33 Introduction

A bipolar electrochemistry approach has recently been employed to research corrosion properties [1–3]. A potential gradient is established along with the

interface of the electrolyte and bipolar electrode (BPE); as a result, both anodic and cathodic reactions are simultaneously occurring along the BPE surface [1–5]. The main advantage of the bipolar electrochemistry for corrosion behaviour is a continuous anodic to cathodic corrosion response can be achieved in one single experiment. The non-contact wireless setup allows for the BPE with either complex shapes or sensitive to electric contact, and simple experiment setup [1–3].

Pitting corrosion is the localised breakdown of a passive film on the metal surface followed by a rapid metal dissolution [6]. The pitting corrosion is influenced by: the concentration of Cl^-, applied potential, and electrolyte temperature [7]. Three pit nucleation mechanisms are discussed, include: penetration, mechanical breakdown, and adsorption [8]. Pitting corrosion has three stages: pit nucleation, metastable pit growth, and stable pit growth or pit repassivate [9]. Both metastable and stable pit growth is under diffusion control [10]. The metastable pit growth requires a lacy cover, act as a diffusion barrier to maintain the pit electrolyte with a high concentration of Cl^- and low pH [11,12]. The stable pits can grow without a lacy cover, as pit depth, pit morphology, or pit volume act as diffusion barrier [13–15]. Stable pits only formed above a critical pitting potential or temperature [13]. In single phase stainless steel, the pits become dish-like with longer exposure time as the salt film at pit bottom [16]. In duplex stainless steel, the direction of pit propagation is also controlled by on the ratio and size of the ferritic/austenitic phases [17]. The FU orientation results the wide-like pits, pit shapes in the FD orientation are narrow ellipsoids like, and the PE orientation has the intermediate shape pits [18]. Different pit shapes are related to the salt film at the pit bottom. Gravity can remove the salt film, results in narrow ellipsoids like pits. For the FU orientation, gravity encourages the salt film deposit at the pit bottom, results in the semi-circular or wide-like shape [14,18]. The pits in the FD orientation grow faster than the FU orientation, as the salt film is removed by gravity [18,19]. The pit growth kinetics is controlled by the pit electrolyte, the Cl^- concentration is lower in the FD and PE orientations, as gravity can move Cl^- out of pit [18,20]. Pits are easier to be stable with a large aspect ratio (pit

depth to pit diameter), as the higher current density is nucleated from high aspect ratio at the same applied potential [12,21,22].

The paper aims to use a bipolar electrochemistry approach to investigate the pit volume, pit corrosion kinetics, and pit shape change on Type 316L and 304L stainless steels over a wide range of applied potentials changed by gravity combined with 3-D laser confocal microscopy. The exposed surfaces of the stainless steels are holding in three different orientations (Faceup, Perpendicular, and Facedown) to achieve gravity influence pitting corrosion. The 3-electrode potentio-dynamic and potentio-static polarisation test are also used to compare the pit shape and pitting potential change by gravity.

9.34 Materials and Methods

The composition (wt%) of Type 316L and 304L stainless steel was 16.7 Cr, 10.1 Ni, 0.02 C, 0.05 N, 2.04 Mo, and (bal.) and 18.4 Cr, 8.7 Ni, 0.02 C, 0.04 N, and (bal.) Fe. The size of rectangular coupons were 30 * 10 mm^2 (length * width) with thickness from 1 to 2 mm. The samples were mounted in Araldite resin with a plastic tube at the backside of the exposed surface, then grinding the exposed surface to a 1200 grit finish. The pitting resistance equivalent number ($PREN_{16}$ = % Cr+3.3 % Mo +16 % N) value was used to compare the pitting corrosion resistance [23]. PREN was 18.9 and 25.4 in Type 304L and 316L stainless steel, indicates Type 316L had a better pitting corrosion resistance.

Figure 9.3- 1 (a) shows the setup of the bipolar electrochemistry experiment, a Keysight E36015A DC was used for power supply. Platinum feeder electrodes have a surface area of 4 cm^2 each. The anodic reactions occurred near the negative feeder electrode, and vice versa for the reduction. The electrolyte chosen was 0.1 M HCl, the distance between the two feeder electrodes was 60 mm, with BPE set at the centre of the feeder electrodes. The voltage applied on the feeder electrode was 10 V. The bipolar electrochemistry experiments were conducted in 5 min intervals, with individual sample removed after 5, 10 and 15 min of exposure. Figure 9.3- 1 (b) shows the different exposed surface orientations. The different surface orientations were achieved by bending the plastic tube to different directions.

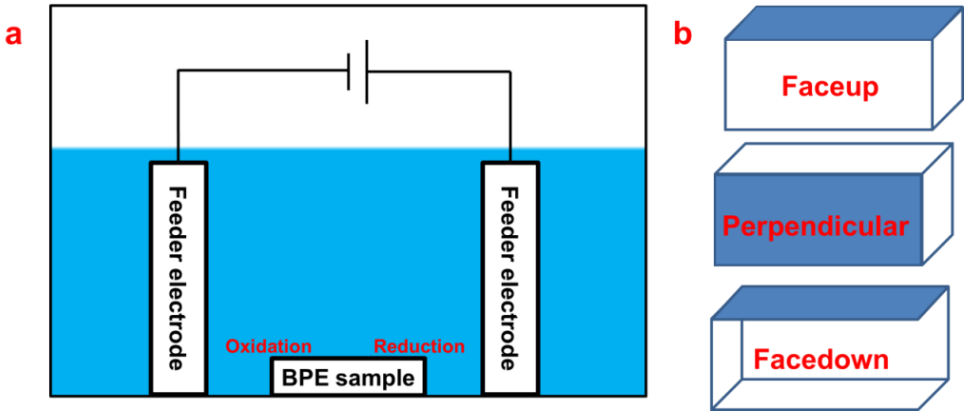

Figure 9.3- 1 (a) Setup for bipolar electrochemistry with (b) the coloured face of the BPE is the sample exposed surface orientation.

Figure 9.3- 2 provides the measured potential and current along with Type 304L BPE under different surface orientations. To measure the local potential and current, a split array BPE electrode consisting of 13 rectangle coupons with a size of 1.9 * 10 mm^2 (length * width) was used. Each segment had an individual electric connection to a copper wire at the backside of the exposed surface, with each segment insulated to each other by the electric insulation tape, and once packed these split BPEs in a sequence by the copper wire, it had a dimension of a single BPE electrode. To measuring the local current at each segment, coupons were connected to ZRAs via copper wire. A ZRA was used to measure the current from each segment BPE to the integrated BPE. For the potential measurement, a Luggin probe was located above the BPE surface (≈ 1 mm), with the Luggin probe connected to a reference electrode (SCE). The Open Circuit Potential (OCP) was stabilised at first, and then the turned on the bipolar electrochemistry experiment. The potential difference between record potential and the OCP value was the local potential change. Figure 9.3- 2 (a) shows the potential distribution linearly reduced from the BPE oxidation edge to the reduction edge. The potential along BPEs was similar for all different surface orientations. The maximum potential was +1.0 V_{ocp} and the minimum potential was -1.0 V_{ocp} on the BPE. Figure 9.3- 2 (b) gives the current density distribution on the BPE. The PE and FD orientations had the similar current density on the BPE, from +5 mA/cm^2 (BPE oxidation edge) to -4 mA/cm^2 (BPE reduction edge). However, a stepper current density distribution was found in the BPE with the FU orientation, from +10 mA/cm^2 to

-10 mA/cm^2. Higher anodic current density was caused by the more localised corrosion, with a higher cathodic current to balance the anodic current density.

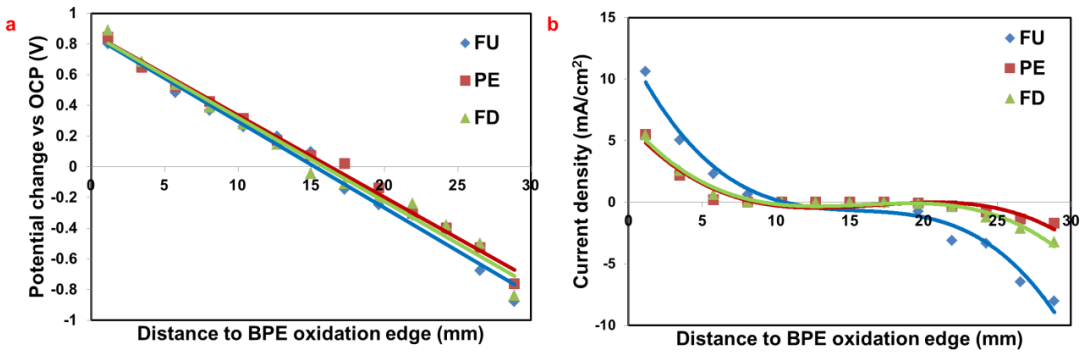

Figure 9.3- 2 The potential distribution and (b) the current density distribution along the BPE with different surface orientations.

The relationship between the pit depth (d) and pit volume (V) follows Equation 1, where r is the radius of the pit mouth (assume the pit mouth is a circle shape).

$$\boldsymbol{V = \frac{1}{2} \times \frac{4}{3} \times \pi \times d \times r^2} \qquad \text{Equation 1}$$

$$\boldsymbol{d = \alpha \times r} \qquad \text{Equation 2}$$

Equation 2 shows the relationship between the pit depth (d) and pit radius (r), α is a pit shape factor depend on the pit shape. To simulating the evolution of pit shapes, topological boundary cavities were introduced. For a wide-like pit, a shape factor was < 1 (here 0.5 was used). For a semi-circular pit, the shape factor was 1. For a narrow ellipsoid pit, the shape factor was >1 (e.g. 2 was used). The assumption was for the same pit depth, a smaller shape factor resulted in a larger volume equivalent to a larger cross-sectional area.

For the 3-electrode cyclic potentio-dynamic polarization and potentio-static polarization tests, samples with size of 30 * 10 mm^2 (length * width) were immersed in 35% HNO_3 for 6 hours, to growth a passive film at the sample edges, to avoid crevice corrosion at the sample edges. Then samples were electric connect to the backside of the exposed surface by copper wire. The samples were mounted in Araldite resin and then ground until 1200 girt. A platinum electrode and SCE reference electrode were used; IVIUM-

Compactstat and IVIUMsoft software was used to measure potentio-dynamic polarisation and potentio-static polarisation curves. The OCP was stabilised for 10 min, followed by the cyclic potentio-dynamic polarisation test from -200 to +1200 mV_{OCP} with a scan rate of 1 mV/s. For the potentio-static polarisation test, a constant potential +900 mV_{OCP} was applied to the sample for 15 min after the OCP stabilised.

After all the experiments, the BPE was removed from the electrolyte and cleaned with soap, followed by an ultrasonic bath to collapse and remove the pit lacy covers for subsequent analysis of pit dimensions. A Keyence VK-200K microscopy was used to determine the pit depth (d) and the corresponding pit volume (V).

9.35 Results and Discussion

Cyclic potentio-dynamic polarisation test

Figure 9.3- 3 (a) and (b) shows the 3-electrode potentio-dynamic polarisation curves for different surface orientations in Type 304L and 316L stainless steels. The E_{rep} for Type 316L stainless steels with the FD and PE orientations is +0.2 V_{SCE}, with the E_{pit} is +0.5 V_{SCE}. The E_{pit} in Type 304L stainless steel is +0.4 V_{SCE} with the $E_{rep} \approx 0$ $V_{SCE,}$ both E_{pit} and E_{rep} in Type 304L stainless steel is lower than Type 316L stainless steel, indicates Type 316L stainless steel has a better pitting corrosion resistance, same as the PREN. From the potentio-dynamic polarisation curves, gravity does not change E_{rep} in both stainless steels for all the surface orientations. However, E_{pit} in the FU orientations is higher than E_{pit} in the PE and FD orientations for both stainless steels, indicates gravity reduce the E_{pit} but no influence to the E_{rep}, so the translation between the metastable pit to stable pit is influenced by gravity. The sale bar is uniform for all the optical images in Figure 9.3- 3. Figure 9.3- 3 (c) shows the optical images of pits in the FU orientation is larger than the PE and FD orientations for the Type 316L stainless steel, pits in the PE and FD orientations have the similar size. Figure 9.3- 3 (d) displays the rank of pit size follows the FU > PE ≈ FD orientations in Type 304L stainless steel. Both of the stainless steels display pits with the FU orientation have larger pit. Pits in the FD and FU orientations have similar size.

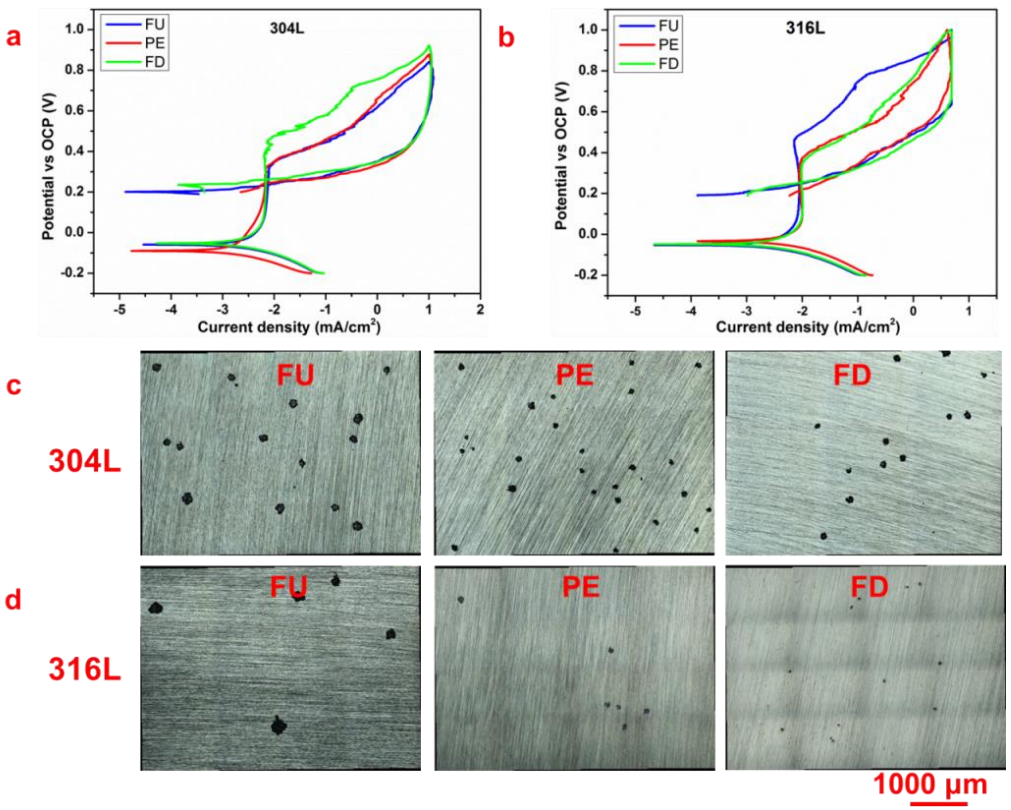

Figure 9.3- 3 The cyclic potentio-dynamic polarisation with different surface orientations in (a) Type 304L and (b) Type 316L stainless steels, with corresponding the optical image (c) Type 304L and (d) Type 316L stainless steels.

Figure 9.3- 4 shows the relationship between the pit depth and corresponding pit volume with different surface orientations after 3-electrode potentio-dynamic polarisation test. Three reference curves are drawn which show the pit depth and related pit volume from Equation 1 and Equation 2, pit shape factor changes from 0.5 (wide pit) to 2 (narrow pit). The largest volume pits are in the FU orientation in both stainless steels, as aggressive electrolyte accumulate inside of the pit, which allows the pits quickly growth [20]. The pits in the PE and FD orientations are narrow ellipsoids like; pits prefer growth in depth direction due a longer diffusion length for the electrolyte diffuse out, which has less influence from gravity. For the same volume pit, the current density is higher for a narrow pit, which support pit stable growth [24].

Gravity also changes the pitting corrosion by: increasing the pH inside of pit, which form protective oxide ($FeCr_2O_4$, NiOH or FeOH), compete with the salt film precipitates [11,25], 2, reducing the concentration of Cl^-,both of them

reduces the stability of the salt film. Gravity also direct remove the salt film formed at pit bottom.

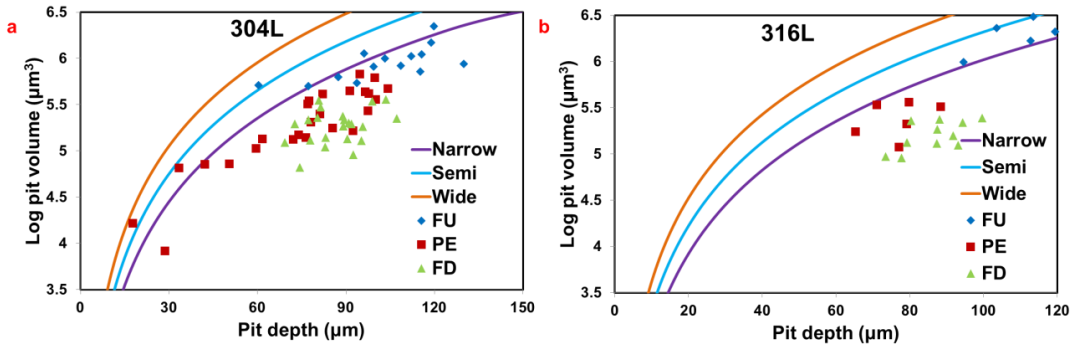

Figure 9.3- 4 The pit depth and related pit volume in Type (a) 304L and (b) 316L stainless steels with different surface orientations.

Potentio-static polarisation test

Figure 9.3- 5 shows the current density response at a constant potential of +900 mV_{OCP}. The sample with the FU orientation shows the largest current density response, and current density response in the PE and FD orientations is similar. Figure 9.3- 5 (a) shows the current density in Type 304L stainless steel with the FU orientation is quickly increased to 20 mA/cm^2 and then slowly to 23 mA/cm^2; for the PE and FD orientations, the current density response is quickly increased to ≈15 mA/cm^2 and stabilised at 13 mA/cm^2. Figure 9.3- 5 (b) shows the current density response in Type 316L stainless steel in the FU orientation is quickly increased to 12 mA/cm^2 and then slowly to 17 mA/cm^2. For the PE and FD orientations, the current density is similar ≈ 7.5 mA/cm^2. In both of the stainless steels, Samples with the FU orientation have the largest current density response, and similar current density response between the PE and FD orientations.

The 3-electrode potentio-dynamic polarisation test shows the similar current density response except the E_{pit}, but not for the 3-electrode potentio-static polarisation test. As gravity only influences the pit growth kinetics, so current response above E_{pit} is changed, but less influence in the other regions (cathodic, passive, or active corrosion region)

Figure 9.3- 5 (c) and (d) give the optical images after 3-electrode potentio-static polarisation test. For both Type 304L and 316L stainless steels, the largest pit size are found in the FU orientation, and the pits have similar size between the FD and PE orientations. The pit sizes influenced by gravity is similar between the 3-electrode potentio-dynamic and potentio-static polarisation test.

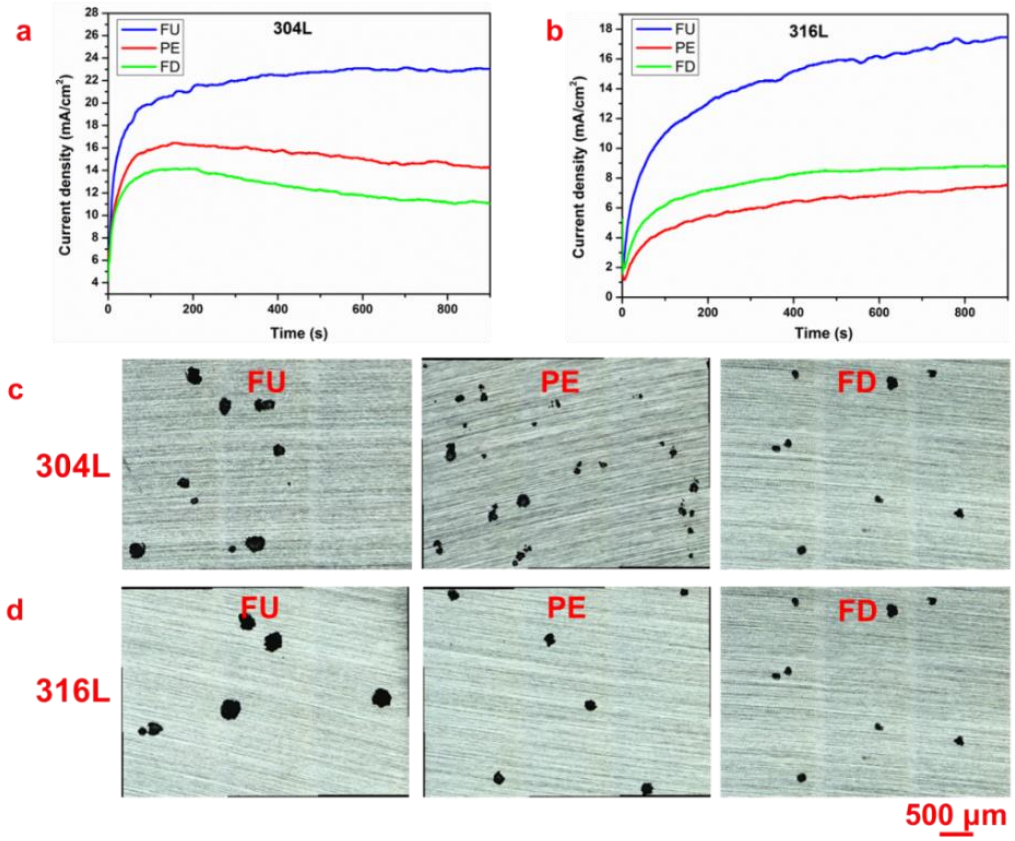

Figure 9.3- 5 The current density from potentio-static polarisation test at the potential of 0.9 V_{OCP} for (a) Type 304L and (b) Type 316 L stainless steels with different surface orientations. and the optical images after experiments for (c) Type 304L and (d) Type 316L stainless steel.

Figure 9.3- 6 (a) gives the pit shape evolution in Type 304L stainless steel after 3-electrode potentio-static polarisation test; pits in the FU orientation are the semi-circular shape. For the PE and FD orientations, all pits have the narrow ellipsoid-like shape. Figure 9.3- 6 (b) shows the pit shapes changed in Type 316L stainless steel by gravity, pits shapes in the FU orientation are slightly wide-like. For the PE orientation, all the pits have the narrow ellipsoids like, and more narrower pits in the FD orientation. Compare with the pit after

the potentio-dynamic polarisation test, wider pits measured from the 3-electrode potentio-static polarisation test for both stainless steels with different surface orientations. Larger pit volume is caused by longer exposure time above E_{pit}, results in wider shape pits.

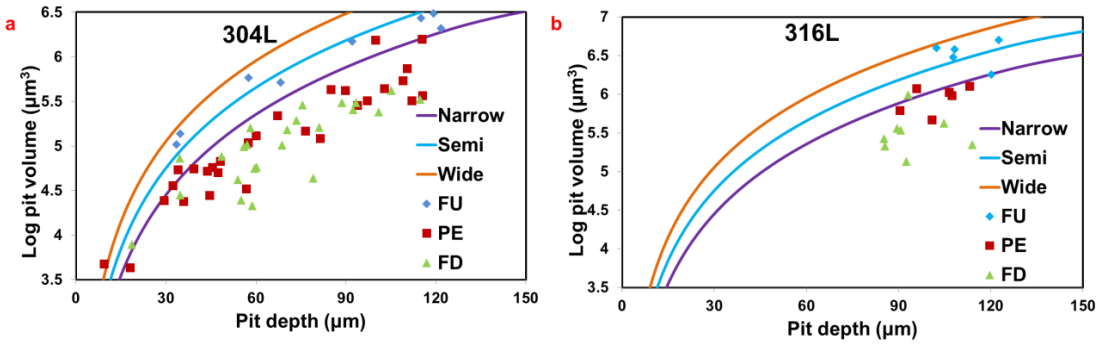

Figure 9.3- 6 The pit shape change with different surface orientations in (a) Type 304L and (b) Type 316L stainless steels after potentio-static polarisation test at 0.9V_{ocp}.

Bipolar electrochemistry result

A summary of the pits covered area and total dissolved volume with different surface orientations is given in Figure 9.3- 7. All the pits on the Type 304L and 316L BPEs are the lacy cover pits. The left side of the optical images are the BPE oxidation edge, and the scale bar is uniform for optical images. Figure 9.3- 7 (a) compares the pit covered length in Type 304L BPE with different exposure time and surface orientations. The observed overall pit covered length is reduced from the FU to FD, and finish at the PE orientation. Pit covered length change is caused by gravity, from the Point Defect Model, pit nucleation caused by the cation vacancy across the passive film [26,27]. Gravity can assist (FU orientation) or prevent (FD and PE orientation) cation vacancy across the passive film. So the pit nucleated at the low applied potential in the PE and FD orientations is harder. Figure 9.3- 7 (b) gives the pit covered length in Type 316L stainless steel changed by surface orientation and exposure time. The pit covered lengths are independent to gravity due to the Mo, Mo increases the passive film properties and the pitting potential by reduction of the local chloride concentration from Mo complexes with chloride [28–30].

Pits nucleated at high applied potential only after 5 min for Type 316L stainless steel, as the higher potential also results in a thicker passive film. Before 5 min, the passive film growth rate is quicker than Cl^- go through the passive film, so no pit is determined. At 10 min, pit nucleation via cation vacancy reaches the metal matrix. The average pit size in the FU orientations is larger than other two orientations. Fewer pits nucleated in the FU orientation, so each pit has a high current to support fast growth. More pits in the PE and FD orientations are nucleated, so each pit has a less current which results in smaller size pit.

Pit covered length is changed by gravity in Type 304L BPE, but the E_{pit} is similar in the potentio-dynamic polarisation test, the possible reason is the properties of the passive film. The passive film is increased during OCP, as selective dissolution of Fe which result in higher Cr in the passive film [31]. A thicker passive film is formed when sweeping through the passive region. The transport of Cl^- in the passive film will be retarded in a thicker passive film [32,33]. With the addition of Mo (Type 316L stainless steel), the stability of the passive film increased, so the pit covered length on the Type 316L stainless steel has less influence from gravity.

Pits covered length in Type 316L stainless steel is longer than Type 304L stainless steel, indicates a lower pitting potential which is oppose to the PREN and E_{pit}, this is caused by more serious pitting corrosion in Type 304L BPE, so pits plunder current from the lower applied potential in BPE region, which reduces the current density at the lower potential region. The current in this region cannot support the pit nucleation, result in a shorter BPE covered region for Type 304L stainless steel.

Figure 9.3- 7 (c) shows pit volume in Type 316L BPE is similar for all different orientations at 5 min, as the influence of growth of passive film compete with pit nucleation. After 5 min, the pits nucleate at higher applied potential region, so pits in FU orientation become larger. Pit volume in PE and FD orientations is similar. Figure 9.3- 7 (d) displays Type 304L BPE in the FU orientation with the largest pit volume, and the PE and FD orientations have similar pit volume.

The total pit volume of Type 304L stainless steel is larger than Type 316L stainless steel, indicates a worse pit corrosion resistance.

The pit growth is higher in the FD orientation and lower in the FU orientation, researched before [18,19], but shows opposite conclusions to this experiment. The reason is the exposure time; former researchers' analysis the pit growth kinetics from 6 hours to 66 hours, but this experiment runs 15 min. For a short exposure time, the pit growth kinetics is more controlled by the pit electrolyte, less aggressive pit electrolyte reduce the pit growth kinetics, so the pit growth kinetics in the FU orientation is higher. For a long exposure time, the pit growth kinetics is more changed by the salt film; the pit growth in depth direction after the salt film removed by gravity. So the pit growth kinetics in the FD orientation is higher.

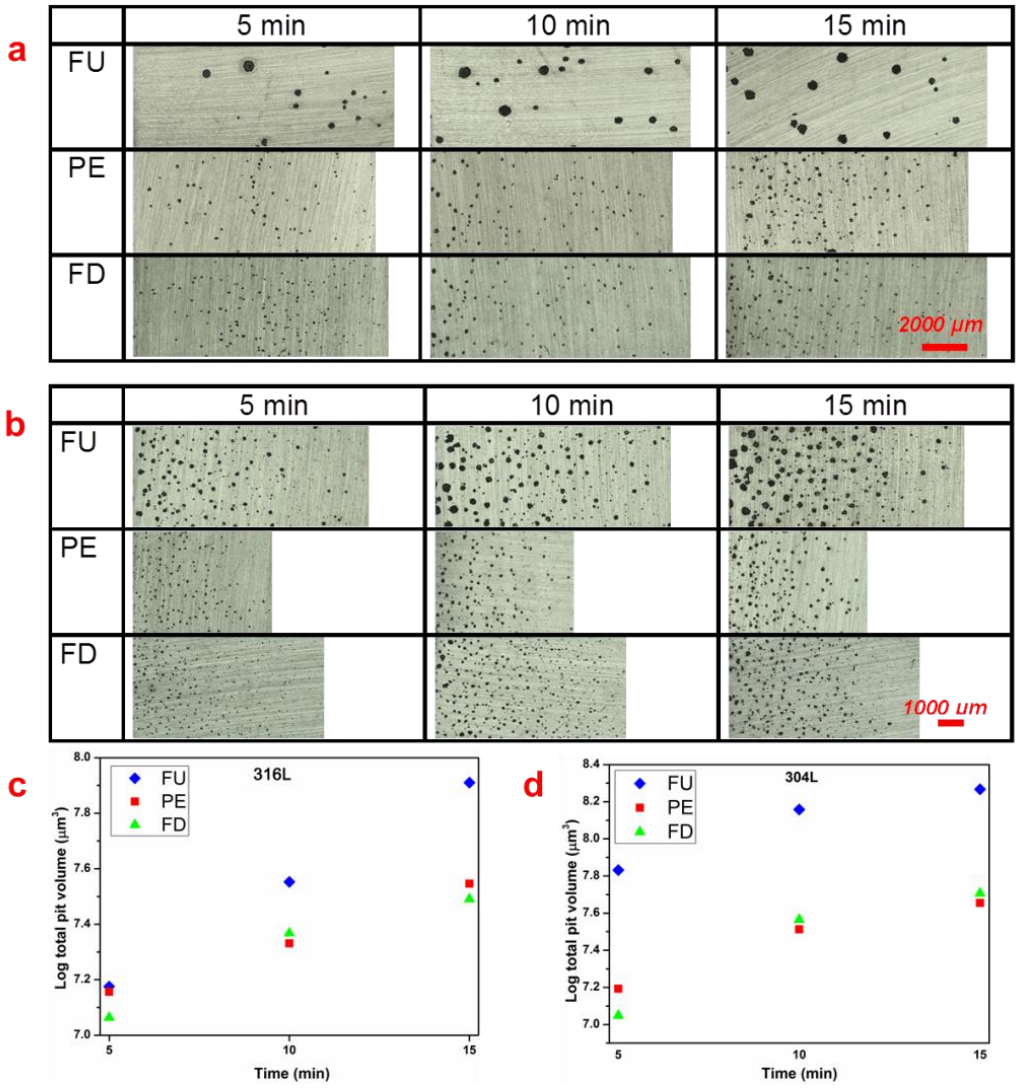

Figure 9.3- 7 Optical images of the pit covered regions in (a) Type 304L and (b) Type 316L BPEs with different exposure time and surface orientations, and corresponding pit volume in (c) Type 304L and (d) Type 316L stainless steels.

Largest pit in the BPE

Figure 9.3- 8 gives the maximum pit depth and corresponding cross-section area with different surface orientation and exposure time. The maximum pit depth and cross-section area are increasing with time, indicates these pits are active. Figure 9.3- 8 (a) shows the maximum pit depth in Type 304L BPE increase from 80 μm at 5 min to ≈ 140 μm at 15 min for all the surface orientations. Figure 9.3- 8 (b) gives maximum pit depth in Type 316L BPEs, pits have similar depth from 5 to 15 min. The maximum pit depth in Type 316L stainless steel is always lower than Type 304L stainless steel. Figure 9.3- 8 (c) and (d) give the maximum cross-section area with different time and surface orientations. Similar pit depth in all exposed surface orientations; but the corresponding pit cross-section area various, the pit cross-section area in the FU orientation is largest, and the pit cross-section area is similar between the PE and FD orientation.

Gravity has little effect to the pit electrolyte at the pit bottom, and more influence to the pit electrolyte near the pit mouth, as different diffusion length. So the pits depth is independent to the surface orientation, but not pit cross-section areas.

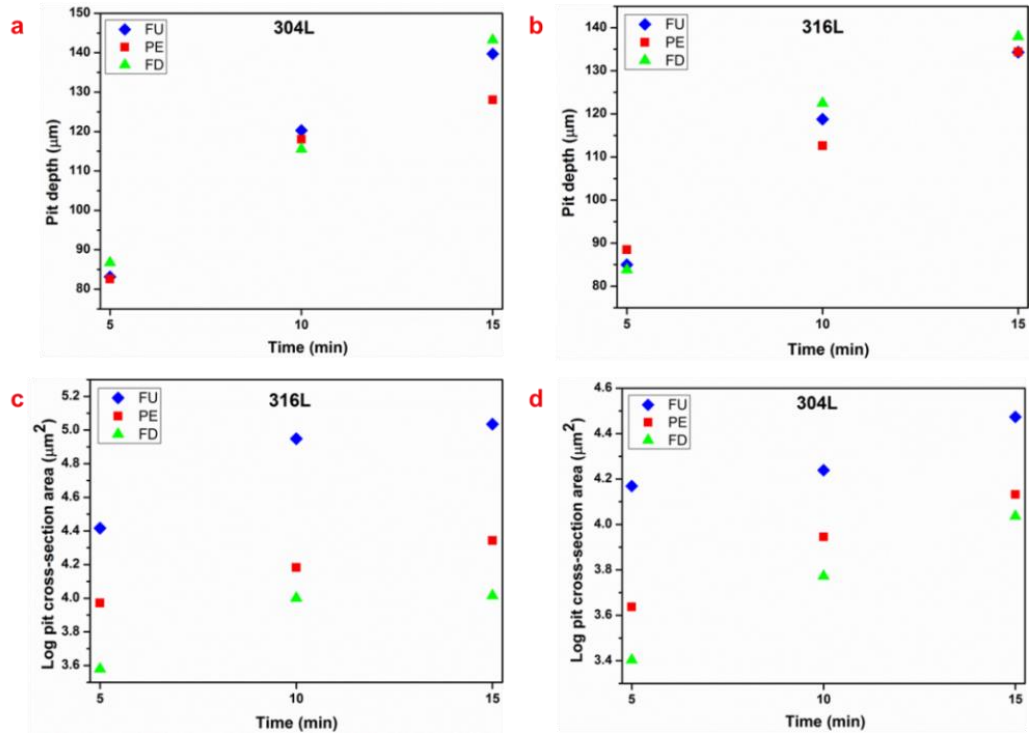

Figure 9.3- 8 The maximum pit depth* with different exposure time and surface orientations in (a) Type 304L and (c) Type 316L BPPEs. The corresponding pit cross-section area in (b) Type 304L and (d) Type 316L BPEs (*the maximum pit before merge).

Pit volume along the BPE

The pit covered region is divided into five groups along the BPE length, and each group contains a size of 1 * 4 mm^2 (length * with). Region 1 represents the highest potential close to the oxidation edge, with region 5 representing lower applied potentials, 4 to 5 mm away from the oxidation edge. From Figure 9.3- 9 (a), (c), and (e), the pit volume in Type 304L BPE is linearly reduced from the region 1 to 5 in all the surface orientations, due to a linearly potential gradient. The FU orientations have the largest pit volume in all the regions. The pit volume between the FD and PE orientations is similar; as same current density distribution on the BPE. The pit volume change along the BPE in the FU orientation is smoother than the FD and PE orientations, indicates gravity influence the pitting corrosion is higher at a lower applied potential. At a high applied potential, a higher current density can compensate the pit electrolyte diffuse out. But at low applied potential, the pit electrolyte diffuse out cannot be easily compensate due to lower applied potential.

Figure 9.3- 9 (b) shows pits are nucleated in Type 316L BPE after region 4 in the FU orientation, but for the FD and PE orientations, pits generated from region 1. For 316L BPE, a more protective passive film is formed due to Mo, the competition between the passive film formation and pit nucleation results in non-linear pit volume along the BPE in all the surface orientations. In Figure 9.3- 9 (d) and (f), Type 316L BPE with PE and FD orientations show the linearly pit volume along the BPE after 10 min, with similar pit volume reduction rate, so the competition between the passive film growth and pit nucleation is finished in the PE and FD orientations. The pit volume along the BPE is not linearly until 15 min in the FU orientation, The pit volume linearly distribution on the Type 316L BPE for the FU orientation need 30 min exposure time [34]. The passive film growth is independent to gravity from the 3-electrode polarisation test but changes by gravity for 316L BPE. The possible reason is the corrosion resistance of passive film reach the maximum before E_{pit}, contribute from the OCP and potential in the passive region. But for the BPE, a high applied potential is direct applied on the BPE, the concentration of Cr in the passive film is reduced which results in a less protective passive film, hence a lower corrosion resistance [35,36]. So the corrosion resistance of the passive film can be increased by longer exposure time. Gravity can reduce the precipitate process, makes a less protective passive film in the FD and PE orientations, so the competition between the passive film growth and pit nucleation finish earlier, results in linearly pits along the 316L BPE after 10 min in PE and FD orientation.

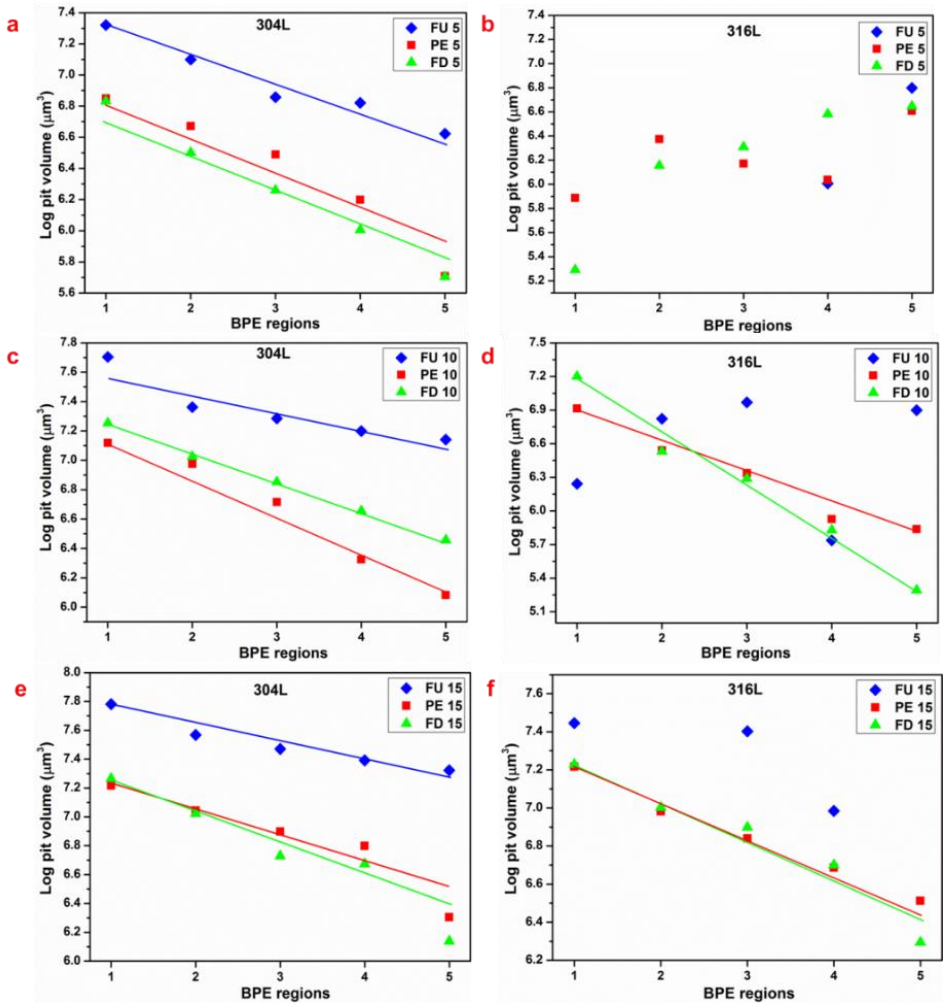

Figure 9.3- 9 Pit volume loss along Type 304L BPE after (a) 5 min, (c) 10 min and, (e) 15 min, and Type 316L BPE after (d) 5 min, (e) 10 min, and (f) 15 min with different surface orientations.

Pit shape with different orientation

Figure 9.3- 10 gives all the pits with depth and corresponding volume as a function of exposure time and exposed surface orientations. For

Figure 9.3- 10 (a), (c), and (e), all pits in Type 304L BPEs with the FU orientation is around semi-circular. For the PE and PD orientations, pits are the narrow ellipsoids like. Pits in the FU orientation is wider, as more aggressive pit electrolyte maintained near the pit mouth. The pits in the PE and FD orientations are narrow ellipsoids like, as the pit electrolyte near the pit mouth is diffuse away. Narrow ellipsoids like pits are dangerous as the pits with higher aspect ratio might penetrate the substrate, or result in the fatigue crack nucleation and expansion, or result in the Stress Cracking

Corrosion (SCC) as higher stress as pit shoulder and higher stain at pit mouth [37–40].

Figure 9.3- 10 (b), (d) and, (f) show the pit shapes evolution in Type 316L BPEs. For the FU orientation, pits are wider than semi-circular. For the PE and FD orientations, pits are narrow ellipsoids like, comes from the pit electrolyte near the pit mouth diluted by gravity. The pit number in FU orientation is little, but the pit volume is much larger.

For the FU orientation, pits in Type 304L BPEs are semi-circular but wide-like pits are found in Type 316L BPE. The reason is the addition of Mo, Mo exists in the salt film, increase the resistance of the salt film, result in longer the diffusion path and lower corrosion rate, so wider pits are found in the Type 316L BPE [41,42].

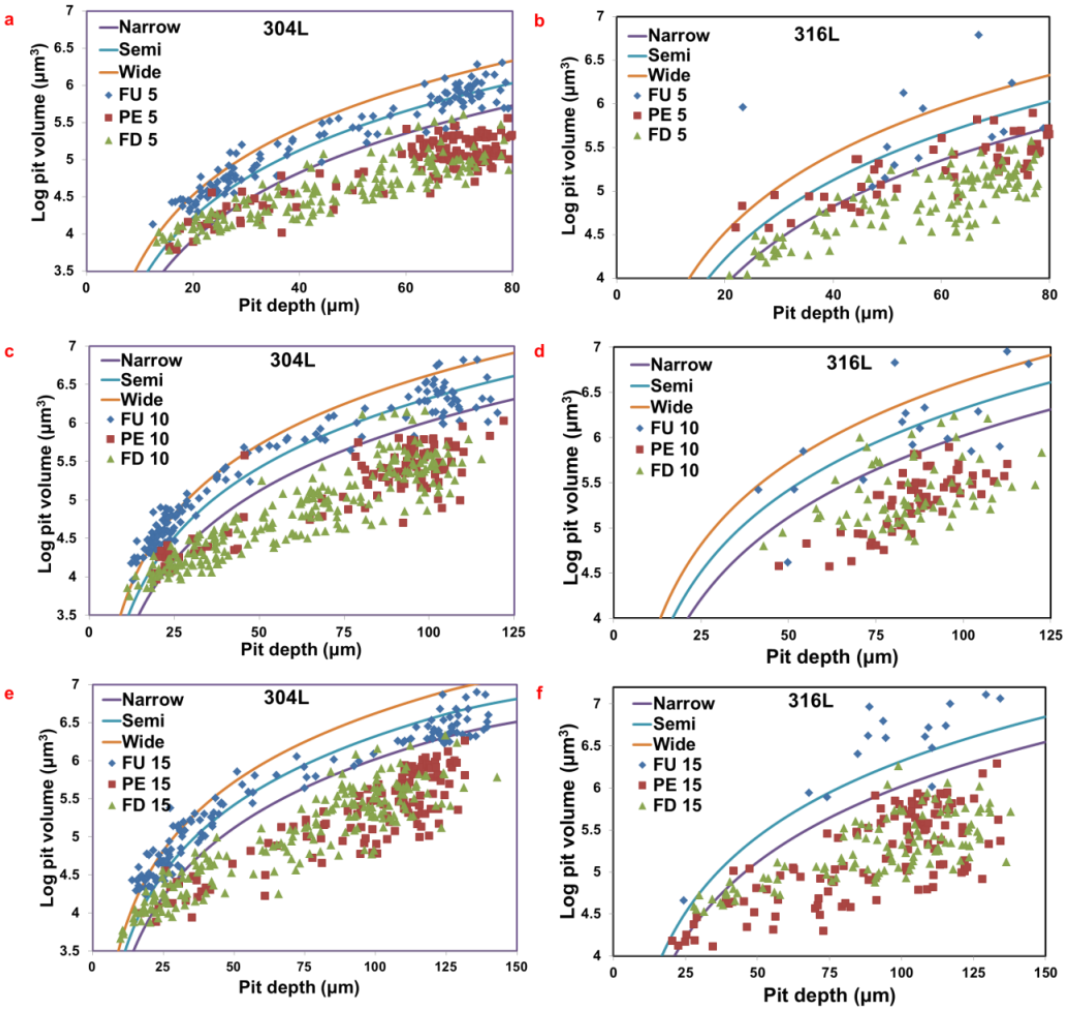

Figure 9.3- 10 Pit depth and the corresponding volume in Type 304L and 316L BPEs with different exposed surface orientations. Type 304L stainless steel runs for (a) 5 min, (c) 10 min, and, (e) 15 min, Type 316L BPEs exposed for (b) 5min, (d) 10 min, and (f) 15 min.

Pit shape along the BPE

Figure 9.3- 11 shows the pit depth and the corresponding volume along Type 304L BPE after 15 min exposure time. Figure 9.3- 11 (a) displays pits in the region 1 are semi-circular shape and the left four regions have the narrow ellipsoids like pits. The maximum pit depths in all regions are similar. More open pits are nucleated at higher applied potential with higher opportunities to become stable pits [15,16]. Figure 9.3- 11 (b) and (c) shows all pits are narrow ellipsoids like in the PE and FD orientations. Slightly deeper pits are measured in region 1, and similar pit shapes in other region. The pit shape influenced by gravity is from dilute pit electrolyte at pit mouth, as the pit depth is similar from region 1 to region 5. The Higher applied potential offer higher current density, which has the potential to the pit mouth diffuse out at the pit mouth. So the pit volume increased without change in pit depth.

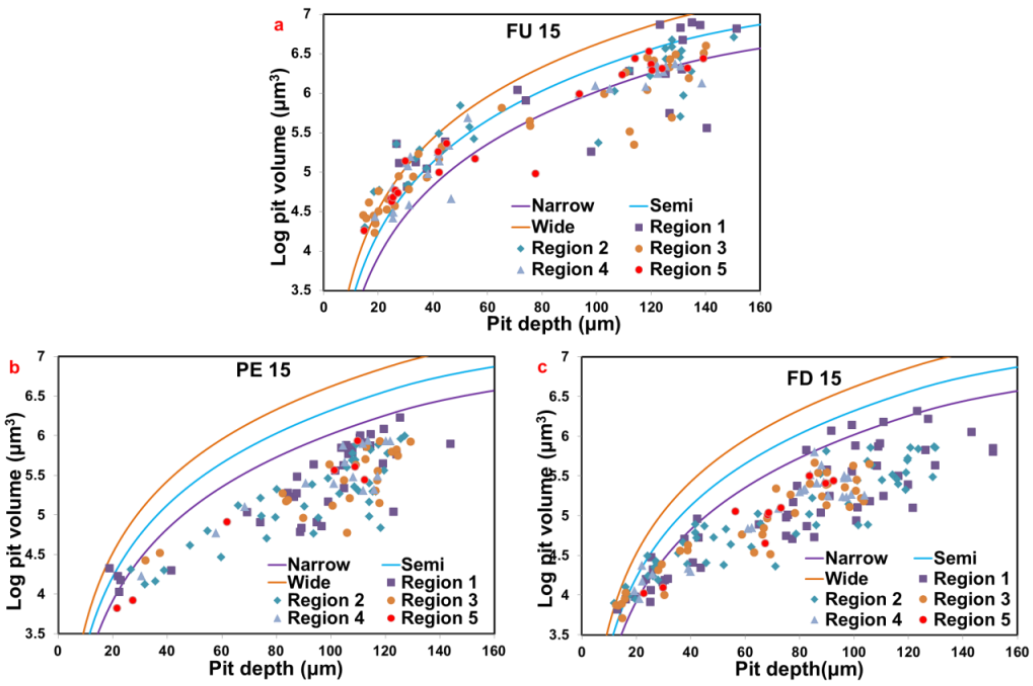

Figure 9.3- 11 Pit shapes along 304L BPE at 15 min from (a) FD, (b) PE, to (c) FU orientation.

Individual pit volume distribution

Figure 9.3- 12 (a), (c), and, (e) shows the pit and related volume distributed on Type 304L BPE with different surface orientations and exposure time. The numbers of pits in the FU orientation are highest. At 5 min, the numbers of pits are similar between the FD and PE orientation. At 10 min, the numbers of pits in the FD orientation is higher, but after 15 min, the pits become similar again between the PE and FD orientations. Figure 9.3- 12 (b), (d), and (f) gives the pit number and related volume distribution in Type 316L BPE. From 5 to 15 min, the pit numbers in the FU orientation is lowest with largest pit volume. The pit numbers in the FD orientation is higher than PE orientation at 5 min; but after 10 min, the pit number and pit size become similar.

For the FU orientation, Type 304L BPEs prefer forming large numbers of pits but smaller volume pit; and Type 316L stainless steel nucleates few numbers of pits but larger individual pit volume. as the addition of Mo can reduce the pit nucleation probability [43,44].The features of pit density and pit size in Type 304L and Type 316L stainless steel are same as literatures [45,46].

Pit volume slope is the increment rate of pit volume in a constant number of pits; the pit volume slope is used to describe the pit nucleation and growth kinetics. Large pit volume slope indicates a lower pit nucleation rate with a higher pit volume expansion rate. For Type 304L BPEs, 2 different pit volume slopes are observed in FD and PE orientations, indicates the metastable pit in the first pit volume slope and stable pit in the second pit volume slope. The pit volume can act as diffusion layer, so stable pits always have a large pit volume. For Type 316L BPEs, pit volume slope in the FU orientation is highest and similar between the FD and PE orientations. Only one pit volume slope is determined for each surface orientation, as not enough pit numbers, the boundary between the metastable pits and stable pits cannot be distinguished from the pit volume slope.

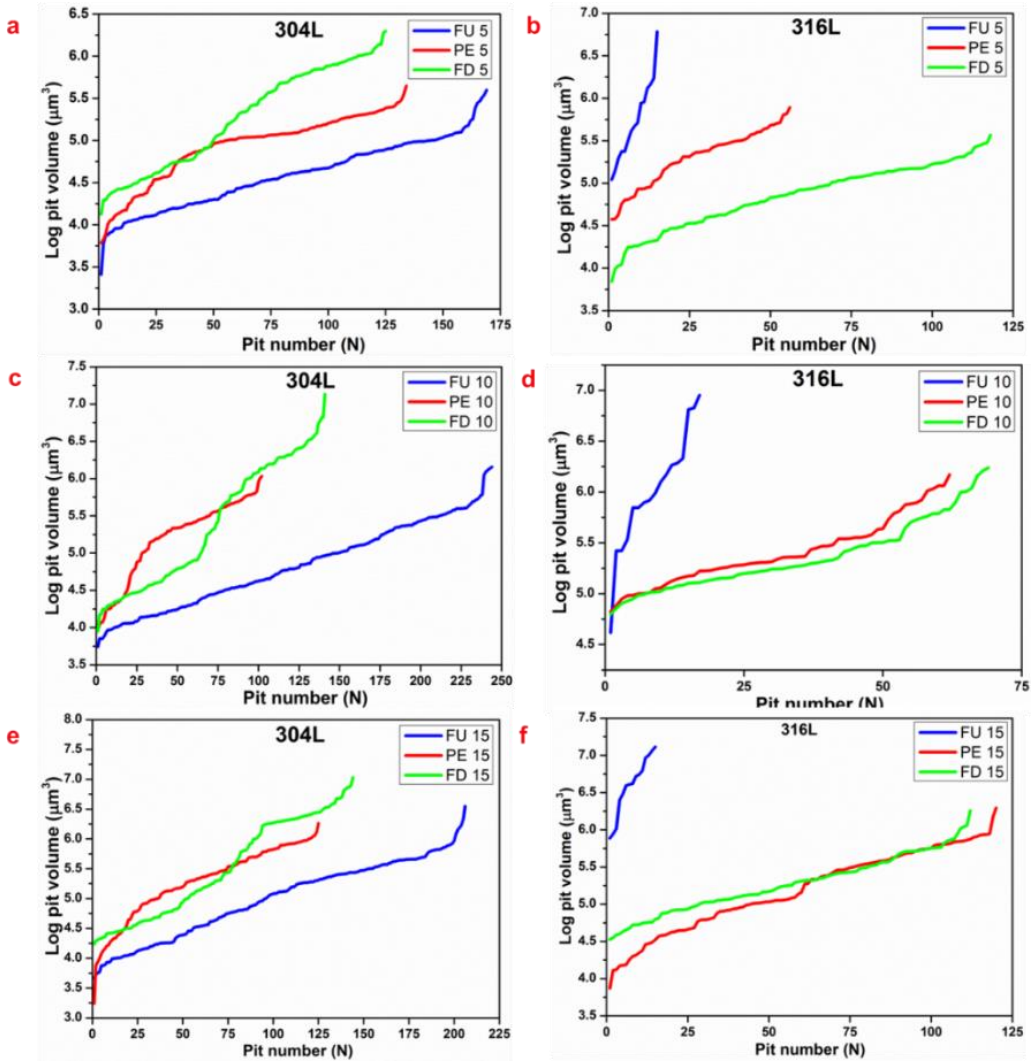

Figure 9.3- 12 The distribution of the pit volume with the different surface orientations, (a) (c), and (e) are the 304L BPE exposed from 5, 10, to 15 min, and (b), (d), and (f) are the 316L BPE runs from 5, 10, and 15 min.

Figure 9.3- 13 gives the value of pit volume slopes for different surface orientations and exposure time in Type 304L BPE. The FU orientation has 1 pit volume slope, and 2 different pit volume slopes are observed for the PE and FD orientations. For the PE orientation, the second pit volume slope is smaller than the first pit volume slope, indicates stable pit volume expansion rate is higher than metastable pits. For the FD orientation, the second pit volume slope is higher than the first pit volume slope, related to the numbers of metastable pits and stable pits, with a more numbers of metastable pits and less stable pits, the current density from the repassivate pits can support the stable growth with a fast speed, which shown as PE orientation. If less numbers of metastable pits and more stable pits, the current from the

repassivate pits cannot accelerate the stable pit growth rate. Only one pit volume slope is determined in the FU orientation, which is almost similar from 5 to 15 min, as a large numbers of pits are generated, pits are close to each other or merge. In this situation, two factors should be noticed; first of all, after pits close to each other, the cathode area surrounds the pit are reduced which cannot support enough cathodic current, so the pit volume expansion rate was retarded [45,46]. Secondly, after pits merge, the local effective potential and/or pit electrolyte change, which also influence the pit growth kinetics [47]. For these two reasons, only one pit volume slope is determined.

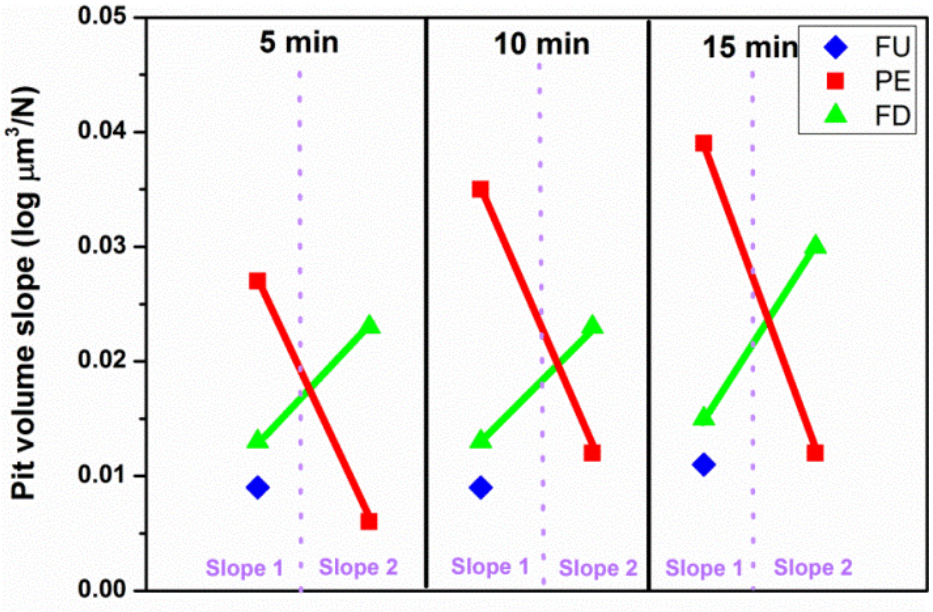

Figure 9.3- 13 The different pit volume slopes for Type 304L stainless steel with different exposure time and surface orientations.

9.36 Conclusions

Bipolar electrochemistry is used to research the pitting corrosion, pit shape, and pit growth kinetics by gravity, allows the pit research under a wide range of potential in one sample. Type 316L stainless steel shows a higher pitting corrosion resistance than Type 304L stainless steel. Before exposed 15 min, the total pit volume and pit growth kinetics are highest in the FU orientation and similar between the PE and FD orientations. The pit volumes are linearly reducing along Type 304L BPE but not for Type 316L BPE. The pit shapes are either semi-circular or wide-like for the FU orientation and the pits are the

narrow ellipsoids like for the PE and FD orientations. The maximum pit depth is independent to the applied potential, but the pit shapes are changed by the local applied potential. The stable pit growth is influenced by the numbers of stable and metastable pits.

9.37 References

[1] S. Munktell, M. Tydén, J. Högström, L. Nyholm, F. Björefors, Bipolar electrochemistry for high-throughput corrosion screening, Electrochemistry Communications. 34 (2013) 274–277.

[2] Y. Zhou, D.L. Engelberg, Application of a modified bi-polar electrochemistry approach to determine pitting corrosion characteristics, Electrochemistry Communications. 93 (2018) 158–161.

[3] N. Pébère, V. Vivier, Local Electrochemical Measurements in Bipolar Experiments for Corrosion Studies, ChemElectroChem. 3 (2016) 415–421.

[4] S.E. Fosdick, K.N. Knust, K. Scida, R.M. Crooks, Bipolar electrochemistry, Angewandte Chemie - International Edition. 52 (2013) 10438–10456.

[5] C. Sequeira, P. Cardoso, F. Gameiro, Bipolar Electrochemistry, a Focal Point of Future Research, Chemical Engineering Communications. 0 (2016) 1001–1008.

[6] G.S. Frankel, Pitting Corrosion of Metals A Review of the Critical Factors, Journal of Electrochemistry Society. 145 (1998) 2186–2198.

[7] B. Krawczyk, P. Cook, J. Hobbs, D. Engelberg, Corrosion Behavior of Cold Rolled Type 316L Stainless Steel in HCl Containing Environments, Corrosion. 73 (2017) 1346.

[8] N. Sato, A theory for breakdown of anodic oxide films on metals, Electrochimica Acta. 16 (1971) 1683–1692.

[9] S. Pahlavan, S. Moazen, I. Taji, K. Saffar, M. Hamrah, M.H. Moayed, S. Mollazadeh Beidokhti, Pitting corrosion of martensitic stainless steel in halide bearing solutions, Corrosion Science. 112 (2016) 233–240.

[10] S.M. G.Burstein, P.Pistorius, The Nucleation and Growth of Corrosion Pits on Stainless Steel, Corrosion Science. 35 (1993) 57–62.

[11] J. Srinivasan, R.G. Kelly, Evaluating the Critical Chemistry for Repassivation at the Corroding Surface Using Mass Transport Model-Based Artificial Pit Experiments, Journal of The Electrochemical Society. 163 (2016) C768–C777.

[12] J. Srinivasan, C. Liu, R.G. Kelly, Geometric Evolution of Flux from a Corroding One-Dimensional Pit and Its Implications on the Evaluation of Kinetic Parameters for Pit Stability, Journal of The Electrochemical Society. 163 (2016) C694–C703.

[13] N.J. Laycock, Metastable Pitting and the Critical Pitting Temperature, Journal of The Electrochemical Society. 145 (1998) 2622.

[14] N.J. Laycock, R.C. Newman, Localised dissolution kinetics, salt films and pitting potentials, Corrosion Science. 39 (1997) 1771–1790.

[15] W. Tian, S. Li, N. Du, S. Chen, Q. Wu, Effects of applied potential on stable pitting of 304 stainless steel, Corrosion Science. 93 (2015) 242–255.

[16] N.J. Laycock, S.P. White, Computer Simulation of Single Pit Propagation in Stainless Steel under Potentiostatic Control, Journal of The Electrochemical Society. 148 (2001) B264.

[17] C. Örnek, F. Léonard, S.A. McDonald, A. Prajapati, P.J. Withers, D.L. Engelberg, Time-dependent in situ measurement of atmospheric corrosion rates of duplex stainless steel wires, Npj Materials Degradation. 2 (2018) 10.

[18] J. Mankowski, Z. Szklarska-Smialowska, The effect of specimen position on the shape of corrosion pits in an austenitic stainless steel, Corrosion Science. 17 (1977) 725–735.

[19] M. Wang, H.W. Pickering, Potential Distribution, Shape Evolution, and Modeling of Pit Growth for Ni in Sulfuric Acid, Journal of The Electrochemical Society. 142 (1995) 2986–2995.

[20] J. Mankowski, Z. Szklarska-Smialowska, Studies on accumulation of chloride ions in pits growing during anodic polarization, Corrosion Science. 15 (1975) 493–501.

[21] M. Sakairi, A. Kageyama, Y. Kojima, Y. Oya, T. Kikuchi, Effect of aspect ratio of artificial pits formed on anodized Al by PRM on localized corrosion in chloride environments, The Electrochemical Society. 16 (2009) 19–28.

[22] P.C. Pistorius, G.T. Burstein, Aspects of the effects of electrolyte composition on the occurrence of metastable pitting on stainless steel, Corrosion Science. 36 (1994) 525–538.

[23] R. Merello, F.J. Botana, J. Botella, M. V. Matres, M. Marcos, Influence of chemical composition on the pitting corrosion resistance of non-standard low-Ni high-Mn-N duplex stainless steels, Corrosion Science. 45 (2003) 909–921.

[24] K. TOHMA, K. YAMADA, Change of corrosion potentials of aluminum and aluminum alloys with pit growth, Journal of Japan Institute of Light Metals. 30 (1980) 85–91.

[25] S. Pyun, J.-D. Kim, Effects of electrolyte composition and applied potential on the repassivation kinetics of pure aluminium, Electrochimica Acta. 40 (1995) 1863–1869.

[26] D. Macdonald, The Point Defect Model for Bi-Layer Passive Films, Journal of the Electrochemical Society. 139 (1992) 3434–3449.

[27] D.D. MacDonald, The history of the Point Defect Model for the passive state: A brief review of film growth aspects, Electrochimica Acta. 56 (2011) 1761–1772.

[28] S. Yang, D.D. Macdonald, Theoretical and experimental studies of the pitting of type 316L stainless steel in borate buffer solution containing nitrate ion, Electrochimica Acta. 52 (2007) 1871–1879.

[29] C. Örnek, M. Långberg, J. Evertsson, G. Harlow, W. Linpé, L. Rullik, F. Carlà, R. Felici, E. Bettini, U. Kivisäkk, E. Lundgren, J. Pan, In-situ synchrotron GIXRD study of passive film evolution on duplex stainless steel in corrosive environment, Corrosion Science. 141 (2018) 18–21.

[30] M. Kaneko, H.S. Isaacs, Effects of molybdenum on the pitting of ferritic- and austenitic-stainless steels in bromide and chloride solutions, Corrosion Science. 44 (2002) 1825–1834.

[31] C. Örnek, C. Leygraf, J. Pan, Passive film characterisation of duplex stainless steel using scanning Kelvin prove force microscopy in combination with electrochemical measurements, Npj Materials Degradation. 3 (2019) 8.

[32] K. Sugimoto, Y. Sawada, The role of molybdenum additions to austenitic stainless steels in the inhibition of pitting in acid chloride solutions, Corrosion Science. 17 (1977) 425–445.

[33] J. Moon, H.Y. Ha, S.J. Park, T.H. Lee, J.H. Jang, C.H. Lee, H.N. Han, H.U. Hong, Effect of Mo and Cr additions on the microstructure, mechanical properties and pitting corrosion resistance of austenitic Fe-30Mn-10.5Al-1.1C lightweight steels, Journal of Alloys and Compounds. 775 (2019) 1136–1146.

[34] Y. Zhou, D.L. Engelberg, Application of a modified bi-polar electrochemistry approach to determine pitting corrosion characteristics, Electrochemistry Communications. (2018) In Press.

[35] C.O.A. Olsson, D. Landolt, Passive films on stainless steels - Chemistry, structure and growth, Electrochimica Acta. 48 (2003) 1093–1104.

[36] G. Okamoto, Passive film of 18-8 stainless steel structure and its function, Corrosion Science. 13 (1973) 471–489.

[37] Y. Kondo, Prediction of Fatigue Crack Initiation Life Based on Pit Growth, Corrosion Science. 45 (1989) 7–11.

[38] K. Jones, D.W. Hoeppner, Pit-to-crack transition in pre-corroded 7075-T6 aluminum alloy under cyclic loading, Corrosion Science. 47 (2005) 2185–2198.

[39] L.K. Zhu, Y. Yan, L.J. Qiao, A.A. Volinsky, Stainless steel pitting and early-stage stress corrosion cracking under ultra-low elastic load, Corrosion Science. 77 (2013) 360–368.

[40] A. Turnbull, L. Wright, L. Crocker, New insight into the pit-to-crack transition from finite element analysis of the stress and strain distribution around a corrosion pit, Corrosion Science. 52 (2010) 1492–1498.

[41] J.R. AMBROSE, The Role of Molybdenum as an Inhibitor of Localized Corrosion on Iron in Chloride Solutions, Corrosion. 34 (1978) 27–31.

[42] J.N. WANKLYN, The role of molybdenum in the crevice corrosion of stainless steels, Corrosion Science. 21 (1981) 211–225.

[43] A. Pardo, M.C. Merino, A.E. Coy, F. Viejo, R. Arrabal, E. Matykina, Pitting corrosion behaviour of austenitic stainless steels - combining effects of Mn and Mo additions, Corrosion Science. 50 (2008) 1796–1806.

[44] G.O. Ilevbare, G.T. Burstein, The Role of alloyed molybdenum in the inhibition of pitting corrosion in stainless steels, Corrosion Science. 43 (2001) 485–513.

[45] M.T. Woldemedhin, M.E. Shedd, R.G. Kelly, Evaluation of the Maximum Pit Size Model on Stainless Steels under Thin Film Electrolyte Conditions, Journal of the Electrochemical Society. 161 (2014) E3216–E3224.

[46] M.T. Woldemedhin, M.E. Shedd, R.G. Kelly, Evaluation of the Maximum Pit Size Model on Stainless Steels under Atmospheric Conditions, Journal of the Electrochemical Society. 58 (2014) 41–50.

[47] N.J. Laycock, D.P. Krouse, S.C. Hendy, D.E. Williams, Computer Simulation of Pitting Corrosion of Stainless Steels, Interface, The Electrochemical Society. (2014) 65–71.

9.4 Optimising brass dezincification with a bipolar electrochemistry technique

Yiqi Zhou[*1], *Sultan Mahmood*[2], *Dirk Lars Engelberg*[1,2]

(1) Corrosion & Protection Centre, School of Materials, The University of Manchester, M13 9PL, Manchester, UK

(2) Materials Performance Centre, The University of Manchester, M13 9PL, Manchester, UK

* Corresponding author: Yiqi.Zhou@postgrad.manchester.ac.uk

9.42 Abstract

A bipolar electrochemistry approach was applied to characterise the dezincification of brass. The dissolution of both Cu and Zn resulted in the formation of Cu_2O, CuO, ZnO and CuClx, with corrosion product formation characterised as a function of the potential gradient. At low potentials, protective corrosion products formed, with compositional changes observed via dezincification up to a critical applied potential threshold. Above the critical potential, no corrosion products could form, resulting in higher corrosion rates. The influence of corrosion product formation after bipolar electrochemistry assessment is compared to results from standard three-electrode potentiodynamic polarisation tests.

Keywords: Bipolar electrochemistry, dezincification, potentiodynamic polarisation, SEM, Raman, XRD

9.43 Introduction

Bipolar electrochemistry produces a potential gradient between two feeder electrodes, resulting in a continuous spectrum of anodic-to-cathodic electrochemical reactions along the exposed bipolar electrode (BPE) [1–3]. The potential gradient provides direct access to electrochemical reactions covering the full spectrum of applied potentials [4], allowing samples with complex shapes, electrically sensitive systems, or even complicated microstructures, such as multi-component welds or additively manufactured materials, to be investigated [5]. A large number of experimental exposure parameters can be assessed in a single bipolar electrochemistry experiment by using a simple, low-cost set-up, allowing its application for both research and assessment of industrial service environments [6–9]. Bipolar electrochemistry is a powerful corrosion assessment technique, which has been used, for example, to probe pitting corrosion of Type 2205 duplex

stainless steel at room temperature, where as other techniques are dependent on higher temperature exposure tests (>40°C) [10].

Commercial brass suffers from dealloying via a mechanism called dezincification, when Zn is selectively dissolved out of the brass matrix, leaving behind a porous Cu enriched surface layer. This phenomenon can lead to brittle crack nucleation sites and mechanical failures, as well as the release of other alloying elements causing health issues [11–13]. De-alloying is also used for the manufacture of nano-porous layers, by establishing the relationship between dissolution parameters and the associated de-alloying response. There are, in general, two common dezincification mechanisms, based on either selective dissolution or dissolution-redeposition reactions. Selective dissolution involves the preferential dissolution of Zn without the electrochemical dissolution of Cu [14,15]. Dissolution-redeposition describes the simultaneous dissolution of both Cu and Zn, after which Cu re-precipitates back onto the brass surface, resulting in a porous metallic Cu-rich surface film [16,17]. The difficulty of identifying underlying dissolution mechanisms of brass from simply observing the current density is due to the potential formation of soluble and insoluble corrosion products [18,19]. The multi-layered corrosion products contain Zn oxides, Cu oxides and can result in a depleted layer of zinc [20,21].

The presence of brass corrosion product in pH ≈ 7 tap water has been reported to accelerate the dezincification rate [22], with dissolution also reported at very low applied potentials (-0.25 V_{SHE}) in NaCl solutions [23,24]. The initial stage of brass corrosion is often not selective, and both components Cu and Zn then dissolve in parallel [25,26]. The release of Cu ions can be used to kill bacteria due to their excellent antimicrobial properties [27–29], with the possibility of corrosion products that can prevent further dezincification [30]. To combat the dezincification of brass, Sn, As, and Nb can be added as alloying element to brass, with these elements forming a passive to suppress Zn dissolution [31,32]. To find the optimised potential to release enough Cu ions is of importance in medical applications, with the idea of forming Cu-containing corrosion products before use in food and tap water systems. This release can reduce the risk of health issues from dezincification.

This study aims to provide a better understanding of the occurrence of brass dezincification at different applied potentials, investigated by using a bipolar electrochemistry method. The corrosion product formation as a function of applied potential gradient was observed and characterised, yielding interesting insights into the relationship between element dissolution and associated redeposition reactions.

9.44 Materials and Methods

Temper half hard Cu_{63}/Zn_{37} brass sheet was used in this study. For the 3-electrode potentiodynamic polarisation test, the sample was cut to a size of 30 mm x 30 mm x 2.4 mm (L x W x T) and tested in an AVESTA cell [45] at room temperature in 0.1M HCl. A Pt electrode and SCE reference electrode were used, in combination with an IVIUM-Compactstat and IVIUMsoft software to measure potentiodynamic polarisation curves. The OCP was measured for 600 seconds, followed by potentiodynamic polarisation tests from -200 mV_{OCP} to +1500 mV_{OCP} with a scan rate of 1 mV/s. Potentiodynamic tests were also carried out up to +200mV_{SCE}, +800mV_{SCE}, and +1300mV_{SCE}, with samples then removed for surface analysis (samples A, B and C in Figure 9.4- 2 respectively).

For bipolar electrochemistry, the BPE had a dimension of 30 mm x 10 mm x 2.4 mm (L x W x T), with Figure 9.4- 1 giving a schematic of the experimental setup. A Keysight E36105A power supply was used, and a constant potential (10 V) was applied between the feeder electrodes with a distance of 60 mm. The BPE was set at the centre of the feeder electrodes. Each Platinum feeder electrode had a surface area of 4 cm^2. Bipolar electrochemistry experiments were run for 900 seconds, and the electrolyte was HCl (0.1 M, 200 ml).

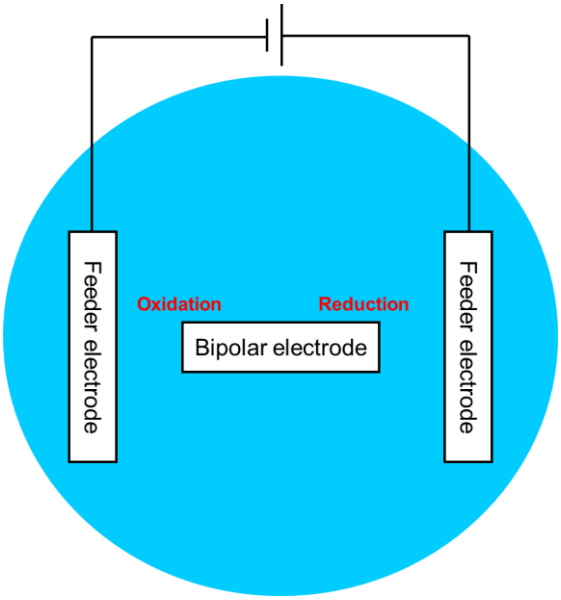

Figure 9.4- 1 Schematic setup of the bipolar electrochemistry experiment.

After each electrochemical experiment, the sample was removed from the electrolyte, washed with detergent and water, and cleaned in an ultrasonic bath with de-ionised water for 600 seconds. The latter was carried out to remove any non-adherent corrosion products. A Keyence VK-200K laser confocal microscope was used to determine the corrosion morphology, with SEM imaging carried out using a Zeiss Sigma VP FEG-SEM at 5 kV. The data analysis from EDX was carried out using Aztec software at 20 kV to characterise the chemical composition of the surface films.

GI-XRD analysis was carried out on a Rigaku SmartLab 3 kW with a copper sealed tube target producing Cu kα and kβ emission lines operating at 40 kV and 30 mA (1.2 kW), and a scan step size of 0.05° (2θ) was applied. An incidence angle of 3^{o} was used for all XRD scans.

Raman spectroscopy analysis was carried out on a Renishaw inVia™ confocal Raman microscope. A 633nm laser was used with an 1800 l/mm grating, the exposure time was 10 second, with 5 accumulations, using a 5x objective lens, with the laser power at 100%.

9.45 Results and Discussion

Potentiodynamic Polarisation Testing

A potentiodynamic polarisation curve of brass in 0.1M HCl is shown in Figure 9.4- 2, The sample had an open circuit potential (OCP) of -0.2 V_{SCE}, followed by an increasing current density from -0.2 V_{SCE} to +0.3 V_{SCE}. At approximately +0.3 V_{SCE} a small current drop is observed. The current then increases again monotonically up to +1.0 V_{SCE}, with higher potentials (> +1.0 V_{SCE}) following a monotonically decreasing current trace. Three samples (A, B, C) with different end potentials (+0.2 V_{SCE}, +0.8 V_{SCE}, and +1.3 V_{SCE}) were prepared for scanning electron microscope (SEM) and energy dispersive X-ray (EDX) analysis, as shown in Figure 9.4- 3.

Figure 9.4- 3 (a) shows an SEM image of Sample A, which had a final exposure potential of +0.2 V_{SCE}, just before the first potential drop. At lower magnification, grinding marks from preparing the sample for exposure are still present, indicating that not much corrosion had occurred on this sample. However, at higher magnifications, the presence of small particles is observed. EDX analysis shows that the particles have a higher Cu/Zn ratio of 87:13, compared to the as received material composition (Table 9.4-1). The brass surface after a polarisation to +0.8 V_{SCE} is shown in Figure 9.4- 3 (b), clearly supporting the presence of corrosion products covering the sample surface. These adhered to the surface and were not removed by the ultrasonic cleaning process. Some cracks were also present within the observed surface layer (Figure 9.4- 3 b and c).

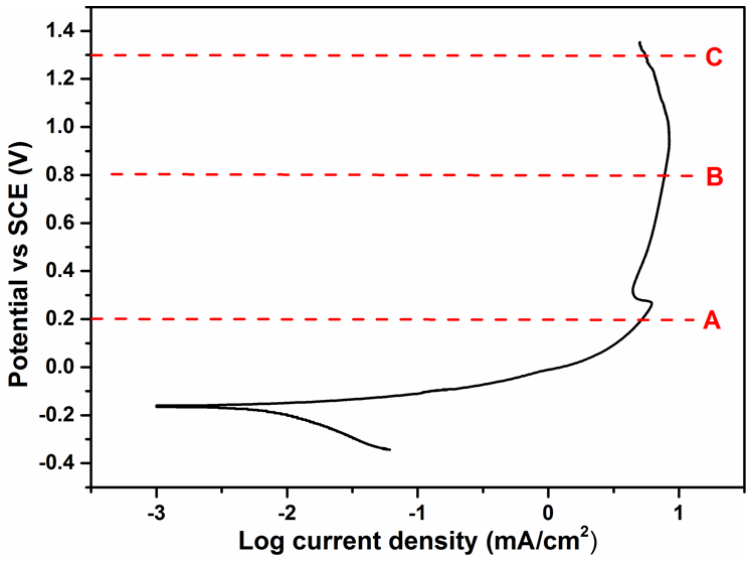

Figure 9.4- 2 The 3-electrode potentiodynamic polarisation curves for brass at room temperature.

The current drop at +0.3 V_{SCE} is therefore believed to be related the formation of corrosion products. The corrosion products seem to initially protect the sample surface, as the current density slowly increases with higher applied potentials. The presence of corrosion products is clearly shown in Figure 9.4- 3 (b), after exceeding a critical potential which results in electro-adsorption of these products on the brass surface, as reported by others [33]. At +1.0 V_{SCE}, the thickness or composition of the corrosion product changes, as it becomes more protective, resulting in the current density reduces with the higher applied potentials. The formation and nucleation of corrosion products has also been related to the overall exposure time [34]. Inspecting the higher magnification images in Figure 9.4- 3 (b), it is apparent that the surface of the corrosion product is not smooth, supporting the presence of smaller particles. In Figure 9.4- 3 (c), the surface of the corrosion products appears then smoother, pointing towards physical or chemical changes in the product layer.

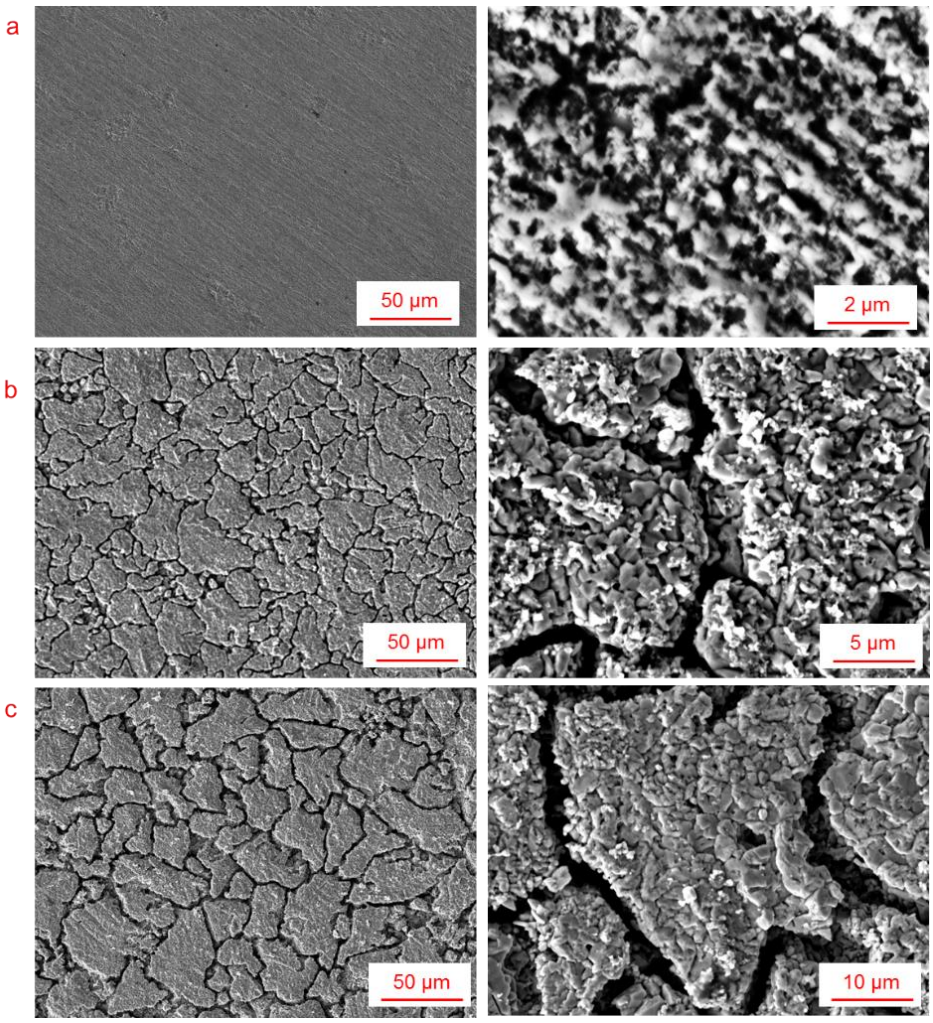

Figure 9.4- 3 SEM images of the brass dezincification during potentiodynamic polarization test at (a) +0.2 V_{SCE}, (b) +0.8 V_{SCE}, and (c) +1.3 V_{SCE}. The left image is at lower magnification and the right image in under a higher magnification.

Table 9.4-1 gives the chemical composition of the brass surface analysed by EDX of the samples exposed to different polarisation end potentials, shown as samples A, B, and C in Figure 9.4- 2. The composition of the as received (AR) sample under EDX measurement is 62% Cu, 35% Zn, and ≈ 3% O. After polarising to +0.2 V_{SCE}, the concentration of Cu significantly increases, with a parallel reduction in Zn and O. Higher applied potential then clearly indicates the preference of Zn to dissolve into the electrolyte, with increasing Cu contents up to a maximum of ≈ 94%. Interestingly, the data can also be interpreted with the dissolution of both Cu and Zn, followed by re-precipitation of Cu-containing corrosion products at the sample surface. The presence of Cl is also observed in all analysed layers.

Table 9.4- 1 Compositions of alloying elements in as received (AR) condition Sample A, Sample B, and Sample C, obtained by EDX.

(wt%)	Cu	Zn	O	Cl
AR	62	34.9	3.1	/
+0.2V	86.7	12.2	0.9	0.2
+0.8V	91.9	5.7	0.4	2
+1.2V	93.9	4.6	0.2	1.2

Combining 3-electrode potentiodynamic polarisation tests with SEM/EDX analysis indicates the formation of corrosion product on the brass surface, which reduces the corrosion rate (E-log(i) curve). Over higher applied potential and longer exposure times the composition of the corrosion products changed (Table 9.4-1).

Bipolar Electrochemistry – Potential Distribution

The bipolar electrochemical set-up with corresponding current and potential distributions is at first introduced. Measurements to determine local potential changes which act during bipolar electrochemistry experiments were carried out, to better understand the potential distribution along the brass sample surface. These experiments were undertaken by spot welding a copper wire to the back of the BPE, and a Luggin capillary connected to a saturated calomel electrode (SCE) set ≈ 1mm above the BPE surface. During these experiments, the OCP of the electrode was first recorded, and the feeder electrode power supply then switched on. The reported potential change on the y-axis in Figure 9.4- 4 is the difference between the measured potential with bipolar feeder electrodes switched on and the OCP with feeder electrode switched off. The potentials were measured along the BPE surface in increments of 5 mm, with the Luggin capillary positioned along the centreline of the brass sample.

Figure 9.4- 4 (a) (a) shows the potential distribution along the BPE, with the recorded potential at each point showing the mean potential over 10 minutes of exposure. The potential distribution is quasi-linear along the centre of the BPE, with the potential at the oxidation edge indicating slightly increased potential responses; i.e. more positive at the oxidation edge and more negative at the reduction edge. This is due the discontinuity of the BPE sample at the interface to the resin, attracting a more concentrated electrical field. The superimposed trend line shows a linear approximation of all points, with the

measured potentials at the BPE edges (0 mm and 30 mm) slightly off-set with respect to the trendline.

Figure 9.4- 4 (b) (b) gives the potential change vs OCP at different locations over time. The values (e.g. 0 mm, 5 mm) describe the distance with respect to the oxidation edge of the BPE. The observed noise at each point is caused by local turbulences due to corrosion and other gas formation reactions. The applied potential here can generate Cl_2 and H_2 gas, which in turn over extended periods of time changes the electrical resistance of the electrolyte.

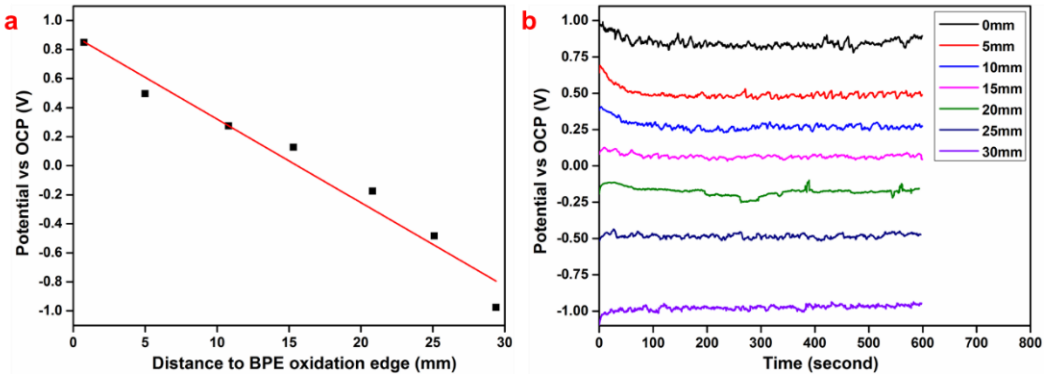

Figure 9.4- 4 (a) measured potential distribution along the BPE (potential change vs OCP) and (b)The potential change vs time at different locations on the BPE (0 - 30 mm).

Bipolar Electrochemistry – Surface Characterisation

Figure 9.4- 5 (a) shows optical images of the brass surface after application of bipolar electrochemistry for 900 seconds at room temperature. The left side of the image is the oxidation edge (close to the negative feeder electrode), resulting in the most oxidised material surface. Five different regions are present at the anodic sites, related to the corrosion response to the acting potential gradient along the BPE shown in Figure 9.4- 4 (a).

The five distinct regions are separated by lines in Figure 9.4- 5 to delineate them. The lines are curved at higher applied potentials due to the edge effect of the surrounding sample interface, consuming more current (similar to the interface in Figure 9.4- 4 (a)). Figure 9.4- 5 (b) gives higher magnification images of these region, with the different areas marked from Region 1 to 5. More than one colour is observed in Regions 1 to 3, highlighted by the arrows in Figure 9.4- 5 (b). The latter areas appear patch-like, indicating a partial loss of the surface films at these regions.

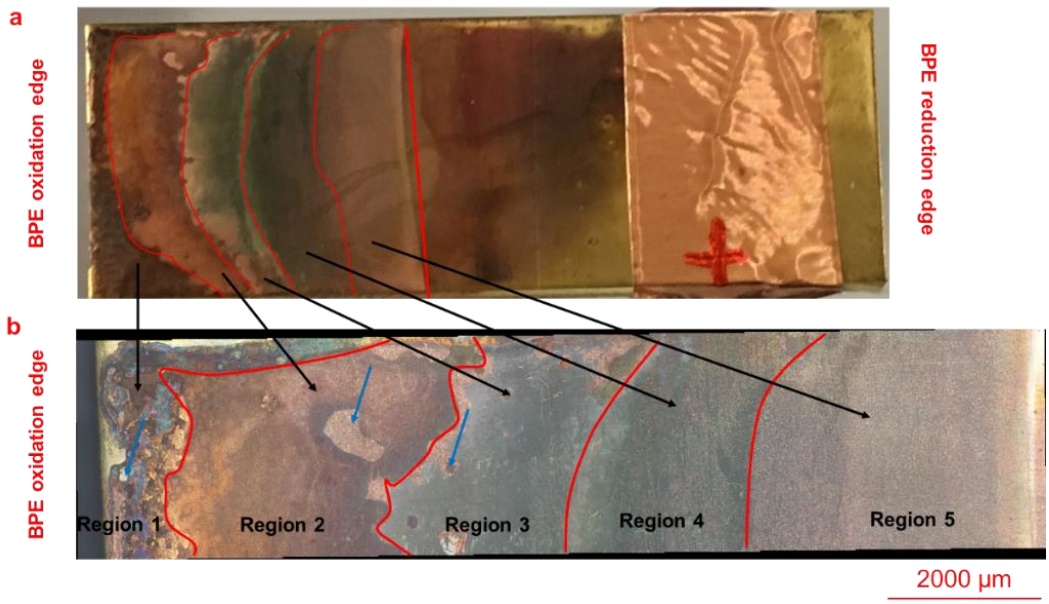

Figure 9.4- 5 (a) View of the bipolar electrode after dezincification, outlining the different corrosion regions along the sample surface; (b) higher magnification optical image of the 5 regions, with arrows outlining areas with different surface colour. (Note: a thin copper strip is placed in (a) over the sample and marked with a + to provide electrical contact to the SEM stab for analysis).

Figure 9.4- 5 summarises the different dezincification regions on one brass sample obtained from a single bipolar experiment. This observation supports literature reports of the applied potential influencing the acting dezincification mechanism [35]. The parameter influencing the dezincification reaction is here only the locally acting potential at the sample surface, as the exposure time is a constant for all the 5 regions. The bipolar technique overcomes the issues of analysing material behaviour using potentiodynamic polarisation tests, by excluding scan rate and exposure time related effects. In Figure 9.4- 6 optical images of the as received brass sample and the different regions after bipolar treatment are shown. The scale bar is the same for all the optical images, with the Regions 1 to 5 referring to the labels in Figure 9.4- 5.

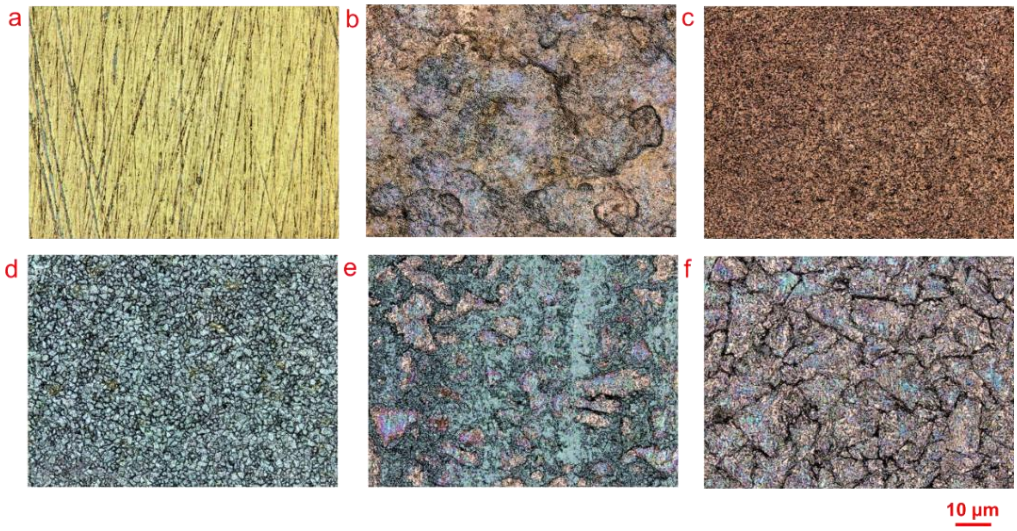

Figure 9.4- 6 Optical images of (a) AR brass and after dezincification along BPE in (b) Region 1, (c) Region 2, (d) Region 3, (e) Region 4, and (f) Region 5.

The surface of the AR sample contains grinding marks, shown in Figure 9.4- 6 (a), highlight the surface condition before sample exposure. Region 1 and 2 are shown in Figure 9.4- 6 (b and c) reflecting an inherently brown colour, indicative of oxidised copper surfaces. The surface in Region 2 is smoother compared to Region 1. In Figure 9.4- 6 (d), the colour of the surface film in Region 3 then changes into cyan, with the sample surface containing a lot of cracks. Region 5 is shown in Figure 9.4- 6 (f), the surface colour is grey and brown, with much larger cracks all over the surface. Figure 9.4- 6 (e) indicates a gradual transition in appearance from region 3 to region 5, with the presence of two distinct corrosion products adhering to the surface. Gas formation has also been observed during the bipolar electrochemistry experiment, indicating an acting potential far in the transpassive region. The gas evolution is most likely linked to oxygen or chlorine gas, which can in turn also result in the reduction of hydrogen ions affecting the overall mechanism of brass dissolution [36].

Figure 9.4- 7 highlights SEM images of the different BPE regions shown in Figure 9.4- 5. In Region 1 and Region 2, spherical and cubic particles are present at the sample surface. The size of the particles in Region 1 is smaller than those observed in region 2, with sizes of approximately > 200 nm. Figure 9.4- 7 (c) gives the surface morphology of Region 3, showing the presence of

cracks and associated surface porosity. Figure 9.4- 7 (e) highlights the corrosion product observed in Region 5, with the surface also containing some cubic particles. The corrosion products in Region 4 is shown in Figure 9.4- 7 (d), having both of the features observed in Region 3 and Region 5.

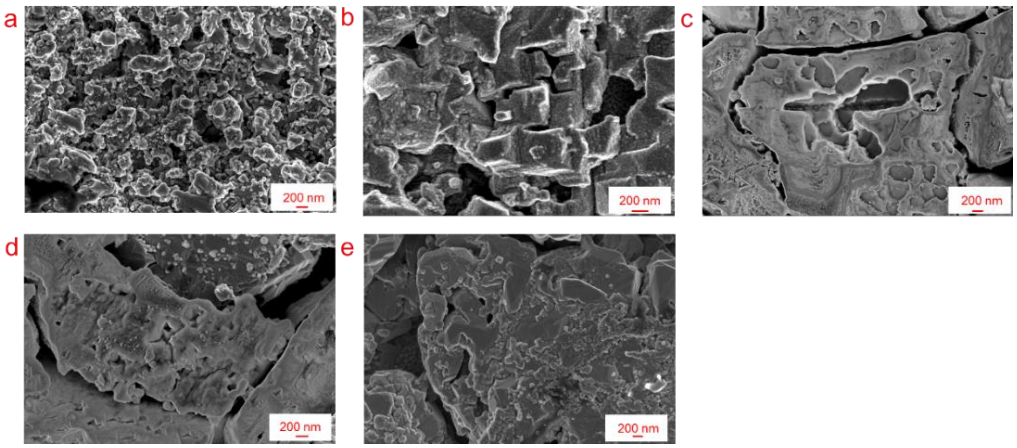

Figure 9.4- 7 SEM images of brass after dezincification along BPE, with (a) Region 1, (b) Region 2, (c) Region 3, (d) Region 4, and (e) Region 5.

Bipolar Electrochemistry – Chemical & Elemental Surface Analysis

Chemical information of the regions highlighted in Figure 9.4- 5 (a) were obtained using EDX analysis, obtaining data from an area of ≈1000 μm^2 for each analysis. Figure 9.4- 8 gives the mean (in wt.%) of each analysed element along the 5 regions, with region 1 seeing the highest acting potential. The concentration of Cu, Cl, and Zn show differences, with almost no change of the weight percentage of oxygen observed across all 5 regions. Zn is only present in Region 1 and Region 2, with chlorides predominately present in Regions 3 to 5. After Region 3, the weight percentage of Zn is very small, as Zn is more soluble than copper in the presence of Cl [37]

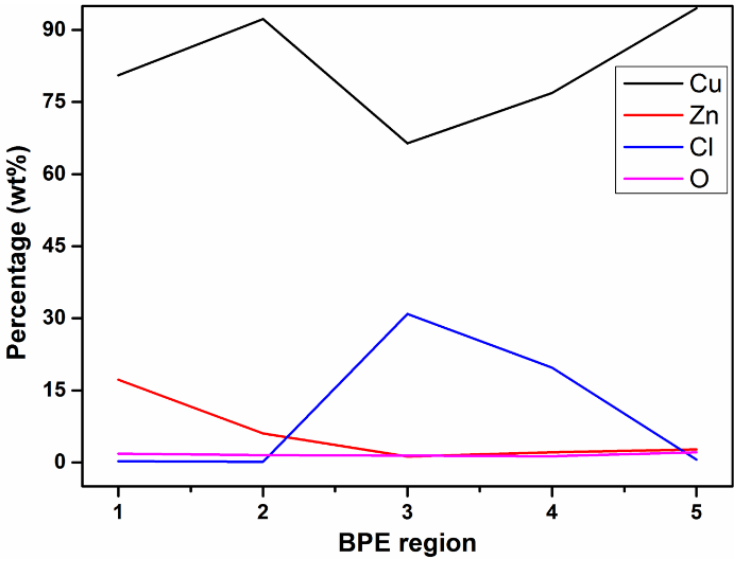

Figure 9.4- 8 The EDX analysis of the main elements along the BPE after dezincification.

The weight percentage of Cu is increasing from Region 1 to Region 2, as the highest applied potential is able to dissolve both the Cu and Zn here. This then changes to a more selective dissolution of the Zn, resulting in a copper rich surface layer found in Region 2. The changes of Cu content from Region 3 to Region 5 are related to corrosion product re-deposition. The weight percentage of Cl is highest in Region 3, and continues to drop with lower acting potentials towards Region 5.

Region 1 has a far rougher surface compared to Region 2, which is caused by more severe dissolution. No re-deposited corrosion products were identified in Region 1 and Region 2, with formation of surface films and products observed from Region 3 onwards. The surface colours in Region 3 and Region 5 are entirely different, and Region 4 is a mixture of both corrosion products, indicating that the corrosion product formed at lower applied potentials and then gradually changed along the potential gradient toward region 3.

Garzing-incidence X-ray diffraction (GI-XRD) phase analysis confirmed the presence of CuO, Cu_2O, CuCl, $CuCl_2$, and ZnO at the sample surface after dezincification, with all XRD spectra summarised in Figure 9.4- 9. The CuZn diffraction peaks identify the α-phase brass matrix structure. In Region 1, only a minor Cu_2O peak is found besides the dominant Cu-Zn peak. In Region 2, both CuCl and $CuCl_2$ are detected, with strong contributions from CuO found

at 71° and 86.5°, and a weak peak for ZnO. In Region 3 and Region 4, the intensity of the CuCl is increased, and further peaks belonging to CuCl (33°, 48.5°, and 56°) are present, with ZnO present at 36.5°. In Region 5, the intensity and numbers of peaks are reduced for the CuCl phase. The difference between corrosion products in Region 3 and Region 5 is the abundance of CuCl. The latter is also supported by EDX analysis, with higher concentrations of Cu and Cl measured.

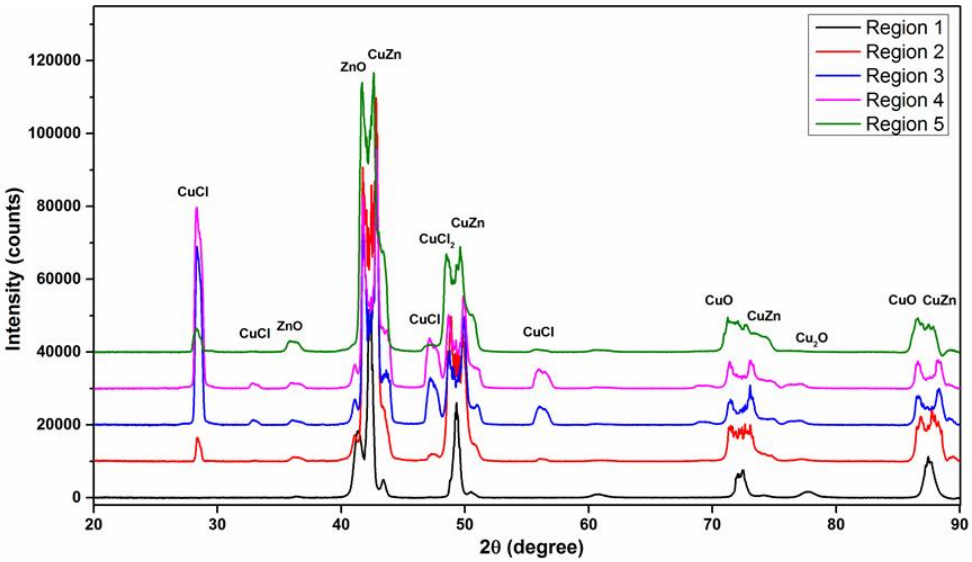

Figure 9.4- 9 X-ray diffraction spectra of brass BPE after dezincification between 20° (2θ) and 90° (2θ).

Figure 9.4- 10 (a) gives the Raman results after dezincification. Region 1 and Region 2 have similar peak profiles. The Raman shift between 100 cm^{-1} to 700 cm^{-1} is shown in Figure 9.4- 10 (b) with peaks at 146 cm^{-1}, 525 cm^{-1}, and 619 cm^{-1} determined in Region 1 and Region 2, which is associated with Cu_2O. In Regions 3 to 5, peaks at 112 $cm^{-1}$and 439 cm^{-1} clearly indicate ZnO. Peaks at 205 $cm^{-1}$and 409 cm^{-1} are $CuCl_2 \cdot H_2O$. The peak at 297 cm^{-1} is CuO. Figure 9.4- 10 (c) displays the Raman shit from 700 cm^{-1} to 1700 cm^{-1}, no peak is determined in Region 1 and Region 2. In the other three Regions 3 to 5, the peak at 761 cm^{-1} indicates CuO, peak at 1619 cm^{-1} is $CuCl_2 \cdot H_2O$, with most other peaks (796 cm^{-1},1073 cm^{-1},1172 cm^{-1}, and 1211 cm^{-1}) identified as CuCl.

For Raman analysis, only Cu_2O is measured in Region 1 and Region 2. ZnO and $CuCl_x$ are found in Region 3 to 5, which confirms corrosion products

formed after Region 3. The corrosion in Region 1 and Region 2 points towards Zn dissolving into the electrolyte and Cu is oxidised into Cu_2O. Clear trends are observed pointing towards selective dissolution with surface scale characteristics associated with in the potential gradient.

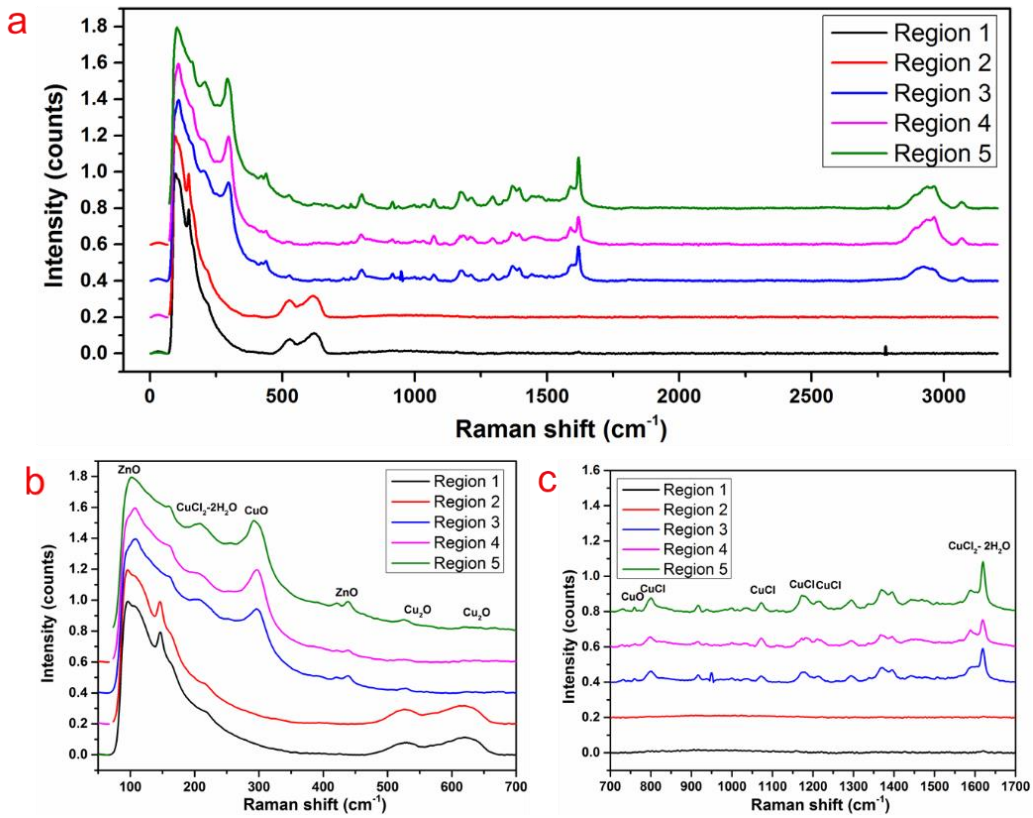

Figure 9.4- 10 (a) Overview of Raman spectra of brass at different BPE after dezincification, the Raman shift is between 100 cm^{-1} to 700 cm^{-1} in (b) and between 700 cm^{-1} to 1700 cm^{-1} in (c). ZnO, $CuCl_2$-H_2O, CuCl, CuO, and Cu_2O are measured [38–43]

Dezincification – Design Optimisation

A summary of all EDX, GI-XRD, and Raman results from Region 1 to Region 5 is shown in Table 9.4- 2. For EDX analysis, the weight percentages of the four main elements (Cu, Zn, Cl, and O) are given. Cu, Zn, and Cl vary in the different regions, with EDX carried out at 20 kV, resulting in typical sampling volumes of several 10's µm in depth. For GI-XRD analysis, predominantly Cu_2O is measured in Region 1, and CuO and CuCl are found in Region 2. After Region 3, the surface contains chiefly ZnO, CuCl, $CuCl_2$, and CuO. For Raman analysis, Cu_2O is measured in Region 1, corresponding with XRD measurements. In Region 2, only Cu_2O is detected. From Region 3, all

compounds observed in the corrosion product correspond to XRD and Raman analysis. Minor differences between the XRD and raman measurement are potentially caused by the choice of measurement location (colour) in Region 2. The occurrence of Cu_2O shows activity against a range of bacterial pathogens [44].

Table 9.4- 2 EDX, GIXRD, and Raman analysis of different corrosion area on the BPE after dezincification.

	Region 1	Region 2	Region 3	Region 4	Region 5
EDX (wt%)	80.6 Cu 17.2 Zn 0.2 Cl 1.8 O	92.3 Cu 6.0 Zn 0.1 Cl 1.5 O	66.4 Cu 1.2 Zn 30.9 Cl 1.4 O	76.9 Cu 2.1 Zn 19.7 Cl 1.3 O	94.5 Cu 2.7 Zn 0.6 Cl 2.1 O
XRD	Cu_2O	CuCl $CuCl_2$ CuO	ZnO CuCl $CuCl_2$ CuO ZnO	ZnO CuCl $CuCl_2$ CuO ZnO	ZnO CuCl $CuCl_2$ CuO ZnO
Raman	Cu_2O	Cu_2O	$CuCl_2{\cdot}2H_2O$ CuO CuCl	$CuCl_2{\cdot}2H_2O$ CuO CuCl	$CuCl_2{\cdot}2H_2O$ CuO CuCl

Compared with the 3-electrode polarisation test, bipolar electrochemistry test for brass dezincification research has several advantages; (1). The composition/structure changes with the applied potential can be determined from a single experiment, which saves time and reduces the number of samples. (2). The relationship between the applied potential and brass dezincification can eliminate the effects of exposure time, scan rate or previously applied potential. (3). The brass dezincification mechanism at high applied potential (without the formation of corrosion product) can be further explored. To reduce dezincification, at potential in BPE Region 3 can be applied, as a more protective corrosion product is formed. To control the release of copper ions, a potential in BPE Region 2 should be chosen, since almost no corrosion product formed on the substrate, and the local applied potential does not corrode the substrate heavily.

9.46 Conclusions

Potentiodynamic polarisation tests revealed differences in the corrosion behaviour with corrosion product formation after dezincification. A bipolar electrochemistry technique was applied to determine the brass dezincification under different applied potentials, utilising the acting potential gradients. Five different corrosion regions were distinguished, with SEM and EDX analysis

showed Cu-rich corrosion products with ZnO at lower applied potentials. Only Cu_xO was determined at higher applied potentials, pointing towards Zn being preferentially dissolved. GI-XRD and Raman analysis confirmed the structure and composition of corrosion product at lower applied potential regions, with only the substrate corrosion present at higher applied potentials. The Region 3 is the best choice for corrosion product formation to prevent further dezincification.

9.47 References

[1] S.E. Fosdick, K.N. Knust, K. Scida, R.M. Crooks, Bipolar electrochemistry, Angew. Chemie - Int. Ed. 52 (2013) 10438–10456. https://doi.org/10.1002/anie.201300947.

[2] N. Pébère, V. Vivier, Local electrochemical measurements in bipolar experiments for corrosion studies, ChemElectroChem. 3 (2016) 415–421. https://doi.org/10.1002/celc.201500375.

[3] Y. Zhou, D.L. Engelberg, Application of a modified bi-polar electrochemistry approach to determine pitting corrosion characteristics, Electrochem. Commun. 93 (2018) 158–161. https://doi.org/10.1016/j.elecom.2018.06.013.

[4] Y. Zhou, D.L. Engelberg, On the application of bipolar electrochemistry to characterise the localised corrosion behaviour of type 420 ferritic stainless steel, Metals (Basel). 10 (2020) 794. https://doi.org/doi.org/10.3390/met10060794.

[5] Y. Zhou, A. Kablan, D.L. Engelberg, Metallographic screening of duplex stainless steel weld microstructure with a bipolar electrochemistry technique, Mater. Charact. 169 (2020) 110605. https://doi.org/10.1016/j.matchar.2020.110605.

[6] A. Kuhn, R.M. Crooks, S. Inagi, A compelling case for bipolar electrochemistry, ChemElectroChem. 3 (2016) 351–352. https://doi.org/10.1002/celc.201500569.

[7] L. Koefoed, S.U. Pedersen, K. Daasbjerg, Bipolar electrochemistry—A wireless approach for electrode reactions, Curr. Opin. Electrochem. 2 (2017) 13–17. https://doi.org/10.1016/j.coelec.2017.02.001.

[8] G. Loget, A. Kuhn, Shaping and exploring the micro- and nanoworld using bipolar electrochemistry, Anal. Bioanal. Chem. 400 (2011) 1691–1704. https://doi.org/10.1007/s00216-011-4862-1.

[9] D.C. Eardley, D. Handley, S.P.S. Andrew, Bipolar electrolysis with intra phase conduction in two phase media, Electrochim. Acta. 18 (1973) 839–848. https://doi.org/10.1016/0013-4686(73)85036-4.

[10] Y. Zhou, D.L. Engelberg, Fast testing of ambient temperature pitting corrosion in type 2205 duplex stainless steel by bipolar electrochemistry experiments, Electrochem. Commun. 117 (2020) 106779. https://doi.org/10.1016/j.elecom.2020.106779.

[11] G. Ghiara, R. Spotorno, S. Delsante, G. Tassistro, P. Piccardo, P. Cristiani, Dezincification inhibition of a food processing brass OT60 in presence of Pseudomonas fluorescens, Corrrosion Sci. 157 (2019) 370–381. https://doi.org/10.1016/j.corsci.2019.06.003.

[12] M. Tang, P. Sinsheimer, E. Sarver, J. Parks, M. Edwards, Evaluating“Lead-free”brass performance in potable water, Corrosion. 75 (2019) 865–875. https://doi.org/doi.org/10.5006/3060.

[13] H. Sugawara, H. Ebiko, Dezincification of brass, Corros. Sci. 7 (1967) 512–513.

[14] H.W. Pickering, P.J. Byrne, On preferential anodic dissolution of alloys in the low-current region and the nature of the critical potential, J. Electrochem. Soc. 118 (1971) 209–215.

[15] H.W. Pickering, Volume diffusion during anodic dissolution of a binary alloy volume diffusion during anodic dissolution of a binary alloy, J. Electrochem. Soc. 115 (1968) 143–147.

[16] A. V Polunin, A.P. Pchelnikov, V. V Losev, I.K. Marshakov, Electrochemical studies of the kinetics and mechanism of brass dezincification, Electrochim. Acta. 27 (1982) 467–475.

[17] A.P. Pchelnikov, A.D. Sitnikov, I.K. Marshakov, V. V Losev, A study of the kinetics and mechanism of brass dezincification by radiotracer and electrochemical methods, Electrochim. Acta. 26 (1979) 591–600.

[18] H.W. Pickering, P.J.Byrne, Partial currents during anodic dissolution of Cu-Zn alloys at constant potential, J. Electrochem. Soc. 116 (1969) 1492–1496.

[19] H.W. Pickering, Electrolytic dissolution of binary alloys containing a noble metal, J. Electrochem. Soc. 114 (1967) 698–706.

[20] M.B. Valcarce, S.R. De Sánchez, M. Vázquez, A comparative analysis of copper and brass surface films in contact with tap water, J. Mater. Sci. 41 (2006) 1999–2007. https://doi.org/10.1007/s10853-006-4499-1.

[21] M.B. Valcarce, S.R. de Sanchez, M. Vazquez, Brass dezincification in a tap water bacterial suspension, Electrochim. Acta. 51 (2006) 3736–3742. https://doi.org/10.1016/j.electacta.2005.10.034.

[22] Y. Feng, The corrosion behaviour of copper in neutral tap water part II: determination of corrosion rates, Corros. Sci. 38 (1996) 387–395.

[23] M.J.Pryor, K.-K. Giam, The effect of arsenic on the dealloying of α-brass, J. Electrochem. Soc. 129 (1982) 2157–2163.

[24] M.J. Pryor, J.C. Fister, The mechanism of dealloying of copper solid solutions and intermetallic phases, J. Electrochem. Soc. 131 (1984) 1230–1236.

[25] R.C.Newman, T.Shahrabi, K.Sieradzki, Direct electrochemical measurement of dezincification including the effect of alloyed arsenic, Corros. Sci. 28 (1988) 873–886.

[26] H.W. Pickering, Characteristic features of alloy polarisation curves, Corros. Sci. 23 (1983) 1107–1120.

[27] N. van Doremalen, T. Bushmaker, D.H. Morris, M.G. Holbrook, A. Gamble, B.N. Williamson, A.Tamin, J.L. Harcourt, N.J. Thornburg, S.I. Gerber, J.O. Lloyd-Smith, E. de Wit, V.J. Munster, Aerosol and surface stability of SARS-CoV-2 as compared with SARS-CoV-1, New Engl J. Med. March 17 (2020) 1564–1567.

[28] J.R. Scully, The COVID-19 Pandemic, Part 1: Can antimicrobial copper-based alloys help suppress infectious transmission of viruses originating from human contact with high-touch surfaces?, Corrosion. Aprial (2020). https://doi.org/10.5006/3568.

[29] P. Airey, J. Verran, Potential use of copper as a hygienic surface:problems associated with cumulative soiling and cleaning, J. Hosp. Infect. 67 (2007) 271–277. https://doi.org/10.1016/j.jhin.2007.09.002.

[30] M.E. Touhami, I. Mansouri, C. Monticelli, Corrosion behavior of different brass alloys for drinking water distribution systems, Metals (Basel). 9 (2019). https://doi.org/doi: 10.3390/met9060649.

[31] C. Hung, C. Lin, C. Hsieh, C. Li, P.T. Wu, K. Chen, W. Wu, A novel approach to improving resistance to dezincification of diphasic brass, J. Alloys Compd. 671 (2016) 502–508. https://doi.org/10.1016/j.jallcom.2016.01.261.

[32] R. Karpagavalli, R. Balasubramaniam, Development of novel brasses to resist dezincification, Corros. Sci. 49 (2007) 963–979. https://doi.org/10.1016/j.corsci.2006.06.024.

[33] J. Diard, J. Le Canut, B. Le Gorrec, C. Montella, Copper electrodissolution in 1 M HCl at low current densities .I. General steady-state study, Electrochem. Acta. 43 (1998) 2469–2483.

[34] P. Zhou, M.J. Hutchison, J.W. Erning, J.R. Scully, K. Ogle, An in situ kinetic study of brass dezincification and corrosion, Electrochim. Acta. 229 (2017) 141–154. https://doi.org/10.1016/j.electacta.2017.01.078.

[35] H.Gladen, H.Kaiser, H.Kaesche, A morphological study of dezincification of ε-brass, Corros. Sci. 30 (1990) 737–741.

[36] L. Burzy, Comparison of the spontaneous and anodic processes during dissolution of brass, Corros. Sci. 43 (2001) 1053–1069.

[37] R. Procaccini, W.H. Schreiner, M. Vázquez, S. Ceré, Surface study of films formed on copper and brass at open circuit potential, Appl. Surf. Sci. 268 (2013) 171–178. https://doi.org/10.1016/j.apsusc.2012.12.050.

[38] A. Khare, B. Himmetoglu, M. Johnson, D.J. Norris, M. Cococcioni, Calculation of the lattice dynamics and Raman spectra of copper zinc tin chalcogenides and comparison to experiments, J. Appl. Phys. 111 (2012) 083707. https://doi.org/10.1063/1.4704191.

[39] R.L. Frost, P.A. Williams, J.T. Kloprogge, W. Martens, Raman spectroscopy of the copper chloride minerals nantokite , eriochalcite and claringbullite–implications for copper corrosion, Neues Jahrb. Für Mineral. - Monatshefte. 10 (2003) 433–445. https://doi.org/10.1127/0028-3649/2003/2003-0433.

[40] R.L. Frost, W. Martens, J.T. Kloprogge, P.A. Williams, Raman spectroscopy of the basic copper chloride minerals atacamite and paratacamite : implications for the study of copper , brass and bronze objects of archaeological significance, J. Raman Spectrosc. 33 (2002) 801–806. https://doi.org/10.1002/jrs.921.

[41] R.L. Frost, Raman spectroscopy of selected copper minerals of significance in corrosion, Spectrochim. Acta - Part A Mol. Biomol. Spectrosc. 59 (2003) 1195–1204. https://doi.org/doi.org/10.1016/S1386-1425(02)00315-3.

[42] Y. Deng, A.D. Handoko, Y. Du, S. Xi, B.S. Yeo, In situ Raman Spectroscopy of copper and copper oxide surfaces during electrochemical oxygen evolution reaction : identification of Cu III oxides as catalytically active species, ACS Catal. 6 (2016) 2473–2481. https://doi.org/10.1021/acscatal.6b00205.

[43] Y. Review, Raman effect in zinc oxide, Phys. Rev. 142 (1966) 570–574.

[44] R.P. Allaker, Chapter 10. Nanoparticles and the control of oral biofilms, Elsevier Inc., 2013. https://doi.org/10.1016/B978-1-4557-3127-5.00010-6.

[45] B. Krawczyk, P. Cook, J. Hobbs, D. Engelberg, Corrosion behavior of cold rolled type 316L stainless steel in HCl containing environments, Corrosion. 73 (2017) 1346. https://doi.org//10.5006/2415.

10 Summary

The key new finding from my PhD research includes: 1, different corrosion response can be direct measured on the BPE. 2, the potential and current density are directly measured on the BPE. 3, the features of the pit (pit depth/volume) to transfer from metastable pits and stable pits is measured. 4, pitting corrosion can be nucleated on DSS 2205 and SDS 2707 on room temperature. 5, gravity influences pitting corrosion (pit depth/volume/cross-section area/nucleation rate) are determined. 6, galvanic corrosion/corrosion under wider potential range/competition between pitting and crevice corrosion are determined by modified bipolar electrochemistry.

Bipolar electrochemistry was used to determine the corrosion behaviour of stainless steels. The potential and current distribution on the BPE were measured from the split bipolar electrode setup. The localised corrosion on type 420 stainless steel were tests by bipolar electrochemistry, and then the potential and current density are compared between 3-electrode potentio-dynamic, potentio-static polarisation, and bipolar electrochemistry. Different corrosion response along type 420 BPE at different local applied potential was measured by SEM. Bipolar electrochemistry with an in-situ camera allowed the in-situ pitting corrosion test. Then analysis cavities shapes which allows the pit nucleation. Pitting growth with/without diluting pit electrolyte are compared. Type 420 martensitic stainless steel was formed after austenitizing treatment, tempering changed the microstructure of MSS 420, result in different corrosion behaviours.

Bipolar electrochemistry could nucleated pitting corrosion on DSS 2205 stainless steel at room temperature in 15 seconds. Then the localised corrosion (pitting and crevice) and general corrosion growth kinetics of DSS 2205 was analysed. Heat treatment changed the microstructure of DSS 2205, result in different pitting corrosion resistance. The corrosion resistance of duplex and austenitic stainless steels were tested and compared by bipolar electrochemistry, potentio-dynamic polarisation test, and PREN.

Three modified bipolar electrochemistry setups were created to test the pitting corrosion under a wide range of applied potential, pittinng and crevice corrosion competition, and galvanic corrosion between stainless steels.

Bipolar electrochemistry is used to test the welded DSS, which allowed corrosion at different microstructure regions on welded 2101 could be directly compared. Gravity influenced the pitting corrosion can be tested by bipolar electrochemistry. Brass dezincification was also tested by bipolar electrochemistry due to a linear potential gradient.

The overall conclusions were listed below:

Corrosion Electrochemistry with a Segmented Array Bipolar Electrode

- Crevice corrosion, pitting corrosion, general corrosion, and cathodic response appeared on the BPE.
- Potential and current density was measured by a split bipolar electrode.
- Potential was linearly distributing along the bipolar electrode, with the corresponding current follows Butler-Volmer relationship.
- Compare with 3-electrode potentio-dynamic polarisation test, the critical pitting potential measured from BPE was lower.
- Compare with 3-electrode potentio-static and potentio-dynamic polarisation test, bipolar electrochemistry saved sample and time consuming.

On the Application of a Bipolar Electrochemistry Approach to Determine the Corrosion Behaviour of Annealed Type 420 Ferritic Stainless Steel

- Pitting with general corrosion, pitting corrosion, general corrosion, and cathodic region were detected on the BPE.
- Pits nucleated near chromium carbides contain $Cr_{23}C_6$, Cr_3C_2, and CrC.
- General corrosion surrounded pit, comes from pit electrolyte diffuse out.
- α-FeOOH was found in the general corrosion region.
- Particles with C, O, and Cl were deposited and measured at the cathodic site.
- Pit growth factor was independent of the applied potential.

Time-lapse, In-situ Observation of Pit Nucleation and Growth in 13%Cr Ferritic Stainless Steel under Bipolar Electrochemistry Control

- Pit nucleation and growth had been observed by in-situ from a camera combined with a bipolar electrochemistry approach.
- The probabilities of pits growing was reducing with longer time exposure.
- Pits nucleated and growth in the cavities with the aspect ratio of 0.4 - 0.6.
- The growing pits became dish-like with time.
- Diluting the pit electrolyte reduced the pit growth kinetics.

Accessing The Full Spectrum of Corrosion Kinetic Behaviour of Tempered Type 420 Martensitic Stainless Steel

- $Cr_{23}C_6$ was measured in the tempered martensitic stainless steel, and Cr_7C_3 and CrC were found in the martensitic stainless steel tempered at 550℃.
- Pitting, passive region, general corrosion, and cathodic response were determined on MSS 420 BPE.
- Intergranular corrosion was determined on MSS 420 tempered at 550 ℃.
- A lower hardness of MSS 420 is measured from higher tempered temperature
- From the BPE, the corrosion resistance rank was tempering at 250 ^oC > no tempering > 400 ^oC > 700 ^oC.

Fast testing of ambient temperature pitting corrosion in type 2205 duplex stainless steel by bipolar electrochemistry experiments

- Pitting can be nucleated on the DSS 2205 BPE at room temperature.
- Pit and selective phase corrosion nucleated at the ferrite phase.
- No lacy covered pits as austenite phase are small.
- Pit growth kinetics is potential independent, but not the pit volume.

Estimating Pitting and Crevice Corrosion Growth Kinetics of Type 2205 Duplex Stainless Steel at Ambient Temperature

- Ferrite enriched in Cr and Mo preferred to corrode away and austenite with a higher concentration of Ni retains.

- The applied potential affected the overall localised corrosion volume, but pit growth kinetics is independent of the potential.
- The critical localised potential was reduced with longer exposure time.
- The height difference between ferrite and austenite was linearly increased with time.

A new approach to assess the corrosion resistance of solution annealed duplex stainless steel microstructure

- Crevice corrosion, pitting, general corrosion, and cathodic area with the passive region were measured on DSS 2205 with different heat treatments.
- Pit growth factor was independent of the applied potential, but influenced the pit volume.
- The fraction of the ferrite phase was increasing with higher temperature.
- Lowest critical pitting potential and pit growth kinetics cannot be achienved by a single heat treatment.
- The pitting corrosion was changed by solution treatments, but the rank of pitting resistance was not the same as PREN, CPT, and bipolar electrochemistry.

Application of a modified bi-polar electrochemistry approach to determine pitting corrosion characteristics

- A modified bipolar electrochemistry was designed by applying a secondary potential applied to the BPE.
- The potential of the BPE was also controlled by the secondary potential.
- No corrosion (cathode + passive region), lacy cover pits, open pits, open pits, and transpassive corrosion were determined on the modified BPE.
- Pits became dish-like at a higher secondary applied potential.

Characterisation of localised corrosion growth kinetics with an orthogonal bipolar electrochemistry technique

- A secondary feeder electrode was set perpendicular to the primary feeder electrodes.

- Overall corrosion volume on the BPE was independent of secondary bipolar potential.
- Crevice corrosion nucleated at a lower potential than pitting corrosion.
- Crevice corrosion got more current than pitting corrosion.

On the application of bipolar electrochemistry for simulating galvanic corrosion behaviour of dissimilar stainless steels

- A parallel bipolar electrochemistry was created to research the galvanic corrosion.
- The galvanic protection effect was determined by the pit volume change.
- Higher secondary potential resulted in higher galvanic protection.
- The galvanic protection was related to the distance to anodic electrode

Application of Bipolar Electrochemistry for Characterising Corrosion Kinetics of Austenitic and Duplex Stainless Steels

- Pitting, general corrosion, and cathode region were detected on DSS 2205. Transpassive corrosion, pitting corrosion, and cathode region were detected on DSS 2101.
- Lacy cover pits were nucleated in Type 304L, 316L, and 2101 stainless steel, and open pits were measured in DSS 2205.
- Critical pitting potential measured from 3-electrode potentio-dynamic polarisation test and bipolar electrochemistry experiments were compared.
- The preferred corrosion phase was the ferritein pitting and general corrosion, but the ferrite retained in transpassive corrosion.
- From pit volume, the rank of pitting corrosion follows 304L > 2101 > 2205 ≈ 316L;

Metallographic Screening of Duplex Stainless Steel Weld Microstructure with a Bipolar Electrochemistry Technique

- Bipolar electrochemistry metallographic highlighted the most susceptible regions of welded lean DSS 2101.
- Crevice corrosion, trans-passive corrosion, and pitting corrosion on different microstructure zones are observed and compared

- The HAZ has the lowest pitting resistance with the fastest pit growth kinetics, and the FZ showed more serious transpassive corrosion and crevice corrosion.
- Pits nucleated by selective dissolve ferrite phase, but transpassive corrosion nucleated in the austenite phase.

Revisiting the effect of gravity on Pitting Corrosion

- Gravity only changed current density distribution on the BPE, not potential distribution.
- Highest pit volume in the FU orientation, and similar in the PE and FD orientations.
- Gravity did not change pit depth, but changed the pit volume.
- Pits were semi-circular or wide-like for the FU orientation, and narrow-like pits were determined in the PE and FD orientations.

Optimising Brass Dezincification with a Bipolar Electrochemistry Technique

- Corrosion products only could be formed at a lower applied potential, which could reduce further dezincification.
- Corrosion products became thicker and enrich in Cu until a critical applied potential.
- Cu ions release could be controlled at high applied potential.
- The corrosion product was determined by SEM/EDX/XRD/Raman.

11 Future work

In the future work, how the electrolyte composition change influence the corrosion kinetics will be researched, it was measured the pH/temperature increased, current density between the feeder electrode, and electrolyte weight loss after the experiment as the gas (Cl_2 and H_2) formation during the experiment, which indicates a lot of electrochemical reactions in the bipolar system. From literatures, lots of high active oxidants will be generated in Cl electrolyte with a high applied potential, these highly active oxidant can reduce the corrosion resistance from lower the free corrosion potential and locally increase the pH during potentio-static polarization test [1,2]. These oxidants also might result in formation of complex surface oxidants, which might influence the corrosion kinetics [3], in the future Nuclear Magnetic Resonance might be used to determine the composition of the electrolyte, change after the experiment

Some different research areas will be analysed by bipolar electrochemistry in the future.

11.1 The applied stress influences the pit corrosion and stress corrosion cracking by bipolar electrochemistry

Pitting corrosion is nucleated on DSS 2205 wire at room temperature. Tensile stress can be applied during the bipolar electrochemistry test. Also, SCC can be measured on the BPE anodic sites and hydrogen embrittlement (HE) can be obtained at the cathodic sites. The paper aims to research the pit changed by the applied stress, and determine SCC and HE.

The left side of the images are BPE oxidation edges. Figure 11- 1 (a) shows the DSS 2205 wire pitting region in 0.1M HCl for 10 min. The distance between the two feeder electrodes is 3 cm with 10 V applied on feeder electrodes. Figure 11- 1 (b) displays the pitting corrosion for DSS 2205 with tensile stress, the numbers of pits are reduced but the average pit sizes are increased, some pits have an elongated pit mouth. In future work, how to quantify applied stress on the wire will be found. Then, the relationship between the pitting and applied stress can be obtained. At last, the parameters to generate the stress corrosion cracking and/or HE in stainless steel BPE will be found out.

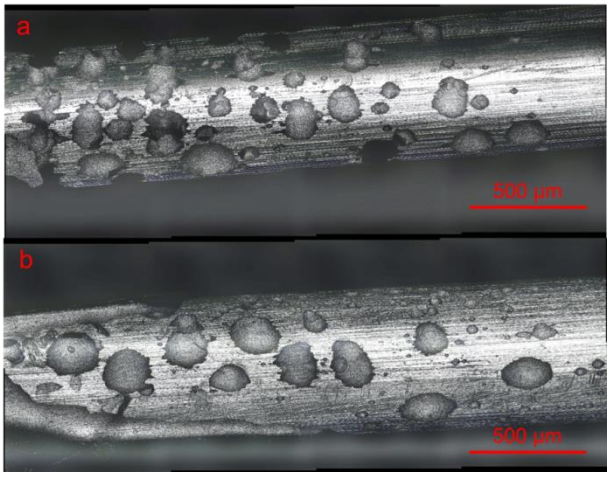

Figure 11- 1 (a) The pitting corrosion in Type 2205 stainless steel without applied stress, and with tensile stress in (b).

11.2 Effect of BPE Set-up Parameter on the Application of Bipolar Electrochemistry to Type 420 ferritic stainless steel

Corrosion screening is only recently analysis by bipolar electrochemistry, how the parameters are shown in Figure 11- 2; (a) the distance of the feeder electrode, (b) the location of BPE, (c) the concentration of HCl and electrolyte temperature, and (d) the applied potential on the feeder electrode influence the corrosion on the BPE influence the corrosion behaviours on the BPE will understand.

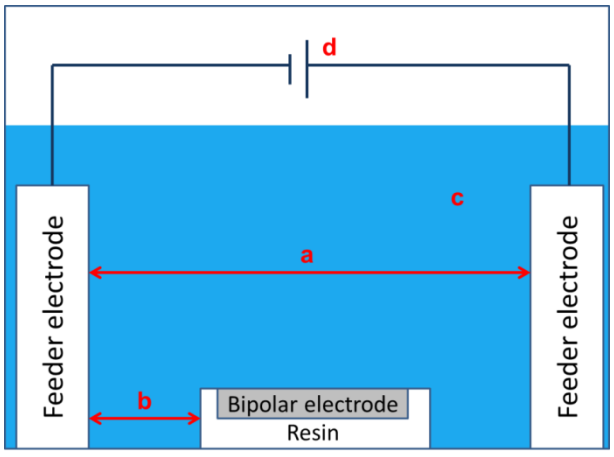

Figure 11- 2 The parameters of the setup could change the corrosion environment.

11.3 Towards Understanding the Corrosion Behaviour of Heat Treated Type 2101 Stainless steel from Bipolar Electrochemistry Experiments

Different heat treatment temperature varies from 850 to 1350 ^{o}C were applied on DSS 2101. The pit volume, depth, shape, and critical pitting potential under different heat treatment temperatures are applied to research the corrosion behaviours changed by heat treatment. The microstructure and composition are determined by EBSD and EDX.

Figure 11- 3 gives the pitting corrosion zone on DSS 2101 under different heat treatment, the critical pitting potential is similar with different heat treatment, but the pit size, pit numbers and tranpassive corrosion change. The distance between the feeder electrodes is 6 cm under constant current (1A), the electrolyte is 0.1M HCl with 15 min exposure time.

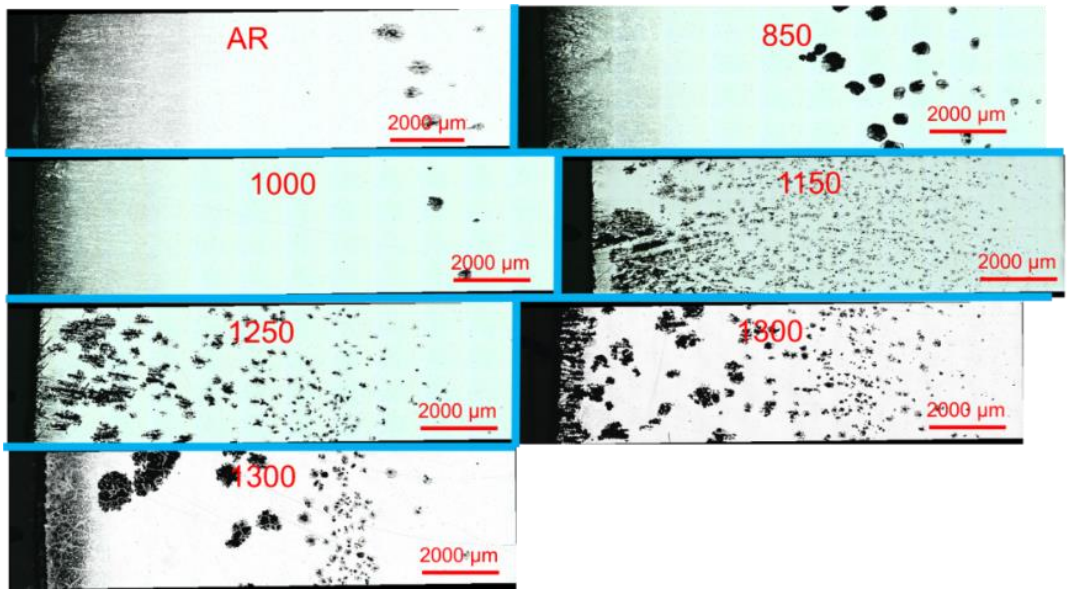

Figure 11- 3 The corrosion region on the Type 2101 stainless steel BPE for different heat treatment (the numbers indicate the heat treatment temperature)

11.4 Determine the influence of the electrolyte temperature and potential to corrosion on the austenitic stainless steel under bipolar electrochemistry

The applied potential and electrolyte temperature influence the corrosion response. The bipolar electrochemistry test is used corrosion test as the boundary between different corrosion types can be detected on the one BPE.

The research aims to determine the corrosion responses from different applied potential and electrolyte, with less influence of passive film formed before the critical pitting potential.

Figure 11- 4 shows 8 corrosion responses at a modified Type 316L BPE. The corrosion responses change from no corrosion, lacy cover pits, mixed pits, open pits, pits with general corrosion, transpassive corrosion, and transpassive corrosion with pits. In future work, different materials (Type 304L) and test method (potentio-dynamic polarisation) will be applied and compared.

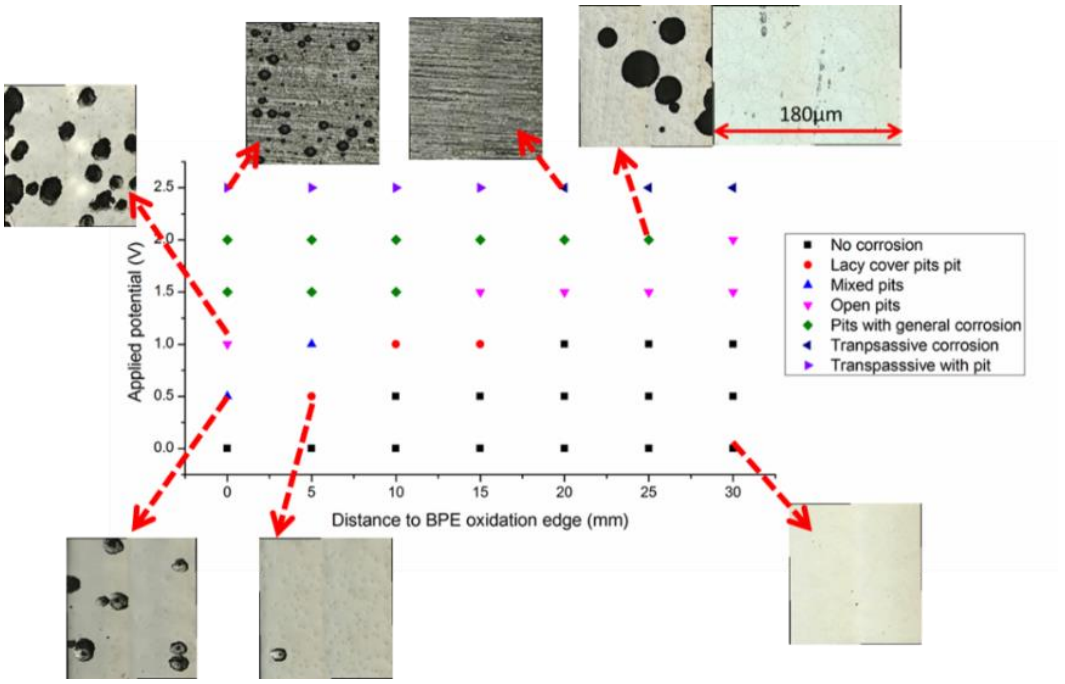

Figure 11- 4 The different corrosion response along the BPE with different secondary applied potential (the width of all the images are 2 µm)

References

[1] Y. Song, K. Dang, H. Chi, D. Guan, Corrosion of marine carbon steel by electrochemically treated ballast water, J. Mar. Eng. Technol. 4177 (2009) 49–55. https://doi.org/10.1080/20464177.2009.11020218.

[2] A. Neville, T. Hodgkiess, X. Destriau, Initiation and propagation of localised corrosion on stainless steels in seawater containing high biocide concentrations, Corros. Sci. 40 (1998) 715–730. https://doi.org/10.1016/S0010-938X(97)00173-X.

[3] J. Llopis, I.M. Tordesillas, J.M. Alfayate, Anodic corrosion of ruthenium in hydrochloric acid solution, Electrochim. Acta. 11 (1966) 623–632. https://doi.org/10.1016/0013-4686(66)87006-8.